ISSN 0288-4534
CODEN: KONAE7

KONA

POWDER AND PARTICLE

No. 16 (1998)
Published by Hosokawa Powder Technology Foundation

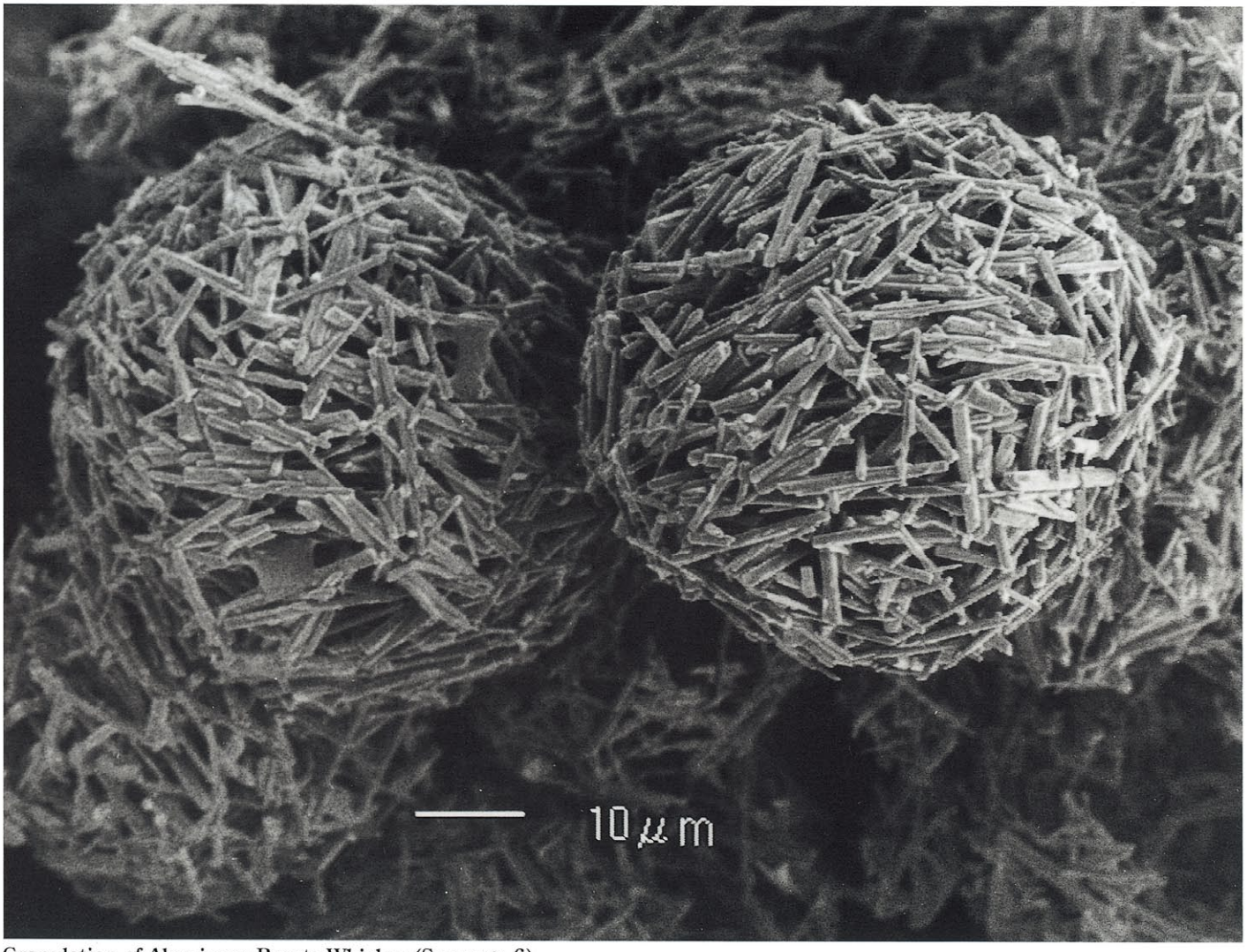

Granulation of Aluminum Borate Whisker (See page 6)

KONA

POWDER AND PARTICLE

KONA is a refereed scientific journal that publishes articles on powder and particle sciences and technology. KONA has been published annually since 1983 by the Hosokawa Powder Technology Foundation in Japan. KONA is distributed to researchers, members of the scientific community, universities and research libraries throughout the world.

About the Cover of Journal "KONA"

The Chinese character "粉" is pronounced "KONA" in Japanese, and means "Powder". The hand written "粉" is after the late Mr. Eiichi Hosokawa, founder of the Hosokawa Micron Corporation.

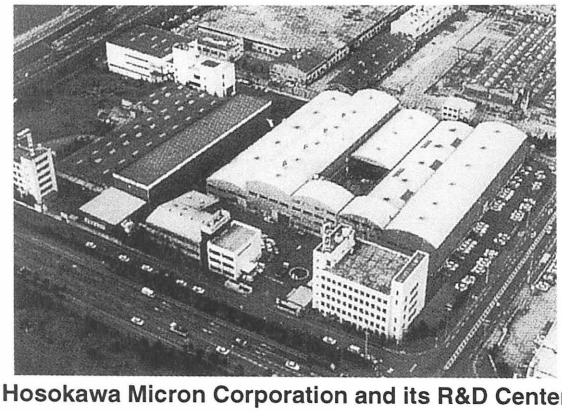

Hosokawa Micron Corporation and its R&D Center

■ Publication Office

Hosokawa Powder Technology Foundation (Japan) in Hosokawa Micron Corporation
No. 9, 1-chome, Shoudai Tajika, Hirakata-shi, Osaka 573 Japan

■ Notes

○ Hosokawa Powder Technology Foundation has entrusted the editorial duty to the editorial board organized by the Council of Powder Technology, Japan.

(Complimentary Copy)

Printed in Japan

Obituary (Amended)

It is with great regret that we inform the readers of this journal of the loss of the great leader of Kona's Science and Technology in Japan. Professor Koichi Iinoya passed away on 26th November, 1998, at the age of eighty one.

No one can doubt his great achievement to establish powder technology, not only in Japan but also around the world.

He founded the Society of Powder Technology, Japan, the first academic Society of this new field, in 1956 in Nagoya, when he was Professor in the Department of Chemical Engineering, Nagoya University. Since then he was always leading Japanese powder science and technology, as the president and honorary president of the society. His academic contributions to this science are clearly shown in over two hundred papers and over thirty publications in Japanese as well as in English.

He was especially active in making Japanese powder science international. He travelled abroad many times, including stays in the University of Wisconsin and in Georgia Institute of Technology in 1959-61 and again in 1964-65 in Georgia. He maintained a very wide academic network around the world. He received many awards and honorary positions, including Honorary Doctor of Engineering from Karlsruhe Technical University.

After he moved to Kyoto University, Kyoto became a worldwide center of powder technology. Many important international congresses and symposia were held, such as International Symposium on Powder Technology in 1981 and the Second World Congress on Particle Technology in 1990, both organized by the Society in Kyoto. Professor Iinoya played a key role in both as the Chairman and the Honorary Chairman. Other smaller, but not less important, sym-

posia can be added to this list.

He also contributed to the foundation of IFPRI, the International Fine Particle Research Institute, and served as an international advisor to stimulate world wide cooperation in this science and technology, especially that between East and West. We should not forget his contributions to the industry related to powder technology. He founded the Association of Powder Process Industry and Engineering in 1971, and led it as director general, president and then as honorary president. Now the Association has grown to have over three hundred member companies, and the main event, Powdertex Tokyo and Osaka, has become one of the largest international powder exhibitions of the world.

Among other social activities, we should never forget that he was from the start a member of the Board of Hosokawa Powder Technology Foundation, the publisher of this KONA journal, and was always very active as advisor for the development of this international journal of our science and technology.

(Genji JIMBO, President of the Council of Powder Technology)

The Letter from the Editor

Kei Miyanami
Editor-in-Chief

It is with our deep regrets that we inform the KONA readers of the death of Professor Koichi Iinoya. He passed away on Friday, November 26, 1998. We have been very surprised and so sorry to hear his sudden death.

On behalf of the KONA Editorial Committee, we all lament his death and extend our condolences heartily. We are also greatly thankful to him for his enormous contributions to the publication of the KONA journal since the first issue. He was one of the chartered members of the Council of Powder Technology, Japan, and of the Board of Hosokawa Powder Technology Foundation. The memorial address by Professor Genji Jimbo, the present president of CPT, Japan, has been included in this issue.

More importantly, we have lost a friend and respected colleague who has left each of us with many fond memories.

Kei Miyanami

KONA

GENERAL INFORMATION

HISTORY OF THE JOURNAL

KONA journal has been published by the Council of Powder Technology, Japan. (CPT), from No.1 to No.12 issues, under the sponsorships of Hosokawa Micron Corporation (No.1 to No.9) and Hosokawa Powder Technology Foundation (No.10 to No.12).

The CPT has been established in 1969 as a non-profit organization to enhance the activities of research and development on powder science and technology in Japan under the sponsorship of Hosokawa Micron Corporation. In 1983, the CPT has decided to issue an international journal named "KONA", which publishes the excellent articles appeared in Japanese journals concerning powder science and technology, after translated into English, throughout the world. After the seventh volume issued in 1989, the CPT has changed its policy to internationalize the "KONA" from the 8th issue (1990) and on by incorporating the monographs originally written in English from the authors throughout the world. Immediately, the present editorial board including Asian, Americas' and European Blocks has been organized.

From the 13th issue and on, the Hosokawa Powder Technology Foundation has taken over the role of KONA publisher from the CPT and the Foundation has entrusted the editorial duty to the present KONA editorial board organized by the CPT without requesting any shift in our present editorial policies. This switching of publisher has been simply and only to make the aim and scope of the Foundation definite. Essentially no change has been observed in continuously editing and publishing this journal except in the designation on a part of the journal cover.

AIMS AND SCOPE OF THE JOURNAL

KONA Journal is to publish the papers in a broad field of powder science and technology, ranging from fundamental principles to practical applications. The papers discussing technological experiences and critical reviews of existing knowledge in specialized areas will be welcome.

These papers will be published only when they are judged, by the Editor, to be suitable for the progress of powder science and technology, and are approved by any of the three Editorial Committees. The paper submitted to the Editorial Secretariat should not have been previously published except the translated papers which would be selected by the Editorial Committees.

CATEGORY OF PAPERS

- Invited papers
  Original research and review papers invited by the KONA Editorial Committees.
- Contributed papers
  Original research and review papers submitted to the KONA Editorial Committees, and refereed by the Editors.
- Translated papers
  Papers translated into English, which were previously published in other languages, selected by the KONA Editorial Committees with the permission of the authors and / or the copyright holder.

SUBMISSON OF PAPERS

Papers should be sent to each KONA Editorial Secretariat.

- Asia / Oceania Editorial Secretariat
  F. Nakagawa
  Hosokawa Micron Corporation Micromeritics Laboratory 1-9, Shoudai Tajika, Hirakata 573 JAPAN
- Europe / Africa Editorial Secretariat
  Dr. P. van der Wel or Mrs. P. Krubeck
  Hosokawa MikroPul GmbH
  Welserstr. 9-11, 51149 Köln
  Postfach 900749, 51117 Köln
  GERMANY
- Americas Editorial Secretariat
  Dr.I. Pikus or D.A. Scort
  Hosokawa Micron International Inc.
  10 Chatham Road, Summit, NJ 07901 USA

PUBLICATION SCHEDULE

KONA is published once a year.

SUBSCRIPTION

KONA is distributed free of charge to senior researchers at universities and laboratories as well as to institutions and libraries in the field throughout the world. The publisher is always glad to consider the addition of names of those who wish to obtain this journal regularly to the mailing list. Distribution of KONA is made by each Secretariat.

INSTRUCTIONS TO AUTHORS

(1) Manuscript format

- Two copies should be submitted to the Editorial Secretariat, in double-spaces typing on pages of uniform size.
- Authorship is to give author's names, and the mailing address where the work has been carried out on the title page.
- Abstract of 100-180 words should be given at the beginning of the paper.
- Nomenclature should appear at the end of each paper. Symbols and units are listed in alphabetical order with their definitions and dimensions in SI units.
- Literature references should be numbered and listed together at the end of paper, not in footnotes. Alphabetical order is accepted. Please give information as in the following examples:
  1) Carslaw, H.C. and J.C. Jaeger: "Conduction of Heat in Solids", 2nd ed., Clarendon Press, Oxford, England (1960).
  2) Howell, P.A.: US Patent, 3,334,603 (1963).
  3) Rushton, J.H., S.Nagata and D.L. Engle: AlChEJ., 10. 294 (1964).
  4) Seborg, D.E.: Ph.D. Dissertation, Princeton Univ., N.J., U.S.A. (1969).
- Original figures with each single copy should be submitted, on separate sheets. Authors' names and figure numbers are marked in the corner.
- Figure numbers and captions are listed on a separate sheet.
- Place of figure insertion is to be indicated in the margin of the manuscript.
- Tables should be typed on separated sheets.
- Submit an IBM-readable floppy disk ($3_{1/2}$) with your unformatted text file in ASCII code. If you use either WORD or WORD PERFECT−as word processing system, please add the formatted text file.

(2) Reprints

- The authors shall receive 50 free reprints. Additional reprints will be furnished when ordered with return of galley proofs.

(3) Publication policy

- All papers submitted for publication become immediately the property of the CPT and remain so unless withdrawn by the author prior to acceptance for publication or unless released by the Editor. Papers are not to be reproduced or published in any form without the written permission of the CPT.

KONA Powder and Particle No. 16 (1998)

Contents

Explanation of the Cover Photograph

Granulation of Aluminum Borate Whisker

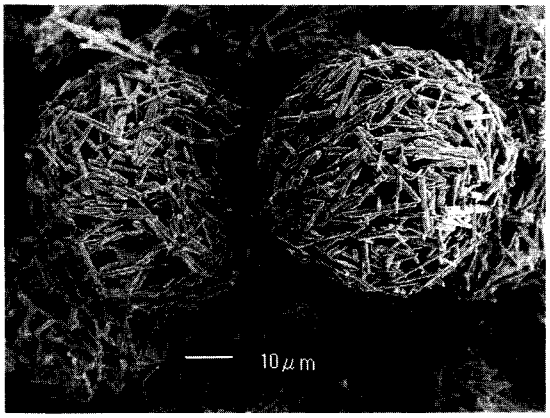

Aluminum borate whisker ($9Al_2O_3 \cdot 2B_2O_3$; diameter is 0.5~1.0μm length is 10~30μm) is promising material as a reinforcement for metal matrix composites, because of its low production cost and high tensile strength at elevated temperatures. However, conventional preforms in which whiskers were distributed randomly and homogeneously are deformed due to compressive stress by molten aluminum alloy during the infiltration. In order to solve this problem, a granulated whisker preform was developed. The whiskers are first dispersed in water to make a slurry. Then, the slurry is granulated by a spray-drier of disk rotary type. SEM image shows the granule whisker with a median diameter of 50μm, and a volume fraction of 30%. The granules are placed in a mold and pressed to make a preform. This granulated whisker preform is able to suppress the deformation, because its permeability is six times larger than that of conventional one.

By
Toshio Yamauchi: Suzuki Motor Corporation
Yoshinori Nishida: National Industrial Research Institute of Nagoya
Hideo Nakae: Waseda University

Review

Dispersion and Characterization of Pharmaceutical Dry Powder Aerosols†

Craig A. Dunbar, Anthony J. Hickey* and Peter Holzner
*Dispersed Systems Laboratory, School of Pharmacy, University of North Carolina**

Abstract

Dry powder inhalers may be employed for the delivery of drugs to the lungs for the treatment of pulmonary and systemic diseases. Dry powder inhalers consist of a formulation, metering system and delivery device. The formulation consists of small drug particles (median aerodynamic diameter <5 μm) usually combined with large excipient particles (30−125 μm). The physico-chemical properties of particles influence flow, fluidization and dispersion. An aerosol is passively inhaled by means of the inspiratory effort of the patient. Active devices use independent energy sources to deliver the aerosol. The aerodynamic particle size of an aerosol significantly effects lung deposition. Inertial deposition of particles, as a function of their aerodynamic diameter, allows measurement of the drug mass in a specific size range. The fine particle dose, or fine particle fraction (FPF) of the metered dose, is the simplest expression of the aerosol particle size. Passive inhalers have been reported to administer up to 50% FPF and active inhalers up to 70% FPF. The criteria for optimal inhaler performance must be defined to facilitate the rapid growth in research and development in this field.

1. Introduction

Epinephrine was the first drug to be incorporated in a chlorofluorocarbon (CFC) propellant driven metered dose inhaler in the 1950s [216]. This aerosol delivery device was a forerunner of current inhalers used in the treatment of asthma [233]. In recent times the success of CFC propellant driven metered dose inhalers has been overshadowed by their contribution to ozone depletion in the upper atmosphere and the concomitant health effects [169]. Therefore, the international community has agreed to phase out CFC propellants by the year 2,000 [52]. Pharmaceutical scientists have been responsive to the concerns over the environmental effects of propellants and have sought alternatives for the delivery of drugs to the lungs. The three major alternatives are the use of propellants that do not deplete ozone [179, 235], aqueous droplet aerosols delivered by nebulizer [178] and dry powder inhalers [2, 175]. Each of these approaches has its merits and their uses have been discussed in detail in the literature [90, 91].

The successful delivery of dry powders as aerosols depends upon a number of closely related factors. The intrinsic physico-chemical properties of the drug particles are the foundation for optimization of their delivery as aerosols [24]. These properties such as particle crystallinity, size distribution, shape and density may be modified in the manufacturing process and must be characterized carefully before proceeding to their incorporation in the dosage form [32]. The forces of interaction between particles in a powder bed are contingent on their physico-chemical properties and can be defined for specific powder forms [208]. The dynamic properties of flow and dispersion, which are related to ease of particle separation, may be evaluated as the basis for modification of powder performance. Finally, the interaction of the powder metering system and the device intended to generate the aerosol must be evaluated to optimize the dose delivery to the lungs. Considering each of these topics at a fundamental level will lead to successful integration of the powder formulation, metering system and inhaler to facilitate aerosol dispersion. The following sections discuss aspects of the dispersion and characterization of pharmaceutical dry powder aerosols and integrate them to define appropriate inhaler quality and performance criteria.

1.1 Physicochemical Properties

Crystallinity, polymorphism, particle size distribution, shape, moisture content and hygroscopicity have an impact on the dispersibility and stability of dry

* Beard Hall CB#7360, Chapel Hill, NC 27599-7360, USA.
† Received, January 1998

powders intended for delivery as aerosols. It should be noted, when considering particles that are included in aerosol powder systems, that the drug is rarely administered alone. The majority of formulations include carrier particles to which the drug particles adhere and from which the drug is dispersed [45].

1.1.1 Crystallinity and Polymorphism

The crystallinity of the powder may be described in terms of the crystal system and crystal habit of the particles. The crystal system is defined by the interatomic or intermolecular spacing within the particle, i.e., bond lengths and angles [247]. The crystal structure can be studied by X-ray diffraction [32]. Determination of phase angles for each Bragg reflection allows the calculation of the electron density map from which the molecular structure can be calculated [77]. The structure of cromolyn sodium is an example of pharmaceutical relevance [50]. Crystallographic studies of this particle structure have evaluated the interaction of the drug with water [189]. There are seven major crystal systems [171]. The crystal habit describes the morphology of the particle which may differ from the unit cell defined by the crystal system if the growth of the particle has been restricted in any dimension [32]. **Figure 1** illustrates the characteristics of the major crystal systems and gives an example of crystal habit.

Different crystal systems of a single chemical entity give rise to polymorphism. Since the bond angles and lengths differ between polymorphs their physical properties also vary [245]. Thus, polymorphs may exhibit different particle shape, solubility, hygroscopicity and moisture content which will have an impact on aggregation, through electrostatic charge, capillary and mechanical interlocking forces. Particles must be very small, $<5\,\mu m$, to be suitable for lung delivery [26, 89, 232]. In order to manufacture small particles, a considerable energy expenditure is required, commonly in the form of attrition milling or spray drying [136]. Much of this energy is expended in breaking the uniform bonds that exist in crystalline structures. Crystallinity must also be considered for carrier particles, notably lactose monohydrate, since this will have an impact on the nature of the mixing process and final distribution of drug particles in an aerosol powder. Elastic particles (low Young's modulus) are difficult to disperse due to deformation of interacting particles, generating large contact surface areas. Deformation increases interparticulate forces and reduces the porosity of the bulk powder.

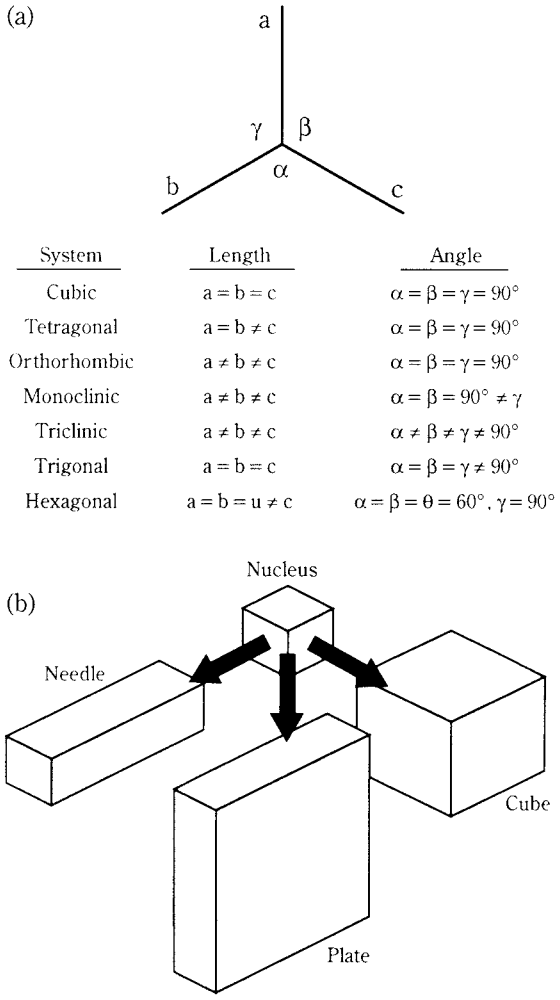

System	Length	Angle
Cubic	$a=b=c$	$\alpha=\beta=\gamma=90°$
Tetragonal	$a=b\neq c$	$\alpha=\beta=\gamma=90°$
Orthorhombic	$a\neq b\neq c$	$\alpha=\beta=\gamma=90°$
Monoclinic	$a\neq b\neq c$	$\alpha=\beta=90°\neq\gamma$
Triclinic	$a\neq b\neq c$	$\alpha\neq\beta\neq\gamma\neq90°$
Trigonal	$a=b=c$	$\alpha=\beta=\gamma\neq90°$
Hexagonal	$a=b=u\neq c$	$\alpha=\beta=\theta=60°,\ \gamma=90°$

Fig. 1 (a) The seven major crystal systems [171] and (b) an example of changes in crystal habit [32].

1.1.2 Particle Size, Distribution and Shape

The particle size and distribution of the drug in the bulk product are not usually controlled. The powder, which is most frequently prepared by crystallization or precipitation from solution [70], must be reduced in size to be suitable for inhalation [9, 136]. Size reduction frequently results in a powder which is log-normally distributed around a median diameter [6]. This type of distribution is typified by a large number of small particles. Individual large particles when broken into small ones produce numbers which are proportional, maximally, to the cube of the diameter. This is not only true of attrition milling but also of spray drying where droplets disintegrate during atomization in a similar geometrical fashion. Particle size reduction often eliminates specific irregular morphologies, or shapes of particles. Most spray drying processes are optimized to produce spheroidal particles [35, 212, 239]. Attrition milling results in particles which have a large number of planes of rotational

symmetry [146] but are not spherical. Supercritical fluid manufacture is a relatively new process that offers control of the physical characteristics of the particle [212]. This method has the advantage of generating respirable particles from heat labile compounds, e.g., peptides and proteins.

The size and shape of carrier particles must be considered when preparing blends with the drug. Lactose monohydrate occurs as a triclinic crystal and must be manufactured or sieved into size ranges suitable for drug delivery. In the original formulation of disodium cromoglycate the range of lactose particle size was 30−60 μm [119]. Various sizes up to 125 μm [47] have been explored for this purpose. The range of particle size employed will effect the flow and packing of the powders [144].

Particle shape is known to influence powder dispersion [199] and lung deposition [142]. In general, large deviations from sphericity are not considered useful in powder formulation, i.e. fibers or plates. Thus, any advantages that shape offers in terms of lung deposition are negated by their effects on reproducibility of dosing. Shape affects particle interactions with other particles in the powder and also with air during fluidization and deaggregation. Particles that have bluff body profiles (high drag coefficients) experience large drag forces and are therefore easier to fluidize. Elongated, fibrous particles have been shown to have unique transport properties that enhance deposition in the lung [33, 68, 99]. The contact state between fibrous particles is extremely unstable, promoting fluidization and deaggregation [186]. Rugosity balances the effects of interparticulate forces and mechanical interlocking. Rugose particles reduce interparticulate forces by the small effective diameters of the asperities but can promote mechanical interlocking as the surface irregularities increase, particulary for small particles in interactive mixtures. Reducing particle rugosity can significantly improve the respirable fraction of a dry powder inhaler [71]. However, smooth particles tend to experience high interparticulate forces, e.g., potato starch.

Particle size may be described by a variety of dimensions. The most common term for expressing the particle size from microscopic examination is the projected area diameter. This equates the diameter of a circular disc with the projected area (A) of the particle resting in the plane of greatest stability [6].

$$D_p = (A4/\pi)^{1/3} \quad (1)$$

For particles which are near spherical, the projected area diameter approximates the diameter of a sphere that has the same volume as the particle, i.e., the equivalent volume diameter (D_{eq}). Laser scattering and diffraction particle sizing methods allow the determination of equivalent volume diameters.

The most appropriate dimension for defining aerosol particles is the aerodynamic diameter [204]. The aerodynamic diameter (D_{ae}) of a particle is equivalent to the diameter of a unit density (ρ_0) sphere that has the same terminal velocity in still air:

$$D_{ae} = D_{eq}\left(\frac{\rho_p}{\rho_0 \chi}\right)^{0.5} \quad (2)$$

Eq.(2) shows that D_{ae} is dependent on both particle shape (χ) and density.

Particle size is statistically represented by two parameters: a representative diameter and a measure of the distribution of particles sizes. These parameters usually take the form of a median diameter and geometric standard deviation for inhalation aerosols, although many other representative diameters and distribution factors can be used [110,139]. The D_{eq} commonly calculated by impaction methods is the mass median aerodynamic diameter (MMAD). MMAD represents the aerodynamic particle size for which 50% of the total aerosol by mass have smaller aerodynamic diameters. MMAD is calculated assuming a log-normal distribution of particle sizes. Distribution of particle sizes is represented by the geometric standard deviation (σ_g) of the log-normal distribution ($D_{ae,\,0.84}$/MMAD).

A recent development in the physical structure of particles has been made with the production of large ($5<D_p<30$ μm), porous particles [60]. Porous particles are less dense than solid particles with equivalent volume diameters, making it possible to increase the particle cross-sectional area (improved fluidization) without increasing the aerodynamic diameter (deposition) (see Eq.(2)). Administering large diameter particles (>3 μm) to the lung also increases bioavailability by reducing phagocytosis [211] and thereby extends the residence time of the particles in the lungs.

The powder packing consists of individual particles in mutual contact with voids filled with gaseous medium. The volume of gas to the total volume of the powder pack is known as porosity (ε). This parameter provides a measure of the compactness of the packed powder bed and can quantify the uniformity of the powder blend. Porosity is effected by particle size distribution, interparticulate forces, mechanical interlocking and friction, random settling and boundary effects [208]. These forces dictate the bulk and tap density. The bulk density, in contrast with the true density, is a measure of the interstitial space between

particles, or the spontaneous packing geometry [32]. The tap density indicates the extent to which the packing of particles can be re-arranged by imparting mechanical energy. This can be viewed as a measure of the stability of the spontaneous packing geometry. Both of these properties will be influenced by particle size, distribution, shape, density, charge and moisture content.

1.1.3 Moisture Content and Hygroscopicity

The moisture content of powders will have an impact on stability. The equilibrium moisture content at ambient temperature and relative humidity may be a good indicator of the suitability of a drug or excipient for use in an aerosol product. **Figure 2** shows the equilibrium moisture contents for lactose and mannitol [244]. The moisture content of most sugars is relatively low at a relative humidity below 90%, e.g., Glucose, lactose, maltodextrins, mannitol exhibit equilibrium moisture contents of <21%, <7%, <6%, ≃0.5%, respectively. The amount of free water in a system is closely related to the magnitude of the capillary forces which hold particles in aggregates. The water confined between particles in narrow pores is highly structured relative to free water, giving rise to strong interactions [61]. Moisture between particles also generates capillary forces which are a function of the surface tension, liquid density and pore radius [70].

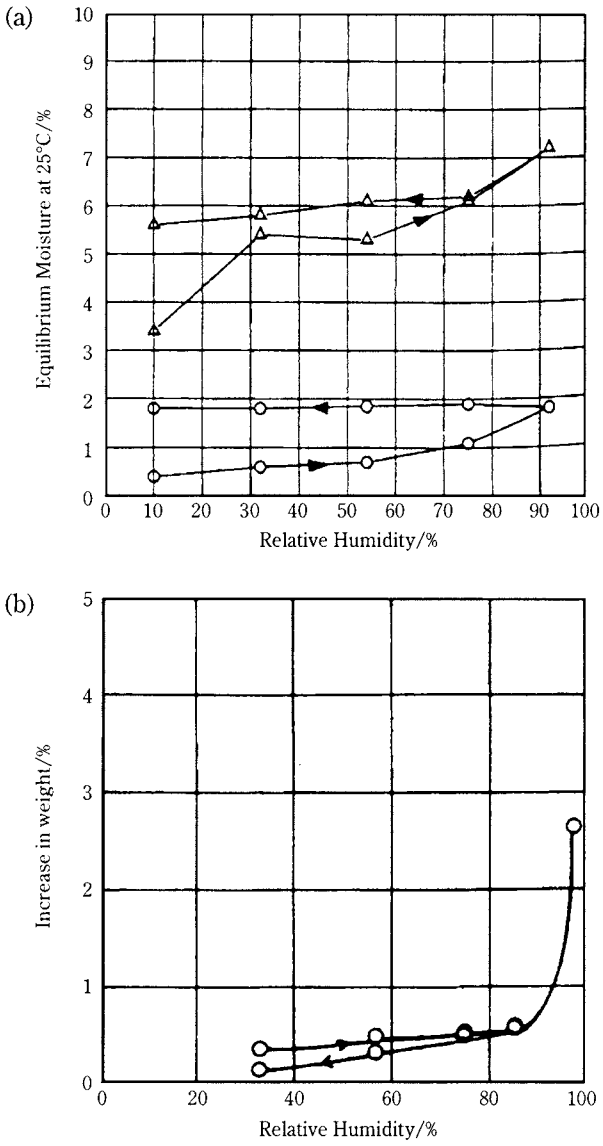

Fig. 2 Equilibrium moisture content (a) anhydrous (o) and spray dried (Δ) lactose, (b) mannitol [244]

The method of manufacture of particles also has an impact on their uptake of moisture. Micronized cromolyn sodium exhibits a decline in respirable particles (0.3−3.3 μm) from 8 to 4%, whereas spray dried particles drop from 17 to below 1% for RH in the range 0−80% [2, 241]. This data was derived from a study in which both products were prepared as 1:1 blends with lactose [241]

Hygroscopicity is the tendency of particles to take on moisture from the atmosphere. Susceptibility to hygroscopic growth can result in physical instability. Moisture uptake and loss over a narrow range of relative humidities can result in dissolution and recrystallization, leading to irreversible aggregation in the form of solid bridging.

Electrostatic charge occurs by a number of methods. The charge associated with certain ionic species at the surface of a particle will influence particle behavior. Contact with specific surfaces and charge transfer by motion will give rise to unique powder charge characteristics. The charge on a particle increases as it approaches the anhydrous state. The forces of interaction between hydrophobic surfaces are generally less charged than hydrophilic ones [5]. The surface energetics may be investigated by inverse phase gas chromatography [116, 117] from which the cohesive energy density of the surface of particles may be obtained. The chemical heterogeneity of the surface can also be studied by gas adsorption with fractal analyses [10].

2. Powder Particles: Flow and Dispersion

2.1 Fundamentals

The fundamental aspects of powder aerosol dispersion for inhalation, illustrated in **Figure 3**, may be considered in terms of static powder properties, flow, fluidization and deaggregation. Static powder properties are the properties of the powder at rest and con-

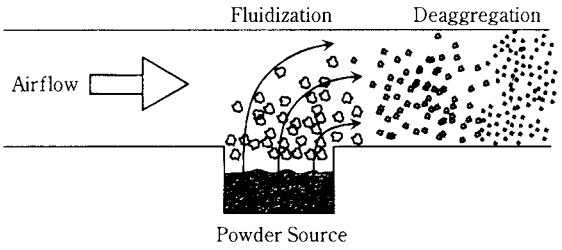

Fig. 3 Schematic of powder aerosol dispersion

sist of single particle characteristics, interparticulate forces and bulk powder and powder packing characteristics. Fluidization is the mobilization of the bulk powder by interaction with air. Shear force fluidization is the most common form of fluidization in passive inhalers. Other fluidization mechanisms include gas-assist, capillary and mechanical. Deaggregation occurs after fluidization of the bulk powder and is the second stage interaction with air. The forces acting on a particle system/agglomerate are generated by relative motion, turbulence, flow shear stresses, electrostatics and collision.

Static powder properties exist in the dry powder inhaler after the powder has been metered and before the powder is dispersed for inhalation. Static powder properties can be described in terms of microscopic (single particle) characteristics (physicochemical properties: section 1.1), interparticulate forces and macroscopic (bulk powder or powder packing) characteristics.

Interparticulate forces that influence particle interactions during the dispersion of powder aerosols include the cohesive/adhesive van der Waals, electrostatic, capillary, mechanical interlocking and friction forces. Cohesive forces are due to the attraction of like materials, e.g., particle to particle. Adhesive forces are due to the attraction of unlike materials, e.g., particle to carrier or device. Particulate interactions are primarily dominated by van der Waals force, which are only effective over a short range ($<10^{-3}$ μm), but can be very strong ($>10^3$ F_g). The van der Waals force of attraction between two spherical, rigid particles of different diameter is given by:

$$F_{vdw} = \frac{AD_{12}}{12h^2} \tag{3}$$

where A is the Hamaker constant, h is a characteristic length scale representing the shortest distance between particles and D_{12} is given by:

$$D_{12} = \frac{D_1 D_2}{D_1 + D_2} \tag{4}$$

Application of Eq.(3) is limited to qualitative calculations due to the difficulty in defining the Hamaker constant and the characteristic length scale [172]. Estimates of these parameters are available in the literature [64, 140, 120, 208, 243, 254]. Values for the Hamaker constant range from to $5\times10^{-20}-1\times10^{-19}$ J, with values for the shortest distance between particles ranging from 0.35−10 nm. A range of van der Waals force of over 1600 is predicted from these values, highlighting the difficulty in quantifying this force. Eq.(4) can be modified for non-spherical particles by defining an effective diameter of the asperity at the point of contact. The magnitude of the van der Waals force will be considerably reduced since the diameter of the asperities will be smaller than that of the particle.

Electrostatic charge is generated when particles are separated from the bulk material or contact other surfaces. This mechanism can significantly affect formulation homogeneity, especially when the powder contacts dissimilar materials [224]. The force of electrostatic attraction between two particles with charges q_1 and q_2, respectively, is given by Coulomb's law:

$$F_q = K_q \frac{q_1 q_2}{h^2} \tag{5}$$

where K_q is the electrostatic force constant. General application of Coulomb's law is limited due to the difficulties in defining the respective particle charges, which change with contact surface, environment and flow conditions. Definition of a characteristic length of charge separation is also required. The magnitude and polarity of charge will be different for the static powder in contact with the device compared to a deaggregated particle. The net charge of the fine particle dose generated by commercial DPIs has a dependency upon the type of inhaler and the method of deaggregation, although it is difficult to delineate these mechanisms [193]. Electrostatic effects are negligible at relative humidities above 65% [100].

Capillary forces are formed by the condensation of water to form high tensile liquid bridges. Liquid bridges can occur at elevated relative humidities, i.e., RH>65% [214, 242], and are dependent on particle material and surface characteristics. The capillary force between two spherical particles of different diameter is given as:

$$F_c = 2\pi\sigma D_{12} \tag{6}$$

where D_{12} is defined by Eq.(4). This force will be significant during transport in the lung (RH→100%) due to its dependence on relative humidity.

Mechanical interlocking and friction are significant effects when considering the relationships between irregular large carrier particles and small drug particles. The magnitude of the forces resulting from

mechanical interlocking are dependent on surface characteristics. Small drug particles can be forced into cavities which require large separation forces. Mechanical interlocking can be enhanced with prolonged blending. Interactive mixtures form stable associations with other particles during blending. Particles continue to relocate to sites of higher stability/lower energy as the blending time is increased, promoting the effect of mechanical interlocking. Friction is generated between surfaces in mutual contact and is dependent on the contact force, area at the point of contact and surface roughness. The force of friction is more apparent for smaller particles, as both the coefficient and angle of friction increase with decreasing particle size [66].

The magnitude of the respective interparticulate forces (with the exception of mechanical interlocking and friction) can be approximated by considering an ideal binary system, i.e., a pair of spherical, rigid particles. Interparticulate forces are estimated in **Table 1** for four binary systems: (I) carrier:carrier; (II) carrier:drug; (III) drug:drug and (IV) asperity:asperity. The model carrier is a 90 μm lactose particle and the model drug is a 2 μm albuterol sulphate particle. Capillary forces are significantly higher than both van der Waals and electrostatic forces but are only produced at high relative humidities (RH>65%). This suggests that capillary forces dominate in the lung and further deaggregation of agglomerates beyond the oropharynx is unlikely to occur. Ranking of interparticulate forces during dispersion within a DPI reveals that van der Waals force dominates with electrostatic forces being an approximate two orders of magnitude less. The magnitude of the forces estimated in **Table 1** are dependent on particle diameter for a binary system, i.e., interparticulate forces decrease with decreasing particle size. However, it becomes increasingly difficult to fluidize small particles since aerodynamic force is proportional to the cross-sectional area.

Table 1 Estimation of interparticulate forces for ideal binary systems

Force	Equation	Parametric Values	Magnitude/10^{-9} N			
			I	II	III	IV
Van der Waals	$\frac{AD_{12}}{12h^2}$	A=7.5×10^{-20} J h=5 nm	11	0.5	0.1	0.01
Electrostatic	$K_q\frac{q_1q_2}{h^2}$	$K_q=9\times10^9$ Nm^2/C^2 $q_d=5.3\times10^{-20}$ C[a] $q_l=1.18\times10^{-18}$ C[a] h=5 nm	0.5	0.03	0.001	–
Capillary	$2\pi\sigma D_{12}$	$\sigma=73\times10^{-3}$ N/m	20640	917	229	23

(I): lactose: lactose; (II)=drug: carrier; (III)=drug: drug and (IV) asperity: asperity (D_{eff}=0.1 μm)
drug=albuterol sulphate, D_d=2 μm, ρ_d=1150 kg/m^3 [108]
carrier=lactose, D_l=90 μm, ρ_l=1540 kg/m^3
[a] q approximated from specific charge measurements of Peart et al [193]

The magnitude of the forces for a 'real' DPI powder will be different to theory due to asperities and powder packing effects. Asperities depend on the rugosity of the particle and are typically <0.1 μm [208]. Thus, the van der Waals force between two particles, approximated in **Table 1**, would be reduced by a factor of nearly 900 if the particles were connected by asperities. The magnitude of the interparticulate forces within a powder packing is also affected by the number of mutual points of contact, i.e., the coordination number (k). Interparticulate forces for a binary system are approximately proportional to D_p (**Table 1**). Thus, small particles have smaller interparticulate forces at a single point of contact. Interparticulate forces acting on a particle within an agglomerate increase by a factor of the coordination number, e.g., a particle within a cubic packing (k=6) will experience interparticulate forces six times greater than that for a binary system.

2.2 Powder Characteristics

The dispersion of particles from a static powder bed may be considered in terms of dilation, flow, fluidization and ultimately aerosol production. These are integrated mechanisms during the dispersion process that can be evaluated individually to construct a model of powder dispersion.

Flow is the first step in the dispersion of aerosol powders, occuring as enough space is created between particles for them to pass over and around each other in the direction of an applied force. In a system of spherical, uniform, non-cohesive particles, this process might be expected to occur in a predictable fashion with the flow rate being proportional to applied force. Unfortunately, pharmaceutical powders are non-uniform in size and shape and are subject to various cohesive and adhesive forces. There are two scales of scrutiny of powder flow as it relates to aerosol dispersion. These are the bulk macroscopic and the discrete microscopic flow characteristics. There are many methods of measuring powder rheological properties [219]. The angle of repose [31], Flodex (Hanson Research Corporation, Chatsworth, CA) and the shear cell [209] are examples of classical methods. The angle of repose indicates the ease of flow in terms of the angle that a pile of powder poured through a funnel makes with respect to the horizontal. A large angle of repose indicates poor flow properties. The Flodex, powder flowability index test

instrument (US Patent #4,274,286), is a simple method in which powder is poured through an orifice from a hopper. The orifice diameter may be reduced until the smallest orifice through which the powder will pass unassisted is identified. The diameter of this orifice becomes the measure of the ease of flow of the powder. The shear cell is analogous to a viscometer. The resistance in the form of torque experienced when a force is applied to the surface of a powder is used to define its ease of flow. The latter technique is particularly useful in evaluating powders that will experience compression but may not be as relevant in the evaluation of aerosol powders. Each of these methods measures bulk flow properties which are known to be inversely proportional to particle size.

Small fluctuations in flow which arise from small stable aggregates within the powder are of additional interest. These fluctuations may be of great significance on the scale of a unit powder dose, i.e., ≤25mg. Alternative methods have been developed for the evaluation of these small variations in flow. Flow from a vibrating spatula has been analyzed to allow derivation of fractal dimensions describing the irregularities in flow [94]. This method measures the powder dispensed gravimetrically and is limited in the speed of data acquisition (~300ms intervals). This is insufficient to adequately distinguish between powders with differing flow properties, exhibiting a range of fractal dimension of 1.003 for smooth flow to 1.057 for irregular flow. A second method has been developed involving chaos data analysis of dynamic angle of repose measurements [95] yielding capacity dimensions, analogous to fractal dimensions, which have the sensitivity to discriminate between the performance of powders, ranging from 1.2 for periodic to 2.6 for random behavior [48]. The phase space plots of the original data may be used to distinguish the effect of particle size distribution compared with particle interaction. **Figure 4** shows a phase space plot of bulk lactose [95]. The distance across the trajectories reflects the breadth of particle size distribution. The radius of the trajectories is inversely proportional to ease of flow. This is a relatively new method for studying powder behavior and it may be possible to derive more information from the data by alternative analytical methods, e.g., avalanching [132]. The concept of self-similarity at all scales of scrutiny may ultimately be applied to many aspects of powder characterization, including particle morphology, powder mixing, flow and dispersion [93].

Particle detachment may be evaluated in a number of different ways. The most commonly used methods

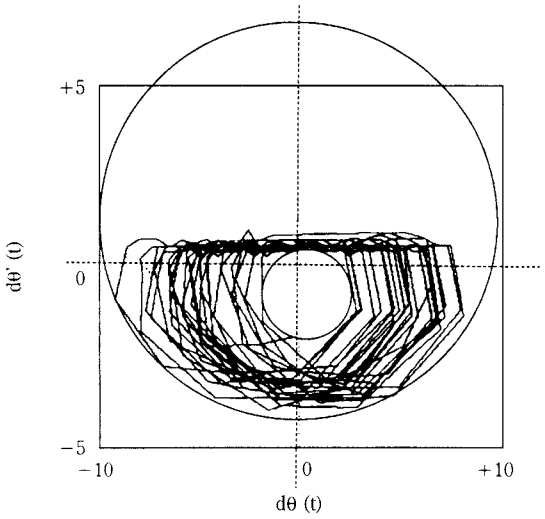

Fig. 4 A phase space plot obtained for a bulk lactose sample [94].

include [172], ultracentrifugation, impact and vibrational forces. Ultracentrifugation is ideal for detachment of particles in small size ranges. However, without attachment to a classifier for the detached particles, or selection of an advanced system such as the spiral centrifuge [153], the method is incapable of distinguishing the nature of the particles, dispersed or aggregated, once they are detached. Impaction and vibration techniques were originally considered for large particles, i.e., D_p>100 μm [186, 187]. The impact force method has recently been modified to allow characterization of particles down to 1 μm [46,48]. This method also characterizes the particle size by microscopy and by quartz crystal microbalance inertial impaction, allowing the degree of dispersion of the particles to be studied. It is possible to characterize detachment in terms of device powder interactions, not just particle-particle interactions, by adopting support surfaces of materials with which the aerosol powder will come into contact.

Particles suitable for deposition in the lung require an approximate aerodynamic diameter of 5 μm. Powders consisting of such small particles are difficult to fluidize due to their small cross-sectional area. Dry powder aerosol formulations typically consist of an interacting or ordered mixture of small drug particles associated with large lactose carrier particles [74, 88]. The purpose of this binary system is to optimize interparticulate forces to obtain an interactive mixture with a high degree of homogeneity that will respond to the fluidization and deaggregation processes. Diluents can also be used to stabilize the active ingredient [23, 40]. Introduction of a third component into the mixture establishes competition between small particles for binding sites [222]. This can result in a

higher proportion of drug particles binding to weaker sites and improved control of the fluidization/deaggregation mechanisms. Addition of tertiary particles has been shown to increase the respirable fraction of the doses emitted from DPIs [131].

Carrier-free powders have the advantage of smaller dosage forms, which can be significant when using potent or expensive drugs. The disadvantage of drug-only formulations is the difficulty in fluidizing the bulk powder and deaggregating particle agglomerates. Difficulty in fluidizing/deaggregating small particles is due to the low drag coefficient (D_p^2) of the individual particles relative to the interparticulate forces, requiring large aerodynamic forces for fluidization.

2.3 Fluidization

Fluidization is the mobilization of the bulk powder by air. This represents the first stage interaction with air in the dry powder inhaler. There are two types of fluidization mechanisms: hydrodynamic and mechanical, which can be further divided into sub-groups. These include gas-assist, capillary and shear force for hydrodynamic fluidization, and vibration and impaction for mechanical fluidization. Powder fluidization is dependent on the ratio of hydrodynamic to interparticulate forces. Hydrodynamic forces take the form of competing effects of viscous drag (D_p^2) and inertial (D_p^3) forces. Interparticulate forces are approximately proportional to D_p. Thus, the interparticulate forces will decrease as the particle size decreases (D_p). However, greater hydrodynamic force in the form of viscous drag (D_p^2) will be required to mobilize the particle, i.e., high air flow rate. The relationship between interparticulate force and inertial force during mechanical fluidization is complicated by the direction of the force vector.

Powders can be characterized by their fluidization properties [75]. Geldhart proposed four distinguishable groups of powder behavior during gas fluidization, three of which can be applied to powder inhalation aerosols. Group A describes fluidized powder beds in which the hydrodynamic forces dominate relative to interparticulate forces, making the powder easy to fluidize. This group usually consists of intermediate size particles (D_p~40 μm) and/or low particle density (<1.4 g/cm^3). Group B powders maintain a balance between interparticulate and hydrodynamic forces (D_p: 40−500 μm) and group C powders are difficult to fluidize due to the predominance of interparticulate forces (D_p<10 μm). Powder fluidization properties can be defined by the Hausner ratio which is the ratio of poured to tapped bulk density [75]. Fluidization is also dependent on the elasticity of the powder particles and viscosity of the gas phase, limiting the general applicability of Geldhart's powder groups [208].

Gas-assist fluidization occurs when a gas is passed through the powder. This form of fluidization can be described by considering a Geldhart group A powder in a gas-assist fluidization bed. This consists of a powder contained in a cylindrical vessel that is sealed at the bottom by a gas permeable plate and open to atmosphere at the top. Gas is forced through the powder via the permeable plate, generating drag forces on the powder particles. Gas flows through the powder pores without disrupting the powder structure at low gas flow rates. Incipient fluidization occurs with increasing gas flow rates, shown in **Figure 5**, resulting in aerodynamic drag forces separating loosely bound particles. Further increases in gas flow rate causes bulk particle separation. Homogeneous fluidization is achieved with further increases in gas flow rate, producing bulk particle separation. The bed becomes unstable at a critical gas flow rate as bubbles begin to form in the powder. The bed height fluctuates as the bubbles are continually produced and collapsed. More complex phenomena occur with other powder groups (B-D), e.g., powder compression and channeling [75, 208]. Active dry powder inhalers are being developed that utilize gas-assist fluidization [42, 59, 69, 82, 122, 191, 215]. Capillary fluidization is a mechanism similar to gas-assist and occurs when a low pressure field is established close to the powder, e.g., recirculation zone. A pressure differential between the air contained in the powder voids and the motion of the air passing over the powder is developed and the powder bed is fluidized.

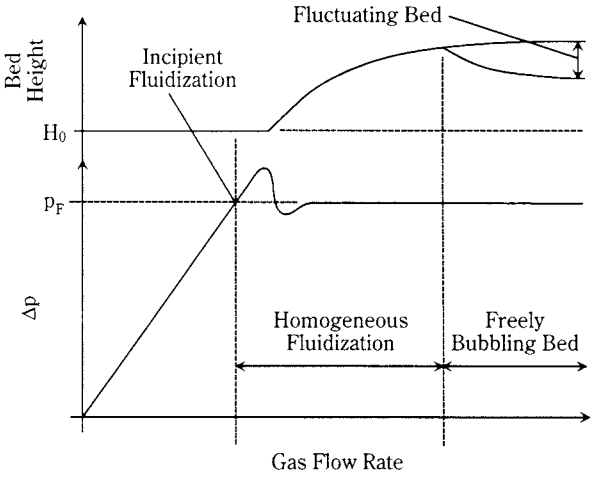

Fig. 5 Fluidized bed characteristics.

Shear force fluidization (also known as saltation) occurs when a gas stream is passed over a powder source, contained in either a pocket or on an open surface. Particles on the surface of the powder source experience reduced interparticulate forces due to the smaller coordination number. Separation by shear force results in the transmission of both translational and rotational motion of the particles as they traverse the powder bed. Collisions with other particles force the particles to bounce, resulting in incipient fluidization. Particles separate from the bulk powder with high rotational velocities (up to 1000 rev/s [38]), generating Saffman lift forces that project the particles vertically. The high viscous shear stresses in the boundary layer close to the powder surface magnify the vertical projection due to the Magnus force. This form of fluidization primarily affects particles with D_p>100 μm and is dependent on the velocity of the air flow around the particle. The critical velocity for shear force fluidization is given as (for D_p>100 μm) [11]:

$$U_{crit} = 1.47\ (D_p)^{0.5} \quad (7)$$

Shear force fluidization predominates in the majority of passive dry powder inhalers.

Mechanical fluidization can be generated by vibration or impaction. Vibrational fluidization occurs when the powder is shaken from its source and falls through air by gravitational forces. The method used to measure the angle of repose exploits vibrational fluidization. The Spinhaler™ was one of the first dry powder devices used for inhalation therapy and employs the principal of vibrational fluidization [16]. Fluidization by impaction when a tangential force is applied to the powder source such that the interparticulate forces forming the bulk powder can be overcome. The impaction force required to fluidize a powder is dependent on particle size and orientation of the powder source. The impaction force must overcome both interparticulate, friction and gravitational forces to fluidized the powder vertically upwards. Inverting the powder source orientation results in the gravitational forces assisting fluidization.

Investigations have been conducted on the effect of particle size and fluidization for dry powder aerosols. Fluidization within the Spinhaler™ occurs by the vibration of a rotating capsule that has been punctured for the powder to pass through. **Figure 6** is a representation of the effect of particle size on fluidization within the Spinhaler™, with maximum fluidization occuring for a particle size of approximately 100 μm. The lower particle size limit is due to small

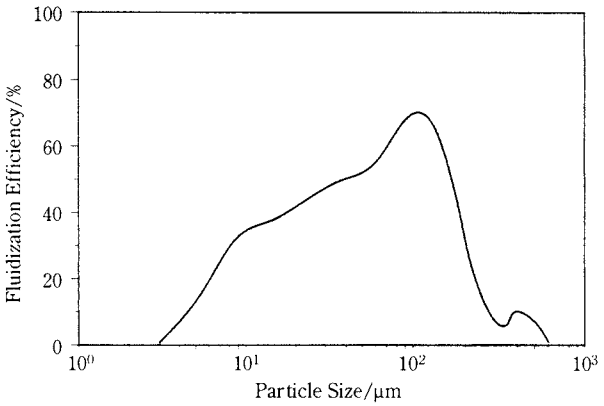

Fig. 6 Relationship between fluidization and particle size for the Spinhaler™ [adapted from 16].

drag forces relative to the interparticulate forces. The large size limit is due to blockage within the capsule hole. Experiments with a fluidized bed generator revealed that large particles (>90 μm) produced smooth and continuous fluidization that was primarily dependent on mean air velocity (shear force fluidization) [144]. Fluidization of smaller particles was dependent on mean air velocity, tube diameter and pressure gradient. This was due to the complex interaction between interparticulate and aerodynamic drag forces. These results imply an optimal particle size for maximum fluidization.

2.4 Deaggregation

Deaggregation and deagglomeration are the processes by which particle aggregates (carrier-drug particle admixtures) and agglomerates (drug clusters) are dispersed into primary particles, ≤5 μm in median diameter, by interaction with an airflow. This is considered to be the primary aerosol dispersion mechanism affecting lung deposition [123]. The interparticulate forces of a binary system or agglomerate must be overcome for deagglomeration to occur. Adhesive/cohesive forces are generally dependent on D_p, whilst forces of separation are dependent on D_p^2 (aerodynamic) and D_p^3 (vibration, rotation and collision).

Deaggregation principally occurs in two regions: the device and the oropharynx. Particle transport beyond the oropharynx affects dispersion of the powder aerosol due to changes in flow geometry and environmental conditions. This ultimately affects lung deposition. Factors affecting lung deposition have been detailed in the literature [151, 152, 230].

Principal forces leading to deaggregation are unclear. The majority of literature points to turbulence being the principal factor without considering the detailed nature of turbulent fluid flow and its

interaction with dispersed particles [72, 131, 138, 234, 238, 246]. The forces contributing to the transport and deaggregation of particle agglomerates travelling in an airstream can be broken down into the following closely coupled categories: (i) relative motion; (ii) turbulence; (iii) shear stress; (iv) electrostatics and (v) collision.

The predominating forces affecting the relative motion of an aerosolized particle can be presented as a supposition of forces:

$$\frac{\pi}{6}D_p^3\rho_p\frac{D\vec{U}_p}{Dt_p}=\frac{\pi}{8}D_p^2\rho C_D|\vec{U}-\vec{U}_p|(\vec{U}-\vec{U}_p)$$
$$-\frac{\pi}{6}D_p^3\frac{\partial P}{\partial\vec{x}}+\frac{\pi D_p^3}{6}\rho|\vec{U}-\vec{U}_p||\omega-\omega_p|$$
$$+1.6(\mu\rho)^{0.5}D_p^2|\vec{U}-\vec{U}_p|\left|\frac{\partial\vec{U}}{\partial\vec{x}}\right|^{0.5}+\frac{\pi D_p^3}{6}\rho_p q_p E-F_g \quad (8)$$

The term on the left-hand side of Eq.(8) represents the inertial force of the particle, with the terms on the right-hand side of the equality respectively representing the drag force, the force due to static pressure gradients in the flow, the Magnus and Saffman forces, the force experienced in the presence of a strong electric field gradient and finally the body force term, taking the form of gravity. The predominating force acting on a particle is usually the drag force. The pressure gradient term becomes significant in turbulent flows typically experienced by dry powder aerosols. Magnus force accounts for translational motion of the particle due to rotation which is significant immediately after shear force fluidization. Saffman force results from free rotation within gas velocity gradients. This force would be experienced close to the powder source in the viscous sub-layer, boundary outer-layers and within swirling eddies. The electrophoresis term is significant for small (<5 μm), charged particles in strong electric fields.

Rotation of carrier particles or agglomerates generates centrifugal forces on surface particles that may be large enough to overcome the adhesive forces. The centrifugal force acting on a small particle can be approximated by considering the particle as a point mass on the periphery of a large carrier particle, as follows:

$$F=0.5\,m_p\omega_p^2D_c \quad (9)$$

where D_c is the diameter of the carrier particle. A binary particle system consisting of a 90 μm lactose carrier particle with a 2 μm albuterol sulphate drug particle attached to the surface requires an ω_p>840 rev/s to overcome the van der Waals force of attraction estimated in **Table 1**. Fluidized sand grains (D_p~200−300 μm) have been observed to rotate with high angular velocities (200−1000 rev/s) [38]. The forces of attraction estimated in **Table 1** are much higher than those experienced by a 'real' binary drug-carrier system due to surface asperities. For a binary system consisting of particles that have asperities with effective diameters of 0.1 μm, the van der Waals force is reduced by an order of 40, requiring an ω_p>130 rev/s for centrifugal separation.

There are three types of fluid flow: laminar, turbulent and transition. Laminar flow usually occurs at low fluid flow velocities and is characterized by stable instantaneous velocities everywhere in the flow field. Turbulence can be defined as a spatially varying mean fluid flow with superimposed three-dimensional random fluctuations which are self-sustaining and enhance mixing, diffusion, entrainment and dissipation [250]. Turbulent fluid flow consists of instabilities known as eddies that occur with various length scales. Large scale turbulence consists of large eddies that contribute to the convective transport of the fluid. Large scale eddies are unstable and break down to fine-scale turbulence that dissipate energy by heat transfer. Transition describes the unstable condition between laminar and turbulent fluid flow. The Reynolds number (Re) is the ratio of inertial to viscous forces:

$$R_e=\frac{(UL)_C}{\eta_g} \quad (10)$$

where U_C and L_C are characteristic velocity and length scales of the fluid flow, respectively. The characteristic scales used to define the Re of fluid flow within a cylindrical pipe are the velocity of the gas and the diameter of the pipe. The characteristic scales for particle motion are the relative velocity of the particle and particle diameter. Re is commonly used to predict the onset of turbulence, e.g., turbulence occurs at Re≈2000 for fully developed flows in cylindrical pipes. The value of Re at which turbulence first occurs is dependent upon geometry, time scales and initial disturbances. The majority of DPIs are composed of short tubes and complex geometries, suggesting the flow through such devices is in an intermediate state, consisting of a turbulent core surrounded by a laminar envelope. Neither flow type will dominate due to the short time scales of the fluid motion through the device. Definition of the type of flow containing suspended particles is further complicated by turbulence modulation. This occurs due to the conflicting effect of particles damping the turbulent flow field by their

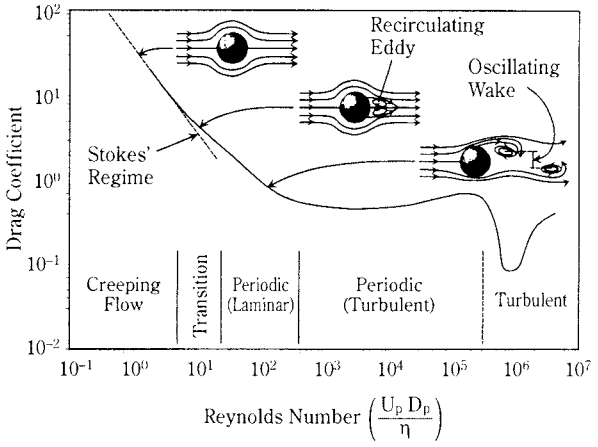

Fig. 7 Flow development of smooth, spherical particles.

inertia as well as instigating instabilities in the flow leading to turbulence production. This process has yet to be fully understood [63, 164].

Flow development around a spherical particle is summarized in **Figure 7**. The fluid flowing past the sphere exerts a drag force due to skin friction (low Re_p) and pressure gradients along the surface. Viscous forces dominate at very low particle Reynolds numbers ($Re_p<0.1$), known as creeping flow or Stokes' regime. As Re_p increases (~ 10), separation of the boundary layer occurs and vortices (large scale eddies) are formed downstream of the particle that are eventually dissipated by the viscous action of the mean flow. Further increases in Re_p result in unstable vortex generation and the production of a wake. At a critical Re_p ($\sim 10^2$), the eddies break off from alternate perimeters of the particle (vortex shedding) and form an oscillating vortex street. Vortex shedding results in alternating lateral forces and may cause forced vibration of the particle if the vortex shedding frequency approaches a resonant frequency of the particle. The limiting values of Re_p, described above, are reduced by increased turbulence of the mean air flow, particle asymmetry, rugosity and the presence of other particles disturbing the mean flow. The Re_p for turbulent flow around a particle is approximately 400 (**Figure 7**).

Shear stresses are established by velocity gradients, defined by:

$$\tau_{ij} = -\mu\left(\frac{\partial U_i}{\partial x_j} + \frac{\partial U_j}{\partial x_i}\right) \tag{11}$$

Efforts have recently been made to relate the shear stress required to deaggregate particles in turbulent flow through a dry powder aerosol device [64] and the oropharynx [140]. The volume flow rate (L/min) required to produce particle deagglomeration was derived by equating the viscous shear force based on a turbulent mixing length hypothesis to the adhesive van der Waals force [64]:

$$Q \ll 0.041 (Dp)^{-4/7} \tag{12}$$

The second approach estimated the viscous shear force in a three dimensional replicate oropharyngeal geometry using computational fluid dynamics. An expression for the minimum diameter of identical particles that can be separated was obtained by equating the viscous shear force to the adhesive van der Waals force:

$$D_{min} = \frac{A}{24\pi h^2 \tau} \tag{13}$$

Both expressions for particle deaggregation highlight the relationship between gas flow rate and particle detachment.

A particle can acquire charge during deaggregation by two mechanisms: static electrification and diffusion charging. Each of these methods affects the transport and deaggregation of particles within a DPI. Static electrification causes particles to become charged as they are separated from the bulk material or other surfaces. This mechanism can significantly affect formulation homogeneity and fluidization, especially when the powder contacts dissimilar materials [193, 225]. A discharge occurs when particles are separated during deaggregation. The electrostatic charge acquired by a particle changes with time due to diffusion charging. Diffusion charging occurs due to random collisions with unipolar ions and particles. The rate of particle charging tends to zero as the particle produces an electrical field that will eventually be strong enough to repel additional ions. Diffusion charging is dependent on the physical and chemical characteristics of the particle, charge and charging time. As particles are charged by diffusion, some will deposit on the surface of the device and discharge. A sufficient number of particles depositing on the device surface could lead to the generation of an electrical field. This effects the transport of the fluidized powder as particles are attracted to (and repelled from) each other and the device surfaces.

Particle collision is an important phenomenon for aerosol dispersion. Particle collision is dependent on particle size, number concentration and particle to particle and gas to particle relative motion. The number concentration and relative velocities are highest during fluidization and therefore the rate of collision is most significant during this process. Deaggregation can occur during collisions of solid, aerosol particles, providing the particles have sufficient relative momentum. Small particles can also adhere to other

particles if there is sufficient settling time for the interparticulate forces to overcome the kinetic energy of the particle. Particle collision is a very complex process and is difficult to quantify *a priori*, especially for polydisperse systems interacting with turbulent fluid flow. Although models of collision have been developed [181], more research in this area is required before the effect of particle collision can be quantified and exploited for dry powder aerosol dispersion.

3. Mechanisms of Dispersion by Inhalers

Dry powder inhalers are designed to generate an aerosol from a powder onto or via the inspiratory airflow. The powder formulation consists of the drug which is usually blended with a carrier (lactose or glucose) to facilitate flow and dispersion [71, 72, 234]. The formulation is either contained as bulk material in a reservoir within the inhaler (multi-dose inhalers) or packed as unit doses in capsules (single dose inhalers) or blisters (multiple unit-dose inhalers). In the case of a powder reservoir, a single dose has to be metered from the bulk and transferred into the inhalation channel prior to inhalation. Pre-metered unit dose packages need to be opened to render the powder accessible for inhalation.

The powder in its static state is characterized by a number of cohesive and adhesive forces (section 3). These consist of van der Waals, electrostatic and capillary forces, mechanical interlocking and friction. Van der Waals forces dominate at low relative humidities (RH<65%) whilst capillary forces control cohesion/adhesion at RH>65%. The extent of these forces is dependent on the powder properties (size, shape, geometry) [34, 93, 99, 100, 144, 242], the formulation (excipients) [30, 64, 224, 225, 228], and ambient conditions (humidity, electrostatics) [28, 76, 193, 200, 222, 224]. Generation of an aerosol in the respirable size range requires the fluidization and deaggregation of the static powder. The cohesive and adhesive forces within the powder have to be overcome by an external supply of energy. This is achieved in passive inhaler devices by the transfer of kinetic energy from the inhaled air stream to the powder, whereas active devices use an additional source of energy, i.e., compressed air or mechanical force. The extent and efficiency of this energy transfer depend upon the construction of the inhaler as well as the inspiratory flow of the patient and ultimately determine the particle size distribution of the aerosol generated [71, 72, 100].

3.1 Dispersion in Passive Dry Powder Inhalers

Passive dry powder inhalers rely on the inspiratory flow as the sole source of energy for powder fluidization and particle deagglomeration. The powder formulation is metered and/or released from the site of storage and primarily fluidized by shear force. Particle deagglomeration can occur due to a variety of mechanisms that include relative motion (the different motion of the particles relative to the air stream), turbulence, shear stress and collision. Each mechanism occurs to a different extent in all inhalers. In the following section, devices used for the generation of dry powder aerosols are described and an attempt is made to pinpoint the dominant mechanisms of powder fluidization and particle deagglomeration (**Table 2**). Fine particle fractions as defined in section 3.3.5 are quoted from the literature to indicate

Table 2 Principal mechanisms of powder fluidization and dispersion in dry powder inhalers

Inhaler	Carrier	Doses	Powder supply	Fluidization	Dispersion
Spinhaler™	–	1	capsules	mechanical	shear force, relative motion
Rotahaler™	lactose	1	capsules	mechanical	turbulence
Inhalator M™	glucose	1	capsules	capillary	shear force
Inhalator Ingelheim™	glucose	6	capsules	capillary	shear force
Diskhaler™	lactose	4, 8	blister	shear force	turbulence
Diskus™	lactose	60	blister	shear force	turbulence
Turbuhaler™	–	200	bulk reservoir	shear force, capillary	shear force
Easyhaler™	lactose	200	bulk reservoir	shear force	turbulence
MAGhaler™	lactose	200–500	tablet	mechanical	mechanical
Spiros™	n/a[1]	1, 16 or 30	unit dose, blister or cassette	mechanical (active)	turbulence, impaction, shear force
Prohaler™	Mannitol[2]			gas assist (active)	turbulence, shear force
Dynamic Powder Disperser™	lactose	12	cartridge	gas assist (active)	turbulence, shear force
Inhale™ Device	lactose	1	blister	gas assist (active)	turbulence, shear force

[1] data not available
[2] [167]

the efficiency of particle deaggregation. A number of other inhalers are currently being developed. These include but are not limited to the Ultrahaler (Rhone-Poulenc Rorer, USA), the Clickhaler (ML Laboratories, UK) and others (Sepracor, USA; Norton, UK; Chiesi, Italy).

3.1.1 Spinhaler™

The Spinhaler™ (Fisons, UK) is a unit dose powder inhaler designed for the inhalation of drugs from gelatin capsules [**Figure 8a**]. The capsules contain 20 mg of micronized drug without carrier and are mounted onto an impeller in the inhaler. A piercing mechanism punctures the inserted capsule. Inhaled air causes the impeller and thus the capsule to rotate at a speed that is dependent on the air flow rate. At sufficiently high flow rates the capsule vibrates leading to mechanical fluidization [16]. This is supported by capillary fluidization due to the pressure drop across the capsule. The powder is conveyed along the capsule walls towards the perforations where it is discharged and enters the airstream. Shear force and relative motion are the predominant mechanisms of powder deaggregation. The high interparticulate forces expected in micronized powders are reflected in low *in vitro* fine particle fractions of 4−12% [55, 228].

3.1.2 Rotahaler™

The Rotahaler™ (GlaxoWellcome, UK) is a single dose device for the inhalation of powder (lactose blends) from gelatin capsules [**Figure 8b**] . A capsule is inserted in the end of the inhaler opposite the mouthpiece. The capsule is broken in half by turning the rear part of the inhaler relative to the mouthpiece, with one half of the capsule falling into the inhaler and the other remaining fixed to the inhaler wall. Powder fluidization from the loose half of the capsule is induced mechanically by vibration and impaction, as well as by shear force, as the capsule swirls around in the inhaler. Powder in the half of the capsule remaining attached to the inhaler will be removed by capillary fluidization and gravity. Particle deaggrega-

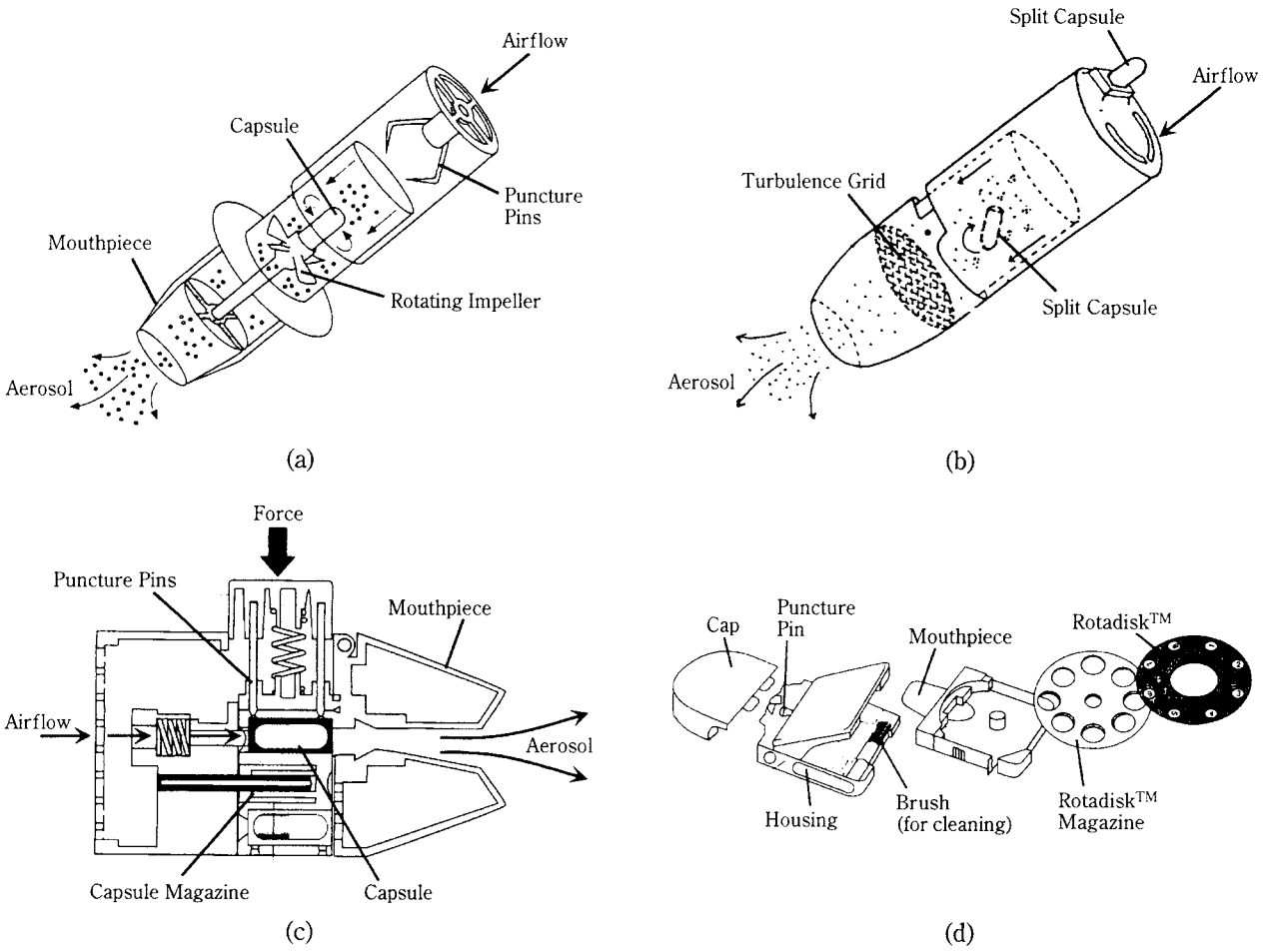

Fig. 8 (a) Spinhaler: modified from [113] (b) Rotahaler: modified from [53] (c) Inhalator M: modified from [113] (d) Diskhaler and Rotadisk: modified from [113].

tion is mainly caused by turbulence promoted by the grid upstream of the mouthpiece. A fine particle fraction of 26% has been reported for this device actuated at 56.5 L/min [190].

3.1.3 Inhalator Ingelheim™

The single dose Inhalator Ingelheim™ (Boehringer Ingelheim, Germany) is designed for the inhalation of drug-glucose blends from gelatin capsules. A capsule is inserted into a narrow container in the inhaler. The capsule is pierced at both ends by pressing a button on the inhaler. In contrast to the Spinhaler™, the capsule is stationary and emptying occurs primarily by capillary fluidization due to the high pressure drop across the capsule. Deaggregation is caused by shear stress and collision. Fine particle fractions (<6.4 μm) for oxitropium bromide have been reported to be approximately 27% at 30 and 60 L/min [228].

3.1.4 Inhalator M™

The Inhalator M™ (Boehringer Ingelheim, Germany) is a multiple unit dose powder inhaler similar to the single dose Inhalator Ingelheim™ [**Figure 8c**]. In contrast to the above, however, Inhalator M™ has a rotating drum magazine for the storage of six capsules. The mechanisms for capsule emptying, powder fluidization and particle deagglomeration are the same due to the construction similarities. Fine particle fractions of 28 and 36%, in the twin and multistage impinger, have been reported for ipratropium bromide [228].

3.1.5 Diskhaler™

The Diskhaler™ (GlaxoWellcome, UK) is a multiple unit dose inhaler. The inhaler housing contains a magazine and a rotating disk that hold the Rotadisk™, a disk-shaped blister pack containing four or eight single doses of powder [**Figure 8d**]. The powder formulation consists of drug blended with lactose. When the hood of the inhaler housing is folded up, a blister is perforated by a pin and the powder becomes accessible for inhalation. As the inhaled air flows across the powder bed, the powder is aerosolized primarily by shear force fluidization and transported to the mouthpiece. The aerosol stream is then mixed with a bypass flow entering through two holes in the mouthpiece. The additional airflow and a grid in the mouthpiece give rise to turbulence that promote deagglomeration [229]. Fine particle fractions (<6.4 μm) for the albuterol sulfate formulation Sultanol™ 200 Rotadisk™ were reported to be approximately 30% [114, 228]. A fine particle fraction (<7 μm) of 23% was measured for the Becotide™ Rotadisks™ [55].

3.1.6 Diskus™

The Diskus™ (GlaxoWellcome, UK) is a multiple unit dose inhaler that contains a foil strip with 60 single dose blisters of drug blended with lactose [**Figure 9a**]. A blister is transported towards the mouthpiece and the lid foil is stripped off prior to inhalation. Air is channeled through the inhaler and the powder is aerosolized by shear force fluidization. Additional air is drawn through two holes in the mouthpiece, similar to the Diskhaler™, to augment particle deaggregation by turbulence [21]. The Flutide™ Diskus™ was reported to deliver a fine particle fraction (<6.4 μm) of 25−30% fluticasone-17-propionate at 60 L/min [228].

3.1.7 Turbuhaler™

The Turbuhaler™ (Astra, Sweden) is a multiple dose inhaler with 200 doses of drug stored in a reservoir [**Figure 9b**]. The micronized drug is spheronized into small pellets rather than blended with a carrier. The pellets are stable in terms of transport and handling but disintegrate into their primary particles during metering and inhalation [249]. The dosing unit is caused to rotate by turning the grip at the bottom of the inhaler. Scrapers actively force drug from the reservoir into conical holes of the dosing unit. The pellets disintegrate and a single dose of drug is metered and ready for inhalation. Air enters the inhaler and passes through the dosing unit across the powder bed during inhalation, fluidizing the powder by shear force. Additional capillary fluidization occurs due to the direction of the air flow entering the inhaler. After fluidization, particle deagglomeration occurs by three mechanisms: turbulence in the narrow inhalation channel, impaction on the bottom of the mouthpiece, and predominantly high shear stress in the swirl nozzle of the mouthpiece [121, 248]. Different studies with the Aerodur™ Turbuhaler™ showed fractions of 47% [114], 50% [121], 32 and 35% [228] terbutaline sulfate below 6.4 μm . Fine particle fractions of 39 − 45% budesonide have been reported for the Pulmicort™ Turbuhaler™ [55, 182, 228].

3.1.8 Easyhaler™

The Easyhaler™ (Orion Farmos, Finland) is a multiple dose powder inhaler with 200 doses of drug-lactose blend stored in a reservoir [**Figure 9c**]. The metering system is based on gravitational flow of the powder from the reservoir into a cavity in the metering cylinder. Potential energy is supplied by shaking the inhaler to assist flow from the reservoir. Depression of the device overcap, similar to a pressurized metered-dose inhaler, causes the metering

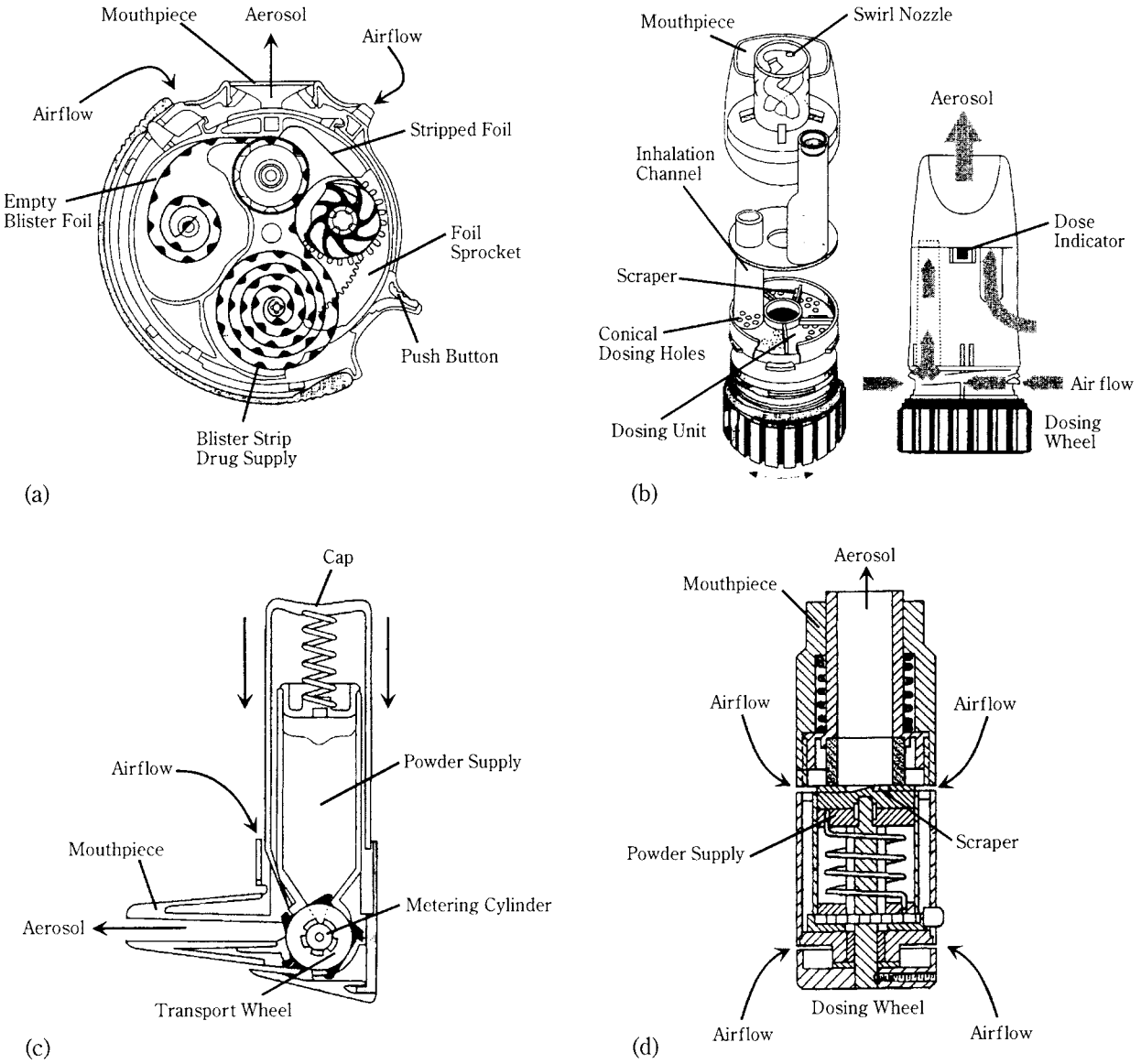

Fig. 9 (a) Diskus: modified from [113] (b)Turbuhaler: modified from [113] (c) Easyhaler: modified from [113] (d) MAGhaler: modified from US patent 5,673,685.

cylinder to rotate and a single dose of powder is transported towards the mouthpiece. Inhaled air passes along the powder bed in the metering cavity and fluidizes the powder by shear force. Turbulence in the long narrow inhaler mouthpiece causes further particle deaggregation. Fine particle fractions (<6.4 μm) of 32% [114], 36–39% [228] and 45%[240] at 60 L/min have been reported for a salbutamol powder blend.

3.1.9 Mechanical Aerosol Generator™

The multi-dose Mechanical Aerosol Generator™, or MAGhaler™, (Gesellschaft für Gesundheits und Umweltforschung GmbH, Germany) is a multiple unit dose inhaler [**Figure 9d**]. The principle of operation differs substantially from other passive devices. The drug is not supplied in the form of a powder, but as a ring-shaped tablet that contains 200 to 500 doses of micronized drug and lactose, compressed by high pressure isostatic compaction. The inner bore of the ring comprises the inhalation channel. Dose metering and powder dispersion are essentially one step, performed by a motor driven ceramic scraper. A fine disperse powder is scraped off the surface of the tablet (mechanical fluidization) into the inhalation channel during inhalation. The aerosol generated is very dilute and is inhaled *in statu nascendi*, before the particles can aggregate. Relative motion and turbulence promote deaggregation. Fine particle fractions (<6.4 μm) between 30 and 50% have been stated for a variety of drugs by the manufacturer.

3.2 Dispersion in Active Dry Powder Inhalers

Active dry powder inhalers have an additional source of energy than that provided by inhalation, using auxiliary means to fluidize and disperse the powder. The basic principles for powder fluidization and dispersion are the same as passive devices, however, the additional energy input decreases or eliminates the dependence of the aerosolization process on the patient's breathing pattern and reduces dose and particle size variabilities [47]. A number of devices are currently under development though to date none have been approved [42, 59, 69, 82, 122, 191, 215]. Hence, no drug formulations for these devices are on the market but studies using both carrier blends and unblended drugs have been published [25, 47, 104, 161, 162, 167].

3.2.1 Spiros™ Dry Powder Inhalation System

Spiros™ (Dura Pharmaceuticals, San Diego, USA) is a power assisted single-unit or multiple-unit dose (blister, cassette) inhalation system [**Figure 10a**]. A mechanical plunger ejects the drug from the reservoir into a mixing chamber (mechanical fluidization). A breath activated, motor driven impeller, rotating at 12000 to 14000 rpm, provides electromechanical energy to disperse the powder formulation by shear force, turbulence and impaction [59, 161]. This mechanism greatly reduces the effect of inspiratory flow on the fine particle fraction. Fine particle fractions between 26 and 32% have been reported using the albuterol sulfate lactose blend from Rotacaps™ at flow rates of 15 to 60 L/min [104].

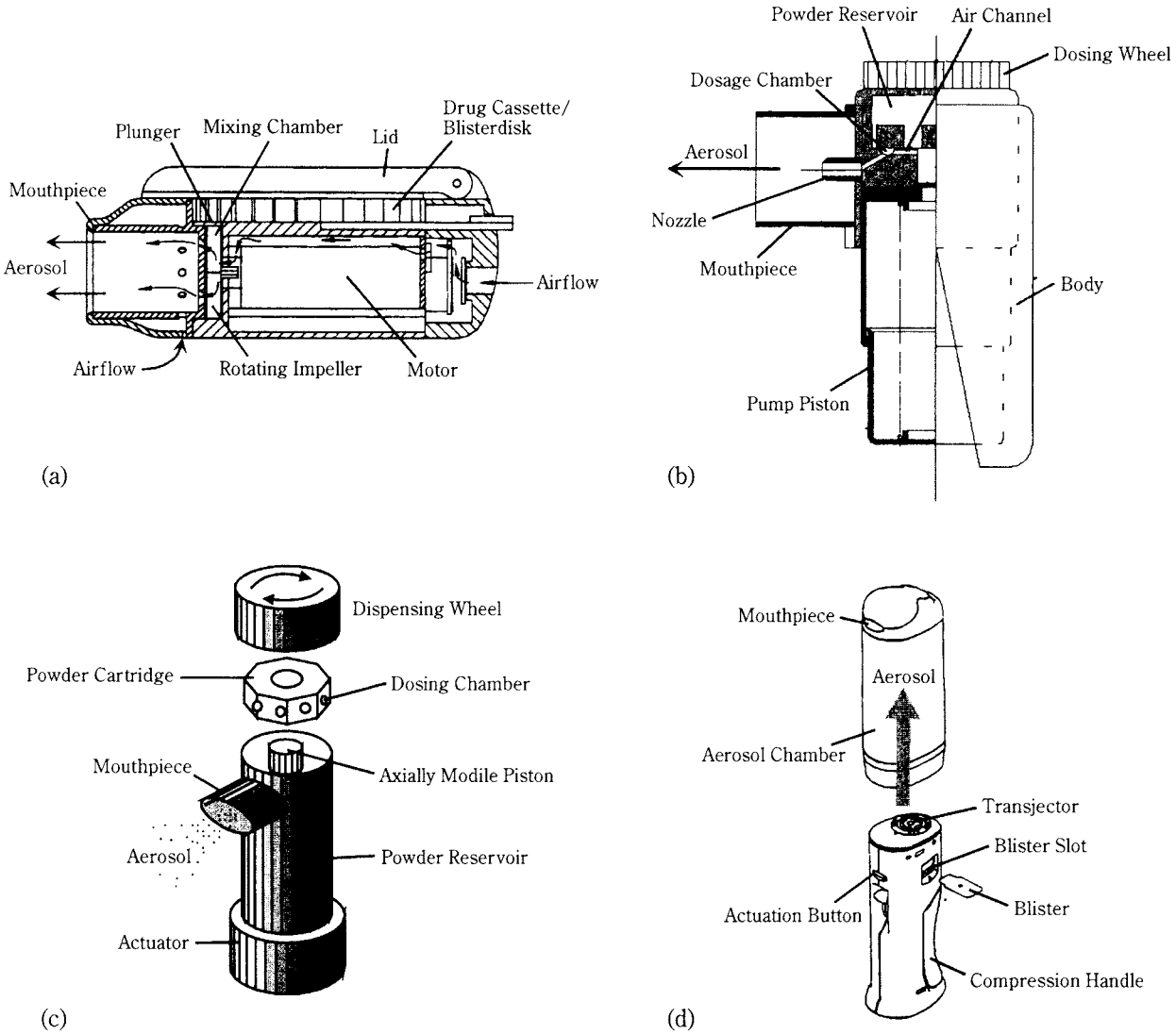

Fig. 10 (a) Spiros: modified from [160]. (b) Prohaler, courtesy of Valois, (c) Pfeiffer Dynamic Powder Disperser: modified from [47]. (d) Inhale dry powder inhaler: modified from [118].

3.2.2 Prohaler™

The Prohaler™ (Valois Pharm, France) is a multi dose powder inhaler where a built-in pump provides compressed air to facilitate dose metering and powder dispersion [**Figure 10b**]. Air assisted powder fluidization reduces the influence of inspiratory flow on fine particle fraction and ensures effective powder dispersion [25]. Fine particle fractions (<6 μm) for a mannitol blend of the leukotriene antagonist SKF-104353 were reported to be 68% [167].

3.2.3 Dynamic Powder Disperser™

The Dynamic Powder Dispenser (Pfeiffer GmbH, Germany) is a multiple unit dose inhaler featuring an exchangable cartridge that holds 12 dosing chambers [**Figure 10c**]. The inhaler is primed by an axially mobile piston that compresses air in the inhaler. The compressed air in the device is expelled through the dosing chamber in the cartridge upon manual actuation and an aerosol is generated by gas assist fluidization. Studies with a 2% albuterol sulfate blend showed fine particle fractions (<5 μm) of up to 40% [47].

3.2.4 Inhale Deep Pulmonary Drug Delivery System

The Inhale deep pulmonary drug delivery system (Inhale Therapeutic Systems, USA) is a gas-assisted dry powder inhaler designed mainly for the systemic delivery of insulin and other biomolecules through the lung [**Figure 10d**]. Insulin is spray dried together with lactose acting as a stabilizing agent. The resulting fine powder (1−3 μm) is packaged in unit dose blisters [118, 191].The base unit of the inhaler contains a mechanical air compression mechanism, a lever to transport and puncture the blister package and a transjector. Prior to inhalation, the inhaler is cocked and a small amount of air is compressed inside the inhaler. A blister is inserted, elevated to the transjector and punctured. When the inhaler is actuated, the compressed air is released through the transjector at sonic velocity. The powder is withdrawn from the blister during this process and aerosolized by gas-assist fluidization. Turbulence and shear force are the main factors for further deagglomeration. The aerosol is then released into a holding chamber with a combined mouthpiece/chamber cap on top from where it can be inhaled.

3.3 Inhaler Performance Criteria

Particles need to have aerodynamic diameters below 5 μm for deposition in the lung [26, 89, 232]. The fine particle fraction delivered from a dry powder inhaler is determined by three independent factors: the powder formulation, the inhaler and the patient [72]. Ideally, an optimal dry powder inhalation would reproducibly generate the same emitted dose and fine particle fraction in order to induce an equivalent pharmacological effect in all patients. In reality, both emitted dose and fine particle fraction vary, depending on patient specific parameters (inspiratory flow rate, handling) and ambient conditions (humidity, electrostatics).

Both powder and air flow have been characterized in a number of idealized systems. Static and dynamic angle of repose and flow from a vibrating spatula have been used to assess global flow parameters of powders [94], as described in section 2.2. Airflow has been characterized in detail in the engineering literature [154, 250]. However, the complex relationship of air flow and particle dispersion in dry powder inhalers is just beginning to be understood and a number of methods have been proposed to gather information that is relevant for these heterogeneous systems [39, 93, 95, 132, 133, 144, 200, 224, 256]. In the following, the relevant criteria influencing the performance of dry powder inhalers are discussed.

3.3.1 Inhaler Flow Resistance

The specific flow resistance of a device is related to pressure difference and volumetric flow rate, as follows:

$$R = \frac{Q}{\sqrt{\Delta P}} \tag{14}$$

where R is the specific flow resistance, Q is the air flow rate and ΔP is the pressure drop across the device [188]. R is dependent on the internal geometry of the inhaler and the dimensions of the air channels. A wide range of values for a variety of commercially available dry powder inhalers has been reported and is summarized in **Table 3** [39, 228]. The flow rate through an inhaler can be approximated as the ratio of the square root of the minimum inspiratory mouth

Table 3 specific resistance and classification of dry powder inhalers [39, 228]

Device	specific resistance [cm $H_2O^{1/2}$/L min^{-1}]	classification
Rotahaler	0.040	low
Spinhaler	0.051	low
ISF Inhaler	0.055	low
Diskhaler	0.067	low
Diskhaler	n/a	medium
Turbuhaler	0.100	medium
Inhalator Ingelheim	0.180	high
Inhalator M	n/a	high
Easyhaler	n/a	high

pressure and the device resistance, the resistance of most inhalers exceeding that of the airways [41]. Minimum inspiratory oropharyngeal pressures reported in the literature are generally in the range of 110−140 cm H_2O for normal, healthy individuals, slightly lower (90−115 cm H_2O) for cystic fibrosis patients and still lower (60−70 cm H_2O) for patients with chronic obstructive pulmonary disease [41]. This has important consequences. The flow rate through an inhaler at a constant inspiratory effort (pressure differential) will be device dependent. Also, the flow rate through a specific inhaler will be dependent on the patients' inspiratory effort. The air flow generated by the patients' inspiratory effort is, however, the sole source of energy for powder fluidization and dispersion in passive dry powder inhalers. Hence, the accuracy of the dose and the fine particle fraction delivered by these devices depend on the specific resistance of the inhaler and the inspiratory flow rate generated by the patient [40, 55, 107, 174, 176, 257]. This has further implications in the selection of the appropriate *in vitro* testing methods. Dry powder inhalers have to be tested at flow rates that match their specific resistance to yield meaningful results. It has been proposed that high resistance inhalers (>0.12 cm $H_20^{1/2}$/L min^{-1}) should be tested at a flow rate of 30 L/min, low resistance devices (<0.07 cm $H_20^{1/2}$/L min^{-1}) at 100 L/min and inhalers with intermediate resistances at 60 L/min [29, 39, 109].

3.3.2 Powder Formulation

Formulation of powders suitable for inhalation require that particles are of sufficiently small size to reach the target site in the lung (D_{ae}<5 μm). However, the intrinsic cohesiveness of such fine powders opposes accurate metering, gives rise to the formation of agglomerates, and impedes the production of primary respirable particles. A variety of approaches have been taken to overcome this challenge and to optimize powder formulations for delivery to the lung in parallel to the development of active inhalers.

A coarse, inert carrier such as lactose or glucose is frequently blended with the drug to facilitate dispersion. In these interactive or ordered mixtures, the fine drug particles adhere to the surface of the carrier [88]. The adhesion force of the drug to the carrier must be sufficient to avoid demixing, but small enough to allow detachment during inhalation [71]. It has been shown that the adhesion between drug and carrier and the fine particle fraction generated from these mixtures can be influenced by a variety of factors. These include the surface properties of both drug and carrier, drug to carrier ratio, carrier particle size, mixing time and method, humidity and electrostatic behavior. Coating cromolyn sodium particles with fatty acids led to changes in the particle morphology and increased the fine particle fraction in the twin impinger approximately threefold [68]. The surface roughness (rugosity) of carriers has a pronounced influence on the adhesion of small particles. Blends using recrystallized lactose with low rugosity gave significantly higher fine particle fractions than crystalline and spray-dried lactose with higher rugosity [127, 226, 258]. Increasing the drug to carrier ratio has been shown to increase the respirable fraction [48, 71, 213], but the opposite effect has also been reported [228]. Decreasing the carrier particle size has been shown to increase the fine particle fraction of a powder blend [48, 128, 129, 228]. The conditions under which a powder blend is processed influence the fine particle fraction. Blending time promotes mechanical interlocking and friction [135], whilst the blending procedure can strongly influence the fine particle fraction [44]. The addition of a ternary component such as magnesium stearate, fine lactose or L-leucine to interactive mixtures can destabilize the mixture and increase the respirable fraction [44, 128, 145, 192, 226].

Spray drying of the drug has been used as an alternative to jet milling in the production of fine powders. The advantages of this method are control of the particle size, shape and surface properties [212]. Vidgrén *et al.* showed that a powder formulation of spray dried sodium cromoglycate produced a significantly higher fine particle fraction than micronized drug [239]. The morphology of spray dried particles has been varied systematically by adding sodium chloride, the fine particle fraction changing proportionally with the salt content [34].

The formulation of carrier-free powder aerosols is a different approach to interactive mixing with carriers. Micronized particles can be agglomerated into soft pellets with small amounts of solvents using conventional granulation methods, which is applied in the Turbuhaler™. These pellets have good flow properties and can be engineered to disintegrate into respirable particles during inhalation [130, 249]. A novel approach to particle engineering has recently been reported by producing large, porous particles with mean geometric diameters up to 30 μm. These particles have good flow properties and are easy to disperse, with an aerodynamic diameter that is small enough to be deposited in the lungs, due to the low particle density [60].

3.3.3 Humidity

Humidity can have a profound effect on the performance of a dry powder aerosol. This can be attributed to two factors: capillary condensation and hygroscopic growth. Capillary condensation between particles in close proximity can occur around or above 65% relative humidity [214, 242]. The resulting capillary force surpasses all other interparticulate forces and strongly adds to particle adhesion (**Table 1**, section 2.1) [19, 200]. Additionally, particles absorb moisture when the ambient humidity exceeds the critical relative humidity of hygroscopic compounds. Hygroscopic growth occurs until the particles start to dissolve and form droplets [96, 123, 184]. Capillary condensation and hygroscopic growth strongly reduce the fine particle fraction of powder aerosols. Fine particle fractions of cromolyn sodium, albuterol and albuterol sulfate powder aerosols were reduced at high temperatures and humidities [25, 123, 124, 220]. Similar effects were reported for the Buventol Easyhaler™, the Intal Spinhaler™ and the Pulmicort Turbuhaler™, though not for the Ventolin Rotahaler™ [109, 114]. Salmeterol xinafoate lactose blends developed strong capillary forces during storage at relative humidities above 75%, that were irreversible after storage at low humidities [200]. The metering and the dose emission of dry powder inhalers can also be affected by humidity, as the capillary forces impede the flow properties of the powder [109, 114].

Protective measures have to be taken to minimize the detrimental effects of humidity on the performance of dry powder aerosols. This can be achieved by using desiccants that adsorb moisture from the air close to the powder formulation (Turbuhaler™). The access of humidity to the powder can be prevented by a protective housing (Turbuhaler™, Easyhaler™) or by hermetically sealing the powder in aluminum blisters (Rotadisk, Diskus™, Spiros™, Inhale device). Another approach is the development of formulations that are less sensitive to humidity. This has been achieved by modifying the particle surface with hydrophobic agents [97], the use of suitable carriers such as lactose [109] or by selecting hydrophobic salts of the drug. Fine particle fractions of free albuterol base and albuterol sulfate both decreased with increased humidity and temperature, whereas the hydrophobic salts, albuterol adipate diethanolate and albuterol stearate, remained largely unaffected [123].

3.3.4 Electrostatics

Two main mechanisms can lead to the formation of electrostatic charges in dry powders. When dry, non-conducting particles come into contact with other particles or surfaces, triboelectric charging occurs. When particles of different work functions are brought into contact, or are detached, a potential difference is formed. The resulting electrostatic forces can contribute significantly to the cohesion of particles in a gaseous environment. However, electrostatic charging is inhibited by humidity due to the adsorption of water on the particle surface which ultimately leads to the system decharging at humidities above 50-60% [125, 242]. Consequently electrostatic and capillary forces in a powder are mutually exclusive. This leaves a narrow window of optimal relative humiditiy (depending on the powder) where the effects of electrostatic charging and capillary condensation are minimized.

Electrostatic charges have influence on all aspects of powder formulation, affecting the flow properties, powder mixing and particle separation [222, 224]. Deposition of particles in the lung is also affected by aerosol charge [12, 87, 163] and drug retention in inhalers is related to the charge on the devices [14, 15, 180]. The electrostatic properties of drugs and blends of albuterol sulphate with lactose in two inhalers have been analyzed. It was proposed that blending powders in metal vessels would aid powder homogeneity, while the plastic of the DPI devices should enhance the separation of drug particles from the carrier [193]. The fine particle charge on budesonide and terbutaline sulphate aerosols emitted from the Turbuhaler™ and on aerosols generated with the Dryhaler™ has recently been determined [28]. While no dependence of the fine particle fraction on the charge was reported, it was shown that charges depended on the powder investigated as well as on the inhaler device and its deagglomeration mechanism [28].

3.3.5 Emitted Dose Characteristics

The quality of dry powder aerosol dispersion is determined by the uniformity of the emitted dose and the fine particle dose. As discussed previously, these parameters depend on the inhaler device, its flow resistance, the powder formulation, humidity, electrostatic effects and last but not least, the patient.

The term "dose" requires clarification as there has been considerable debate and confusion regarding the terms metered-, delivered-, emitted-, respirable-, fine particle dose and fine particle fraction [**Figure 11**]. The dose dispensed from the bulk powder by the metering mechanism of a multiple dose inhaler, or the dose contained in pre-packed units in single or multiple-unit dose inhalers is generally defined as the metered dose [73]. The dose delivered by the inhaler

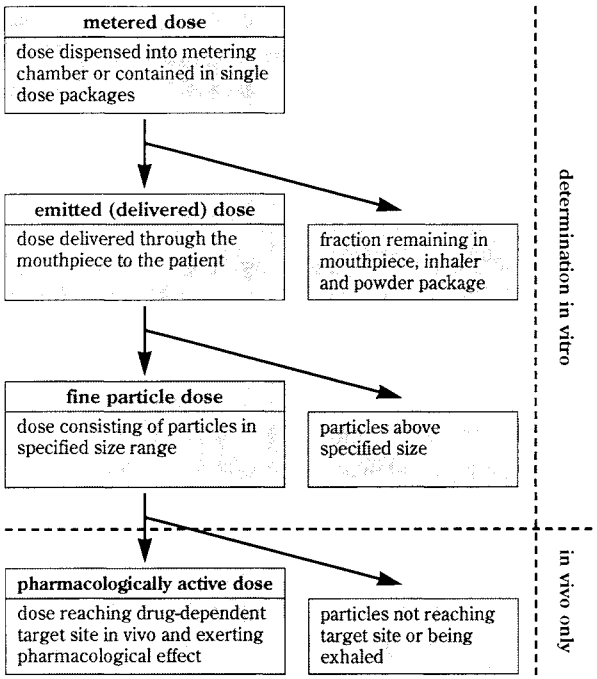

Fig. 11 Definition of terms used in describing the dose from a dry powder inhaler.

to the patient is called the emitted dose or delivered dose. Hence, emitted dose equals the metered dose minus the fractions of the dose remaining in mouthpiece, inhaler, metering chamber and unit dose container. The emitted dose is composed of particles of varying size that will partially deposit in the airways depending on their aerodynamic characteristics, inhalation characteristics and airway geometry. The terms "respirable" versus "non-respirable" dose are often used to further characterize the emitted dose. This may lead to confusion as the term "respirable" neither defines a certain particle size nor indicates a specific site of deposition, but simply indicates inhalation and transport into the airways beyond the oropharyngeal region. Further consternation is added as the terms fine particle fraction and dose have specific definitions relating to inhalation hazards in the field of occupational and environmental medicine [110]. Moreover, for development and quality control purposes, inhalers are generally characterized *in vitro* by methods based upon impaction, whereas a number of additional mechanisms contribute to particle deposition *in vivo* [89, 141, 232]. Hence, the term "respirable" cannot legitimately be used for fractions determined by *in vitro* deposition. In contrast, the term fine particle aerosol dose, or fraction, appears superior, as it does not promote speculative interpretation, especially when stated with the respective particle size range. The fine particle dose is thus defined as the dose that can be inhaled and is theoretically available for pharmacological activity. It has become the convention to consider the fine particle dose (FPD) rather than the fine particle fraction (FPF), since it is the dose which will result in a pharmacological effect. FPF is useful to compare the dispersion properties of different inhalers or formulations, but does not allow conclusions to be drawn in terms of pharmacological activity unless quoted with the emitted dose.

Few comparative studies characterizing the emitted dose of commercially available dry powder inhalers have been published. The dose accuracy and reproducibility of the Spinhaler™, Turbuhaler™ and Diskhaler™ at different flow rates as recommended by the USP advisory panel on aerosols [27] have been determined [107, 109]. Steckel and Muller focused on the fine particle dose of 11 commonly used dry powder inhalers at different flow rates using a twin and four stage impinger, listing the delivered and emitted doses found at 60 L/min [228]. The results are summarized in **Table 4**. De Boer *et al.* determined the effect of inspiration time and flow rate on the dose discharge of Turbuhaler™, Diskhaler™ and Spinhaler™ (since no numbers are given, these data are not included in [**Table 4**]) [55]. Generally, the emitted doses differed substantially from the label claim and increased with higher flow rates. Exceptions were the Easyhaler™ and the inhalers using cromolyn sodium capsules, for which label claims and emitted dose were in reasonable agreement (±15%). The emitted dose for the Spinhaler™ decreased at a higher flow rate. Unit dose variations were generally below ±15% [107] and thus meet the criteria presently advocated [29], with the exception of the Turbuhaler™. The metering of small doses of micronized powders is difficult, especially if the powders are unblended, due to their intrinsically poor flow properties. This is particularly relevant for the Turbuhaler™ which has a powder load of only 0.5 mg, leading to variations in dose uniformity. Nevertheless, the Turbuhaler™ has been an effective device in Europe and has recently been approved in the USA [51, 185, 218]. It has been postulated that the dose variabilities of dry powder inhalers may be within the extreme variability of drug deposition in the lungs [107].

The fine particle fractions emitted from dry powder inhalers and their dependence on flow have been analyzed in numerous studies [40, 55, 104, 114, 115, 121, 160, 174, 176, 228, 240]. Generally, the fine particle fraction increases with air flow rate. The strength of this effect depends on the formulation and the device. Air flow rate is of particular importance for medium

Table 4 Dose delivery of commercially available dry powder inhalers [107, 228]. Results determined at the flow rates proposed by the USP advisory panel on aerosols [27] are printed in bold.

Dry Powder Inhalation	Emitted dose[1] [%]		Delivered dose[2] [%]		Fraction remaining in mouthpiece [%]	
	60 L/min	100 L/min	TSI	MSI	TSI	MSI
Intal Spinhaler™	100.2 ± 7.6	**88.4 ± 8.9**	102.9 ± 0.6	98.7 ± 1.1	2.4 ± 0.6	1.9 ± 0.4
Flui SCG Inhaler™	–	–	101.8 ± 3.1	104.6 ± 3.8	11.9 ± 1.7	8.7 ± 0.2
Cromolyn Orion Inhaler™	–	–	106.0 ± 4.2	101.5 ± 4.6	8.2 ± 1.5	8.8 ± 0.7
Atrovent/Inhalator M™	–	–	72.1 ± 1.5	69.4 ± 1.2	21.4 ± 1.4	21.1 ± 0.3
Ventilat/Inhalator Ingelheim™	–	–	81.7 ± 3.2	76.4 ± 1.6	15.2 ± 0.9	14.0 ± 1.2
Ventolin Rotahaler™	62.7 ± 16.1	**76.3 ± 14.0**	–	–	–	–
Becotide Rotahaler™	59.5 ± 18.8	**75.7 ± 9.5**	–	–	–	–
Ventolin/Sultanol[3] Diskhaler™	52.0 ± 23.3	**68.6 ± 10.2**	72.9 ± 2.1	75.2 ± 2.4	13.3 ± 3.7	10.2 ± 0.4
Becotide Diskhaler™	55.4 ± 18.3	**72.7 ± 8.8**	–	–	–	–
Flutide Diskus™	–	–	**78.8 ± 3.0**	**84.0 ± 2.1**	**12.4 ± 0.9**	**12.3 ± 0.4**
Bricanyl/Aerodur[4] Turbuhaler™	**62.5 ± 13.7**	69.1 ± 21.1	**66.3 ± 2.1**	**64.8 ± 3.0**	**13.8 ± 1.6**	**17.3 ± 3.7**
Pulmicort Turbuhaler™	**58.1 ± 18.3**	65.7 ± 29.3	**60.3 ± 4.3**	**61.0 ± 3.6**	**28.7 ± 1.0**	**27.7 ± 2.2**
Buventol Easyhaler™	–	–	83.6 ± 2.7	86.2 ± 3.5	19.9 ± 0.2	15.8 ± 1.3
Beclomet Easyhaler™	–	–	87.7 ± 1.5	89.9 ± 2.6	17.1 ± 0.2	13.9 ± 0.1

[1] mean value ± standard deviation (n=25) of emitted dose of five single doses from five different inhalers as percent of label claim determined in the unit dose sampling apparatus [107].

[2] mean value ± standard deviation (n=3) of delivered dose as percent of label claim determined in the Twin Impinger (TSI) and the Multistage Liquid Impinger at 60 L/min. Note: single doses were determined for Intal Spinhaler™, Flui SCG™ and Cromolyn Orion™ inhalers, whereas 10 doses were determined in the other inhalers [Steckel and Müller 1997(1)].

[3] Sultanol™ and Ventolin™ Diskhaler™ are identical salbutamol sulphate Diskhalers™ marketed under different names in Germany and the US

[4] Aerodur™ and Bricanyl™ Turbuhaler™ are identical terbutalin sulphate Turbuhalers marketed under different names in Germany and the US.

and high resistance inhalers. A reduction of the air flow rate from 60 to 30 L/min resulted in a decrease of the fine particle fraction of the Turbuhaler™ to approximately one third of the original value *in vitro* [55, 160]. *In vivo* studies for the same device with flow rates of 57 and 28 L/min showed reduction of pulmonary deposition of terbutaline sulfate to approximately 50%, though the pharmacological response was not significantly affected. A strong effect of the flow rate on the fine particle fraction *in vitro* has also been shown for the Spinhaler™ with unblended cromolyn sodium. The fine particle fraction approximately doubled when the flow rate was increased from 30 to 60 and from 60 to 100 L/min [55, 228]. In contrast, the effect for cromolyn sodium lactose blends was less pronounced [228]. A strong increase in the fine particle fraction between 20 and 60 L/min was reported for the beclomethasone dipropionate Diskhaler™ [55], while in another study with the salbutamol Diskhaler™ no major change was observed between 60 and 90 L/min [228]. This may be attributed to the different powder formulations. Only small variations of the fine particle dose with flow rate were reported for Inhalator M™, Inhalator Ingelheim™ and the Easyhaler™ [228]. Few data for active dry powder inhalers are available, but it is anticipated that the fine particle fraction will be far less dependent on air flow rate, as shown for the Spiros™ inhaler [104].

Comparing these findings is difficult for a number of reasons. Firstly, the test conditions used vary widely in regard to impactor type, inlet port, onset of flow, flow rates, sampling time, environmental conditions etc., and it is known that each of these can influence the fine particle fractions determined. Secondly, the definition of the fine particle fraction itself may lead to confusion, as it depends on the impactor type and the flow rate. The mean cut-off diameter of an impactor is a function of the flow rate. Increasing the flow rate shifts the cut-off diameter of an impactor stage and the corresponding fine particle fractions towards smaller diameters [110, 252], a factor that is often ignored in the pharmaceutical literature.

With an awareness of these limitations, **Table 5** offers a comparison of the published data. A relative fine particle fraction (rFPF) is defined as the ratio of the fine particle fraction at the low flow rate to the respective fraction at the high flow rate, expressed in percent. The rFPF is a simplified measure of the effect of the flow rate on the fine particle dose of the inhaler, indicating the change in fine particle fraction when the flow rate is reduced. The cut-off diameters were recalculated for the impactors at the flow rates used, to take into account the effect of flow rate on the fine particle size range and the data included in the table [8].

The rFPF values at reduced flow rates for the different inhalers and powder formulations vary. Four groups of inhalers can be determined. The Spinhaler™,

Table 5 Effect of flow rate on the fine particle fraction (FPF) in different dry powder inhalers. The relative fine particle fraction (rFPF) is the ratio of the fine particle fractions at the low and the high flow rate, expressed in percent. The size range of the fine particle fractions has been recalculated (in italics), unless stated by the authors.

Inhaler	drug	carrier	flow rates [L/min]	Cut-Off Diameter [μm] For FPF low / high flow		rFPF [%]	Method	Ref.
Spinhaler™	cromolyn sodium	–	60/90	<6.4	<5.2	52,5	twin stage impinger (tsi)	228
	cromolyn sodium	–	60/120	n/a	n/a	42.0	lung deposition in vivo	174
	cromolyn sodium	–	60/120	<6.8	*<4.9*	54.9	multistage impinger	174
	cromolyn sodium	–	30/60	*<9.9*	<7	ca. 30	four stage impactor	55*
ISF Inhaler™	cromolyn sodium	lactose	60/90	<6.4	<5.2	80.2	tsi	228
Diskhaler™	salbutamol sulfate	lactose	60/90	<6.4	<5.2	94.8	tsi	228
	Beclomethasone dipropionate	lactose	30/60	*<9.9*	<7	ca. 68	four stage impactor	55*
Diskus™	fluticasone propionate	lactose	28/60	<5.8	<6.4	ca. 60	Andersen impactor/ tsi	67
Inhalator M™	ipratropium bromide	glucose	30/60	<9.1	<6.4	87.2	tsi	228
Inhalator Ingelheim™	oxitropium bromide	glucose	30/60	<9.1	<6.4	97.2	tsi	228
Easyhaler™	salbutamol sulfate	lactose	30/60	<9.1	<6.4	91.0	tsi	228
	salbutamol sulfate	lactose	28/60	<5.8	<6.4	69.7	Andersen impactor/ tsi	240
Turbuhaler™	terbutaline sulfate	–	28/60	<5.8	<6.8	48.0	Andersen impactor/ multistage impinger	122
	terbutaline sulfate	–	28/57	n/a	n/a	54.2	lung deposition in vivo	176
	terbutaline sulfate	–	28/60	<5.8	<6.4	24.8	Andersen impactor/ tsi	160
	Budesonide	–	30/60	*<9.9*	<7	ca. 49	four stage impactor	55*
Spiros™	albuterol sulfate (Rotacaps™)	lactose	15/60	*<12.8*	<6.4	81.7	tsi	104
	11% albuterol sulfate	lactose	15/60	*<12.8*	<6.4	121	tsi	104
Prohaler™	terbutaline sulfate	–	30/60	*<9.1*	<6.4	129	tsi, 50% RH	25
	SKF-104353-Q	mannitol	28/60	<6	<6	99.3	Andersen impactor	167

*data for 3 sec. inhalation, approximated from fig. 7 in [55]

the beclomethasone Diskhaler™ and the Turbuhaler™, produced rFPFs ≤50%. This implies that for these inhalers and respective powder formulations the fine particle dose is strongly reduced with decreasing flow rate. For a second group of inhalers, the beclomethasone Diskhaler™, the Easyhaler and Inhalator Ingelheim™, the relative fine particle fractions were between 60-80%, indicating an intermediate effect of flow rate on fine particle fraction. The salbutamol Diskhaler™, Inhalator M and Inhalator Ingelheim have rFPF values of approximately 90%, indicating a weak effect of flow rate on particle dispersion. Finally, for the active inhalers Spiros™ and Prohaler™, little effect of flow on fine particle fraction can be seen, with the exception of Spiros™ using the Rotacaps™ blend. The rFPF values above 100% can be attributed to the increase in the impinger's cut-off diameter and thus do not imply a better dispersion at lower flow rates. It is intersting to note that rFPFs calculated from lung deposition data *in vivo* for the Turbuhaler™ [176] and the Spinhaler™ [176] are in accordance with the rFPF from *in vitro* deposition studies. Despite the inherent simplifications and limitations in deriving rFPF values from different studies, it is a useful parameter when comparing the susceptability of inhalers and powder formulations to changes in flow rate.

4. Characterization

4.1 Particle Size Analysis

4.1.1 Inertial methods

The first inertial samplers were developed in the 1940s [155]. These methods were quickly adopted for evaluation of environmental and occupational exposure to airborne hazardous materials [143]. Inertial methods of particle size measurement are considered the most relevant for the description of pharmaceutical aerosols for a number of reasons. The estimation of particle size based on mass of the whole aerosol as determined by chemical analysis, such as spectrophotometry, is necesssary from a therapeutic and regula-

tory perspective [1, 27]. In addition, determination of size based on aerodynamic behavior is of relevant to particles intended for drug delivery to the lung. Deposition in the lungs occurs predominantly by inertia, similar to cascade impaction. However, lung deposition also involves other mechanisms such as interception, sedimentation, diffusion and other less significant forces [173].

4.1.1.1 Theory

Inertial methods of aerosol particle sampling are conducted by passing the airflow and suspended aerosol through an orifice of known dimensions and impinging it onto a collection surface at a fixed distance from the orifice. The Stokes number (St) is the ratio of the persistence of the particle to travel in the direction of flow to the magnitude of the barrier [206].

$$St = (\rho_p D_p U_p C)/(9 \eta \phi) \quad (15)$$

where ρ_p is the particle density, η is the air viscosity, ϕ is the jet diameter, D_p is the particle diameter, U_p is the linear velocity and C is Cunningham slip correction factor. For spherical orifices the cut-off diameters occur at a $St^{0.5}$ of 0.47.

All impactors are made to well-defined design specifications. Thus, the geometrical factors that influence the collection efficiency at a stage are constant, i.e., orifice diameter and orifice to surface distance. Flow rate is the only remaining variable influencing the collection efficiency of each stage of an impactor. The theoretical collection efficiency curve is a step function of percentage collection versus particle size [110]. From this curve there is a discrete size at which a particle population is collected with 100% efficiency and below which particles are not collected. The actual curve is sigmoidal and fractional collection efficiencies occur over a range of particle sizes [110], as shown in **Figures 12–17**. The cut-off diameter of a stage is the particle size which is collected with 50% efficiency. Most inertial impactors were designed for sampling aerosols in an industrial hygiene, occupational and environmental medicine setting [143, 147, 149, 221]. These devices were designed to operate at fixed airflow rates such that the cut-off diameters were constant. Indeed, some impactors employed critical orifices to control flow which render the system operator independent [217]. Many dry powder aerosols are delivered by the inspiratory effort of the patient, therefore, the patient's performance dictates the degree of aerosol dispersion. Variation of airflow rate affects the collection efficiency of each stage, requiring recalculation or, more appropriately, recalibration of the cut-off diameter. Impactor theory and design are based on the prerequisite of laminar airflow through the whole device. If the airflow is increased significantly, as has been suggested, then the Reynolds numbers must be recalculated and the suitability of each device to operate at a particular airflow rate must be established.

Laminar flow exists when no convective motion occurs perpendicular to the direction of airflow. The Reynolds number (Re) is based upon the kinematic viscosity of air and characteristic velocity and length of the system, e.g., diameter of the pipe/orifice or particle (see section 2.4). This must be considered as it applies not only to the passage through pipes, where the length scale is the diameter of the pipe, but also to the motion of the particles within an air stream, where the length scale is the particle diameter. The motion of respirable particles is dominated by viscous forces, i.e., low Re (<400) [110]. This is shown in **Figure 7**. Turbulence can be promoted within an impactor in regions of high fluid flow activity (Re <2–3,000 [80, 236]), e.g., flow between stages, leading to "wall loss" errors. These observations are important to the validity of impactor theory, especially when operating at high flow rates.

Inertial impactors have been employed to characterize pharmaceutical aerosols for almost 30 years [201] and have continued to be used for evaluation of propellant driven metered dose inhalers (pMDIs) throughout that period [85, 235]. The first inertial samplers to be used for pharmacopoeial standards were single stage devices [4]. These devices were used to define the "respirable fraction" or "respirable dose" for analytical purposes. Multi-stage inertial impactors have been employed for characterization of pMDIs for a number of years [103]. In the last decade multi-stage devices have also been added to the United States Pharmacopoeia [4]. However, the use of inertial samplers to characterize dry powder inhalers has a number of drawbacks. The method of sampling cannot be conducted independently of flow rate for passive inhalers [102]. Initial attempts to conduct isokinetic sampling [29, 131] were superceded by studies conducted at a number of flow rates [166]. The latter methods have the advantage of sampling the whole aerosol and avoid the potential for sampling errors. Hard collection surfaces, such as glass or stainless steel, give rise to re-entrainment by bounce and blow-off [101]. It is recommended that these surfaces are coated prior to sampling with a viscous fluid, such as silicon fluid or glycerol [78, 81]. The

doses of aerosol administered from a dry powder inhaler are large (≤25mg) in comparison with a pMDI (100μg), consequently greater wall losses occur, particularly in the upper stages of the sampler [207].

Inertial impactors offer no intrinsic description of aerosol particle size. In order to be effective instruments for the measurement of particle size these devices must be calibrated. It is usual to employ monodisperse aerosols for the calibration of inertial sampling systems. Monodisperse aerosol generators must be capable of producing aerosols with a narrow particle size distribution, as signified by a geometric standard deviation <1.2 [65]. The common methods of producing monodisperse aerosols includes the vibrating orifice aerosol generator [17], spinning top/disk generator [36, 54, 156] and the evaporation/condensation aerosol generator [170, 194, 231]. Suspensions of monodisperse polymeric lattices may be employed to calibrate inertial samplers if care is taken in the conditions of their generation [202, 205].

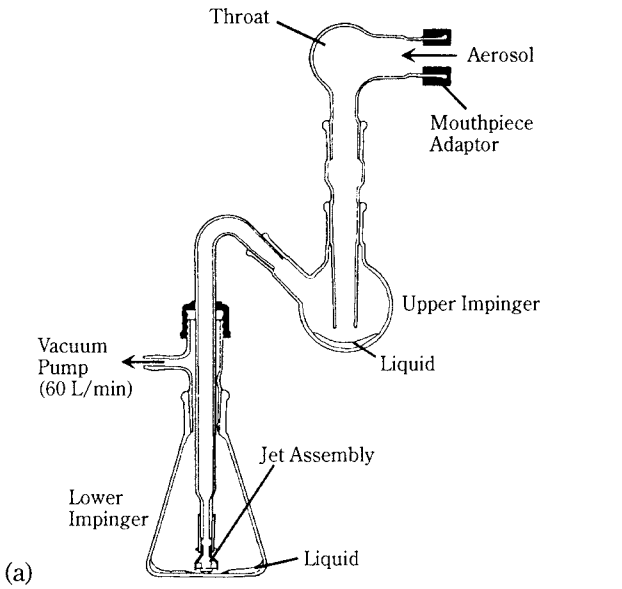

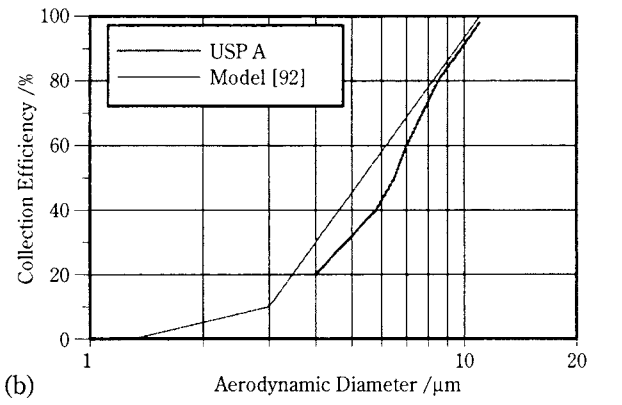

Fig. 12 (a) USP Apparatus A [85] and its (b) collection efficiency and semi-empirical oropharyngeal deposition curves [92].

4.1.1.2 Inertial Sampling Devices

USP Apparatus A

This device is a glass system composed of interconnecting flasks [84]. The device was designed to be operated at 60L/min and consists of one stage with an operational cut-off diameter of 6.4 μm. Samples are collected into a suitable liquid. **Figure 12** shows the device and its characteristic collection efficiency curve. This curve is very broad and indicates a relatively inefficient size selective sampling. However, this curve is remarkably similar to the oropharyngeal deposition curve [92].

USP Apparatus B

The USP Apparatus B is a two stage device with a cut-off diameter of 9.8 μm. The impinger consists of a metal body in which a right angled throat delivers the aerosol into the impactor [183]. The inlet to this device is apparently size selective, acting as an elutriator [115]. Thus, a proportion of the aerosol that enters the device for sizing is preclassified. Samples are collected on a solid surface and a filter which are washed to collect the drug. The standard operating flow rate of this system is 60L/min. **Figure 13** shows a diagram of the apparatus and a plot of the collection efficiency curve. This collection efficiency curve is

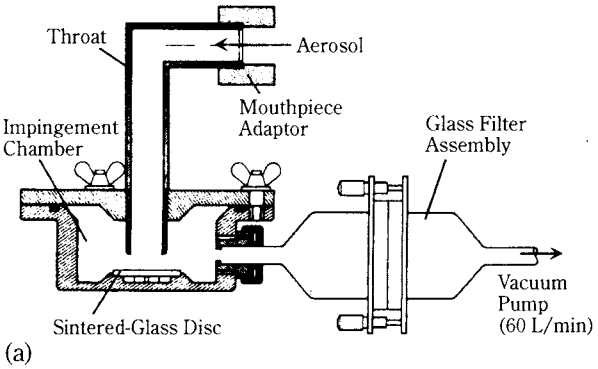

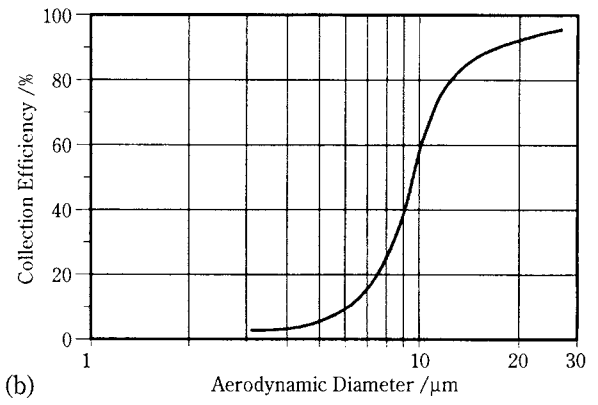

Fig. 13 (a) USP Apparatus B [22] and its (b) collection efficiency curve [43].

broad and again resembles the oropharyngeal deposition curve.

Multistage Impinger

The Multistage impinger is a four stage impinger constructed of glass (Erweka, Milford, CT) with manufacturer's cut-off diameters of 0.8, 3.3, 5.5 and 10.5 μm [210]. The use of this apparatus has become more prominent as it provides information on the particle size distribution in the respirable range. The instrument is arranged vertically and samples are collected into an appropriate liquid medium at an operating airflow rate of 60L/min. **Figure 14** shows a diagram of the device and a plot of the collection efficiency curves for a flow rate of 60L/min. This system has been calibrated at alternative flow rates of 30, 40, 50, 60, 80 and 100L/min, making it suitable for the evaluation of dry powder inhalers [8].

Andersen Impactor

The Andersen Non-Viable 1ACFM Sampler (Graseby-Andersen, Smyrna, GA) is an eight stage device with manufacturer's cut-off diameters of 9.9 (preseparator), 9.0, 5.8, 4.7, 3.3, 2.0, 1.0, 0.7, 0.4 and 0.22 (filter) μm at operating flow rates of 28.3L/min. The sampler is constructed of aluminum stages and is vertically orientated with multiple orifices at each stage, as illustated in **Figure 15**. The collection surfaces are stainless steel but may be replaced with filter paper or aluminum foil. The collection efficiencies have been recalculated for two other flow rates of 60L/min and 90L/min [236]. New stages have been manufactured to supplement or replace the original stages and maintain cut-off diameters at various flow rates. **Figure 15** also shows the efficiency curves for uncoated collection surfaces at 28.3L/min. A thor-

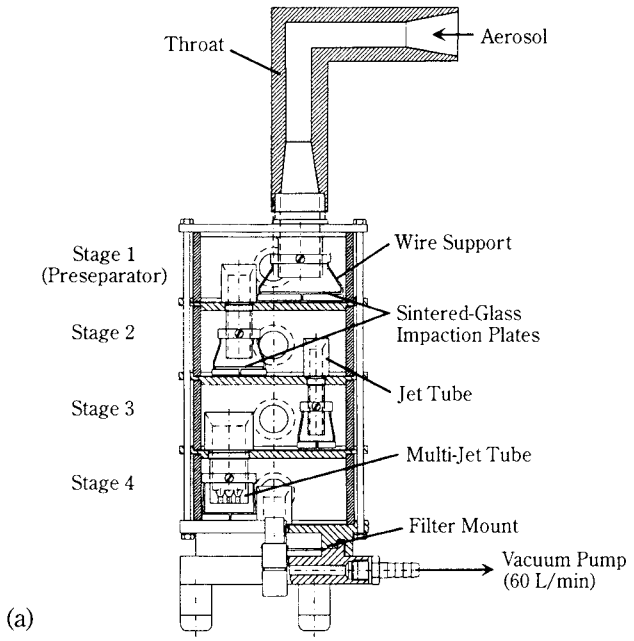

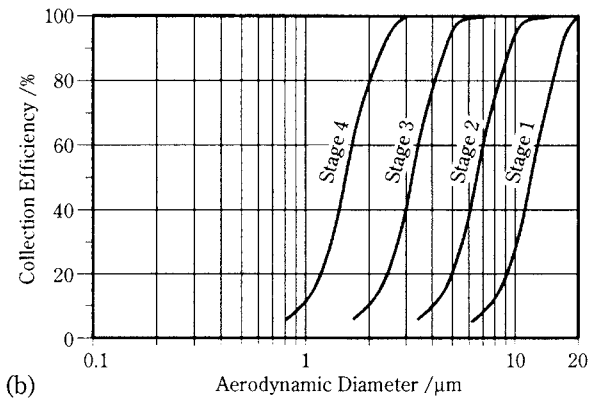

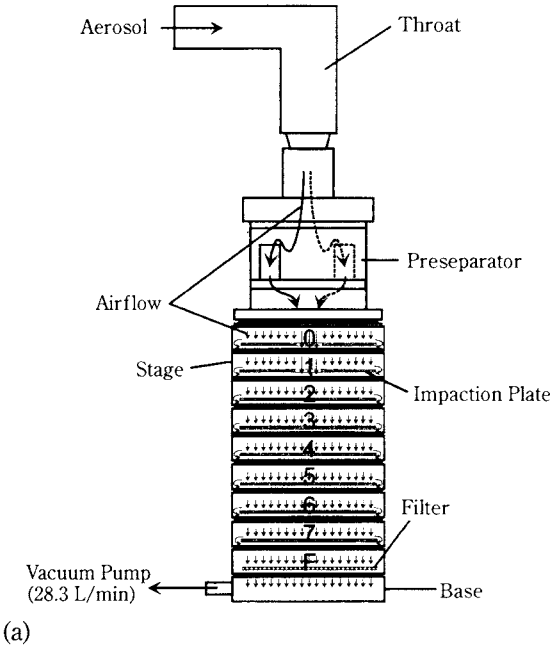

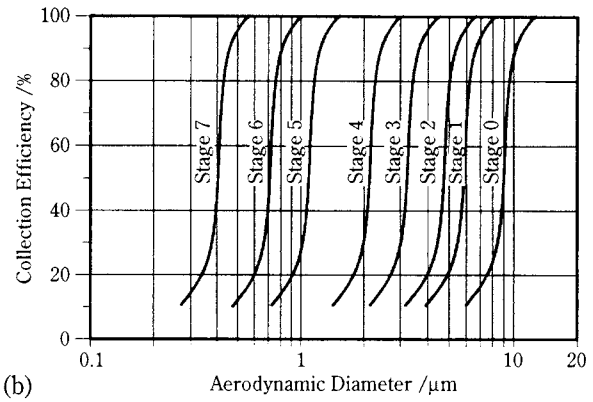

Fig. 14 (a) Multi-Stage Impinger [195] and its (b) collection efficiency curves [8].

Fig. 15 (a) Andersen Non-Viable Mark II Sampler and its (b) collection efficiency curves (courtesy of Graseby-Andersen).

ough calibration of this impactor is reported in the literature [237].

Marple Miller Impactor

A vertically orientated zig-zag inertial sampler, Marple Miller impactor (MMI) is designed specifically for evaluating pharmaceutical aerosols (MSP, Inc., St. Paul, MN [166]). This impactor consists of five stages with manufacturers' calibrated cut-off diameters of 0.62, 1.25, 2.5, 5.0 and 10.0 μm. Each stage has a single orifice and is made of anodized stainless steel. The system is arranged with collection cups which can be washed directly and was designed to operate at 30, 60 and 90L/min. **Figure 16** shows a diagram of the device and collection efficiency curves expressed at each of the operating flow rates. **Figure 16** shows a relatively narrow range of collection efficiences at each of the operating flow rates, indicating that each of these flow rates may be used providing the correct cut-off diameters are adopted

Delron Impactor

The Delron, or Batelle, impactor was one of the original vertical impactors employed for use in industrial hygiene. The DCI-6 model is a six stage stainless-steel device with manufacturers' cut-off diameters of 16, 8, 4, 2, 1, 0.5 and 0.22 (filter) μm for uncoated collection surfaces. The operating flow rate is fixed at 12.5L/min by the use of a critical orifice. The collection plates are glass and must be removed for washing. **Figure 17** Shows a diagram of the impactor and a characteristic collection efficiency curve for stage 1.

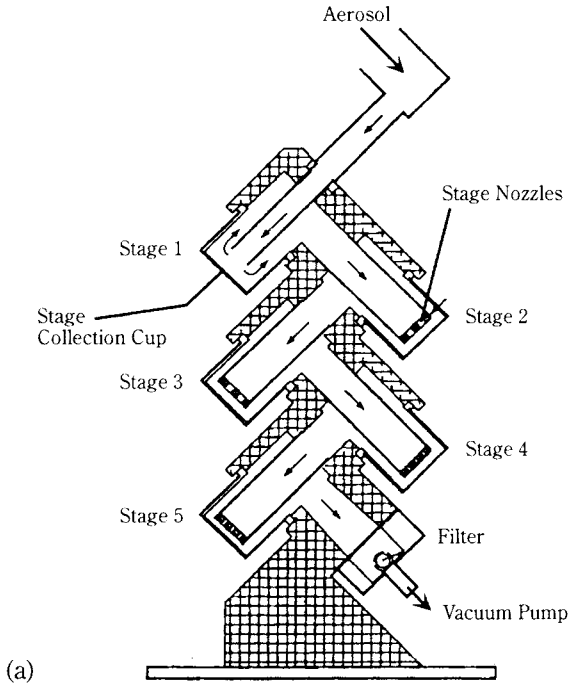

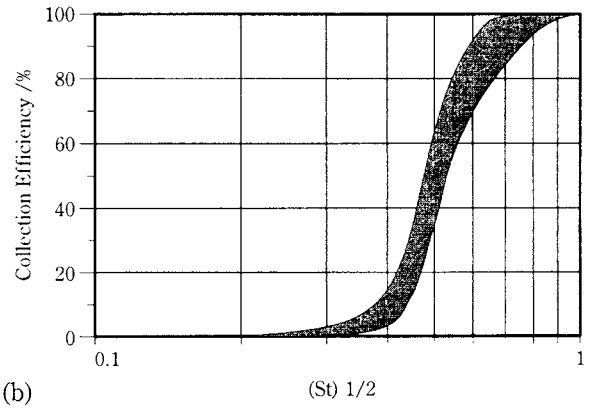

Fig. 16 (a) Marple-Miller Impactor and its (b) range of collection efficiency at 30, 60 and 90 L/min [166].

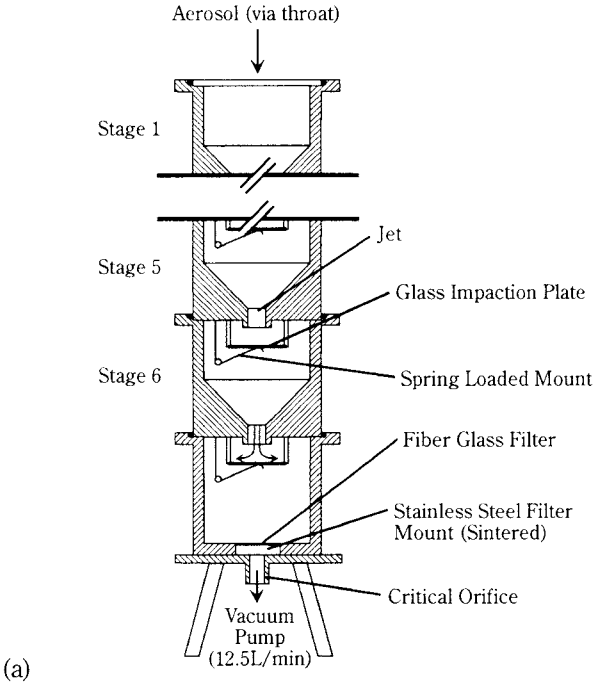

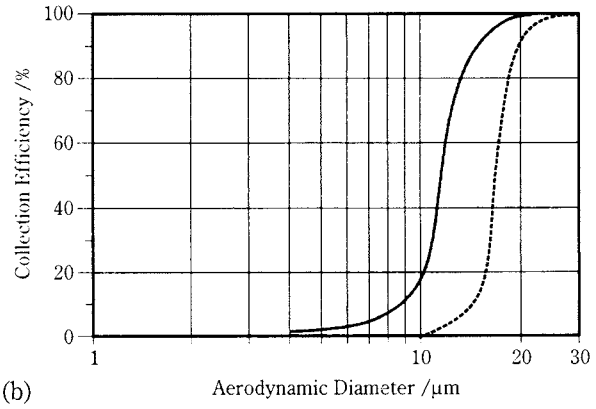

Fig. 17 (a) Delron DCI-6 and a (b) stage 1 collection efficiency curve as specified by the manufacturer (−) and calibrated with coated collection surface (−)[78].

Table 6 Calibrated Cut-Off Diameters (D_{50}, μm) for USP Apparatus A and B, Multi-Stage Liquid Impinger, Andersen Non-Viable, MSP (MMI 150 and 160) and Delron DCI-6.

Apparatus	USP A	USP B	MSI[1]				Andersen[2] (calculated[3])			MSP[4]			Delron
Flow Rate L/min / Stage	60	60	30	60	80	100	28.3	60	90	30	60	90[5]	12.5
−1	–	–	–	–	–	–	–	8.6	6.5	–	–	–	–
0	6.4	9.8	–	–	–	–	8.7 (9.0)	6.5 (6.2)	5.7 (5.1)	–	–	–	–
1	–	–	16.9	13.3	11.8	10.4	6.1 (5.8)	4.5 (4.0)	3.4 (3.3)	10.0	10.0	8.0	11.2
2	–	–	9.3	6.7	5.6	4.9	5.0 (4.7)	3.2 (3.2)	2.7 (2.6)	5.0	5.0	4.0	5.5
3	–	–	4.5	3.2	2.7	2.4	2.8 (3.3)	1.9 (2.3)	1.7 (1.9)	2.5	2.5	2.0	3.3
4	–	–	2.5	1.7	1.4	1.2	1.8 (2.1)	1.1 (1.4)	1.1 (1.2)	1.2	1.2	1.0	2.0
5	–	–	–	–	–	–	1.0 (1.1)	0.5 (0.8)	0.5 (0.6)	0.6	0.6	0.6	0.9
6	–	–	–	–	–	–	0.5 (0.7)	0.2 (0.5)	0.1 (0.2)	–	–	–	0.5
7	–	–	–	–	–	–	0.3 (0.4)	–	–	–	–	–	–

[1][8]; [2][79]; [3][236]; [4][166]; [5]As [166] 80% of 30, 60L/min. cut-off

This plot indicates the deviation of the collection efficiency from the manufacturer's specifications if the collection surface is coated, in this case with silicon fluid [78].

Table 6 is a summary of the calibrated cut-off diameters for the stages of each of the inertial sampling devices. The cut-off diameters for the multi-stage devices with solid collection surfaces, i.e., Andersen, MMI and Delron, were calibrated with coatings. The MSI was also calibrated. In each case the calibrated cut-off diameters differ from the manufacturers' specifications which highlights the need for calibration, particularly if different flow rates and collection surfaces are being employed.

4.1.1.3 Data Interpretation

It is sufficient from a quality control and regulatory perspective to plot the amount of drug sampled at each stage of the inertial impactor against the cut-off diameter for the stage. Specifications can be set on the batch to batch and through life reproducibility of inhaler performance based on this data. The multi-stage impactor data can be analyzed further. The cumulative percentage undersize, on a probability scale, can be plotted against the logarithm of cut-off diameter, so that the mass median aerodynamic diameter and geometric standard deviation can be derived [49, 110]. This information is useful in referring to data that conform to log-normality, i.e., a linear plot. The mass median aerodynamic diameter may also be derived for data that is not log-normal, i.e., a non-linear plot, but the geometric standard deviation may be misleading. It is possible to analyze the data by fitting to the calibration collection efficiency curves using non-linear methods [203].

USP Apparatus A and B were designed with deliberately broad collection efficiency curves. This follows a tradition of impactor design to approximate oropharyngeal deposition for the purposes of contrasting *in-vitro* samples with the limits established for exposure to hazardous aerosols [58, 150, 253]. The interpretation of estimates of "respirable fraction" derived by such methods has been debated in the pharmaceutical sciences and the current concensus favors the use of multi-stage devices which give more detailed information on the particle size distribution of the aerosol.

4.1.2 Optical Methods

Particle size characterization of dry powder aerosols by optical methods involves the interaction of light with individual particles (single particle counters) or with the aerosol (global characterization). The principal advantages of optical techniques are that they are generally non-intrusive, acquire rapid, real-time data and have high temporal and spatial resolution. *In situ* measurements obtained by optical methods can reveal detailed interactions between device parameters and the resultant aerosol characteristics. The main drawback of these techniques is that no discrimination between therapeutically active and inactive particles can be made. There are clear benefits of using optical particle sizing techniques to complement inertial impaction methods.

4.1.2.1 Theory

Light scattered from a surface is governed by the laws of reflection and refraction. Reflection occurs when light is redirected from a non-luminous object. Specular reflection is the simplest form of reflection and occurs when light is incident on a smooth sur-

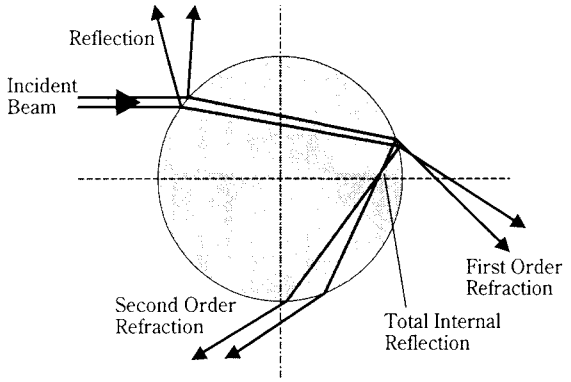

Fig. 18 Light scattering mechanisms from a spherical particle.

face. A light ray that undergoes specular reflection will have an equal angle of incidence and reflection. All surfaces exhibit, to some extent, both specular and diffuse reflection. Diffuse reflection occurs when light is incident on a rough, irregular surface and is scattered in many directions. More complex phenomena can occur depending on the material, e.g., selective absorption or scattering, fluorescence and luminescence. Refraction occurs when light is incident on the interface between two transparent media. Light will be reflected and refracted, as illustrated in **Figure 18** for a spherical particle. The degree to which light is refracted is related to the refractive index of the material (η). Total internal reflection occurs when the angle of incidence exceeds the critical angle and $\eta_p > \eta_{air}$. This affect is illustrated in **Figure 18**.

Diffraction effects occur when incident light waves interact with an obstacle, causing the light to bend. When light interacts with a single obstacle, e.g., a particle, a diffraction pattern (concentric circles of light intensity, described by the Bessel function) is produced by the superposition of secondary Huygens' sources. This is known as Fraunhofer diffraction. The diffraction pattern is uniquely related to the cross-sectional area of the particle.

4.1.2.2 Imaging Methods

Imaging techniques provide direct visual data that are easily interpreted. They may be useful to obtain information regarding particle shape, size and structure. The traditional methods of microscopy can be combined with automated methods of image analysis to measure larger particle samples and derive information on particle shape.

Microscopy

Microscopy is a method that allows the direct physical measurement of particle size and morphology. For dry powder aerosols this method may help to distinguish between drug and carrier particles and may help to detect particle agglomeration or changes in crystal form. However, limitations regarding the size resolution and the number of particles measured have to be taken into account.

Optical microscopy uses the spectrum of visible light (400−700 nm). Although it is possible to measure particles down to 0.25 μm, the measurement of particles below 1 μm is limited by the optical resolution of the instrument. This drawback can be overcome by electron microscopy that has a much higher size resolution due to the shorter Compton wavelength of the electron. The resolution of scanning electron microscopy (SEM) and transmission electron microscopy (TEM) are approximately two and three orders of magnitude greater than the optical microscope, respectively. However, artifacts due to the coating process may occur, particularly for SEM, e.g., surfaces can appear smoother than in TEM, an effect that has been attributed to the coating process [98].

A general drawback of microscopy is the extensive time required to measure sufficient numbers of particles to obtain a representative sample. A representative sample is defined as a sample in which the concentration and size distribution of particles are equivalent to the entirety. In order to achieve that aim opinions vary on the numbers of particles that should be counted. The American Society for Testing and Materials recommends that the modal class of the size distribution should contain at least 100 particles and that at least 10 particles should be present in each size class [7]. Another approach of "stratified sampling" recommends collecting data on at least 10 particles in every size class that has a significant influence on the size curve [255] Moreover, effects of the sample collection and preparation on the particle size have to be taken into account, as well as observer error due to the arbitrary determination of particle size (Martin-, Feret-, or projected area diameter). Hence, microscopy is a useful method for the acquisition of visual powder characteristics, but not a substitute for other particle sizing methods.

Image Analysis

Image analysis is used to quantitatively count, measure or classify a variety of particulate system characteristics. The image is recorded by a camera, electronically captured and subsequently processed by suitable software. Features are discriminated on the basis of gray level values to appropriate thresh-

olds. Data that can be obtained include length, diameter, area, aspect ratio and shape parameters. Image analysis can be automated, making it suitable for the analysis of large numbers of particles, so that frequency distributions, such as particle size distributions can be obtained. Automation can help to overcome the long process time of analyzing large samples when combined with microscopy. Limitations of image analysis are the difficulty to analyze aggregates and artifacts due to overlapping particles. A variety of advanced image analysis systems are currently on the market (e.g. Leica, Wetzlar, Germany; Leco, St. Joseph, MI, USA; Brinkmann, Westbury, NY, USA; Juliet, Iowa City, IA, USA). In addition to complete, automated image analysis systems, a microscope may be used to obtain images that can be scanned and analyzed using image analysis software [62], e.g., SigmaScan, Jandel Scientific, Sunnyvale, CA, USA.

Particle Image Velocimetry

Particle image velocimetry (PIV) is a relatively new technique that provides particle velocity characteristics of the whole flow field being studied [3]. PIV consists of a double-pulsed laser sheet that illuminates the flow at two discrete points in time. This generates a staggered pair of particle images that can be analyzed to yield particle velocity information. The velocity operating range of PIV is $0.1<U_p<1000$ m/s with a viewing area of $1\text{-}10^6$ mm^2. PIV offers the advantages of quantitative information on the particulate velocity vector field along with a detailed visualization of the fluid flow. This is of particular use in fluidization studies.

4.1.2.3 Light Scattering Methods

Light scattering and extinction of dispersed particles are widely used to gather information on the concentration and size of aerosols. Numerous techniques have been reviewed in the literature [251]. This chapter focuses on techniques that are applicable to pharmaceutical dry powder aerosols.

Laser Doppler Methods

Laser-Doppler methods are based on the principal of the light scattered from a particle traversing a measurement volume (approximate diameter=0.5 mm) established by the intersection of two spatially separated laser beams, illustrated in **Figure 19**. Light from the two laser beams interfere, producing parallel lines of alternating light intensity. When a particle traverses these parallel lines, it acts like a lens and scatters light by reflection and refraction. The scattered light interferes and produces a Doppler burst interference fringe pattern. The frequency of the Doppler burst is proportional to the velocity of the particle, irrespective of shape. This is the principal of laser Doppler anemometry (LDA), also known as laser Doppler velocimetry (LDV). Phase shift, produced by viewing the Doppler burst via spatially separated photodetectors, is proportional to particle size for spherical particles only. This is the principal of phase-Doppler analysis (PDA), providing information on both particle size and velocity characteristics. The operational range of both LDA and PDA is $U_p<500$ m/s with a concentration limit of 10^6/cm^3. The size range of particles obtained by PDA is $0.5<D_p<10^4$ μm. LDA has been used to characterize both dry powder aerosols and pressurized metered dose inhalers [137, 138]. Characterization of pMDIs and nebulizers has been conducted using PDA [57, 227]. However, application of PDA to dry powder aerosols is restricted by the requirement of spherical particles to obtain size information.

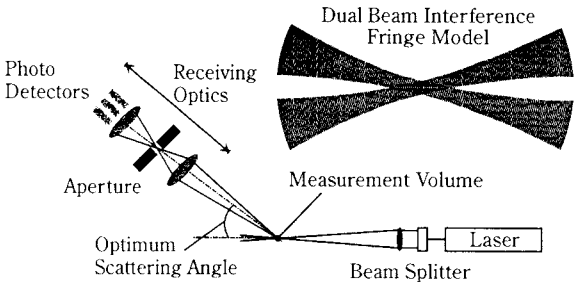

Fig. 19 Schematic of laser-Doppler method of particle size analysis.

The shadow-Doppler particle analyzer (SDPA) is a PDA based method that is being developed to characterize irregular shaped particles [86]. This method obtains particle velocity similar to LDA. Particle size is obtained by focusing the images of the particle projected by the light within the measurement volume onto a linear array of photodetectors. The two signals produced by the light projected from the individual laser beams is related to the equivalent particle diameter. This method overcomes the intrinsic problem of measurement volume particle size bias, as well as providing information on particle size, shape, orientation and velocity. This technique is currently being validated for a wide range of spherical and non-spherical particulate systems [148]. The particle analyzing system (PAS) is a phase-Doppler based instrument that can measure both the size and velocity of non-spherical particles (Dantec Measurement Technology, Inc., Mahwah, NJ). The laser beams are modified to

produce 'top-hat' intensity profiles rather than Gaussian beam profiles. Particle size is correlated with the intensity of the light scattered from the particle using generalized Lorenz-Mie theory (GLMT). PAS has yet to be rigorously validated.

The single-particle, aerodynamic relaxation time (SPART) analyzer is based on the phase lag produced when a particle is subjected to a given acoustic vibration within the measurement volume of an LDA [157]. The aerodynamic diameter is determined by relating the response of the particle to the acoustic excitation. Electric SPART (E-SPART) is a modified version of SPART in which an electric field and acoustic vibration are both applied to the particle [158, 83]. This produces a migration velocity component, providing information on the magnitude and polarity of the particle electrostatic charge as well as aerodynamic diameter. The operational range of the instrument is $0.3<D_{ae}<75$ μm, a data acquisition range of 10−2000 particles/s and an electrostatic charge measurement range from zero to saturation. SPART and E-SPART have been used to characterize both dry powder aerosols and pMDIs [105,106, 196, 197, 198].

The advantages of LDA and PDA are that they are non-intrusive, provide rapid, real-time data acquisition *in-situ* and high spatial and temporal resolution. The disadvantages of the respective methods are that LDA provides information on particle velocity alone and PDA requires the particles to be spherical to obtain size information. The small measurement volume results in a small fraction of the aerosol being characterized that may not be representative of the whole aerosol. The advantage of SPART analysis is that it provides an aerodynamic diameter of the whole aerosol. E-SPART has the additional advantage of generating information on the electrostatic charge of the particles. However, the aerosol emitted from the device must be diluted to prevent particle coincidence, requiring intrusive characterization. Chemical identity of the particles being analyzed cannot be obtained using laser Doppler methods.

Time-of-Flight Methods

Two types of time-of-flight particle sizing systems are currently on the market: the Aerodynamic Particle Sizer™ (TSI, St. Paul, USA) and the Aerosizer™ (Amherst Process Instruments, Hadley, USA). Both systems are single particle analyzers that measure the time-of-flight of accelerated aerosol particles between two laser.

The principle of operation includes three steps: generation of an aerosol beam, determination of the particle time-of-flight and conversion of the data into a corresponding particle size distribution [13, 37, 177]. The aerosol is drawn into the acceleration nozzle, along with additional sheath of air, by a pressure gradient between the partly evacuated measurement region and the ambient air. The aerosol beam is formed and stabilized by the surrounding air sheath. Due to their lower inertia, smaller particles are accelerated faster and reach higher velocities relative to large particles. Upon leaving the nozzle, the particles pass two laser beams [**Figure 20**]. The light scattered by the particles generates start and stop signals from which the time-of-flight of the individual particles are calculated. The time-of-flight is then converted to particle size by internal calibration curves.

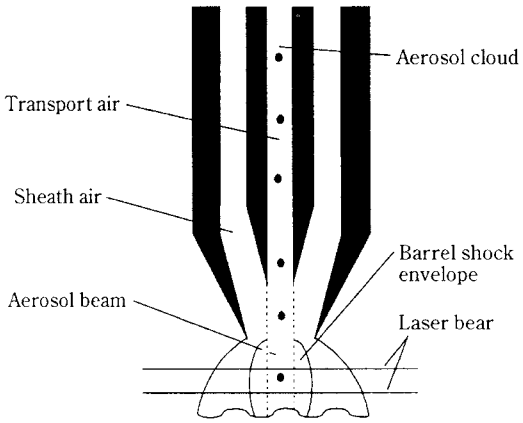

Fig. 20 Aerosizer nozzle [111].

The Aerodynamic Particle Sizer™ (API) measures up to 1000 particles/cm^3 in a size rage of 0.5 to 30 μm. The size range of the Aerosizer™ is 0.1 to 700 μm with an acquisition rate of up to 10^5 particles/s. A number of additional components for specialized applications are available for the Aerosizer™. These include the Aerodisperser™, for the measurement of powders, the AeroDiluter™, to control the volume flow rate of the aerosol into the Aerosizer™, and the AeroBreather™, to generate and analyze aerosols from dry powder inhalers. The latter is a microprocessor controlled sampling system that sits on top of the Aerosizer™ housing. Its inner plenum chamber is attached directly to the nozzle entry. A piston on the upper side of the chamber is moved upwards and draws air through the DPI into the chamber, generating the aerosol. Speed, acceleration and displacement of the piston are variable, so that different inspiratory profiles can be generated. The aerosol is subsequently drawn through the sonic nozzle into the Aerosizer™ and analyzed.

The advantage of time-of-flight methods is the rapid

acquisition of data and calculation of the particle size distribution. Disadvantages are that information about the chemical identity or the mass of particles cannot be obtained. Thus it is not possible to differentiate between drug and carrier particles and the dose measured cannot be assessed. Also, coincidence effects due to particle overload may give rise to phantom particles and distorted size distributions [13]. Studies using the Aerosizer™/AeroBreather™ were able to show the effect of air flow and acceleration on the particle size distribution of the Turbuhaler, but also gave rise to possible particle overload at higher drug doses [111]. It has been proposed that concentrated aerosols need to be diluted for accurate measurement [168]. Time-of flight methods are beneficial as an additional sizing method for the screening of formulations and during the development of dry powder aerosols [18, 108, 112, 168, 213].

Laser Diffraction

Laser diffraction provides a global measurement of the powder aerosol *in situ*. The method is based on Fraunhofer diffraction of particles in a beam of parallel, monochromatic light. Particles diffract light as a function of their diameter, with the angle of diffraction decreasing with increasing particle size [**Figure 21**]. The diffraction pattern produced by a polydisperse population of particles consists of a number of concurrent, concentric diffraction rings, each of which is associated with a certain particle size. These diffraction patterns are focused onto a radial multi-element photodetector that measures the energy distribution of the diffracted light, which is subsequently transformed into a volume distribution by the software.

A number of laser diffraction systems suitable for the measurement of sprays and powders are available. However, only one of these can be equipped for the measurement of dry powder inhalers (Sympatec Helos; Sympatec, Clausthal-Zellerfeld, Germany). The inhaler is attached to a special adapter, that allows air to be drawn through the inhaler. This generates the aerosol and passes the aerosol through the laser beam. The measurement is started by a trigger system as soon as particles are detected. The advantage of this technique is that a rapid measurement of the particle size distribution of dry powder aerosols *in situ* is possible. It is not possible, however, to differentiate between drug and carrier particles. Dry powder aerosol particle size distributions characterized by laser diffraction yielded similar results to those obtained using an Andersen impactor [159]. This method appears to be a promising method to gain information on the particle size distribution of dry powder aerosols in a very short time.

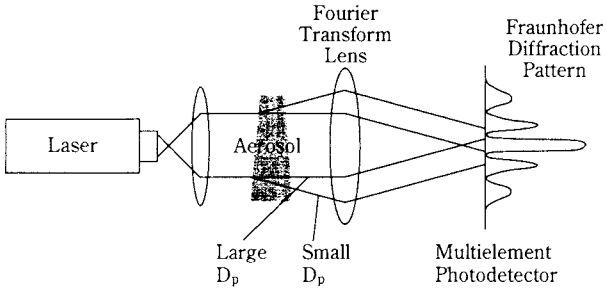

Fig. 21 Schematic of laser diffraction method of particle size analysis.

4.1.3 Summary

A number of inertial impaction devices are available for sampling and size classifying dry powder aerosols. The most useful of these can be operated at more than one airflow rate and have multiple stages. The information from these devices can be used to reconstruct the particle size and distribution of an aerosol under different flow conditions. This allows evaluation of ease of dispersion which is useful both in product development and quality control. Inertial impaction may be used to sample aerosols <15 μm (**Table 6**). This method has the advantage of utilizing chemical analysis of the drug in specific particle size ranges. The major disadvantages of these methods are that they are tedious, time consuming and subject to operator error.

A variety of optical methods are available to characterize dry powder aerosols. These methods are capable of discriminating particles in a range of sizes. In general, the laser techniques described measure particles from 0.5−1000 μm. These techniques have the advantage of rapid *in situ* data acquisition. The major limitation of these methods is the inability to distinguish drug from excipient particles and to specify the dose in a particular size range.

4.2 Stability

Moisture has a significant impact on the physical and chemical stability of particles. Small particles have a greater tendency to take on moisture due to their large surface area to mass ratio and the presence of large interstitial space. Moisture may cause particles to associate and this physical instability results in aggregates which cannot be dispersed adequately. Individual particles may also undergo changes in crystal system or habit based on association with water.

Drugs which are subject to hydrolytic cleavage or undergo chemical reactions with the excipients or

packaging may be unstable and therefore unsuitable for inclusion in dry powder formulations.

4.3 Contamination

Particulate contaminants must be minimized to avoid the introduction of foreign objects into the lungs where they might result in toxic side effects [83]. The purity of the bulk chemicals is usually monitored and handling is controlled to avoid the introduction of contaminating species. Possible contaminants include impurities produced during manufacturing and particulates associated with the containers and closures.

Impurities and contaminants in a dry powder product can be identified and quantified by a number of methods. Any visually observable contaminant, as indicated by color or shape, will be >50 μm in diameter, the resolution limit of the human eye. This may be seen by direct examination of the powder or for insoluble contaminants by dissolving the powder and observing residual particulates in the solution, i.e., turbidity. Small insoluble contaminating particles may be observed by microscopy. Indirect methods such as electrical resistance, light obscuration or laser diffraction may also be used to quantify insoluble particulates in the product. Soluble materials may be identified by spectroscopic methods, such as UV/VIS spectrophotometry or Infra-Red Spectroscopy. The resolution of quantitative methods can be increased by coupling them with chromatography to allow species separation.

Micro-organisms have the capacity to degrade certain compounds in the presence of moisture. The production of esterases and proteases by micro-organisms may result in the degradation of the active ingredient, instability and problems in drug storage. It is very important, therefore, to monitor the powder for the presence of such micro-organisms. These may be bacterial or fungal contaminants. Pnosocomiosis, the introduction of infective micro-organisms as contaminants in aerosols, has been identified as a problem in the delivery of nebulized solutions [20, 126]. In addition, contamination in multidose solutions has been identified [134]. There have been no cases reported in which normal patients have experienced this phenomenon when using dry powder aerosols. However, their use in the treatment of immunocompromised patients would require rigorous attention to potential microbial contamination. Products of biological origin may be more susceptible to degradation by micro-organisms. Close attention to the microbial burden is required as the biotechnology industry considers this route of administration for its products. The Microbial Limits Test states that no more than ten colony forming units/gram of product should exist [165]. There should be a complete absence of coliform bacteria.

5. Conclusion

Figure 22 illustrates the complexity of the issues surrounding dry powder aerosol delivery. The overlapping performance characteristics shown by the inner rings represent the true performance of the aerosol delivery device, its perfomance as estimated by an *in vitro* testing approach, most notably focused on particle size analysis and the ultimate *in vivo* performance. Efficacy is only one aspect of *in vivo* performance. The challenge is to develop or adopt *in vitro* techniques that measure the actual performance of the inhaler with respect to *in vivo* performance. Certain characteristics are known to have a direct impact on general performance and these are indicated as particle size, airflow and the operator (in the case of in-vitro evaluation) or patient. As technologies are developed to control the specific variables (itemized on the periphery of **Figure 22**), it is anticipated that the degree of overlap in actual physical, estimated physical and biological performance will increase to allow predictable therapeutic effects.

There is increasing interest in the administration of drugs to the lungs and a need for delivery systems to achieve this goal. Fundamental approaches to the development of dry powder inhalers may render them an increasingly attractive option. It is important when considering dry powders that their physicochemical, flow and dispersion properties are integrated with device performance and characterization. A framework has been presented indicating the major considerations in any development program based on an understanding of powder properties and behavior.

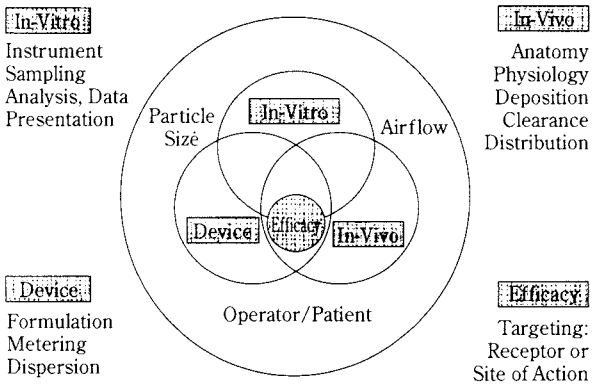

Fig. 22 The influence of device, in-vitro and in-vivo performance on efficacy.

There are a number of issues which still need to be addressed. These include stability, as influenced particularly by electrostatic charge, moisture temperature, active or passive mechanisms of powder dispersion, methods of analysis, presentation and interpretation of performance data. All of these issues are important in setting valid performance criteria.

It should be clear that not all drugs, excipients and packaging materials will be suitable as components of powder inhalers. These systems are developed as complementary dosage forms to aqueous and non-aqueous solution and suspension systems, delivered by nebulizers and propellant driven metered dose inhalers. However, this is a burgeoning scientific field and the rewards for success will include novel approaches to the treatment of pulmonary and systemic diseases.

Acknowledgements

The research that has justified the preparation of this review article has been sponsored by the National Institutes of Health (NHLBI, HL55789), Glaxo Wellcome, Inc., and a German Federal Government Fellowship (for PH). The inclusion of specific devices as examples should not be considered an endorsement by the authors. The omission of other devices was a matter of expediency and brevity in an already lengthy manuscript. We look forward to a future opportunity to thoroughly review the status of device development.

Nomenclature

A	area, Hamaker constant
C	Cunningham slip correction factor
C_D	discharge coefficient
D	diamater
D_{ae}	aerodynamic diameter
$D_{ae,\,0.84}$	aerodynamic diameter, 84th percentile
D_{eff}	effective diameter
D_{eq}	equivalent diameter
D_{min}	minimum diameter for separation by shear force
D_{12}	cumulative diameter of binary system
DPI	dry powder inhaler
E	electric field strength
F	force
FPD	fine particle dose
FPF	fine particle fraction
h	characteristic length scale of separation
k	coordination number
K_q	electrostatic force constant
L	characteristic length scale
m	mass
MMAD	mass median aerodynamic diameter
P	pressure
q	electrostatic charge
Q	volumetric flow rate
R	specific flow resistance
Re	Reynolds number
rFPF	relative fine particle fraction
RH	relative humidity
St	Stokes number
t	time
U	velocity
x	directional coordinate

Greek

ε	porosity
ϕ	diameter
η	kinematic viscosity (μ/ρ), refractive index
μ	absolute viscosity
ρ	density
ρ_0	unit density
σ	surface tension
σ_g	geometric standard deviation
τ	shear stess
χ	dynamic shape factor
ω	rotational velocity

Subscript

b	bulk
c	capillary
C	carrier, characteristic
crit	critical
d	drug
g	gravity
i, j	tensor notation
l	lactose
min	minimum
p	particle
q	electrostatic charge
vdw	van der Waals

References

1) Adams, W.P., G. Poochikian, A.S. Taylor, R.M. Patel, G.P. Burke and R.L. Williams, J. Aerosol Med., 7.119 (1994).
2) Adjei, A.L. and P.K. Gupta: in "Inhalation Delivery of Therapeutic Peptides and Proteins", A.L. Adjei and P.K. Gupta (eds.), Marcel Dekker, Inc., New York, NY, p.625 (1997).
3) Adrian, R.J.: Ann. Rev. Fluid. Mech., 23. 261 (1991).
4) Aerosols <601> United States Pharmacopoeia XXII, 7th Supplement, 3123(1992).
5) Al-Chalabi, S.A.M., A.R. Jones and P.F. Luckham: J. Aerosol Sci., 21. 821 (1990).
6) Allen T.: "Particle Size Measurement", Fourth Edition, Chapman and Hall, New York, NY (1990).
7) American Society for Testing and Materials: "Recommended Practice for the Analyses by Microscopical Methods", Philadelphia, PA (1973).
8) Asking, L. and B. Olsson: Aerosol Sci. Technol., 27, 39 (1997).
9) Austin L.G.: in "Handbook of Powder Science and Technology", Fayed, M.E. and L. Otten (eds.) Van Nostrand Reinhold Company, Inc., New York, NY, p.562 (1984).
10) Avnir, D.: "The Fractal Approach to Heterogeneous Chemistry", John Wiley and Sons, New York, NY (1989).
11) Bagnold, A.: "The Physics of Blown Sand and Desert Dunes", Methuen and Co., Ltd, London (1941).
12) Balachandran, W., C.N. Ahmad and S.A. Barton: Institute of Physics Conference Series, 118. 57 (1991).
13) Baron, P.A., M.K. Mazumder and Y.S. Cheng: in "Aerosol measurement: principles, techniques and applications", K. Willeke and P.A. Baron (eds.), Van Nostrand Reinhold, New York (1993).
14) Barry, P.W. and C. O'Callaghan: Br. J. Clin. Pharmacol., 40. 76 (1995).
15) Barry, P.W. and C. O'Callaghan: Thorax, 49. 402 (1994).
16) Bell, J.H., P.S. Hartley and J.S.G. Cox: J. Pharm. Sci., 60. 1559 (1971).
17) Berglund, R.N. and B.Y.H. Liu: Environ. Sci. and Technol., 7. 147 (1973).
18) Bohan, J.: in "Respiratory Drug Delivery IV", P.R. Byron, R.N. Dalby and S.J. Farr (eds.), Interpharm Press, Buffalo Grove, IL, p.330 (1994).
19) Böhme, G., W. Kling, H. Krupp, H. Lange, G. Sandstede and G. Walter: in "Chemistry, Physics and Application of Surface Active Substances", T.G. Overbeek (ed), Gordon and Breach, London, Vol. II, p.429 (1967).
20) Botman, M.J. and R.A. Krieger: J. Hosp. Infect., 10. 204 (1987).
21) Brindley, A., B.S. Sumby, I.J. Smith, D. Prime, P.A. Haywood and A.C. Grant, Pharm. Technol. Eur., 1/1995. 14 (1995).
22) British Pharmacopoeia, HMSO, London Appendix XVIIC, A196, (1998)
23) Broadhead, J., S.K. Edmond Rouan and C.T. Rhodes: Drug. Dev. Ind. Pharm., 18. 1169 (1992).
24) Brown, K.: in "Drug Delivery to the Respiratory Tract", D. Handerton and T. Jones (eds.), Ellis Horwood/VCH Publishers, New York, NY, p.119 (1987).
25) Bruna, P., O. Fourment, and G. Williams: in "Respiratory Drug Delivery IV", P.R. Byron, R.N., Dalby and S.J. Farr (eds.), Interpharm Press, Buffalo Grove, IL. p.352 (1994).
26) Byron, P.R.: "Respiratory Drug Delivery", CRC Press, Boca Raton (1990).
27) Byron, P.R., E.L. Kelly, M.J. Kontny, E.G. Lovering, G.K. Poochikian, S. Sethi, C.G. Thiel and E.B. Vadas: Pharm. Forum, 20: 7477 (1994).
28) Byron, P.R., J. Peart and J.N. Staniforth, J.N.: Pharm. Res., 14. 698 (1997).
29) Byron, P.R.: in "Respiratory Drug delivery IV", P.R. Byron, R.N. Dalby and S.J. Farr (eds.), Interpharm Press, Buffalo Grove, IL, p.153 (1994).
30) Byron, P.R., V. Naini, and E.M. Phillips,in "Respiratory Drug Delivery V", R.N. Dalby, P.R. Byron and S.J. Farr (eds.), Interpharm Press, Buffalo Grove, IL. p.103 (1996).
31) Carstensen, J.T.: "Pharmaceutical Principles of Solid Dosage Forms", Technomic, Lancaster, PA, (1993).
32) Carstensen, J.T.: "Pharmaceutics of Solids and Solid Dosage Forms", John Wiley and Sons, New York, NY (1989).
33) Chan, H.-K. and I. Gonda: J. Aerosol Sci., 20. 157 (1989).
34) Chan, H.K., A. Clark, I. Gonda, M. Mumenthaler and C. Hsu: Pharm. Res., 14. 431 (1997).
35) Chawla, A., K.M.G. Taylor, J.M. Newton and M.C.R. Johnson: Int. J. Pharm, 108. 233 (1994).
36) Cheah, P.K.P. and C.N. Davies: J. Aerosol Sci., 15.741 (1984).
37) Cheng, Y.S., E.B. Barr, I.A. Marshall and J.P. Mitchell: J. Aerosol Sci., 24. 501, (1993).
38) Chepil, W.: Soil Science, 60. 305 (1945).
39) Clark, A.R. and A.M. Hollingworth: J. Aerosol Med., 6. 99 (1993).
40) Clark, A.R. and R. Bailey: in "Respiratory Drug Delivery V", R.N. Dalby, P.R. Byron and S.J. Farr (eds.), Interpharm Press, Buffalo Grove, IL. p.221 (1996).
41) Clark, A.R.: in "Respiratory Drug Delivery IV", P.R. Byron, R.N. Dalby and S.J. Farr (eds.), Interpharm Press, Buffalo Grove, IL. p.117 (1994).
42) Clark, A.R., Aerosol Sci. Technol. 22. 375 (1995).
43) Clark, A.R.: Personal Communication
44) Clarke, M. J., M.J. Tobyn and J.N. Staniforth: Pharm. Res., 14. S-130 (1997).
45) Concessio, N.M. and A.J. Hickey: Pharm. Technol., 20(6). 60 (1996).
46) Concessio, N.M., M.M. Van Oort and A.J. Hickey: in "Respiratory Drug Delivery VI", R.N. Dalby, P.R. Byron and S.J. Farr (eds.), Interpharm Press, Buffalo Grove, IL, p.251 (1998).
47) Concessio, N.M., R. Jäger-Waldau and A.J. Hickey: Part. Sci. Technol., 15. 51 (1997).
48) Concessio, N.M.: Ph.D. Dissertation, University of North Carolina, Chapel Hill, U.S.A. (1997).
49) Cooper, D.W.: J. Aerosol Sci., 13. 111 (1982).

50) Cox, J.S.G., G.D. Woodward and W.C. McCrone: J. Pharm. Sci., 60, 1458 (1971).
51) Crompton, G.K.: J. Aerosol Med. 10. S23 (1997).
52) D'Souza, S.: J. Aerosol Med., 8 (suppl.1). S-13 (1995).
53) Dalby, R.N., S.L. Tiano and A.J. Hickey, in: "Inhalation Aerosols: Physical and Biological Basis for Therapy", A.J. Hickey (ed.), Marcel Dekker, New York, p.447 (1996).
54) Davies, C.N. and P.K.P. Cheah: J. Aerosol Sci., 15. 719 (1984).
55) De Boer, A.H., D. Gjalteme and P. Hagedorn: Int. J. Pharm., 138. 45 (1996).
56) Dewsbury, N.J., C.J. Kenyon and S.P. Newman: Int.. J. Pharm. 137. 261 (1996).
57) Dunbar, C.A., A.P. Watkins and J.F. Miller: J. Aerosol Med., 10. 351 (1997).
58) Dunnett, S.J. and D.B. Ingham: J. Aerosol Sci., 19. 365 (1988).
59) Dura Pharmaceuticals Inc., Spiros® Dry Powder Inhalation (DPI) System, San Diego, USA (1996).
60) Edwards, D.A., J. Hanes, G. Caponetti, J. Hrkach, A. Ben-Jebria, M.L. Eskew, J. Mintzes, D. Deaver, N. Lotan and R. Langer: Science, 276. 1868 (1997).
61) Etzler, F.M. and D.M. Fagundus: J. Colloid Interface Sci., 115. 513 (1987).
62) Evans, R.: Pharm. Technol. 17(3). 146(1993).
63) Faeth, G.M.: Prog. Energy Combust. Sci., 13. 293 (1987).
64) French, D.L., D.A. Edwards and R.W. Niven: J. Aerosol Sci., 27. 769, (1996).
65) Fuchs, N.A. and Sutugin: in "Aerosol Science", C.N. Davies (ed.), Academic Press, NY, p.1 (1966).
66) Fuchs, N.A.: "The Mechanics of Aerosols", Dover Publications, Inc., NY, USA (1964).
67) Fuller, R.: J. Aerosol Med., 8. S11 (1995).
68) Fults, K.A., I.F. Miller and A.J. Hickey: Pharm. Dev. Technol., 2. 67 (1997).
69) Galli, R.: World Patent No. WO 93/18812 (1993).
70) Ganderton, D. and A.J. Hickey: in "Encyclopedia of Pharmaceutical Technology" Volume 16, J. Swarbrick and J.C. Boylan (eds.) Marcel Dekker, Inc., New York, NY, p.22 (1997).
71) Ganderton, D. and N.M. Kassem: 'Advances in Pharmaceutical Science', Academic Press, London, UK. 165 (1992).
72) Ganderton, D.: J. Biopharm. Sci., 31. 101 (1992).
73) Ganderton, D.: Pharmeuropa, 8. 245 (1996).
74) Geldhart, D., N. Harnby and A.C. Wong: Powder Technol., 37. 25 (1984).
75) Geldhart, D.: Powder Technol., 7. 285 (1973).
76) Geuns, E.R.M., J. Toren, D.M. Barends and A. Bult: Eur. J. Pharm. Biopharm., 44. 187 (1997).
77) Glusker, J.P., M. Lewis and M. Rossi:"Crystal Structure Analysis for Chemists and Biologists" VCH Publishers Inc., New York, NY (1994).
78) Gonda, I., J.B. Kayes, C.V. Groom and F.J.T. Fildes: in "Particle Size Analysis", N. Stanley-Wood and T. Allen (eds.), John Wiley and Sons, New York, NY, p.31 (1981).
79) Graseby-Andersen, Personal Communication.
80) Greenspan, B.J.: Pharm. Forum, 22. 3288 (1996).
81) Groom, C.V. and I. Gonda: J. Pharm. Pharmacol., 32, 93P (1981).
82) Gupte, A.R., D. Hochrainer, J. Poss, J. Wittekind, B. Zierenberg and A. Knecht: World Pat. No. WO 92/00115 (1992).
83) Hailey, D.M., A.R. Lea and C.E. Kendall: J. Pharm. Pharmacol., 34. 615 (1982)
84) Hallworth, G.W. and U.G. Andrews: J. Pharm. Pharmacol., 28. 898 (1976).
85) Hallworth, G.W.: in "Aerosols in Medicine. Principles, Diagnosis and Therapy", Moren, F., M.B. Dolovich, M.T. Newhouse and S.P. Newman (eds.) Elsevier Science Publishers, Amsterdam, The Netherlands, p.351 (1993).
86) Hardalupas, Y., K. Hisdida, M. Maeda, M. Morikita, A.M.K.P. Taylor and J.H. Whitelaw, 3rd Congress on Optical Particle Sizing, Yokohama, Japan. (1993).
87) Hashish, A.H., A.G. Bailey and T.J. Williams: Physics in Medicine and Biology, 39. 2247 (1994).
88) Hersey, J.A., Powder Technol., 11. 41 (1975).
89) Heyder, J., J. Gebhart, G. Rudolf, C.F. Schiller and W. Stahlhofen: J. Aerosol Sci., 17. 811 (1986).
90) Hickey, A.J. (ed.): "Inhalation Aerosols", Marcel Dekker, Inc., New York, NY (1996).
91) Hickey, A.J. (ed.): "Pharmaceutical Inhalation Aerosol Technology", Marcel Dekker, Inc., New York, NY (1992).
92) Hickey, A.J. and C.A. Dunbar: Pharm. Technol., 21(6). 116 (1997).
93) Hickey, A.J. and N.M. Concessio: Adv. Drug Del. Rev., 26. 29 (1997).
94) Hickey, A.J. and N.M. Concessio: Part. Part. Syst. Charact., 11. 457 (1994).
95) Hickey, A.J. and N.M. Concessio: Particulate Sci. Technol., 14-15 (1996).
96) Hickey, A.J.: Drug Dev. Ind. Pharm., 14. 337 (1988).
97) Hickey, A.J., I. Gonda, W.J. Irwin and F.J.T. Fildes: J. Pharm. Sci., 79. 1009 (1990).
98) Hickey, A.J.: in: "Pharmaceutical Inhalation Aerosol Technology", A.J. Hickey (ed.), Marcel Dekker, New York, p.219 (1992).
99) Hickey, A.J., K.A. Fults and R.S. Pillai: J. Biopharm. Sci., 31. 107 (1992).
100) Hickey, A.J., N.M. Concessio, M.M. Van Oort and R.M. Platz: Pharm. Technol., 18 (8). 58 (1994).
101) Hickey, A.J.: Drug Dev. Ind. Pharm., 16.1911 (1990).
102) Hickey, A.J.: Pharm. Technol. 19(3). 58 (1995).
103) Hickey, A.J.: Pharm. Technol., 14(9). 118 (1990).
104) Hill, M.: in: "Respiratory Drug Delivery IV", P.R. Byron, R.N. Dalby and S.J. Farr (eds.) Interpharm Press, Buffalo Grove, IL. p.109 (1994).
105) Hiller, F.C., M.K. Mazumder, J.D. Wilson and R.C. Bone: Am. Rev. Resp. Dis., 118. 311 (1978).
106) Hiller, F.C., M.K. Mazumder, J.D. Wilson and R.C. Bone: J. Pharm. Pharmacol, 32. 605 (1980).
107) Hindle, M. and P.R. Byron: Int. J. Pharm., 116. 169 (1995).
108) Hindle, M. and P.R. Byron: Pharm. Technol., 19 (6). 64 (1995).

109) Hindle, M., R.N. Jashnanai and P.R. Byron: in "Respiratory Drug Delivery IV", P.R. Byron, R.N. Dalby and S.J. Farr (eds.), Interpharm Press, Buffalo Grove, IL. p.137 (1994).
110) Hinds, W.C.: 'Aerosol Technology – Properties, Behaviour and Measurement of Airborne Particles', John Wiley & Sons, New York, USA (1982).
111) Holzner, P. and B.W. Müller: Part. Sci. Technol., in press (1998).
112) Holzner, P., A.J. Hickey and H. Schreier: Pharm. Res., 14. S-62 (1997).
113) Holzner, P.: Med. Monatsschr. Pharm., 20. 177 (1997).
114) Holzner, P.: PhD Dissertation, Christian-Albrecht-University Kiel, Germany (1995).
115) Holzner, P.M. and B.W. Muller: Int. J. Pharm., 116. 11 (1995).
116) Huu-Phuoc, N., H. Nam-Tran, M. Buchmann and U.W. Kesselring: J. Pharm. Sci., 76. 406 (1987).
117) Huu-Phuoc, N., R. P.T. Luu, A. Munafu, P. Ruelle, H. Nam-Tran, M. Buchmann and U.W. Kesselring, J. Pharm. Sci., 75. 68 (1986).
118) Inhale Therapeutic Systems, Technology overview, Palo Alto, USA (1997).
119) Intal – Cromolyn Sodium – A Monograph, Fisons Corporation, Bedford, MA, p.140 (1973).
120) Israelachvili, J.N.: 'Intermolecular and Surface Forces', Academic Press, London, UK (1992).
121) Jaegfeldt, H., J.A.R. Andersson, E. Trofast and K.I.L. Wetterlin, in: "A New Concept in Inhalation Therapy", S.P. Newman, F. Morén and G.K. Crompton (eds.), Medicom, London, p.90 (1987).
122) Jäger-Waldau, R. and H. Mehring, in: "Respiratory Drug Delivery IV", P.R. Byron, R.N. Dalby and S.J. Farr (eds.), Interpharm Press, Buffalo Grove, IL. p.344 (1994).
123) Jashnani, R.N. and P.R. Byron: Int. J. Pharm., 130. 13 (1996).
124) Jashnani, R.N., P.R. Byron and R.N. Dalby: Int. J. Pharm., 113. 123 (1995).
125) Johnson, M.A.: Spray Technol. Marketing, 11, 28 (1997).
126) Johnson, W.G., A.K. Pierce, J.K. Sanford and G.D. Thomas: Ann. Intern. Med., 77. 701 (1972).
127) Kassem, N.M. and D. Ganderton: J. Pharm. Pharmacol., 42. 11 (1990).
128) Kassem, N.M., K.K.L. Ho and D. Ganderton: J. Pharm. Pharmacol., 41. 14P (1989).
129) Kassem, N.M., M. Yianneskis and D. Ganderton: J. Pharm. Pharmacol., 41. 13P (1989).
130) Kassem, N.M., M.A. Shamat and C. Duval: Int. J. Pharm., 43. 75P (1991).
131) Kassem, N.M.: Ph.D. Dissertation, London University, London, UK (1990).
132) Kaye, B.H. in: "Respiratory Drug Delivery V", R.N. Dalby, P.R. Byron and S.J. Farr (eds.), Interpharm Press, Buffalo Grove, IL. p.95 (1996).
133) Kaye, B.H.: "A Random Walk Through Fractal Dimensions", VCH Publishers, Weinheim (1991).
134) Kuhn, R.J., A.H. Lubin, P.R. Jones and M.C. Nahata: Am. J. Hosp. Pharm., 39. 308 (1982).
135) Kulvanich, P. and P.J. Stewart: J. Pharm. Pharmacol., 39. 732 (1987).
136) Lalor, C.B. and A.J. Hickey: in "Physico-chemical Properties of Aerosols", I. Colbeck (ed.), Chapman and Hall, London, UK, p.391(1998).
137) Lee, K.C., K.O. Suen and M. Yianneskis: "Proc. 4th Conf. On Laser Anemometry, Adv. and Appl.", Cleveland, Ohio, USA (1991).
138) Lee, K.C., K.O. Suen, M. Yianneskis and C. Marriott: Int. J. Pharm., 130. 103 (1996).
139) Lefebvre, A.H.: "Atomization and Sprays", Hemisphere Publishing Corp., NY, USA (1989).
140) Li, W-I, M. Perzl, J. Heyder, R. Langer, J.D. Brain, K.-H. Englmeier, R.W. Niven and Edwards, D.A: J. Aerosol Sci, 27. 1269 (1996).
141) Licht, W.: J. Cosmet. Chem., 23. 657 (1972).
142) Lippman, M. and V. Timbrell: J. Aerosol Med., 3S. 155 (1991).
143) Lodge, J.P. and T.L. Chan: "Cascade Impactor", American Industrial Hygiene Association, Akron, OH (1986).
144) Lord, J.D. and J.N. Staniforth: in "Respiratory Drug Delivery V", R.N. Dalby, P.R. Byron and S.J. Farr (eds.), Interpharm Press, Buffalo Grove, IL, p. 75 (1996).
145) Lucas, P., K. Anderson and J.N. Staniforth: Pharm. Res., 14. S-130 (1997).
146) Luerkens, D.W.: "Theory and Appplication of Morphological Analysis, Fine Paricles and Suraces", CRC Press, Inc., Boca Raton, FL (1991).
147) Lundgren, D.A. and W.D. Balfour: J. Aerosol Sci., 13. 181 (1982).
148) Maeda, M. and H. Morikita: Proc. ICLASS-97, Seoul, Korea. (1997).
149) Marple, V.A., and C.M. Chien: Environ. Sci. Technol., 14. 976 (1980).
150) Marple, V.A.: J. Aerosol Sci., 9. 125 (1978).
151) Martonen, T. and I. Katz: "Inhalation Aerosols: Physical and Biological Basis for Therapy", A.J. Hickey (ed.), Marcel Dekker, Inc., New York, NY. p. 29 (1996).
152) Martonen, T. and Y. Yang: "Inhalation Aerosols: Physical and Biological Basis for Therapy", A.J. Hickey (ed.), Marcel Dekker, Inc., New York, NY. p. 3 (1996).
153) Martonen, T.B.: Am. Ind. Hyg. Assoc. J., 43. 154 (1982).
154) Massey, B.S.: "Mechanics of Fluids", 6th edition, Van Nostrand Reinhold, London (1989).
155) May, K.R.: J. Aerosol Sci., 13. 37 (1982).
156) May, K.R.: J. Sci. Instrum., 43, 841 (1966).
157) Mazumder, M.K. and K.J. Kirsch: Rev. Sci. Instrum., 48. 622 (1977).
158) Mazumder, M.K., R.E. Ware and W.G. Wood: "Measurements of Suspended Particles by Quasi-Elastic Light Scattering", John Wiley & Sons, New York, NY (1983).
159) MacRitchie, H.B., G.P. Martin, C. Marriott and L. Murphy, DDL VI, London, The Aerosol Society, Bristol, UK, p.118 (1995).
160) Meakin, B.J., J.M. Cainey and P.M. Woodcock: Int. J. Pharm., 119. 91 (1995).
161) Mecikalski, M.B. and D.R. Williams: World Patent No. WO 94/08552 (1994).

162) Meisner, D., C. Kelemen, C. Shabold and E. Vadas: Pharm. Res., 10: S139 (1993).
163) Melandri, C., G. Tarroni, V. Prodi, T. De Zaiacomo and M. Formignani: J. Aerosol Sci., 14. 657 (1983).
164) Michaelides, E.E., T. Fukano and A. Serizawa (Eds): "Turbulence Modification in Multiphase Flows", ASME, 110 (1991).
165) Microbial Limits Test <61>, United States Pharmacopoeia, XXII, 1479 (1990).
166) Miller, N.: in "Respiratory Drug Delivery IV", P.R. Byron, R.N. Dalby and S.J. Farr (eds.), Interpharm Press, Buffalo Grove, IL. p.342 (1994).
167) Milosovich, S.M., C. Evans and V. Jobeck: Pharm. Res., 14. S143, 1997.
168) Mitchell, J.P. and M.W. Nagel: Aerosol Sci. Technol., 25. 411 (1996).
169) Molina, M.J. and F.S. Rowland: Nature, 249. 810 (1974).
170) Muir, D.C.F.: Ann. Occup. Hyg., 8. 233 (1965).
171) Mullin, J.W.: "Crystallization", Third Edition, Butterworth-Heinemann, Oxford, UK, p.12 (1993)
172) Mullins, M.E., L.P. Michaels, V. Menon, B. Locke and M.B. Ranade: Aerosol Sci. Technol., 17. 105 (1992).
173) Newman, S.P. and S.W. Clarke, Thorax, 38.881 (1983).
174) Newman, S.P., A. Hollingworth and A.R. Clark: Int. J. Pharm., 102. 127 (1994).
175) Newman, S.P., F. Moren and G.K. Crompton: "A New Concept in Inhalation Therapy", Medicom Europe BV, Bussum, The Netherlands (1987).
176) Newman, S.P., F. Morén, E. Trofast, N. Talaee and S.W. Clarke: Int. J. Pharm., 74. 209 (1991).
177) Niven, R.W., Pharm. Technol., 17(1): 72 (1993).
178) Niven, R.W.: in "Inhalation Aerosols Aerosols: Physical and Biological Basis for Therapy", A.J. Hickey (ed.), Marcel Dekker, Inc., New York, NY, p.273 (1996)
179) Noakes, T.J.: J. Aerosol Med., 8 (suppl.1). S-3 (1995).
180) O'Callaghan, C., J. Lynch, M. Cant and C. Robertson: Thorax, 48. 603 (1993).
181) O'Rourke, P.J. and F.V. Bracco: "I.Mech.E. Stratified Automotive Engines Conference", C404/80. 101 (1980).
182) Olsson, B.: J. Aerosol Med., 8. S13 (1995).
183) Olsson, B., J.M. Aiache, H. Bull, D. Ganderton, P. Haywood, B.J. Meakin, P.J. Schorn and P. Wright: Pharmeuropa, 8. 191 (1996).
184) Orr Jr., C., F.K. Hurd and W.J. Corbett: J. Colloid Sci., 13. 472 (1958).
185) Osterman, K., E. Stahl and A. Kallen: Eur. Respir. J., 4. 175 (1991).
186) Otsuka, A., K. Iida, K. Danjo and H. Sunada: Chem. Pharm. Bull., 36. 741 (1988).
187) Otsuka, A., K. Iida, K. Danjo and H. Sunada: Chem. Pharm. Bull., 31. 4483 (1983).
188) Ower, E. and R.C. Pankhurst, in: "The Measurement of Airflow", 5th edition, Pergamon press, Oxford, UK, in press (1997).
189) Paronen, P., A. Poso, M. Vidgren, J. Gynther and P. York: Pharm. Res., 10. S162 (1993).
190) Patel, U.B., A.E. Bell, G.P. Martin and C. Marriott: J. Pharm. Pharmacol., 37. 108P (1985)
191) Patton, J. and R.M. Platz: US Patent No. 5458135 (1995).
192) Peart, J., J.N. Staniforth and B.J. Meakin: Pharm. Res., 14. S142 (1997).
193) Peart, J., J.N. Staniforth, P.R. Byron and B.J. Meakin: in "Respiratory Drug Delivery V", R.N. Dalby, P.R. Byron and S.J. Farr (eds.), Interpharm Press, Buffalo Grove, IL. 85 (1996).
194) Perry, D.G. and G.C. Smaldone: J. Aerosol Sci., 16. 427 (1985).
195) Pharmeuropa, 8. 245 (1996)
196) Phillip, V.A., R.C. Mehta, P.D. DeLuca and M.K. Mazumder: Part. Sci. Technol., 15. 303 (1997).
197) Phillip, V.A., R.C. Mehta, M.K. Mazumder and P.D. DeLuca: Int. J. Pharm., 151. 165 (1997).
198) Phillip, V.A., R.C. Mehta, M.K. Mazumder and P.D. DeLuca: Int. J. Pharm., 151. 175 (1997).
199) Pietsch, W.: "Size Enlargement by Agglomeration", John Wiley, New York, NY p.65 (1991).
200) Podczeck, F., M.J. Newton and M.B. James: Int. J. Pharm., 149. 151 (1997).
201) Porush, I., C.G. Thiel and J. G. Young: J. Am. Pharmaceutical. Assoc., 49. 70 (1960).
202) Raabe, O.: Am. Ind. Hyg. Assoc. J., 29. 439 (1968).
203) Raabe, O.G.: Env. Sci. Technol., 12. 1162 (1978).
204) Raabe, O.G.: J. Air Pollut. Control Assoc., 26, 856 (1976).
205) Raable, O.: in "Fine Particles", B.Y.H. Liu (ed.), Academic Press, New York, NY, p. 59 (1976).
206) Ranz, W.E. and J.B. Wong: Arch. Ind. Hyg. Occup. Med., 5. 464 (1954).
207) Rao, A.K. and K.T. Whitby: J. Aerosol Sci., 9. 87 (1978).
208) Rietema, K.: 'The Dynamics of Fine Powders', Elsevier Science Publishing Co., Inc., New York, USA (1991).
209) Rippie, E.G. and C.H. Chou: Powder Tech., 21. 205 (1978).
210) Ross, D. and R.K. Schultz: J. Aerosol Med., 9. 215 (1996).
211) Rudt, S. and R.H. Muller: J. Controlled Release, 22. 263 (1992).
212) Sacchetti, M. and M.M. Van Oort: in "Inhalation Aerosols: Physical and Biological Basis for Therapy", A.J. Hickey (ed.), Marcel Dekker, New York, NY. p.337 (1996).
213) Schreier, H., W.C. Mobley, N.M. Concessio, A.J. Hickey, and R.W. Niven: S.T.P. Pharma Sciences, 4. 38 (1994).
214) Schubert, H.: Powder Technol., 37. 71 (1984).
215) Schultz, R.K., N.C. Miller, D.K. Smith and D.L. Ross, J. Biopharm. Sci., 31. 115 (1992).
216) Sciarra, J.J. and A.J. Cutie:in "Modern Pharmaceutics", Second Edition, G.S. Banker and C.T. Rhodes (eds.), Marcel Dekker, Inc., New York, NY, p.605 (1990).
217) Sciarra, J.J. and D. Adelman: J. Soc. Cosmet. Chem., 22. 867 (1971).
218) Selroos, O.: J. Aerosol Med., 10. S27 (1997).
219) Shinohara, K.: in "Handbook of Powder Science and Technology", M.E. Fayed and L. Otten (eds.), Van Nostrand Reinhold Company, New York, NY, p. 129 (1984).
220) Smith, G., C. Hiller, C., M. Mazumder and R. Bone: Am. Rev. Resp. Dis., 121. 513 (1980).
221) Sporenberg, F., G. Ruther and E. Weber: J. Aerosol

Sci., 14. 308 (1983).
222) Staniforth, J.N. and J.E. Rees: J. Pharm. Pharmacol., 34. 69 (1982).
223) Staniforth, J.N.: Aerosol Sci. Technol., 22. 346 (1995).
224) Staniforth, J.N., in: "Respiratory Drug Delivery IV", P.R. Byron, R.N. Dalby and S.J. Farr (eds.), Interpharm Press, Buffalo Grove, IL. p.303 (1994).
225) Staniforth, J.N.: in "Respiratory Drug Delivery V", R.N. Dalby, P.R. Byron and S.J. Farr (eds.), Interpharm Press, Buffalo Grove, IL. p.65 (1996).
226) Staniforth, J.N., J.E. Rees, F.K. Lai and J.A. Hersey: J. Pharm. Pharmacol., 34. 141 (1982).
227) Stapleton, K.W. and W.H. Finlay: J. Aerosol Sci., 26. 137 (1995).
228) Steckel, H. and B.W. Müller: Int. J. Pharm., 154. 19 (1997).
229) Sumby, B.S., K.M. Churcher, I.J. Smith, A. Grant, K.G. Truman, R.J. Marriot and S.J. Booth: Pharm. Technol. Int., 6. 20 (1993).
230) Swift, D.L.: "Inhalation Aerosols: Physical and Biological Basis for Therapy", A.J. Hickey (ed.), Marcel Dekker, Inc., New York, NY. p.51 (1996).
231) Swift, D.L.: Ann. Occup. Hyg., 10. 337 (1967).
232) Task Group on Lung Dynamics: Health Physics, 12. 173 (1966).
233) Thiel, C.: in "Respiratory Drug Delivery V", R.N. Dalby, P.R. Byron and S.J. Farr (eds.), Interpharm Press, Buffalo Grove, IL, p. 115 (1996).
234) Timsina, M.P., G.P. Martin, C. Marriott, D. Ganderton and M. Yianneskis: Int. J. Pharm., 101. 1 (1994).
235) Tzou, T.T., R.R. Pachuta, R.B. Coy, and R.K. Schultz: J. Pharm. Sci., 86. 1352 (1997).
236) Van Oort, M., B. Downey and W. Roberts: Pharm. Forum, 22. 2211 (1996).
237) Vaughan, N.P.: J. Aerosol Sci., 20, 67 (1989).
238) Vidgén, M., A. Kärkkäinen, P. Karjalainen, P. Paronen and J. Nuutinen: Int. J. Pharm., 42. 211 (1988).
239) Vidgén, M.T., P.A. Vidgrén and T.P. Paronen: Int. J. Pharm., 35. 139 (1987).
240) Vidgrén, M., M. Slivasti, P. Vidgrén, H. Sormunen, K. Laurikainen and P. Korhonen: Aerosol Sci. Technol., 22. 335 (1995).
241) Vidgrén, M.T., P.A. Vidgrén and T.P. Paronen, Acta Pharm. Fenn., 98. 71 (1989).
242) Visser, J.: Powder Technol., 58: 1 (1989).
243) Visser, J.: Adv. Colloid Interface, 3. 331 (1972).
244) Wade, A. and P.J. Weller (eds): "Handbook of Pharmaceutical Excipients", Second Edition, APhA Association, Washington DC (1994).
245) Wadke, D.A., A.T.M. Serajuddin and H. Jacobson, in "Pharmaceutical Dosage Forms", Volume 1, Second Edition, H.A. Lieberman, L. Lachman and J.B. Schwartz (eds.) Marcel Dekker, Inc., New York, NY p.1 (1989).
246) Ward, A.J.M., N. Kassem, J.M. Evans, J. Moxham and D. Ganderton: Resp. Med., 86. 237 (1992).
247) Wert, C.A. and R.M. Thomson: "Physics of Solids", Second Edition, McGraw Hill, Inc., New York, NY, p10 (1970).
248) Wetterlin, K.I.L., in: "A New Concept in Inhalation Therapy", S.P. Newman, F. Morén, G.K. Crompton (eds.), Medicom, London. A85 (1987).
249) Wetterlin, K.I.L., Pharm. Res., 8. 506 (1988).
250) White, F.M.: 'Viscous Fluid Flow', 2nd edition, McGraw-Hill, Inc., New York, USA (1991).
251) Willeke, K. and P.A. Baron: in "Aerosol Measurement: Principles, Techniques and Applications", Van Nostrand Reinhold, New York (1993).
252) Willeke, K.: Am. Ind. Hyg. Assoc. J., 39. 317 (1978).
253) Willeke, K., R.E. Pavlik, W.C. Friedman, J.D. Blanchard and S.A. Haberman: in Atmospheric Pollution 1980, M.M. Benarie (ed.) Studies in Environmental Science, Volume 8, Elsevier, Amsterdam, p 309 (1980).
254) Woods, D.R. and E. Diamadopoulos: "Surfactants in Chemical/Process Engineering", Marcel Dekker, Inc., New York, USA. 369 (1988).
255) Yamate, G. and J. Stockham: in "Particle Size Analysis", J.D. Stockham and E.G. Fochtman (eds.), Ann Arbor Publishers, Ann Arbor, MI, p 28 (1977).
256) Yianneskis, M., K.C. Lee, D. Ganderton, D. Marriott and G.P. Martin: in "Respiratory Drug Delivery IV", P.R. Byron, R.N. Dalby, S.J. Farr (eds.), Interpharm Press, Buffalo Grove, IL. p.99 (1994).
257) Zanen, P., P.I. van Spiegel, H. van der Kolk, E. Tushuizen and R. Enthoven: Int. J. Pharm., 81. 199 (1992).
258) Zeng, X.M., G.P. Martin, C. Marriot and J. Pritchard: Pharm. Res., 14. S136 (1997).

Author's short biography

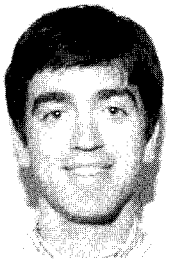

Craig A. Dunbar

Craig Dunbar is currently Senior Scientist at Advanced Inhalation Research, Cambridge, MA. Previously (1996-1998) he was a post-doctoral research fellow in the Dispersed Systems Laboratory at the School of Pharmacy, University of North Carolina at Chapel Hill. He obtained a BEng(Hons) in mechanical engineering at the Victoria University of Manchester and a PhD in thermo-fluids at the University of Manchester Institute of Science and Technology. He has published over twenty research articles, book chapters and abstracts on the characterization of inhalation aerosols, device design and formulation development.

Anthony J. Hickey

Dr. Hickey is Professor of Pharmaceutics and Biomedical Engineering at the University of North Carolina in Chapel Hill. He obtained a B.Sc.(Hons.) in Biology from Portsmouth Polytechnic in 1977 and a M.Sc. in Toxicology in 1980 from the University of Birmingham. He was awarded a Ph.D. in 1984 from the University of Aston in Birmingham for work conducted under the supervision of Drs. Igor Gonda and Bill Irwin. Following postdoctoral positions, with Dr. Peter Byron (1984-1986) and Dr. Patrick DeLuca (1986-1988), Dr. Hickey joined the faculty in Pharmaceutics at the University of Illinois at Chicago in 1988. In 1990 he received the Young Investigator Award in Pharmaceutics and Pharmaceutical Technology from the American Association of Pharmaceutical Sciences. In 1993 he accepted a faculty position in the School of Pharmacy at UNC-CH. He has published over seventy papers and chapters in the pharmaceutical and biomedical literature and has edited two texts on the subject of pharmaceutical inhalation aerosols. He is a reviewer for a number of scientific journals and is currently a member of the editorial advisory boards of Pharmaceutical Technology, Pharmaceutical Development and Technology and Particulate Science and Technology. Dr. Hickey supervises a multidisciplinary group of biomedical engineers and pharmaceutical scientists studying aerosol drug delivery to, disposition in, and from the lungs. Research projects in the areas of physical chemistry, aerosol physics, pulmonary physiology, pharmacology and cell biology are addressed by the group and are focused on novel approaches to the treatment of lung diseases.

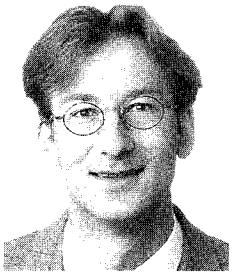

Peter Holzner

Dr. Holzner is Assistant Professor in the Department of Pharmaceutics and Biopharmaceutics at the Institute of Pharmacy, University of Kiel, Germany, since August 1998. He received his undergraduate training in Pharmacy at the University of Regensburg, Germany, and the University of Colorado at Boulder, USA. He became a licensed pharmacist in 1991 and received a Ph.D. (Hons.) in Pharmaceutical Technology from the University of Kiel in 1995. In 1996, following military service as chairman of the Division of Quality Assurance in the hospital pharmacy at the Bundeswehrkrankenhaus in Hamburg, Germany, he became a post-doctoral research fellow with Dr. Anthony J. Hickey at the University of North Carolina in Chapel Hill.

Dr. Holzner is a member of the International Association for Pharmaceutical Technology (APV) and the American Association for Pharmaceutical Scientists (AAPS). He has published 20 research articles, book chapters and abstracts on the characterization of pharmaceutical aerosols, inhalation devices, formulation development and gene delivery to the lung. Current research interests focus on pharmaceutical biotechnology, the stabilization of liposomes and plasmid-lipid complexes for formulation development, and powder aerosols for pulmonary gene delivery.

Review

The Modification of Fine Powders by Inorganic Coatings†

T. A. Egerton
*University of Newcastle upon Tyne, UK**

Abstract

This review describes the modification of fine particles by the formation of an inorganic coating. It shows how a technology, which has been developed in, but mainly confined to, the titanium dioxide pigment industry, has considerable potential in other areas. Inorganic coatings may be used to encapsulate a solid or modify its dispersion properties. They may also be used to impart desired properties, e.g. electrical conductivity or to obtain specific optical effects. In ceramics, inorganic coatings offer a way of distributing minor components, such as stabilisers for zirconia or toughening agents for alumina, in a way that does not depend on the vagaries of mixing. Examples of different coating procedures are presented, and for two of these – dense silica and silica-alumina – the mechanism is briefly described. The uses and limitations of gas adsorption, electron microscopy, electrophoresis, ESCA and SIMS for coatings characterisation are summarised. It is shown that each is useful for coating characterisation but none can unambiguously differentiate between uniform and patchy coating. Finally, specific examples of improved dispersion, improved barrier performance and beneficial powder properties are presented.

Introduction

Fine powders may be used to modify the properties of a continuous organic medium – for example titanium dioxide can be an opacifier in paints and inks, or aluminium hydrates a flame retardant in plastics. Alternatively, powders may be the constituents from which ceramic or other components are fabricated – for example barium titanate for multi-layer capacitors or silicon nitride for the fabrication of turbo-charger rotors. In each case the powder is selected because of its desirable bulk properties – the high refractive index of TiO_2, the endothermic evolution of water from aluminium hydrates, the dielectric properties of barium titanate or the high temperature strength, coupled with low density, of silicon nitride. However, to optimise its opacity the titanium dioxide must be dispersed in the paint and resist flocculation during film formation. The aluminium hydrate must be incorporated into the polymer. Barium titanate may have to be dispersed into an ink to allow screen printing, and the silicon nitride requires a sintering aid to promote densification of the fired component. Hence, as is normally the case, the processing of these powders is controlled by their surface properties. Modification of powder dispersion by the use of organic surface active molecules is widely practised, but this review describes an alternative means of surface modification – the deliberate formation of an inorganic surface layer, or coating. It also demonstrates that modification of particle surfaces by the formation of inorganic coatings has many uses other than dispersion control and some of these applications are demonstrated by the following examples. Although many of the examples above have been drawn from the literature of pigment technology, the aim of this review is not to discuss pigment technology. Rather, it is to draw the readers attention to the possibilities that inorganic coatings may provide in many other application areas.

Control of Dispersion

In order to turn the potential opacity, implicit in the high refractive index of titanium dioxide, into observable opacity in a paint film, it is necessary to optimise the pigment dispersion. This is normally done by coating the surface of the pigment. Typical coatings include hydrous oxides or phosphates of alumina, silica and zirconia. A large literature demonstrates that important properties such as the medium demand of the pigment, the viscosity of the paint mill-base and the optical properties of the derived paints are all modified by the presence or absence of an inorganic coating (1, 2). Coating of iron oxide pigments has also been shown to be beneficial, for instance in the improved flow and gloss of powder coatings (3).

* Department of Chemistry, The Bedson Building, Newcastle NE1 7RU, UK
† Received May 20, 1998

Control of Photoactivity

Solar UV induces photocatalytic activity in titanium dioxide, which would, if not controlled, destroy the organic media to which TiO_2 pigments impart opacity. A suitable inorganic coating can reduce the photoactivity and significantly extend the UV resistance of the pigmented system (2, 4).

Encapsulation to Prevent Leaching

An encapsulating layer may also be used as a physical barrier. Alumina, silica-alumina and antimony oxide- silica -alumina coatings on chromate pigments can reduce leaching of potentially toxic ions and prevent discolouration reactions with the organic matrices (1, 5). Similarly, work on inorganic coatings for organic pigments has been prompted by the goal of reducing their solubility, and also of improving their rheological properties (6). Composite pigments in which a core particle is covered first with a layer of water soluble organic colorants and then sealed by an optically transparent film have also been described (7).

Electrically Conducting Coatings

In contrast to the two previous examples in which the coating is a barrier, it may itself contribute to a desirable property. Thus, inorganic coatings are used to manufacture electrically conductive powders, suitable as anti-static pigments or for the formation of conductive layers on paper. The challenge is to manufacture a product that is conductive but not black. Antimony-containing tin oxide is conductive but it cannot by itself be produced as a powder with uniform particle size and good dispersibility. Also, as the antimony content is increased the colour becomes bluish and less white. One solution to this problem has been to coat titanium dioxide with antimony-containing tin oxide and thus combine conductivity, dispersion and whiteness. The resistivity of a 10% $(Sb+Sn)O_2$ coated powder is five orders of magnitude less than that of a physical mixture of the components (8).

Novel Optical Effects

Coatings also contribute directly to desired effects in pearlescent, or 'effect' pigments which are manufactured by forming an iron oxide or titanium dioxide film of carefully controlled thickness on substrates of mica or aluminium flakes. A portion of incident light is reflected at the coating surface and a further portion is reflected at the substrate. The consequent interference gives rise to an appearance which depends on the thickness of the coating and on the angle from which it is viewed. If the substrate is mica, different colours may be seen in reflection and transmission and if the coating itself absorbs light, e.g. Fe_2O_3 on aluminium flake, the highest colour brilliance is observed when the interference colour is close to the absorption colour of the coating. It is important that coatings of this type are relatively smooth and if they are formed by precipitation they may be subsequently calcined (9). Alternatively, the coating on, e.g, aluminium flakes may be deposited in a fluidized bed by chemical vapour deposition (10).

Electrorheology

Certain suspensions of polarizable particles dispersed in insulating oils exhibit a rapid reversible change in the viscosity following the application of an electrical field. This phenomenon is called electrorheology. Composite particles consisting of an acrylic polymer core coated with titanium hydroxide particles have been shown to give excellent electrorheological suspensions (14).

Applications in Ceramics

Coatings of precipitated hydrous metal oxides have been found to be very effective binders for ceramic powders. They give high compacted densities and higher green strengths than those obtained with organic binders (11).

The control of stabilising additives is a key to the successful production of partially-stabilised zirconia ceramics. Inorganic coatings have been found to be a very efficient way of controlling the amount and distribution of additions, such as yttria or ceria (12). During the firing process the stabilizer migrates from the surface of the ceramic into the zirconia particle. The derived ceramics have high strength, and sinter at 1350°C to >97% theoretical density (13). Such coatings may be formed by precipitation from aqueous salt solutions or by hydrolysis of alkoxides.

The Preparation of Coated Powders

The most usual means of forming a coated powder is by the precipitation of an inorganic hydrous oxide onto the surface of the particles to be coated. For reasons of convenience the coating constituents are usually designated by such terms as 'alumina', 'silica', 'zirconia' etc. This should not be take to imply the existence of a discrete oxide phase – it is merely a convenient shorthand for the hydrous oxide, silicate or phosphate that has been precipitated. Unless the coated particles are subsequently deliberately calcined, or dried at high temperatures, the coatings are

heavily hydrated and it is therefore not surprising that they are non-crystalline. In some cases an anhydrous layer may be formed on a substrate particle, e.g. by a solid gas reaction in a process of chemical vapour deposition. However, even in these cases the coating is usually amorphous. **Figure 1** shows a typical coating on the surface of crystalline titanium dioxide. The contrast between the crystallinity – exemplified by the clear lattice images – of the substrate and the amorphous coating is clear.

The following sections provide an introduction to a few of the many methods that have been used to modify the surface of fine inorganic powders, and for the two most important classes a brief description of the coating mechanism is included.

1. Dense Silica coatings

Perhaps the most widely applicable method of applying an inorganic coating to a substrate is Iler's 'dense-silica' method. (16, 17, 18). The original patent describes examples of the formation of dense silica on attapulgite, haloysite and kaolin clays, chrysotile and crocidolite asbestos, vermiculite and talc, iron powder, nickel and aluminum flake, glass fibres, cotton and nylon cloths, and on titania pigments. The method is illustrated by the following two examples.

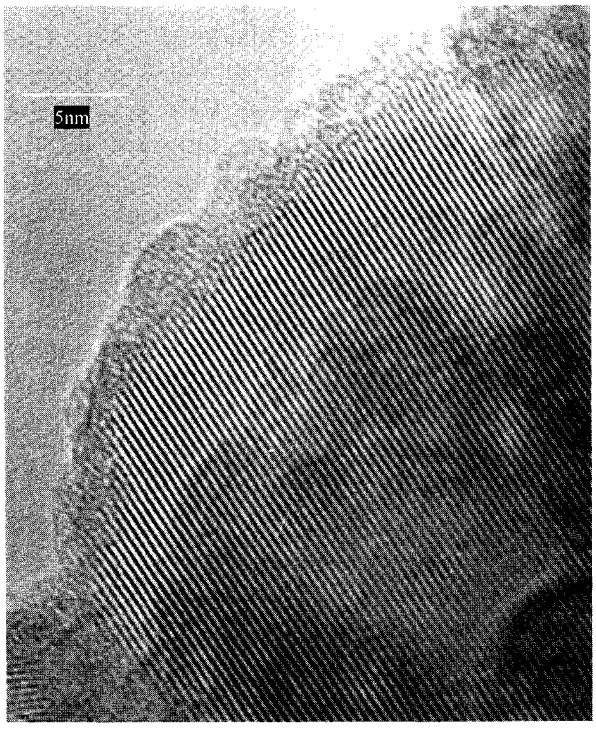

Fig. 1 High resolution electron micrograph of a rutile crystal coated with silica-alumina type coating. The contrast between the crystalline substrate and the amorphous coating is evident.

Dense Silica on Aluminium Flake

Aluminium flake was pre-treated in 0.25% sodium silicate solution and was then suspended in water at 2.4% solids concentration. Sufficient sodium sulphate was added to make the solution 0.2M in sodium ion. The suspension was then heated to 95°C and 1000 cm^3 each of a sodium silicate solution (4% SiO_2 and 1.25% Na_2O, equivalent to 0.33 gms of silica per gram of aluminium) and 1.57% sulphuric acid solution were added simultaneously, but separately over a period of 2 hours during which the pH hardly changed (9.3 at start, 9.5 at end). The final free-flowing product was 15.6% SiO_2 and had a surface area of 40 m^2/g (compared with 51 m^2/g. initially). One criterion of the applied coating being 'dense', i.e. not porous to nitrogen, is that coated particles whose core density is comparable with that of silica should have a surface area that is the same as, or lower than, the un-coated material.

Dense Silica on Titania

In another example, a dense silica coating was applied to a 200 g.p.l dispersion of rutile in water at pH 10. The slurry was then heated to 95°C and to the vigorously stirred suspension 1 litre each of sodium silicate (4% SiO_2 and 1.25% Na_2O) and of 1.57% sulphuric acid were added separately but simultaneously at a rate of 15 ml/min. During this addition the pH fell to 8.7. The suspension was filtered, washed and the pH adjusted to 6.5 before further washing and air drying. An electron micrograph of a titanium dioxide particle coated by a dense silica method is shown in **Fig. 2**. It shows

Fig. 2 Electron micrograph of a silica coated rutile prepared by the dense silica method. The coherent nature of the coating is demonstrated.

clearly the dense skin of substantially uniform thickness bound to the core particle and composed of amorphous hydrated silica. Iler demonstrated that a key advantage associated with this skin is the reduction of the photo-activity of the resulting titanium dioxide pigments.

Mechanism of Dense Silica Coating

Although the steps in this mechanism are broadly understood their relative importance probably varies between different modifications of the process. However, it is probable that the first step in the coating is the adsorption of silicate on the surface of the substrate particle (e.g. in the coating of aluminium flake) and that this adsorbed material provides the surface on which subsequent coating occurs.

It is generally considered that the next step in the mechanism of the dense silica coating process is the generation of silicic acid, $Si(OH)_4$. This may be formed by the addition of silicon tetrachloride to water, by the ion exchange of sodium silicate solution, or by the addition of acid to sodium silicate solution. However, at pH 9 the solubility of $Si(OH)_4$ is only ca 0.01% (expressed as SiO_2) at 25°C (ca 0.04% at 90°C) and if its concentrations exceed a few hundredths of one percent it polymerises to form silica particles (19). However, provided that the particle growth is not allowed to continue, this polymerisation is reversible and Iler considered that the 'active silica' which is a precursor to dense silica coating contains both monomeric silica and particles up to 1–2 nm diameter. Further, since silica particles smaller than ca 5 nm are more soluble than large particles, large particles – e.g. substrate particles with an initial layer of adsorbed silica – would be expected to grow relative to discrete 2 nm particles by a process of Ostwald ripening – that is surfaces with a small curvature (large particles) grow at the expense of particles with a high curvature (small particles).

Therefore, putting these observations together, Iler concluded that dense silica coating occurred as a result of molecular deposition of $Si(OH)_4$.

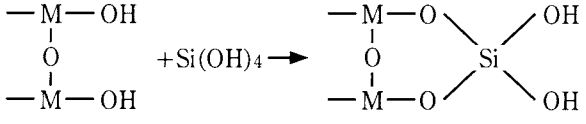

If the sodium silicate and acid are added too quickly the 2 nm silica particles will grow, the reverse reaction will become more difficult, and at ca 5nm the driving force for Ostwald ripening will be lost. Depending on the ionic strength and the pH the silica particles would then either form stable colloidal silica or form a gel and, at best, this will represent an inefficient use of the coating silica. The aim is to have sufficient super-saturation to coat the substrate without having so much super-saturation as to form a silica sol.

The choice of reaction conditions follows. The pH of 9 is sufficiently high to minimise the tendency of the 2 nm particles to form gels but is below the level, 10.5, at which the silica will redisolve as silicate ions. Further, at pH9 the base catalysed depolymerisation and condensation reaction rate is at its maximum and this will increase the rate of Ostwald ripening. Also, the rate of $Si(OH)_4$ transfer is accelerated at high temperature because of the increased solubility of silica. Iler (17) gives formulae relating the maximum permissible silica deposition rate to the temperature and the total surface area to be coated :

$$S = \frac{A\,(2)^n}{200}$$

where A is the specific area of the substrate (m^2/g)
n=(T-90)/10 where T is the temperature (K).
and S is the amount of SiO_2 added (g/hr per g. of substrate).

Developments of the Dense Silica Method

This 40 year old method still forms the basis of a wide range of coatings and has been developed extensively. In this summary I restrict myself to its DuPont descendants. Alexander (20) has described an extension of the method to produce silica coatings which contain chemically combined polyvalent metal ions. For example aluminium may be incorporated into a silica coating by simultaneously adding sodium silicate and sodium aluminate to a suspension of fine particles kept at a pH between 10 and 11. Zinc or copper may be incorporated by dissolving zinc sulphate or copper sulphate in sulphuric acid and then simultaneously adding the silicate and acid solutions. Other examples describe the incorporation of lead, magnesium and iron. Werner (21) has described the preparation of a titanium dioxide pigment with the improved durability resulting from a dense silica coating, but which, as a consequence of a subsequent precipitation of alumina, does not suffer from the poor dispersion associated with single component silica coatings. In this case the dense silica was deposited by first adding sodium silicate and subsequently raising the pH. The process described by Werner is slow and West (22) has described a faster method, suitable for continuous production. The essence of this faster process is increased pH and higher temperatures.

Other patents in this family claim the benefits of incorporating small amounts of boron at the dispersion stage (23, 24). Many of the other developments of the dense silica coating procedure focus on making the process more convenient at an industrial scale or on optimising pigmentary properties other than durability.

2. Silica Alumina Coatings

The molecular deposition of silica is believed to be central to the formation of dense silica coatings. However, the deposition of alumina-silica coatings can occur by a quite different route.

The Mechanism of Silica Alumina Coating

Howard and Parfitt (hereafter HP, 25) and subsequently others (26, 27) have provided insight into the mechanism of silica/alumina coating precipitation. The first stage in this process is the adsorption of polysilicate anion. HP described the addition of sodium silicate solution (containing the equivalent of 100 gm SiO_2/ℓ) to a slurry of TiO_2 at pH 3. Silicate adsorption continued throughout the addition as the pH increased to 10.5 but at maximum adsorption (0.5% SiO_2) only one quarter of the added silica was adsorbed on the substrate. This adsorption caused no significant change in surface area but was demonstrated by a decrease in the isoelectric point of the substrate from pH 3.5 to 2.7. Since the non-adsorbed silica was present in amounts considerably greater than the known solubility of silica at these pH s it was inferred that much of the unadsorbed silica was present as multimeric anions in stable dispersion.

The second stage of this coating process is the acidification of the titanium dioxide/silicate slurry by the addition of an aluminium salt. In the absence of aluminium salts, the acidification of the TiO_2/sodium silicate slurry simply causes the progressive desorption of silicate species from the titanium dioxide surface. In the absence of silicate, the addition of aluminium sulphate to an alkaline titanium dioxide slurry rapidly lowers the pH. At pH 10 the slurry becomes saturated with respect to aluminium salt and, therefore, during further addition of aluminium sulphate practically all the added aluminium is precipitated. This continues until the pH had dropped to ca. 3. At this pH the aluminium becomes soluble once more and therefore as the pH falls from 3.0 to 2.8 the additional aluminium sulphate is neither precipitated nor adsorbed – even though for a total of 2.8% (based on TiO_2) most of the aluminium is added over this range. **Figures 3** and **4**, derived from HP's results, summarise these changes and contrast them with the addition of aluminium salts to the titanium dioxide/silicate slurry. The addition of aluminium nitrate or aluminium sulphate to the silicate/titanium dioxide slurry caused the precipitation of all the aluminum ions, and ca 50% of the silicate, from solution at pH 9 to pH 10.

The remaining silica is precipitated from colloidal solution at pH 3.8 to 4, the point at which soluble aluminium cationic species become stable. HP con-

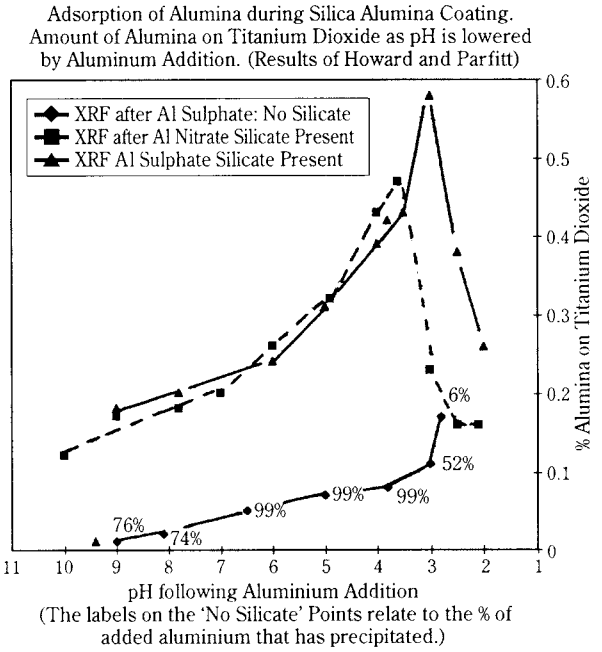

Fig. 3 The Adsorption of Alumina as the pH is reduced during the second stage of Silica Alumina Coating. For the silicate dispersed pigment, the amount of adsorbed alumina reaches a maximum at pH between 3.5 and 3.

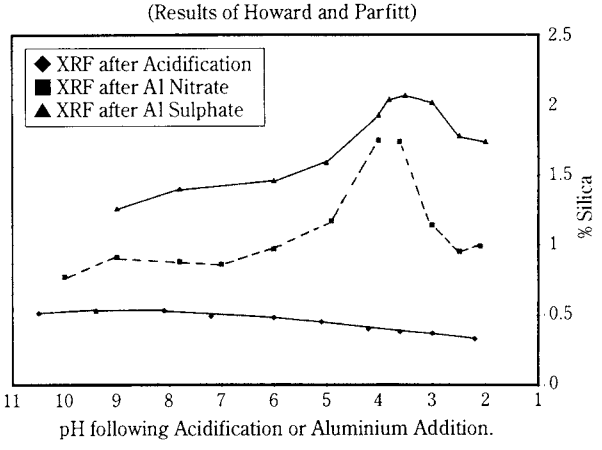

Fig. 4 The Adsorption of Silica accompanying the reduction of pH during the second stage of Silica Alumina Coating. When the pH is reduced with acid, previously adsorbed silicate desorbs. If the pH is reduced by the addition of aluminium sulphate there is considerable adsorption of silica.

cluded that to a first approximation the precipitation of the aluminium is governed by the solubility of aluminium hydroxide. The first stage of this precipitation is the formation of hydroxy aluminium polymeric species and these heterocoagulate with the anionic (poly-)silicate species. Thus both silica and alumina are precipitated. The maximum in the silica precipitation may correspond to the formation of higher molecular weight polymeric aluminium species at pH 6 to pH 4. Similarly, when the pH is lowered below 3.5, the polymeric aluminium cations, particularly those with nitrate counter-ions, de-polymerise to form soluble cationic aluminium species and release some of the hetero-coagulated silica. (To demonstrate this point, Fig. 3 and 4 include points for which the pH was lowered below 3 by nitric acid or sulphuric acid addition.) The resulting sol particles, aggregated at the titanium dioxide surface, form, after drying, a surface coating. The electrophoretic mobility of samples extracted from suspension at different stages of the coating process suggest that the external surface is silica rich.

During the third stage of this coating the pH is raised by adding alkali. Precipitation of the alumina and small amounts of silica in solution is essentially completed between pH 4.5 and 5.0 and the surface area shows a minimum at ca. pH 4. Further increases in pH remove sulphate from the coating, presumably as a result of hydroxide ion exchange, and increase surface area. After 'neutralisation' to pH 8.5 these silica-alumina coated titanias have surface areas of 16−18 m^2/gm, significantly greater than those of the dense-silica analogues.

A recent study (28) of coprecipitation of hydrous alumina and silica precipitated in an aqueous neutral suspension of titanium dioxide showed that the surface area decreased from 40 to 30 m^2/gm as the preparation time increased from 1 to 15 minutes.

Silica-Alumina Coating on Titania.

In a representative example of this procedure(26) sodium silicate solution (SiO_2: Na_20=3.2) was added to a 300 g.p.l. suspension of TiO_2 particles at 60°C. The stirred slurry was held at this temperature for 30 minutes during which adsorption of silicate occurred. Aluminium was then added as a solution of aluminium sulphate. During the initial stages of this addition the pH fell to ca 4 and complete precipitation of the residual silica and of the added alumina occurred. Further aluminium sulphate addition lowered the pH further, without further alumina precipitation but with dissolution of a small portion of the precipitated silica. The slurry was then neutralised with NaOH and this caused complete precipitation of alumina and silica in solution.

Other Silica-Alumina Coatings.

A very large number of silica-alumina coating variations have been described and used and it not possible to summarise them all here. The most important variation is the use of sodium aluminate in place of aluminium sulphate and mechanistic studies of this coating route have been described (26, 27). High pH probably facilitates the formation of the pseudo-bohemite phase in the coating alumina (29). Other variants have include the incorporation of titania or zirconia in the coatings (4) and the use of phosphate dispersants rather than sodium silicate (30).

3. Alkoxide-derived Coatings.

The methods described above have all made use of conventional inorganic reagents, aluminium sulphate, sodium silicate etc. It is also possible to coat from alkoxides of e.g., aluminium, silicon or titanium, and methods of this sort have been attractive for academic studies because they eliminate the counter-ions which can otherwise increase the ionic strength of the suspension (and hence cause flocculation of the coated particles) or else be incorporated into inorganic coatings (as with the sulphate ions derived from aluminium sulphate).

The coating of gold sols by a two stage process involving first the hydrolysis of an alkoxide (a Stober silica step) and subsequently an Iler type dense silica step has been described, together with the optical properties of the resulting sols (31).

4. Coatings on Ceramic Particles.

A number of studies of dense silica deposition on alumina have been published (18, 34) but there has been much less effort directed towards understanding the mechanism of other coatings on ceramic particles and the coating procedures are much less well developed.

In a very simple example (11), focused on production of zirconia toughened alumina, alumina (Sumitomo AKP 30) was ultrasonically dispersed in water and the pH adjusted to 0.8 by the addition of nitric acid. Sufficient zirconyl sulphate solution to give 15% zirconium oxide was then added drop by drop, with vigorous stirring. The pH was raised to 8.5 with ammonia solution and was held at this level for 20 minutes. During the addition hydrous zirconia was precipitated on the alumina particles. The coated product, after

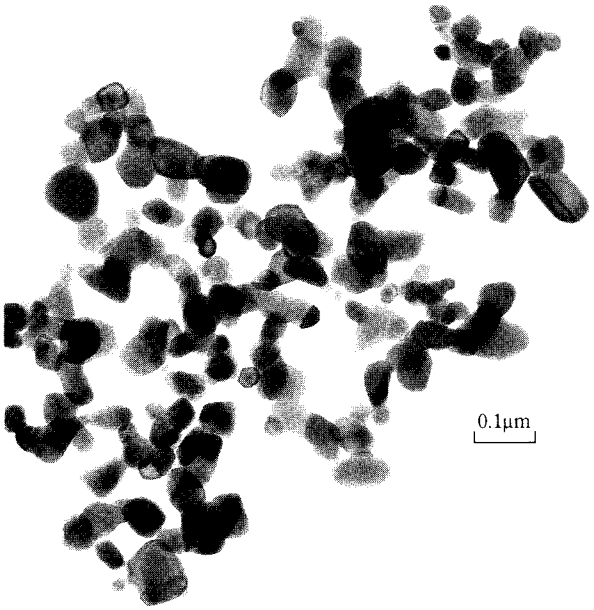

Fig. 5 Uncoated Zirconia Particles

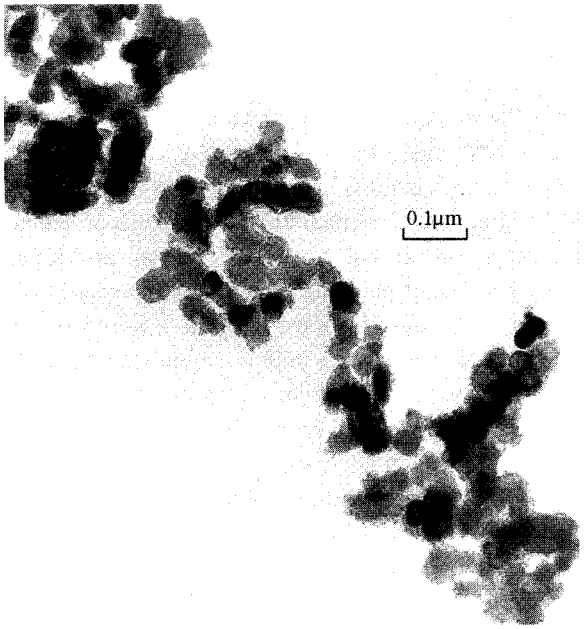

Fig. 6 Zirconia Particles Coated with Ceria

filtration, washing and drying at 110°C, had surface area of 54 m^2/gm compared with the alumina surface area of 7.4 m^2/gm. Electron microscopy suggested that the coating was well distributed but very fluffy and density measurements by gas pycnometry showed the density of the coated particle to be significantly lower than the uncoated substrate. It is clear that the voluminous coating is heavily hydrated and this was confirmed by both thermogravimetric analysis and surface area measurements after calcination at increasing temperatures. The initially amorphous coating became crystalline after calcination and microscopy showed a number of zirconia islands distributed over the surface of each alumina crystal. Similar experiments have been reported using zirconyl chloride as the starting reagent (32). A preparation using zirconium alkoxide hydrolysis also led to a fluffy coating and increased surface area from an initial 12 m^2/gm to 100 m^2/gm for the coated sample (nominally, 20% zirconia) (33). As with the samples prepared by hydrolysis of zirconyl sulphate, the alkoxide-derived samples showed significant weight loss during firing and continued to lose weight up to 500°C (35).

The coating of zirconia particles with stabilisers such as yttria and ceria has been much more successful (12, 13). For example, a dispersion (200 g.p.l) of 0.1 μm zirconia particles was coated by first heating to 50°C and then adding an aqueous solution of acid zirconium sulphate in an amount sufficient to introduce 1% (w/w as ZrO_2) of hydrous zirconia. An aqueous solution of yttrium chloride was then added in an amount sufficient to introduce 6% (w/w as Y_2O_3). The pH was then raised to 8.0 over 45 minutes and the dispersion was then stirred for a further 30 minutes before filtration, washing and drying. **Figures 5** and **6** are electron micrographs of uncoated and ceria coated zirconia prepared by this route. Fired ceramics prepared by this route had strengths>1000 MPa and fracture toughness >15 MPa $m^{0.5}$ (36).

Ceria stabilised zirconia powders have been coated with yttria or alumina using a homogeneous hydrolysis process in which the pH change is induced by heating an acidic solution of reactants containing urea (15).

5. Vapour Phase Coating or Chemical Vapour Deposition (CVD)

The previous four sub-sections have described the formation of inorganic coatings by controlled precipitation of the coating components from an aqueous phase onto the surface of fine particles in an aqueous suspension, or slurry. An alternative coating route – particularly suited to the treatment of particles which have been formed in the gas phase – is by deposition from the vapour phase.

As might be expected there is a voluminous patent literature (e.g. 37) but the elements of the method are summarised in recent papers (38, 39) which describe the gas-phase coating of titania with metal oxides. The coating precursors (e.g. $SiCl_4$, $AlCl_3$, $ZrCl_4$) may be introduced, either singly or in combination, into the vapour phase down stream of a $TiCl_4$ oxidation reactor. Introduction of $SiCl_4$ at 1500°C gave relatively uniform silica coatings 5–20 nm thick. Similar uniform

coatings could be achieved at 1300°C if some water vapour was also added to the reactor. Results were reported for silica, alumina, zirconia, silica/alumina and zirconia/alumina coatings and simple models of the competing processes were proposed (40). In general, the gas phase oxidation of $SiCl_4$, $AlCl_3$ and $ZrCl_4$ is slower than that of $TiCl_4$ and it is likely that the coating is achieved by reaction of the coating precursor with the already formed TiO_2 surface

$$TiO_2 + SiCl_4 \rightarrow SiO_2 + TiCl_4$$

rather than by initial gas phase oxidation of $SiCl_4$ to SiO_2 followed by deposition on the TiO_2 surface. At lower temperatures, exchange reactions of the type

$$Al_2Cl_6 + TiO_2 \rightarrow AlOCl + TiCl_4$$

have been shown to occur by X-ray identification of the AlOCl (41) and the kinetics studied.

Commercial application of these methods would eliminate the need for first wetting and then drying titanium dioxide pigment. However, despite the apparent attractiveness of a simpler process, as described in numerous patents (37, 42, 43), the route has not been commercially exploited, most probably because of the practical difficulties of neutralising the acid surface that results from the oxidation of metal chlorides, the only economical coating precursors for bulk chemicals. However routes involving more expensive coating precursors – e.g. decomposition of alkanoyl oxysilanes (44) – have been studied for specialist applications.

An interesting recent variant on vapour phase coating is a report of the in situ synthesis of palladium powders coated with, e.g. ZnO and CaO by a spray pyrolysis method.(45).

The Characterization of Coated Powders

An ideal coating process would lead to each particle of material A acquiring a uniform coherent coating of component B. Alternatively B will coat A, but will do so unevenly, so that, instead of a uniform coating, islands of B will form and uncovered, bare patches of A will persist. By contrast, a totally unsuccessful coating procedure will lead to the precipitation of B as a separate phase and will leave the entire surface of A uncoated. (See **Fig. 7**) The possibilities become more complex if a multi-component coating is required, and it is therefore not surprising that the characterization of coated powders remains a significant challenge for the materials scientist.

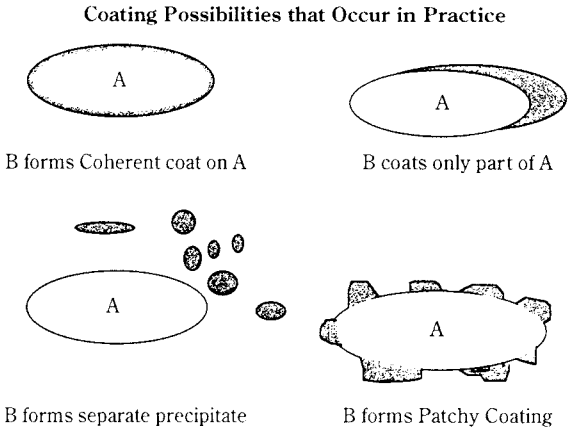

Fig. 7 Different Coating Possibilities that can occur in Practice. The ideal characterization method would differentiate between all of these options.

Surface Area and Adsorption

For the development technologist the simplest method of characterization is usually surface area determination and the most useful is electron microscopy. The specific surface area (SSA) of a spherical particle of radius r and density ρ is given by

$$(SSA)_{uncoated} = 3/(r \cdot \rho)$$

If a truly coherent non-porous coating has been achieved the SSA of the coated particle will, to a first approximation, be

$$(SSA)_{coated} = 3/(r \cdot \rho \, [\, 1+x/300])$$

where x is the amount of coating, expressed as weight %, and it is assumed that the density of the coating is equal to that of the underlying particle. In theory, the coated sample will thus have a lower surface area than the uncoated parent material as exemplified by 40 m^2/gm for dense silica on 51 m^2/gm aluminium flake. Dense silica coatings on 7 m^2/gm TiO_2 typically have a surface area of ca 10 m^2/gm as measured by nitrogen adsorption. By contrast silica alumina coatings, of the type described earlier, often have areas in the range 15–20 m^2/gm. An increase of surface area of 10 m^2/gm can easily result from 5% of coating. It follows that the coating must have an area of ca. 200 m^2/gm and most of this must be internal area – that is, the coating must be porous to nitrogen. It is therefore unsurprising that the changes in surface area accompany the incorporation and replacement of sulphate ions during the neutralisation of silica alumina coatings (**Fig. 8**).

The use of adsorptives other than nitrogen gives additional information. Thus it has been shown that, for n- pentane, the B.E.T. 'C constants' (a measure of

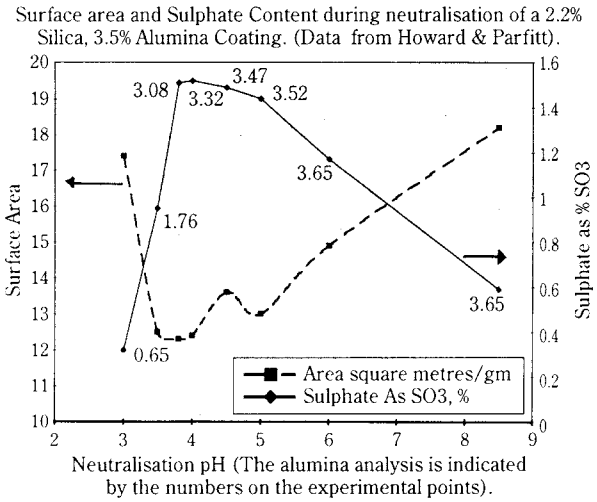

Fig. 8 Surface Area and Sulphate Content During Neutralization of Silica-Alumina Coating

the adsorption strength) and the molecular areas, σ, are quite different for rutile alumina and silica (46). The n-pentane isotherms on a of a rutile base coated with 3% silica, alumina or titania gave values similar to those of the pure oxides and thus demonstrated the similar surface characters of the coatings and the corresponding pure oxides. High levels of water adsorption have been ascribed to the reversible desorption of water from the hydrous coatings during outgassing, whilst ethanol – which cannot penetrate the bulk of the coating material – has been used to probe the hydrophilic nature of the exterior surface of the coating (47).

Electron Microscopy

The primary method of assessing coating quality is electron microscopy. Figure 2 shows a transmission electron micrograph of a silica coated titanium dioxide. The coherent coating layer can be seen clearly. However, because transmission microscopy of this type measures through the particles it averages thicknesses which may vary over the depth dimension. Thus, the appearance of uniformity is enhanced. **Fig. 9** shows a scanning electron micrograph of a pigment which has been coated with both dense silica and alumina. The underlying, darker areas, in this micrograph are believed to be due to silica which has formed a coherent coating on the TiO_2. The lighter patches are due to alumina which has formed patches on the underlying silica even though the alumina is present in amounts which, if evenly distributed, would form a coherent overcoat over the silica. Both the silica only and the silica plus alumina coatings were prepared using a dense silica method of the general type described above.

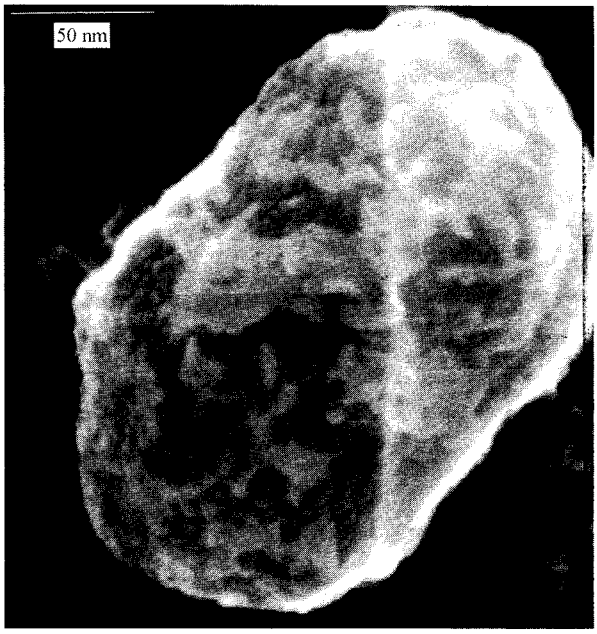

Fig. 9 Scanning Electron Micrograph showing alumina patches on a dense silica coating.

The major limitation of the electron microscopy is that only a very few crystals are examined. One gram of a fine powder contains about 10^{14} crystals of 100 nm radius, but it is highly unlikely that more than a few hundred crystals will be examined in a high resolution t.e.m. study. Therefore, although it is tempting to interpret micrographs, such as Fig. 2, as demonstrating a successful coating, they can easily mislead the optimistic development scientist. They are particularly difficult to interpret if the coating level is low. However, microscopy will detect both changes in the texture of the coating and the formation of bulk precipitates.

Electrophoresis and Point of Zero Charge

The next characterization method in the coating technologist's armoury is the measurement of electrophoretic or acoustophoretic mobility of the coated particle as a function of pH. Unlike the other methods considered here, this technique does not need the sample to be exposed, with risk of surface modification, to vacuum conditions. Surface ionization and isoelectric points vary from oxide to oxide and therefore this measurement may be used to infer surface composition. Further, because the surface potential controls the colloid stability and hence the rheological behaviour of the modified particles, the measurement is directly relevant to their behaviour in many applications, particularly if the measurements can be made at high particle concentration, e.g. by using acoustophoretic methods.

Pure silica has a much lower point of zero charge (p.z.c.) than pure titania. Therefore it would be expected that a silica coating would lower the p.z.c. **Figure 10**, based on results for silica on a pure rutile (48) shows that this is indeed the case. Deposition of 2.5% dense silica on pure titania of 20 m^2/gm gave isoelectric points judged to be consistent with pure silica. However, to obtain reversible mobility/pH curves which did not exhibit coating-solubility of the coating at low pH, a 5% coating was necessary.

The variation of isoelectric point with coating composition has also been reported and **Figure 11** shows measurements of the point of zero charge, taken from Losoi (27) and Parfitt and Ramsbotham (49), plotted as a function of the fraction of alumina in a silica alumina coating. Both sets of results show a general increase in the p.z.c. as the fraction of alumina in the coating is increased. Losoi's results also show that the coating sequence can be important: silica followed by alumina, gave a higher p.z.c. than alumina followed by silica, giving credence to the belief that some layering of the coating had resulted from the sequential deposition. The p.z.c plateau for the four Parfitt coatings that were richest in alumina is probably a consequence of the increase in weight fraction being almost entirely controlled by a decrease in silica – the actual alumina analyses were all close to 2.2%.

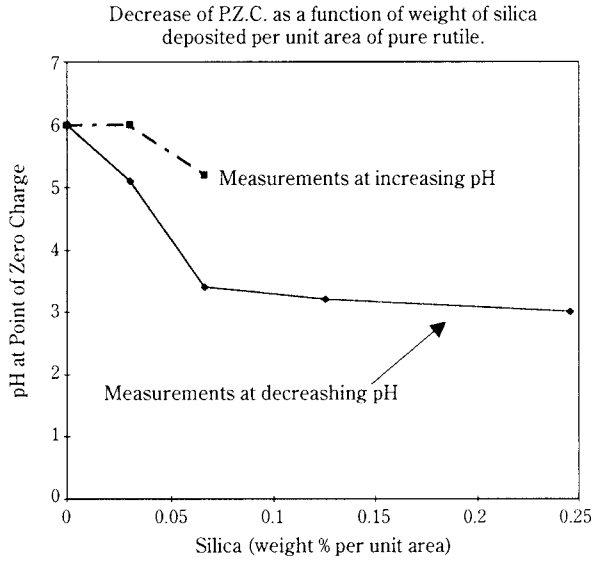

Fig. 10 Decrease of P.Z.C. as a function of weight of silica deposited on rutil. The difference in p.z.c. measured at decreasing pH and increasing pH are attributed to silica solubility at low pH.

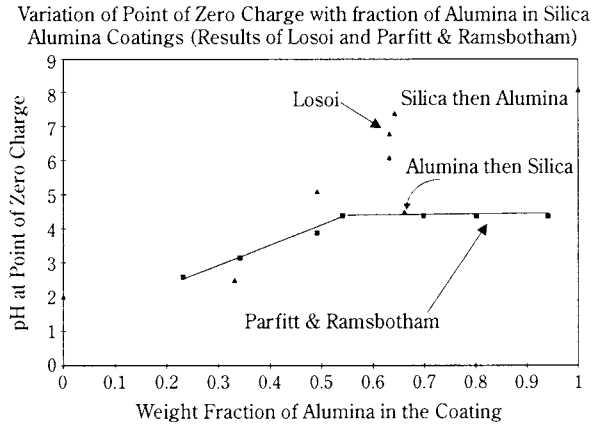

Fig. 11 Variation of P.Z.C. with increasing fraction of Alumina in Silica Alumina Coatings. Parfitt's results show the general trend. Losoi's results show that the detailed coating procedure also effects the P.Z.C.

Zeta potential curves for alumina coated with zirconia were similar for 1:8 and 1:1 zirconia alumina compositions and were taken to provide good evidence that the zirconia coats the surface of the alumina (32) but the possibility that the measurements were simply dominated by the zirconia because of its much higher (×8) surface area was not explicitly considered.

In summary, there is good evidence that electrophoretic measurements can differentiate between major changes of coating type.

Surface Analytical Methods

Since none of the classical surface characterization methods outlined above is able to answer all of the questions that can be asked about coating quality, a number of attempts have been made to use modern surface analytical techniques. These include X-ray Photo-electron Spectroscopy (XPS) often known as ESCA, and Secondary Ion Mass Spectrometry (SIMS). A limited number of Auger studies have also been carried out (26).

XPS measures the energy of electrons that are ejected from the solid by incident X-ray photons. The electron energy is characteristic of the element from which the electron is ejected, and the probability, P, that an electron originating from a depth, t, within a solid will reach a detector at an angle α to the normal to the solid surface is given by

$$P = K \exp(-t/\lambda \cos \alpha)$$

where K is a constant and λ is a characteristic escape depth (of the order of 1–2 nm for the cases of interest). As approximately 95% of the emitted electrons originate from a depth of 3λ (3–6 nm) from the solid surface, ESCA signals are dominated by the surface. For typical coatings the ratio of (coating element)/(substrate element) may be two orders of magnitude higher than those calculated from bulk analyses (27,

50). If the coating had simply precipitated as particles similar to the substrate particles the XPS ratio would approximate to the bulk ratio. Therefore, a high ratio confirms that the a coating rather than a bulk precipitate has formed.

However, for a 200 nm diameter particle, the outermost 5nm accounts for 15% of the mass. Since most coatings are less than 15% of the substrate mass, they are equivalent to less than 5 nm thick. (Because the coatings are porous the geometrical thickness may be greater than this, but there is a corresponding decrease in atom density.) As the ESCA sampling depth is typically 3–6 nm, it follows that at normal coating levels the underlying substrate can contribute significantly to the measured signal even when perfect encapsulation has been achieved. This conclusion has been confirmed experimentally for dense silica coatings on both alumina (18, 34) and titania (50). Thus although ESCA is highly surface sensitive, it is not sufficiently sensitive to readily differentiate between, e.g., a 3% coating spread evenly over a 200 nm particle, and the same amount of material covering only 50% of the surface with a coating that is twice as thick. (If $\lambda=2$ and the density of the coating is half that of the core, the core signal for the fully coated case falls to ca. 56% of the uncoated value, whilst the signal for the half coated core is 37% of the uncoated value) For planar surfaces greater surface specificity may be achieved by collecting the electrons that escape at large angles from the normal – that is by increasing the path length of solid through which they must travel. However, for an assembly of fine particles this angular dependent surface enhancement is negligible because of the complex geometry of the real surface (50). An alternative approach has been to use an ion beam to etch away the surface layer and measure the increase of substrate signal and decrease of coating signal as the upper layers are removed. This approach also is complicated for fine powder assemblies. The process is analogous to slicing the top from a box full of oranges – not matter how deep you slice, some skin will always be apparent. However, theoretical etching profiles have been calculated and compared with experiment (51). Despite these sophistications the overall conclusion remains: ESCA, like the classical techniques, will show gross coating differences but is less well suited to monitoring the practically important small deviations from perfect encapsulation by a thin coating.

Secondary Ion Mass Spectrometry measures the ions sputtered from a surface by a beam of incident ions. The technique is significantly more surface sensitive than ESCA and for a 4% silica coating on a titanium dioxide signal the SIMS Si:Ti ratio was 50:1 whilst the corresponding ESCA Si:Ti ratio was 10:1 Therefore SIMS is probably better suited than ESCA to studies of coating integrity. Although quantification of SIMS is extremely difficult it has been used with some success in studies of the mechanism of coating alumina with silica (18).

Examples of Specific Effects

In the introduction to this review various applications of coatings were indicated. In this final section three of these examples are described in more detail.

Coatings for Ceramics

The simplest example of the effect of surface modification on powder properties may be observed in the properties of the powders themselves. Both the bulk density and the cohesivity of TiO_2 are modified by the formation of a surface layer of, e.g., alumina or silica and similar effects are observed when zirconia is coated with yttria.

A beneficial application is found in the increased strength of compacts of coated particles in comparison with the uncoated starting materials (11). The first stage of ceramic processing is the preparation, by pressing, of a 'green' body with the form of the desired final article. These bodies must have a strength adequate to withstand the mechanical disturbance associated with transport within the factory, loading into furnaces etc. Typically the powders are compacted with a polymer binder, e.g. PVA, in order to obtain the required strength. However, these binders must be burnt out during firing and this can be a rate determining step in the kiln cycle. When zirconia-coated alumina ceramics, of the type described earlier, were isostatically pressed at 400 MPa the resulting compacts had strengths, measured in 4-point bend, of 13.5 MPa. This is significantly higher than the figure of 0.8 MPa for the same alumina coated with a PVA binder. Uncoated powder compacted at 400 MPa was too weak to be measured by this method. Similar results have been demonstrated for both titania and magnesia powders.

Dispersion

Coating affects the dispersion of particles in three ways. First it reduces the Van der Waals interactions which are responsible for the attractive forces between colloidal particles. For a constant electrostatic repulsion and steric stabilisation, this leads to a greater energy barrier to flocculation and therefore

stability is increased. The effect is particularly significant for core particles of a high Hamaker constant, e.g. iron oxide or titanium dioxide, coated by a material of low Hamaker constant, e.g. silica or alumina. For such particles in a 5mM 1:1 electrolyte, calculations (assuming a constant surface potential of 30mV) show that coatings of even 1 or 2 nm can increase the colloid stability by 10–20 kT and can therefore turn an unstable system into a stable one. Of course if one material is coated by another the surface potential at fixed pH will not remain constant because the number and type of ionizable groups will be altered, as demonstrated above for both silica (Figure 10) and silica-alumina (Figure 11) coatings. Therefore adsorption of surfactants and dispersing agents will also be changed and at a given pH adsorption of an anionic surfactant will drop to zero if the isoelectric point of the adsorbing surface is below the suspension pH, whilst the opposite trend will occur with a cationic detergent (52). In a key study of the effect of coatings on titanium dioxide pigments (53) it was shown that in alkyd paint systems the surface potential increased with increasing fraction of alumina in the coating. However, the magnitude of the increase was insufficient to account for the observed increases in opacity of the pigment. On the basis of adsorption from solution, it was demonstrated that the alumina coatings were more basic than the silica ones and, it was suggested, they could interact only with the few (two or three per polymer molecule) acid sites in the alkyd molecules. These molecules therefore adopted a looped configuration on the pigment surface. The more acidic silica surface was able to interact with the many basic groups (hydroxyls, esters) on the molecule which was therefore constrained to lie flat on the pigment surface. It was concluded that the increased pigment opacity was a result of steric stabilisation associated with the changed polymer conformation. Hence, in this example the chemistry of the particle surface – specifically its acid base nature – is also affecting the particle dispersion.

Control of Photoactivity

Photocatalytic oxidation of alcohols by titanium dioxide has been widely studied. The reaction is believed to involve the UV photo-generation of electrons in the conduction band, and holes in the valence band of titanium dioxide. The holes migrate to the oxide surface where they combine with surface hydroxyl anions to form hydroxyl radicals, OH'. These radicals then abstract a hydrogen from the isopropanol. Hence, if the surface is modified by coating, the photocatalysis should be reduced because of a barrier between the hydroxyl radicals and the isopropanol molecules.

Figure 12 shows how the activation energy for the reaction is increased as increasing amounts of coating are applied to a titanium dioxide catalyst. The increase in activation energy from ca. 48 to ca 75 kJ/mol occurs between 0.04 and 0.09% coating/m^2 of substrate and this range stradles the figure (0.07% coating/m^2) at which Furlong et al. (48) found that the p.z.c. of a silica coated pure rutile becomes relatively independent of coating level, as shown in Figure 10. This figure corresponds to coating thicknesses of ca 0.3 to 0.5 nm which may be compared with a distance of 0.16 nm for the Si–O bond length in silica. Yet again the profound effect of very thin coatings is demonstrated.

Acknowledgements

The electron micrographs used to illustrate this review were kindly made available by, and are reproduced by permission of, Tioxide.

Dependence of Activation Energy for IsoPropanol Photo-Oxidation on Coating Level. (Results of Day and Egerton (47))

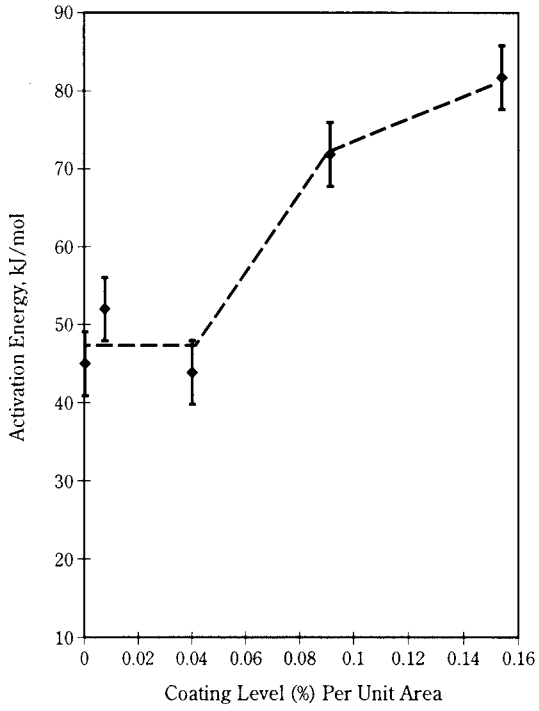

Fig. 12 The Activation Energy for Photocatalyzed Isopropanol Oxidation. The increased activation energy occurs at ca 0.06% silica/m^2, the same value at which the p.z.c. became constant (Fig. 10).

References

1) Solomon, D.H., and D.G. Hawthorne: "Chemistry of Pigments and Fillers", John Wiley and Sons, New York, U.S.A. (1983).
2) Blakey, R.R. and J.E. Hall: 'Titanium Dioxide', p. 1 in P.A. Lewis (ed.) "Pigment Handbook: Vol. 1: Properties and Economics" 2nd ed., John Wiley and Sons, New York, U.S.A. (1988).
3) Thometzek, P. et al.: Proceedings of 13th FATIPEC Congress, Brussels 1996.
4) Howard, P.B.: (to Tioxide Group Ltd.) U.K. Patent 1 479 988 (1977).
5) Shimazawa, K. et al.: (to Toda Kogyo Corp.) Japan Kokai 78 36 538 (1978).
6) Bugnon, P.: Prog. Organic Coatings, **29**, 39 (1996).
7) Otterstedt, J.E. et al.(to Small Particle Technology AB): International Patent Application WO 92/21726 (1992).
8) Yoshizumi, M. (to Mitsubishi Kinzoku Kabushiki Kaisha): European Patent 0 025 583 (1982).
9) DeLuca, C.V. (to the Mearl Corporation): U.S. Patent 5 4333 779 (1995).
10) Ostertag, W.E. and N.D. Mronga (to BASF): U.S. Patent 4 978 394 (1990).
11) Bromley, A.P., F.L. Riley, G.P. Dransfield and T.A. Egerton: Solid State Phenomena, **25 & 26**, 97 (1992).
12) Egerton, T.A., E.J. Lawson and P.W. Frost (To Tioxide Group): U.K. Patent 2 181 723 (1986).
13) Dransfield, G.P., K.A. Fothergill and T.A. Egerton: In Euro Ceramics, vol. 1, p. 275 ed. G. De With, R.A. Terpstra, and R.M. Metsalaar, Elsevier Applied Science Publishers, London (1989).
14) Otsubo, Y.: Kona, **15**, 43 (1997).
15) Djuricic, B.D. Mc Garry & S. Pickering: Third Euro Ceramics, vol. 1, p. 237 ed. P. Duran and J. Fernandez. Faenza Editrice Iberica, Spain (1993).
16) Iler, R.K.,(to E.I. du Pont de Nemours): U.S. Patent 2 885 366 (1959).
17) Iler, R.K.: "The Chemistry of Silica" John Wiley & Sons, New York, U.S.A. (1979).
18) Bergna, H.E., L.E. Firment and D.G. Swartzfager: in "Uses of Colloidal Silicas" Advances in Chemistry **234,** 561 (1994). American Chemical Society.
19) Iler. R.K. 'Colloidal Silica' in E. Matijevic, ed., "Surface and Colloid Science; Vol. **6**, p. 1, John Wiley, New York (1973).
20) Alexander, G.B. (to E.I. du Pont de Nemours): U.S. Patent 2 913 419 (1959).
21) Werner, J.W. (to E.I. du Pont de Nemours): U.S. Patent 1 179 171 (1970).
22) West, W. (to E.I. du Pont de Nemours): U.S. Patent 4 125 412 (1978).
23) Bettler, C.R. et al (to E.I. du Pont de Nemours): International Patent WO96015197 (1995).
24) Jacobson, H.W.: (to E.I. du Pont de Nemours): European Patent Application 0245 984 (1987).
25) Howard, P.B. & G.D. Parfitt : Croatica Chemica Acta, **50,** 15 (1977).
26) Bruni, M. et al.: Ind. Eng. Chem. Prod. Res. Dev., **24,** 579 (1985).
27) Losoi, T.: J. Coat. Technol., **61,** 57 (1989).
28) Gesenhues, U.: J. Coll. Interface Sci., **168,** 428 (1994).
29) Van Straten, H.A., B.T.W. Holtkamp and P.L. De Bruyn: J. Coll. Interface Sci., **98,** 342 (1984).
30) Howard, P.B. (to Tioxide Group Ltd.) U.K. Patent 1 479 989 (1977).
31) Mulvaney, P. et al: Langmuir **12**, 4329 (1996).
32) Rao, A.S. and R.W. Cannon: Ceramics International **15,** 179 (1989).
33) Fegley, B., P. White and H. Kent Bowen: J. Am Ceram. Soc., **68**, C60 (1985).
34) Firment, E.L. et al: Surf. And Interface Anal. **14**, 46 (1989).
35) Cortesi, P., and H. Kent Bowen: Ceramics International, **15** 173 (1989).
36) McColgan P., G.P. Dransfield and D.J. King: Third Euro Ceramics, vol. 1, p. 225 ed. P. Duran and J. Fernandez. Faenza Editrice Iberica, Spain (1993).
37) Hughes, W. (To British Titan Products) U.K. Patent 867 479 (1958).
38) Fotou, G.P. and T.T. Kodas: Adv., Mater. **9,** 420 (1997).
39) Fotou, G.P. et al.: Vol. 1V p. 784, 5th World Conference of Chemical Engineering, San Diego, California USA, 1996.
40) Jain, S., G.P. Fotou and T.T. Kodas: Vol. 1V p. 25, 5th World Conference of Chemical Engineering, San Diego, California USA, 1996.
41) Santacesaria, E. et al: Ind Eng. Chem. Prod. Res. Dev., **21**, 496 (1982). Santacesaria, E. et al: Ind Eng. Chem. Prod. Res. Dev., **21**, 501 (1982).
42) Scotti, C. et al: (to SIBIT s.p.a.) Italian Patents 19156A/80 and 1957A/80 (1980).
43) (to Kemira Pigments): International Patent WO 9603644 (1995).
44) (to BASF AG): U.S. Patent 5505991 (1994).
45) Jain, S. et al: Vol. 1V p. 31, 5th World Conference of Chemical Engineering, San Diego, California USA, 1996.
46) Day, R.E., G.D. Parfitt, & J. Peacock: J. Coll. Interface Sci., **70,** 130 (1979).
47) Day, R.E. & T.A. Egerton: Colloids and Surfaces **23,** 137 (1987).
48) Furlong, D.N., K.S.W. Sing and G.D. Parfitt: J. Coll. Interface Sci. **69,** 409 (1979).
49) Parfitt, G.D. and J. Ramsbotham: J. Oil Col. Chem. Assoc., **54** 356 (1971).
50) Egerton, T.A. et al: Colloids and Surfaces, **7**, 311 (1983).
51) Cross, Y.M. and J. Dewing: Surf. and Interface Analysis, **1**, 26 (1979).
52) Morrison, W.H.: J. Coatings Technol., **57**, 55 (1985).
53) Franklin, M.J.B., K. Goldsbrough, G.D. Parfitt and J. Peacock: J. Paint Technol., **42**, 740 (1970).

Author's short biography

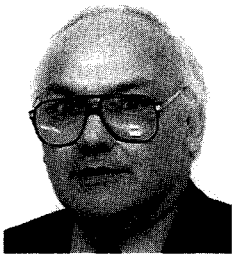

T. Egerton

Terry Egerton's career has been divided between Industry and University.
After a Chemistry degree from Imperial College, London and research in Physical Chemistry at Bristol University he was appointed as an ICI Research Fellow at the University of East Anglia. He subsequently held lectureships at Makerere University, Uganda, and University College Cardiff, Wales.
From Cardiff, he joined the Research and Development Department of Tioxide – Europe's largest manufacturer of Titanium Dioxide. He remained with Tioxide after its purchase by ICI and ultimately became a Company Research Associate on the ICI Scientific Ladder. During his 20 years experience with Tioxide he has been particularly concerned with research on the photoactivity of titanium dioxide pigments and on the formation of fine particles by both solution and gas phase routes.
In October 1998 Dr. Egerton joined the Department of Chemistry at the University of Newcastle as Senior Lecturer in Physical chemistry. His research interests are in the areas of Formation and Modifications of Fine Particles, their Surface Characterization and Applied Photocatalysis.

Review

Crystallization and Precipitation†

A. Mersmann
*Department B of Chemical Engineering, Technical University Munich**

Abstract

The paper deals with the design and operation of cooling and evaporation crystallizers and precipitators for reaction crystallization. It will be shown that the median crystal size L_{50} of a crystalline product and the Crystal Size Distribution (CSD) mainly depend on the crystallization kinetics, e.g. the rates of nucleation and crystal growth, and that this kinetics is controlled by supersaturation. Therefore, the main objective in crystallization and precipitation is to choose and to maintain the optimal supersaturation with respect to product quality at all times and all locations in the crystallizer or precipitator.

1. The role of supersaturation for the median crystal size

The selection of the apparatus or reactor and its operation condition depend on the chemico-physical properties of the system which can be described by the dimensionless solubility c^*/c_c (c^* is the solubility of the solute and c_c the density of the crystalline material) and the slope $d(\ln c^*)/d(\ln T)$ of the solubility curve $c^*=f(T)$ with T as the absolute temperature, see **Fig. 1**. Evaporative crystallization is necessary in the case of flat solubility curves $d(\ln c^*)/d(\ln T)<1$.

Drowning out crystallization is carried out by the addition of an antisolvent, for instance alcohols or ketones. The maximum possible supersaturation in the absence of any formation of solid matter (e.g. a theoretical supersaturation not occuring in crystallizers) is given by

the ratio $\frac{\text{solution flow rate}}{\text{cooling rate}}$ in cooling crystallization or

the ratio $\frac{\text{solution flow rate}}{\text{evaporation rate}}$ in evaporative crystallization or

the ratio $\frac{\text{solution flow rate}}{\text{antisolvant flow rate}}$ in drowning out crystallization

However, we demonstrate that the actual supersaturation $\Delta c \equiv (c\text{-}c^*)$ or relative supersaturation $\sigma=\Delta c/c^*$ is the result of crystallization kinetics and the presence of crystals and foreign particles in the apparatus.

In reaction crystallization, two or more components react chemically with the result that a new product is formed. If the initial concentration of the reactants is high and, therefore, the initial concentration c_{max} of the product is also very high but the solubility c^* is very low, the resulting high supersaturation $S_{max}=1+\sigma_{max}=c_{max}/c^*$ or $\sigma_{max}=\Delta c_{max}/c^*$ leads to high rates of primary nucleation. Since foreign particles in the nanometer range are always present in the reactant

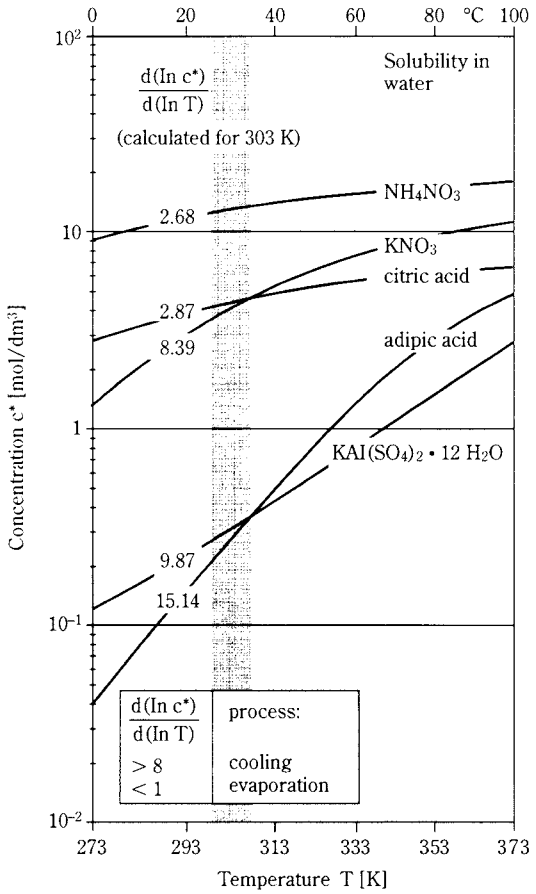

Fig. 1 Solubility of various solutes

* Boltzmannstr. 15, D-85747 Garching, Germany
† Received May 20, 1998

solutions, heterogeneous nucleation will take place. Homogeneous nucleation can be dominant at very high supersaturation ($\Delta c/c_c > 0.1$ for non-dissociating products).

Primary nucleation is an activated process which means that local or temporary peaks of supersaturation Δc are quickly reduced to the metastable supersaturation Δc_{met} ($\Delta c \rightarrow \Delta c_{met}$). The rate, B_{prim}, of primary nucleation is a function of the actual local supersaturation S. After this nucleation step, particles grow at the moderate supersaturation $\Delta c \leq \Delta c_{met}$ with the growth rate $G = f(\Delta c)$. If the residence time τ of nuclei in the precipitator or the batch time are small, the size increase $\Delta L = G\tau$ is small, too. When the crystal size exceeds approximately 100 µm, attrition fragments are formed which can act as secondary nuclei. The total nucleation rate is the sum $B = B_{prim} + B_{sec}$ of the contributions of primary and secondary nucleation. The median crystal size and the crystal size distribution (CSD) depend on the kinetic parameters B and G.

In the case of MSMPR (Mixed Suspension Mixed Product Removal) crystallizers or precipitators, the median crystal size L_{50} is given by

$$L_{50} = 3.67 \left(\frac{G\, m_T}{6\, \alpha\, B\, \rho_c} \right)^{1/4}$$

with the suspension density m_T and the density ρ_c of crystals. With reaction crystallization, the suspension density results from a mass balance of the reactants in the case of complete conversion. According to equation (1), nanoparticles can be obtained by applying very high nucleation rates, B_{prim}, which require very strong supersaturations S_{max}. Such high supersaturations can be achieved by

- high concentrated reactants
- products with high concentrations c_{max} but low solubilities c^*
- rapid micromixing at the feed point of the reactants

for a fast chemical reaction. If, however, a coarse product is desired, the supersaturation must be kept low by

- low concentrated reactants (perhaps by dilution)
- good macromixing in the entire precipitator and
- seeding by high recycling rates of slurry in order to reduce local supersaturation peaks by crystal growth.

In systems with high solubilities ($c^*/c_c > 0.01$), the supersaturation is so small ($\sigma < 0.1$) that activated nucleation does not take place and new nuclei are only formed as attrition fragments.

In this case large median sizes L_{50} can be obtained if

- the attrition rate $B_{att} \sim B_{sec}$ is low,
- the crystal growth rate G has the maximum allowable value with respect to crystal purity and
- the mean residence time of the slurry is optimum.

In the case of batch crystallizers, the median crystal size L_{50} as well as the CSD are dependent on the actual supersaturation which varies with time and also with the location, if a voluminous apparatus is not ideally mixed.

The kinetic crystallization parameters, i.e. the nucleation rate, B, and the growth rate, G, are necessary for the evaluation of the median crystal size.

2. Nucleation rate

The rate of primary nucleation depends on the diffusivity D_{AB}, the solubility c^*, the density c_c of the crystals and the supersaturation S, and can be calculated according to the classical theory of nucleation [6]. However, with respect to a very high particle or nuclei density N in the form of particles/m^3, a very rapid perikinetic agglomeration takes place with the result that observed nucleation rates, B_{prim}, of nuclei in the micrometre range are several orders of magnitude smaller than predicted by theory [9]. In addition, foreign particles are present in every solution leading to heterogeneous nucleation. According to experiments carried out with foreign particles added to the reactants, the nucleation work is reduced to approximately 10% of the value for homogeneous primary nucleation [1, 8]. Furthermore, the rate of heterogeneous primary nucleation is proportional to the specific surface area of foreign particles present in the solution [1, 8]. These results and further considerations allow evaluation of the metastable zone widths for homogeneous and heterogeneous nucleation. Below a certain supersaturation $\sigma_{met,sec}$ or $\Delta c_{met,sec}/c^*$, the nucleation rate induced by activated nucleation is so small that new nuclei can only originate from attrition fragments [6].

In **Figure 2**, the nucleation rate is plotted against the relative supersaturation S for activated (surface) nucleation (theoretical lines) and for attrition-induced nucleation (shaded area). Further theoretical considerations and experimental results lead to **Figure 3** where the dimensionless metastable zone width, $\Delta c_{met}/c_c$, (valid for $B \gg 10^{12}$ m^{-3} s^{-1}), is plotted against the dimensionless solubility, c^*/c_c, with c_c as the density of the solid crystals (valid for non-dissociating systems). In such a diagram, lines of constant relative supersaturation S can be drawn according to $\Delta c/c_c = (\Delta c/c^*)(c^*/c_c) = \sigma \cdot c^*/c_c$.

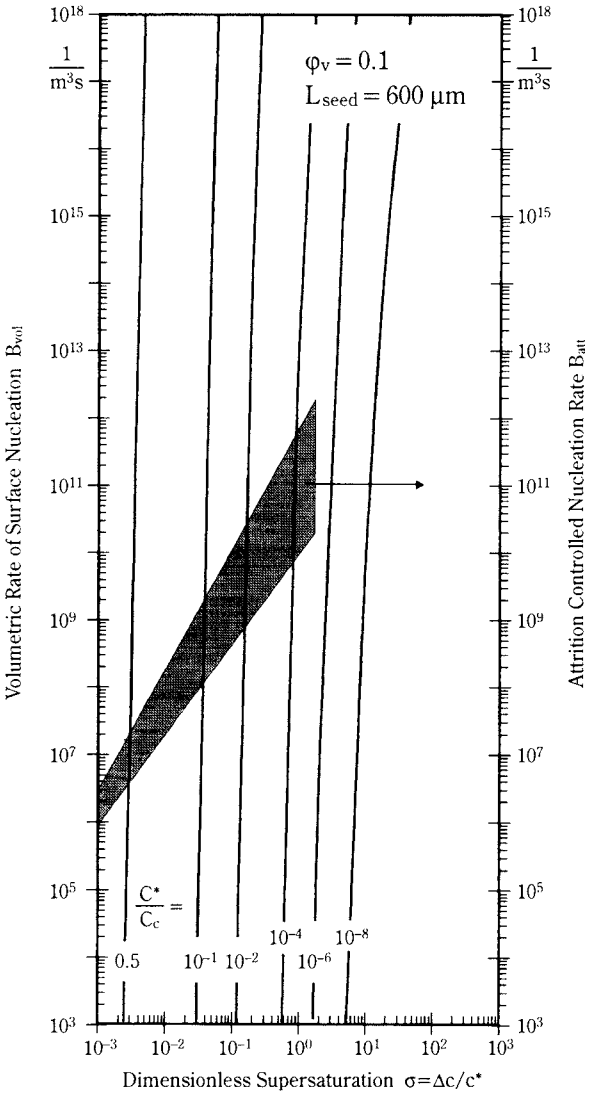

Fig. 2 Volumetric nucleation rate against the dimensionless supersaturation for activated and attrition-controlled nucleation

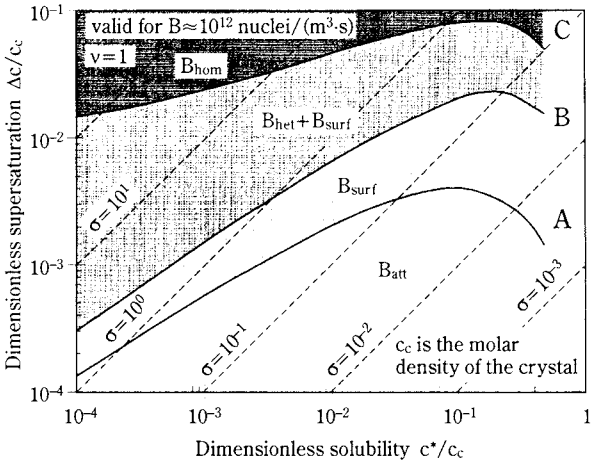

Fig. 3 Metastable zone widths $\Delta c_{met}/c_c$ against the dimensionless solubility c^*/c_c for homogeneous, heterogeneous and attrition-controlled nucleation

3. Growth rates

Experimental results and theoretical considerations have shown that the mean growth rate, G, of a crystal collective depends mainly on the mass transfer coefficient k_d, the dimensionless solubility, c^*/c_c, and the relative supersaturation $\sigma = \Delta c/c^*$ [4]. In **Figure 4**, the ratio v/k_d with $G = 2v$ is plotted against σ with c^*/c_c as the parameter. As can be seen from the shaded area in this figure, the growth rate G is often in the range

$$10^{-9}\ m/s < G < 10^{-7}\ m/s$$

and can be calculated for growth controlled by diffusion for $\sigma > 1$ from

$$G = \frac{\beta}{3\alpha} k_d \frac{\Delta c}{c_c}$$

α and β are the volume or surface shape factors, rsp.

Since the maximum supersaturation is $\Delta c_{met,act}$ after activated nucleation, the supersaturation Δc with $\Delta c_{met,het} > \Delta c > 0$ is decisive for the growth of nuclei. With batch crystallizers, the growth rate depends on the time-averaged supersaturation

$$\overline{\Delta c} = \frac{1}{\tau} \int_0^\tau \Delta c\, dt$$

Here, τ is the residence time of the crystals in the crystallizer. The curves in **Figure 4** show maximum possible growth rates in the absence of impurities or additives which retard or even block crystal growth. Only agglomeration of submicron particles of high particle density N may enhance the increase of crystal size per unit time. With needle-like crystals or platelets, the definition and prediction of crystal growth rates are difficult.

If the crystallizer is not ideally mixed, the local distribution of supersaturation has to be taken into account. This can be done by dividing the total active volume into sections with approximately constant supersaturation.

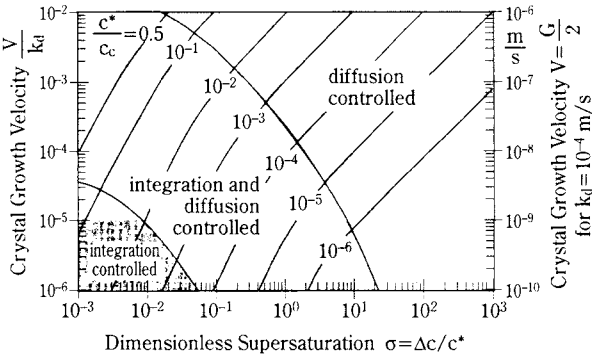

Fig. 4 Crystal growth rate against the relative supersaturation with the ratio c^*/c_c as the parameter

4. Median crystal size

In the case of activated nucleation, the rate B_{act} increases very rapidly with the supersaturation S (B_{act}~S^{10} up to B_{act}~S^{50} in the absence of agglomeration depending on c^*/c_c, see **Fig. 2**). In reality, however, strong agglomeration takes place for nuclei smaller than one micrometre [9]. The higher the initial supersaturation the smaller is the median crystal size L_{50} in the absence of agglomeration. In **Figure 5**, the median crystal size is plotted against the mean relative supersaturation σ (or the maximum supersaturation $\sigma_{max}=S_{max}-1$ for reaction crystallization) for inorganic and organic systems with different solubilities c^* or ratios c^*/c_c (the density of crystals is in the range 5 mol/dm^3<c_c<40 mol/dm^3). Additionally, the diagram shows experimental results of the aqueous systems of $BaSO_4$, $BaCO_3$, $CaCO_3$, $Mg(OH)_2$ and $MgC_2O_4y2H_2O$. As can be seen from this figure, the median crystal size drops with increasing relative supersaturation. In reaction crystallization, the relative supersaturation which is decisive for the median crystal size depends on

- the rate constant of the chemical reaction,
- the number and size of foreign particles present in the reactants,
- the effectiveness of macro and micromixing, and
- the maximum product concentration.

Experiments carried out with continuously operated precipitators have shown that the mean crystal size is much larger in comparison to products obtained with batch precipitators in which large differences of supersaturation occur with respect to time and space.

Systems with high solubilities (c^*/c_c>0.01) lead to median crystal sizes L_{50}>100 mm. The larger the crystal and the higher the collision velocity w_{col} of

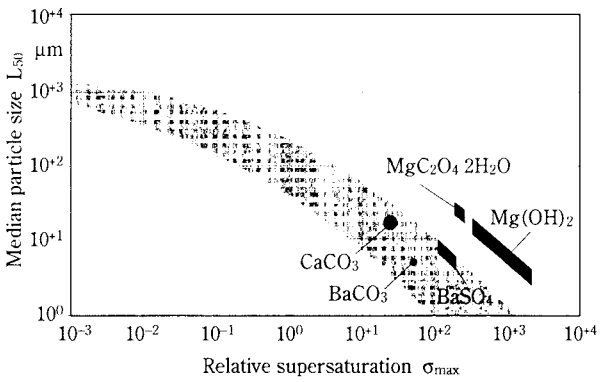

Fig. 5 Median crystal size against the initial (maximum possible) supersaturation; shaded are: results of inorganic and organic systems [5]

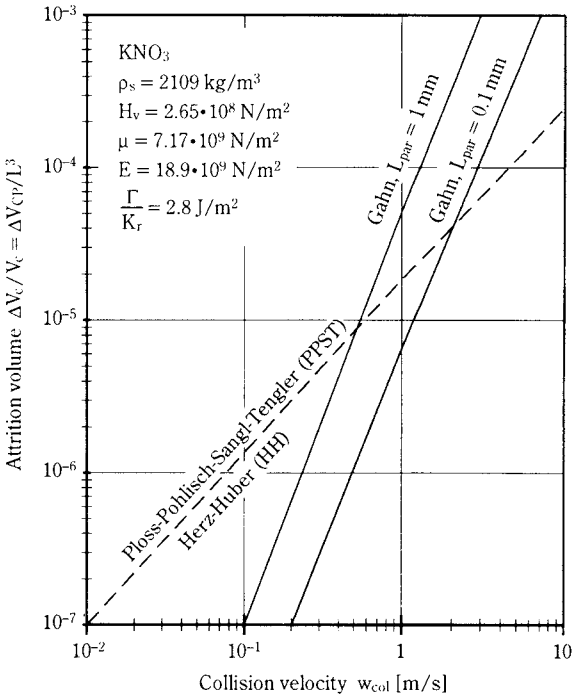

Fig. 6 Relative attrition volume against the collision velocity (crystal resistance) for KNO_3 according to different models

crystals against a resistance (rotor, wall, other crystals), the stronger are the attrition effects which lead to attrition fragments in the size range 1 µm<L_{att}<150 µm [11]. In **Figure 6**, the relative abraded crystal volume $\Delta V_c/V_c$ based on the volume V_c of a single crystal is plotted against the collision velocity w_{col} for 0.1 and 1 mm KNO_3 crystals according to a model of Gahn [11]. The diagram also shows lines according to a model developed earlier [12, 13, 14, 15]. In all cases, a huge number of attrition fragments are produced in industrial crystallizers with crystals larger than 100 µm. Therefore, it is necessary to restrict the circumferential velocity of rotors (stirrer, pumps) to <10 m/s and the mean specific power input in stirred vessels to $\bar{\varepsilon}$<0.5 W/kg when a coarse product is desired. The growth rate, G, of small attrition fragments is reduced due to crystal deformation and an increased chemical potential [16].

This reduction can be described by

$$G = k_g \left[\frac{c - c^* \exp\left(\frac{\Gamma_s}{\Re T L_{att}}\right)}{c^*} \right]^g$$

with k_g as the growth coefficient and g as the growth exponent usually in the range 1<g<2. The higher the fracture resistance Γ_s and the smaller the size L_{att} of the attrition fragment, the more the growth rate is reduced, see **Figure 7** valid for KNO_3 attrition fragments. With respect to individual differences in defor-

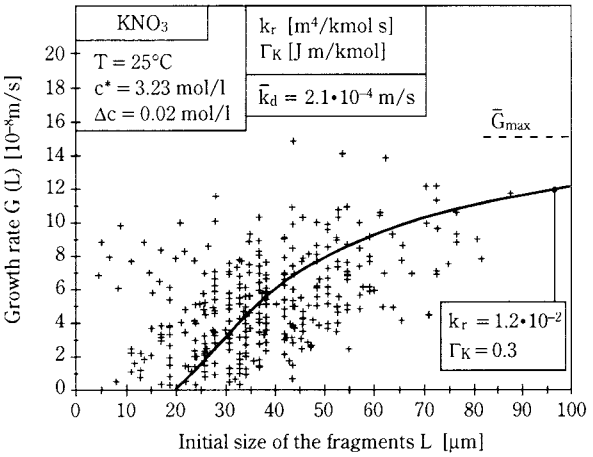

Fig. 7 Growth rate of 356 KNO_3 attrition fragments against their initial size

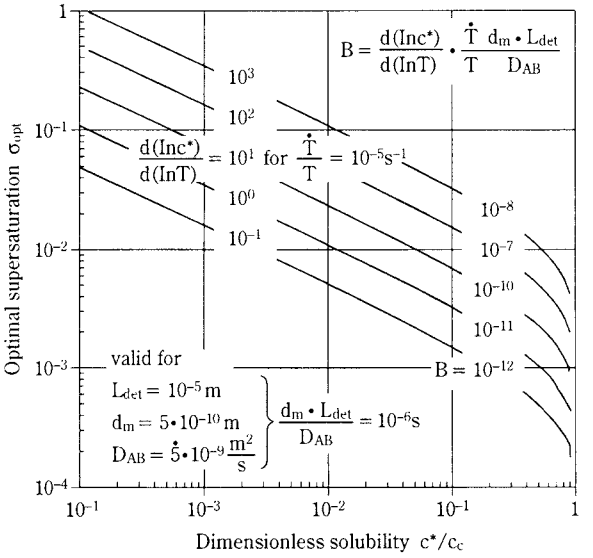

Fig. 8 Optimal supersaturation for cooling crystallization against the dimensionless solubility for different cooling rates or slopes of the solubility curve

mation, the growth rate differs from fragment to fragment (Growth Rate Dispersion, GRD). As a result of these considerations, large median sizes can only be obtained under the following conditions:

- the supersaturation has to be optimum (see **Fig. 8**), i.e.
- the residence time (continuously operated crystallizer) or the batch time has to be optimum (see below)
- the circumferential velocity u_{tip} of a rotor should be low and
- the specific power input should be low, too.

However, with respect to the suspension of coarse crystals in stirred vessels, a minimum value of $[u_{tip}(D/T)^{3/2}]$ of the stirrer is necessary for a given suspension [17]:

$$\left[u_{tip}\left(\frac{D}{T}\right)^{3/2}\right]_{min} = \frac{1}{0.088\,Ne^{7/18}}\left[3c_w \bullet L_p \bullet g\,\frac{\Delta\rho}{\rho_L} \bullet w_s^2 \varphi_v\right]^{1/4}$$

with D/T as the diameter ratio (stirrer D and tank T) and w_s as the settling velocity of the largest crystal with the drag coefficient c_w and the density difference $\Delta\rho = \rho_c - \rho_L$ between the crystal (c) and the liquid (L), φ_v is the volumetric crystal hold-up and Ne the Newton number of the stirrer. As can be seen from this equation, crystals with a large settling velocity w_s are mostly endangered by attrition.

5. Supersaturation in crystallizers

The actual local supersaturation in a crystallizer under isothermal condition is the result of the following parameters and processes:

• Concentration of the reactants • Velocity of the chemical reaction • Intensity of macro and micromixing • Dilution of solution • Agglomeration	important for sparingly soluble systems
• Crystallization kinetics (nucleation, growth Creation of crystal surface by attrition.	important for highly soluble systems

Let us assume that precipitation is initiated by a very fast chemical reaction with the result that the progress of this reaction is controlled by macro and micromixing. This will be explained in more detail.

5.1 Effect of macro and micromixing

In **Figure 9**, the supersaturation S is plotted against a dimensionless time t* which is defined by

$$t^* = \frac{1}{\tau_{macro}}\left(\frac{V}{\dot{V}_A + \dot{V}_B}\right) = \frac{\tau}{\tau_{macro}}$$

for MSMPR crystallizers and

$$t^* = t \bullet \left(\frac{\dot{V}_A + \dot{V}_B}{V}\right)$$

for batch crystallizers. With continuously operated crystallizers, the actual supersaturation depends on the ratio of the mean residence time $\tau = [V/(\dot{V}_A + \dot{V}_B)]$ and the macromixing time τ_{macro} according to

$$\tau_{macro} \approx 5\frac{T^{2/3}}{\bar{\in}^{1/3}} \approx 5\left(\frac{\pi}{4\,Ne}\right)^{1/3}\left(\frac{T}{D}\right)^{5/3} \bullet \frac{1}{N}$$

Here, $\bar{\in}$ is the mean specific power input equivalent to $\bar{\in} = (1/V)\int \in dV$, T is the tank diameter and N is the speed of the stirrer. In batch crystallizers, the ratio $V/(\dot{V}_A + \dot{V}_B)$ is the time of the addition of the two reactants A and B or the solution, respectively. Let us assume that the addition time of a reaction crystal-

lizer is very short compared to the total batch time. If the micromixing time of the liquid mixture with the viscosity ν according to

$$\tau_{micro} \approx 50 \ln Sc \frac{\nu^{1/2}}{\in_{loc}^{1/2}}$$

is very short ($\tau_{micro} << \tau_{macro}$ or $\tau_{macro}/\tau_{micro} \to \infty$), the maximum possible supersaturation S_{max} is obtained after a short time (batch crystallizers) or a short residence time (continuously operated crystallizers), see point A. The supersaturation decreases with increasing t*. The longer the micromixing time τ_{micro} in comparison to the macromixing time τ_{macro}, the smaller is the supersaturation for a given t* and, consequently, the nucleation rate.

5.2 Effect of dilution

Let us consider a T-mixer and a stirred vessel, see **Figure 10**. In the case of a stirred vessel, the flow rates $\dot{V}_A$ and $\dot{V}_B$ of the reactants are diluted in the vessel and the degree of dilution increases with the vessel volume V. Therefore, the actual concentration and supersaturation depend on the ratio $(\dot{V}_A + \dot{V}_B)/V$. The actual local supersaturation can be influenced by the processes of

- dilution ($\sigma \sim 1/V$), see point B in **Figure 9**
- macromixing ($\sigma \sim 1/N$) and
- micromixing ($\sigma \sim \in_{loc}^{-1/2}$).

Therefore, the prediction of the median crystal size requires the prediction of the mixing phenomena and the calculation of local concentrations and supersaturation profiles.

5.3 Effect of attrition

In the case of strong attrition (e.g. high settling velocity w_s of crystals), the maximum and the median crystal size are reduced with the result that the coefficient of variation CV decreases. The CSD can be controlled by attrition, see **Figure 11**. In this diagram, the median crystal size is plotted against the residence time τ of a continuously operated crystallizer. Since KNO_3 (as well as potash alumn and citric acid) are very prone to attrition, the optimum residence time τ_{opt} is only one hour. With attrition-resistant materials such as KCl, NaCl, $(NH_4)_2SO_4$ and tartaric acid, the residence time τ_{opt} can be two or three hours. Therefore, it is very important to know the attrition behaviour which depends mainly on the fracture resistance of the crystalline matter [11].

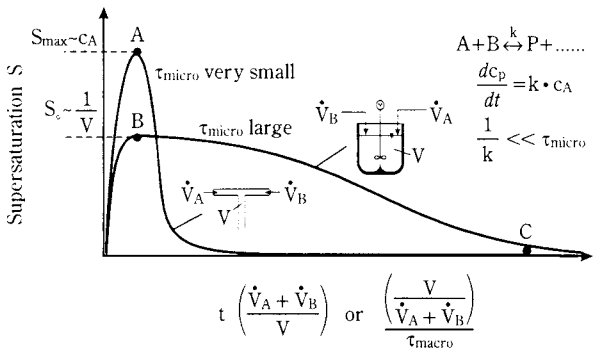

Fig. 9 Supersaturation S against the dimensionless time with τ_{micro} as the parameter

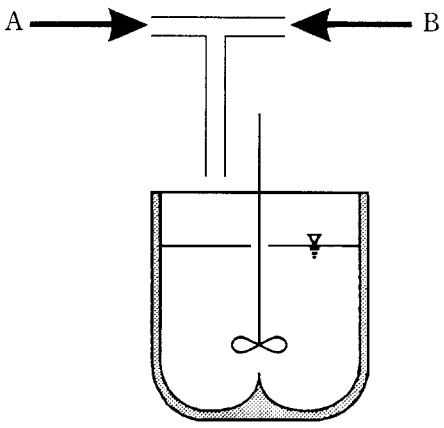

Fig. 10 Operation of a T-mixer and a stirred vessel

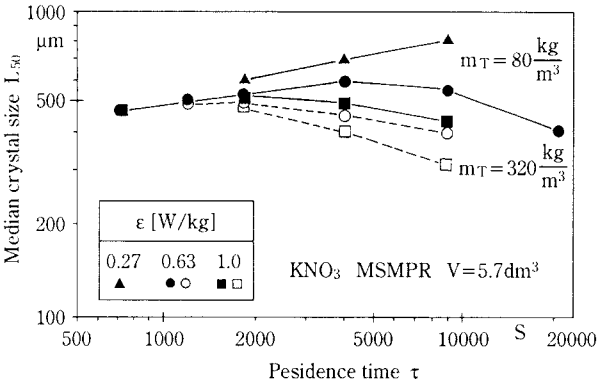

Fig. 11 Median crystal size of KNO_3 crystals against the mean residence time

6. How to influence the median crystal size

The median crystal size L_{50} depends on the crystallization kinetics via B(S) and G(S) and on the growth time (batch) or
$t = V/(\dot{V}_A + \dot{V}_B)$ with $L_{50} = 3.67 \times G\tau$ for MSMPR crystallizers.

6.1 Continuously operated crystallizers

Very small particles (nanoparticles) can be produced by

- highly concentrated reactants and high $\Delta c/c_c$ ($\Delta c/c_c > 0.1$)
- avoidance of agglomeration (addition of surfactants and/or change in pH)
- rapid quenching or diluting in order to stop growth
- fast local micromixing of the reactants but poor macromixing
- no dilution (T-mixer) in order to produce many nuclei

The contrary is true for obtaining large particles. The reduction of attrition is the prerequisite for producing coarse crystals. As a rule, particles in the micrometre range are agglomerates formed from nanoparticles [8, 9].

6.2 Batch crystallizers

In order to produce very fine particles, the remarks given under 6.1 are valid. The addition tubes of the two reactants should be very close together at a point of a very high specific power input (discharge region of the impeller, preferably a Rushton turbine). Another possibility is to premix the reactants in a T-mixer where the fast chemical reaction takes place, see **Figure 10**. The suspension is then introduced into the vessel where a very weak (or zero) supersaturation leads to no further activated nucleation (or growth).

Large particles can be produced if

- the supersaturation is optimum (only very few nuclei but sufficient growth) and
- the residence time of the crystals is long ($L_{50} \sim G\tau$) [10].

Nomenclature

B	: nucleation rate	$[m^{-3}s^{-1}]$
c	: concentration	$[kmolm^{-3}]$
c_w	: drag coefficient	[−]
D	: stirrer diameter	[m]
D_{AB}	: diffusion coefficient	$[m^2s^{-1}]$
f	: factor	[−]
G	: growth rate	$[ms^{-1}]$
k_d	: mass transfer coefficient	$[ms^{-1}]$
k_g	: growth coefficient	$[ms^{-1}]$
L	: crystal size	[m]
m_T	: suspension density	$[kgm^{-3}]$
N	: stirrer speed	$[s^{-1}]$
$\Re$	: gas constant	$[Jmol^{-1}K^{-1}]$
S	: supersaturation	[−]
T	: tank diameter	[m]
T	: temperature	[K]
t	: time	[s]
V	: vessel volume	$[m^3]$
$\dot{V}$	: volumetric flow rate	$[m^3s^{-1}]$
w_s	: settling velocity	$[ms^{-1}]$
α,β	: shape factors (volume, surface)	[−]
ϵ	: specific power input	$[Wkg^{-1}]$
ν	: kinematic viscosity	$[m^2s^{-1}]$
ρ	: density	$[kgm^{-3}]$
τ	: residence or mixing time	[s]
Γ_s	: fracture resistance	$[Jmol^{-1}m]$
φ_v	: volumetric hold-up	[−]
Ne	: Newton number of the stirrer	[−]
$Sc \equiv \nu/D_{AB}$	: Schmidt number	
t^*	: dimensionless time	[−]

Subscripts and superscripts

A,B	: component A, B
act	: activated
att	: attrition
c	: crystalline
het	: heterogeneous
hom	: homogeneous
L	: liquid
max	: maximum
p	: parent
prim	: primary
sec	: secondary
tip	: tip speed
*	: equilibrium
50	: 50 percent

References

1) Angerhöfer, M.: Untersuchungen zur Kinetik der Fällungskristallisation von Bariumsulfat, Thesis, TU Munich, (1994)
2) Nore Ph., Mersmann, A.: Batch Precipitation of Barium Carbonate, Chem. Eng. Sci. 48 (1993) 3083-3088
3) Franke, J.: Über den Einfluß der Prozeßparameter auf die Fällungskristallisation am Beispiel von Calciumcarbonat und Calciumsulfat Dihydrat, Thesis, TU Munich, (1994)
4) Mersmann, A.: General Prediction of Statistically Mean Growth Rates, J. of Crystal Growth, 147 (1995) 181-193
5) Mersmann, A.: Crystallization Technology Handbook, Marcel Dekker, New York, (1995)
6) Mersmann, A.: Supersaturation and Nucleation, TransIChemE, 74A (1996) 812-820
7) Schubert, H., Mersmann, A.: Precipitation and Filtration – an Experimental Study, Proc. 5th World Congress on Chemical Engineering, San Diego, (1996)
8) Schubert, H., Mersmann, A.: Determination of Heterogeneous Nucleation Rates, TransIChemE, 78A (1996)

9) Schubert, H., Mersmann, A.: How Agglomeration Processes Affect Experimentally Determined Nucleation Rates, Proc. Int. Conf. on Mixing and Crystallization, Tioman Island, Malaysia, (1998)
10) Kühberger, M., Mersmann, A.: How to Meet Product Requirements During Cooling Crystallization by Control of Supersaturation, Int. Conf. On Mixing and Crystallization, Tioman Island, Malaysia, (1998)
11) Gahn C., Mersmann A.: Theoretical Prediction and experimental determination of attrition rates, Trans-IChemE, 75A2 (1996) 125
12) Ploss, R., Tengler, T., Mersmann, A.: Scale-up of MSMPR-Crystallizers, Ger.Chem.Eng., 9 (1986) 42-48
13) Pohlisch, J., Mersmann, A.: The Influence of Stress Attrition on Crystal Size Distribution, Chem.Eng.Technol, 11 (1988) 40-49
14) Tengler, T.: Wachstum und Keimbildung bei der Kühlungskristallisation von Ammoniumsulfat, Thesis, TU München, (1990)
15) Sangl, R., Mersmann, A.: Attrition and Secondary Nucleation in Crystallizers, Proc. 11th Symp. Ind. Cryst., ed. A. Mersmann (1990) 331-336
16) Zacher, U., Mersmann, A.: J. Crystal Growth, 147 (1995) 172
17) Mersmann, A., Werner, F., Maurer, S. Bartosch, K.: not yet published

Author's short biography

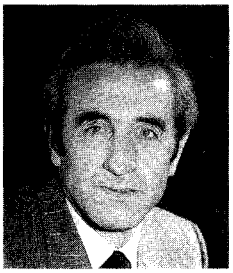

A. Mersmann

1931	Alfons Mersmann was born in Oer-Erkenschwick, Germany
1952-1957	he studied Mechanical Engineering at the Technical University of Hannover
1957-1961	worked at the Max-Planck Institute in Goettingen, Germany in the field of heat and refrigeration technology
1961	wrote his doctorate on: Pressure drop and foam thickness of liquid layers in a gas penetrated sieve tray
1961-1969	worked at Dynamit Nobel, Germany
since 1969	is dean of the Institute of Mechanical Engineering at the Technical University Munich, Germany
1983-1985	was dean of the department of Mechanical Engineering
1994	received the Emil-Kirschbaum-Medal for his continued research in the field of Thermal Process Technology
1996	received the Ernest-Solvay Prize

Prof. Mersmann prepared many international conferences, published more than 280 articles. He was and still is member of various special research projects.

Review

Prediction of the Porosity of Particle Mixtures†

A.B. Yu and R.P. Zou
School of Materials Science and Engineering
The University of New South Wales *

Abstract

Particle characteristics affect porosity mainly via three factors: dimensionless particle size distribution, particle shape and absolute particle size, giving various packing systems from the simple coarse spherical particle packing to the complicated fine and nonspherical particle packing. Consequently, the modelling of the relationship between porosity and particle characteristics may be carried out by considering these three factors, either successively or simultaneously. This paper presents a review of the work in this area since the early 1980s. The dependence of porosity on particle size, shape and their distributions is examined from typical examples for different packing systems. The need for further development is also discussed.

1. Introduction

Particle packing, recognised by Dallavalle [1] as a core research area in particle/powder technology, is of prime importance to many industries, the material and mineral industries in particular [2]. For example, the densification of a powder mass is important in the shaping of solids in ceramics, powder metallurgy or composite synthesis; proper description of particle packings at either microscopic or macroscopic level is also fundamental to many mineral processes such as solid-liquid separation (sedimentation, thickening and filtration), raw material handling (stockpiling, blending, drying, storage and transportation), and pyrometallurgical processes (agglomeration, coke making, ore sintering, blast furnace ironmaking and iron ore pre-reduction process). Not surprisingly, it is very useful to develop a method for predicting the packing properties of particulate materials for property and/or process control.

Porosity is known to be the simplest and most accessible parameter for characterising particle packing. Previous studies indicate that it is affected by many factors [3]. However, as far as particle characteristics are concerned, a situation often encountered in practice, there are three main factors: (dimensionless) particle size distribution, particle shape, and absolute particle size. These factors may lead to various complex packing systems from spherical to non-spherical, and/or from coarse to fine particle packing. Understanding and modelling of the relationship between porosity and particle characteristics has been a subject of research since the turn of this century, namely since the work of Fuller and Thompson [4], progressing from the simple spherical particle packing to the complicated fine and non-spherical particle packing. Previous work is mainly experimental and has been summarised by Gray [3], Cumberland and Crawford [5] and then German [2]. In the 1980's, significant progress was made in the modelling of the packing of coarse spherical particles [6-15]. On this basis, in the recent years, attempts have also been made to model the packing of nonspherical and fine particles [16-21]. This paper presents a review of the work in this area and highlights the need for future development.

* Sydney, NSW 2052 Australia
† Received 4 June, 1998

2. Mathematical Modelling

2.1 Model Framework

The system considered is assumed to be composed of n components, with each characterised by its (initial) porosity ε_i and effective (packing) diameter d_{pi} (i=1, 2, ..., n). In general, the porosity of this system ε can be expressed as

$$\varepsilon = f(X_1, X_2, ..., X_n; d_{p1}, d_{p2}, ..., d_{pn}; \varepsilon_1, \varepsilon_2, ..., \varepsilon_n) \quad (1)$$

where X_i is the fractional solid volume of the ith component. For convenience, d_{pi} are so ordered that $d_{p1} \geq d_{p2} \geq ... \geq d_{pn}$. When particles of different sizes are mixed and packed, the volume occupied by a unit volume of solid particles, commonly referred to as the specific volume V [$=1/(1-\varepsilon)$], will vary, e.g. decreasing as compared with the packing of mono-sized

spheres. Analogous to the solution dynamics, V can be written as

$$V = \sum_{i=1}^{n} X_i \overline{V}_i \qquad (2)$$

where $\overline{V}_i$ is the partial specific volume of component i and may be treated as though it represents the specific volume of the component in a packing. The packing mechanisms can then be elucidated from the quantitative analysis of $\overline{V}_i$ and hence the role of individual components in forming a packing, as discussed by Yu and Standish [13]. For binary packing, it is postulated that two components will either "mix" or "unmix" with each other depending on their size ratio. As shown in **Fig. 1**, if the size ratio (small/large) is less than the critical ratio of entrance, equal to 0.154 as determined from a simple geometrical consideration [22], a binary packing is dominated by the unmixing mechanism; otherwise it is dominated by the mixing mechanism. For a packing formed by the unmixing mechanism, the existence of the other component does not affect the packing, i.e. the "skeleton" or "connection", of the controlling component, with $\overline{V}_i$ independent of X_i. On the contrary, for a packing formed by the mixing mechanism, the packing is controlled by both components and the "skeleton" of the previous component is distorted, with $\overline{V}_i$ varying with X_i. **Fig. 1** also demonstrates geometrically these concepts.

The above consideration has been extended to the packing of multi-component mixtures by use of the concept of controlling mixture [15]. It is argued that a component can be either one of the controlling components of the mixing effect or one of the components of the unmixing effect. The controlling components act as an arbitrary component of the unmixing effect but they themselves are also a mixture, i.e. they are a sub-mixture in the whole mixture. An important property of the controlling mixture is that the packing of the controlling mixture, like in a binary packing, does not change with the addition of the components of the unmixing effect. **Fig. 1** only shows a situation when small particles are introduced into large particles. In reality, the controlling components not only change with particle sizes but also with the fractional solid volumes of the components. In general, the packing of a particle mixture can be represented by **Fig. 2**, which suggests that the specific volume decreases mainly due to the mixing effect of medium particles, i.e. the controlling mixture, and the unmixing effect of small and large particles.

Corresponding to component i, the medium particles of the mixing effect are assumed to be composed of the Mth to Nth ($1 \le M \le i \le N \le n$) components and hence the large and small particles of the unmixing effect should be composed of the 1st to (M-1)th and (N-1)th to nth components, respectively. Since the partial specific volume of the medium particles, $\overline{V}_{Mi}$, is not affected by the addition of small and/or large particles, if the partial specific volumes of small and large particles, $\overline{V}_{Sj}$ (j=1, 2, ..., M-1) and $\overline{V}_{Lj}$ (j=N+1,

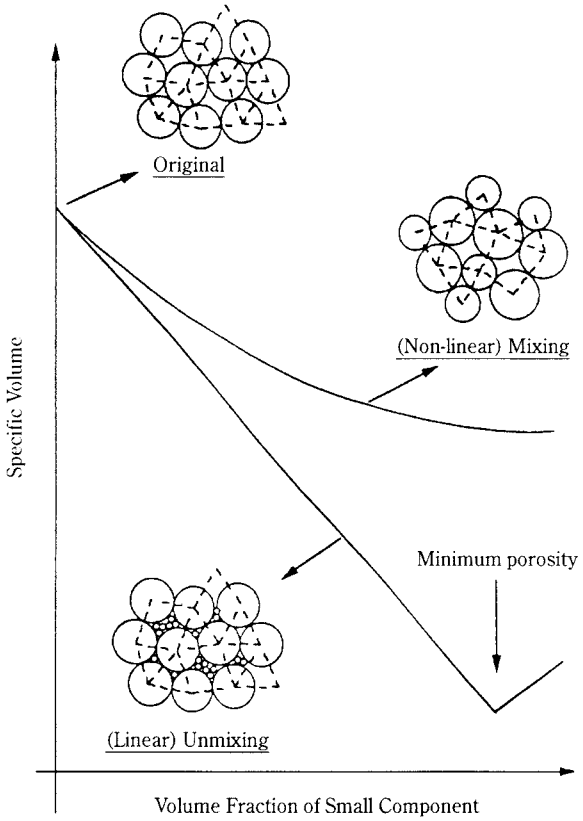

Fig. 1 Schematic illustration of the mixing and unmixing packing mechanisms when small spheres are introduced into the packing of large spheres.

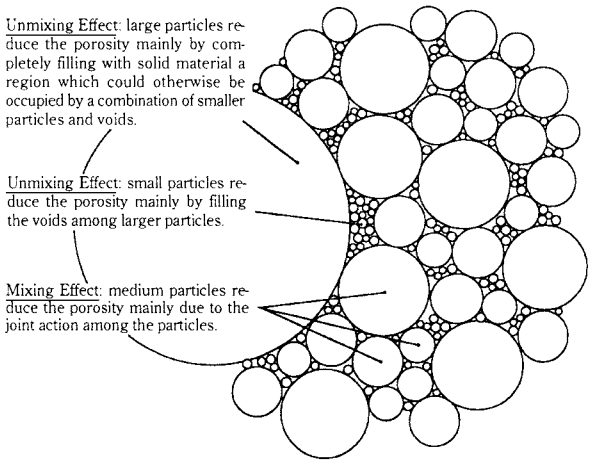

Fig. 2 Two dimensional illustration of the random packing structure of spheres.

N+2, ..., n), are assumed to be dependent on their individual sizes relative to the representative size of the controlling mixture, then eqn. (2) can be re-written as

$$V_i^T = \sum_{j=1}^{M-1} \overline{V}_{Lj} X_j + \overline{V}_{Mi} \sum_{j=M}^{N} X_j + \sum_{j=N+1}^{n} \overline{V}_{Sj} X_j \quad (3)$$

Depending on the particle sizes and volume fractions involved, a component may be categorised into any of the above three groups of particles. It is difficult to determine *a priori* whether a particle has a mixing or unmixing effect. However, once the model equations have been developed, this problem can be readily solved by the physical consideration that the volume occupied by a unit solid volume of particles should not be less than the volume which can accommodate all the particles. Therefore, the specific volume of a particle mixture should be the maximum of the calculated V_i^T, i.e.

$$V = \text{Max.} \{V_1^T, V_2^T, \ldots, V_n^T\} \quad (4)$$

The above treatments may be used as a general model framework for developing a model for porosity prediction [15]. Different models, as they are developed based on different geometrical and/or analytical assumptions, may give different equations for evaluating the values of M and N and partial specific volumes, resulting in different predicability.

According to Yu and Standish [15], the models proposed in the literature may be categorised into two groups: geometrical and analytical. A geometrical model often starts with a simple geometrical unit which is convenient for analysis but may be too simple to represent the real complex packing structure. In particular, the use of a geometrical unit implies that such a model considers the mixing mechanism only, as particles of different sizes are treated in the same way. Consequently, a geometrical model can not reliably predict the porosity of particle mixtures of large size range without modification. For example, the simplest statistical geometrical model of Dodds [6] is only applicable to packings when d_n/d_1 is greater than 0.154. This is also the case for the early version of the model proposed by Ouchiyama and Tanaka [7] and, as demonstrated in [14], its variant by Suzuki and Oshima [9]. One advantage of a geometrical model is its capacity to predict the mean coordination number of a particle mixture, in addition to porosity. However, as recently demonstrated by Pinson et al. [23,24], a geometrical model predicts a varying mean coordination number, which is in conflict with experimental observations that the mean coordination number is essentially a constant, independent of particle size distribution. Another deficiency of the existing geometrical models is their inability to handle the packing involving varying initial porosity [25], in spite of the efforts made to improve the predicability of a model for fine or nonspherical particles [9, 14, 26]. Compared with the geometrical approach, the analytical approach appears to be more flexible, as seen from the development of the linear packing model [10, 12, 20]. Therefore, the following will emphasise the analytical treatments, focussing on the linear [10, 12, 20], mixture [13] and linear-mixture [15] packing models.

2.2 Calculation of Partial Specific Volumes

The controlling components can be treated as either a sub-mixture or a pseudo-component. When treated as a pseudo-component, a representative particle size can be ascribed to this component so as to determine its interaction with other components. This representative size can be simply assumed to be the same as component i corresponding to V_i^T. Since the interaction between two components is dependent on their relative size, appropriate use of the binary packing results can lead to the determination of M and N, and partial specific volumes.

For binary packing, the mixing mechanism will be effective if the size ratio between two components is larger than 0.154, i.e. the critical ratio of entrance. Application of this value to multi-component packing suggests that M and N should be evaluated by

$$M = \begin{cases} k & d_{p,k-1} > \dfrac{d_{pi}}{0.154} \geq d_{pk} \quad (k=2, 3, \ldots, i) \\ l & \dfrac{d_{pi}}{0.154} \geq d_{pl} \end{cases} \quad (5a)$$

and

$$N = \begin{cases} k & d_{p,k-1} \geq 0.154 d_{pi} > d_{pk} \quad (k=1, i+1, \ldots, n) \\ n & 0.154 d_{pi} < d_{pn} \end{cases} \quad (5b)$$

Eqn. (5) means that any components whose sizes are within the range $[0.154d_{pi}, d_{pi}/0.154]$ are controlling components. As discussed above, the partial specific volume $\overline{V}_{Sj}$ or $\overline{V}_{Lj}$ is dependent on the particle size of component j relative to the representative size of the controlling mixture. According to Yu et al. [20], $\overline{V}_{Sj}$ $(i<j\leq n)$ is given by

$$\overline{V}_{Sj} = V_j [1 - f(r_{ij})] \quad (6)$$

and $\overline{V}_{Lj}$ $(1\leq j<i)$ is

$$\overline{V}_{Lj} = V_j - (V_j - 1) g(r_{ij}) \quad (7)$$

where $f(r_{ij})$ and $g(r_{ij})$ are referred to as the interaction functions that depend on the (small to large) size ratio

between component j and the controlling mixture, r_{ij}. The two functions should meet the boundary conditions: $f(0)=g(0)=1$; and $f(1)=g(1)=0$; they can be evaluated theoretically [10] or empirically [12]. Since the packing of binary mixtures has been well established, the latter approach is favoured. Empirical formulation based on the well established packing results of binary mixtures leads to [20]

$$f(r_{ij}) = (1-r_{ij})^{3.3} + 2.8r_{ij}(1-r_{ij})^{2.7} \quad (8)$$

and

$$g(r_{ij}) = (1-r_{ij})^{2.0} + 0.4r_{ij}(1-r_{ij})^{3.7} \quad (9)$$

On the other hand, the partial specific volume $\overline{V}_{Mi}$ can be evaluated when the controlling components are treated as a sub-mixture. This evaluation should be made by means of a mathematical model developed on the basis of the mixing mechanism. One such model is the so-called mixture packing model [13], which gives

$$\overline{V}_{Mi} = \sum_{j=M}^{N} Y_j V_j + \sum_{j=M}^{N-1} \cdot \sum_{k=j+1}^{N} \beta_{jk} Y_j Y_k + \sum_{j=M}^{N-1} \cdot \sum_{k=j+1}^{N} \gamma_{jk} Y_j Y_k (Y_j - Y_k) \quad (10a)$$

where

$$Y_j = \frac{X_j}{\sum_{k=M}^{N} X_k} \qquad (j = M, M+1, ..., N) \quad (10b)$$

Eqn. (10b) highlights the fact that the controlling components are themselves a mixture, but as implied by eqn. (3), its (partial) specific volume is not affected by other components of the unmixing effect. Coefficients β_{jk} and γ_{jk}, related to the interaction between components j and k, should be dependent on their size ratio r_{jk}, and initial porosities ε_j and ε_k [note that $V_j=1/((1-\varepsilon_j)]$. For the case when $\varepsilon_j=\varepsilon_k=\varepsilon_o$, Yu and Standish [15] obtained

$$\beta_{jk}(r_{jk}, \varepsilon_o) = 10.288\times10^{-1.457(1-\varepsilon_o)}(-1.000+0.113r_{jk} + 5.846r_{jk}^2 - 7.949r_{jk}^3 + 3.122N_{jk}^4) \quad (11)$$

and

$$\gamma_{jk}(r_{jk}, \varepsilon_o) = [-1.309+15.039(1-\varepsilon_o) - 37.453(1-\varepsilon_o)^2 + 40.869(1-\varepsilon_o)^3 - 17.110(1-\varepsilon_o)^4] \cdot (-1.003+0.359r_{jk} + 10.970r_{jk}^2 - 22.197r_{jk}^3 + 12.434r_{jk}^4) \quad (12)$$

Incorporation of eqns. (5-12) into eqn. (3) allows the calculation of the porosity of a particle mixture, leading to the so-called linear-mixture packing model [15] as it is developed from the linear and mixture packing models. In fact, the linear-mixture model can be reduced to the linear packing model when M=N=i and $\overline{V}_{Mi}=V_i$ or to the mixture packing model when M=1 and N=n. For the packing of spherical particles, the linear-mixture model can provide better predictions than the linear or mixture model because of its consistency with the packing mechanisms as implied by eqn. (3) [15]. However, because eqns. (11) and (12) do not take into account the case when $\varepsilon_j \neq \varepsilon_k$, it is not generally applicable to the packing of non-spherical and/or fine particles, which usually involves a significant difference in initial porosities. At this stage of development, the only model that can overcome this deficiency is the (modified) linear packing model [20]. Therefore, in this paper, model applications will be discussed with special reference to the linear-mixture model for the packing of spherical particles and the linear model for the packing of non-spherical and/or fine particles.

2.3 Evaluation of the Packing Characteristics of Mono-sized Particles

Use of the above model in the porosity calculation requires the information of the packing characteristics such as ε_i and d_{pi} a priori. It has been established that initial porosity is constant for coarse spherical particles, generally taking the value of 0.4 for the loose random packing or 0.36 for the dense random packing [2, 3]. However, initial porosity increases with decreasing particle size because of the effect of weak forces if particle size is smaller than a certain value; it also varies with particle shape. If the particle size and shape of component i are, respectively, represented by its equivalent volume diameter d_{vi} and sphericity ψ_i, this gives

$$\varepsilon_i = f(d_{vi}, \psi_i) \quad (13)$$

On the other hand, the so-called effective diameter d_{pi} is the equivalent packing diameter which is obtained from the similarity analysis, as done for nonspherical particles [16-19]. It is also dependent on both d_{vi} and ψ_i, i.e.

$$d_{pi} = f(d_{vi}, \psi_i) \quad (14)$$

The dependence of initial porosity on particle size and shape can be illustrated in **Figs. 3** and **4**. It is evident from **Fig. 3** that initial porosity decreases with particle size for fine particles and then reaches to a constant value for coarse particles. The scatter observed is probably due to the effects of other particle characteristics and material properties, in addition to experimental conditions (note that the data were obtained from different literature sources) [21]. **Fig. 4** shows that different shapes give different rela-

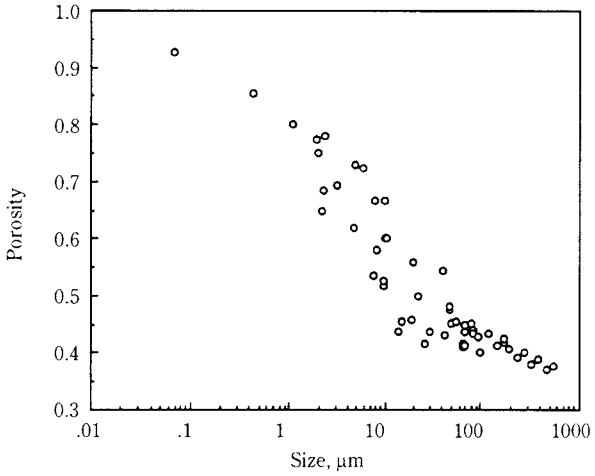

Fig. 3 Initial porosity vs. particle size [21].

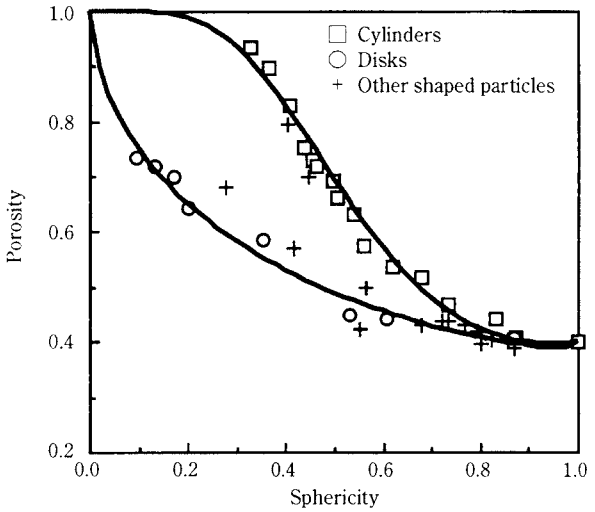

Fig. 4 Initial porosity vs. particle shape under the loose packing condition [19].

tionships between initial porosity and sphericity, suggesting that a single shape parameter, i.e. sphericity, can not fully represent the effect of particle shape on porosity [19]. To date it is not clear how particle shape interacts with particle size. Further studies are therefore necessary in order to establish eqn. (13). On the other hand, it should be noted that for a given packing system, ε_i or V_i for individual components can be readily measured. These measured V_i can be used directly in the model calculation; this treatment may improve the accuracy of prediction.

The similarity between spherical and nonspherical particle packings has led to the development of the concept of equivalent packing diameter [16-19]. In particular, for coarse particles of convex shape, the dependence of d_{pi} on ψ_i has been established, as given by [19]

$$d_{pi} = \frac{d_{vi}}{\psi_i^{2.785} \exp[2.946(1-\psi_i)]} \qquad (15)$$

Recently, the concept of equivalent packing diameter has been extended to the packing of fine particles [21]. As will be discussed later, satisfactory predictions can be obtained for alumina powders, indicating the approach is very promising. However, the effect of d_{vi}, together with its interaction with ψ_i, on d_{pi} is not understood yet, which will limit the model's application [27].

3. Model Application

In this section, the application of the above treatments will be examined for packings involving respectively coarse spherical, coarse nonspherical, and fine particles. The dependence of porosity on particle size and shape, and their distributions, will also be discussed via typical examples for different packing systems.

3.1 Packing of Coarse Spherical Particles

For this packing system, porosity is only dependent on the particle size distribution that may be either discrete or continuous, which has been studied extensively [2, 15, 28]. Representative examples are given below to demonstrate the application of the linear-mixture model. As implied by eqn. (15), this model is also applicable to packings of non-spherical particles of the same shape. However, initial porosity should change to reflect the effect of particle shape.

The packing of ternary mixtures of spherical particles has been studied by various investigators [29-35]. **Fig. 5** shows two typical measured results. It can be seen that the change of particle sizes in a ternary system may result in different porosity patterns. Therefore, it is difficult to obtain a complete picture of ternary packing from the previous experimental studies. However, a validated model can readily solve this problem. **Fig. 6** shows the porosity results for six representative ternary systems of different size ratios. Since there is a common binary mixture between any two connecting ternary systems, the six ternary systems can be combined together and plotted in one figure. Inspection of the results in **Fig. 6** suggests that the ternary packing has the following features: i) there is a minimum porosity for each ternary system, located either inside a triangle or at the small-large boundary line; and ii) starting with this minimum porosity, a triangular diagram may be considered to be composed of three regions dominated, respectively, by the large, medium and small components. The variation of the minimum porosity and corresponding fractional solid volumes with size ratios has been established [15].

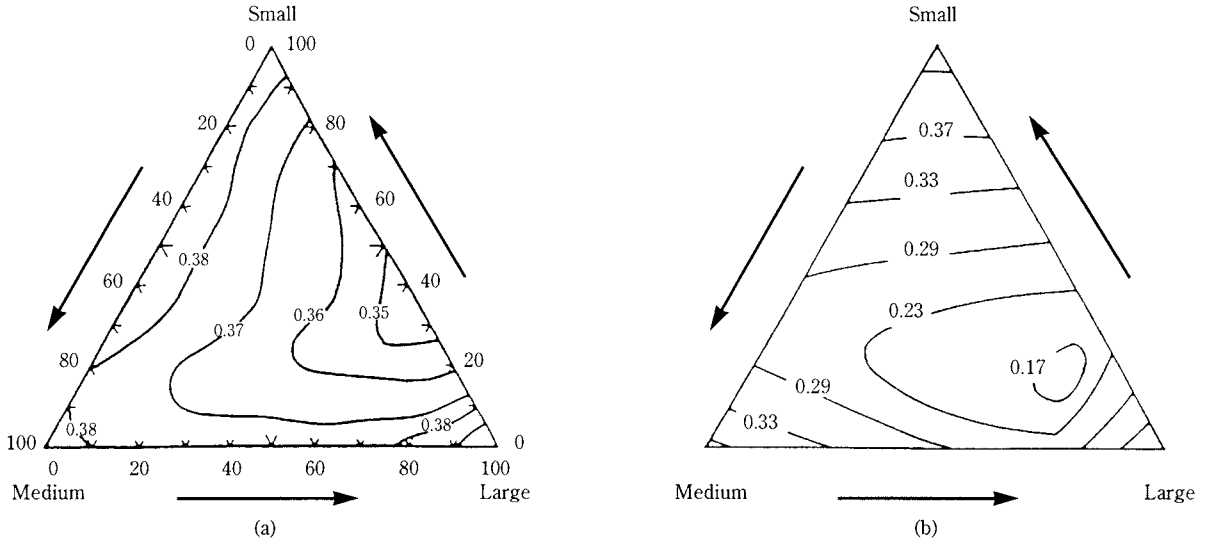

Fig. 5 Measured porosity of ternary mixtures for different size ratios: (a), $d_1:d_2:d_3=20:12:9$ [31]; (b), $d_1:d_2:d_3=50:8:1$ [29].

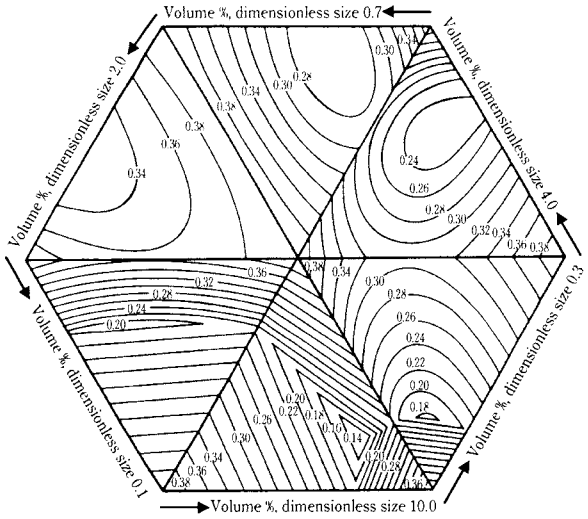

Fig. 6 Porosities of six ternary systems with the dimensionless diameter of the central component equal to unity ($\varepsilon_o=0.4$).

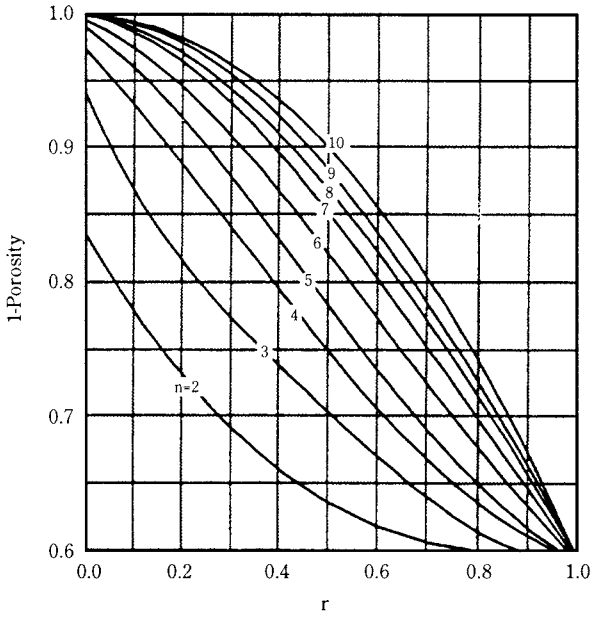

Fig. 7 Dependence of porosity on n and r, obtained when $\varepsilon_o=0.40$.

An interesting finding due to Ouchiyama and Tanaka [36] is that for a given n (=3 or 4) and d_n/d_1, the minimum porosity should be achieved when the other particle sizes d_i ($1<i<n$) are so arranged that $d_{p,i+1}/d_{pi}$=const. This may provide a good support for the use of the present screening system of a constant successive size ratio. Indeed, many practical packings are subject to the constraint: $d_{p,i+1}/d_{pi}=r$ (const.), as a result of the well-established sieving/screening practice. It is therefore of significance to understand the relationship among the minimum achievable porosity, number of components, n, and size ratio between successive components, r. This has been investigated by Furnas in his classical paper [37] and more recently by other investigators [21]. **Fig. 7** shows the results of Yu and Standish [15], which clearly indicates low porosities should be obtained by increasing the number of components and/or size gaps between successive components.

Practical packing usually involves continuous size distributions. To demonstrate the predicability of the proposed model, a comparison has been made for the packing of particles with the volumetric log-normal size distribution given by

$$f_v(d_p)=\frac{1}{\sqrt{2\pi}d_p\ln\sigma_g}\exp\left[-\frac{1}{2}\left(\frac{\ln d_p-\ln d_{p,0.5}}{\ln\sigma_g}\right)^2\right] \quad (16)$$

where $d_{p,0.5}$ and σ_g are, respectively, the median size

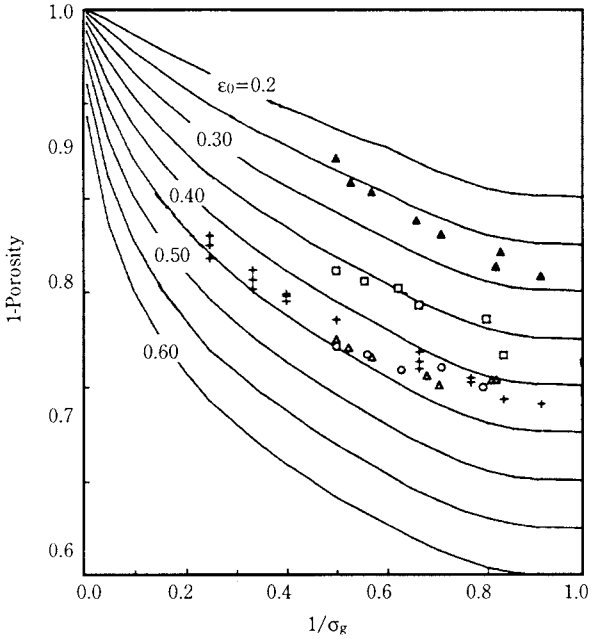

Fig. 8 The packing of particles with the log-normal size distribution: ○ & +, Sohn and Moreland [38]; □, Dexter and Tanner [39]; △ & ▲, Wakeman [40]; predictions.

and standard geometric deviation. For coarse particles, porosity is dependent on σ_g only. **Fig. 8** shows the calculated results for different initial porosity ε_o, indicating that porosity decreases with the increase of σ_g. The results measured by various investigators [38-40] are also included in **Fig. 8**. It is evident that although these measurements were obtained under different packing conditions, they can be well matched by the model predictions if initial porosity ε_o is properly chosen. The small discrepancy between the model prediction and the measurement for large σ_g may be attributed to the limited size ranges available in an experiment. As discussed by Yu et al. [28, 41], size range is an important factor affecting particle packings.

If a component itself is a mixture of particles and its cumulative size distribution is represented by $f_{vi}(d_p)$, then the (overall) particle size distribution should be written as

$$f(d_p) = \sum_{i=1}^{n} X_i f_{vi}(d_p) \qquad (17)$$

This gives a so-called mixture size distribution. This packing system may be more often encountered in practice, although not so well appreciated in the literature [38, 42]. $f_{vi}(d)$ may significantly affect the porosity results, so that the effect of X_i may be quite different from that for mixtures of uniformly sized particles. This can be seen from the results in **Fig. 9** for ternary mixtures of lognormal distributions of constant standard deviation (σ_g=2.0). Although comparable, the results in **Fig. 9** are different from those shown in **Fig. 6**. As demonstrated by Yu and Standish [42], the use of eqn. (17) in the porosity calculation provides a convenient way to solve more complicated packing problems in practice.

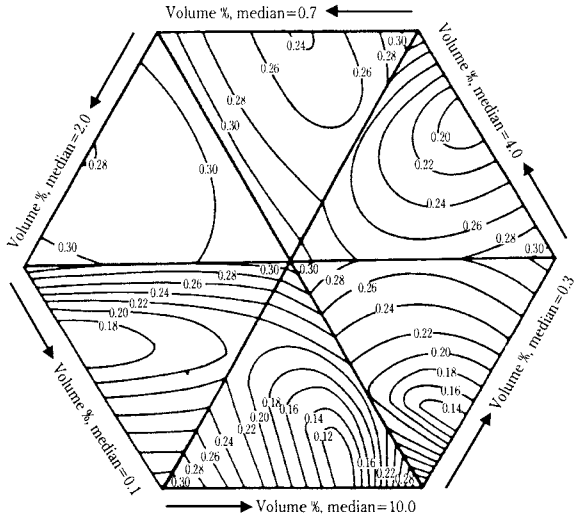

Fig. 9 Porosity of ternary mixtures of the log-normal distribution with the dimensionless median of the central component equal to unity (ε_o=0.40 and σ_g=2.0).

3.2 Packing of Coarse Nonspherical Particles

The porosity prediction of nonspherical particle mixtures should be made by use of the modified linear model and equivalent packing diameter determined according to eqn. (15). Previous studies were mainly concerned with the binary packing of spherical and cylindrical particles [43]. **Fig. 10** shows typical measured results, together with the predictions,

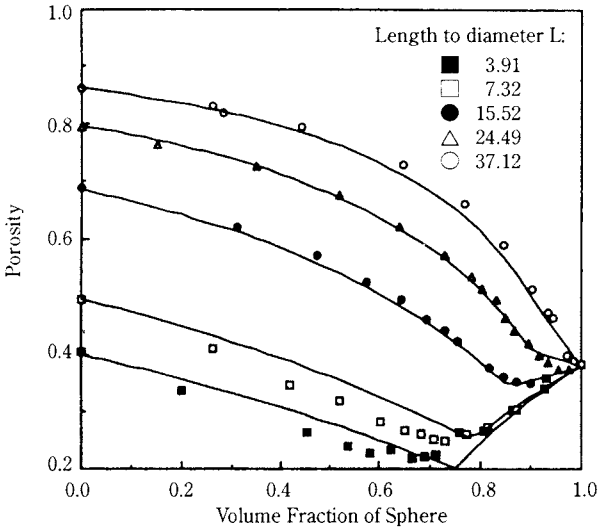

Fig. 10 Porosities of binary mixtures of sphere and cylinders of different dimensionless length L when the diameter ratio of sphere to cylinder is 17.40: points, measurements of Milewski [43]; —, predictions.

the results indicating that the predictions are in good agreement with the measurements. Such good agreement can also be found in the ternary packing, as shown in **Fig. 11** for a ternary packing of disk, cylinder and sphere.

The results in **Fig. 11** are in terms of specific volume variation, ΔV, which is defined as the difference in specific volume between the initial (unmixing) and final (mixing) states of a packing, i.e.

$$\Delta V = \sum_{i=1}^{n} X_i V_i - V \tag{18}$$

Different types of particles are put layer by layer in the initial state and well mixed in the final state, as schematically shown in **Fig. 12**. As such, the two states are not the same as the mixing and unmixing concepts in the above discussion of packing mechanisms. For spherical particles, since $\varepsilon_i = \varepsilon_j$ $(i \neq j)$, porosity patterns are the same as those in terms of specific volume variation. However, because of the effect of initial porosity, the porosity patterns of nonspherical particle mixtures may be quite different from those of spherical particle mixtures. For example, for the ternary packing shown in **Fig. 13**, the features observed in **Fig. 6** can be observed in the plot in terms of specific volume variation (**Fig. 13(b)**) but not in the plot in terms of porosity (**Fig. 13(a)**). It is found that the reduction of porosity due to the mixing of different sized particles should be elucidated in terms of specific volume variation, so is the similarity between spherical and nonspherical particle packings [16-20]. It is based on this finding that the concept of equivalent packing diameter and the modified linear packing model result.

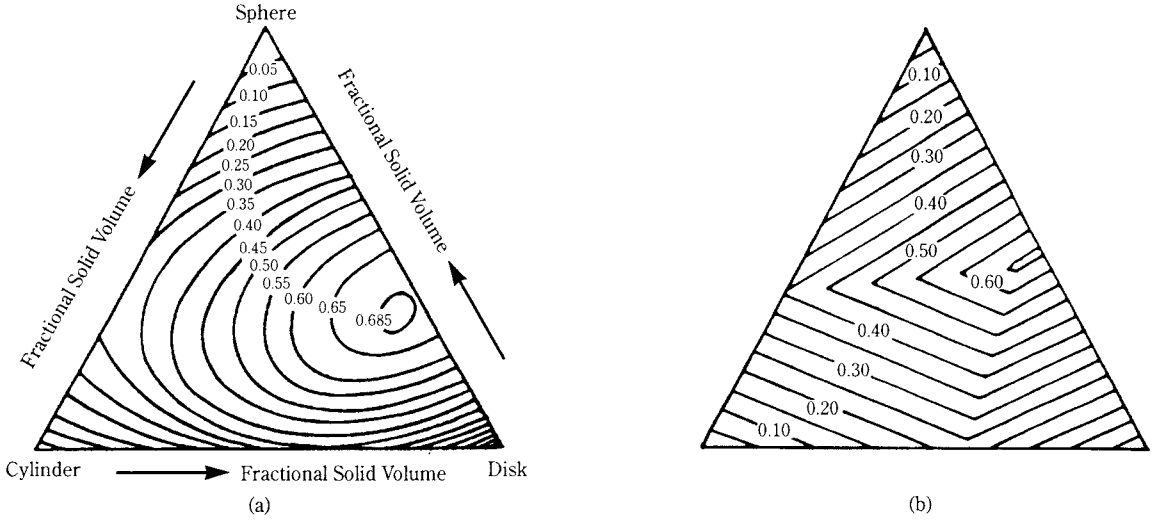

Fig. 11 Comparison between the measured (a) and calculated (b) specific volume variations for a disk-cylinder-sphere ternary system: disk, $d_{p1}=20.59$ mm, $V_1=2.653$; cylinder, $d_{p2}=10.95$ mm, $V_2=2.155$; sphere, $d_{p3}=3.00$ mm, $V_3=1.639$.

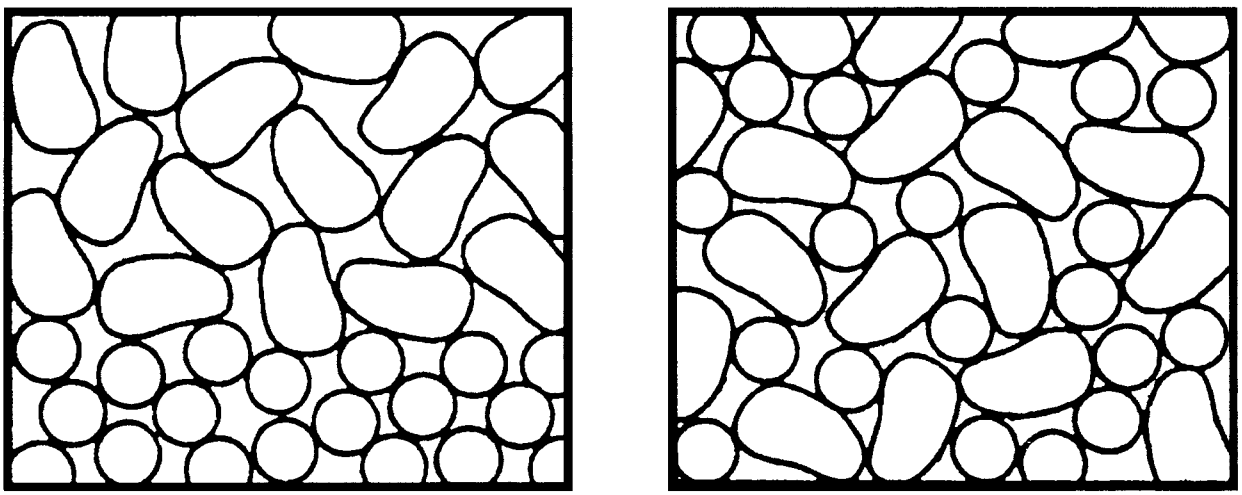

Fig. 12 The initial (a) and final (b) packing states of a particle mixture.

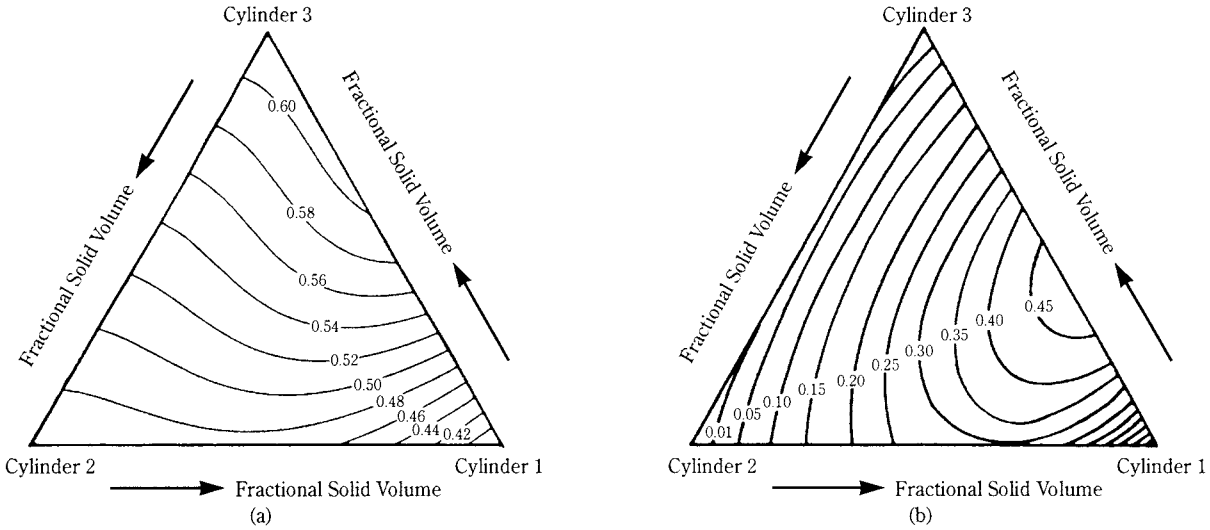

Fig. 13 The measured packing results for a ternary system of cylindrical particles in terms of: (a), packing density (=1-porosity); (b), specific volume variation, with particle sizes given as $(DxL)_1$=19.374x0.071, $(DxL)_2$=4.0x7.5, $(DxL)_3$=6.0x2.0 mm; and initial specific volumes as V_1=2.653, V_2=2.155, V_3=1.616 [16].

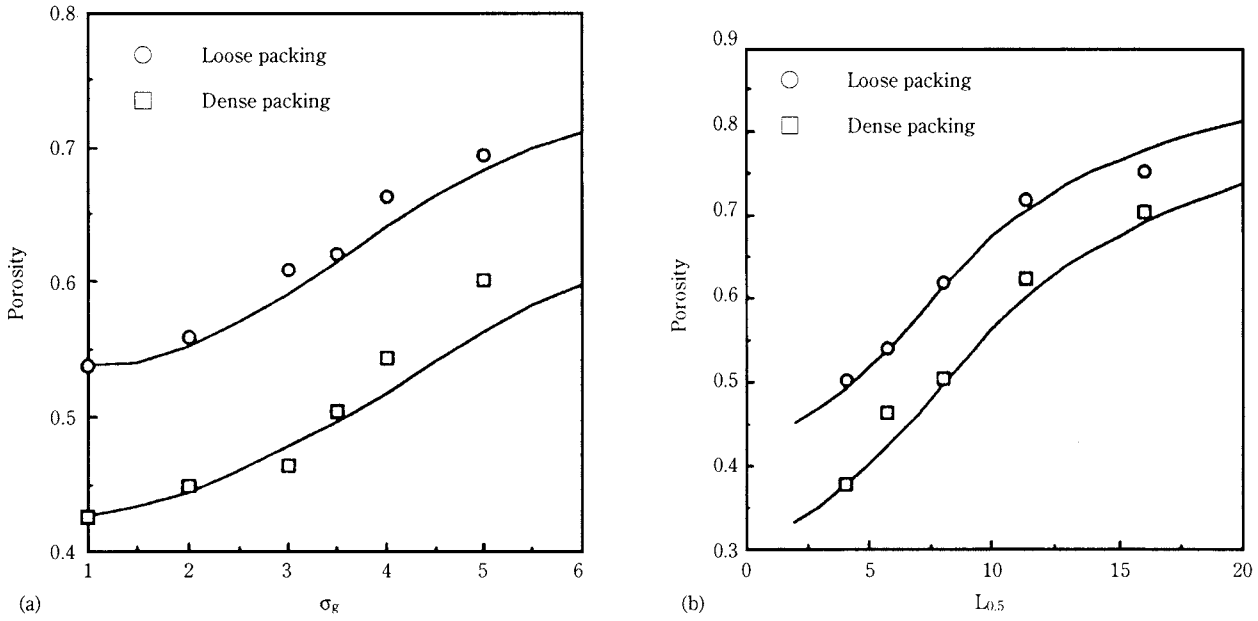

Fig. 14 Variation of the porosity of cylinders with the log-normal length distribution with: (a), σ_g when $L_{0.5}$=8.0; (b), $L_{0.5}$ when σ_g=3.5: points, measurements [44]; ——, predictions.

The model can be used to predict the porosity of multi-component mixture of nonspherical particles. This can be demonstrated from the packing of fibres (cylindrical particles) with a constant diameter but a length distribution. In particular, the length distribution is assumed to follow the log-normal length distribution

$$f_v(L) = \frac{1}{\sqrt{2\pi}} \frac{1}{L} \frac{1}{\ln\sigma_g} \exp\left[-\frac{1}{2}\left(\frac{\ln L - \ln L_{0.5}}{\ln\sigma_g}\right)^2\right] \quad (0 \leq L < +\infty) \quad (19)$$

where L is the ratio of length to diameter of a cylinder/fibre. Zou et al. [44] found that porosity is dependent on both median length $L_{0.5}$ and standard deviation σ_g. **Fig. 14** shows their results, together with the predictions which are obtained consistent with their experimental conditions. It is obvious that the predictions are in reasonably good agreement with the measurements. The model should be useful to advanced materials processing, e.g. ceramic and composite manufacturing, where fibrous particles are widely used.

3.3 Packing of Fine Particles

As discussed earlier, at present it is difficult to give an explicit equation to determine ε_i as a function of both ψ_i and d_{vi} because of the lack of quantitative information about the interaction between particle size and shape. Size range is also an important factor affecting the interaction between particles of different sizes [27]. On the other hand, for a given packing system, the initial porosity ε_i can be measured readily and then related to d_{vi} which should be associated with ψ_i. In this case, eqn. (13) can be re-written as

$$\varepsilon_i = f(d_{vi}) \tag{20}$$

with ψ_i considered implicitly. The above consideration is also applicable to the evaluation of d_{pi}. For simplicity, it can be further assumed that the ratio of packing sizes between components i and j, r_{ij}, is dependent on the corresponding ratio of equivalent volume diameters, R_{ij}, i.e.

$$r_{ij} = f(R_{ij}) \tag{21}$$

In this case, for a given type of powder, if eqns. (13) and (14) can be developed empirically, then the porosity of a powder mixture can be predicted by the above model.

The proposed approach has been tested by considering the packing of alumina powders ranging from about 0.1 to 60 μm under the poured and tapped conditions [21]. **Fig. 15** shows the initial porosity results, which can be well represented by the equation

$$\varepsilon_i = 0.567 + 0.433\exp(-0.247 d_{vi}^{0.749}) \tag{22a}$$

for the poured packing, and

$$\varepsilon_i = 0.433 + 0.567\exp(-0.446 d_{vi}^{0.579}) \tag{22b}$$

for the tapped packing.

On the other hand, the results in **Fig. 16** suggests that the relationship between r_{ij} and R_{ij} can be represented by a power law function

$$r_{ij} = R_{ij}^{p} \tag{23}$$

where parameter p is 0.293 for the poured packing and 0.593 for the tapped packing. Incorporation of eqns. (22) and (23) into the linear model allows the porosity of a multi-component mixture of alumina powder to be calculated. As shown in **Fig. 17(a)**, the calculated results are in good agreement with the measured results for ternary mixtures.

The need to use the concept of packing size in the porosity calculation can be highlighted from its accurate determination of the optimum packing for this ternary system. The use of R_{ij}, i.e. p=1.0 in eqn. (23), in the model calculation can also give the porosity results (**Fig. 17(b)**). The results differ from **Fig. 17(a)**. In fact, **Fig. 17(b)** suggests the minimum porosity is equal to 0.459 when X_1=0.71, X_2=0.16 and X_3=0.13. Experimental measurement at the nearby point (X_1=0.72, X_2=0.15 and X_3=0.13) gives a porosity of value 0.610. The measured porosity is quite different from that predicted with use of R_{ij}. However, as seen in **Fig. 17(a)**, this problem can be avoided by use of r_{ij}.

Application of the approach to the packing of particles with continuous distributions can be illustrated for the case when the cumulative particle size distribution is given by

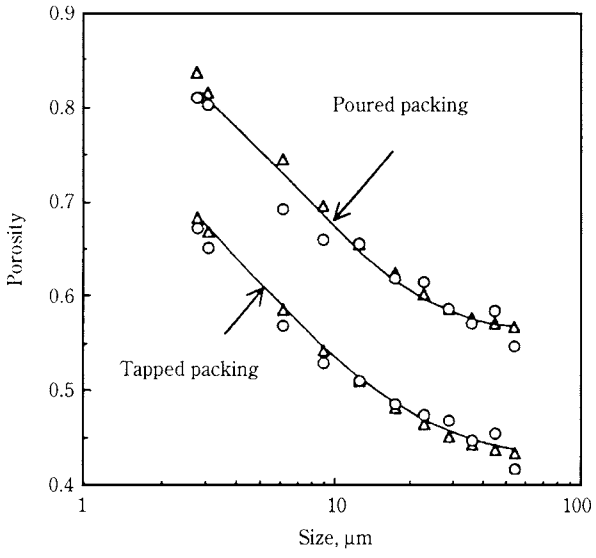

Fig. 15 Initial porosity vs. particle size for the alumina powders: points, measured; ___, fitted by eqn. (22).

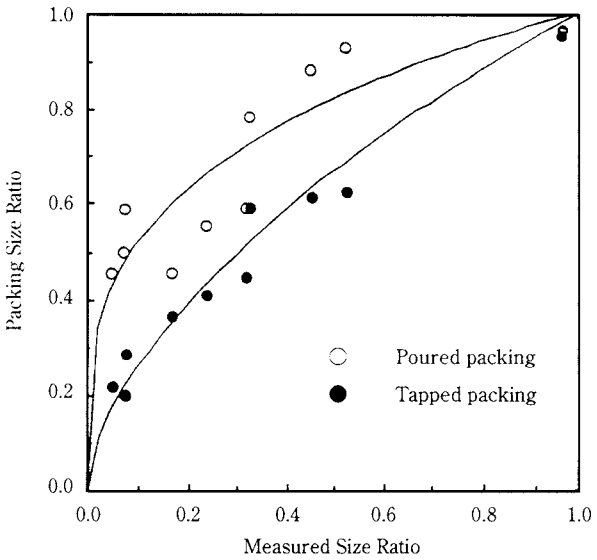

Fig. 16 Relationship between r_{ij} and R_{ij}.

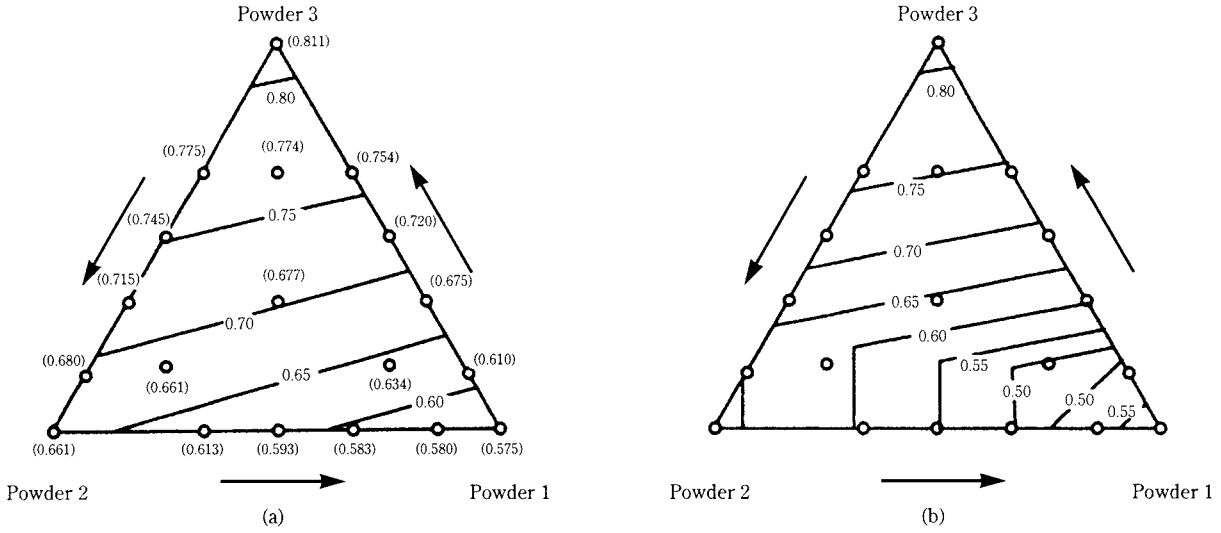

Fig. 17 Porosity of ternary mixtures (d_p=36.4 μm for Powder 1, 9.1 μm for Powder 2, and 3.1 μm for Powder 3) for the poured packing: ○, measured; —, predicted by use of: (a), r_{ij}; and (b), R_{ij}.

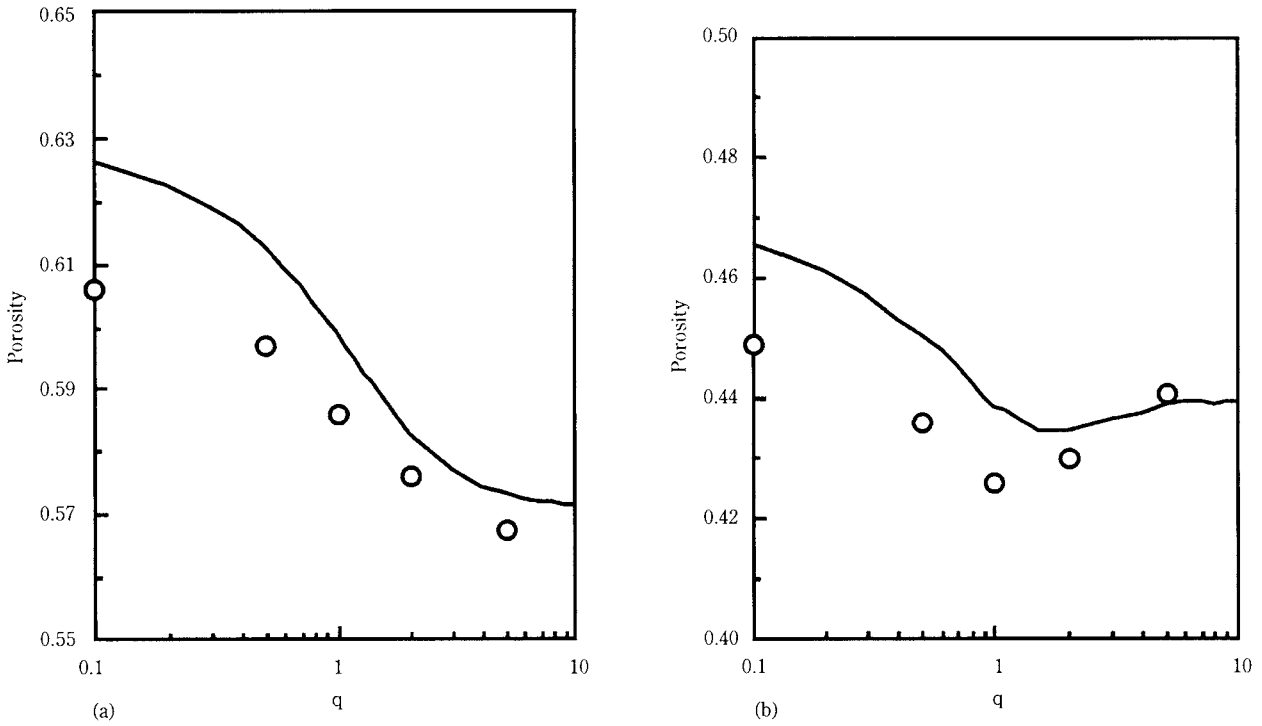

Fig. 18 Porosity vs. parameter q in eqn. (24) for the poured (a) and tapped (b) packings: ○, measurements; —, predictions.

$$F(d_v) = \frac{d_v{}^q - d_{v,min}{}^q}{d_{v,max}{}^q - d_{v,min}{}^q} \tag{24}$$

The minimum and maximum particle sizes $d_{v,min}$ and $d_{v,max}$ were assumed to be 6 and 57 μm, respectively, to match the experimental condition. **Fig. 18** shows the results. For the packing of (coarse) spherical particles, it has been established that porosity decreases to a minimum and then increases with the increase of q, though the minima may vary with the size range [15, 36]. Such behaviour can be observed for the tapped packing (**Fig. 18(b)**) but is absent for the poured packing (**Fig. 18(a)**). As seen in **Fig. 18(a)**, increasing q results in a continuous decrease in porosity, indicating the minimum porosity should be obtained when q is extremely large. This behaviour could be attributed to the agglomerate formation of fine particles resulting from the attractive forces. Application of external (mechanical) forces, e.g. the use of tapping/vibration or compaction, may break

down the agglomerates, leading to a denser packing with its limit matching the packing of coarse particles, a fact highlighting the importance of the study of the packing of coarse particles.

4. Concluding Remarks

Macroscopic modelling of the packing of particles can be made on the basis of the macroscopic packing mechanisms, such as mixing and unmixing, and facilitated by simple but physically sound concepts, such as initial porosity and equivalent packing size. In the past decade or so, significant progress has been made in this direction, particularly for the packing of coarse particles, leading to a comprehensive understanding of the dependence of porosity on particle characteristics including particle size, shape and their distributions. Such successful modelling provides a powerful means to solve various packing problems in a range of applications.

Acknowledgement

The authors would like to thank KCC, CSIRO, ARC and ERDC for financial supports, Prof. N. Standish and Prof. P. C. Arnold (Univ. of Wollongong), Dr. J. K. Wright (CSIRO), Dr. P. Zulli (BHP Research), Dr. J. A. Dodds (Ecole des Mine d'Albi), and Prof. J. Bridgwater (Univ. of Cambridge) for their encouragement, helpful discussions and/or direct involvement at various stages of the work.

Nomenclature

D = diameter of a cylindrical particle, m
d_p = equivalent packing diameter, m
d_v = equivalent volume diameter, m
$d_{p,0.5}$ = median size, m
d_{pi} = equivalent packing diameter of ith component, m
d_{vi} = equivalent volume diameter of ith component, m
$d_{v,min}$, $d_{v,max}$ = minimum and maximum particle sizes in eqn. (24), respectively, m
$f(r_{ij})$ & $g(r_{ij})$ = interaction functions between two components of size ratio r_{ij}, dimensionless
$f_v(d_p)$ = volume-frequency distribution of a powder, m^{-1}
$f_v(L)$ = volume-frequency distribution in terms of dimensionless length L, dimensionless
i, j, M, N = integer, dimensionless
L = ratio of length to diameter of a cylindrical particle, dimensionless
$L_{0.5}$ = median length in eqn. (19), dimensionless
n = number of components in a packing system, dimensionless
q = parameter in eqn. (24)
r = size ratio between successive components, dimensionless
r_{ij} = size ratio between the component i and j, dimensionless
V = overall specific volume of a packing system, dimensionless
V_i = initial specific volume of ith component, dimensionless
$\overline{V}_i$ = partial specific volume of component i, dimensionless
$\overline{V}_i^T$ = calculated specific volume under the assumption that the controlling mixture corresponding to component i is the controlling component, dimensionless
$\overline{V}_{Lj}$ = partial specific volume of jth (large) component in calculating V_i^T, dimensionless
$\overline{V}_{Mi}$ = partial specific volume of the controlling mixture in calculating V_i^T, dimensionless
$\overline{V}_{Sj}$ = partial specific volume of jth (small) component in calculating V_i^T, dimensionless
ΔV = specific volume variation, dimensionless
X_i = fractional solid volume of ith component, dimensionless
Y_k = defined by eqn. (10)

Greek Letters

β_{jk} = coefficient given by eqn. (11), dimensionless
γ_{jk} = coefficient given by eqn. (12), dimensionless
ε = porosity of a packing system, dimensionless
ε_o = initial porosity of a system with constant initial porosity, dimensionless
ε_i = initial porosity of ith component, dimensionless
σ_g = standard deviation of the log-normal distribution, dimensionless
ψ = sphericity, dimensionless
ψ_i = sphericity of ith component, dimensionless

References

1) J.M. Dallavalle, Micromeritics: The Technology of Fine Particles, Pitman, Chicago, New York, 1943.
2) R.M. German, Particle Packing Characteristics, Metal Powder Industries Federation, Princeton, New Jersey, 1989.
3) W.A. Gray, The Packing of Solid Particles, Chapman and Hall, London, 1968.
4) W.B. Fuller and S. E. Thompson, "The law of Proportioning Concrete," *Trans. Am. Soc. Civ. Engrs.*, 59 (1907), 67-172.
5) D.J. Cumberland and R.J. Crawford, The Packing of

Particles, Elsevier Science, Amsterdam, The Netherlands, 1987.
6) J.A. Dodds, "The Porosity and Contact Points in Multicomponent Random Sphere Packing Calculated By a Simple Satistical Geometric Model," *J. Colloid Interface Sci.*, 77 (1980), 317-327.
7) N. Ouchiyama and T. Tanaka, "Porosity Estimation for Random of Spherical Particles", *Ind. Eng. Chem. Fundam.*, 23 (1984), 490-493.
8) N. Ouchiyama and T. Tanaka, "Porosity Estimation from Particle Size Distribution," *Ind. Eng. Chem. Fundam.*, 25 (1986), 125-129.
9) M. Suzuki and T. Oshima, "Verification of a Model for Estimating the Void Fraction in a Three Component Randomly Packed Bed," *Powder Technol.*, 43 (1985), 147-153.
10) T. Stovall, T.F. De Larrard and M. Buil, "Linear Packing Density Model of Grain Mixtures," *Powder Technol.*, 48 (1986), 1-12.
11) J.S. Marshall and V.K. Dhir, "On the Prediction of Porosity of Beds Composed of Mixtures of Spherical Particles," *Chem. Eng. Commun.*, 48 (1986), 261-285.
12) A.B. Yu and N. Standish, "Porosity Calculation of Multi-Component Mixtures of Particles," *Powder Technol.*, 52 (1987), 233-241.
13) A.B. Yu and N. Standish, "An Analytical-Parametric Theory of the Random Packing of Particles," *Powder Technol.*, 55 (1988), 171-186.
14) N. Ouchiyama and T. Tanaka, "Porosity estimation of Mixed Assemblages of Solid Particles with Different Packing Characteristics", *J. Chem. Eng. Jpn.*, 21 (1988), 157-163.
15) A.B. Yu and N. Standish, "Estimation of the Porosity of Particle Mixtures by a Linear-Mixture Packing Model," *Ind. Eng. Chem. Res.*, 30(1991), 1372-1385.
16) A.B. Yu, R.P. Zou and N. Standish, "The Packing of Ternary Mixtures of Non-Spherical Particles," *J. Am. Ceram. Soc.*, 75 (1992), 2765-2772.
17) A.B. Yu and N. Standish, "Characterisation of Non-Spherical Particles from Their Packing Behaviour," *Powder Technol.*, 74 (1993), 205-213.
18) A.B. Yu, N. Standish and A. McLean, "Porosity Calculation of Binary Mixtures of Non-spherical Particles", *Journal of American Ceramic Society*, 76 (1993), 2813-2816.
19) R,P. Zou and A.B. Yu, "Evaluation of the packing characteristics of monosized non-spherical particles", *Powder Technol.*, 88 (1996), 71-79.
20) A.B. Yu, R.P. Zou and N. Standish, "Modifying the linear packing model for predicting the porosity of nonspherical particle mixtures", *Industrial & Engineering Chemistry Research*, 35 (1996), 3730-3741.
21) A.B. Yu, J. Bridgwater and A. Burbidge, "On the modelling of the packing of fine particles", *Powder Technology*, 92 (1997), 185-194.
22) L.C. Graton and H.J. Fraser, "Systematic Packing of Spheres with Particular Relation to Porosity and Permeability," *J. Geol.*, 43 (1935), 785-909.
23) D. Pinson, A.B. Yu and P. Zulli, "Calculation of the Coordination Number of Particle Mixtures: An Assessment of the Predictability of Some Proposed Packing Models", *Proc. Int. Ceramics Conference Australasian 94*, Sydney, Australia, July 1994, pp. 892-898.
24) D. Pinson, R.P. Zou, A.B. Yu, P. Zulli and M.J. McCarthy, "Coordination Number of Binary Mixtures of Particles", *Journal of Physics D: Applied Physics*, 31 (1998), 457-462.
25) A.B. Yu and N. Standish, "Limitation of the Proposed Mathematical Models for the Porosity Estimation of Nonspherical Particle Mixtures", *Industrial & Engineering Chemistry Research*, 32 (1993), 2179-2182.
26) A. Mayadunne, S.N. Bhattacharya and E. Kosior, "Modelling of Packing Behaviour of Irregularly Shaped Particles Dispersed in a Polymer Matrix," *Powder Technol.*, 89 (1996), 115-127.
27) C.L. Feng, R.P. Zou and A.B. Yu, "Packing of Binary Particulate Mixtures: Effect of Size Range", *Proc. 6th Int. Conf. on Bulk Materials Storage, Handling and Transportation*, Sept. 1998, pp. 389-395.
28) A.B. Yu, R.P. Zou, N. Standish and D.L. Xu, "Effect of Particle Size Distribution on Porosity of Packed Particles", *Proc. of the 1st Int. Particle Technology Forum*, Denver, U.S.A., August 1994, Vol. 2, pp. 60-65.
29) A.E.R. Westman, and S. E. Thompson, "The Packing of Particles," *J. Am. Ceram. Soc.*, 13 (1930), 767-779.
30) R.K. McGeary, "Mechanical Packing of Spherical Particles," *J. Am. Ceram. Soc.*, 44 (1961), 513-522.
31) K. Ridgway and K.J. Tarbuck, "Particulate Mixture Bulk Densities," *Chem. and Proc. Eng.*, 49 (1968), 103-105.
32) A.R. Dexter and D.W. Tanner, "Packing Density of Ternary Mixtures of Spheres," *Nature Physical Science*, 230 (1971), 177-179.
33) R. Jeschar; W. Potke; V. Petersen and K. Polthier, "In Blast Furnace Aerodynamics," Standish, N., Ed.; Aust. I.M.M. Press: Wollongong, Australia, 1975; pp.136-147.
34) N. Standish and D.E. Borger, "The Porosity of Particulate Mixtures," *Powder Technol.*, 22 (1979), 121-125.
35) N. Standish and D.N. Collins, "The Permeability of Ternary Particulate Mixtures for Laminar Flow," *Powder Technol.*, 36 (1983), 55-60.
36) N. Ouchiyama and T. Tanaka, "Predicting the Densest of Ternary and Quaternary Mixtures of Solid Particles," *Ind. Eng. Chem. Res.*, 28 (1989), 1530-1536.
37) C.C. Furnas, "Grading Aggregates I – Mathematical Relations for Beds of Broken Solids of Maximum Density," *Ind. Eng. Chem.*, 23 (1931), 1052-1058.
38) H.Y. Sohn and C. Moreland, "The Effect of Particle Size Distribution On Packing Density," *Can. J. Chem. Eng.*, 46 (1968), 162-167.
39) A.R. Dexter and D.W. Tanner, "Packing Densities of Mixtures of Spheres with Log-normal Size Distributions," *Nature Phy. Sci.*, 238 (1972), 31-32.
40) R.J. Wakeman, "Packing Densities of Particles with Log-normal Size Distribution," *Powder Technol.*, 11 (1975), 297-299.
41) N. Standish, A.B. Yu and R.P. Zou, "Optimization of Coal Grind for Maximum Bulk Density", *Powder Technol.*, 68 (1991), 175-186.
42) A.B. Yu and N. Standish, "A Study of the Packing of

Particles with a Mixture Size Distribution," *Powder Technol.*, 76 (1993), 113-124.
43) J.V. Milewski and H.S. Katz, Handbook of Fillers and Reinforcements for Plastics, Van Nostrand Reinhold, New York, 1987, pp.14-33.
44) R.P. Zou, X.Y. Lin, A.B. Yu and P.L. M.Wong, "The packing of cylindrical particles with a length distribution," *Journal of American Ceramic Society,* 80 (1997), 646-652.

Author's short biography

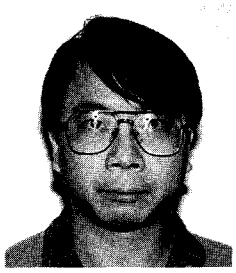

A.B. Yu

Dr. A. B. Yu specilised in chemical metallurgy, obtaining his BEng in 1982 and MEng in 1985 from Northeastern University (PR China) and PhD in 1990 from the University of Wollongong (Australia). He worked as a postdoctoral fellow with CSIRO Division of Mineral & Process Engineering and then a research fellow with the University of Wollongong. He has been with the University of New South Wales since June 1992 and is currently associate professor in the School of Materials Science and Engineering. He has published about 120 journal and conference papers, mainly in the areas of particle technology and process metallurgy.

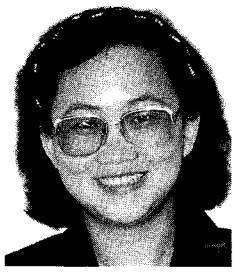

R.P. Zou

Dr. R. P. Zou specilised in physical chemistry, obtaining her BEng in 1986 from Northeastern University (PR China), MEng in 1990 from the University of Wollongong and PhD in 1997 from the University of New South Wales (Australia). She has published over 20 journal and conference papers. She is currently a postdoctoral fellow with the University of New South Wales, continuing her research on particle packing and fluid flow in packed beds.

Review

Present State and Prospects of Aerosol Research Application in Korea†

Kil-Choo (K.C.) Moon
Environment Research Center
*Korea Institute of Science and Technology (KIST)**

Abstract

Aerosol research in Korea started in the beginning of 1970's in various fields of hygiene, air pollution control, inhalation toxicology, atmospheric physics, clean room and powder manufacturing. The first aerosol related association in Korea was established in 1984 under the name of Subcommittee of Powder Technology (SCPT) of the Korea Institute of Chemical Engineers (KIChE).

The aerosol science research has grown continuously with various application fields in science and engineering. The importance of the aerosol science was recognized in newer technology fields such as clean room for semi-conductor, manufacturing for material science, and combustion for diesel engines in 1980's. The Korean Association for Particle and Aerosol Research (KAPAR) was founded in September 1994 with various background of aerosol science researches. The main purpose of KAPAR is to exchange the knowledge of aerosol science and let public recognize the importance of particle technologies.

The KAPAR started to promote the aerosol research through advancing the arts and sciences in the fields of aerosol science and particle technology with various science and engineers backgrounds. In four years, KAPAR has more than 200 individual members of scientists and engineers from research institutions, universities and private companies. These two associations of SCPT and KAPAR promote mutual understanding and technology exchange.

1. Introduction

Aerosol technology is the study of the properties, behavior, and physical principles of aerosol and the application of this knowledge to their measurement and control. The particulate phase of an aerosol represents only a very small fraction of its total mass and volume. The bulk properties of aerosols, such as viscosity and density, differ imperceptibly from those of pure air. Consequently, to study the properties of aerosols one must adopt a microscopic point of view. This approach considers one particle at a time and deals with questions about the forces on the particles, its motion, and its interaction with the suspending gas, with electromagnetic radiation, and other particles. [1]

At the turn of the century, the study of aerosols was at the forefront of the physical sciences because aerosols represented the smallest observable division of matter. With the advent of atomic physics, interest in aerosol waned until world War II, when their military application received great attention. Following World War II, and particularly during the 1970s, aerosol technology grew in importance because of an increased environmental awareness and a concern for the health effects arising from air pollution in community and occupational environments. It has become an important tool in understanding the effect we have on our environment and the impact of that environment on us. Any subject that touches such diverse phenomena as sunsets, silicosis, rain, cascade impactors, cross pollination, electrostatic precipitation, and rainbows is not a simple one. Aerosol technology draws on physics, chemistry, and engineering. It uses some of the tools, concepts, and terminologies of power technology. It is used in the fields of industrial hygiene, air pollution control, inhalation toxicology, atmospheric physics and chemistry, and radiological health.

As described above, the aerosol technology expanded along with the major industry changes, such as environmental control in 1970s, aerosol technology applied for semiconductor in 1980s and atmospheric science application in 1990s in Korea.[2] Before 1980s, the Korea's industry was very premature without any

* P.O. Box 131, Cheongryang, Seoul, 130-650, KOREA
Tel: +82-2-958-5802/Fax: +82-2-958-5805
† Received 15 June, 1998

higher technology application of aerosol science. However, many Korean studied aerosol related subjects and established an association such as the Subcommittee of Powder Technology (SCPT) of the Korean Institute of Chemical Engineers (KIChE). The SCPT was established in 1984, but the SCPT research was very limited in the fields of powder technology rather than broad fields of aerosol science. The SCPT contributed to adopt the concept of powder and aerosol technologies in Korea. The Korean Association for Particle and Aerosol Research (KAPAR) was founded in September 1994. Professor Sang Soo Kim was the first President of the Association, and now Dr. Kil-Choo (K.C.) Moon is the second President. The main purpose of KAPAR is to exchange the knowledge of aerosol science and let the public recognize the importance of the particle technologies.

The KAPAR started to promote the aerosol research through advancing the arts and sciences in the fields of aerosol science and particle technology with various science and engineering backgrounds. In the beginning, the members were very limited in number with chemical, mechanical and electrical engineers and scientists who have aerosol and particle backgrounds. In four years, KAPAR attracted more than 200 individual scientists and engineers from research institutions, universities and private companies with various background of aerosol and particle technologies such as electronics and chemistry.

2. Major Activities of KAPAR and SCPT Association

As described already, there are two associations for powder technology and aerosol science researches in Korea. It is not easy to distinguish the main difference of these organizations' function but they have the same purpose in aerosol and particle technology, i.e. to exchange and introduce newer technologies for industry.

KAPAR:

The Association has two annual meetings in Spring and Fall and one continuing education and training program. Usually, Spring Conference invites famous aerosol researchers to give lectures and Fall conference presents papers as annual meeting. One of the best activities of this association is continuous education and training program for young scientists and engineers in different fields. The curriculum of continuous education program includes fundamental theories, experiment and application of aerosol instruments for various cases. This continuous education and training program has been already offered four times for graduate students and engineers in the aerosol fields such as electrical, chemical and mechanical engineering.

Another major activity is to promote participation in famous international conferences, such as AAAR, European Aerosol Conference, International Aerosol Conference, National Heat Transfer Conference, KSME-LSME Thermal Engineering Conference, AIChE conference, International Conference of Contamination Control Society, Microcontamination and A&WMA and more.

The future activities will be the issue of periodical journals and joint the organization of workshop with other associations. Furthermore, KAPAR wishes to establish an Asian Aerosol and Particle Conference together with Asian countries. The KAPAR is now four years olds with second executive boards members, Second President K.C. Moon with aerosol control technology background. The Executive board member consist of two vice presidents and ten directors of general affairs, treasure, activities and publications. The executive boards also include one former president, Dr. Sang Soo Kim, and one councilor, Dr. Kyoo Won (Ken) Lee.

Table 1 shows the list of steering member of KAPAR and their major research fields, which are very wide range from aerosol dynamic to air pollution controls including pharmacology, gas-particle two phase flow, clean room control technology, semiconductor processing, fluids mechanics of aerosol system, indoor air pollution and so forth. There are many other universities, research institutions and companies in the membership.

SCPT (Subcommittee of Power Technology):

The SCPT was established in 1984 as one of 13 expert subcommittees in the Korea Institute of Chemical Engineers (KIChE), which was established in 1962. The steering member of the SCPT and their major fields of interest are listed in **Table 2**. The number of membership of the SCPT is about 5-10% of the total 4300 membership of KIChE. The exact number of membership is not fixed, because the membership fee is free and any member in KIChE can at the same time enroll several subcommittees. The SCPT has regular meetings, i.e., the annual meeting in spring and fall, a summer symposium, and the occasional seminar of basic education on power technology. The newsletter of the SCPT has been distributed widely since 1989 to regular members and potential

Table 1 KAPAR key members and their activities

No	Name/affiliation	Major fields of interest
1	Dr. Lee, Kyoo Won (councilor) Kwangju Institute of Science & Technology (K-JIST) e-mail : lee@env.kjist.ac.kr	- Aerosol dynamics - Filtration - Aerosol instrumentation
2	Dr. Kim, Sang-Soo (past president) Science & Technology Policy Institute (STEPI) e-mail : sskim@stepimail.stepi.re.kr	- Gas-particle two-phase flow - Environmental control - Electrostatic precipitation
3	Dr. Moon, Kil-Choo (president) Korea Institute of Science & Technology (KIST) e-mail : kcmoon@kistmail.kist.re.kr	- Air pollution control - Clean air technology - Diesel particle charging
4	Dr. Kim, Sun-Geon (vice president) Chung-Ang University	- Ultrafine particle technology - Flue gas treatment
5	Dr. Lee, Jin-Won (vice president) Pohang University of Science & Technology (POSTECH)	- Health related aerosols - Respiratory depostion
6	Dr. Hwang, Jungho (general secretary) Yonsei University e-mail : hwangjh@bubble.yonsei.ac.kr	- Material synthesid - Combustion particles
7	Dr. Kim, Yong-Jin Korea Institute of Machinery & Metals (KIMM) e-mail : yjkim@boss.cee.uc.edu	- Precipitation and acid gas control - Fluid mechanics of aerosol system
8	Dr. Choi, Man-Soo Seoul National University e-mail : mchoi@alliant.snu.ac.kr	- Heat transfer - Aerosol synthesis - Materials processing
9	Dr. Ahn, Kang-Ho Hanyang University e-mail : khahn@hyunp2.hanyang.ac.kr	- Instrumentation of aerosol measurements - Particle contamination control
10	Dr. Kim, Young-Joon Kwnagju Institute of Science & Technology (K-JIST)	- Aerosol physics - Atmospheric aerosols - Sampling and analysis
11	Dr. Jung, Yongwon Inha University e-mail : jungyw@dragon.inha.ac.kr	- Air cleaning - Dust collection - Waste recycling
12	Dr. Lee, Jae-Keon Pusan University e-mail : jklee@hyowon.pusan.ac.kr	- Unburned particle separation - Ultra clean technology

nonmembers who are working in this field. As an international meeting, the Korea-Japan Power Technology Joint Seminar has been held every 2 years since 1985. This international joint seminar helps mutual understanding and technology exchange, and will be continued for mutual cooperation.

3. Major Research Organization

Aerosol technology research brings together many different research areas of academic and industrial organizations related to air pollution and control, contamination control, material processing, health and industrial hygiene and instrumentation and measurements. Most of aerosol researchers are affiliated at

Table 2 List of Steering Members of SCPT

No	Name/affiliation	Major fields of interest
1	W.S.Choi (Professor, Chairman) Pusan National University Department of Pharm, Manufac.	Communication, Agglomeration, Powder processing
2	P. Z. Ryu (Professor, Secretary) Seimyung University Department of Resource Engineering	Mixing, Kneading
3	J. H. Choi (Professor) Kangwon National University Department of Paper Engineering	Filtration, Wet processing
4	C. S. Choi (Professor) Seogang University Department of Chemical Engineering	Crystallization
5	K. R. Chung (Professor) Cheunbook National University Department of Chemical Engineering	Particle size measurement
6	S. C. Chung (Professor) Pusan Industrial College Department of Chemical Engineering	Reaction process
7	S. H. Kang (Professor) Youngnam University Department of Chemical Engineering	Particle size measurement, Dust collection, Filtration
8	K. S. Kim (Professor) Kangwon National University Department of Chemical Engineering	Aerosol science
9	S. K. Kim (Professor) Joongang University Department of Chemical Engineering	Production of fine particles
10	T. S. Seo (Director) Korea Institute of Chemistry Laboratory of Powder technology	Classification, Pigment
11	J. I. Shon (Director) Korea Institute of Energy and Technology	Dust collection, Coal utilization
12	J. K. Yang (Director) Sangyong Cement Indstury Co.	Powder processing, Cement

Universities, National Research Laboratories and Private Research Institutions. As shown in the **Table 3**, the major role of the different institutions are distinguishable – university focuses on basic research, National Laboratory focuses on project and application research and the private institution focuses on development and improvement of products research.

This report covers very limited but representative research oriented organizations for aerosol research among many universities, national and private research institutions in Korea. Report describes the limited research programmes of Seoul National University, University of Kyungpook, Kwangwon and Pusan University, YonSei and Pohang University of Science and Technology, and also describes about the aerosol research activities of several National Laboratories of Korea Advanced Institute of Science and Technology (KAIST), Kwanju Institution of Science and Technology (K-JIST), Korea Institution

Table 3 Research Function of Different Institution

Categories	Major Roles	Research Topics
University	• Fundamental Research • Basic Science • Limited Application • Education Purpose	- Aerosol dynamics - Fundamental aerosol movement/characterization - Air quality modelling - Plasma and corona discharge research for SOx/Nox - Nano particle research - Particle motion in lung airways
National Research Laboratory	• Application base on Fundamental Theory • Project Oriented Research and Development • Target Oriented Research than pure Science • Public Awareness Oriented Research	- Instrument development - Environmental monitoring and Development modeling - Development of high efficiency Industrial ESP. - Development of semi-Dry electrostatic scrubber
Private Research Institution	• Development and Improvement Oriented research • Problem Solving Research • Small Scale Research	- Gas cleaning technology - Develop high efficiency ESP - Develop clean and ultra clean room - Production improvement oriented research

of Machinery and Material (KIMM), and Korea Institution of Science and Technology (KIST). Report does not describe on research function of private research institution in detail to avoid the conflict of the interest.

Seoul National University: The aerosol related researches go on in many departments, however this paper describes on the researches at the Department of Mechanical Engineering, because this department was recently (Dec. 1997) nominated as "Center for Nano Particle Control (CNPC)" that is supported as one of Creative Research Initiatives (CRI) Programs by the Ministry of Science and Technology in Korea for six to nine years. This research group has been carrying out aerosol related research in thermal material processing and developing research programs of heat transfer and aerosol studies in the manufacturing of optical fibers and planar waveguide, both of which are currently made by aerosol processes. Their research includes both experimental and theoretical works for several aerosol processes such as Modified Chemical Vapor Deposition, Outside Vapor Deposition, Flame Hydrolysis Deposition and they are interested in establishing aerosol control technology by controlling heat and flow in the processes. The leader of research group is Professor Mansoo Choi who obtained Ph.D. degree from the University of California, Berkely.

Kyungpook National University: Many departments have conducted aerosol researches but this paper describes on Laboratory of Eco-Electrostatic Engineering for aerosol research. This group's main concerns and interests are the electro-physicochemical and electro-hydrodynamic interactions in high electric fields, submicropulses and/or nonhomogeneous fields discharges as well as electrostatic phenomena. The fundamental theory of these phenomena are studied and many projects focus on the engineering applications, such as air pollution gas control by nonthermal discharge plasma, development and application of ozone generation system, effective control means for submicron fine particles, and many other fine particle control devices. This group is lead by Professor Jae-Duk Moon.

Kangwon National University: The Department of Chemical Engineering research group conducts on many aerosol research. The major research topics of this group are analysis of aerosol dynamics for ultra fine particle generation and transportation. Also aerosol dynamics in flame aerosol reactor and in furnace aerosol reactor are the major project topics to meet the ultimate goal to make efficiency TiO_2 photocatalysts and to make uniform films of ultra fine SiO_2 particles by controlling wall temperature. Also they analyze the particle generation and growth in silane PCVD reactor in order to reduce the particle contamination in semiconductor processing. The research group is lead by Professor Kyo-Seon Kim, who obtained his Ph.D. degree from the University of Cincinnati.

Pohang University of Science and Technology (POSTECH): POSTECH offers research-oriented graduate school program rather than that for undergraduates. The Department of Mechanical Engineering and School of Environment Engineering have aerosol related research programmes. The aerosol research group focuses on the analysis of air flow and particle motion in dust collector and particle motion respiratory airways as well as air pollution related researches. One of their research objective is to establish numerical techniques for simulating particle

motion in turbulent flows and establish in boundary layers. The numerical techniques will be developed and applied to accurate modeling of ESP's and cyclone. Also they focus on the research of particle transportation in human airways which is very sensitive to the geometry and velocity profile at the inlet. The airway modeling of particle collection and diffusion for human lung are studying using a multiple model. This research group is lead by Professor Jin W. Lee who obtained his Ph.D. from Northwestern University.

Pusan National University: Aerosol research program at the School of Mechanical Engineering started in 1993. This group focuses on gas cleaning and separation of fine and ultra fine particles of unburned carbon from flyash. They investigate the technical feasibility of a dry triboelectrostatic process to recover unburned carbon from flyash into economically valuable products. Particles of unburned carbon and ash can be charged in different electrical polarity by copper tribocharge, and can be separated by passing them through an external electric field. The two stage separation system of the centrifugal classifier and the triboelectrostatic separator showed potential application removing unburned carbon from flyash. This group also has interests on the development of clean room, ultra clean technology and classification & waste recycling of powers such as coal, flyash and plastics. This research group is lead by Professor Jae-Keun Lee who obtained Ph.D. degree from the University of Minnesota.

Yonsei University: The Department of Mechanical Engineering has an applied aerosol research studies. This research group focus on application of aerosol technology to material synthesis and thermal behavior of metal aerosols in waste incineration. In the beginning of their aerosol research, they focused on the electric field enhanced deposition processes in optical fiber preform fabrication. Now they work on more application oriented project of particle technologies, such as reduction of diesel particle matters using pulsed plasma technology, improvement of scrubbing efficiency of SO_2 using electrospraying technology, and control of killer wear particles generated in hard diskette drivers. This research group is lead by Professor Jungho Hwang who obtained Ph.D. degree from the University of California, Berkely.

Kwangju Institute of Science and Technology (K-JIST): K-JIST is a research-oriented graduate school that focuses on essential fields of technology. The aerosol research group at the Department of Environmental Science and Engineering was founded in 1993 for aerosol technology and air quality laboratory. The main research focus on the behavior and mechanics of suspended particle including measurements of composition, concentration, size distribution, aerosol deposition, agglomeration and various physical, electrical and chemical properties. The application includes atmospheric science, contamination control, clean room technology, semiconductor manufacturing processes, combustion engineering, public health and nuclear reactor safety analysis. The Air Quality Laboratory carries out research into processes that relate to air quality and atmospheric changes concentration on the transport, dispersion, transformation and removal of gaseous and particulate air pollutants, the development of new measurement techniques, calibration and analysis techniques and the development of air quality management strategies. This research group is leading by Professor Kyoo(Ken) Won Lee who obtained Ph.D. from the University of Minnesota.

Korea Institute of Machinery and Material (KIMM): The Aerosol Research Group at KIMM, national laboratory, investigates the transport and behavior of aerosol in industrial and environmental systems. The research group studies on both basic and application researches for development of innovative industrial aerosol control devices minimizing the impact of hazardous aerosols to the environment. Their main research area is to develop a high efficiency industrial ESP, especially for submicron particles and semi-dry electrostatic scrubber, development of a plasma de-SOx and de-NOx system and development of a hybrid indoor air cleaner. This research group develops higher efficiency ESP which can be used to control air pollutants of sulfates and nitrates particles including pollutants gases. Most of their research is related to the projects bases for national and private industries. The research group is lead by Dr. Yong-Jin Kim who obtains Ph.D. degree from KAIST.

Korea Advanced Institute of Science and Technology (KAIST): One of the oldest aerosol research laboratories with very wide spectrum of research topics. The Department of Mechanical Engineering has Aerosol and Particle Technology Laboratory for their own aerosol research. This laboratory focus on basic research on droplet growth in a capillary expansion,

absorption into a wavy falling liquid film and charge effects on coagulation between particles, and application research on filtration of fibrous filters with external electric field, air sampling system for air borne particles, and particle collection by inertial impaction in solid-gas two-phase flow system. This research group also works on many combustion related particle projects, such as particle trap for low emission control combustion technique and analysis of heat and mass transfer of sludge particles in a sludge dryer system and more. The aerosol and particle research laboratory offers aerosol short courses for industry and graduate student during summer periods since 1995. This short course is very popular and recognized in Korea. This research group is lead by Sang Soo Kim who obtained his Ph.D. from the Northwestern University.

Korea Institute of Science and Technology (KIST): KIST engages in a wide spectrum of research related to particle and aerosol technologies, such as air pollution phenomena in local, regional and global scale including long range transportation. The main emphasis of the research is placed on the aerosol dynamic, which is vital to understand a variety of air-pollution phenomena ranging from smog in urban area, acid rain precipitation to global warming. Recent rapid industrialization of the East-Asia region made Korea to be in more vulnerable position for protecting the nation's environmental quality. The center is currently involved in the research activities to develop the monitoring and prediction tools for long-range transport of air pollution and acid-rain precipitation in order to devise mitigation strategies for the increasing environmental strain causes by regional pollution. Particle transformation modeling research is going on under various conditions, such as particle to particle, gas to particle and particle to gas formation. This research will be contributed to aerosol dynamics and long range transportation to understand the actual aerosol dynamic phenomenon. The fine particle control is one of major active research now. This research fields covers from electrostatic precipitator control to ultra fine particle contamination on a wafer surface. The particle size response of the wafer surface scanner is studied. This group also studies basic particle behavior characterization including partial diffusion on semiconductor and indoor aerosol particles. This is one of the largest aerosol research group in Korea. This research group is lead by Kil-Choo (K.C.) Moon who obtained his Ph.D. from the University of Minnesota.

4. Conclusion

The SCPT member established a fundamental basis for particle applied research in Korea. Moreover the association contributes the application of particle technology to industry as well as exchange knowledge between researchers and industries. With their foundation, the new association of KAPAR was easy to formulated for next generation researches.

The KAPAR members and activities are in premature stage, however individual members' activities are recognized in the aerosol research fields. The application and importance of aerosol and particle science in industry are being recognized in Korea, slowly. In four years history of KAPAR, it achieved a great role of continuous education and exchanged individual knowledges. In future, SCPT and KAPAR will recruit more memberships and expand activities for exchange knowledge between members and collaboration between other related associations. Furthermore KAPAR would like to participate Asian International Aerosol Conference with other Asian countries in Nagoya in 1999.

In conclusion, these two associations will be resorts for Korean aerosol research and become a seed for Asian Aerosol Conference in the near future. On behalf of SCPT and KAPAR members, it is a very honour and pleasure to have chance to introduce Korean aerosol research.

Acknowledgment

The author wishes to thank all the Korean members of SCPT and KAPAR, especially who contributed to write their institution research description.

References

1) William C. Hinds, "Aerosol Technology, Properties, Behavior and Measurement of Airborne Particles", A Wiley Interscience Publication, U.S.A., 1982
2) N.J. Baik, T.H. Kim, Y.p. Kim, K.C. Moon, "Cause and Verification of Visibility Impairment Phenomenon", KAPAR Vol. 10, No.1 pp1-23, Seoul , Korea, 1994

Author's short biography

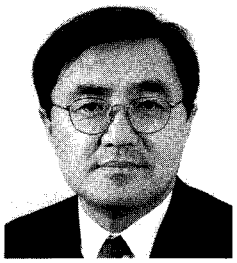

Kil-Choo (K.C.) Moon

Dr. Kil Choo Moon, Director of Environment Research Center of KIST who has a broad of experience in all aspects of atmospheric sciences, from the technical and management perspectives. He joins KIST in 1991, before Dr. Moon joined KIST, he had more than 10 years working experiences in U.S.A.. Recently at KIST, he manages many other related project as well as works on his own project such as Seoul Smog project and Ozone project at industrialized area in Korea with developing special region air dispersion modeling project for Korea Electric and Power Company. He is using his wide experience for international cooperation projects in Korea. He successfully carried out already international projects such as aerosol measurement and research center between Korea and China November 1993, and working on Asia-Pacific Technology Research Network between Korea and Japan. Dr. Moon has his Ph.D. degree at Department of Mechanical Engineering, Particle Technology Laboratory at the University of Minnesota.

Review

Applications of Supercritical Fluids in Powder Processing†

Tadafumi Adschiri
*Dept. of Chem. Eng., Tohoku Univ.**

Abstract

This paper reviews methods of producing particles using supercritical fluids. First it explains the properties of supercritical fluids, phase behaviors of supercritical solutions, and reaction equilibrium and reaction rate in supercritical fluids. Next it explains the principles of new crystallization methods using supercritical fluids. These explanations cover the RESS method, GAS method, retrogressive crystallization, supercritical drying, and hydrothermal synthesis in SCW. The use of rapid expansion of supercritical solutions (RESS) through a nozzle obtains extremely high supersaturation, which brings about rapid nucleation.

This leads to the formation of ultrafine particles. Changing the expansion conditions allows one to control particle morphology and size. Using two nozzles makes it possible to coat particles with other materials. Supercritical CO_2 can be used as an antisolvent. This gas anti-solvent (GAS) method is used to recrystallize the solute, which is thermally or chemically unstable. The solubility of a solute in a supercritical fluid is largely dependent on temperature and pressure, and this temperature and pressure dependence differs from one substance to another. Thus, manipulating temperature makes it possible to precipitate only one solute from a mixture solution. This method is called retrogressive crystallization. Supercritical fluid extraction can be used for drying particles. Using this method eliminates capillary force among particles because there is no gas-liquid interface during drying, thereby inhibiting particle coagulation. Hydrothermal synthesis in supercritical water is an attractive method for producing metal oxide fine particles while controlling particle size, morphology, and crystal structure. Since SCW is miscible with O_2, H_2, or CO gas, these gases can be used to control the oxidizing or reducing atmosphere. The reaction equilibrium for hydrothermal reactions varies greatly around the critical point by slightly varying pressure and/or temperature, which brings about change in the morphology of the produced particles. This paper also considers the possibilities of creating new powder processing processes.

Introduction

In the development of technologies for the chemical industry the selection of solvents is of obvious importance, but as people have until now been shackled by the established idea that solvents are liquids, the selection of solvents has been very difficult. Of particular interest in recent years are trial attempts at using, as new solvents to replace liquid solvents, supercritical fluids whose physical properties can be broadly controlled by temperature and pressure.

Beginning in the 1980s attention focused on the controllability of the solvent power and phase equilibrium of supercritical fluids, and people have worked on their use as new extraction and separation solvents to take the place of liquid solvents. Supercritical carbon dioxide in particular is not only nontoxic, odorless, and inexpensive, but also has a critical temperature that is near room temperature. It is therefore capable of separation operations at low temperatures and can be used in the separation of substances that are thermally unstable. It also promises high selectivity in separation, and there is no problem whatsoever with post-separation residual solvent. For these reasons development has proceeded on supercritical carbon dioxide extraction processes chiefly in the areas of food and pharmaceuticals [1].

The controllability of supercritical fluid physical characteristics is not limited to extraction and separation solvents, but also offers promise for reaction solvents [2, 3] and crystallization solvents [4-6], and recently research and development are proceeding in these applications. This paper will explain the characteristics of supercritical fluids as a powder processing field.

* Aoba-ku, Sendai City 980-8579, Japan
Phone/Fax 022-217-7246

† This report was originally printed in J. Soc. Powder Technology, Japan. **35**, 371 (1998) in Japanese, before being translated into English by KONA Editorial Committee with the permission of the editorial committee of the Soc. Powder Technology, Japan.

First comes an explanation about the physical characteristics and solvent characteristics of supercritical fluids, which is followed by an explanation about the principle of a new crystallization method using supercritical fluids, and examples of applications. The paper will also consider the possibilities of creating new processes.

1. Physical Characteristics and Solvent Characteristics of Supercritical Fluids

1.1 What Are Supercritical Fluids?

Whether a fluid is in a gaseous phase or liquid phase depends on the kinetic energy of its molecules and the energy of intermolecular force. When intermolecular force governs to a greater extent than molecular kinetic energy, a fluid will be a liquid with a certain measure of order, but when kinetic energy is dominant, it will be a gas with a chaotic structure. Kinetic energy grows as temperature rises, and the shorter the distance between molecules (i.e., the higher the concentration), the more dominant intermolecular force will become. Thus, in general a liquid will become a gas when its temperature is raised, and a gas will liquefy when it is compressed. However, above a certain temperature, molecular kinetic energy is the greater force no matter what the distance between molecules, and the substance will become a noncondensable fluid. This temperature (the critical temperature) is unique to each substance, and a fluid at or above its critical temperature is a supercritical fluid.

Because the state of molecules near the critical temperature is characterized by the balance between the formation of system order by intermolecular force and dissipation by molecular kinetic energy, on a microscopic level this is a state in which the molecules are changing places very actively while maintaining a certain extent of order, and rather small changes in temperature and pressure will bring about major changes in average fluid density and cluster structure.

All physical properties of a fluid depend on its average structure and dynamic structure, and because these structures change greatly near the critical point, various physical characteristics (such as density, viscosity, diffusivity, dielectric constant, and ionic product) also undergo great changes in conjunction with them [6]. Here the author presents graphical representations of the temperature and pressure dependence of water density (**Fig. 1**) and of water's dielectric constant ε (**Fig. 2**). The graphs show that near the critical temperature of 374°C these physical property values change greatly. Solvent characteristics such as the fluid's solvent power, as well as its reaction rate and equilibrium there, also change greatly as these values change. An example would be the solubility of SiO_2 in supercritical water (**Fig. 3**). It is evident that near the critical point solubility changes greatly along with temperature and pressure.

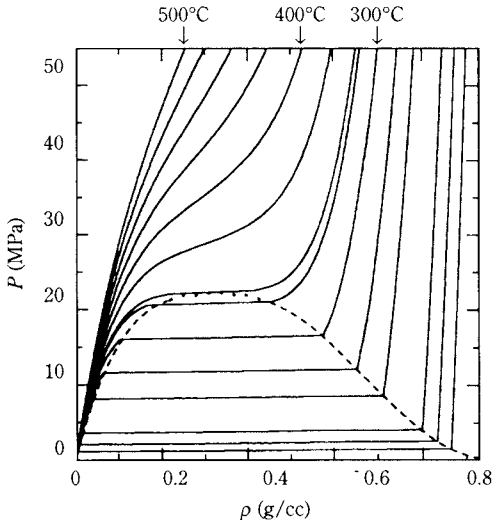

Fig. 1 Dependence of Water Density on Temperature and Pressure

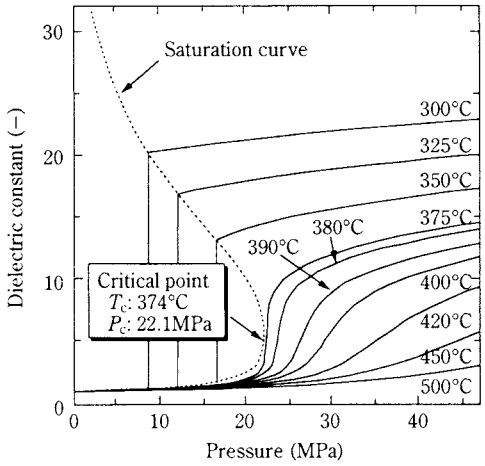

Fig. 2 Dependence of Water Dielectric Constant on Temperature and Pressure

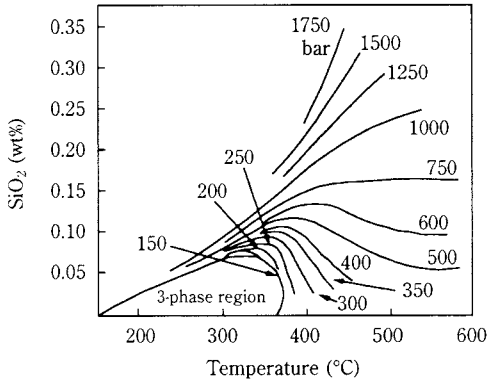

Fig. 3 Solubility of Silica (SiO_2) in Water at High Temperature and Pressure

1.2 Phase Behavior of Systems in which Supercritical Fluids Are Involved

Actual fields are multi-component systems, so determining the states of such systems necessitates considering also the energy of interaction between molecules of different kinds. When a supercritical fluid is involved, interaction between molecules of different kinds also changes greatly near the critical point, and as a result the phase behavior also changes greatly. Thus, when a supercritical fluid is involved, there are large changes in phase behavior even when the system is a simple one with two components [7-9].

Let us examine the phase behaviors of a water-gas system (**Fig. 4**) and a water-hydrocarbon system (**Fig. 5**) near their critical points. The curves are the gas-liquid critical loci. In the higher-temperature regions (right hand sides), components mix uniformly in arbitrary compositions.

At room temperature forcing a gas into water will produce bubbles, but supercritical water, which is high-density vapor, will completely mix with a gas. Similarly, water and hydrocarbons in the low-temperature range will refuse to mix and undergo phase separation, but when water is supercritical they will mix uniformly. This mutual solubility with hydrocarbons is understandable when considering that the dielectric constant of supercritical water, as shown in **Fig. 3**, is about 2 to 10 and approximately equivalent to that of a polar organic solvent.

Recent years have seen the development of a "supercritical water oxidation" technology that completely and rapidly decomposes by oxidation, which

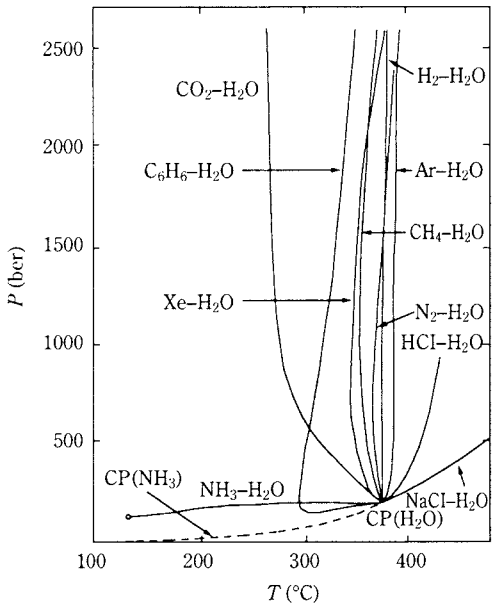

Fig. 4 Critical Loci of a Two-Component (Water-Gas) System

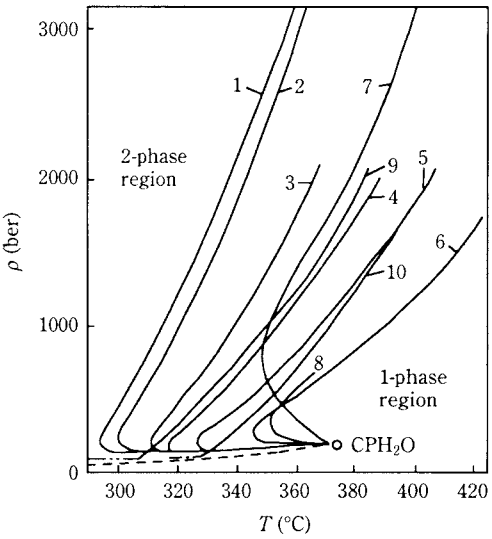

Fig. 5 Critical Loci of a Two-Component (Water-Hydrocarbon) System
1. Benzene, 2. Benzene-D_2O, 3. Toluene, 4. o-xylene, 5. 1,3,5-trimethyl benzene, 6. Cyclohexane, 7. Ethane, 8. n-butane, 9. Naphthalene, 10. Biphenyl

works by forcing oxygen into foul water and other sewage that is in a supercritical state [10, 11]. This technology takes advantage of the ability to cause the reaction of water, organic substances, and oxygen in a homogeneous phase by putting the sewage water into a supercritical state. Just as with crystallization and other powder preparation techniques, there is promise for the creation of new technologies that utilize such controllability of phases [4-6].

1.3 Reaction Equilibrium and Reaction Rate in Supercritical Fluid Fields

Let us examine a reaction activation barrier (**Fig. 6**). The difference in potential between the transition

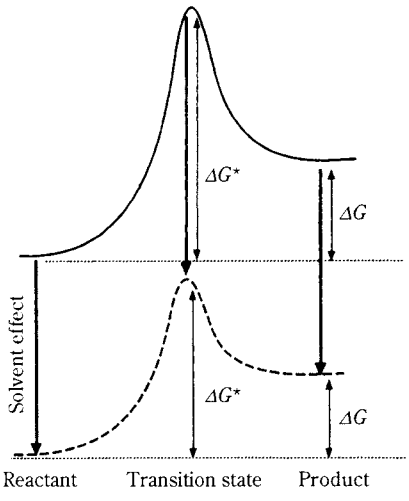

Fig. 6 Activation Energy of Reaction and Solvent Effect

state and the reactant is the activation energy. When there is a solvent the states of the reactant and the molecules in transition state will change, and activation energy will also change. The theory of Kirkwood and Amis expresses the reaction rate in a solution with the following equation [12, 13].

$$\ln k = \ln k_0 - \frac{c}{RT}\left(\frac{1}{\varepsilon} - 1\right) \quad (1)$$

where the first term is the reaction rate constant in a vacuum, the second is the solvent effect, ε is dielectric constant of the fluid, and constant c is the difference in polarity between the transition state and the reactant.

As seen in **Fig. 2**, the dielectric constant will change greatly near the critical point due to slight changes in temperature and pressure, showing that the reaction rate will change greatly [3].

The reaction equilibrium constant, as in Equation (1), is written as the function of the dielectric constant ε, while C is written using the polarity difference between the reactant and product.

$$\ln K = \ln K_0 - \frac{C}{RT}\left(\frac{1}{\varepsilon} - 1\right) \quad (2)$$

The foregoing suggests that reaction rate and equilibrium change greatly near the critical point, and that it is possible to control them by manipulating pressure and temperature.

2. Powder Processing with the Rapid Expansion of Supercritical Solutions (RESS) Method

2.1 Principle of the RESS Method

The solvent power of supercritical fluids changes considerably by slight manipulation of temperature and pressure, which makes it possible to decrease the solubility of a solute at least several orders of magnitude by dissolving the solute in a high-density supercritical fluid, and then expanding and lowering its density to nearly atmospheric pressure by passing it through a nozzle. Let us examine the solubility of SiO_2 in a supercritical fluid, shown in **Fig. 3**. Near the critical point a slight decrease in pressure translates into a substantial drop in solubility, and a high degree of supersaturation is obtained. Because expansion occurs at the speed of sound, an extremely high degree of supersaturation is obtained in a short time of under 10^{-5} sec, which results in the formation of fine particles. Matson et al. [14] called this method the rapid expansion of supercritical solutions, or RESS.

2.2 RESS Application

In the diagram showing the RESS method proposed by Matson et al. (**Fig. 7**), supercritical water is fed into a high-pressure cell containing sample material, which is dissolved. The solution is sprayed from a nozzle, thereby undergoing rapid depressurization from a supercritical state to a gaseous state and crystallizing the solute. Unlike ordinary crystallization methods, the process is not governed by mass transfer rate or heat transfer rate, and the attainment of an extremely high degree of supersaturation at the speed of sound makes it possible to crystallize fine particles of sizes ranging from nano to micron [13]. Altering conditions makes it possible to crystallize whiskers or membranes [14, 15].

An example of a product obtained with this method appears here in a photograph (**Fig. 8**). Heretofore work has been done on a variety of systems including SiO_2-H_2O; GeO_2-H_2O; SiO_2, $KI-H_2O$; $Si-NH_3$; $ZrO(NO_3)_2$-ethanol; $Si_3N_4-NH_3$, polystyrene-pentane; poly (propylene)-pentane; poly (carbosilane)-pentane; poly (phenyl sulfone)-propane; poly (methyl methacry-

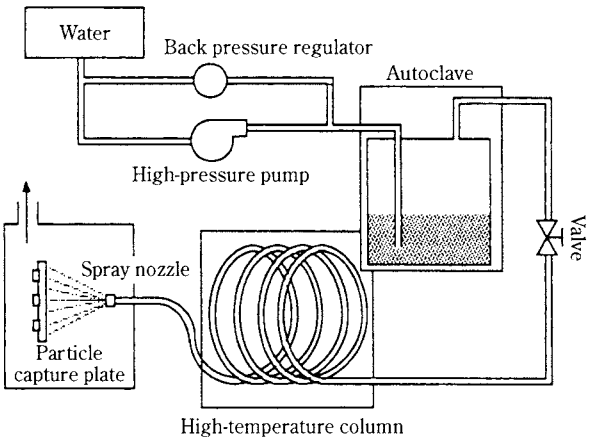

Fig. 7 Diagram of Experimental Apparatus for RESS Method

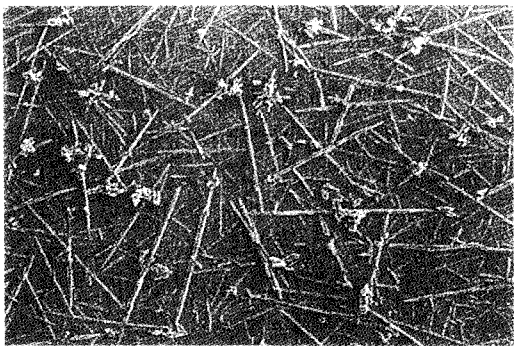

Fig. 8 Particles of the Drug Levostatin Formed with the RESS Method (extraction temperature: 55°C; extraction pressure: 200-250 bar; preliminary expansion temperature: 100-110°C)

late)-propane; and poly (vinyl chloride), KI-ethanol. There are reports on the great possibilities of this method for making fine particles and membranes [14, 15].

Recently there are many reports on organic macromolecules using supercritical CO_2, pharmaceuticals, and the like.

In the area of pharmaceuticals, Chan et al. [16] used supercritical ethylene to make β-carotene into fine particles. Other experimenters have observed that using supercritical CO_2 in RESS processing of polylactic acid [17] and stigmasterol [18] results in the formation of whisker crystals and amorphous spherical particles.

Debeneditti et al. [19] attempted the making of compound materials and the capsulation of particles by forcing different solutes from two nozzles. An example appears here (**Fig. 9**). The solvent was supercritical CO_2. They report that coating the drug levostatin with lactic acid made possible the manufacture of a preparation for drug delivery. Changing the conditions resulted in the creation of lactic acid-coated levostatin in spherical, flat, and thin-film forms. They also made network materials.

Mishima et al. also made a flavonoid PEG coating using a similar method [20]. Tsutsumi et al. [21] proposed a dry coating method for fine particles that combines the RESS method with a spouted bed, which fluidizes particles by spraying them through a nozzle. Unlike techniques that use liquid solvents, supercritical fluids change to a gaseous state after ejection, which eliminates clinker trouble in the fluidized bed and makes it possible to continuously create uniform coats in large quantities.

There are also reports on research using supercritical fluids on catalyst loading in porous carriers. Mclaughlin et al. [22] dissolved a metallic salt catalyst in a supercritical solvent and used decompression to precipitate it as a film on porous alumina and a porous zirconia surface. They report that this method demonstrated high catalytic activity.

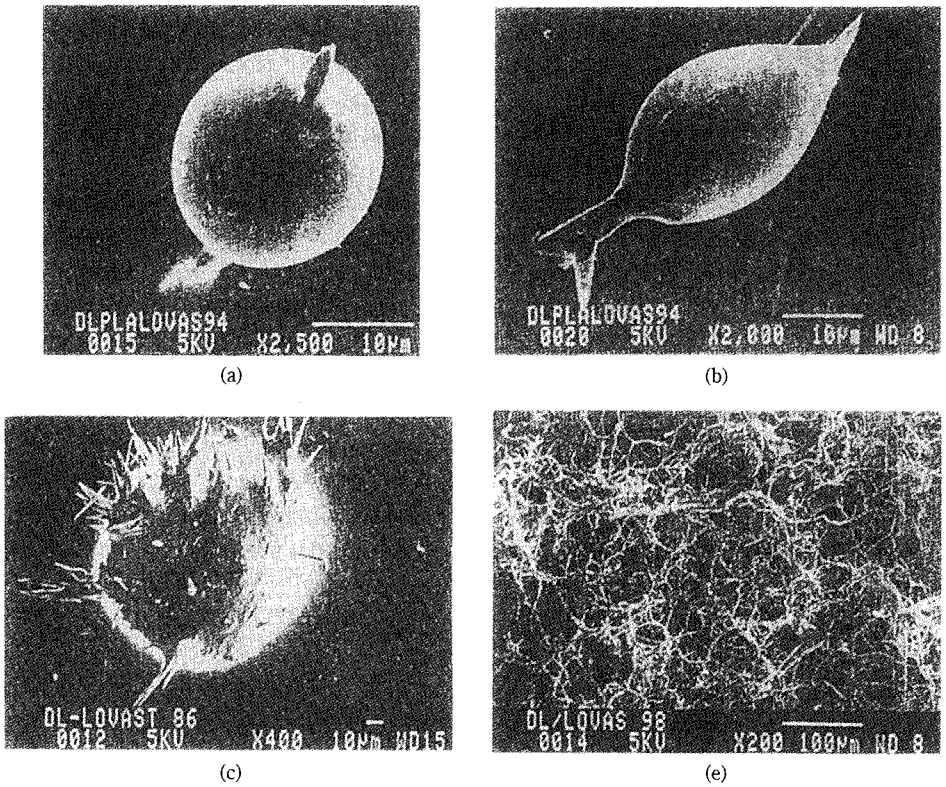

Fig. 9 Experimental Conditions for Producing the Drug Levostatin Coated with a Polymer (DL-PLA) Using the RESS Method
(a) & (b) Molecular weight (DL-PLA): 5,300; extraction temperature: 55°C; extraction pressure: 200 bar; preliminary expansion temperature: 75-80°C
(c) Molecular weight (DL-PLA): 5,300; levostatin+DL-PLA mixture extraction tank temperature: 55°C; levostatin extraction tank temperature: 35°C; extraction pressure: 200 bar; preliminary expansion temperature: 75-80°C (when using two extraction tanks and spraying after mixing the two fluids)
(d) Molecular weight (DL-PLA): 10,000; extraction temperature: 55°C; extraction pressure: 200 bar; preliminary expansion temperature: 80°C

2.3 Theoretical Analysis

Involved in phenomena occurring with the RESS method are temperature decline caused by decompression, solvent expansion, and the increase of a solute's degree of supersaturation. These depend heavily on the structure and size of the nozzle used (orifice, capillary, sintered plate).

Debeneditti [23] theoretically examined the formation of nuclei in the rapid expansion process after nozzle ejection. He made a system of fluid dynamics and Peng-Rebinson equation of state and assessed the processes of fluid expansion, temperature drop, and pressure drop, as well as the accompanying decline in solubility and increase in degree of supersaturation. Using the results, he assessed the rate of nucleus formation and critical nucleus diameter on the basis of classical homogeneous nucleation theory.

It is known that, depending on the ejection conditions, nucleation already occurs inside the nozzle, which makes it important to describe not only the expansion process after nozzle ejection, but also phenomena at the nozzle inlet and in its interior. Research on the nozzle interior has reported the same kind of analyses as that above [24, 25]. Lele [24] used this analysis to show that needle crystals were obtained when nuclei formed at the nozzle inlet.

Kwauk and Debeneditti [26] incorporated a nucleus growth model into the aforementioned nucleation model and conducted a theoretical analysis of the RESS method. They used this model to explore the relationship between the size distribution of particles formed and ejection conditions.

3. Powder Processing Using the Gas Anti-Solvent (GAS) Method

3.1 Principle of the GAS Method

Phase behavior undergoes great changes in the mixed systems involved in supercritical fluids, and these characteristics can be used in crystallization. Dissolving a supercritical fluid into a solvent makes the solvent into a poor one, and separates and precipitates solute phases. This is the GAS method. If a supercritical fluid is used, the manipulation of pressure and temperature makes it possible to control the extent of fluid dissolution, so this allows one to search with comparative ease for the optimum poor solvent (crystallization) conditions [27-29].

Krukonis [27] was the first to publish on the GAS method, and it was proposed as a method for making fine particles of, and recrystallizing, explosives and other substances that are difficult to mechanically pulverize. It is possible to adjust the rate at which fluid components dissolve by varying pressure, and this brings about large changes in the properties of the crystals formed. In general, solubility in supercritical fluids is nearly two orders of magnitude lower than in liquid solvents, which sometimes creates serious problems in process productivity. Because the GAS method involves dissolving a solute in a good liquid solvent and then making that solvent poor, it does not suffer from that limitation, which is a feature of the method.

3.2 GAS Application

The GAS method is used also in synthesizing fiber or needle macromolecular polymers, but recent research actively promotes its use as a recrystallization method for pharmaceuticals and other thermally unstable substances.

Randolph [30] and Foster et al. [31] used the GAS method to form submicron particles of polylactic acid (PLA), a biodegradable polymer, for the purpose of making sustained release capsules for drug delivery. They formed fine particles by dissolving PLA in methylchloride and adding supercritical CO_2.

Yeo et al. [32] added supercritical CO_2 to insulin that had been dissolved in an organic solvent, by which they obtained fine insulin particles smaller than 4 μm (**Fig. 10**).

Shishikura et al. [33] used the GAS method to refine citric acid obtained by fermentation. They first added supercritical CO_2 to fermentation liquid at a comparatively low pressure, then crystallized and separated organic acids other than citric acid, other substances, and impurities. Next they crystallized high-purity citric acid by once again bringing in supercritical CO_2 after setting the pressure high. This demonstrated that it is possible to control particle diameter more simply and faster than the ordinarily used calcium salt precipitation method.

Kitamura et al. [32] dissolved the drug sulfathiazole ($C_9H_9N_3O_2S_2$) in ethanol and crystallized it by introducing supercritical CO_2 as a poor solvent. They conducted a detailed study of the relationship between pressurization operation and precipitation behavior in the GAS method, including instances of multi-stage pressurization.

Because redissolution occurs with the GAS method when decompressing after precipitation, generally the precipitate and liquid slurry are removed while maintaining pressure. Some researchers are developing a process that conducts this operation continuously [35, 36].

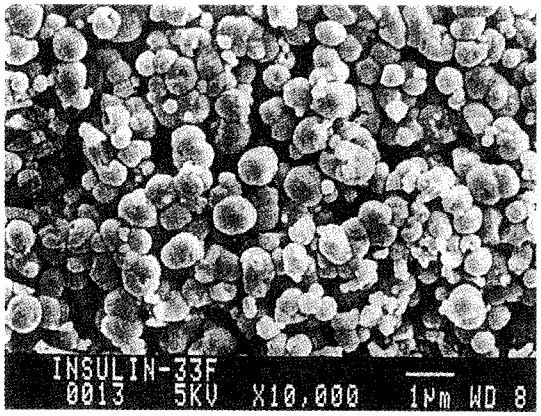

(a)

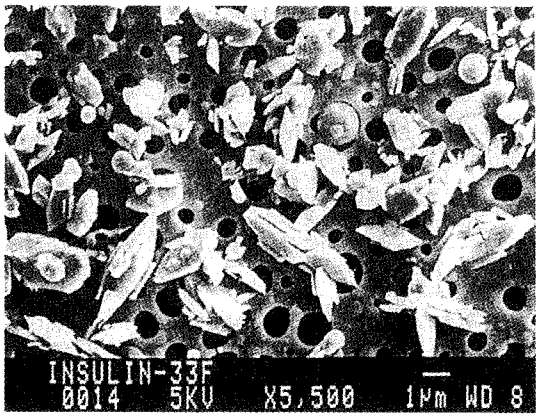

(b)

Fig. 10 Fine Insulin Particles Formed with the GAS Method [32]
Solvent: 90% ethanol solvent; poor solvent: supercritical CO_2 (35°C, 80 bar)
(a) Particles that passed through filter (spherical particles under 1 μm)
(b) Particles captured by filter (needle particles about 5 μm)

4. Retrograde Crystallization Method

Solubility of a solute in a supercritical fluid rises with the density of the fluid and with the volatility of the solute. If temperature is raised while maintaining the same pressure the solute's volatility will increase, but the fluid's density will decrease. Thus, when raising temperature there is a pressure range in which solubility increases, and another in which it decreases, a fact illustrated also by pressure dependence near the critical point in **Fig. 3**. The relationship between solubility and pressure as a parameter of temperature (**Fig. 11**) shows that there are pressures at which solubility curves intersect. These intersecting pressures differ according to the solutes. Thus, if one manipulates temperature between the two components' intersecting pressures, the solubility of one solute will increase, while the other will decrease. By taking advantage of this phenomenon, it is possible in

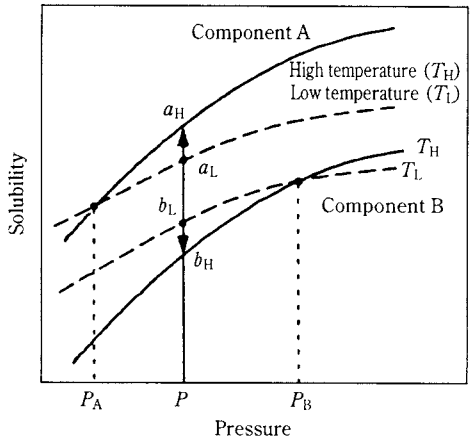

Fig. 11 Principle of Retrograde Crystallization Method

principle to precipitate only certain components from a mixture [37]. Iwai et al. tried separating isomers using this method [38, 39].

5. Processing of Particles Using Supercritical Drying

When removing a solvent from a gel with the usual evaporation, the drying process results in the formation of a gas-liquid interface, and surface tension causes problems such as crack formation and fragmentation. A way to limit this is the supercritical drying method, which involves removing the solvent in a supercritical state. The principle is the extraction of solvents using supercritical fluids. Use of this method eliminates gas-liquid interfaces, which makes it possible to suppress the formation of cracks and fragmentation and to obtain a dry product. The supercritical drying method has been practicalized, especially as a method of synthesizing aerogels [40]. Work is also in progress on the application of the same sort of method to defatting molds.

In recent years this method has been considered as a way to make fine particles. Synthesizing fine particles by the wet method necessitates a drying process, and the drying of particles results in strong agglomeration by capillary force when the solvent vaporizes, which often has major effects on the physical properties of the final powder [41]. The supercritical drying method, which uses supercritical fluids to extract solvents, differs from ordinary drying methods in that the absence of a gas-liquid interface makes it possible to suppress the strong agglomeration caused by capillary force. Another capability is crystallization by heat treatment during supercritical drying [38].

Powders crystallized in supercritical nonaqueous solvents have finer particles and better dispersion

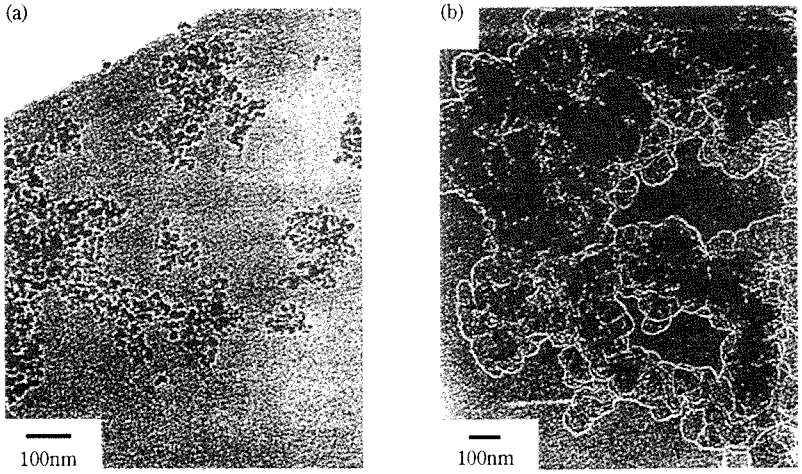

Fig. 12 12% mole CeO_2-ZrO_2 Powder Made with the Supercritical Drying Method
(a) Ethanol (250°C) (b) Hot water (250°C)

than those crystallized by hydrothermal processing (**Fig. 12**) [42].

In the presence of adsorbed water on a powder surface, bridges form between adjacent particles by hydrogen bonds through the water, and the particles agglomerate into a hard mass when dehydrating, but because treatment with an organic solvent suppresses the formation of bridges by hydrogen bonds, the formation of hard agglomerations is prevented [41, 42]. Because inorganic salts generally have low solubility in nonaqueous solvents, crystal growth in nonaqueous solvents is restrained, yielding microcrystals. Sato [42] found that by using supercritical ethanol in the crystallization of a CeO_2-ZrO_2 amorphous gel whose agglomeration he curbed by subjecting it to supercritical drying, it was possible to obtain microcrystals of about 2 μm with excellent sinterability.

Gunnarsson et al. [43] prepared an oxide of zirconium/yitrium (water) in a mixed methanol/water solvent, and treated it by supercritical drying. They fired these particles at 1,400°C and were able to attain a high density that was above 97.4% of the theoretical density. They conclude that the reason it is possible to obtain such a high density at a comparatively low temperature is that supercritical drying enabled them to suppress the agglomeration of particles by capillary force.

There are reports on powder (microcrystal) synthesis and drying with similar methods for the following systems: ZrO_2 [44], TiO_2-SiO_2 [45], organic microcrystals [46], SiO_2 [47], $MgFe_2O_4$ [48, 49], and Fe_3O_4 [50].

Recently there are attempts at using this method to make catalysts. Jarzebski et al. [51] prepared a catalyst by supercritical drying of an anhydrous maleic acid-ethyl vinyl ether copolymer to which had been added a cobalt (II) catalyst. They explored catalyst activity and selectivity in isopropanol dehydration and dehydrogenation reaction, and obtained a reaction rate that was greater than that of catalysts prepared with the usual vacuum drying method. Temperature stability had also improved. They attribnted it to that supercritical drying increased the number of meso- and macro-pores, which increased the total surface area.

6. Reaction Crystallization in Supercritical Fluids

6.1 Hydrothermal Synthesis in Supercritical Water

Heating an aqueous metallic salt solution will hydrolyze the metallic salt and produce a metallic hydroxide. At high temperatures a dehydration reaction occurs and forms fine metallic oxide particles. This is hydrothermal synthesis.

$$M(NO_3)_x + xH_2O = M(OH)_x + xHNO_3$$
$$M(OH)_x = MO_{x/2} + \frac{x}{2}H_2O$$

The equilibrium and transport physical properties of supercritical water (critical temperature, 374°C; critical pressure, 22.1 MPa) vary greatly depending on pressure and temperature. This means there is great variability in the field of the aforementioned hydrothermal synthesis reaction, its attendant nucleation, and particle growth. The author and others are experimenting with the use of supercritical water as a field for hydrothermal synthesis [4-6, 52-56].

Using the experimental apparatus shown in **Fig. 13**, I supplied an aqueous metallic salt solution by HPLC pump, and brought it into contact with supercritical water supplied through a different line, thereby

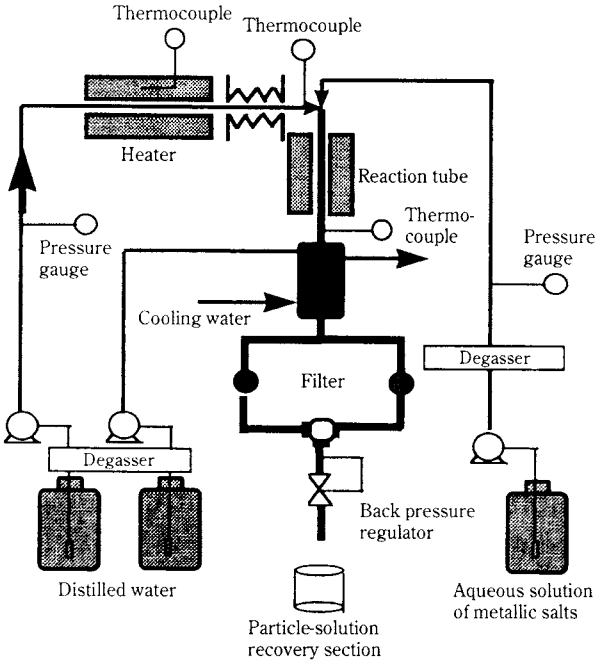

Fig. 13 Diagram of Experimental Apparatus Used with the Supercritical Water Crystallization Method

rapidly putting the solution into a supercritical state and causing a hydrothermal synthesis reaction. While water-cooling externally at the reaction tube outlet, I rapidly cooled the crystals by supplying them directly with cold water to stop the reaction.

The results are presented here in **Table 1**. Synthesis of fine metal oxide particles with this method has heretofore been tried for nitrates, chlorides, and sulfates of Al, Fe, Mn, Ni, Ti, Zr, Co, Ce, Rh, and Pt, and in every instance the fine particles formed were on the order of 1 μm to several nm [52, 53].

Table 1 Fine Metal Oxide Particles Synthesized in Supercritical Water

Metal salt	Crystalline structure	Particle diameter (nm)	Shape
$Al(NO_3)_3$	AlOOH	100−60	Hexagonal plates Ellipsoids Needles
$Fe(NO_3)_3$	$\alpha-Fe_2O_3$	Up to 50	Spheres
$Fe_2(NO_4)_3$	$\alpha-Fe_2O_3$	Up to 50	Spheres
$FeCl_2$	$\alpha-Fe_2O_3$	=50	Spheres
$Fe(NH_4)_2H(C_6H_5O_7)_2$	Fe_3O_4	Up to 50	Spheres
$Co(NO_3)_2$	Co_3O_4	Up to 100	Octahedra
$Ni(NO_3)_2$	NiO	Up to 200	Short rods
$ZrOCl_2$	ZrO_2(cubic)	=10	Spheres
$Ti(SO_4)_2$	TiO_2	=20	Spheres
$TiCl_4$	TiO_2(anatase)	=20	Spheres
$Ce(NO_3)_4$	CeO_2	=300	Octahedra
$Fe(NO_3)_3+Ba(NO_3)_2$	$BaO\cdot 6Fe_2O_3$	Up to 600	Hexagonal plates

Comparisons with similar experiments performed in subcritical water as well showed that reaction crystallization forms fine particles more easily in supercritical water. In supercritical water the hydrolysis rate of metal salts is extremely fast, and the solubility of the monomers and precursors yielded is lower than substances produced in subcritical water. Thus hydrothermal synthesis in supercritical water instantly yields a very high degree of supersaturation and a high nucleation rate. This seems to be the reason that fine particles are easily formed [55].

Changes in the physical properties of supercritical fluid crystallization fields also affect particle shape. In the case of boehmite, the shapes of the particles formed changed considerably depending on reaction conditions, yielding hexagonal plates, rhombic plates, swordlike shape, and football shapes with laminar plates (**Fig. 14** (a)-(d)). This appears to be the result of great changes in physical characteristics near the critical point, and there is promise that we can control not only particle diameter, but particle shape as well [54].

When using ferrous ammonium citrate the product was magnetite, which means that Fe^{3+} ions were reduced to Fe^{2+} ions. Probably what happened is that a reduction reaction occurred because of the CO that was a product of the pyrolysis of ammonium citrate. Supercritical water is miscible with not only CO, but also oxygen, hydrogen, and other substances, so if a gas is injected into the crystallization field, it is easy to control the oxidation-reduction environment [53].

The author and others are working on a continuous synthesis method for fine barium ferrite particles. This process involves the use of a HPLC pump to supply a mixture of barium nitrate and ferric nitrate in aqueous solution, bringing it into contact with heated potassium hydroxide supplied through a separate line, and forming hydroxides. Then we supply supercritical water, within which hydrothermal synthesis takes place. While water-cooling externally at the reaction tube outlet, we rapidly cool the crystals by the direct supply of cold water, then recover the barium ferrite particles with an in-line filter. The reaction takes between 5 seconds and 2 minutes. This method provides pure barium ferrite particles (**Fig. 15**).

It is also possible to produce barium ferrite with the usual hydrothermal method, but a problem is that it does not provide good magnetic characteristics. The author found that this method provides about the same extent of magnetic characteristics as the commercial glass crystallization method.

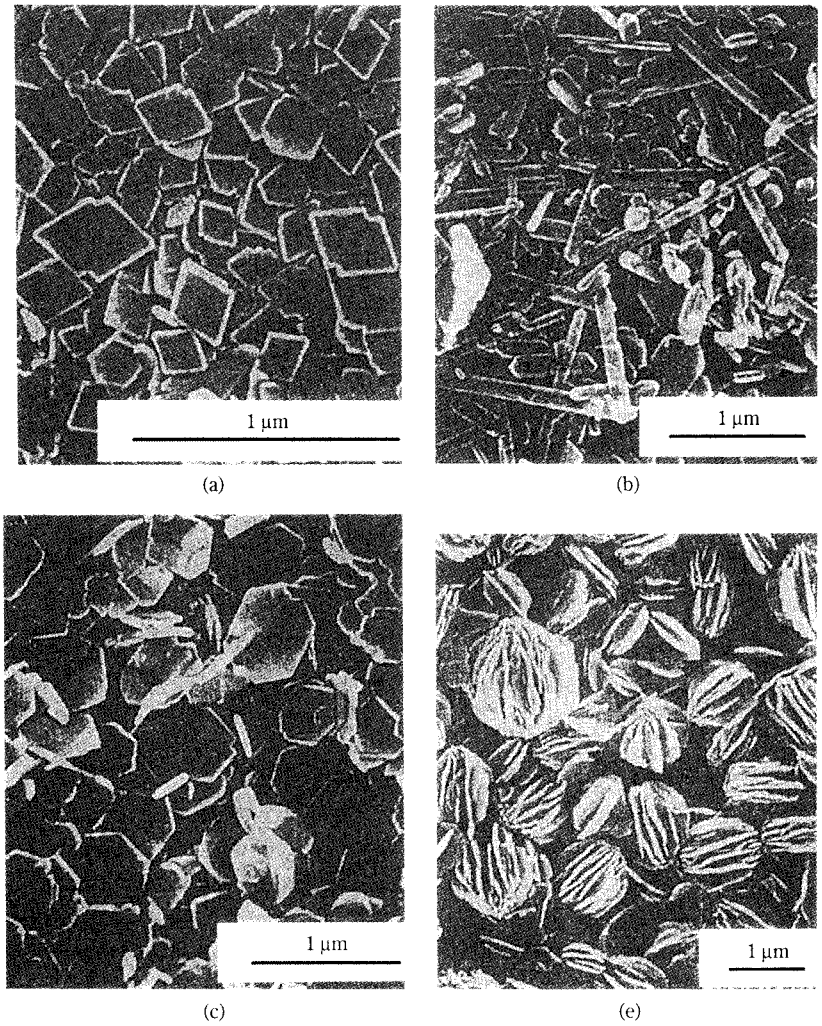

Fig. 14 Particle Shape and Reaction Conditions ($Al(NO_3)_3$ Concentration, Reaction Temperature, Reaction Pressure) of Boehmite (AlOOH) of Various Shapes Created by the Supercritical Water Crystallization Method
(a) Rhombic shape: 0.006 M; 350°C; 35 MPa
(b) Swordlike shape: 0.02 M; 400°C; 35 MPa
(c) Hexagonal plates: 0.05 M; 400°C; 40 Mpa
(d) Football shape with laminar plates: 0.05 M; linear temperature rise from 100 to 300°C; 30 Mpa

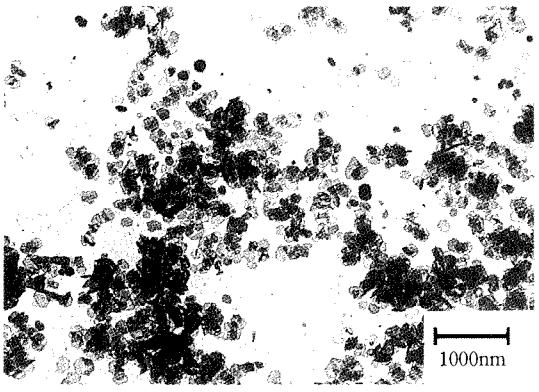

Fig. 15 Fine Barium Ferrite ($BaO{\cdot}6(Fe_2O_3)$) Particles Created with the Supercritical Water Crystallization Method
Reaction conditions
$Fe(NO_3)_3$, 0.05M; $Ba(NO_3)_2$, 0.025M; alkaline molar ratio ($[KOH]/[NO_3]_T$), 4; temperature, 400°C; pressure, 30 Mpa; residence time, 63 seconds

6.2 Fine Particles Synthesized in Supercritical Nonaqueous Solvents

Research is also underway on synthesizing fine particles with the alkoxide method and other methods that use supercritical fluids other than water as solvents.

A series of research projects by Pommier, Bocquet, and Chhor et al. use supercritical fluids as solvents in synthesizing oxide particles by the hydrolysis of metal alkoxides [57-59].

They performed hydrolysis and polycondensation on titanium-isopropoxide or ethoxide in supercritical ethanol or propanol, and produced 0.5-3 μm anatase particles consisting of 30-60 nm primary particles [57]. They also hydrolized Mg [Al (O-secBu)$_4$]$_2$ in

supercritical methanol at 350°C and 15 Mpa, and produced spinel $MgAl_2O_4$ crystals [58, 59].

Some features they note are that, compared with the sol-gel and spray methods, there is no residual solvent in the particles, thereby providing particles of very high purity; the particles are also very stable, which allows the omission of pre-sintering heat treatment, and endows particles with excellent sinterability.

Wood et al. [60] caused the reaction of K_2Se_4, Se and Ag (1:2:1) in supercritical ethylenediamine at 300°C and 2,400 psi. They report the formation of porous $K_2Ag_{12}Se_7$ crystals with a yield of at least 80%.

6.3 Synthesis of Organic Particles in Supercritical Fluids

Kendall and DeSimore [61] conduct polymerization using supercritical carbon dioxide as the reaction solvent. The industrial use of organic solvents is being restricted around the world, and in that sense as well there are hopes for supercritical carbon dioxide as a substitute solvent. Unlike other organic solvents, a reaction characteristic of carbon dioxide is that it is totally inactive in free-radical reactions. In precipitation polymerization, surfactants used as stabilizers can be recovered and reused. The CO_2 used can be completely recovered and recycled by decompression.

Investigations are also in progress on precipitation polymerization reactions using dehydration enzymes as catalysts [62]. Reactions take place in the solvents, and precipitation stops the reactions. Solvent power is controlled by manipulating the pressure, which in turn makes it possible to control the polymerization degree of the precipitated polymers. It is reported that with this method it is possible to synthesize polymers with a very sharp distribution in the degree of polymerization.

Because supercritical CO_2 dissolves in the polymer phase, rapid decompression causes polymer/CO_2 spinodal phase separation, thereby forming porous polymers with minute cells [61, 63].

7. Other Supercritical Fluid Processing

Multi-component polymers are provided with multiple functions and high performance by controlling the phase separation structure [63]. There is currently a great deal of research on the use of supercritical CO_2 in making polymers. Making supercritical carbon dioxide coexist in polymer systems lowers polymer melting points and increases fluidity, and there is also promise for its function as a third component that controls phase separation structure. As noted previously, because CO_2 dissolved in polymers foams and becomes fixed as is upon decompression, this technique is used in synthesizing porous polymers.

Nakanishi et al.'s group [64] is experimenting with the synthesis of phthalocyanine with various crystal structures by dissolving phthalocyanine, which has no good solvent in the vicinity of room temperature, in a supercritical water/alcohol system, and making it a poor solvent while rapidly cooling by the introduction of cold water/alcohol.

8. Conclusion

This paper has explained the principles, and given application examples, regarding the characteristics of supercritical fluids as solvents for powder processing. Although research and development have just begun, this discussion has no doubt provided the reader with an understanding about the possibilities for new processes. There are hopes that once more is learned about the mechanism of crystallization in supercritical fluids, it will lead to the creation of material preparation processes that do not exist at present.

References

1) Saito, S.: *Supercritical Fluid Science and Technology*, Sankyo Business (1997) (in Japanese)
2) Adschiri, T.: *High Pressure Science and Technology*, 12 (4), 287 (1993) (in Japanese)
3) Adschiri, T. and K. Arai: *Hydrothermal Science Handbook*, Gihodo, p. 571 (1997) (in Japanese)
4) Adschiri, T.: *Recent Chemical Engineering*, 43, Crystallization 52 (1991) (in Japanese)
5) Adschiri, T. and K. Arai: *Hydrothermal Science Handbook*, Gihodo, p. 388 (1997) (in Japanese)
6) Arai, K.: *New Ceramics*, 7 (1995) (in Japanese)
7) Adschiri, T. and K. Arai: *Hydrothermal Science Handbook*, Gihodo, p. 39 (1997) (in Japanese)
8) P. H. van Konynenberg, R. L. Scott: *Phil. Trans. Roy. Soc.*, **298**, 195 (1980)
9) Arai, K. and S. Saito: *Oil Chemistry*, 35, 240 (1986) (in Japanese)
10) Oe, T., A. Suzuki, O. Takahashi, and T. Nakamura: *Journal of the Japan Energy Society*, 868 (1997) (in Japanese)
11) Timberlake S. H., G. T. Hong, M. Simson and M. Modell: *SAE Technical Papers # 820872*, 12th, *Intersociety Conf. On Environmental Systems*, San Diego (1982)
12) Amis, E. S.: Solvent Effects on Reaction Rates and Mechanisms Academic Press, New York (1966)
13) Isaacs, N.: *Liquid Phase High Pressure Chemistry*, John Siley & Sons. New York (1987)
14) R. C. Petersen, D. W. Matson, and R. D. Smith: *J. Am.*

Chem. Soc., **108**, 2100 (1986)
15) D. W. Matson, J. L. Fulton, R. C. Petersen and D. Smith: *Ind. Eng. Chem. Res.*: **26**, 2298 (1987)
16) Chan, C. J. and A. D. Randolph: *AIChE J.*, **35**, 325 (1989)
17) Jean, W. T. and P. G. Debeneditti: *Biotechnol. Prog.*, **7**, 403 (1991)
18) Ohgaki, K., H. Kobayashi, T. Katayama and N. Hirokawa: *J. Supercrit. Fluids*, **3**, 103 (1990)
19) Jean W. Tom, Gio-Bin Lim, Pablo G. Debeneditti, and Robert K. Prud' Homme: 238, *ACS Symposium Series*, **514**, 238 (1993)
20) Mishima, K., Matsuyama, K., Uchiyama, H. and M. Ide: Proc. 4th Int. Symp. Supercrit. Fluids, 267 (1997)
21) Tsutsumi, A., S. Nakamoto, T. Mineo and K. Yoshida: Powder Technology, **85**, 275 (1995)
22) McLaghlin, D. F., M. C. Skriba and C. Michael: United States Patent, 496108, Apro. 10 (1990)
23) Debeneditti, P. G.: *AIChE Journal*, **36**, 1289 (1990)
24) Lele, A. and Shine, A. D.: *AIChE J.* **38**, 742 (1992)
25) Brend, J. I. and Miller, D. R.: *Thin Solid Film*, **166**, 139 (1988)
26) Kwauk, X. and Debeneditti, P. G.: *J. Aerosol Sci.*, **24** (4), 445 (1993)
27) Krukonis, V. J.: Proc. *Int. Symp. on Supercritical Fluids*, 541 (1988)
28) Gallagher, P. M, M. P. Coffey, V. J. Krukonis, N. Klas utis: *SCF Science and Technology, ACS Symp. Ser.* **406**, 334 (1989)
29) P. M. Gallagher, Val J. Krukonis and L. J. Vandekieft: Proc. 2nd International Symposium on Supercritical Fluids, 45 (1991)
30) Randolph, T. W., A. D. Randolph, M. Mebes and S. Yeung: *Biotechnol. Prog.* **9**. 429 (1993)
31) A. K. Dillow. F. Dehghani, and N. Foster: Proc. 4th Int. Symp. Supercrit. Fluids, 247 (1997)
32) Tom, J. W., G. B. Lim, D. G. Debcntdetti and P. K. Prud, homme, ACS Symposium Series, 514, 238 (1993)
33) Shishikura, A., H. Takahashi, S. Hirohama, K. Arai: *J. Supercritical Fluids*, , (1992)
34) Kitamura, M., M. Yamamoto, Y. Yoshinaga, and H. Matsuoka: *Chemistry Engineering Symposium Series*, 49, 200 (1995) (in Japanese)
35) Wubbolts, F. E., O. S. L. Bruinsma, J. de Graauw, G. M. van Rosmalen: Proc. 4th Int. Symp. Supercrit. Fluids, 63 (1997)
36) Jaarmo, S., M. Rantakyla, O. Aaltonen: Proc. 4th Int. Symp. Supercrit. Fluids, 263 (1997)
37) Johnston, K. P., S. E. Barry, N. K. Read T. R. Holcomb: *Ind., Eng. Chem. Res.* , **26**, 2372 (1994)
38) Iwai, Y., Y. Koga, H. Maruyama and y. Arai: *J. Chem. Eng. Data*, **38**, 506 (1993)
39) Iwai, Y., Y. Mori, N. Hosotani, H. Higashi, T. Furuya, Y. Arai, K. Yamamoto and Y. Mito: *J. Chem. Eng. Data*, **38**, 509 (1993)
40) H. D. Gesser and C. Goswami: *Chem. Rec.* **89**. 765-788 (1989)
41) Readey, M. J., R. Lee, J. W. Halloran and A. H. Heuer: *J. Am. Ceram. Soc.*, **73**, 1499 (1990)
42) Sato, T.: *Chemical Industry*, 46, 308 (1995) (in Japanese)
43) Gunnarsson, G., E. L., Sveinsdottir, A. K. Westman, T. Lepisto, T. Mantyla and O. T. Sorensen: Ceram. Powder Process, Sci., Proc. Int. Conf. 2nd, Meeting, 197 (1989)
44) Miao, C. X., Gao, Z.: *Mater. Chem. Phys.*, **50** [1], 15-19 (1997)
45) Lee, J. H. Choi, S. Y., Kim, C. E., Kim, G. D.: *J. Mater. Sci.*, **32** [13], 3577-85 (1997)
46) Lu, X., Caps, R., Fricke, J., Alviso, C. T., Pekala, R. W.: *J. Non-Cryst. Solids*, **188** [3], 226-34 (1995)
47) Heley, J. R., Jackson, D., James, P. F.: *J. Sol-Gel Sci. Technol.*, **8** [1-3], 177-81 (1997)
48) Oliver, S. A., Willey, R. J., Hamdeh, H. H. Oliveri, G., Busca, G.: *Scr. Metall. Mater.*, **33** [10-11], 1695-701 (1995)
49) Hamdeh, H. H., Xia Z., Foehrweiser, R., McCormick, R. J., Willey, R. J., Busca, G.: *J. Appl. Phys.*, **76** [2], 1135-40 (1994)
50) Yuan Chunbo, Yang Xiaomin, Fu Degang, Lu Zuhong, and Liu Juzheng: *J. Solid State Chemistry*, **121**, 492-494 (1996)
51) Jarzebski, A. B., A. I. Lachowski, J. Lorene, J. Mas linska-Solich and W. Turek: *Chem. Eng.* **47** (5), 1321 (1992)
52) Adschiri, T., M. Kanazawa, and K. Arai: *Chemical Engineering*, 55, 223, (1991) (in Japanese)
53) T. Adschiri. K. Kanazawa and K. Arai: *J. Am. Ceram. Soc.*, **75**, 1019 (1992)
54) T. Adschiri. K. Kanazawa and K. Arai: *J. Am. Ceram. Soc.*, **75**, 2615 (1992)
55) Hakuta, Y., H. Terayama, S. Onai, T. Adschiri, and K. Arai: Proc. 4th, Int. Symp. Supercrit. Fluids, 255 (1997)
56) Hakuta, Y., T. Suzuki, K. Seino, T. Adschiri, and K. Arai: Submitted to J. Amer. Cerm Soc. (1998)
57) Chhor, K., J. F. Bocquet and C. Pommier: Mater. *Chem. Phys.*, **32**, 249 (1992)
58) Barj, M., J. F. Bocquet, K. Chhor and C. Pommier: *J. Mater. Sci.*, **27**, 2187 (1992)
59) Pommier, C. K. Chhor, J. F. Bocquet and M. Barj: *Matet, Res. Bull.*, **25**, 213 (1990)
60) Wood, P. T., W. T. Pennington and J. W. Kolis: *J. Am. Chem. Soc.* **114**, 9233 (1992)
61) Kedall, J. L. and J. M. DeSimone: Proc. 4th, Int. Symp. Supercrit. Fluids, 771 (1997)
62) Chaudhary A. K., Beckman E. J., Russell A. J. *J. Am. Chem. Soc.*, **117**, 3728 (1995)
63) McHugh. M. A.: 4th, Int. Symp. Supercrit. Fluids, 785 (1997)
64) Nakanishi, et al.: Proc. Organic Materials for Electronics and Photonics, (1998)

Author's short biography

Tadafumi Adschiri

About the author: Graduated from the Tokyo University Faculty of Engineering in 1981, held posts as assistant professor in Tokyo University and Tohoku University, and has since 1991 been an associate professor at Tohoku University. Has Ph.D. in engineering.

Specialties: Research in chemical engineering, and in the use of supercritical fluids as reaction solvents. Currently conducting research in areas including reforming reactions for biomass, heavy oils, plastics, and coal in supercritical water, and the hydrothermal synthesis of metal oxides.

Review

Photon Correlation Spectroscopy – Extending the limits of concentration –†

A.W. Willemse, E.J. Nijman, J.C.M. Marijnissen, H.G. Merkus, and B. Scarlett

*Particle Technology Group, Department of Chemical Engineering, Delft University of Technology, Netherlands**

1. Introduction

Photon correlation spectroscopy (PCS) is a light-scattering technique for measuring the size of sub-micrometer particles. It is also often known as Quasi Elastic Light Scattering (QELS). The technique is based on the fact that small particles exhibit Brownian motion. This motion is random and depends on the size of the particles: the smaller the particles, the more intense their movement. This motion is measured by monitoring the fluctuations in the intensity of light scattered by the particles. From the frequency of these fluctuations, it is possible to deduce the particle size.

PCS is widely used in both research and quality control applications. The conventional technique, however, is limited to a maximum and a minimum particle concentration. When the concentration is too high, particle interactions and multiple scattering distort the size measurement. This is a real limitation in applications such as pharmaceuticals, pigments and paints where the suspensions become unstable or change their composition upon dilution.

At the other limit, when the particle concentration is too low, the measured intensity fluctuations arise not only from the Brownian motion of the particles but also from the changing number of particles in the measuring volume. This additional fluctuation can be interpreted to indicate large particles which are not really present.

This paper proposes solutions to both the high and the low concentration problems. The theory of PCS and the problems that arise at high and at low concentrations are described in section 2. In sections 3 and 4 the new developments and measurements made at both high and low concentrations are presented.

* Julianalaan 136, NL–2628 BL Delft, The Netherlands

† Received August 10, 1998

2. Theory

Brownian motion

Brownian motion is the movement of particles due to the thermal motion of the surrounding molecules. The particle motion is random and the frequency of the movements increases with decreasing particle size. This motion was first observed in 1827 by botanist Robert Brown who noticed a continuous random motion of pollen grains in water. Diffusion and Brownian motion are related in that diffusion is the net movement caused by the Brownian motion. The net transport is always from a region with high concentration to a region of lower concentration and can be characterised by the particle diffusion coefficient, D. The more vigorous the Brownian motion, the larger the diffusion coefficient and, therefore, the faster the transport [Hinds].

In liquid dispersions of low concentration, the diffusion coefficient of a particle is related to the particle diameter by the *Stokes-Einstein equation*, which assumes that the net diffusion force is balanced by the resistance of the liquid to the particle's motion:

$$D = \frac{k_B T}{3\pi\eta d} \tag{1}$$

The diffusive behaviour of particles in more concentrated liquid dispersions and also in aerosols deviates from the Stokes-Einstein equation and is related to particle size in a more complex manner.

Light scattering

When a small particle is illuminated by a laser beam it scatters light in all directions. When the particle is moving, the frequency of the scattered light is altered slightly compared to the frequency of the incident beam. This change in frequency is caused by an optical Doppler shift, and can be calculated by

$$\Delta\omega = \vec{q}\cdot\vec{v} \tag{2}$$

ω = frequency

v = velocity
q = scattering vector

Consider now a monochromatic laser beam, incident on a dispersion of particles with a scattering geometry as shown in **figure 1**.

Because the particles are in Brownian motion and thus have a distribution of velocity in all directions, the scattered light also acquires a frequency spectrum as illustrated in **figure 2**. This intensity spectrum is given by:

$$I(\omega) = \frac{\langle I_s \rangle}{\pi}\left[\frac{Dq^2}{(Dq^2)^2+(\omega_0-\omega)^2}\right] \quad (3)$$

Here $q = |\underline{q}|$

The shape of the spectral curve is Lorentzian [Berne and Pecora] and the translational diffusion coefficient is related to the half-width at the half-height.

$$\Delta\omega_{1/2} = Dq^2 \quad (4)$$

The magnitude of the incident wave vector is given by

$$|\underline{k_I}| = \frac{2\pi n}{\lambda_0} \quad (5)$$

n is the refractive index of the surrounding medium.

The change in frequency due to the Brownian motion is only small compared to the frequency of the incident beam. Assuming that the incident and scattered beams have the same frequency, the scattering vector can be determined by

$$q = \frac{4\pi n}{\lambda_0}\sin(\theta/2) \quad (6)$$

θ is the angle relative to the direction of the incident light. λ_0 is the wavelength of the incident light

The frequency and wavelength of the electric field are inversely related:

$$f = \frac{c}{\lambda} \quad (7)$$

The wavelength, λ_0, is typically $500*10^{-9}$ m and c is the *speed of light*. Thus the *frequency* f has a typical value of 10^{15} Hz. At normal temperatures the frequency shift, Δf, is of the order of 100 Hz. Thus, for a typical PCS experiment $\Delta f/f \approx 10^{-13}$. Therefore, in order to obtain reliable values of the particle diffusion coefficient, accurate measurements of the frequency spectrum are required. It can be obtained by using a spectrum analyser but these devices do suffer from the 'law of conservation of trouble' [Finsy]. When only a small part of the scattered light energy is detected in the range $f+\delta f$, where δf is the bandwidth of the filter, only a weak and noisy signal is recorded. On the other hand, when the filter bandwidth is increased the accuracy of the measurement is reduced.

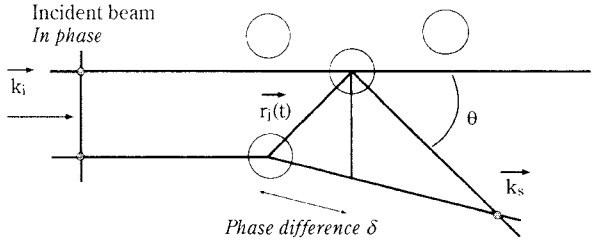

Fig. 1 Scattering geometry

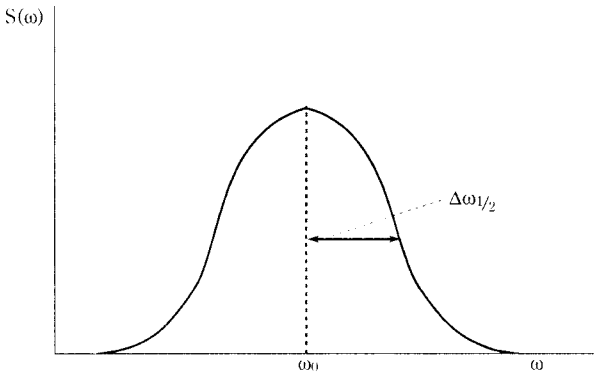

Fig. 2 Spectral density curve of scattered electric field

autocorrelation

The limitations of spectrum analyzers can be circumvented by measuring in the time domain because the diffusion coefficient can equally well be obtained from the Fourier transform of the frequency spectrum. This Fourier transform is the autocorrelation function of the scattered light intensity I(t), because the change in scattering intensity from particles in Brownian motion is a time-invariant random process.

The *intensity autocorrelation function*, $G^{(2)}(\tau)$, can be described as

$$G^{(2)}(\tau) = \langle I(t)\cdot I(t+\tau)\rangle = \langle I(0)\cdot I(\tau)\rangle \quad (8)$$

The superscript (2) refers to the fact that the intensity is the square of the scattered electric field component of the electromagnetic radiation. This autocorrelation function is normally measured using a digital autocorrelator. The detector used is a photomultiplier and because the number of detected photons is proportional to the intensity, $G^{(2)}(\tau)$, can be written as

$$G^{(2)}(\tau) = \langle n_{ph}(0)\cdot n_{ph}(\tau)\rangle \quad (9)$$

The normalised intensity autocorrelation function $g^{(2)}(\tau)$ is given by

$$g^{(2)}(\tau) = \frac{\langle I(0)\cdot I(\tau)\rangle}{\langle I\rangle^2} \quad (10)$$

intensity based detection and measuring modes

Two modes of detection should be distinguished; the homodyne and heterodyne modes. With the homodyne mode only the scattered light is detected whilst with the heterodyne mode a part of the incident beam, or of a separate monochromatic beam, acts as a local oscillator and is mixed with the scattered light. There is, however, a confusing difference between the American and English terminology which is explained in **Table 1**. In this paper we will use the English (UK) terms to define the detection modes.

Table 1 *Modes of detection, defined in two cultures*

	Detection of scattered light only	Detection of scattered light mixed with frequency shifted incident beam	Detection of scattered light mixed with non-frequency shifted incident beam
American Term	Self-beat	Heterodyne-beat	Homodyne-beat
English Term	Homodyne mode	Heterodyne mode	

Homodyne detection of monodisperse samples

For monodisperse particles in Brownian motion, $g^{(2)}(\tau)$ is related to the modulus of the *normalised electric field autocorrelation function, $g^{(1)}(\tau)$,* by the Siegert relationship:

$$g^{(2)}(\tau) = 1+\beta|g^{(1)}(\tau)|^2 \tag{11}$$

This equation can also be written for the non-normalised intensity autocorrelation function, $G^{(2)}(\tau)$, as:

$$G^{(2)}(\tau) = A+B|g^{(1)}(\tau)|^2 \tag{12}$$

Here A and B are factors dependent on the instrumental configuration.

The normalised electric field autocorrelation function can be written as:

$$g^{(1)}(\tau) = \frac{\langle E(0)\cdot E^*(\tau)\rangle}{\langle I\rangle} \tag{13}$$

Heterodyne detection of monodisperse samples

If both scattered light and local oscillator light are received by the detector at similar intensities, the correlation function $g^{(2)}(\tau)$ may be written as

$$g^{(2)}(\tau)=1+2\frac{I_{LO}I_s}{(I_{LO}+I_s)^2}f_1|g^{(1)}(\tau)|+\frac{I_s^2}{(I_{LO}+I_s)^2}f_2|g^{(1)}(\tau)|^2 \tag{14}$$

It can easily be seen from equation 14 that this simplifies to the homodyne case when the local oscillator intensity is small compared to the particle scattered light; $I_s \gg I_{LO}$. On the other hand, if $I_{LO} \gg I_s$, equation 14 simplifies to the purely heterodyne case

$$g^{(2)}(\tau) = 1+2\frac{I_{LO}I_s}{(I_{LO}+I_s)^2}f_1|g^{(1)}(\tau)| \tag{15}$$

This equation shows that the electric field autocorrelation function, $g^{(1)}(\tau)$, can be obtained directly from the intensity autocorrelation function.

determination of particle diameter

Experimental data are always contaminated with noise and with experimental faults. This means that equation 12 should be rewritten as

$$G^{(2)}(\tau) = A+B|g^{(1)}(\tau)|^2+\varepsilon_i \tag{16}$$

To extract the field autocorrelation function, $g^{(1)}(\tau)$, the baseline A has to be evaluated as accurately as possible. Two experimental strategies are used.

1. For large time delays, $G^{(2)}(\tau)$ decays to its background value A. The baseline can, therefore, be determined by the measurement of $G^{(2)}(\tau)$ for large decay times. This is sometimes referred to as the *measured baseline.*
2. The baseline can be measured by an estimation of the time-averaged intensity. Separate counters are then used in the instrumentation. This is often referred to as the *calculated baseline.*

Monodisperse samples

For particles in Brownian motion, the time decay of $g^{(1)}(\tau)$ is determined by the diffusion coefficients of the dispersed particles. In particular, for monodispersed particle samples, $g^{(1)}(\tau)$ and $g^{(2)}(\tau)$ are exponentially decaying functions since the spectral density curve $I(\omega)$ has a Lorentzian shape

$$g^{(1)}(\tau) = e^{-\Gamma\tau} \tag{17}$$

The decay rate, Γ, is related to the diffusion coefficient D as

$$\Gamma = Dq^2 \tag{18}$$

Here q is the modulus of the scattering vector given by equation 6. The diffusion coefficient can be related to the particle diameter via the Stokes-Einstein relationship. The particles are assumed to be spherical and to have no interaction with each other. When the particles are not spherical, an 'equivalent sphere' diameter is obtained.

Polydisperse samples

The inversion of equation 12 is normally not possible due to the experimental uncertainties in $G^{(2)}(\tau)$ and the baseline A. Without knowledge of $\varepsilon(\tau)$, $g^{(1)}(\tau)$ will be biased. At large values of time delay, the experimental estimates for $[G^{(2)}(\tau)-A]$ can be negative, so that it is not possible to extract the square root. To overcome this problem, several strategies are used:

1. Reject measurements with $[G^{(2)}(\tau)-A] < 0$
2. If $[G^{(2)}(\tau)-A] < 0$, put $g^{(1)}(\tau)$ equal to zero
3. If $[G^{(2)}(\tau)-A] < 0$, $g^{(1)}(\tau)$ is assigned the positive value $|G^{(2)}(\tau)-A|$

The first two options lead to a biased estimation of $G^{(1)}(\tau)$ but the third option does not. Although A is normally taken to be independent of time, it should be realised that A can be time dependent due to several reasons such as laser fluctuations and dust. This effect should be taken into account by rewriting A as A(t).

For polydisperse samples, the generalisation of equation 17 is a sum of exponentials

$$g^{(1)}(\tau) = \sum_{j=1}^{n} c_j e^{-\Gamma_i \tau} \tag{19}$$

In this equation, the coefficient c_j represents the intensity due to the particles with diffusion coefficient

$$D_j = \frac{\Gamma_j}{q^2} \tag{20}$$

This equation can also be written in a continuous form as

$$g^{(1)}(\tau) = \int_0^\infty C(\Gamma) e^{-\Gamma\tau} d\Gamma \tag{21}$$

inversion of the autocorrelation function

In principle, $C(\Gamma)$ can be recovered by inverse Laplace transformation of $g^{(1)}(\tau)$. However, the problem is ill-conditioned which means that a small amount of noise on the measured autocorrelation function can lead to a totally different calculated distribution of the decay rates. In the past years, approaches have been developed to evaluate these autocorrelation functions. The first approach does not require prior information whilst the second increases the resolution of the particle size distribution by assuming correlation between neighbouring size classes.

Cumulants

The cumulants method is an analysis method which does not require prior knowledge and is most commonly used in PCS. The cumulants method supposes that for monodisperse samples, $g^{(1)}(\tau)$ is an exponentially decaying function. A power expansion leads to the following equation

$$g^{(1)}(\tau) = \exp(-\bar{\Gamma}\tau) \exp\left(\frac{\mu_2}{2!}\tau^2\right) \exp\left(-\frac{\mu_3}{3!}\tau^3\right) \ldots\ldots \tag{22}$$

where $\bar{\Gamma}$, μ_2, μ_3, ... are the moments of the distribution of decay rates.

The first cumulant is defined as

$$\bar{\Gamma} = \int_0^\infty \Gamma C(\Gamma) d\Gamma \tag{23}$$

and the succeeding ones are defined as

$$\mu_n = \int_0^\infty (\Gamma - \bar{\Gamma})^n C(\Gamma) d\Gamma \tag{24}$$

From the average decay rate, the average, intensity weighted, particle size can be calculated. The second cumulant, μ_2, is related to the relative variance, also known as the 'polydispersity index' of the particle size distribution. This polydispersity index (PI) can be expressed as

$$PI = \frac{\mu_2}{\bar{\Gamma}^2} \tag{25}$$

The third and fourth cumulants are related to the skewness and the kurtosis of the distribution.

When $C(\Gamma)$ is known to be a bimodal distribution, this is a simple, nonlinear, least-square fit with three unknown parameters Γ_1, Γ_2 and A_1 (or A_2). The equation can then be written

$$g^{(1)}(\tau) = A_1 \exp(-\Gamma_1\tau) + A_2 \exp(-\Gamma_2\tau) \tag{26}$$

where $A_1 + A_2 = 1$.

Singular value and reconstruction (SVR)

The first step in this procedure gives the number of exponential decay rates that can be recovered from noisy data. In the next step, the Laplace inversion is reduced to a singular value problem and an eigenvalue problem. Both of these problems are well conditioned and can be solved by reliable and fast algorithms. As a result the solution finally obtained for the (discrete) distribution function is unique. The main limitation of the method is that it can only be applied to data sampled at equidistant time delays.

Non Negativity constrained Least Square fit (NNLS)

The NNLS algorithm uses the prior knowledge that distribution functions are represented only by positive values. Therefore only solutions with $c_i > 0$ are retained.

CONTIN

The CONTIN algorithm is a smoothing technique that tries to overcome the ill-posed nature of the Laplace transform inversion. CONTIN assumes that the simplest solution, the one that reveals the least amount of information, is the best one. This principle is also known as the 'parsimony principle'. The parsimony principle limits the details obtained about the distribution function but also discards many extreme solutions. Both constraints, parsimony and non-negativity, are achieved by constrained regularisation. This regularisation scheme was developed by [Provencher].

Maximum Entropy Method (MEM)

In this method, the *Shannon-Jaynes entropy function* is used to find the particle size distributions that are most likely to describe the real particle system. The

most probable solution is the set of intensity values that maximises this entropy function.

[Chu] showed, using simulated data without noise, that NNLS, SVR, Contin and MEM all give similar results for a broad, log-normal distribution. Additionally, it was shown that the cumulant fitting procedure is not suited for broad or multimodal distributions. In practice, the method of cumulants is the most suitable method to analyse relatively narrow, monomodal, distributions as it is accurate and insensitive to noise compared to the other methods mentioned. SVR is especially useful to determine the information content of an autocorrelation function. MEM and Contin are needed for the reconstruction of multimodal and broad distributions. Compared to NNLS, these methods are relatively insensitive to noise.

experimental set-up

The classical PCS system consists of a goniometer arrangement as shown in **figure 3**. The laser light falls onto the suspended particles in the sample cell of the goniometer. The scattered light is recorded at a certain scattering angle by a photomultiplier. The autocorrelator and computer then calculate the autocorrelation function and the diffusion coefficient of the particles. With this system, the average particle diameter can be determined accurately if the temperature is well controlled. The detector can be either a lens-and-pinhole arrangement or an optical fibre.

In either configuration it is necessary to detect only a small angular fraction of the scattered light in order to limit the number of coherence areas on the photomultiplier. A pinhole can be used to restrict the angle or alternatively a single-mode optical fibre can be used. A single mode fibre has the advantage that it works as a spatial filter; only light of the desired mode is detected. Furthermore, the high angular resolution of the optical fibre is almost ideal for PCS. The scattering volume is determined by the detector optics and the diameter of the focussed laser beam. Generally, this scattering volume is only of the order of 10^{-6} cm^3 (at a 90 degree scattering angle). With a

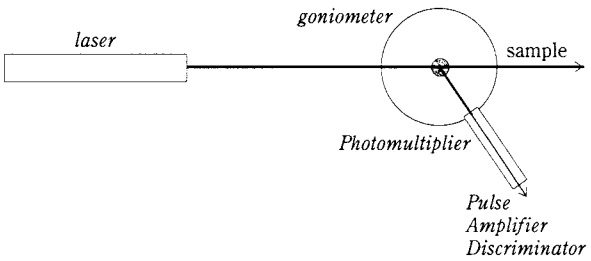

Fig. 3 Classical PCS set-up using a goniometer
The PMT is the photomultiplier.

lens-and-pinhole detector a typical value of about 0.6 to 0.8 is achieved for the baseline value A , as defined in equation 12. A single mode fibre detector has a typical value for A of 0.95.

Correlator

In the experiments reported in this paper two types of correlator were used: a Brookhaven BI-8000AT and an ALV-5000/E. With the Brookhaven correlator the sampling times are constant but the delay times can be exponentially increased. With the ALV correlator the sampling times are also increased.

Laser

The laser used was a water-cooled Lexel 95 Argon-Ion laser with adjustable wavelength and output power. The maximum output power is 1800 mW. Only two lines of the laser are normally used, 514.5 nm and 488 nm, as these lines are the most powerful ones.

Photomultiplier

In combination with the Brookhaven correlator, a Hamamatsu R649 photomultiplier was used. This photomultiplier has a built-in PAD (Photon Amplifier and Discriminator) which delivers ECL (Emitter Coupled Logic) arrangement signals at the output connector. The photomultiplier was connected either to a lens-and-pinhole or to a single mode optical fibre detector operating at a wavelength of 488 nm. The lens-and-pinhole detector is a part of the Brookhaven (BI-SM200) equipment, which has pinholes of 100 µm, 200 µm, 400 µm, 1 mm, 2 mm or 3 mm available. The optical fibre detector has a gradient index lens fitted to the detecting end of the fibre.

3. Measurements at High Concentration.

If the PCS technique is to be used at high concentration, the signal must be received at a scattering angle of 180°, that is backscatter. This can be achieved by using an optic fibre to transmit both the incident and scattered light. This technique is know as FOQUELS (Fibre Optic Quasi Elastic Light Scattering). A schematic diagram of a FOQUELS equipment is shown in **figure 4**. Laser light of 635 nanometer wavelength (4 mW) is fed into a single mode optical splitter which has a splitting ratio 50/50 with a tolerance of 5%. The optical fibre transports the light into the sample and the back scattered light to the detector, which is double photomultiplier arrangement (**figure 5**). The signals from the two photomultipliers are cross-correlated by an ALV5000/E correlator board.

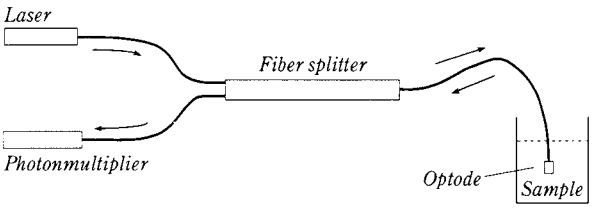

Fig. 4 Schematic overview of a typical fibre optics PCS arrangement (FOQELS). The arrows indicate the direction in which the light travels.

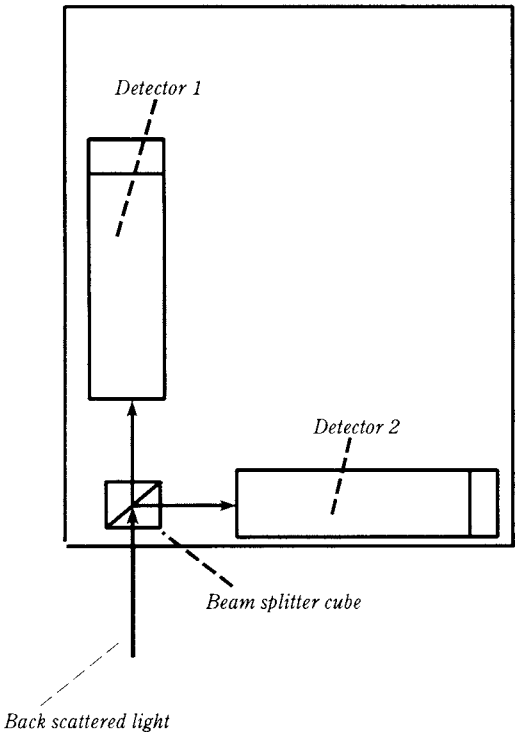

Fig. 5 Double photomultiplier arrangement

Electronic distortions which arise within or after the photomultipliers are thus decorrelated and do not contribute to the measured autocorrelation function.

Conventional measurements are usually made in the homodyne mode and the results interpreted using equation 11. The alternative is to operate completely in the heterodyne mode and to interpret the results using equation 15. In the literature various configurations have been suggested to ensure one of these limiting modes of operation using a FOQUELS arrangement. They are listed in **Table 2** and shown in **Fig. 6**.

The basic optode is the *straight ended* heterodyne 1. Light is transported through the optical fibre into the dispersion to be examined. Since the refractive index of the optical fibre and the fluid are different, the end of the fibre acts as a semi-transparent mirror. Some of the light is, therefore, reflected back without entering the dispersion and is called the *local oscillator light*.

Table 2 *Properties of the different optode configurations given in figure xxx*

Set-up Parameter	Heterodyne 1	Homodyne 1	Homodyne 2	Homodyne 3
Commercial instrument	Malvern High-C	—	—	BI-FOQELS
Researcher	Auweter 1985	Lilge 1991	van Keuren 1993	Dhadwal 1991
Fouling sensitivity	High	High	Moderate	Moderate
Detection angle	180 degrees	180 degrees	Variable	Variable
Particle concentration (%v/v)	50 – 60	50 – 60	30 – 40	30 – 40
Alignment	Easy	Easy	Difficult	Moderate

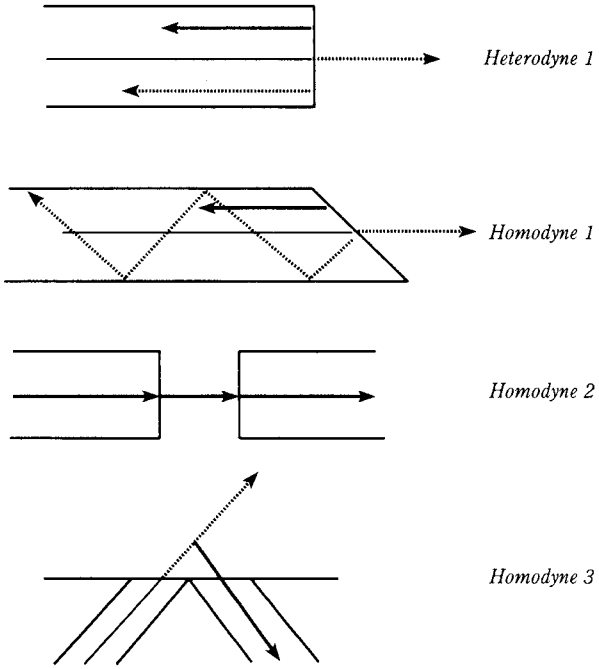

Fig. 6 Schematic view of known optodes.

The other light enters the dispersion and is scattered by the particles present. The light backscattered at 180 degrees is received by the same optical fibre and is called the *signal* light. Since the total backscattered signal contains a large contribution of local oscillator light, this optode measures in the heterodyne mode.

To prevent the local oscillator light being reflected back into the fibre, the *slanted* homodyne 2 optode can be used. By using a slanted optode, the local oscillator light is refracted at a certain angle out of the optical fibre. It is trapped in the shell of the optical fibre and is damped out. The non-reflected part of the incident light enters the dispersion and is scattered by the particles present. The backscattered light is

received by the optical fibre and only this light is transported through the system. Since the local oscillator component is now absent, this optode measures in the homodyne mode.

Instead of using a single fibre to act as both transmitter and receiver, two independent fibres can be used. These solutions are the homodyne 3 and homodyne 4 optodes. They are not suitable for very high concentrations since the light has to travel through the dispersion to reach the receiving fibre an alignment is difficult. The two most suitable optodes to be used in highly concentrated media are, therefore, the conventional straight ended fibre and the slanted version. The problem which arises with the slanted optode in highly concentrated dispersions is due to fouling. Particles sticking to the optical reflect the light and thus act as a local oscillator. This means that there is an increasing heterodyne component with increasing fouling of the fibre and the value of the intercept decreases. Thus, the conditions change into a mixed homodyne-heterodyne mode which is changing with time, straight ended optode: when the particle concentration increases the homodyne component increases due to the increase of signal scattered by the particles.

There are, therefore, two choices. The first is to operate always in the heterodyne mode. The fouling which inevitably occurs in a concentrated suspension poses then a much reduced problem. Since the signal-to-noise (S/N) ratio is already extremely low (~0.01 – 0.1), fouling only lowers this ratio. The alternative is to operate in the mixed mode, described by equation 14, and to adjust the coefficients with time as the fouling changes.

Heterodyne Mode.

Several techniques which ensure operation in the heterodyne mode are known from the literature. They use mixing of the scattered and reference beam outside the scattering cell [Sasaki] [Bott]. A typical set-up for an outside mixing point is shown in **figure 7**.

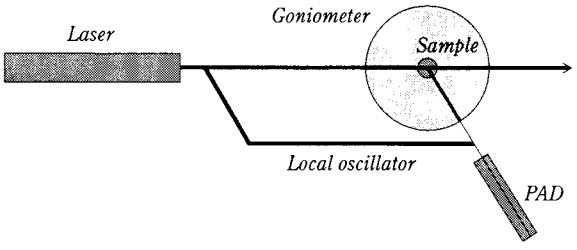

Fig. 7 Set-up for an outside mixing point

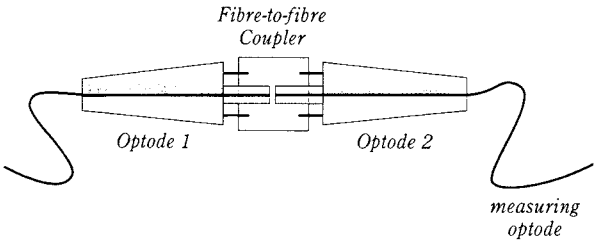

Fig. 8 Fiber coupler for FOQUELS to remain in heterodyne mode

These arrangements are, however, based on a conventional goniometric set-up and still need optical trannmission of the scattered light. Furthermore, these solutions suffer from a high sensitivity to mechanical vibrations. For use at really high concentrations we suggest that the local oscillator can be provided by making a break in the fibre. This is achieved using an optical fibre-to-fibre coupler. Due to the difference in refractive index at the glass-air surface, extra local oscillator light is added at the end of the first fibre. This solution is illustrated in **figure 8**.

This set-up provides a rigid and stable solution for the homodyne-heterodyne mixing problem in concentrated dispersions since heterodyne operation is retained at every concentration. The fibres are coupled using a 3M FC-PC connector. Index matching gel (Spindler & Hoyer) was applied between the two optodes to reduce the local oscillator working of the coupling. The intercept values without the index matching gel were smaller than 0.01. With the gel they were smaller than 0.1 which gives a better signal/noise ratio within the heterodyne regime.

Mixed Mode.

[Bremer] developed a method to derive the normalised diffusion coefficient (D/D_0) when the conditions lie within the mixed homodyne/heterodyne regime. He rewrote the autocorrelation function $G^{(2)}(\tau)$ as:

$$G^{(2)}(\tau)=BKX^2|g^{(1)}(\tau)|^2+BK2X(1-X)|g^{(1)}(\tau)|+B \quad (27)$$

Here B is the baseline, K (assuming $f_1 = f_2$) is an instrumental factor and X represents the fractional homodyne component of the signal:

For FOQUELS measurements, K is the value of the intercept if the measurement is operating in the homodyne mode and has been reported to have a value of 0.8 ± 0.1. The following equations give the relationship between the apparent diffusion coefficient D, the true diffusion coefficient D_0 and the ratio A/K, where A is the intercept value of the measured autocorrelation function. When the intercept is defined, then

$$g^{(2)}(\tau=0) = G^{(2)}(\tau=0)/B = 1+A$$

$$\text{Thus: } X = 1-\left(1-\frac{A}{K}\right)^{1/2} \tag{29}$$

Substituting equation 27 and equation 29 into equation 11 for $|g^{(1)}(\tau)|$ yields

$$g^{(1)}(\tau) = \frac{\left(1-\frac{A}{K}+\frac{G^{(2)}(\tau)-B}{BK}\right)^{1/2}-\left(1-\frac{A}{K}\right)^{1/2}}{1-\left(1-\frac{A}{K}\right)^{1/2}} \tag{30}$$

The relationship between the apparent diffusion coefficient D, the true diffusion coefficient D_0 and the ration A/K is thus given by:

$$\frac{D}{D_0} = \frac{2}{\sqrt{\left(1-\frac{A}{K}\right)+1}} \tag{31}$$

In **figure 9**, the ratio D/D_0 is plotted against the intercept, $g^{(2)}(t=0)-1$, for a value of $K=1$.

It is clear from this figure that the diffusion coefficient can only be uniquely determined if the ambient value of the intercept is known. In the case of heterodyne measurements there is, however, another problem. As can be seen from **figure 9**, the correct diffusion coefficient can only be found at an intercept value of zero. This implies that the signal-to-noise ratio is also zero and that there is no signal from which the diffusion coefficient can be calculated. Of course, a measurable signal-to-noise ratio is necessary but this introduces, in turn, an increasing error in the determination of the diffusion coefficient. From the literature it is suggested that the heterodyne regime dominates if the intercept value is less than 0.1. This was easily achieved with the coupler fibre arrangement. As can be seen from **figure 9**, an error of about 3% is introduced into the measured diffusion coefficient at this value of the intercept. Bremer also stated that the intercept of the intensity autocorrelation function cannot be used to determine whether or not a signal is purely homodyne or heterodyne. Bremer suggested that the ratio of intercept to instrumental constant A/K should be in the range of 0.1 to 0.3 to reliably extract the field autocorrelation function from heterodyne measurements. These values are a good compromise between the speed of acquisition of the data and the error made in the calculation.

However, his theory can be used to correct the measurement mode with the single fibre if the value for K is known. Equation 31 can be re-written as:

$$D_0 = \frac{\left(1-\frac{A}{K}\right)^{1/2}+1}{2} D \tag{32}$$

From the single fibre results, the diffusion coefficient D and the intercept values of the autocorrelation function, A are known. These can be substituted into equation 32 and the true diffusion coefficient, D_0, is calculated. The values of D_0 which are thus determined are shown in **figure 10** and are compared with those measured directly with the fibre coupler arrangement. The instrumental factor K is assumed to be 0.7. This figure shows that the coupled fibre data and the corrected single fibre data give very similar results at all concentrations. The hardware solution and the software solution are equally successful. Of course, in practice the single fibre corrections can be made on-line as the intercept changes with the fouling.

Measurements and results

Measurements were performed to test the new coupled fibre arrangement against the conventional single fibre set-up. The measurements were made on a sample of BASF Styronal 176 nanometer latex with a stock concentration of 50% vol/vol. This latex was

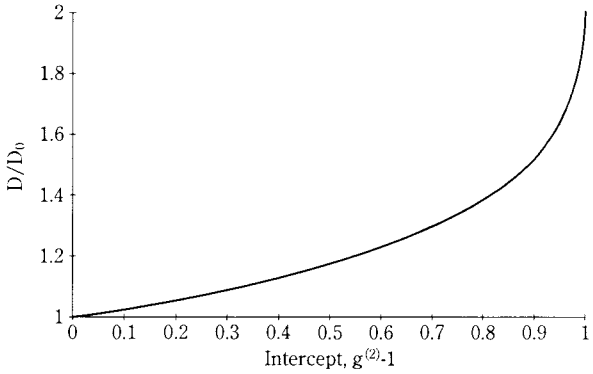

Fig. 9 Plot of D/D_0 for various values of the intercept of the autocorrelation function for $K=1$

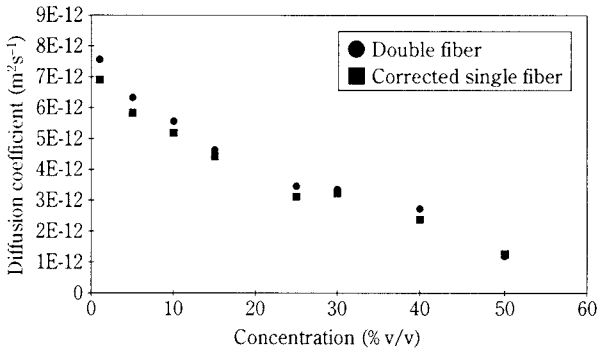

Fig. 10 Diffusion coefficients obtained from measured data using the double fibre set-up and data obtained using the single fibre set-up after correction for the intercept of the autocorrelation function

diluted using Millipore water which was filtered via a Sterivex 200 nanometer filter. The results are given in **figure 11**.

This figure clearly shows the difference between the intercept values obtained for the single and coupled fibre arrangements. The intercept value of the single fibre set-up already reaches the homodyne-heterodyne mode at a concentration of 10% v/v whilst the coupled fibre set-up remains below an intercept value of 0.1 at every concentration. The influence of the intercept on the value of the diffusion coefficient calculated via the CONTIN method and assuming heterodyne operation is given in **figure 12**. It is clear that, although the experimental parameters and the sample are the same, the results only coincide at very low and very high concentrations.

The use of the coupler fibre is a hardware solution to the problem which ensures operation in the heterodyne mode. The alternative solution is to use the single fibre in the mixed mode but to make a software correction.

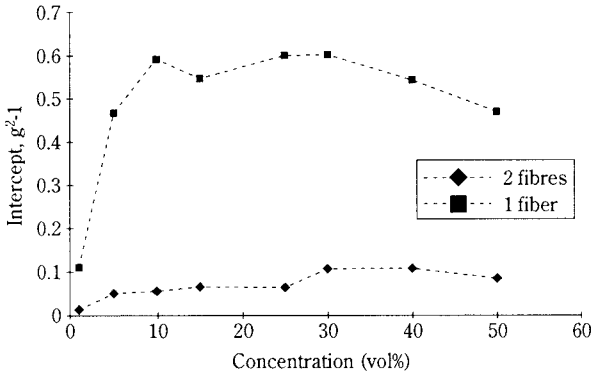

Fig. 11 Intercept of the autocorrelation function from the single and the coupled fiber arrangements using different concentrations of a 176 nm BASF Styronal latex

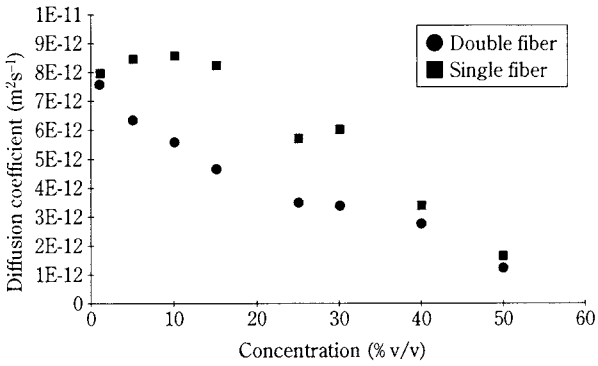

Fig. 12 Values of the diffusion coefficient derived from single and coupled fibre arrangements using different concentrations of a 176 nm BASF Styronal latex

Relationship to Particle Size

For concentrated dispersions the relationship between the diffusion coefficient and the particle size is complicated. In the first instance, the coefficient measured depends upon the relative values of the scattering vector, q, and the average interparticle distance. If the measuring volume includes many particles, then a collective diffusion coefficient is measured. If the measuring volume contains few particles, then the self diffusion coefficient is measured. Much more complicated are the numerous hydrodynamic and inter-particle interactions which can occur.

There are two clearly separate roles for the PCS technique. The first is as a research tool, perhaps a unique one, by which these interactions can be investigated and the proposed theories verified, or not as the case may be. Used in this way, it is obviously best to carry out the experiments with well defined, monosized particles. An example of a set of measurements made on the BASF, 176 nm latex particles is shown in **Fig. 13**. The questions then relate to the relative importance of the attractive/repulsive forces and to the order of the particle interactions. Measurements of the particle motion, made locally and in situ, are the most convincing way to investigate these phenomena. It will be a long time before the models, even the computer simulations, will supercede the need for good measurements.

A more practical way to use the PCS technique is to calibrate it arbitrarily to monitor a particular system. In **Fig. 14** is an example of the use of the coupled fibre equipment to monitor the grinding of a magenta, waterborne paint. The arbitrary system parameter is derived from the apparent diffusion coefficient by applying the Stockes-Einsteinequation; in this way it is also corrected for the change of temperature during the process. Again it is remarked that the system

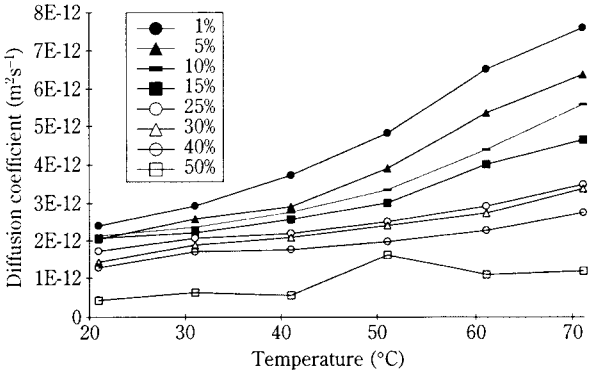

Fig. 13 Diffusion coefficient of 176 nm BASF Styronal latex measured at various concentrations and temperatures using the coupled fibre (FOQELS)

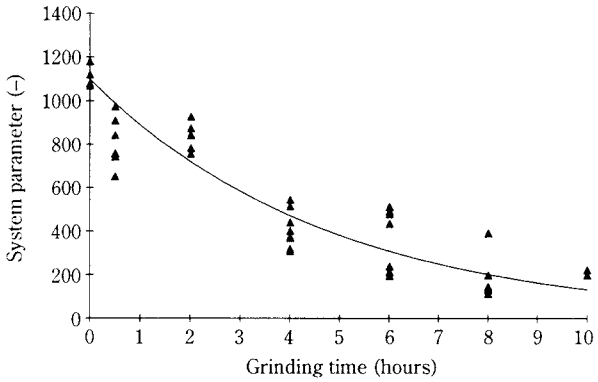

Fig. 14 Monitoring the grinding of an undiluted magenta 611, waterborne paste using the coupled fibre equipment

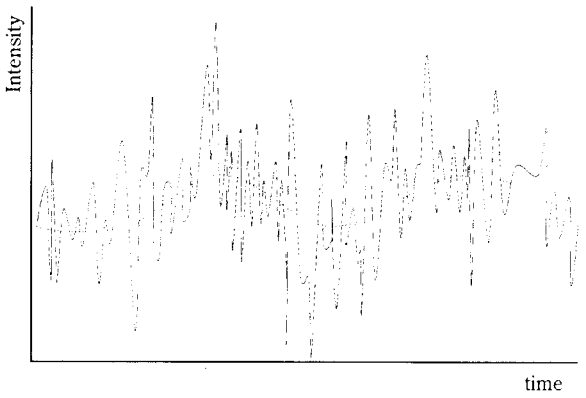

Fig. 16 Graphical representation of a PCS signal consisting of a high-frequency Brownian motion part and a low-frequency number fluctuations part.

parameter does not represent a particle size, due to the strong particle interactions.

Between these two extremes of use lies the way forward. The research on the model materials helps to interpret the completely empirical use.

4. Measurements at low concentrations

number fluctuations

In dispersions of low concentration, number fluctuations give rise to a slowly flucuating signal. The conventional PCS measuring system assumes a constant measuring volume of about $1*10^{-6}$ cm^3. Particles will move in and out of this measuring volume, but when the total number of particles present, $\langle N \rangle$, is large it can be taken to be constant. As the concentration becomes smaller, the number present at any moment varies and should be written as a function of time.

$$N(t) = \langle N \rangle + \delta N(t) \tag{33}$$

The process is illustrated in **Fig. 15**. In practice it has an appreciable effect on the results when the average number of particles present is less than one hundred. The varying concentration usually leads to a fluctuation in the recorded intensity, as illustrated in **Fig. 16**. Usually, the frequency domain of these fluctuations is much lower than that due to the Brownian motion and thus they can be separated. The regime can be estimated as follows:

At low concentrations, the number of particles in the scattering volume can be described with Poisson statistics

$$P(N) = \frac{\langle N \rangle^N}{N!} e^{-\langle N \rangle} \tag{34}$$

Using Poisson statistics, so that $\langle N^2 \rangle = \langle N \rangle^2 + \langle N \rangle$, and combining equations (8) and (34), the second order correlation function can be written as:

$$G^{(2)}(\tau) = \langle N \rangle^2 + \langle N \rangle^2 |G^{(1)}(\tau)|^2 + \langle \delta N(0) \cdot \delta N(\tau) \rangle \tag{35}$$

Dividing by $\langle N \rangle^2$ yields the normalised autocorrelation function. This equation now contains the number

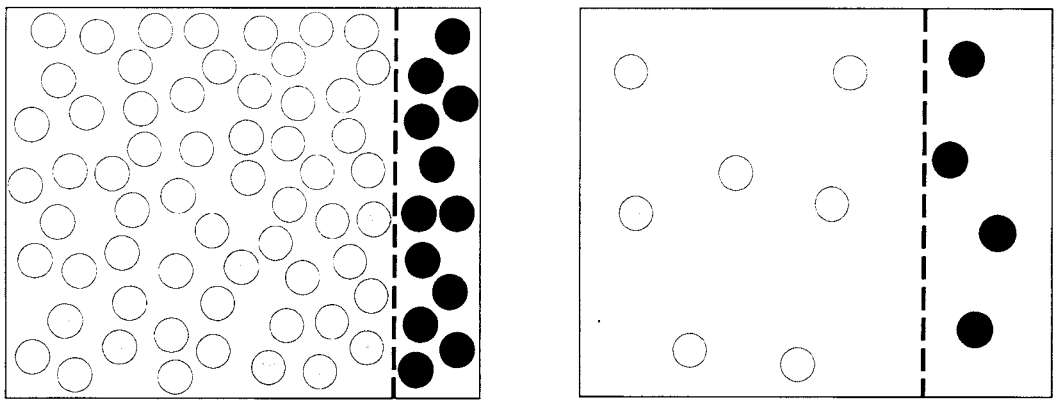

Fig. 15 Illustration of the number fluctuations.

fluctuations which contribute a second component to the decay in the measured autocorrelation function. The time constant of this decay, τ_N, can be estimated by the quotient of the diameter of the scattering volume and the diffusion coefficient of the particles

$$\tau_N \propto \frac{L^2}{D} \tag{36}$$

Measurements and result.

In order to separate the two regimes of intensity fluctuation, solutions are possible both by hardware or by software. The low frequency measurements offer, of course, an excellent method of measuring a very low concentration of particles. If this is the required parameter, then the hardware solution offers some advantages. In this case a low-pass filter can be combined with a comparator as shown in **Fig. 17**. Such a filter was tested in combination with a standard lens and pinhole arrangement, using 90° scattering and the Brookhaven correlator. The particles were latex of 176 nm diameter. The results obtained

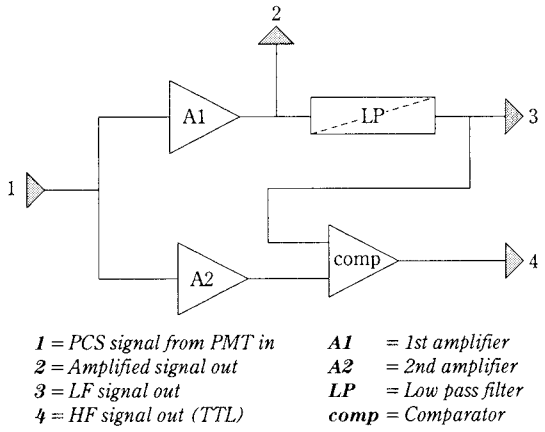

Fig. 17 Overview of the electronic filter used for the low concentration PCS

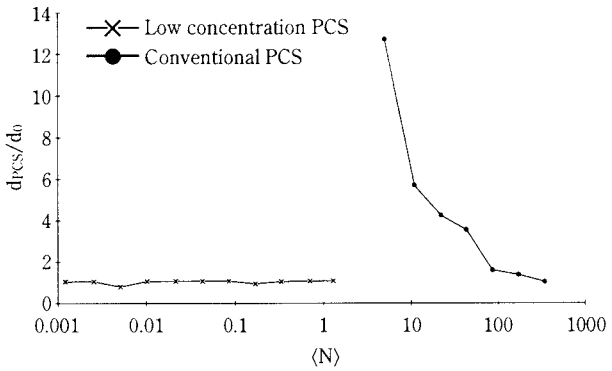

Fig. 18 Normalised particle diameter of 176 nm latex particles obtained with both the conventional and the low concentration PCS system using a lens-and-pinhole detector

are shown in **Fig. 18**. When the two components of fluctuation are not separated, the apparent diameter increases dramatically when the average number of particles present is less than about one hundred. By separating the signals, reliable measurements of particle size can be made at concentrations at least five decades lower.

These concentrations are so low that it was necessary to show that this count rate did not originate from any unwanted electronic source but was only due to scattered photons. This confirmation is consistent with the following observations:

1. When the detector was covered, the count rate decreased to the dark count values
2. When the laser output was reduced, the count rate decreased
3. When a clean, particle-free, sample was used, no correlation was found

It seems that some of the light scattered by the particles must be originating from scattering events outside the conventional scattering volume. The probability is that the detector is receiving light which has been multiply scattered. This is illustrated in **Fig. 19**. This component is also present at higher concentrations but is too weak to be significant. Only at low concentrations does it become appreciable.

Of course, the signals can also be separated in the software. The hardware solution can only be used if a continuous DC signal is generated. If the signal is recorded as individual pulses in sufficient number then the filter is not necessary. Modern correlators are capable of operating in this mode, that is the time constant of the amplifier is less than that of the pulse duration. If the required parameter is the size of the particles, it may be easier to operate in this mode. Examples of measurements made on latex samples of

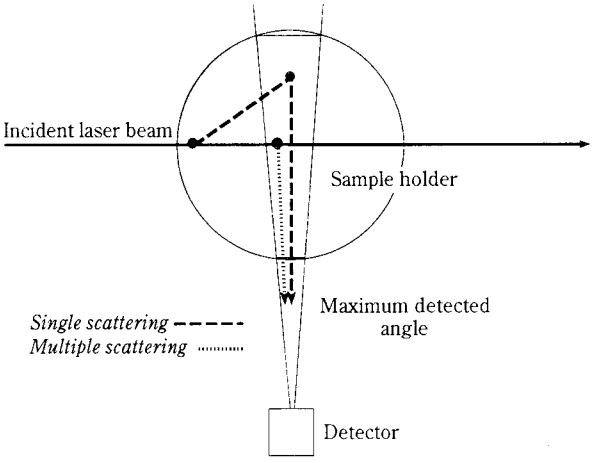

Fig. 19 Signals can originate from both single and multiple scattering.

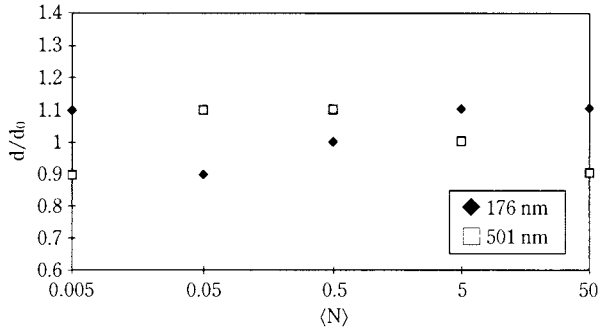

Fig. 20 Normalised particle diameters of samples of 176 and 501 nanometer latex measured at low concentration

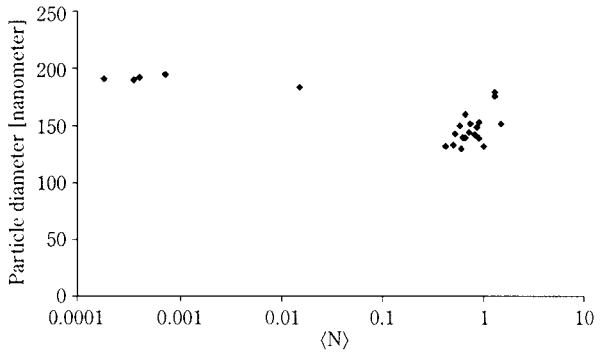

Fig. 21 Monitoring cigar smoke

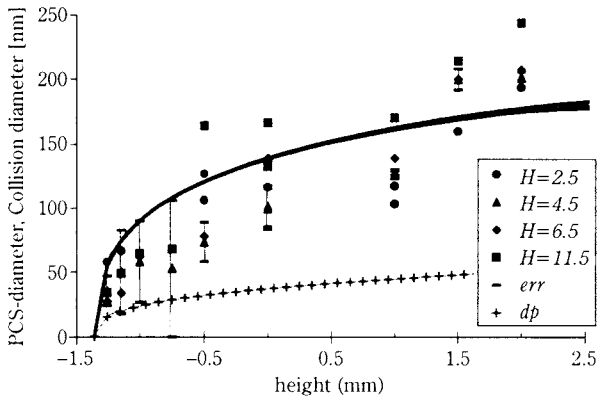

Fig. 22 Monitoring the formation of particles of Si_3N_4 in an aerosol reactor

176 nm and 501 nm are shown in **Fig. 20**. Here, the correlator has been able to discriminate the Brownian fluctuations without the help of a filter. Measurements may be made not only on particles in liquids but also in air, that is on aerosol particles. The instrument was tested with cigar smoke as illustrated in **Fig. 21**, where the mean size is plotted as a function of the number fluctuations. **Figure 22** shows the growth of particles of Si_3N_4 in an aerosol reactor monitored by this technique [van Drunen et al.]. The indication is that photon corelation techniques can be developed to become a standard method of measuring both the size and the concentration of aerosol particles.

5. Conclusions

Photon Correlation Spectroscopy is the standard technique for the measurement of sub-micron particles. Properly used, it yields an accurate measurement of the mean size of the particles. Modern deconvolution techniques make it possible to also make an estimate of the most likely distribution of particle size. Both the upper and lower limits of concentration can be considerably extended.

In concentrated dispersions, optical fibre PCS is used for measuring the diffusion coefficient. In order to measure reliably at high concentrations, a split fibre arrangement has been developed which operates always in the heterodyne mode. This equipment performed well compared to known optodes and is able to measure the diffusion coefficient of particles in the concentration range from 1 to 50% vol/vol. Fouling of the optode is not an insuperable problem, although sufficient light must, of course, be able to reach the dispersion and be reflected to the detector. At concentrations below 1% vol/vol, the signal-to-noise ratio is too small to record good autocorrelationfunctions by this heterodyne technique.

At low concentrations, although number fluctuations are present, the system is still capable of obtaining the correct particle size from both liquid and aerosol dispersions. There are at least two different frequency ranges present in the signal recorded in a PCS signal at low concentration. One cause of the low frequency signal is due to variation of the number of particles in the detection zone. The signal obtained contains information about both the particle size and concentration. The lower limit of concentration is now determined by the scattering behaviour of the particles, the sensitivity of the detector and the power of the incident laser beam.

List of Symbols

β	: spatial coherence of the scattering volume	[-]
Γ	: average decay rate	[1/s]
Γ	: decay rate	[1/s]
λ	: mean free path of the gas	[m]
λ	: wavelength of light	[m]
η	: solvent viscosity	[Pa s]
ω	: circular frequency of light	[rad/s]
θ	: scattering angle	[rad]
ω_0	: circular frequency of the incident light	[rad/s]
μ_2	: second moment of the distribution of decay rates	[1/s^2]

μ_3 : third moment of the distribution of decay rates [$1/s^3$]
ε_i : (unknown) experimental uncertainty [-]
τ_N : time constant of the decay due to number fluctuations [s]
A : intercept value of the measured autocorrelation function [-]
B : baseline [-]
c : speed of light [m/s]
$C(\Gamma)$: distribution of decay rates [-]
C_C : Cunningham slip correction factor [-]
c_j : intensity weight of the particles with diffusion coefficient D_j [ ]
d : particle diameter [m]
D : particle diffusion coefficient [m^2/s]
D_0 : true diffusion coefficient [m^2/s]
d_m : collision diameter of a molecule [m]
E : electric field [a.u.]
f : frequency of the scattred electric field [1/s]
f_1 and f_2 : experimental parameters, normally <1 [-]
$G^{(2)}(\tau)$: intensity autocorrelation function [-]
$g^{(2)}(\tau)$: normalised intensity autocorrelation function [-]
I_{LO} : intensity of the local oscillator [# photons/s]
Is : scattered intensity by the particles [# photons/s]
K : instrumental factor [-]
k : wave vector [1/m]
k_B : Boltzman costant [J/K]
L : dimension of the scattering volume [m]
N : # of particles in the scattering volume [-]
n : refractive index of the medium [-]
n_{ph} : # of photons impinging on the detector [#]
n_z : average # of collisions of a molecule per second [#/s]
P(N) : chance of having N particles in the scattering volume [-]
$\underline{q}$: scattering vector [-]
T : absolute temperature [K]
v : speed of the particle [m/s]
X : fractional homodyne component of the signal [-]

References

1) Berne J.B., Pecora, R., Dynamic light scattering, with applications to chemistry, biology and physics, John Wiley & Sons, New York, 1976
2) Bott S.E., System for measuring the size distribution of particles dispersed in a fluid, *U.S. Patent 4.676.641* (1987)
3) Bremer L.G.B., Deriemaker L., Finsy R., Geladé E., Joosten J.G.H., Fiber optic dynamic light scattering, neither homodyne nor heterodyne, *Langmuir*, **9** (1993), 2008-2014
4) Chu, B., Laser light scattering – Basic principles and Practice, Second edition, Academic Press, San Diego, 1991
5) Drunen, M.A. van, Tuinman I.L., Marijnissen J.C.M., Merkus H.G. and Scarlett B., Measurement of aerosols in a silicon nitride flame by optical fiber photon correlation spectroscopy, *J. Aerosol Sci.*, 895-908, 1994
6) Finsy R., Particle sizing by quasi-elastic light scattering, *Adv. Coll. Int. Sci.*, **52** (1994) 79-143
7) Hinds W., Aerosol Technology – Properties, behaviour and measurement of airborne particles, John Wiley & Sons, New York, 1982
8) Provencher S.W., A constrained regularization method for inverting data represented by linear algebraic or integral equations, *Computer Phys. Comm.*, **27** 213, 1982
9) Sasaki S., Mandel M., Equipment for photon correlation spectroscopy measurements in the heterodyne mode, *J. Phys. E: Sci. Instrumen.*, **17** (1984)

Author's short biography

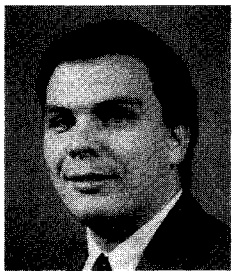

Dr.ir. A.W. Willemse

Alexander Willemse graduated in Chemical Engineering from Delft University of Technology in 1994. He then proceeded with Ph.D. research in the Particle Technology Group of Professor Scarlett which he completed in 1998. He is currently working as a Group Leader Solids Section, at the pharmaceutical Product Development Department of NV Organon, Oss, The Netherlands.

Author's short biography

Ir. E.J. Nijman

Evelien Nijman received her M.Sc. degree in Chemical Engineering from Delft University of Technology, The Netherlands, in 1996. She is now working on a Ph.D. project on Photon Correlation Spectroscopy in Aerosols in the Particle Technology Group in Delft.

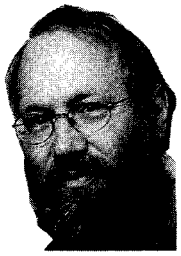

Dr.ir. J.C.M. Marijnissen

Dr.ir. J.C.M. Marijnissen is Associate Professor Aerosol Technology in the Particle Technology Group of the Department of Chemical Engineering of Delft University of Technology in the Netherlands. He has some twenty-five years experience in the field of mine ventilation and aerosol technology and is especially involved in the development of advanced aerosol measuring instrumentation. He has authored more than hundred articles, is the editor of three books on aerosols and teaches extensively. He is a member of the Netherlands Air Association, Netherlands Institute of Mining Engineers, he is the chairman of the Netherlands Flemish Aerosol Association, he is committee member of the European Aerosol Assembly, a member of the editorial board of the Journal of Aerosol Science and associate editor of the Journal of Nanoparticle Research. He hold a Masters from Delft University of Technology and a Ph.D. Environmental Engineering from the University of Minnesota, U.S.A.

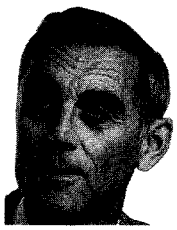

H.G. Merkus

Henk Merkus, graduated in organic chemistry from the University of Amsterdam, the Netherlands. After working in various jobs at Shell Research Amsterdam, he joined the Delft University of Technology, where he became a senior staff member in the Department of Chemical Engineering. He is supervisor of the analytical service group of this department, which covers an extensive range of analytical techniques for particle characterisation, surface area and porosity determination as well as chemical analysis. He is chairman of the Dutch Working Party for Particle Characterisation and convenor for the ISO Working Group for Particle Size Measurement by Laser Diffraction Methods.

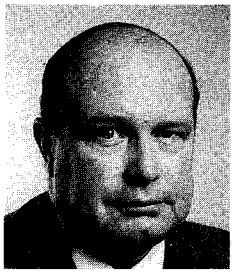

B. Scarlett

Brian Scarlett graduated originally in Physics from the University of Durham. His first job was in a nuclear power station. He later studied powder technology in Nottingham and progressed to become a lecturer and then senior lecturer at Loughborough University of Technology. He was here leader of the Particle Technology Group for 19 years. For a period he was simultaneously Chairman of Water Management in the Severn Trent Water Authority.

Since 1983 Brian Scarlett has been Professor of Particle Technology at Delft University of Technology. Amongst other functions he is currently chairman of ISO TC24/SC4, the international committee which concerns particle size measurement. He is an editor of the journal Particle Characterisation and is Series Editor of the Chapman Hall books on Powder Technology. Brian Scarlett is currently the European Adviser to IFPRI, the International Fine Particle Research Institute.

Review

High Performance Ferrite Magnets
—From the Perspective of Powder Technology† —

Hitoshi Taguchi
*TDK Materials Research Center**

Abstract

Coercivity in hexa-ferrite magnets originates in the magnetic behavior of so-called "single domain particles" with uniaxial magneto-crystalline anisotropy. The critical diameter, below which a single domain is stable, is estimated at around 1 micrometer (10^{-6} m) for M-type Sr-ferrite, which means that control of grain size to under a micron is significant for achieving high coercivity. For this reason studies were performed on a process for obtaining submicron powder and sintered grains, as well as on techniques for obtaining high orientation under magnetic fields when using submicron powder. For analytical purposes, particle size distribution, magnetic properties, and lattice defects of Sr-ferrite particles were investigated to explain the observed behavior.

1. Introduction

In general, the crucial properties of permanent magnets are not only their high energy product (BH)max, which allows volume reduction, but also high reliability (chemical and magnetic stability) and low price. Selection of magnet materials should be based on these criteria. Over the past few decades, many materials have been studied and proposed, but only ferrite, NdFeB, SmCo, and some AlNiCo magnets are still in use today. At 32-40 kJ/m^3, ferrite magnets have a considerably lower (BH)max than NdFeB-magnets with 320-400 kJ/m^3, but ferrite magnets account for an estimated 95% of world production by weight, which testifies to the unsurpassed cost efficiency of ferrite magnets. Another advantage is the chemical stability of these oxides, which makes them environmentally safe, further establishing their continued use.

The first "ferrite magnet" was Co-ferrite with a spinel structure (OP-magnet) invented by Prof. Y. Kato and Prof. T. Takei of Tokyo Institute University in 1932. The OP-magnet is now considered a landmark of scientific progress, although it was produced on a very small scale due only to its poor magnetic properties and weak mechanical strength. Later J. J. Went et al. (Philips N.V.) systematically studied Ba-ferrites with hexagonal structures and in 1952 released the M-type Ba-ferrite as a new permanent magnet material called "Ferroxdure" [1]. Since then, much basic research has been directed at improving the properties and productivities of these materials. Typical and successful examples are the discovery of Sr-ferrite with larger magnetic anisotropy (K1), and the development of pressing technology under a magnetic field, which doubles the residual flux density (Br). For this reason anisotropic M-type Sr-ferrite is now dominant in mass production.

* 570-2, Matsugashita, Minamihatori Narita, Chiba 286-8558 Japan
Tel (0476)37-1642 Fax. (0476)37-1648
e-mail: htaguchi@mb1.tak.co.jp

† Received 12 October, 1998

2. General Description of Ferrite Magnets

2.1 Crystal Structure of Ferrite Magnets

Fig. 1 shows a magnetoplumbite (M) type crystal structure. Oxygen ions that form hexagonal closed

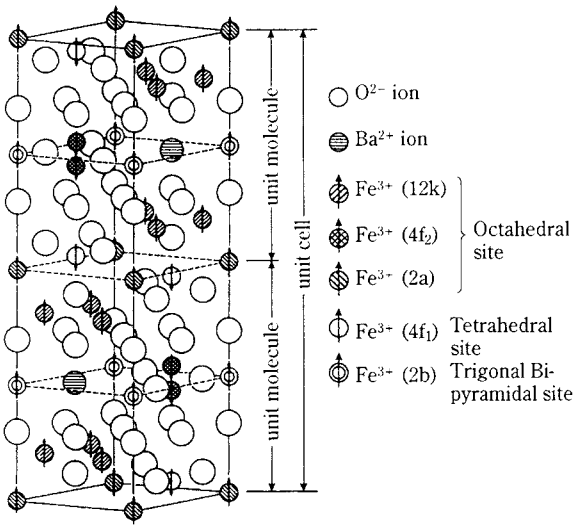

Fig. 1 Perspective illustration of M-type Ba-ferrite

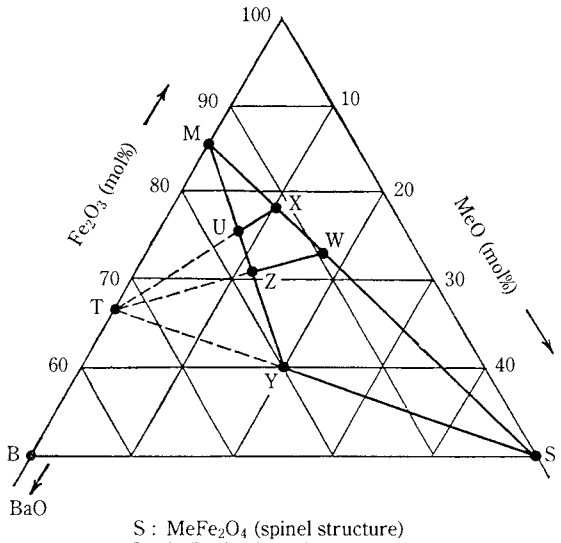

Fig. 2 BaO-MeO-Fe_2O_3 system, showing the relationships of chemical compositions among ferrimagnetic hexagonal compounds The symbol Me represents a divalent ion.

packing are partially substituted by strontium ions (Sr^{2+}). Ferrous ions (Fe^{3+}) lie between the oxygen ions and are magnetically connected with each other. These generate uniaxial magnetic anisotropy along the c-axis in the M-structure, which is the basic reason why M-type ferrite is a permanent magnet. Other than M-type ferrite, W- and X-type ferrites also have uniaxial anisotropy, which means they have the potential to be permanent magnets. Their compositions lie on the line between M and S (spinel) as shown in **Fig. 2**.

Table 1 shows the fundamental properties of these hexa-ferrites. M-type Sr-ferrite (SrM) has a 10% larger anisotropic constant (K1) than M-type Ba-ferrite (BaM). Magnetization of W-type ferrites is 10% greater than M-type ferrite, but its K1 is relatively small in general. Despite a great number of studies concerning cation substitution in the M-type structure, very few attempts to increase magnetization have succeeded.

Similar to spinel ferrites, the saturation magnetization of M-type ferrites will increase when non-magnetic ions such as Zn occupy the tetrahedral 4f1 sites; Fe^{3+} at 4f1 sites has down-spins. Recently the partial substitution of La^{3+} and Zn^{2+} for Sr^{2+} and Fe^{3+} achieved magnetization that was 5% higher than conventional M-type Sr-ferrite, while retaining the K1 value of conventional M-type Ba-ferrite, thereby resulting in the highest (BH)max value of 41 kJ/m^3, as shown in **Table 2** [7].

2.2 Theory of Single Domain Particles

It is assumed that coercivity in ferrite magnets originates in the magnetic behavior of "single domain particles" [8]. In general, magnetic materials form a "magnetic domain structure" in order to reduce static magnetic energy. Boundaries between two domains are magnetic walls where magnetic moments gradually change direction. When reducing the particle or

Table 1 Fundamental magnetic properties of hexa-ferrite magnet materials

Symbol	Chemical formula	σs $\times 10^{-6}$(Hm^2/kg)	Tc (K)	HA (MA/m)	K_1 (J/m^3)	Reference
SrM	$SrO \cdot 6Fe_2O_3$	1.14	733	1.59	0.35	
SrFe2W	$SrO \cdot 2FeO \cdot 8Fe_2O_3$	1.23	783	1.55		[2]
SrZn2W	$SrO \cdot 2ZnO \cdot 8Fe_2O_3$	1.25	643			[3]
SrZnX	$2(SrO \cdot ZnO \cdot 7Fe_2O_3)$	1.21	703	0.98	0.26	[4]
BaM	$BaO \cdot 6Fe_2O_3$	1.08	723	1.35	0.32	[5]
BaFe2W	$BaO \cdot 2FeO \cdot 8Fe_2O_3$	1.19	773	1.4		[2]
BaZn2W	$BaO \cdot 2ZnO \cdot 8Fe_2O_3$	1.23	643	1	0.26	[6]

Table 2 Magnetic properties of newly developed Sr-ferrite

	Fundamental properties			Sintered samples						
Composition	Js (T)	K_1 (J/m^3)	Tc (K)	Br (T)	HcJ (kA/m)	Ir/Is (%)	Hk/HcJ (%)	(BH)max (kJ/m^3)	Density (Mg/m^3)	Reference
$SrFe_{12}O_{19}$	0.465	0.35	728	0.44	320	97.5	91.5	37	5.00	[11]
$Sr_{0.7}La_{0.3}Fe_{11.7}Zn_{0.3}O_{19}$	0.485	0.33	693	0.46	207	98.3	94.4	41	5.06	[7]

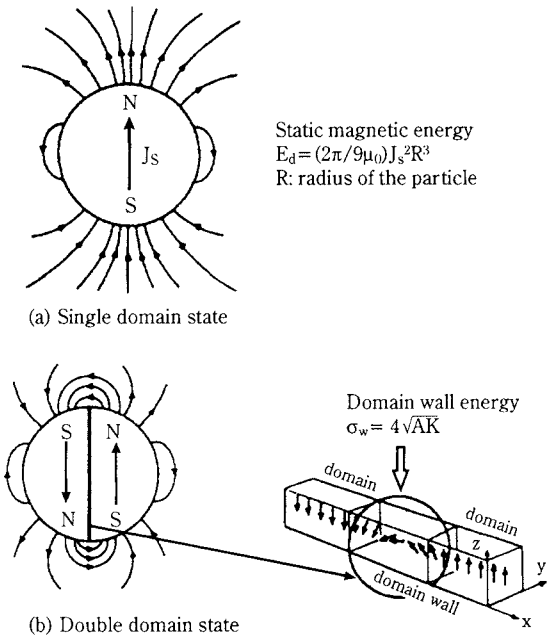

Fig. 3 Domain structure of one particle with uniaxial anisotropy

grain size of magnetic materials, the "non magnetic wall state" (i.e., single domain state) becomes energetically more stable as shown in **Fig. 3**. And once this single domain state is realized, coercivity will be maximized because magnetic reversal mechanisms are limited only to spin rotation.

2.3 Conventional Process for Sintered Ferrite Magnets

Fig. 4 shows the conventional manufacturing process of ferrite magnets. The raw materials strontium carbonate (or barium carbonate) and iron oxide are mixed and calcined at 1250-1300°C in air. Especially in the case of anisotropic ferrite production, ferrite formation must be concluded at this stage because it is necessary to orient the ferrite particles at the pressing stage. For this reason, higher calcination temperatures (higher than 1250°C) have been conventionally employed, causing grain growth. The calcined products, which are usually hard pellets of more than a few mm in size, are crushed and pulverized. For the production of anisotropic magnets, calcined pellets are first dry-pulverized and then wet-milled to submicron order.

Ferrite magnets can be classified into two groups according to their manufacturing process: isotropic magnets and anisotropic magnets. Anisotropic magnets are mainly manufactured by pressing in a magnetic field. There are two methods for pressing, wet and dry. Wet-pressing is a process for compacting a slurry of fine-milled powder mixed with a solvent

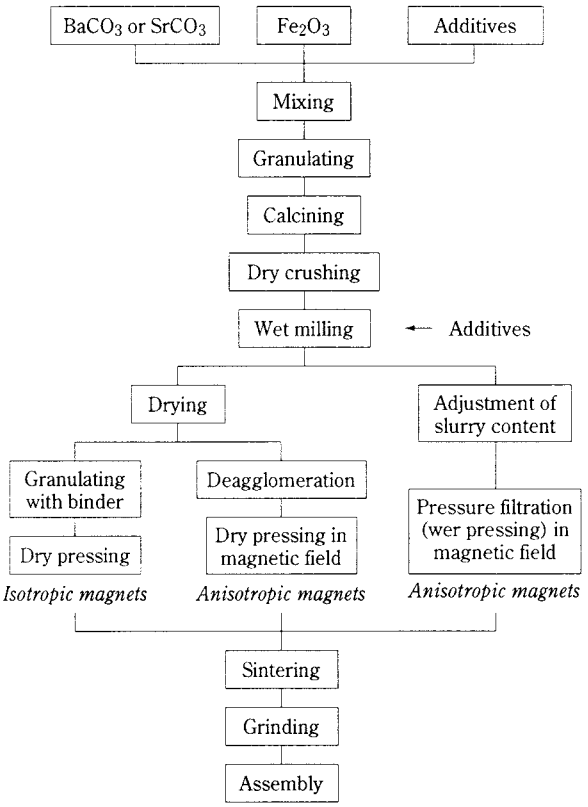

Fig. 4 Conventional production technology of sintered ferrite magnets

such as water in a magnetic field. Although the flotation of the particles in the solvent facilitates their rotation and orientation, dewatering takes a longer time. SiO_2 and $CaCO_3$ are usually added at the pulverizing stage in order to promote densification and inhibit grain growth at the next sintering stage. Compacts are sintered at 1200-1250°C in air.

2.4 A Concept for High-Performance Ferrite Magnets

From the perspective of materials research, residual flux density (Br) and intrinsic coercivity (HcJ) are the most important properties. Both Br and HcJ consist of factors originating in the crystal structure and micro- or nano-structure, as shown in **Fig. 5**. All these factors should be improved simultaneously in order to improve magnetic properties.

Br is determined by the product of density, the

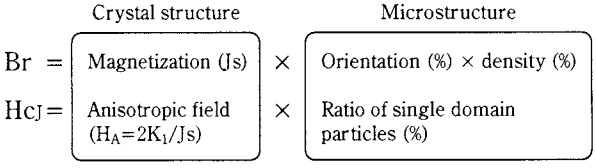

Fig. 5 Factors of magnetic properties (Br and HcJ) in ferrite magnet

degree of orientation, and the saturation magnetization (Js). M-type Sr-ferrite has a Js value of about 0.465 T. The density and the degree of orientation have upper limits of about 98% for sintered magnets, which afford the highest values. Therefore, the practical limit of Br in a sintered ferrite magnet with conventional M-type composition is around 0.445 T (i.e., $0.465\times0.98\times0.98$), resulting in (BH)max of 37 kJ/m^3.

The limit of HcJ, on the other hand, is determined by the anisotropic field ($H_A=2K_1/Js$), which is estimated at 1.5 MA/m for M-type Sr-ferrite. Large grains in excess of one micrometer show multi-domain behavior and reduce coercivity. The ratio of single domain particles or grains should therefore be increased in order to reach the theoretical value of HcJ.

The critical diameter below which a single domain is stable is estimated at around 1 μm for SrM-ferrite. This means controlling grain size to under a micron is significant for achieving high HcJ as mentioned above. Taking into account grain growth, ferrite particles for sintered magnets should be around 0.3 μm before sintering. There are some problems in obtaining this powder with conventional processing (e.g., simply long milling) because very fine particles (0.01-0.02 μm) also appear, as shown in **Fig. 6**. These ultrafine particles have low magnetic properties due to thermal fluctuation, and decrease productivity especially at the pressing stage. Similarly, particles prepared by the co-precipitation method, hydrothermal

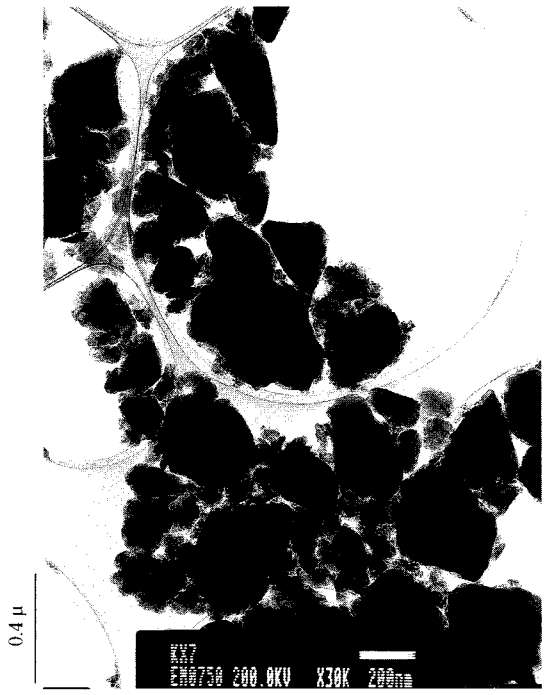

Fig. 6 TEM image of Sr-ferrite particles after long milling showing ultra-fine (under 0.05 μm) particles

synthesis, or by glass crystallization are too small (under 0.1 μm) to be oriented in a magnetic field. Our research therefore centered on conventional ceramic methods for obtaining submicron-sized primary particles *after calcination and before pulverization*, having an adequate size between 0.1 and 1 μm for the production of sintered magnets. From this point of view, calcination temperatures should be lowered through careful mixing of fine raw materials. In addition, the molar ratio Fe_2O_3/SrO should be nearly stoichiometric (6.0) to inhibit grain growth.

3. Process for Submicron Calcined Powder

First was a study of the wet mixing of raw materials in order to understand ideal mixing [9]. Iron oxide from pickling liquors (α-Fe_2O_3) having 0.3 μm primary particle size was agitation milled (attritor) in a Na_2CO_3 aqueous solution. By adding a $SrCl_2$ solution to the slurry, fine-$SrCO_3$ particles were synthesized and mixed with the Fe_2O_3 particles in the mill. The reaction is indicated below. The $Fe_2O_3/SrCO_3$ molar ratio was about 6.0.

$$SrCl_2+Na_2CO_3 \rightarrow SrCO_3\downarrow+2NaCl$$

After removing NaCl by washing, the slurry was dried and granulated to about 50 μm by spray drying, and calcined at 1150-1200°C for 3 hours in air. TEM observation showed that $SrCO_3$ precipitated particles were uniformly fine (0.02 μm) and dispersed well among the Fe_2O_3 particles. By means of a SEM observation (**Fig. 14**) of Sr-ferrite primary particles calcined at 1200°C, the average size of the particles was around 0.3 μm as shown in **Fig. 9**. The magnetic properties of the powder were $\sigma s=1.12\times10^{-6}$ Hm^2/kg, HcJ=422 kA/m. Judging from the fact that σs was approximately the theoretical value (1.13×10^{-6} Hm^2/kg), ferrite formation was almost completed. These excellent properties are due to the high dispersion of the fine raw materials (Fe_2O_3 and $SrCO_3$) and low calcination temperature. As a result of further investigation, similar powders were also obtained by using commercial-grade raw material $SrCO_3$, and even by a dry mixing process [10].

4. Process for High Orientation Using Submicron Calcined Powder

4.1 Experimental Process for Pulverizing Submicron Calcined Powder [11]

Fig. 7 illustrates the following pulverization process. First, calcined powder was dry-pulverized with a

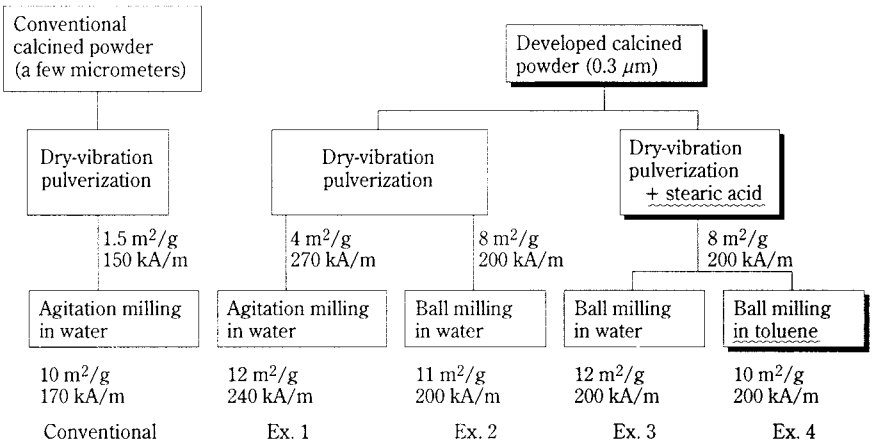

Fig. 7 Block diagram of pulverization process
The numerals indicate specific surface area (m^2/g) and HcJ (kA/m) of the powder.

Table 3 Magnetic properties of pressed and sintered samples

	Pressed samples			Sintered samples					
Sample	S_{BET} (m^2/g)	Jr/Js (%)	HcJ (kA/m)	Br (T)	HcJ (kA/m)	Jr/Js (%)	Hk/HcJ (%)	(BH)max (kJ/m^3)	Density (Mg/m^3)
Conventional	10	75	170	0.425	263	95.5	93-95	35.2	4.95
Ex. 1	12	65	240	0.382	353	89.9	88.0	27.4	4.94
Ex. 2	11	72	200	0.402	367	91.5	90.8	30.3	4.98
Ex. 3	12	72	200	0.396	367	91.3	87.9	29.5	4.93
Ex. 4	10	80	200	0.435-0.440	321-343	97.5	91.5-94.2	37.1-37.7	4.96-5.00

vibrating mill using 19 mm dia. steel rods. In Ex. 1 and Ex. 2, SiO_2 (0.6 wt%) and $CaCO_3$ (1.9 wt%) were added during pulverization. In Ex. 3 and Ex .4, stearic acid (2.0 wt%) was also added. All powders were then wet-pulverized by agitation milling (attritor) or ball milling, using water or toluene, to the extent of 10-12×10^3 m^2/kg. After increasing slurry concentration, the slurry was wet-pressed into pellets of 30×15 mm dia. in a magnetic field of about 1.0 MA/m. Pellets were sintered at 1180°C in air. **Table 3** shows the magnetic properties of the pressed and sintered samples. Pulverization with stearic acid in toluene (Ex. 4) achieved a remarkable improvement in orientation. Orientation degree was over 97%. This resulted in the highest magnetic properties, such as Br=0.44 T, HcJ=320 kA/m, and (BH)max=37 kJ/m^3. Sintered density was about 97% of the theoretical value. As shown in **Fig. 8**, SEM examination revealed highly uniform and well oriented grains. **Fig. 9** shows particle (grain) size distribution measured by counting 300-400 particles (grains) in the SEM micrographs of **Fig. 7** and **Fig. 8**. Average grain size was about 0.7 μm. A combination of oleic acid and xylene,

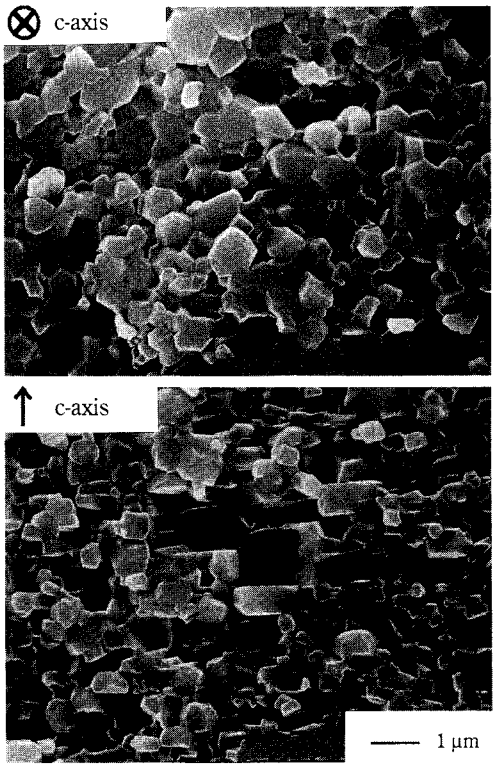

Fig. 8 Microstructures of high-performance Sr-ferrite magnet

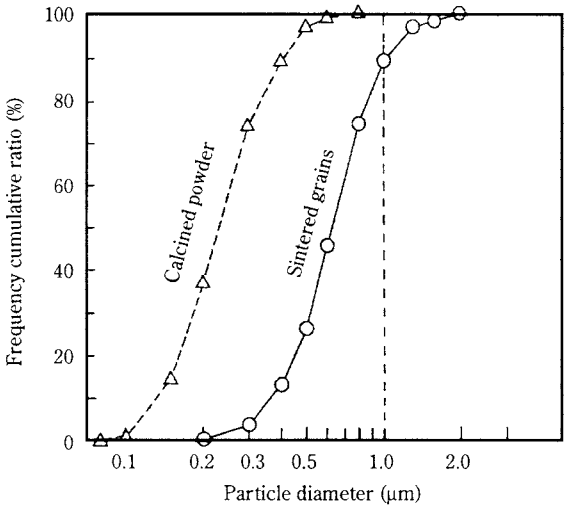

Fig. 9 Particle size distribution of calcined powder and sintered grains Size of the sintered grains was measured from the c-plane SEM micrograph.

instead of stearic acid and toluene, yielded similar or improved results.

The orientation degree decreased in the conventional process (water-based without surfactant, Ex. 1). The following subsection considers the reasons for this change in orientation.

4.2 Mechanism for Magnetic Agglomeration of Sr-Ferrite Particles

It is believed that single domain particles attract each other magnetically, thereby creating agglomerates that prevent orientation. **Fig. 10** shows an expected B-H hysteresis curve of one Sr-ferrite particle. Magnetic flux density at the working point (B1), which is determined by the particle shape, relates to magnetic agglomeration force. Thus, the surface flux density of the particle must be reduced (B1→B2) by reducing HcB. The magnetic moment of the particle in the magnetic field (Hex) is proportional to Js, which is best maximized. It was found that dry-vibration pulverization in particular was effective in reducing Hc values. This is treated in Section 5.

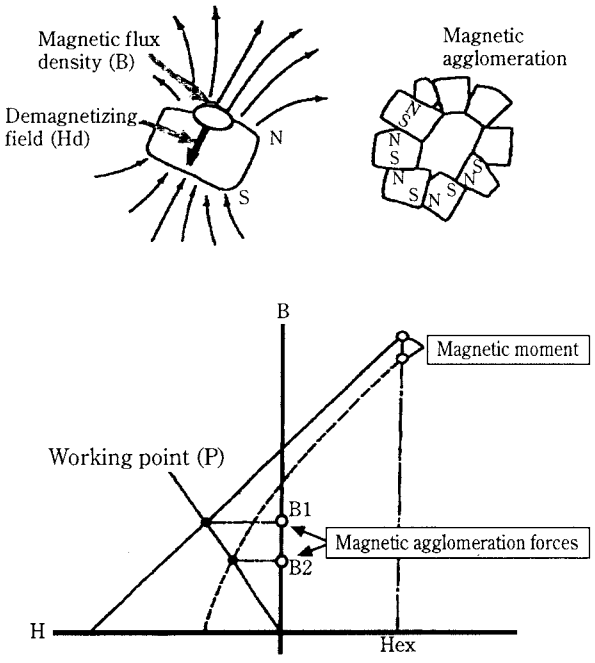

Fig. 10 Magnetic agglomeration forces of single domain particles

4.3 Wet Pressing Using an Organic Solvent and Surfactant

The wet process using an organic solvent (e.g., toluene or xylene) and a surfactant (e.g., stearic acid or oleic acid) brought about a remarkable improvement in the degree of orientation for submicron particles, as shown in **Fig. 11**. In a magnetic fluid, for instance, it is well known that fine ferrite particles (0.01 μm) are dispersed well in organic solvents with an added surfactant such as oleic acid. In the same way, it appears that Sr-ferrite particles coated with oleic acid or stearic acid dispersed well in toluene or xylene during milling and pressing. This gave rise to the improvement of orientation under a magnetic field. The relation between the amount of stearic acid

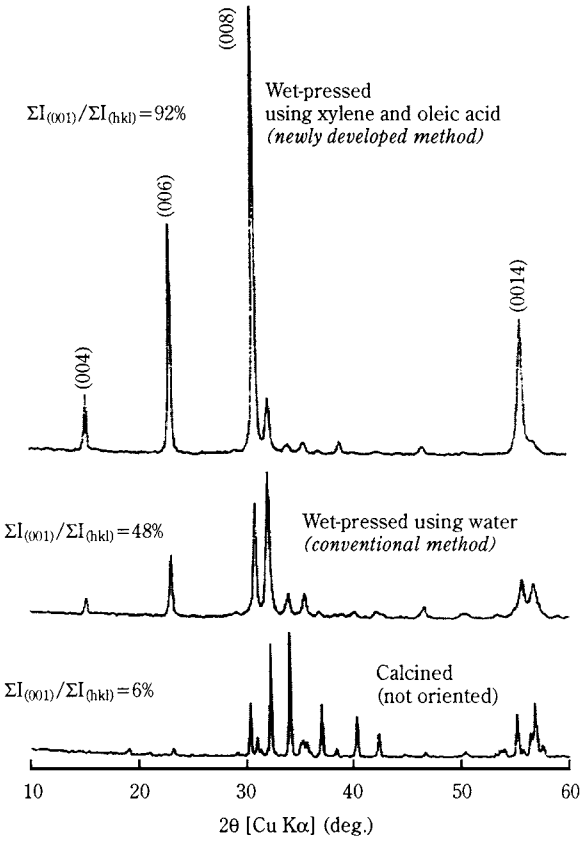

Fig. 11 XRD patterns of submicron Sr-ferrite particles

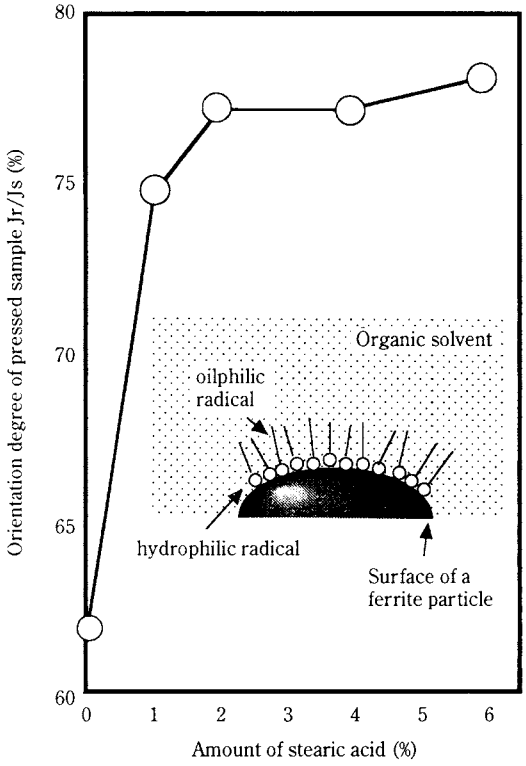

Fig. 12 Relationship between amount of stearic acid and orientation degree

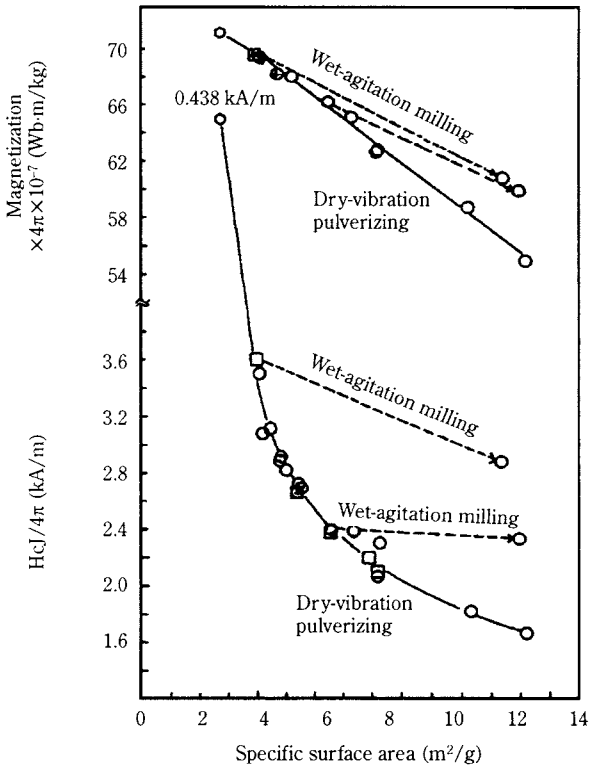

Fig. 13 Change of specific surface area and magnetic properties of Sr-ferrite powder during pulverization

and the degree of orientation (Jr/Js) of the pressed samples was investigated. More than 2 wt% of stearic acid seems to be required for optimum orientation, as shown in **Fig. 12**. This corresponds to a complete coating by stearic acid, as calculated for particles of 10 m^2/g surface area based on a cross sectional stearic acid area of about 2.0 nm^2.

5. Analysis of Sr-Ferrite Powder

5.1 Influence of Pulverization on Magnetic Properties

Fig. 13 shows the changes in magnetic properties of submicron Sr-ferrite powder when pulverized by dry-vibration milling. As pulverization proceeded, and the specific surface area of the powders increased, both magnetization and coercive force decreased. However, the respective changes are very different. Compared at 8×10^3 m^2/kg for example, the pulverized powder's HcJ decreased to 40% of the initial value, HcJ=438 kA/m, HcB=366 kA/m→HcJ (=HcB) =199 kA/m, while the decrease of σs (saturation magnetization per weight) was within 10%. These changes can be utilized to avoid magnetic agglomeration of the Sr-ferrite particles as mentioned in the previous section. Furthermore, with wet-pulverization by agitation milling (attritor), the changes are relatively small, as shown in **Fig. 13**. In addition to σs and HcJ,

Table 4 H_{CJ} curie temperature and temperature dependence of Sr-ferrite

	S_{BET} (m^2/g)	HcJ (kA/m)	Tc (K)	ΔHcJ/ΔT (A/m/K)
Calcined powder (Before pulverization)	3.0	438	763	600
Vibration pulverization	8.3	167		140
Vibration pulverization	13.0	135	766	
Agitation milling (Attritor)	13.0	183	761	

the temperature dependence of HcJ was considerably changed by pulverization, although Tc was not, as shown in **Table 4**. The torque curve of the pulverized powder was measured by using a highly sensitive torque measurement. The dependence of K2/K1 on the applied magnetic field increased [12].

5.2 SEM and TEM observation

Fig. 14 shows SEM images of pulverized Sr-ferrite particles prepared by dry-vibration milling. Primary particle size distribution differed little from the initial state, which means that the change in powder HcJ cannot simply be explained by a change in particle size. **Fig. 15** is a TEM image of pulverized Sr-ferrite particles. Moire fringes (parallel) indicate lattice defects.

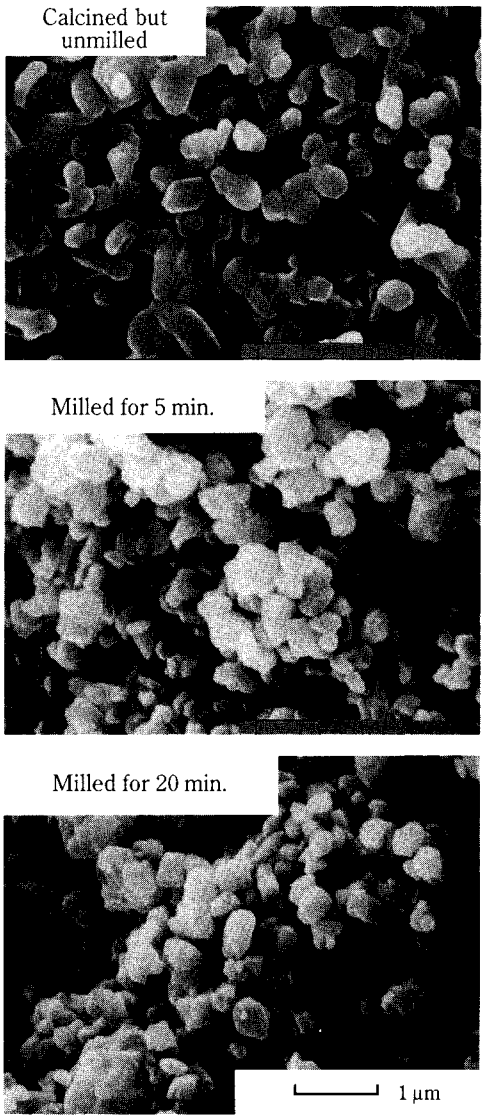

Fig. 14 SEM image of submicron Sr-ferrite particles pulverized by dry-vibration mill

Fig. 15 TEM image of pulverized Sr-ferrite particle
Moire fringes (parallel) are observed.

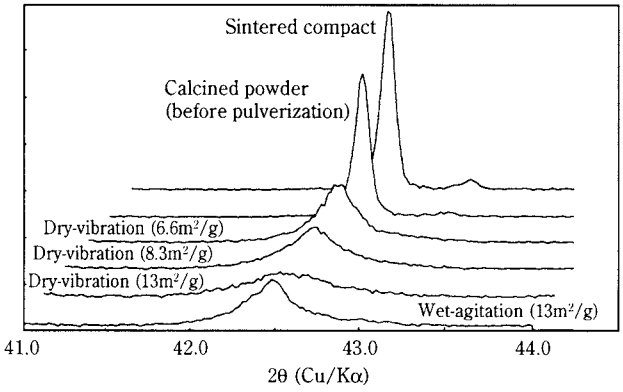

Fig. 16 XRD profile of (206) plane of Sr-ferrite
The pattern changes in accordance with pulverization.

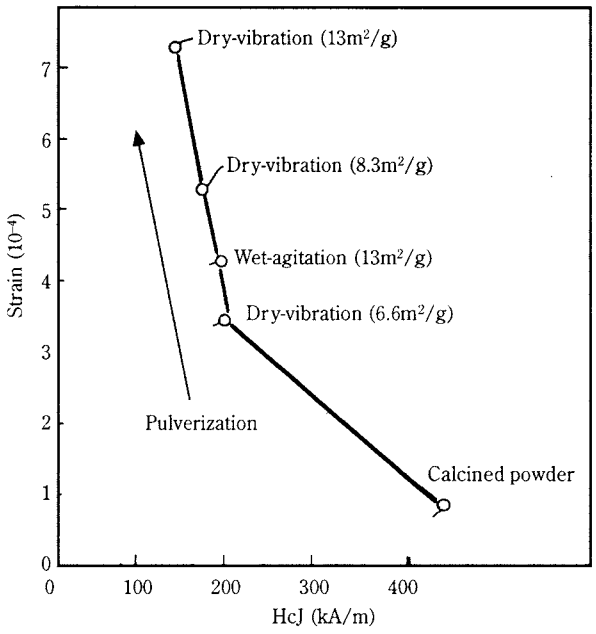

Fig. 17 Lattice strain of (206) plane and HcJ of Sr-ferrite powder

5.3 XRD Analysis

Lattice defects can cause a decrease in pulverized powder HcJ. Pulverized powder was analyzed by XRD in order to characterize lattice defects. The crystal system (hexagonal) did not change, and lattice constants were almost the same. **Fig. 16** shows the XRD profile of the (206) peak of Sr-ferrite powder. Apparently the diffraction peak broadened as pulverization proceeded. In consideration of crystallite size reduction as well as the crystal strain responsible for this broadening, the XRD profiles were analyzed with the Warren and Averbach method [13], yielding the conclusion that the strain induced by pulverization is isotropic and closely related to the coercivity of the particles, as shown in **Fig. 17**.

6. Conclusions

Processes for preparation of submicron-sized powder, for high orientation, and for high density are significant for high performance ferrite magnets. However, this study found that submicron sized particles (with high Hc) are oriented with great difficulty in a magnetic field at the pressing stage. A detailed study of the pulverization process to solve this problem revealed that over 97% high orientation and high density could be achieved, with an average grain size of 0.7 μm, by dispersing this powder with surfactant (stearic or oleic acid) into an organic solvent (toluene or xylene), while at the same time reducing the coercive force of the powder by introducing lattice defects [14].

References

1) J.J. Went, G.W. Rathenau, E.W. Gorter, and G.W. van Oosterhout, *Philips Techn. Rev.* 13 (1952) 194-208.
2) H. Kojima, C. Miyakawa, T. Sato, and K. Goto, *Jpn. J. Appl. Phys.*, 24, 51 (1985).
3) H. Graetsch, F. Haberey, R. Leckebusch, M.S. Rosenberg, and K. Sahl, *IEEE Trans. Magn.*, MAG-20, 495 (1984).
4) F. Leccabue, R. Panizzier, G. Bocelli, G. Calestani, C. Rizzoli, and N. Suarez Almodovar, *J. Magn. Magn. Mat.*, 68, 365 (1987).
5) D.V. Ratnam and W.R. Buessem, *IEEE Trans. Magn.*, MAG-6, 610 (1970).
6) F. Leccabue, R. Panizzieri, G. Salviati, G. Albanese, and J.L. Sanchez Liamazares, *J. Appl. Phys.*, 59, 2114 (1986).
7) H. Taguchi, T. Takeishi, K. Suwa, K. Masuzawa, and Y. Minachi, "High Energy Ferrite Magnets," *ICF7*, Bordeaux (1996).
8) H. Kojima, *Ferromagnetic Materials* 3, North-Holland Publishing Company, Amsterdam, 1982, pp. 305-391.
9) H. Taguchi, F. Hirata, T. Takeishi, Y. Tokoyama, and T. Mori, *J. Japan Soc. Powder and Powder Metallurgy* 39 (1992) 959-963.
10) H. Taguchi, F. Hirata, T. Takeishi, and T. Mori, "Dry process for Submicron Sr-ferrite Particles," *Japan Soc. Powder and Powder Metallurgy* Spring Meeting, Kyoto (1994) pp. 29.
11) H. Taguchi, F. Hirata, T. Takeishi, and T. Mori, "High Performance Ferrite Magnets," *ICF6*, Tokyo (1992), T. Yamaguchi and M. Abe, eds. pp. 1118-1121.
12) H. Taguchi, N. Nishio, F. Hirata, T. Takeishi, and T. Mori, *J. Mag. Soc. Japan* 18 (1994) 197-200.
13) B.E. Warren and B.L. Averbach, *J. Appl. Phys.* 21 (1950) 595-599.
14) H. Taguchi, F. Hirata, and T. Takeishi, *J. Japan Soc. Powder and Powder Metallurgy* 43 (1996) 19-24.

Author's short biography

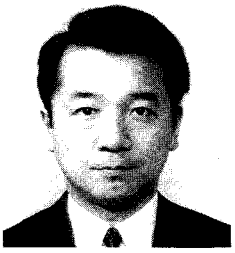

Hitoshi Taguchi

Dr. H. Taguchi is a chief scientist at the Materials Research Center of TDK Corporation. He graduated in Electronics Engineering from Saitama University and joined TDK in 1981. He has been engaged mainly in developing high performance ferrite magnets. He received his Doctorate in Engineering from Saitama University in 1995. He received "Technology Advancement Award" from the Japan Society of Powder and Powder Metallurgy in 1995. He is a member of the Magnetics Society of Japan.

Measuring Slugging Bed Dynamics with Acoustic Sensors†

C.E.A. Finney
Department of Mechanical and Aerospace Engineering and Engineering Science
*University of Tennessee**
C.S. Daw
Engineering Technology Division
*Oak Ridge National Laboratory***
J.S. Halow
*Federal Energy Technology Center****

Abstract

We describe experimental observations of slugging bed dynamics with passive acoustic sensors. Our results indicate that acoustic signals contain both similar and complementary information relative to dynamic pressure signals. We find that selective preprocessing of acoustic signals is a key step in separating information about microscale and macroscale processes. With such preprocessing, both linear and nonlinear dynamical features are apparent. Nonlinear features appear to be especially useful for practical diagnostics.

1. Introduction

In many commercial and research applications of fluidized beds, dynamic pressure measurements are routinely employed to assess the quality and/or regime of fluidization. While such measurements are extremely useful, they present several engineering difficulties, including tap penetration of the vessel wall, plugging of the taps by particulates, and modulation of the dynamic signal by lines connecting the taps and pressure sensors. These difficulties provide an incentive to develop other options for making dynamic measurements, especially in cases where installation of pressure taps is constrained by severe process conditions or cost (*e.g.*, pressurized fluidized-bed combustion).

We selected acoustic measurements for study because of our qualitative observation that audible sound changes correlate with fluidization state. In particular, rhythmic "whooshing" sounds associated with rising bubbles seem to be a characteristic feature of many fluidized beds. Acoustic measurements are also attractive from the standpoint that they can be completely nonintrusive and are not subject to erosion, corrosion, or plugging. Although we found we could clearly distinguish fluidization states in laboratory beds by ear, an inspection of the raw acoustic signals showed them to be highly complex with a broad frequency spectrum. Thus it appears that the human ear does some rather sophisticated processing of the raw bed sounds.

From the results of this study we demonstrate that, at least in some cases, it is possible quantitatively to distinguish fluidization states by analyzing passive acoustic signals from the bed. Further, we show that acoustic signals can provide an alternative source of fluidization information which can be used to complement or even replace dynamic pressure measurements. Our working hypothesis is that acoustic signals from fluidized beds contain information about both microscale events (*e.g.*, particle-particle and particle-wall collisions) and macroscale events (*e.g.*, bubbles, global bed motion). The degree to which useful fluidization diagnostics can be developed depends upon the ability to separate these two different types of information.

In the following discussion, we illustrate signal processing techniques that work well for beds with large particles operating in a slugging or near-slugging mode. Our technique allows us to determine physical bubble/slug features and nonlinear dynamical (*i.e.*, chaotic) features which are important to bed performance and scale-up.

* 414 Dougherty Engineering Building, Knoxville TN 37996-2210 USA
** Oak Ridge TN 37831-8087 USA
***P.O. Box 880, Morgantown WV 26507-0880 USA
† Received August, 1997

2. Background

Many different measurement systems have been used to monitor fluidized-bed dynamics (*i.e.*, observe the time evolution of the bed or its parts), ranging from sophisticated three-dimensional x-ray and capacitance imaging to optical and conductivity probes to flush, wall-mounted pressure taps. Example descriptions of many of these techniques are given in Clark *et al.* [1], Clift and Grace [2], Fan [3], Geldart [4], and Kühn *et al.* [5], and reviews are given by Yates and Simons [6] and Chaouki *et al.* [7].

Recent studies of the nonlinear and chaotic nature of fluidized beds have focused primarily on high-speed pressure measurements because they are relatively easy to make (at least in the laboratory) and they are commonly available on commercial beds. It is also believed that, at least in bubbling beds, pressure measurements strongly reflect the bubble patterns that dominate heat and mass transfer. Skrzycke *et al.* [8], Hay *et al.* [9], Schouten *et al.* [10], vander Stappen [11], and Karamavruç and Clark [12] illustrate implementations of dynamic pressure measurements and analysis for bubbling or slugging beds.

Studies of acoustic measurements such as that by Cody *et al.* [13] have focused primarily on microscale dynamics; specifically, on the "random" component of particle motion associated with the granular temperature. In contrast, we are primarily interested in obtaining information about larger-scale dynamic phenomena such as bubbles and slugs.

We specifically want to use acoustic signals collected externally either through the bed wall or from the surrounding air to make inferences about fluidization quality. There are a number of practical problems associated with interpreting such signals, among which are attenuation or modulation of the sound by the bed wall and surroundings, background noise (*e.g.*, from gas flow or building vibrations), and distinguishing features associated with large-scale, collective solids motion from small-scale individual particle motion.

In order to start with a well-defined problem, we ran our experiments with ambient-temperature, transparent beds of large particles (*i.e.*, particles in Geldart groups D and B). Our objective was to explore the potential for extracting information from bed sounds that would be useful for diagnostics and possibly control. In the discussion below, we do not mean to imply that our results can be extended generally to all beds. Rather, we propose that our basic concepts for sound processing are likely to be suited for slugging conditions with Group D or B particles.

3. Experimental apparatus and procedure

In this study we investigated three different bed sizes and five different particulate solids. The first fluidized bed consisted of a 7.6-cm-diameter by 68-cm-long acrylic tube equipped with a perforated-plate grid. The grid contained 185 0.15-cm-diameter holes. Air was drawn through the bed by an acoustically insulated blower. Various materials, including an ellipsoidal crisp rice cereal with spherical equivalent diameter of 0.58 cm and density of 0.107 gm/cc, millet seed with equivalent diameter of 0.35 cm and density of 0.97 gm/cc, and corn (maize) with equivalent diameter of 0.91 cm and density of 1.25 gm/cc, were fluidized in the bed. Settled bed heights ranged from 15 to 45 cm. Sounds from the bed were captured by a directional microphone, then bandpass filtered (1600−6300 Hz) through a graphic equalizer and recorded with a DAT recorder at 44.1 kHz. After the experiment, the recorded sounds were processed by passing them to a computer sound card and digitizing at 22.05 kHz.

The second fluidized bed consisted of a 10.2-cm-diameter by 260-cm-long plexiglass tube. Regulated pressurized air from the building compressor was introduced into the plenum, where the air passed through seven tuyeres into the bed. The bed material was uniform 0.45-cm-diameter steel spheres with material density of 7.5 gm/cc, and the static bed height was 23.5 cm. The sound system was an analog sound-level meter, and the meter output signal was recorded, as-measured or bandpass filtered (0.1−6 Hz), with a 12-bit digitizing oscilloscope (Nicolet 440) at 200 Hz. The meter was set to a fast response rate with an "A" weighting, which integrated the acoustic intensities between 0.5 and 10 kHz, and was mounted horizontally 2.5 cm from the bed wall 17.5 cm above the grid. Additionally, a Baratron differential pressure transducer measured the pressure drop between taps located 10 and 23 cm above the distributor. The pressure signal was bandpass filtered (0.1−20 Hz) and recorded with the digitizing oscilloscope at 200 Hz.

The third fluidized bed was a 15.9-cm-diameter by 280-cm-long plexiglass tube with a similar air supply system as the 10.2 cm bed. The bed material was polyethylene powder between 0.25 and 1.0 mm diameter (0.63 mm mean diameter) with a particle density of 0.83 gm/cc, and the static bed height was 31.8 cm. Based on size and density, these particles are classified as Geldart Group B. The sound system was a piezoelectric acoustic pickup (model AGT 100 from Engineered Products Marketing Ltd. of St. Thomas,

Ontario, Canada), which is commercially produced for the amplification of acoustic guitars. The output from the pickup was bandpass filtered (0.1−20 Hz) and recorded with the digitizing oscilloscope at 200 Hz. Additionally, a Baratron differential pressure transducer measured the pressure drop between taps located 18.5 and 28.5 cm above the distributor, and the pickup was mounted on the outside bed wall 23.5 cm above the distributor between the two pressure taps. The transducer signal was bandpass filtered (0.1−40 Hz) and recorded with the digitizing oscilloscope at 200 Hz.

The filter settings for the latter two beds were chosen to enhance signal features associated with bubble and slug events, which were expected to be primarily concentrated in frequencies less than 30 Hz [8]. Such filtering also reduces 60-Hz contamination from nearby AC power systems and prevents signal aliasing.

For all three beds, we recorded between 20 and 300 seconds of sound from each bed after it was fully fluidized. As bubbles or slugs approached the surface, they expanded the solids locally and caused the surface to rise. Particle-particle or particle bed wall collisions during this expansion, rise and subsequent collapse appear to be the source of the "whooshing" sound captured in the recordings. With the 7.6-cm bed system, there was significant background noise from the nearby blower and other sources, whereas the 10.2- and 15.9-cm bed systems were relatively free of background noise.

4. Results

4.1 General features of our acoustic signals

Figure 1 illustrates typical acoustic time series from the three different measurement systems. The microphone time series from the 7.6-cm bed contains much high-frequency information, but the low-frequency amplitude modulation appears to reflect bubbles. The time series from the 10.2- and 15.9-cm beds appear less complicated, partly because of the nature of the instrumentation and partly because of signal preprocessing. The time series from all three measurements exhibit longer timescale (0.5 to 1.0 sec) dynamics corresponding with slugging and overall bed motion. Thus, one expects that an appropriate filter could emphasize either small- or large-scale dynamics, depending on the cutoff frequency.

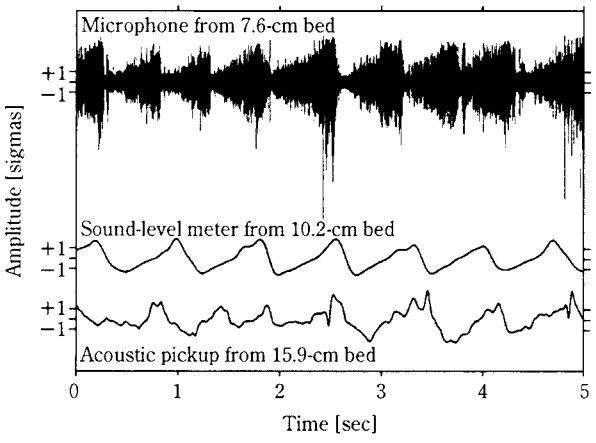

Fig. 1 Segments of typical acoustic-sensor measurements. Notice the predominant longer-timescale (0.5−1.0 sec) oscillations or modulations in all time series.

4.2 Slugging patterns

The general fluidization behavior that we observed followed patterns described in Daw *et al.* [14] and M'chirgui *et al.* [15]. Specifically, we observed a transition from defluidized solids to turbulent fluidization as gas velocity was increased. For gas flows slightly above the *minimum fluidization velocity*, U_{mf}, particles near the bed surface vibrate but experience no net translation. The layer of vibrating particles deepens with increasing flow rate, but the movement still occurs at spatial scales on the order of 1−2 particle diameters. Pressure differential measurements across the layer of vibrating particles suggest complex dynamics involving a large number of inter-particle collisions, but these fluctuations are very small relative to those in the slugging regime.

With further increase in gas flow, macroscopic motion begins in the form of gas bubbles. The bubbling regime for Group D particles occurs only over a narrow flow range and changes abruptly to slugging at higher flow, whereas the bubbling regime for Group B particles occurs over a wider flow range before slugging occurs. In slugging, each rising bubble spans nearly the entire cross section of the bed and pushes a large mass of particles in front of it. We refer to each set of upward-moving particles as a *solid slug*, and the gas pocket is referred to as a *slug*. Particles move downward through and around the rising slug until it reaches the top of the bed, whereupon a settled bed is re-established, and the cycle repeats.

As the fluidizing velocity approaches a critical value, slugging becomes nearly periodic and appears to be very regular. We refer to this condition as *maximum stable slugging* and to the critical gas flow as the *maximum stability flow*, U_{mss} [14]. As flow increases beyond U_{mss}, the slugging amplitude increases and the time interval between slugs becomes more irregular. This irregularity occurs in the form of intermittent "stutters" in the otherwise periodic slugging

pattern. Eventually, as the gas flow reaches a significant fraction of the terminal flow, fluidization approaches the turbulent regime.

4.3 Slugging diagnostics

For steel particles in the 10.2-cm bed, acoustic and pressure data were recorded at three fluidization conditions. **Figure 2** displays representative time-series segments of the acoustic and pressure measurements at flows of U/U_{mf} of 1.3, 1.4 and 1.7. The time series in these plots have been normalized to have unit standard deviation. From this figure, it is apparent that the acoustic and pressure signals provide complementary information, although there is a visible phase difference. This phase difference is actual and not an artifact of the lowpass filtering. The fluidization states for U/U_{mf} values of 1.3 and 1.4 (both near U_{mss}) are fairly regular and very similar, whereas that at U/U_{mf} of 1.7 is less regular and rather different than the other two states.

For polyethylene particles in the 15.9-cm bed, acoustic-pickup and pressure data were recorded at three fluidization conditions. **Figure 3** displays representative time-series segments of the acoustic and

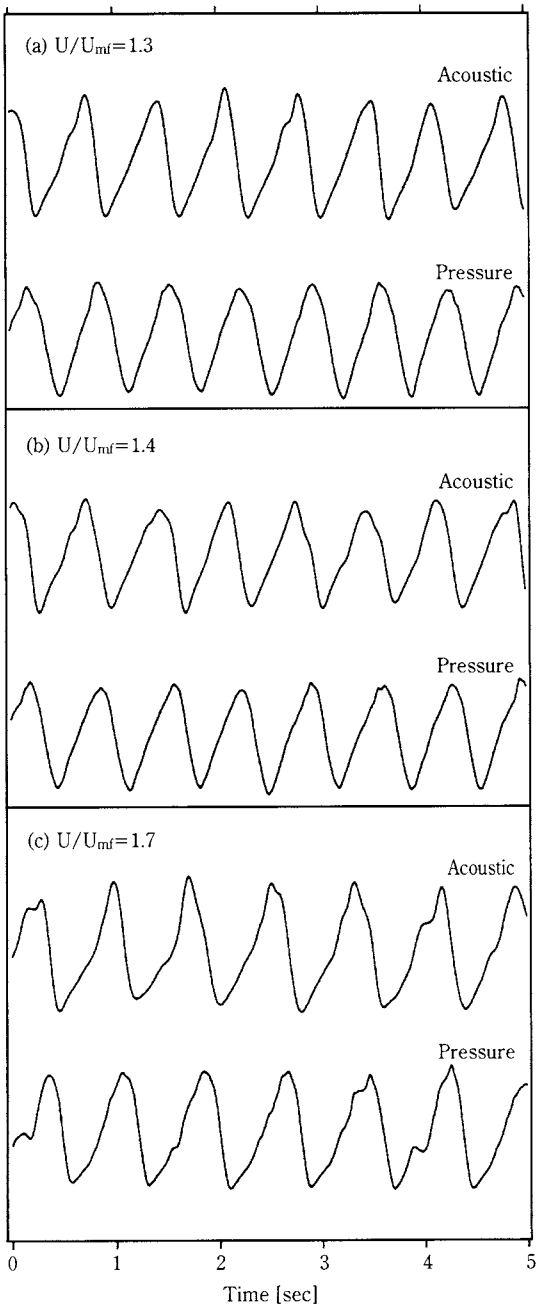

Fig. 2 Filtered sound-meter and pressure time series from the 10.2-cm bed at three different fluidization conditions.

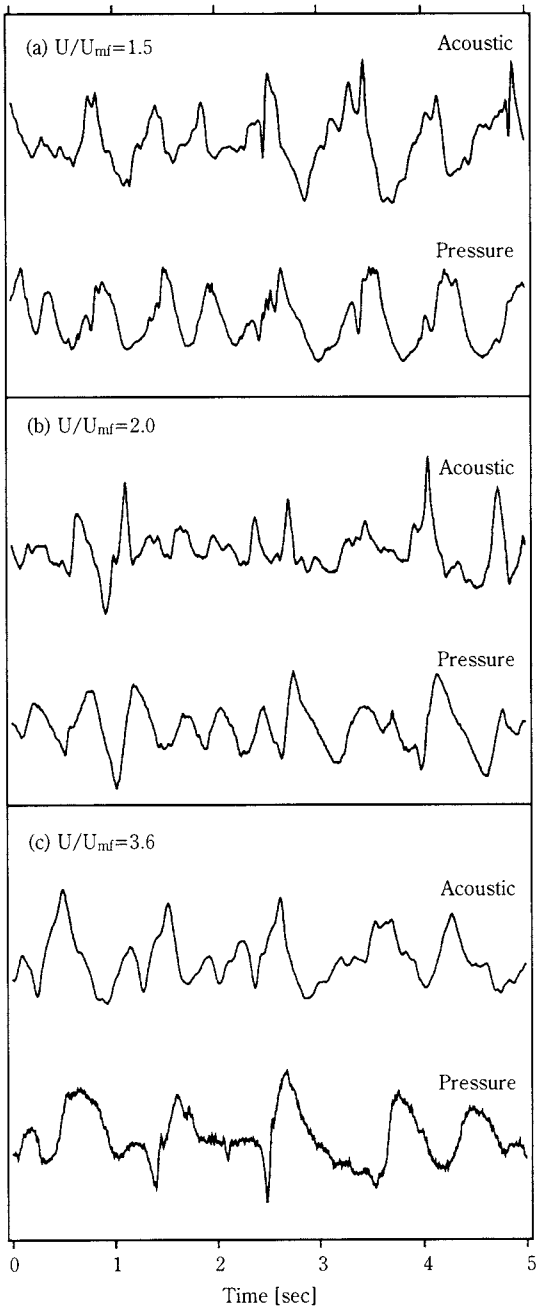

Fig. 3 Filtered acoustic-pickup and pressure time series from the 15.9-cm bed at three different fluidization conditions.

pressure measurements at flows of U/U_{mf} of 1.5, 2.0 and 3.6. The acoustic pickup appears to detect vibrations along the wall corresponding to the disturbance of particles caused by a bubble passage. However, the maximal vibratory disturbance occurs when the bubble has passed through the bed and the solids collapse, as the acoustic signal precedes peaks in the pressure signal with sharp peaks. At the highest flow condition (**Figure 3(c)**), the bed is slugging and vibrating very vigorously, so the acoustic signal, lowpass filtered at 20 Hz, appears fairly noisy. The figure displays the acoustic signal lowpass filtered at 4 Hz, which helps to highlight large-scale features as seen in the simultaneously measured pressure signal. Thus, for sharp changes in the pressure signal, corresponding large peaks in the acoustic signal are visible.

4.4 Physical interpretation of acoustic signals

It is evident from **Figures 2–3** that acoustic signals correlate fairly well with pressure signals. Visual observation of a slugging bed in the acrylic tubes also indicates a correlation of sound with slug motion and that most of the sound comes from the particles flowing around or falling through the slug. To demonstrate this correlation, slugging frequencies were measured in the 7.6-cm bed by both visual observation and by recording and counting the acoustical pulses. The measurements were made with several materials over a range of fluidization velocities. **Figure 4** shows the strong correlation between the visually and acoustically determined slug frequencies. The deviations were cases in which small bubbles were present and there was some uncertainty, either visually or acoustically, in determining whether a bubble was actually present.

Taking the impact of particles falling around or through slugs as the principal sound source, we can estimate the relationship between acoustic measurements and physical parameters. We assume particles free fall and accelerate prior to impact. The kinetic energy of a particle at impact equals its potential energy at the start of its fall:

$$K.E. = m_p\, g\, L_{slug} \tag{1}$$

where m_p is the mass of the particle, g is the acceleration of gravity and L_{slug} is the length of the slug.

The rate of impacts can be related to the slug rise velocity. For the slug to rise, an equal volume of solids must flow around or fall through the slug. Multiplying this volumetric flow rate by the bulk density gives the mass flow rate:

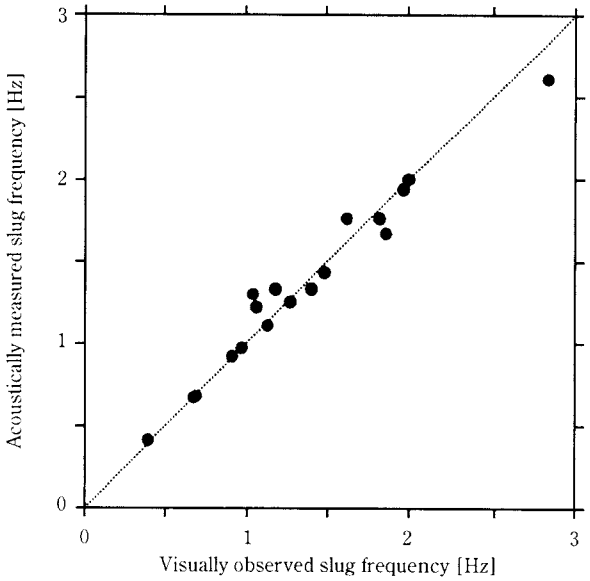

Fig. 4 Correlation between visually observed and acoustically measured slugging frequencies. Results are for two different solids over a range of bed depths and fluidization velocities: corn (23-cm bed height, 143<U<174 cm/sec; 35-cm bed height, 137<U<159 cm/sec) and millet (15-cm bed height, 65<U<95 cm/sec; 30-cm bed height, 77<U<112 cm/sec; 45-cm bed height, 68<U<138 cm/sec).

$$Mass\ flow\ rate\ of\ particles = \rho_{mf}\, U_{slug}\, A_{tube} \tag{2}$$

where ρ_{mf} is the density of the solids at minimum fluidization, U_{slug} is the rise velocity of the slug, and A_{tube} is the cross-sectional area of the tube. The number of particles falling per second equals the mass rate divided by the mass of a single particle. The rate of total kinetic energy released from the impact of falling particles is:

$$Total\ rate\ of\ K.E. = g\, \rho_{mf}\, A_{tube}\, L_{slug}\, U_{slug} \tag{3}$$

Only a fraction, α, of the total kinetic energy will be converted to acoustic energy, transmitted through the wall, and captured by the microphone and recorded. The slug rise velocity is proportional to the square root of the slug length [16]. Substituting for the slug velocity, including the α, and collecting the constant terms into a parameter Z gives:

$$Rate\ of\ acoustic\ energy\ recorded = Z\, L_{slug}^{3/2} \tag{4}$$

where

$$Z = \alpha\, g\, \rho_{mf}\, A_{tube} \sqrt{\frac{g}{2+\left(\frac{A^*}{1-A^*}\right)^2}} \tag{5}$$

A^* is the ratio of the slug cross-section to the bed cross-sectional area. In round-nosed slugs this is usually about 0.75 and in wall slugs about 0.82.

Slugs form in fluidized beds by coalescence of small bubbles released at the grid. They continue to grow as long as any bubbles remain within about two bed diameters of them. During the growth period, the slug length is increasing and therefore the acoustic intensity will increase. A reasonable assumption for the rate of growth is that the slug collects all of the gas in excess of minimum fluidization velocity, so the slug length increases linearly with time. The acoustic intensity therefore increases with time to the 3/2 power. Once the stable size has been reached, the slug length will remain constant and the acoustic intensity will remain constant.

Because the acoustic energy is released during discrete impact events, the signal consists of numerous spikes superimposed on a background noise signal. The energy release in each impact may vary depending on the exact angle between the centers of the impacting particles. Essentially the parameter α varies with each impact. The raggedness in the microphone signal in **Figure 1** illustrates this point. An integral of the RMS value of the acoustic signal over the duration of the passage of a slug through the bed can be used to smooth out these impacts and variations. We divide the slug history into a growth period ending in t_{growth}. This period is followed by a stable non-growing period which ends when the slug reaches the surface at $t_{surface}$. With these definitions, the integral of the RMS becomes:

$$Integral\ RMS = Z(U - U_{mf})^{3/2}\frac{2}{5}t_{growth}^{5/2} + Z\,L_{slug}^{3/2}(t_{surface} - t_{growth}) \qquad (6)$$

where U is the bed superficial velocity.

Figure 5 presents the integral RMS signal for slugs in a fluidized bed. The experiments were performed in the 7.6-cm bed with millet seed, fluidized at 110 cm/sec. Each point is derived from the signal for an individual slug. Most slugs appear reasonably similar in size and velocity with a relatively small number of small bubbles. The upper line in the figure has a slope of 1, illustrating the linear relationship of the RMS integral with duration for stable slugs. The lower line with a slope of 2.5 is what would be expected for slugs during their growth stage. The data in this region show more scatter, probably because there are fewer impacts being averaged for each signal. However, the trends seem to be consistently above the 2.5 sloped line, indicating some less-sensitive dependence. Data from other velocities and bed conditions give similar results. The figure suggests that the basic interpretation of the origin of acoustic signals is correct, but more experimental work is needed to generalize these results.

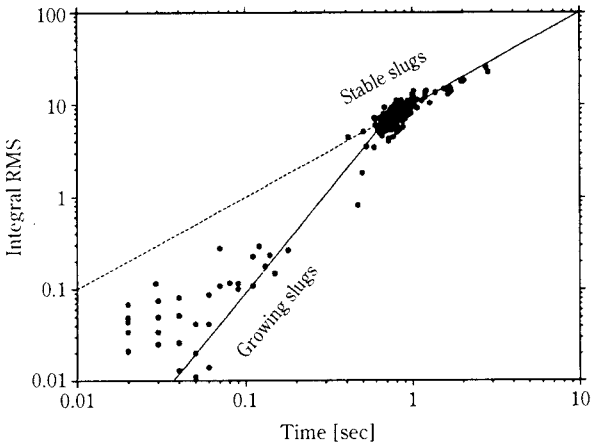

Fig. 5 Audio signal dependence on time. Lines represent expected behaviors based on **Eq. 6**.

4.5 Linear and nonlinear dynamical features

We employ three widely used time-series statistics for characterizing the recorded signals: power spectral density function, mutual information and Kolmogorov entropy.

We use a standard FFT-based power spectral density (PSD) function estimator to describe the frequency content of recorded signals. Similar PSDs between simultaneously measured acoustic and pressure signals should help to demonstrate that acoustic measurements contain similar and complementary frequency information to pressure measurements. As noted recently by other researchers, PSDs are of limited usefulness for characterizing fluidized beds because they assume an underlying linear structure in the signal [17,18]. This assumption does not hold when strong nonlinearities are present, and the resulting spectra can be inadequate to distinguish significantly different fluidization states.

The mutual information function [19] has become a standard tool in nonlinear signal processing, and the bivariate mutual information function has been demonstrated as a useful tool to measure coupling between simultaneously measured signals in fluidized beds [20,21]. Mutual information measures the amount of predictability of a test signal as a function of time based on a reference signal. Given two simultaneous measured time series, R for reference and T for test, the average mutual information of a future or past measurement T_{i+k} with respect to present measurement R_i is

$$I(R_i \mid T_{i+k}) = H(R_i) + H(T_{i+k}) - H(R_i \mid T_{i+k}) \qquad (7)$$

where $H(R)$ and $H(T)$ are unconditional entropies of measurements R and T and $H(R|T)$ is the conditional entropy of T given R, and k is the delay. Entropy takes the form

$$H(X) = -p(X_j) \log p(X_j) \quad (8)$$

where $p(X)$ represents the binned probability of event X, where j is summed over all bins. For base-2 logarithms, H and I are expressed in bits.

Large values of mutual information denotes strong coupling between the signals. When k is allowed to range from negative values to positive values, the average phase differences between the signals are highlighted. For a peak in I for time series T with respect to R, for $k<0$ certain events in T are said to "lead" those in R, whereas for $k>0$ certain events in T and said to "lag" those in R. For physical systems in which measurement errors or unstable dynamics are present, the amount of mutual information is expected to decrease as the delay increases.

Kolmogorov entropy quantifies the amount of information loss in a signal, and we use a form of the maximum-likelihood estimator of Kolmogorov entropy (K_{ml}) by Takens [22]. The K_{ml} has been proved to be a reliable standard measure of fluidized-bed pressure signals [10,11]. As described by Schouten *et al.* [22], it is necessary to specify an appropriate embedding window and an upper lengthscale for determining maximum-norm separations between trajectory segments (*i.e.*, points on the embedded trajectory). We use the term "entropy spectrum" to describe the values in K_{ml} when either the embedding window or the upper lengthscale is varied and the other parameter is held constant [23].

A useful measure based on the maximum-likelihood Kolmogorov entropy is to normalize the entropy value with respect to the entropy value taken from a randomized time series with the same probability distribution as the test time series. This "normalized entropy" thus ranges in value from 0 (purely periodic and infinitely predictable) to 1 (purely random and unpredictable).

Figure 6 shows PSDs for the acoustic and pressure signals at three fluidization conditions in the 10.2-cm bed. With both signals, the PSDs for U/U_{mf} of 1.3 and 1.4 are very similar and dissimilar to those for U/U_{mf} of 1.7. The differences between the U/U_{mf} of 1.3 and 1.4 PSDs are most visible in the 0−1 and 4−5 Hz ranges in the acoustic signal and beyond 2 Hz in the pressure signal, and differences at other frequencies are hard to distinguish as either being real dynamical differences or artifacts of the PSD construction

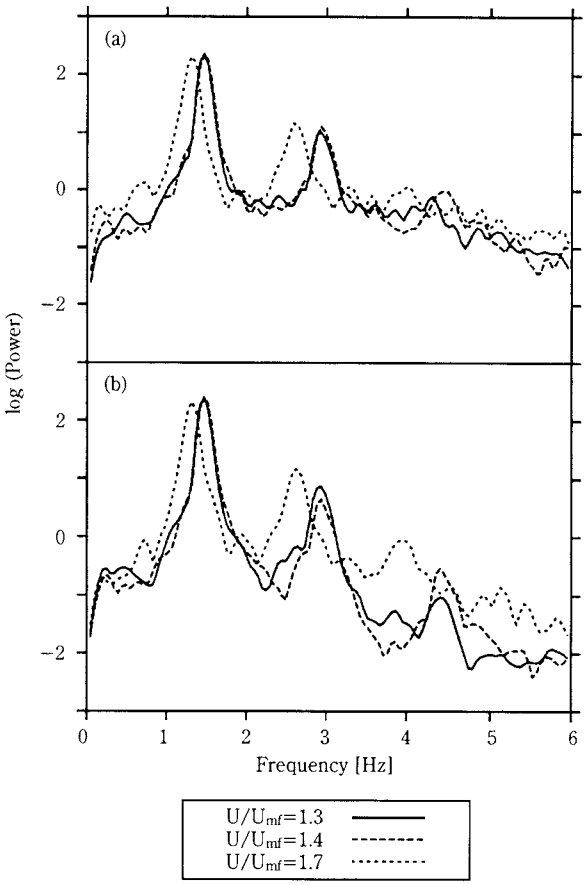

Fig. 6 PSDs for acoustic (a) and pressure (b) signals from the 10.2-cm bed at three fluidization conditions.

(limited, nonstationary data). However, the acoustic and pressure signals share similar content in the major peaks which represent the dominant slugging frequencies. Nevertheless, it is difficult to distinguish signals at U/U_{mf} of 1.3 and 1.4 using only the PSDs and to assign a statistical confidence to degrees of difference.

We present two types of entropy spectra. In the first type, the embedding window is held constant to a value equal to the average orbital time (defined as the average number of measurement timesteps between successive up-crossings of the data mean), and entropy is calculated as a function of upper lengthscale. This type is displayed in **Figure 7**. In the second type, the upper lengthscale is held constant to a value equal to one average absolute deviation about the mean (AAD), and entropy is calculated as a function of the embedding window. This type is displayed in **Figure 8**.

In the entropy-lengthscale spectra, there are several important features. First, the spectra of the two lower-flow cases are distinct from the highest-flow case in both the acoustic and pressure signals. Second, the

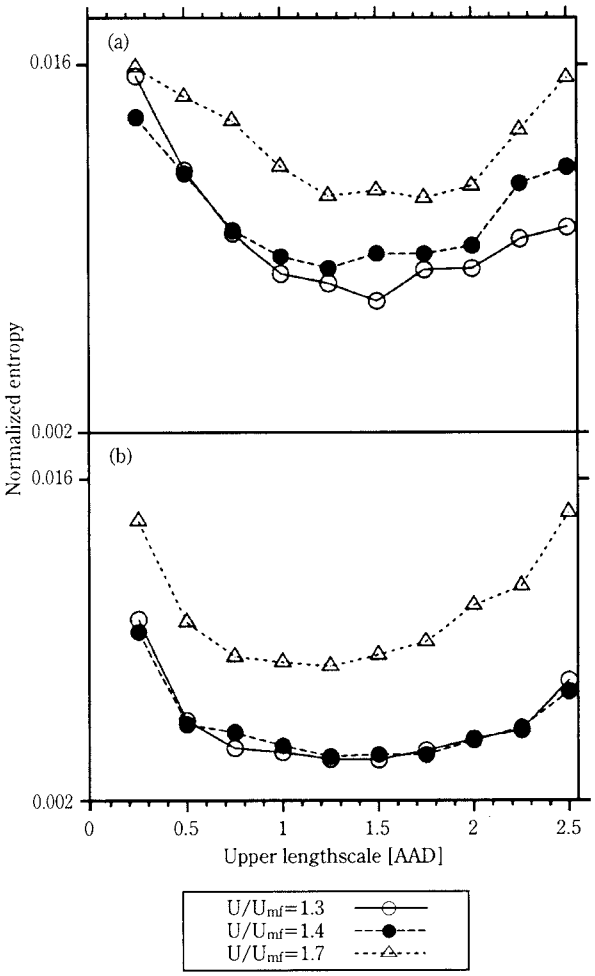

Fig. 7 Normalized entropy-lengthscale spectra for acoustic (a) and pressure (b) signals from the 10.2-cm bed at three fluidization conditions.

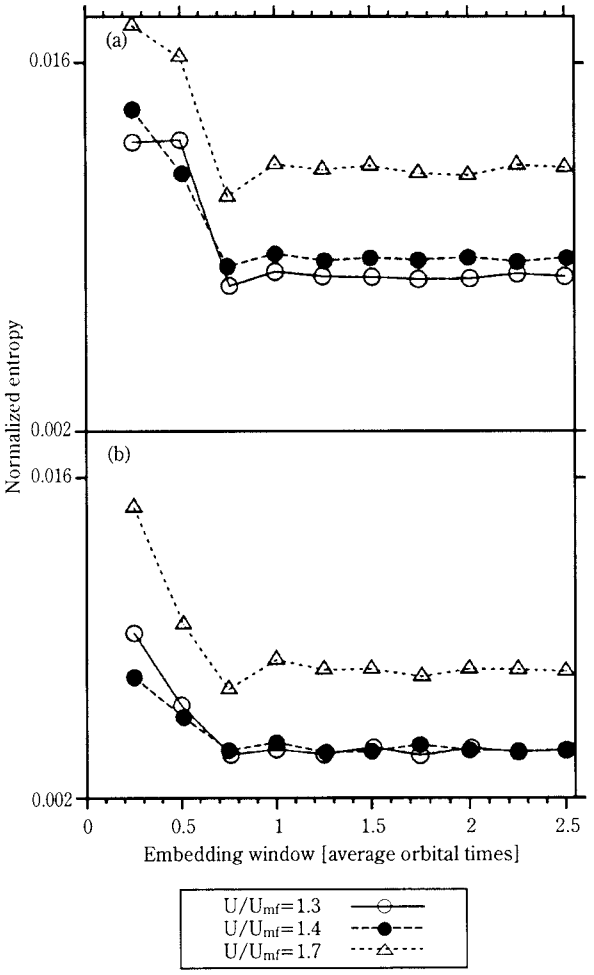

Fig. 8 Normalized entropy-timescale spectra for acoustic (a) and pressure (b) signals from the 10.2-cm bed at three fluidization conditions.

acoustic signals (**Figure 7(a)**) seem to offer better distinction between the two lower-flow cases than is seen in the pressure signals (**Figure 7(b)**). Third, entropy decreases from small (0.2 AAD) to moderate (approximately 1.5 AAD) lengthscales yet increases at much larger upper lengthscales. The lengthscale at which the normalized entropy is minimal (1.5 AAD) represents the optimal lengthscale for predictive observation based on the chosen embedding window. Fourth, entropy is lowest at U_{mss} (here, near $U/U_{mf}=1.3$ and 1.4) and increases at other fluidization conditions because maximum stable slugging implies regularity and low entropy.

In the entropy-timescale spectra, there are several prominent features. First, the spectra of the two lower-flow cases are distinct from the highest-flow case in both the acoustic and pressure signals. Second, the acoustic signals (**Figure 8(a)**) seem to offer better distinction between the two lower-flow cases than is seen in the pressure signals (**Figure 8(b)**). Third, all spectra have the same general shape – entropy is high at short timescales, decreases to a minimum (at 0.8 average orbital times), and stays fairly constant for longer timescales. Where entropy first reaches the minimal value (0.8 average orbital times) represents a sufficiently long embedding window – shorter windows result in less predictability (and higher entropy) because the cycle of the sinusoidal shape of the slugging oscillations is not well-enough defined, and the nearly periodic nature of slugging, in the fluidization cases examined, means that entropy will be low for embedding windows of several average orbital times. Fourth, entropy is lowest at the condition of maximum stable slugging and increases at other fluidization conditions.

Figure 9 shows the mutual information functions of the acoustic-pickup signals with respect to the simultaneous pressure signals in **Figure 3**. Peaks in the MIF represent timescales of strong coupling between the simultaneously measured signals. Several

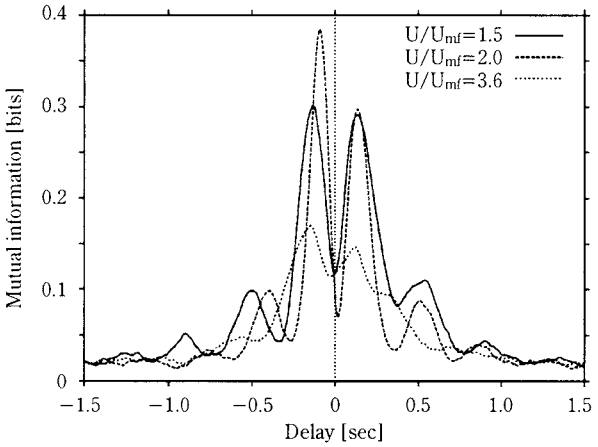

Fig. 9 Mutual information functions of acoustic-pickup with respect to pressure signal from the 15.9-cm bed at three fluidization conditions.

features are noteworthy in this figure. First, for all three fluidization conditions, the largest peaks in the MIFs occur between −0.1 and −0.2 seconds − this means that events in the acoustic signals lead or precede events in the pressure signals, as was observed in the time-series plots (**Figure 3**). Second, at long delays (>1 second), the MIF has reached the "noise floor", meaning that on average there is little discernible predictability of the acoustic signal based on the current value of the pressure signal. Third, the signals at U/U_{mf} of 3.6 have the lowest mutual information (minimal coupling between the acoustic and pressure signals), as might be expected for near-turbulent slugging. Conversely, the signals at U/U_{mf} of 2.0 have the highest degree of mutual information (maximal coupling), as might be expected for periodic slugging.

The first large peak at negative lags represents the average phase difference between the signals. Physically, the time lag between acoustic and pressure signals corresponds to their different sources. The large peaks in the acoustic signal (time series) represent the collapse of solids after a slug has erupted at the bed surface, whereas peaks in the pressure signal represent the subsequent compression wave as a new slug begins. The MIFs constitute a unique signature of the slugging state at each fluidization condition.

5. Conclusions

Based on observations with Group D and B particles under slugging conditions in three ambient, laboratory fluidized beds, it appears that significant information about the bed dynamics can be obtained with simple acoustic signal recording and processing. We were able to monitor slugging events by measuring and processing bed sounds to highlight the low-frequency sound-intensity modulation. This technique could prove useful for monitoring fluidized-bed systems, especially in hazardous systems where avoiding direct contact with the process is an advantage. Such monitoring capability could be used for process diagnostics (*e.g.*, the detection of agglomerates) and possibly for dynamic slugging control [24].

Acknowledgement

The authors thank Prof. Ke Nguyen and Mr. M. Vasudevan of the University of Tennessee for experimental assistance.

Nomenclature

A_{tube} : Tube cross-sectional area
A^* : Ratio of slug cross section to bed cross section
g : Acceleration of gravity
K.E. : Particle impact kinetic energy
K_{ml} : Maximum-likelihood estimator of Kolmogorov entropy
L_{slug} : Slug length
m_p : Particle mass
t_{growth} : Time for slug to grow to stable size
$t_{surface}$: Time for slug to rise to bed surface
U : Superficial gas velocity
U_{mf} : Minimum fluidization velocity
U_{mss} : Maximum stability flow
U_{slug} : Slug rise velocity
Z : Constant parameter
α : Fraction of kinetic energy converted to acoustic energy
ρ_{mf} : Solids density at minimum fluidization

Abbreviations

AAD : Average absolute deviation about the mean
AC : Alternating current
DAT : Digital audio tape
FFT : Fast Fourier transform
MIF : Mutual information function
PSD : Power spectral density function
RMS : Root mean square

References

1) Clark, N.N., E.A. McKenzie Jr. and M. Gautam: Differential Pressure Measurements in a Slugging Fluidized Bed, Powder Technology, 67, 187–199 (1991).
2) Clift, R. and J.R. Grace: Continuous Bubbling and Slugging, in "Fluidization", J.F. Davidson, R. Clift, and D. Harrison, eds., Academic Press, 73–132 (1985).
3) Fan, L.S.: "Gas-Liquid-Solid Fluidization Engineering", Butterworths (1989).
4) Geldart, D.: "Gas-Fluidization Technology", John Wiley and Sons (1986).
5) Kühn, F.T., J.C. Schouten, R.F. Mudde, C.M. van den Bleek and B. Scarlett: Analysis of Chaos in Fluidization Using Electrical Capacitance Tomography, Meas. Sci. Technol., 7, 361–368, (1996).
6) Yates, J.G. and S.J.R. Simons: Experimental Methods in Fluidization Research, Int. J. Multiphase Flow, 20, Suppl., 297–330 (1994).
7) Chaouki, J., F. Larachi and M.P. Dudukovic: "Non-Invasive Monitoring of Multiphase Flows", Elsevier Science (1997).
8) Skrzycke, D.P., K. Nguyen and C.S. Daw: Characterization of the Fluidization Behavior of Different Solid Types Based on Chaotic Time Series Analysis of Pressure Signals, Proceedings of the 12th International Conference on Fluidized Bed Combustion, 155–166 (1993).
9) Hay, J.M., B.H. Nelson, C.L. Briens and M.A. Bergougnou: The Calculation of the Characteristics of a Chaotic Attractor in a Gas-Solid Fluidized Bed, Chem. Eng. Sci., 50, 373–380 (1995).
10) Schouten, J.C., M.L.M. vander Stappen and C.M. van den Bleek: Scale-Up of Chaotic Fluidized Bed Hydrodynamics, Chem. Eng. Sci., 51, 1991–2000 (1996).
11) Stappen, M.L.M. vander: "Chaotic Hydrodynamics of Fluidized Beds", Ph.D. Dissertation, Technical University of Delft (Netherlands), Delft University Press (1996).
12) Karamavruç, A.I. and N.N. Clark: Local Differential Pressure Analysis in a Slugging Fluidized Bed Using Deterministic Chaos Theory, Chem. Eng. Sci., 52, 357–370 (1997).
13) Cody, G.D., D.J. Goldfarb, G.V. Storch, Jr. and A.N. Norris: Particle Granular Temperature in Gas Fluidized Beds, Powder Technology, 87, 211–232 (1996).
14) Daw, C.S., C.E.A. Finney, M. Vasudevan, N.A. van Goor, K. Nguyen, D.D. Bruns, E.J. Kostelich, C. Grebogi, E. Ott and J.A. Yorke: Self-Organization and Chaos in a Fluidized Bed, Phys. Rev. Lett., 75, 2308–2311 (1995).
15) M'chirgui, A., H. Tadrist and L. Tadrist: Experimental Investigation of the Instabilities in a Fluidized Bed Origin of the Pressure Fluctuations, Phys. Fluids, 9, 500–509 (1997).
16) Halow, J.S., G.E. Fasching, P. Nicoletti and J.L. Spenik: Observations of a Fluidized Bed Using Capacitance Imaging, Chem. Eng. Sci., 48, 643–659 (1992).
17) Stappen M.L.M. vander, J.C. Schouten and C.M. van den Bleek: Deterministic chaos analysis of the dynamical behaviour of slugging and bubbling fluidized beds, Proceedings of the 12th International Conference on Fluidized Bed Combustion, 129-140 (1993).
18) Stappen M.L.M. vander, J.C. Schouten and C.M. van den Bleek: Application of deterministic chaos theory in understanding the fluid dynamic behavior of gas-solids fluidization, AIChE Symposium Series 89:296, 91-102 (1993).
19) Fraser, A.M. and H.L. Swinney: Independent Coordinates for Strange Attractors From Mutual Information, Phys. Rev. A, 33, 1134–1140 (1986).
20) Daw, C.S. and J.S. Halow: Evaluation and Control of Fluidization Quality Through Chaotic Time Series Analysis of Pressure-Drop Measurements, Chemical Engineering Progress Symposium Series, American Institute of Chemical Engineers, Vol. 89, No. 286, 103–122 (1993).
21) Karamavruç, A.I., N.N. Clark and J.S. Halow: Application of Mutual Information Theory to Fluid Bed Temperature and Differential Pressure Signal Analysis, Powder Tech., 84, 247–257 (1995).
22) Schouten, J.C., F. Takens and C.M. van den Bleek: Maximum-Likelihood Estimation of the Entropy of an Attractor, Phys. Rev. E, 49, 126–129 (1994).
23) Finney, C.E.A., K. Nguyen and C.S. Daw: Entropic Characterization of Cyclic Variability in Internal Combustion Engines Using Chaotic Time Series Analysis, Proceedings of the 32nd Japanese Symposium on Combustion, 400–402 (1994).
24) Vasudevan, M., C.E.A. Finney, K. Nguyen, N.A. van Goor, D.D. Bruns and C.S. Daw: Stabilization and Destabilization of Slugging Behavior in a Laboratory Fluidized Bed, Proceedings of the 13th International Conference on Fluidized Bed Combustion, 1001–1014 (1995).

Author's short biography

Charles E.A. Finney

Charles Finney is a Graduate Research Assistant and Ph.D. student in mechanical engineering at the University of Tennessee, Knoxville. He received his B.A. in astronomy-physics in 1991 from the University of Virginia and B.S.M.E. in 1993 and M.S. in mechanical engineering in 1995 from the University of Tennessee. The focus of his Ph.D research is on the analysis of time-series measurements from nonlinear systems.

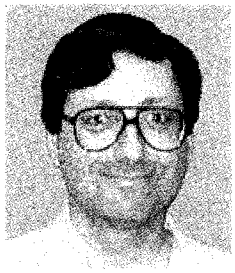

C. Stuart Daw

Dr. Stuart Daw is a research scientist at the Engineering Technology Division of the Oak Ridge National Laboratory. He also is Adjunct Professor of Mechanical and Chemical Engineering at the University of Tennessee, Knoxville. He received his B.S. in 1973 from the University of Florida and his M.S. in 1978 and Ph.D. in 1985 from the University of Tennessee, all with majors in chemical engineering. From 1973 to 1979, he was a R&D engineer with E.I. DuPont de Nemours in New Johnsonville, Tennessee, before joining the development staff at ORNL. His principal research interests include fluidization, chemical reactors, combustion, and nonlinear dynamics.

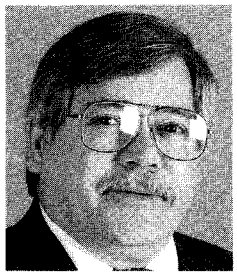

John S. Halow

Dr. John Halow is director of the Gaseous Fuels and Cleanup Division of the Federal Energy Technology Center in Morgantown, West Virginia. He received his B.S. in chemical engineering from Pennsylvania State University in 1964 and his Ph.D. in chemical engineering from Virginia Polytechnic Institute and State University in 1967. Prior to joining the Department of Energy, Dr. Halow was employed by Exxon Research and Engineering Company doing applied research and corporate consulting on fluid-solid systems. His principal research interests include fluidization, combustion, multi-phase flow, and nonlinear dynamics.

Effect of the Addition of Organic Binders on the Behavior of Iron Ore Pellets†

Monica Speck Cassola
mining engineer, PhD
*Institute for Technological Research of the State of São Paulo S.A.**
Arthur Pinto Chaves
metallurgical engineer, full professor
*Department of Mining Engineering, Escola Politécnica, University of São Paulo***

Abstract

The authors describe their experience with organic binders in pelletization plant. It started with carboxi-methyl-cellulose and hematite concentrates. The addition of sodium tri-poli-phosphate (TPP) was demonstrated to be essential. In pelletizing limestone fines, it has been shown to be possible to use dispersants like soda ash, for this particular case, it was possible to make use of no binder and to work only with the dispersant. This fact has been understood as a consequence of the dispersing effect of the chemicals. To check this hypothesis, a set of different kinds of organic dispersants were prepared to test on pellet feed, with the interesting results described herein.

The conclusion is a model for the behaviour of these binders as: 1 – the dispersion of colloidal particles on the surface of the particles to pelletise increases the viscosity in the liquid film between the particles, and 2 – it provides the physical way to link then by bridging. As a practical consequence, in principle, any dispersant may become the binder for pelletization and there is potential to achieve greater mechanical values than by using the conventional binders, bentonite and lime.

1. Introduction

The evolution of the steel industry in the last decades went in the directions of increasing the productivity of the blast furnaces, of saving coke, of keeping the uniformity of the product, of automating handling operations and of decreasing the man-power incidence. The evolution of the processes of direct reduction seeks, also, the same objectives. To reach them, one of the most important factors is the constancy of the metallurgical properties of the iron ore charge and its preparation in the form of pellets.

This tendency resulted mainly from the fact that the greater iron ore producers, with the progressive exhaustion of the richest ore bodies, must treat now lower grade ores, producing fine concentrates. As in this size they can not be used in the blast furnaces or in the direct reduction kilns, its metallurgical use depends on their agglomeration, mainly via pelletization.

The physical, chemical and metallurgical requirements for the pellets demand a narrow and continuous control of a series of process variables and their uniformity with time. The complexity of this problem is increased by the scale of the operations involved in each plant. This is of the order of three million metric tons of products per year. The fact that the product must have a low unitary value adds to that complexity.

The pelletization process is achieved by the agglomeration of ultra-fine particles of hematite, with the use of some binding agents. Spherical agglomerates, of about 8 to 20 mm diameter, are formed and then heated at high temperature.

The product, named pellet, presents the desired combination of chemical composition and compression and abrasion resistance when loaded in the blast furnace.

Furthermore, it conserves, and in general improves, in relation to the natural ores, some metallurgical

* Rua Prof. Almeida Prado, 535-05508-901 – São Paulo (SP) – Brazil, phone 00 55 11 268-2211 Ramal 246, e-mail: mrnc@dce03.ipt.br
**Av. Prof. Mello Moraes, 2373 – 05508-900 – São Paulo (SP) – Brazil, phone 00 55 11 818-5431, e-mail: apchaves@usp.br
† Received December, 1997

properties, such as reducibility, porosity and thermal conductivity.

Besides allowing the rational and economic use of friable and dusty ores, the use of pellets in the blast furnaces or in the direct reduction kilns assures higher productivity levels and easier operation than with lump ores.

The pelletization technique, and its wide scale, resulted from research and development mainly done in North America, on their low grade ores, the taconites. It can be said that the pelletization, as today practised, constitutes a recent technique, begun at the end of the decade of 1950.

2. Theoretical Aspects

In the pelletization mechanism, the ore particles are kept together by surface moisture. The water film in the space between very close particles, or even in contact, acts as a capillary, where the phenomena of surface tension (very well known from the Physics) are manifested. The surface tension not only keeps the particles together but also allows the pellet to grow. As this water evaporates, the ball will dismantle itself, unless other mechanisms seem to maintain the coherence of the particles.

It is a very well-known fact that the fine lamellar high grade hematite offers great difficulties to the formation of agglomerates. The spheres, formed with great difficulty, are not resistant to handling, and cannot be used in the steel plants.

Pellets with acceptable composition and diameter, and having the desired physical and metallurgical characteristics, can only be obtained by the use of additives. Thus must also be submitted to thermal processing in high temperatures to assure the constitution of new phases and the recrystallization, at least partial, of the original hematite.

Moreover, with high specific gravity minerals like hematite, the surface tension of water by itself is not adequate to maintain cohesion. Therefore "binders" must be added to the mixture, with the objectives of:

- increasing the viscosity of the liquid phase inside the capillaries;
- maintains the integrety of the green pellets;
- helping, during heating, the formation of bridges, ceramic or iron oxide bonding, or still, the slagging in discrete points, so contributing to the resistance of the pellet after firing.

ULRICH and HAN's work[1] is one of the first ones to evidence the decisive influence of the formation of the new phases in the pellets. In summary, the new phases and the recrystallization of small granules inserted among the hematite crystals give to the heated pellets the properties of strength, porosity, thermal conductivity and reducibility, demanded by the good operation of the reduction kilns. Such a product presents better behaviour than natural ores, what explains the gains in productivity and coke economy in the blast furnaces. The processes of direct reduction are in general still more exigent in relationship to the characteristics of the charge but, in principle, it is always possible to adjust the production conditions so that they behave as demanded by those ovens.

ARIAS and MANHEIMER[2], studying ore from CVRD[1], clearly identified the textural modifications, and thus the alteration of the original nature of the hematite. At the temperature of 1100°C, the finest particles, of about 2 mm diameter, start to recrystallize and to grow. Such particles distribute themselves among larger lamellar granules. These manifest changes in shape. At such a temperature, also the silica gangue granules, those of lime, of limestone or of the added bentonite, start to constitute a new binding phase, which ULRICH and HAN[1] believe to be a ferrite.

Increasing the temperature up to 1370°C, appreciably increases the pellet strength followed by an increase in the FeO grade, due to the transformation of part of the hematite in magnetite. Furthermore, and what is very important, significant changes in the chemical composition happen, lowering the sulphur and phosphorus grades*).

An appreciable growth of the grains is observed: grains which had 2 to 4 mm diameter at 1315°C grow to 7 to 15 mm when the temperature comes to 1400°C. *The presence of fines is a factor of amount importance for the improvement of the pellet properties.*

The chemical composition of concentrates for pelletization is very strict, specially for those destined to direct reduction. Specifically, they admit very low limits for contaminants.

The most widely used binder for iron ore is bentonite. This thixotropic clay-mineral gives the pellets the desired properties, has a low price and does not interfere with their metallurgical behaviour. However, the amount to be added is relatively high (about .5% by weight), which brings significant contamination with silica and alumina.

Chemical binders able to burn without leaving any residue would be extremely interesting. They would have over bentonite many advantages like:

*) CVRD – Companhia Vale do Rio Doce – Brasil

- as they are industrial products, they do not suffer quality variations;
- the added amount may be reduced, what is important from the economic point of view.

Several products have been studied, such as carboximethyl-cellulose (CMC), guar gum, hemicellulose, starch acrilate and many others. The disadvantages verified in practice are especially their price, the possibility of deterioration for some of the products and the bad results after firing.

3. Experimental Work

3.1 Preliminary experiments

In 1992, LIMA[3,4,5] presented his PhD thesis on the use of CMC as a pellet binder. The previous published experience with the use of organic binders had taken pellets poor mechanical properties, especially hot, of very high production costs, or to very high moistures — to the point of causing the deformation of the pellet (ovalization) under its own weight. These problems were overcome by him via the addition of a dispersant, in the case the sodium tripolyphosphate (TPP).

The hematite concentrate was supplied by CVRD and the CMC by Ultraquímica São Paulo S.A. The pellets were built in a disk pelletizer 1 m diameter, 43° inclined, 19 rpm. The feed mixture was prepared in a Sympson mixer. After pelletization, 10 pellets were taken, randomly for the measure of the green strength and an other 10 pellets for the measure of the dry strength, an other 5 pellets were finally tested as to the number of successive falls from the height of 45 cm.

After all, each lot was checked against the resistance to the thermal shock, according to CVRD's standards. The conclusions of this experimental work were the following ones:

- CMC presents good possibilities for use as a binder. It shows, however, significative result variations depending on the considered product. The greater the viscosity of the solution of CMC in water, the better is the binding power and the larger is the difficulty for dissolving it;
- by itself, CMC is not suited, because the resulting pellet does not resist to high temperatures, undergoes disintegrated. This problem was solved by the addition of TPP, which was the important contribution of LIMA;
- this dispersant improves the mechanical properties either green or after firing. There is an optimum value for its addition, which gives the best hot properties, as well as an optimum value for the rate CMC/TPP;
- the addition of soda ash to the CMC/TPP mixture has a synergetic effect.

In 1993, CHAVES[6,7,8,9] studied, in North America, the problem of agglomerating limestone fines. He started to work using CMC and TPP, as well as bentonite and portland cement. In the effort to replace TPP for products of lower price, other dispersants were checked. Finally, the advantages and a convenience of soda ash were identified. The following step was to vary the rate CMC/soda ash in the mixture. It was verified that the mechanical properties of the pellet improved with the amount of soda ash and that the best results were attained with 100% of soda ash (that is to say — without CMC!).

In 1996, CASSOLA AND CHAVES[10,11] worked with chemicals provided by Hoechst of Brazil (now Clariant) and a sample of pellet feed supplied by FERTECO, as will be described in sequence.

Two research lines were followed: the first one considered the classic *modus operandi* of using CMC plus TPP. The second one considered the substitution of CMC for alternative products.

The tests with CMC showed that TPP alone provided more resistance than the mixture CMC/TPP. This allowed the elaboration of the work hypothesis that: *the truly important effect in the acquisition of mechanical strength for the pellets is due to the action of the dispersant and not to the action of the organic binder;* this will be described later. To check this conclusion, Hoechst prepared different organic dispersant formulas which were tested and compared.

3.2 Systematic experiments

The research program consisted of the evaluation of the behaviour of different organic and inorganic binders, in different amounts. This was done via agglomeration through pelletization and characterization of the agglomerates with relation to their mechanical resistance.

The pellet feed sample was supplied by FERTECO. It was homogenised without previous drying. Representative samples were taken for size distribution analysis, chemical analysis, determination of the humidity and preparation of mixtures with the organic binders.

The characterization test had the purpose of determining the physical characteristics of the pellet feed. The humidity of the sample was determined by drying it for 105°C till constant weight. The actual specific gravity of the samples was determined in a

picnometer and the chemical analysis was done via conventional methods. The results are presented in **Table 1**.

The size distribution analysis was done by dry screening with the Tyler series of sieves. The results are presented in **Table 2**.

Table 1 Chemical analysis, humidity and actual specific weight

humidity (%)	specific weight (g/cm^3)	oxide (%)			
		P_2O_5	Al_2O_3	SiO_2	Fe_2O_{3t}
9.02	4.4	.11	.81	3.1	92.3

Table 2 Size distribution of the pellet feed

mesh Tyler (#)	FERTECO iron ore	
	% weight	% cummulative
−48+65	.30	.30
−65+100	.85	1.15
−100+150	1.89	3.04
−150+200	5.54	8.58
−200+270	22.81	31.39
−270+325	28.52	59.91
−325+400	33.78	93.68
−400	6.32	100.00

The mixtures were made in an Eirich muller mixer, model R-7, with capacity of 70 l and speed of 80 rpm. The minimum amount of material for each recipe was 3.0 kg for the pelletization tests. The tests were accomplished with moist ore or with dry ore, but the amount of chemicals added was always calculated on a dry basis.

For the test work, the following binders were used: P/D2114/E11, P/D2114/E12, P/D2114/E69, P/D2114/E21, P/D2114/E24, FONGRABOND, TPP, lime, limestone and bentonite.

As a research cryterion, these three last products were always tested as a **reference "standard"** formulation. The organic chemicals are commercial line products or developed by Hoechst specifically for this program. For commercial reasons we are not able to provide their structural or physical-chemical characteristics.

The chemicals were diluted with mild agitation in a magnetic mixer/heater under low temperatures, so as to avoid any eventual degradation. The limestone, lime and bentonite were always added dry.

The chemicals dilution in the solutions varied due to their high viscosity. Every morning a fresh amount

Table 3 Pelletization tests results. Sample of iron ore from FERTECO

Binders dosage (%)				crushing strenght (N/pel)		Shock temperature (N/pel)				
				green	dry	200°C	300°C	400°C	500°C	600°C
iron ore		—		.33	.61	.60	.56	.33	.41	.47
limestone	2.60	bentonite	.70	.46	1.75	2.00	2.10	1.60	1.10	1.80
limestone	2.60	lime	1.50	.32	2.40	1.70	1.90	1.70	2.00	1.60
PD/2114-E11	.05	TPP	.10	.60	3.30	3.00	3.00	1.16	.18	1.54
PD/2114-E11	.10	TPP	.05	.53	1.38	1.26	1.21	1.17	1.82	1.54
PD/2114 E11	.15	—	—	.35	.55	1.76	.47	.22	.70	.18
PD/2114-E12	.05	TPP	.10	.54	2.70	1.60	.80	1.46	.70	1.20
PD/2114-E12	.10	TPP	.05	.65	1.38	1.06	1.43	.71	.88	.80
PD/2114-E12	.15	—	—	.28	.34	.16	.04	.09	.00	.07
TPP	.05	—	—	.45	1.65	1.50	1.60	1.60	1.50	1.30
TPP	.10	—	—	.47	1.65	1.20	1.64	1.29	1.24	1.00
TPP	.12	—	—	.49	1.25	1.20	1.40	1.44	1.47	1.00
TPP	.15	—	—	.69	4.15	n.d.	n.d.	2.20	n.d.	1.58
TPP	.20	—	—	.40	3.35	3.30	2.70	1.50	1.50	1.10
FONGRABOND	.05	—	—	.22	.80	.63	.54	.56	.48	.50
FONGRABOND	.10	—	—	.36	1.65	1.49	.80	1.10	.96	1.08
FONGRABOND	.10	TPP	.05	.29	1.95	1.60	1.62	1.35	1.40	1.12
FONGRABOND	.12	—	—	.38	2.25	1.22	1.28	1.17	1.19	1.32
FONGRABOND	.15	—	—	.49	2.50	1.40	1.70	1.28	2.02	1.35
FONGRABOND	.20	—	—	.50	4.05	3.10	2.80	2.60	1.84	1.50
PD/2114-E24	.10	TPP	.05	.28	1.05	.76	.93	.64	.79	.34
PD/2114-E24	.15	—	—	.41	.66	.48	.40	.31	.58	.48
PD/2114-E21	.15	—	—	.31	.40	.17	.28	.10	.18	.17
P/D2114-E69	.15	—	—	.32	.56	.46	.17	.17	.27	.21

Table 4 Pelletization tests results. Sample of iron ore from MBR

Binders	Level of addition (%)	Crushing strength (N/pel) green	dry
Bentonite Brasgel	.50	2.16	13.72
Bentonite Brasgel	.75	2.45	26.95
Bentonite Brasgel	1.00	2.25	29.89
FONGRABOND	.15	2.45	22.54
TPP	.15	2.65	37.24
MBR iron ore	—	3.53	2.55

of solution was prepared for that day. At the end of the day, the amount that had not been used was discarded.

The pelletization tests were done in a disk 1.2 m diameter with speed of 20 rpm and inclination of 45°.

The pellets were screened out when reached the range of 9.5 to 12.5 mm. The different binders were tested in varied amounts.

The pellets were submitted to the tests of successive falls either green and dry (for 105°C), green and dry strength resistance, thermal shock (200°C, 300°C, 400°C, 500°C and 600°C). **Table 3** presents the results for the whole series and the experimental conditions.

Some additional test were realized with another iron ore sample, supplied by MBR**). The results are presented in **Table 4**.

3.3 Analysis of the results

evaluation of the action of TPP

In this phase of the studies, an addition of .15% binders to the mixture was done. The rate TPP/binders varied from 0 to 100%. The tested binders were: P/D2114-E11, P/D2114-E12. Reference tests with the standard mixtures of lime + limestone and limestone + bentonite were also done. **Figure 1** shows these results.

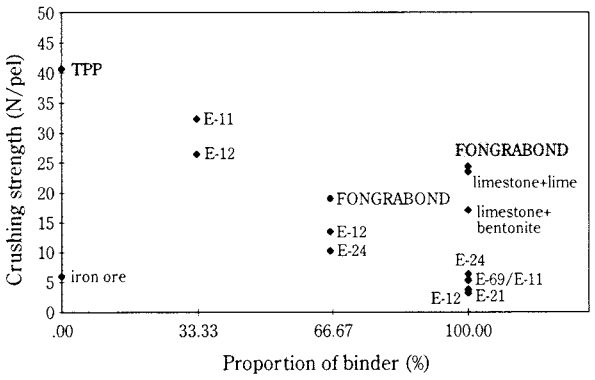

Fig. 1 Evaluation of the action of TPP

**) Supplied by MBR for the PhD thesis experimental work of Ayres F. Morgado from the Federal University of Santa Catarina.

It was verified that TPP is superior to the other chemicals, providing the best results. Even so this product has the disadvantage of introducing phosphorus in the pellet, what is undesirable.

Other reagents, when used together with TPP showed better results but, by themselves did not show satisfactory results. This lead to the hypothesis of being the dispersing effect of the chemical the main agent for their performance.

In the sequence, the best level of TPP addition to the mixture was studied and alternative products to TPP were chosen, based on their dispersant properties.

evaluation of the variation of the dosage of TPP on the mixture

The best addition to the mixture, found to be around .15%, was optimised in this stage. **Figure 2** shows the results. As one can observe, for all the addition levels (that varied of 0 to .15% TPP) there is a fall in the strength of the pellets at the level of .12% and, starting from there, the curve ascends up to .15, although .20% was the largest level tested. This behaviour repeats it self for the different sets of tests.

evaluation of the action of the other binders (dispersants actives)

To verify if the dispersing characteristic of TPP was what in fact contributed for the improvement of the mechanical strength of the pellets, a series of tests was accomplished with other pure dispersants. These were FONGRABOND, P/D2114-E21, P/D2114-E69 and P/D2114-E24. The results were compared with the **standard mixtures**. The results are presented graphically in **Figure 3**.

TPP is again the product that provides the best mechanical properties. However, FONGRABOND presents similar results to those obtained with limestone + bentonite, being therefore a potential binder.

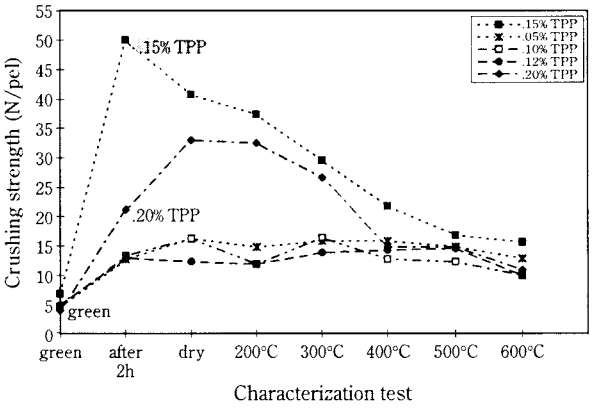

Fig. 2 Evaluation of the variation of the dosage of TPP

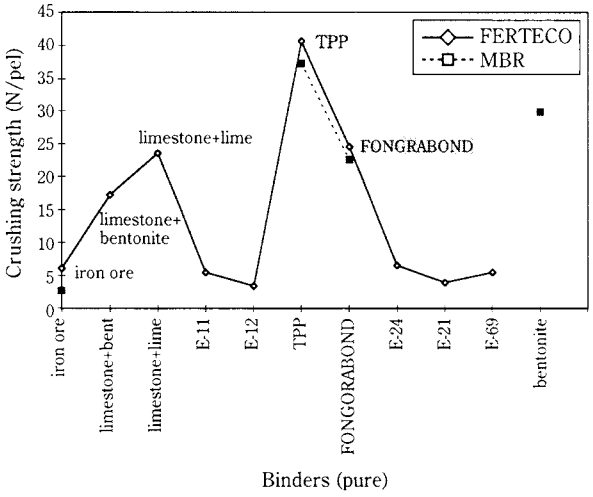

Fig. 3 Evaluation of the action of the other binders

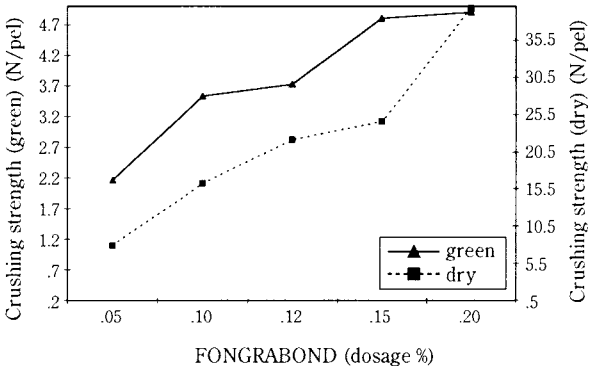

Fig. 4 Evaluation of the level of addition of FONGRABOND

evaluation of the level of addition of FONGRABOND

To evaluate the optimum addition level of FONGRABOND on the mixture, tests were carried out varying from 0 up to .20%. **Figure 4** shows these results.

It can be observed that until the level of .20%, the mechanical properties of the pellets improve. As, in the level of .15%, these values are satisfactory, in the sequence of the studies this level was maintained.

4. Discussion of the Results and Conclusion

LIMA e CHAVES[4,5,6] developed their experimental work based on the hypothesis that the effect of the mixture CMC/TPP was due to two different mechanisms that summed up to give the final result:

1 – the viscosity of the solution of CMC would improve the mechanism of capillary action by keeping the cohesion the particles into the green pellet;

2 – the dispersing action of TPP would disperse colloidal particles of limonite, always present on the surface of the hematite particles. This dispersion would act in two ways: increasing still more the viscosity of the CMC solution (contributing like this to the stability of the green pellet) and during firing, promoting the formation of iron oxide bridges between the particles. This mechanism is recognized for the sintering of the particles in the fired pellet.

CHAVES[7,8,9,10] working with limestone, followed the same reasoning and verified that the soda ash alone was enough to allow stability to the green pellets. The limestone pellets were not fired, just cured.

It was verified that the cured pellet had remarkable mechanical properties. He interpreted this green behaviour as the result of the dispersing action of the soda ash on the colloidal particles of limestone and on the present clay-minerals.

The behaviour after curing was seen as the result of the chemical reaction:

$$CaCO_3 + Na_2CO_3 = Na_2CO_3 + CaCO_3,$$

where the ions Ca^{++} and Na^{+} of the solution and of the mineral surface are changed, forming bridges of carbonate between particles.

The verification of CASSOLA and CHAVES[10,11] in the experimental work herein described is more comprehensive and completes the picture, allowing full understanding of the phenomenon. Effectively, the dispersion of the limonites on the surface of the hematite particles is the fundamental mechanism for the whole process. It assures the necessary viscosity to keep the green pellet stable, as well as it allows the construction of the iron oxide bridges that provide the stability to the burnt pellet. This is achieved without disturbing the other binding mechanisms such as slagging, melted points or sintering.

The main development is that this dispersion can be provided by any chemical that possesses such a dispersing action. Especially, organic dispersants that do not bring undesirable contaminants to the pellet (Al, Si, P, S) are interesting options to bentonite or lime.

Finally, the authors have shown to exist potential for the development of organic binders able to provide superior strength to that obtained with bentonite, limestone and lime.

References

1) ULRICH, D.M.; HAN, T.M. The progress report on the effect of grind, temperature and pellet size upon the quality of specular hematite pellets. *International Symposium on Agglomeration, I.* W.A. Kneper, ed., New York, Interscience, 1964, p. 669-714.
2) ARIAS, H.D.; MANHEIMER, W.A. Uso da microscopia eletrônica na observação de pelotas de minério de ferro. *Metalurgia*, 28 (171) 101-9, 1972.
3) LIMA, J.R.B. *Estudo da carboxi-metil-celulose como aglomerante para pelotização.* Dissertação de mestrado, EPUSP, São Paulo, 1992.
4) LIMA, J.R.B, CHAVES, A.P. Estudo da carboxi-metil-celulose como aglomerante para pelotização. *Technical bulletin*, USP, Department of Mining Engineering, BT/PMI/014, EPUSP, São Paulo, 1992.
5) LIMA, J.R.B, CHAVES, A.P. Study of surface properties in agglomeration processes. MINERAL INTERNATIONAL PROCESSING CONGRESS, 17. *Annals.* Sydney, 1993. p. 1395-1402.
6) CHAVES, A.P. Recycling of limestone quarry fines through pelletization. *Internal report.* Southern Illinois University, Carbondale, 1993.
7) PAUL, B.C.; CHAVES, A.P.; WHITE, C.M.; McKINNEY, G. Pelletization solution to fines-handling problem. *Pit and Quarry*, Jun. 93, p. 30-3 and Jul. 93, p. 34-7.
8) CHAVES, A.P.; PAUL, B.C. Pelotização de finos de calcário. *Reciclagem of rejeitos na indústria mínero-metalúrgica.* ABM/COREME, São Paulo, 1992, p. 469-82.
9) PAUL, B.C.; CHAVES, A.P.; WHITE, C.M. Recycling of limestone quarry fines entrusts pelletization. Congresso Italo-brasiliano d'ingegneria mineraria, 2. *Resoconti.* São Paulo, 1993, p. 883-97.
10) INSTITUTO DE PESQUISAS TECNOLÓGICAS DO ESTADO DE SÃO PAULO S.A.. Relatório nº 34.084/96-*Ensaios de aglomeração de pellet-feed com diferentes tipos de ligantes.* Final report. IPT, São Paulo, 1996.
11) CASSOLA, M. S. ; CHAVES, A . P. Efeito da adição de aglomerantes orgânicos no comportamento de pelotas de minério de ferro. I Simpósio Brasileiro de Minério de Ferro: Caracterização, beneficiamento e pelotização. Anais Out/96. Ouro Preto – MG.

Author's short biography

Monica Speck Cassola

From 1972 to 1976 she studied mining engineering at the Escola Politécnica, University of São Paulo. She got his MSc. (1992) and PhD (1997) degrees at the same university in the field of flotation of salt type minerals.

She worked six years at the Paulo Abib Engineers, a private consulting company; eight years at a phosphate mine in Jacupiranga, São Paulo, and since 1990 she is a research engineer in the Department of Metallurgy of the Institute for Technological Research of the State of São Paulo.

She's current research interests are the influence of chemical products on the micro-mechanism during pelletization of ore.

Arthur Pinto Chaves

Dr. Arthur Pinto Chaves is a full professor and the main lecturer in Mineral Processing at the Department of Mining Engineering, Escola Politécnica, University of São Paulo. He graduated as a Metallurgical Engineer in 1968. Before becoming a full time prefessor and researcher , Dr. Chaves worked for important engineering and consulting companies such as Paulo Abib Engineers and Promon Engineering Co. or for mining companies like the Brumadinho Group. His research interests lie on minerals processing and materials handling (including dewatering and agglomeration).

In-Situ Sizing of Powders and Crystals Using Phase Doppler Measurement Technique†

Amir A. Naqwi & Chris W. Fandrey
*TSI Inc.**
Rebanta Bandyopadhyay and
David J.W. Grant
*Dept. of Pharmaceutics, Univ. of Minnesota***

Abstract

Phase Doppler technique is a non-intrusive optical device for in-situ measurement of single particles. In the case of an irregular particle, it provides a deterministic measure of particle velocity and statistical information about the particle size in the form of a phase shift signal. By collecting sufficient signals, velocity-resolved particle size distributions can be reconstructed. This is demonstrated by comparing phase Doppler measurements of irregular particles with an aerodynamic particle sizer. Preliminary measurements in a crystallizer are also presented. The present device is shown to work with near back-scatter collection of scattered light; hence, leads to a robust setup that can be used under the conditions of limited optical access.

1. Introduction

In many industrial particulate flows, the particles under investigation have irregular and complex structures. It is desirable to use these real particles in field tests as well as laboratory studies that may be aimed at understanding the corresponding particulate process. Optical techniques provide a convenient means for in-situ measurement of such particles. However, the light scattering characteristics of the irregular particles deviate significantly from those of homogeneous spherical particles, that are frequently used as models for estimating the particle response.

In fact, an irregular particle of a given size can generate many different values of a certain light scattering property. The corresponding ambiguity in the measurements is dealt with in many different ways in the previous works. Some of the previous approaches are reviewed by Naqwi and Fandrey [1].

In an earlier experimental work, Bottlinger and Umhauer [2] took into consideration the entire histogram of scattered intensities generated by a single irregular particle. These probability functions were used to relate the size distribution of a polydisperse suspension to the corresponding measured intensity distribution, using a matrix formulation.

The present technique is similar to the above approach; however, instead of intensity, phase shift between sinusoidal signals of a phase Doppler system is measured. As shown by Naqwi [3], the measured phase distribution can be expressed as an integral involving the unknown size distribution and a kernel function, referred to as monosize phase distribution (MPD) function. The MPD function represents the phase distribution corresponding to a single particle size.

The phase Doppler technique is superior to the intensity based instrumentation, as phase shift is less susceptible to electronic noise than intensity. Also phase is not affected significantly by variations in the laser power due to presence of particles in the path of the laser beam. Furthermore, phase Doppler provides a deterministic measure of the particle velocity in addition to a stochastic measure of its size, so that velocity resolved phase distributions can be measured.

For the sake of completeness, the principle of the phase Doppler technique is briefly reviewed in the following section. The stochastic model for the response of irregular particles is given in Sec. 3. An experimental setup for measurement of MPD is described in the subsequent section, which also presents the measured MPDs and their moments for different type of irregular particles. In Sec. 5, measurements in a bench-top crystallizer are presented. The final section summarizes the progress so far and highlights the future plan of work.

* St. Paul, MN 55164, U.S.A.
** Minneapolis, MN 55455, U.S.A.
† Received March, 1998

2. Principle of Phase Doppler Technique

The phase Doppler system for sizing and velocimetry of particles is shown in **Fig. 1**. The output beam of an Argon-Ion laser is transmitted to the beam conditioning optics which is connected to the transmitting probe that focuses pairs of monochromatic beams, such that they cross at the focal point, where interference fringes are produced. As a particle crosses these fringes, it scatters light, which oscillates in time with a frequency that is proportional to the velocity component normal to the fringes. Laser beam pairs of different color are used to measure different components of velocity.

The oscillatory signals collected by the two receivers have the same frequency but are shifted in phase, which is used to measure the particle size. The signal conditioning electronics employ photomultipliers to convert the optical signals into electrical signals.

The output of the electronics is routed to a signal processor, which determines the frequency of the individual signals and phase shift between the phase Doppler signals. The modern processors are capable of transferring the measured data at a high speed to a computer where a software package reduces the results and displays them in real-time.

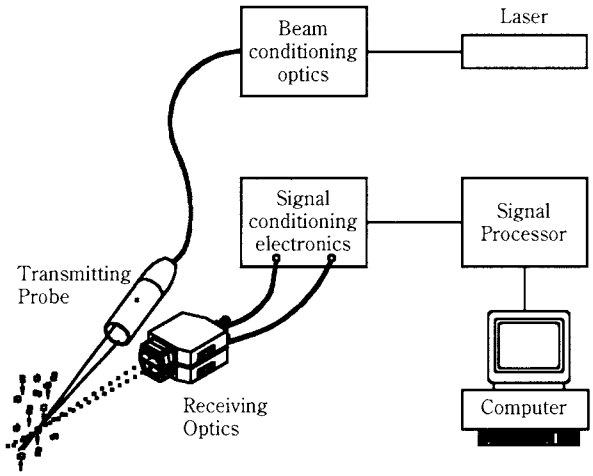

Fig. 1 Layout of a phase Doppler system

3. Stochastic Model for Response of Irregular Particles

A stochastic model is described by Naqwi [3] for the response of irregular particles. This model assumed that a single 'size' can always be associated with a particle. In the previous work, this size was the particle volume as measured by a Coulter counter. The aerodynamic size, as measured by an Aerodynamic Particle Sizer, is used in the present work to represent the particle size.

Various irregular particles of the same size respond differently to a phase Doppler system as their features differ from each other at random and they cross the measuring volume with random orientations. In a hypothetical experiment, many particles with the same size D are measured by a phase Doppler system, or the same particle is made to cross the measuring volume many times with random orientations. The resulting phase distribution function $q(D,\Phi)$ represents the broadening of the phase Φ for a given size D. Function q will be referred to as *monosize phase distribution* (MPD) function. It is very narrow for small particles and becomes broader with increasing particle size. Using an appropriate optical configuration, MPD may be confined to a 360° range of phase shift, so as to avoid the ambiguity associated with the periodic nature of phase.

Using the concept of MPD, the probability density function $P(\Phi)$ for the phase shift signals generated by a polydisperse suspension, may be expressed as

$$P(\Phi)=\int_{D=D_{\min}}^{D_{\max}} q(D,\Phi)p(D)\,dD, \tag{1}$$

where $p(D)$ is the particle size distribution.

In Eq. (1), the functions p and q are assumed to satisfy the normalization condition, i.e. when they are integrated over the entire range of D and Φ respectively, the net result is 1. As a consequence, P also satisfies the normalization condition.

After calibrating a system, i.e. specifying the function q, Eq. (1) represents the relationship between the measured phase distribution $P(\Phi)$ and the unknown size distribution $p(D)$. The latter can be deduced if Eq. (1) is discretized as below:

$$\vec{P}=[Q]\,\vec{p}\,\Delta D, \tag{2}$$

where $\vec{P}$ and $\vec{p}$ are vectors with n elements of $P(\Phi)$ and $p(D)$ respectively; i.e. both the phase distribution and the size distribution are divided into n bins each. The n columns of matrix $[Q]$ – hereafter referred to as MPD matrix or calibration matrix – represent MPDs for n discrete particle sizes.

In order to solve Eq. (2), inverse of the above matrix is needed, so that

$$\vec{p}=\frac{[Q]^{-1}\vec{P}}{\Delta D}. \tag{3}$$

However, the above solution is numerically unstable.

As shown by Naqwi and Fandrey [1], inversion can be obtained by imposing linear constraints on the least squares solution to the above problem.

4. Measurement of Monosize Phase Distribution Function

The experimental setup for the measurements of MPD function is shown in **Figs. 1-3**. The laser beams passed through a window in the Aerodynamic Particle Sizer (APS) nozzle assembly (**Figs. 2** and **3**), where they were focused at the exit of a nozzle.

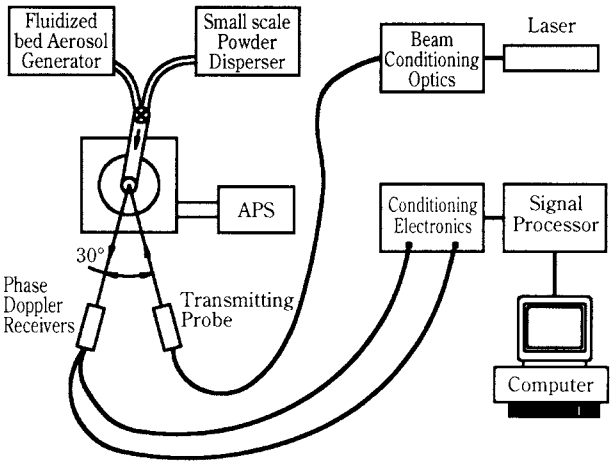

Fig. 2 Calibration setup

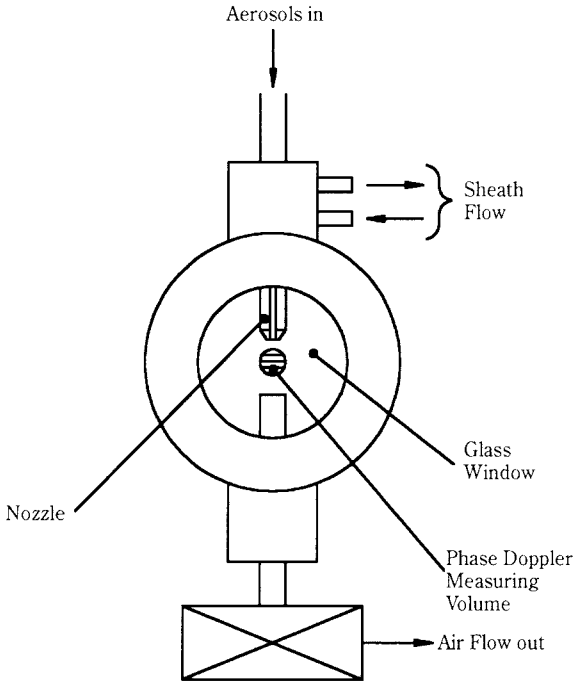

Fig. 3 APS nozzle assembly

These beams generated interference fringes with a spacing of 6.27 μm.

The nozzle assembly itself was connected to the APS which controlled the flow through the nozzle. The purpose of the APS and nozzle assembly was to accelerate particles so that a relationship between their velocity and aerodynamic size could be determined. The assembly was also connected to a particle generation instrument such as a small-scale powder disperser (TSI model 3433) or a fluidized bed aerosol generator (TSI model 3400).

The experimental procedure consisted of calibrating the relationship between velocity and aerodynamic size using spherical PSL particles of known size and then gathering and analyzing data with two samples of crystalline Alumina (Al_2O_3) powder of mean sizes 2.44 μm and 4.98 μm. Also measurements were taken with Arizona road dust, corn starch and quartz powder.

Immediately following the calibration of the system the two samples of Alumina particles were aerosolized using a Fluidized Bed Aerosol Generator. For each sample, a large set of data was collected. Only the data points with valid measurements for both velocity and phase were used in the analysis. Each data set was broken up into velocity bins which were then changed into an aerodynamic size using the APS calibration data.

The phase distributions and their moments are computed for bins with over 500 data points in them. Bins with less than 500 points were considered to be statistically unreliable and were not used for purposes of analysis. Typical phase distributions are shown in **Fig. 4**. These correspond to alumina and corn starch particles. Microscopic images of these particles are also included in **Fig. 4**.

As expected, MPDs broaden with increasing particle size. For similar aerodynamic sizes, the MPD of corn starch is broader than that of alumina. These data may be indicative of a general trend; i.e. MPDs of particles with external irregularities would tend to be sharp-peaked like a Laplace distribution and those of smooth particles with internal inhomogeneities would be Gaussian-like.

The data in **Fig. 4** have clearly shown that the size information can be obtained with phase shift measurements near backscatter. They also show that the mean values of MPD functions are nearly zero. Also, MPDs are symmetric; i.e. the odd moments of phase distribution are zero. The particle size information is contained in the even moments.

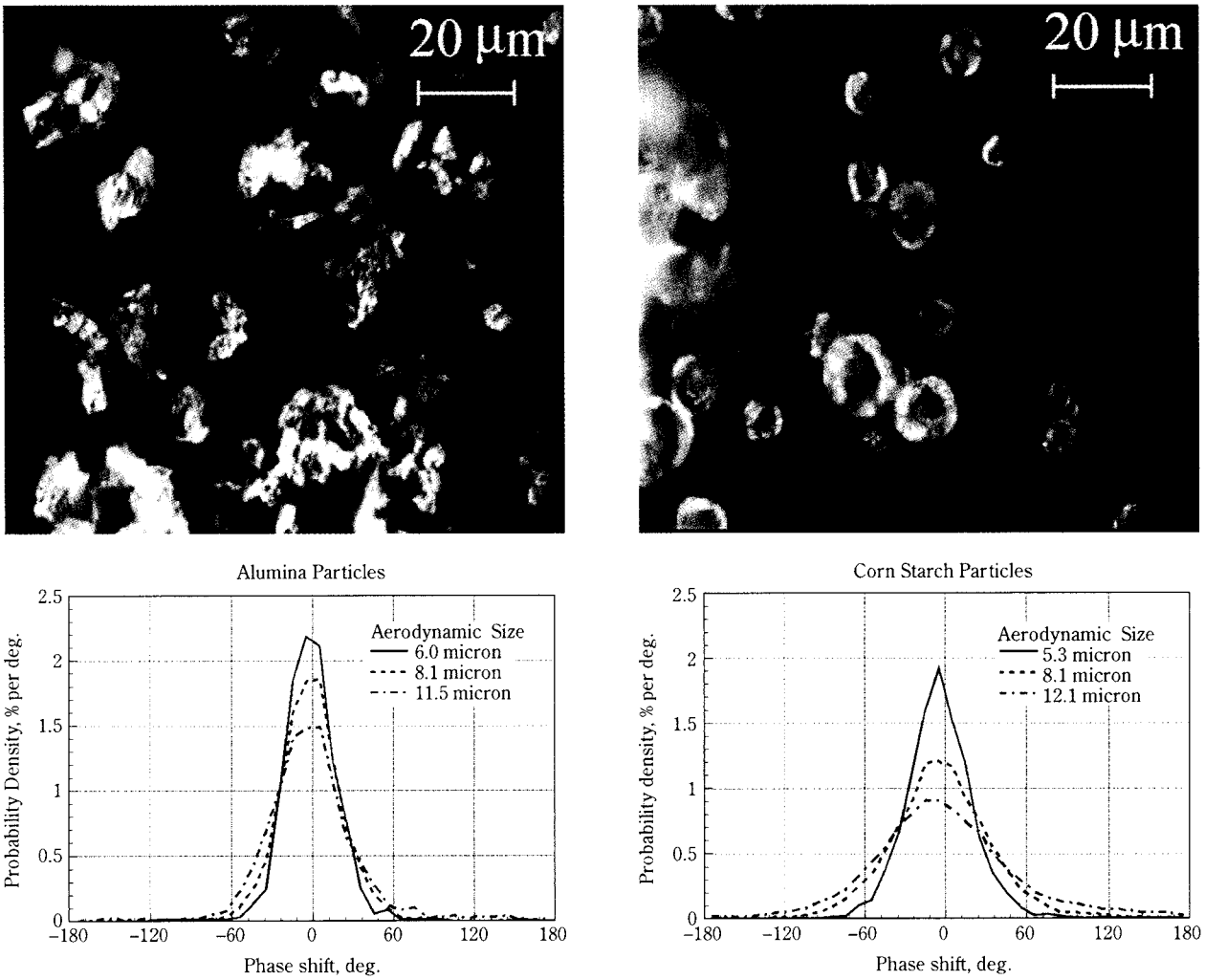

Fig. 4 Measured MPDs for Alumina and corn starch

Figure 5 show the relationship between the aerodynamic particle size and the first three even moments of the alumina, corn starch and test dust particles. The following parameters are plotted:

$$\left(\frac{1}{N}\sum_{i=1}^{N}\Phi_i^n\right)^{1/n}=\left(\int_{-180^\circ}^{+180^\circ}\Phi^n q(D,\Phi)d\Phi\right)^{1/n},$$

where n = 2, 4 & 6. (4)

The parameter Φ_i represents the individual phase shift signals for a given particle size, so its moment can be expressed as an integral of the corresponding MPD function.

Good linear fits with the line passing through the origin are obtained between the above parameter and the aerodynamic particle size D for all the samples considered. The slopes of the lines are comparable for alumina and test dust as these particles have similar morphology. Phase distributions are broader for corn starch particles. Mathematically, the linear fits of **Fig. 5** can be expressed as

$$\int_{-180^\circ}^{+180^\circ}\Phi^n q(D,\Phi)d\Phi=f_n D^n, \quad (5)$$

where f_n is the proportionality constant for the nth moment.

The correlation in Eq. (5) applies to monosize particles. An equivalent of this correlation for a polydisperse suspension can be obtained by integrating Eq. (5) over the entire particle size range; i.e.,

$$\int_{D_{\min}}^{D_{\max}}\int_{-180^\circ}^{+180^\circ}\Phi^n q(D,\Phi)d\Phi\, p(D)dD=f_n\int_{D_{\min}}^{D_{\max}}D^n p(D)dD. \quad (6)$$

Rearranging the order of integration on the left-hand side of Eq. (6) and invoking Eq. (1),

$$\int_{-180^\circ}^{+180^\circ}\Phi^n P(\Phi)d\Phi=f_n\int_{D_{\min}}^{D_{\max}}D^n p(D)dD. \quad (7)$$

Alternatively,

$$\frac{1}{N}\sum_{j=1}^{N}\Phi_j^n=f_n\frac{1}{M}\sum_{k=1}^{M}D_k^n, \quad (8)$$

where Φ_j is one of the N phase shift signals generated by a polydisperse suspension, and D_k is the size of one of the M particles in that suspension. The above

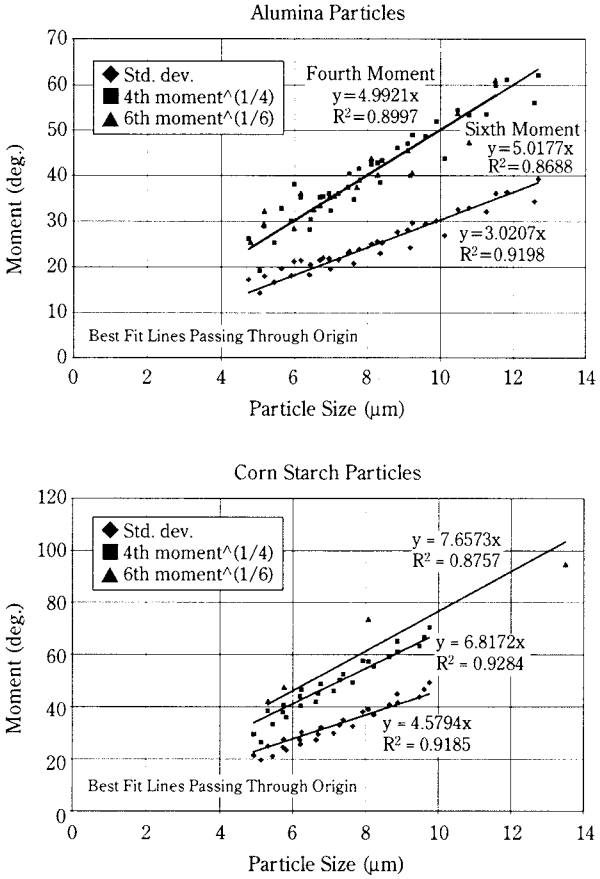

Fig. 5 Higher moments of phase distribution

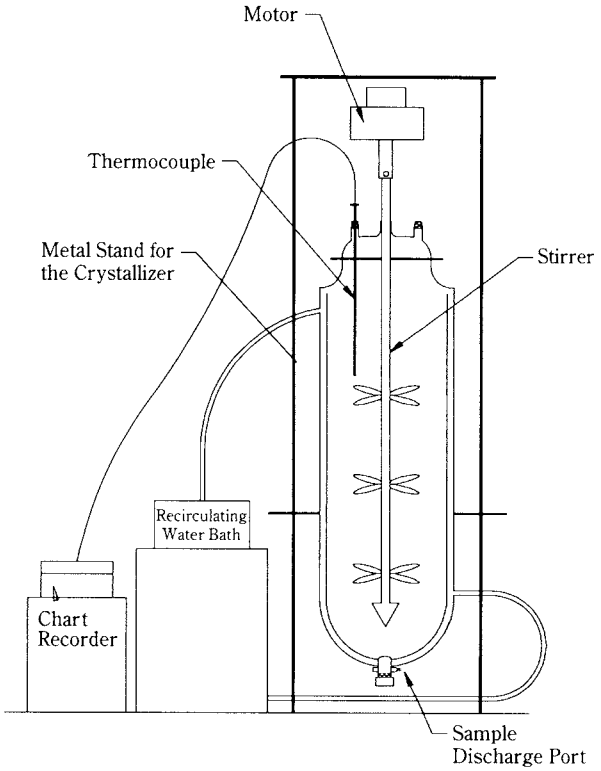

Fig. 6 Schematic diagram of the batch crystallizer

equation shows that the nth moment of the measured phase distribution is proportional to the nth moment of the particle size distribution. In other words, the correlations shown in **Fig. 5** imply that if the second, fourth and sixth moments of phase distribution are measured on a polydisperse suspension, then the mean, square-mean and cube-mean of D^2 can be determined. These moments of D^2 can be reduced to mean, standard deviation and skewness of D^2 distribution. If it is known that D^2 (or D) has a mono-modal distribution, then the first three moment would allow to reconstruct the distribution fairly well, without resorting to an elaborate inversion scheme, as discussed by Naqwi and Fandrey [1].

5. Measurements in a Crystallizer

Measurements were conducted in a model batch crystallizer with controlled-cooling as shown in **Fig. 6**. The design and use of such a crystallizer has been described by Brown et al. [4]. The rate of cooling and hence the degree of supersaturation can be controlled using external circulation of a coolant by means of a bath circulator that can be programmed to cool at any pre-planned linear rate. The crystallizer consists of a 6-liter cylindrical, jacketed glass vessel with a motor-driven agitator that ensures small and uniform crystals and reduced run-time.

The optical system used for the measurements was similar to the one illustrated in **Fig. 1**. The fringe spacing in the measuring volume was 46.3 μm and there were about 10 fringes in the measuring volume. Measurements could be taken as much as 10 mm inside the crystallization vessel as, under the conditions of complete crystallization, the crystal concentration became so high that the laser beams did not penetrate farther.

Typical signals are shown in **Fig. 7**. Each plot in this figure contains two curves – depicted by the solid line and the dotted line – representing the bursts collected by the two receivers of the phase Doppler system. About 80% of signal pairs had comparable amplitudes as shown in the top plot of **Fig. 7**. Also the phase shift was nearly constant along the burst. This result is in disagreement with the results of similar tests done by Onofri [5].

In the experimental setup of Onofri, the fringe spacing was about 12 μm and the irregular metallic particles were 400-500 μm in size, i.e. about 40 times larger than the fringe spacing. On the other hand, the ratio of particle size to fringe spacing was confined to

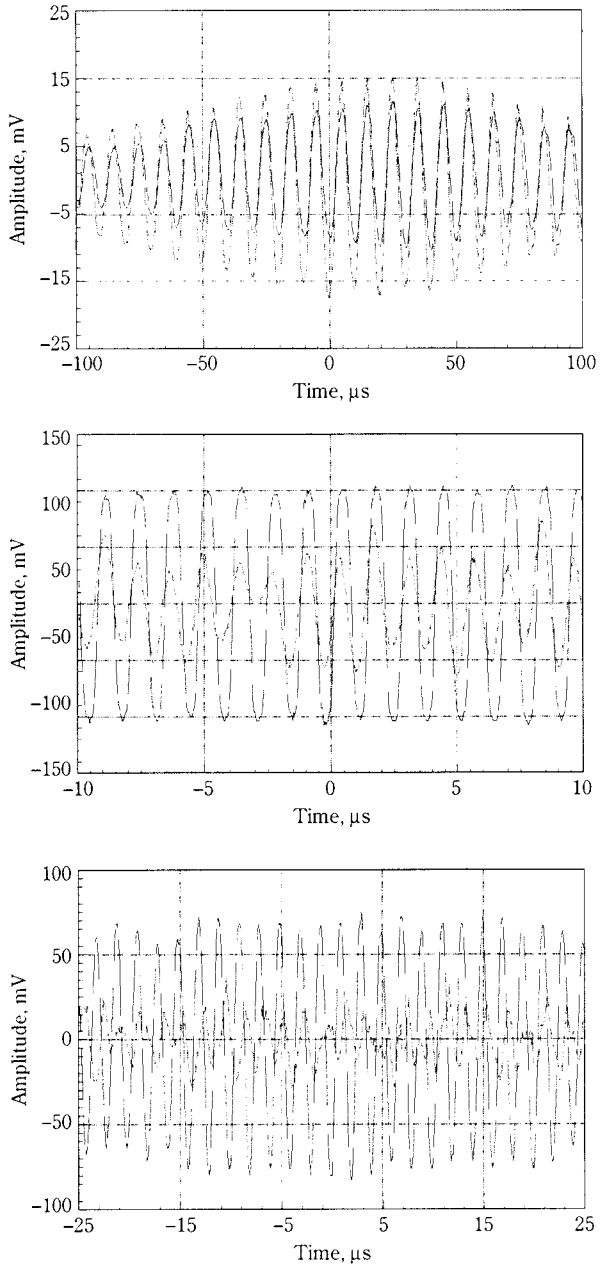

Fig. 7 Microscopic views of burst pairs with probability of occurrence of 80%, 15% and 5% respectively

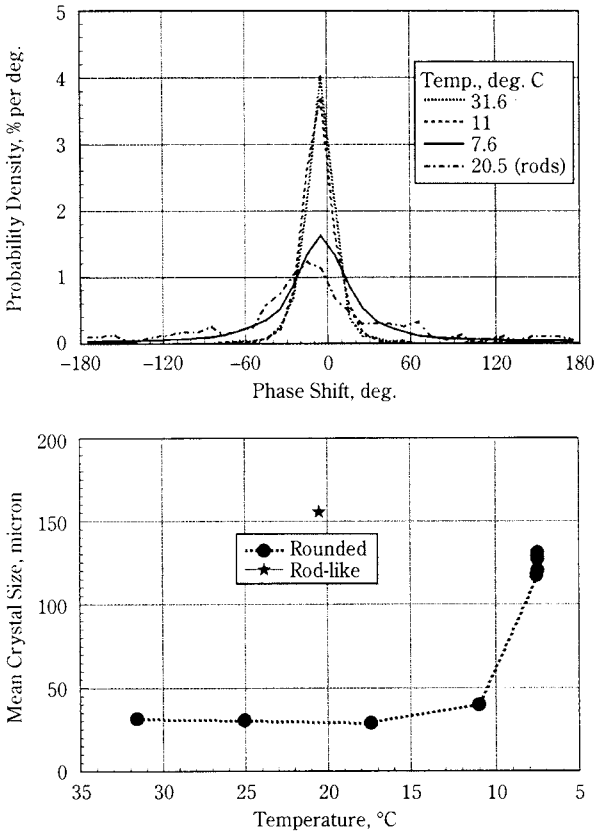

Fig. 8 Evolution of phase distribution and mean size during solution cooling.

about 4 in the present experiments. This difference between the two experimental settings explains the discrepancy in the phase behavior. Earlier work by Naqwi [3] has shown that a meaningful relationship between phase response and particle size is obtained only if the largest particle size does not exceed 4 times the fringe spacing. Direct examination of the signals suggests that constancy of phase shift within a burst is a pre-condition for the statistical behavior of the phase shift to be sensitive to particle size.

In-situ measurements in a crystallizer were conducted with a solution of lysine monohydrochloride in a mixture of methanol and water. Elongated rod-like crystals and rounded crystals were produced with a 1:1 and a 3:2 weight-by-weight ratio of water to methanol respectively. The histograms of signal phase shift, measured at different temperatures are shown in **Fig. 8**. The phase histogram broadens with the decreasing temperature, i.e. with the growth of the crystals. Standard deviation of the phase shift is converted to mean particle size using an estimated conversion factor. The final crystal size is comparable to the SEM micrograph shown in **Fig. 9**.

According to **Fig. 8**, mean particle size appears to be invariant over a wide range of initial temperatures (from 35°C to 15°C). The measured standard deviation over this range was about 10°. The actual standard deviation may have increased from a very small value to about 10°, i.e. the measurement resolution appears to be limited to 10°.

Figure 10 shows the correlation between the velocity and the standard deviation of phase shift for rounded particles. These curves represent size-velocity correlations and indicate that the fastest upward motion (>0.6 m/s) is clearly exhibited by smaller crystals.

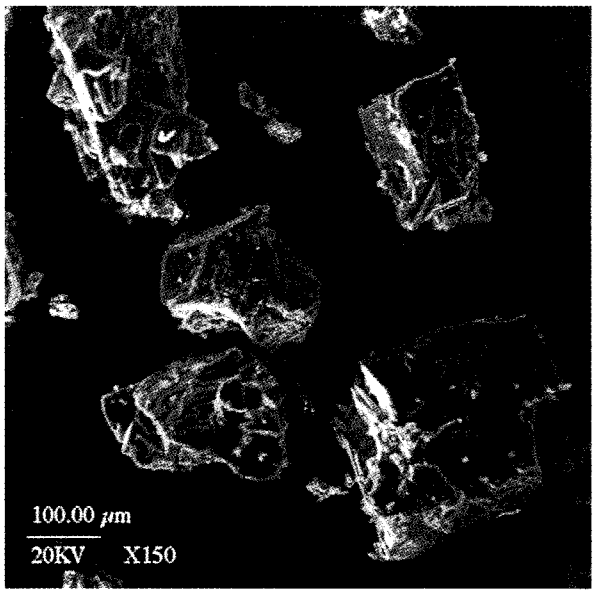

Fig. 9 SEM micrograph of the rounded crystals

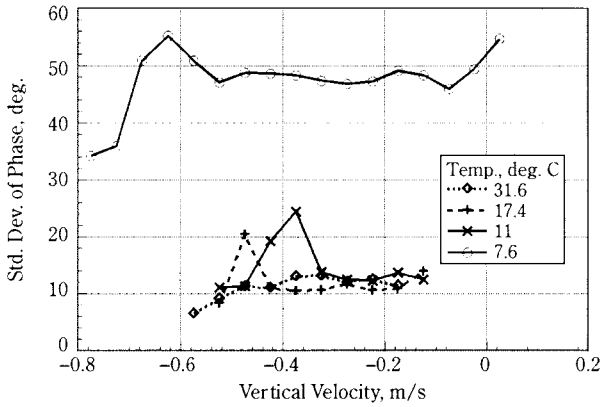

Fig. 10 Size- velocity correlations for the rounded crystals

For intermediate temperatures, large values of standard deviation occur only over a narrow range of velocity; i.e. crystals appear to grow within streams that flow fairly uniformly and streams wander around, so they do not remain in the phase Doppler measuring volume all the time.

6. Conclusions

This work has clearly demonstrated that the phase Doppler technique can be used for in-situ measurement of crystal size and velocity, while collecting data in backscatter. Experimental studies show a linear relationship between the standard deviation of the phase shift and the aerodynamic particle size. Also the fourth and sixth roots of the fourth and sixth moments of the phase distribution respectively are related linearly to the aerodynamics particle size. These relationships hold for irregular particles of diverse structures and morphology.

The above relationships allow a convenient means to convert the measured phase distribution into a size distribution. However, the present hardware limits the dynamic range of particle size to about 5:1. The variance of the phase shift is determined not only by the optical signals but also by the random time delay in the photomultipliers that are used to convert the optical signals into electronic signals.

Although the random delay variations are small, i.e. limited to ±2 ns, they cause large phase errors as the in-coming optical signals have a 40 MHz carrier frequency that is needed to determine the direction of motion of the crystals. The period of the optical signals is about 25 ns, so the standard deviation of random delay variations is about 10°. Hence, the instrument is not sensitive to small crystals whose standard deviation for the phase shift is smaller than 10°. Also there is an upper limit of about 50° for the standard deviation of the largest measurable particle. At the upper limit, the entire phase shift range of 360° is filled and phase signals begin to wrap around for larger particles.

Given the above upper and lower limits on the standard deviation of the phase shift, the measurable particle size range is limited to 5:1.

The above limitation can be overcome by reducing the carrier frequency. The electronic delay problem can be completely eliminated by using a frequency of 1 MHz, instead of 40 MHz. In the present hardware, one of the two laser beams is shifted by 40 MHz using an acousto-optic modulator (AOM). Although AOM cannot be operated at a much lower frequency, two such devices can be used to shift both the beams by say 40 and 39 MHz, so the effective shift between the beams would be 1 MHz. The above option will be evaluated in the future work. It is expected that a 50:1 dynamic range of particle size can be covered with appropriate hardware.

Acknowledgment

The authors are grateful to the National Institute of General Medical Sciences of USA for the financial support of this work. Program Director: Dr. Peter Preusch.

References

1) Naqwi A. and Fandrey C.: Phase Doppler measurements of irregular particles and their inversion to velocity-resolved size distributions, *Powder Handling & Processing* 9 (1997) 45–51
2) Bottlinger M. and Umhauer H.: Single particle light scattering size analysis: quantification and elimination of the effect of particle shape and structure, *Part. Part. Syst. Charact.* 6 (1989) 100–109
3) Naqwi A.: Sizing of irregular particles using a phase Doppler system, *Part. Part. Syst. Charact.* 13 (1996) 343–349
4) Brown R., York P. and Maclaine J. Q.: The role of crystallization conditions in the control of final product character, *Pharm. Res.* 7 (1990) S-107
5) Onofri, F.: Prise en compte de la dimension finie des faisceaux d'éclairage en granulométrie optique: Anémomètrie Phase Doppler – Diagnostics des Milieux Diphasiques, Doctoral Thesis, Faculty of Science, University of Rouen (1995).

Author's short biography

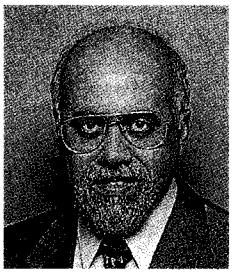

Amir A. Naqwi

Dr.Naqwi received his Ph. D. in Mechanical Engineering from Stanford University in 1987 and has worked for several years at the University of Erlangen, Germany. He is author of numerous publications and patents pertaining to laser instrumentation, especially instrumentation for diagnostics of particulate flows. He is currently the Advanced Products Manager in Laser Diagnostics Division of TSI Incorporated and serves on several scientific committees, including the Advisory Board of the journal Particle and Particle System Characterization.

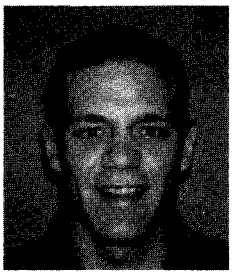

Chris W. Fandrey

Chris Fandrey is a graduate of the University of Minnesota in Mechanical Engineering and has worked in the Paticle Technology Laboratory there for over three years. He has been employed at TSI Incorporated, initially as an engineering intern, and now as a Research Engineer. He is the author of several publications on the phase Doppler technique for sizing irregular particles and glass fibers.

Rebanta Bandyopadhyay

Rebanta Bandyopadhyay is Research Investigator in the Advanced Candidates Liquids Area at the Bristol-Myers Squibb Pharmaceutical Research Institute in New Brunswick, NJ. He obtained B. Pharm. (first class, honors) in 1991 from Jadavpur University, Calcutta, India, and M. S. in Pharmaceutical Sciences from the University of Mississippi in 1993. In 1998, he graduated from the University of Minnesota with a Ph. D. in Pharmaceutics under the supervision of Professor David J. W. Grant. The focus of his research was the influence of crystal properties on the tableting performance of lysine derivatives. The influences of the crystallization conditions on the hydration state and the morphology of the recrystallized phase were also studied. Rebanta Bandyopadhyay received the Best Poster Award at the Midwest Meeting of the American Association of Pharmaceutical Scientists, held at Chicago in May, 1997, for his work on the influence of thermodynamic activity of water on the hydration state and the crystal habit of L-lysine monohydrochloride. During his graduate studies, Rebanta Bandyopadhyay held a research assistantship at the University of Minnesota and received a Honors Fellowship from the University of Mississippi. He also received the Emami Award from the Indian Pharmaceutical Association for his performance in the undergraduate program. Memberships include AAPS, Rho Chi, Phi Kappa Phi, and Sigma Xi.

Author's short biography

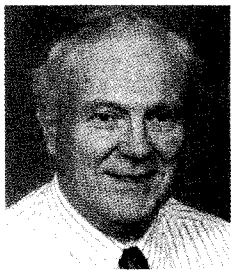

David J.W. Grant

David Grant is Professor of Pharmaceutics, College of Pharmacy, University of Minnesota, Minneapolis. He is a graduate of Oxford University, UK: B.A. in Chemistry in 1960; D.Phil. in Physical Chemistry in 1963; M.A. (Keble College, 1963); and D.Sc. for recognized published research on the physical chemistry of pharmaceutical systems (October 1990). He has held academic appointments at the University College of Sierra Leone (then affiliated to the University of Durham, UK), at the University of Nottingham, UK, and at the University of Toronto, Canada. In 1988, he was appointed to the William and Mildred Peters Chair in Pharmaceutics, University of Minnesota. Since January 1994 David Grant has served as Associate Editor of the Journal of Pharmaceutical Sciences. He is also a member of the Editorial Advisory Board of the journals "Pharmaceutical Development and Technology" and "Kona Powder and Particle". In April 1998 he was elected to the Board of Directors of Hosokawa Micron International, Inc. David Grant has worked on bacterial drug resistance and metabolism and, since 1972, on the physical chemistry of pharmaceuticals in which he is co-author of an undergraduate text. In 1978 and 1980 he worked on the intermolecular interactions of drugs in solution at the University of Kansas in the laboratory of the late Dr. Takeru Higachi, with whom he is the co-author of a book on the solubility behavior of organic compounds. Since 1978 David Grant has been studying the crystal engineering of drugs and the properties of the solid state, particularly the thermodynamics, solvation, polymorphism, crystallization, compaction, solubility, and dissolution of drugs. His recent work has focused on doping, hydration, hydrogen bonding, and chirality in the solid state. He is the author or co-author of over 120 scientific articles and reviews and serves as a consultant for numerous companies that manufacture fine chemicals and pharmaceuticals. David Grant is a Fellow of AAPS and the Royal Society of Chemistry (Chartered Chemist, UK). Memberships also include AAAS, AACP, ACA, ACS, AIChE, APhA and Rho Chi.

Deposition of Particulate Materials into Confined Spaces — New Tester Development and Experimental Results† —

P.S. Dhanoa and V.M. Puri
Department of Agricultural and Biological Engineering
*The Pennsylvania State University**

Abstract

The filling of particulate material into confined spaces such as dies (typical volume a few cubic centimeters) presents problems that affect the quality of the final product. Some researchers have studied the effects of filling method on fundamental particulate properties and load distribution in large storage systems such as bins and silos. However, there is a lack of quantitative analysis of the process of deposition of particulates into small storage systems such as dies. A low-cost tester capable of acquiring real-time data has been developed for experimental analysis of the process of filling of dies. A literature review and preliminary study of the effect of die filling methods (funnel fill and sieve fill) impact on spatial fill distribution (for spray-dried Alumina) in a cylindrical die have been carried out. Cumulative mass profile plots show that the load cells record a flatter profile in the case of sieve fill than the funnel fill case. This suggests a more uniform powder fill for the sieve filling method compared to the funnel fill method.

1. Introduction

A wide variety of products such as feed pellets, tablets, tool inserts, electronic components and automobile parts are produced by subjecting a fixed mass or volume of dry cohesive particulate material, poured into a die, to high pressures. This manufacturing technique is referred to as compaction or pelletization and the pressed part is referred to as a compact. The quality of the product made by pelletizing is recognized to be dependent upon many factors such as intrinsic material properties, particulate material properties, nature of applied load, and die geometry. Many pelletization defects such as lamination, end-capping, and stress cracking etc. are caused by anisotropic compaction of the particulate material. It is further recognized by researchers that the anisotropic compaction, among other factors, is attributable to non-uniform pre-compaction fill-density of the particulate material in the die. Filling (deposition) of powders in confined spaces (e.g., dies) is the required first step in the process of manufacture of pressed parts/products. Since errors get compounded in any manufacturing process, it stands to reason that ensuring a pre-compaction uniform particulate deposition in the die or mold would be an effective method of ensuring and enhancing quality of the pressed compacts.

A review of literature revealed that researchers have studied the effect of filling methods on fundamental particulate properties and load distribution in large storage systems but there exists a significant lack of qualitative and quantitative analysis of the process of die filling *vis-à-vis* particulate material's pre-compaction density distribution within the die volume. This study is a systematic attempt to deal with the issue of effect of die filling methods and other related factors such as die cross-section, die aspect ratio, and rate of die filling on the spatial, pre-compaction powder (fill) density distribution within the die volume. This is a work-in-progress and only preliminary results of the newly developed tester's capability to determine the effect of die fill method is discussed herein.

2. Literature Review

The literature review is divided into two sections. The first section deals with the review of literature pertinent to die filling. In the second section, literature review about the determination of in-situ spatial density distribution is presented.

* University Park, PA 16802 U.S.A
† Received March, 1998

2.1 Die filling:

Molenda et al. (1994) have reported that the spatial arrangement of individual wheat grain kernels, forming a granular bed using three different fill methods, significantly influenced the loads on the walls and the radial distribution of vertical pressure on the floor of the flat-bottom model bin. The three methods of bin filling used by Molenda et al. (1994) are shown schematically in **Figure 1**. The filling methods were: central, circumferential, and sprinkle. Measured data showed that the highest mean vertical pressure on the floor was caused by the sprinkle filling method. Circumferential filling of the smooth wall container resulted in the highest vertical pressure at the center of the container, while the highest pressure for central filling was on the second ring from the center. For the rough wall and all filling methods, the minimum vertical pressure was observed on the ring second from the wall. An increase in the vertical pressure on the ring nearest to the wall was observed for all tests except for the smooth wall bin and central filling where the pressure on the ring nearest to the wall decreased.

Moysey (1984) investigated the effect of the use of grain spreaders on the friction properties of grains and on bin wall pressures. Two filling methods were employed — sprinkle filling (achieved using a grain spreader) and stream filling (grains flowing in a stream into the bin). For both bins, sprinkle filling resulted in lateral pressures that were appreciably lower than stream filling. Sprinkle filling also resulted in a 7-8% higher bulk density than stream filling. In the same study, Moysey has also shown that in shear box tests to determine the internal friction angle in some cereal grains, the method of filling the box has a significant effect on the bulk density of the sample and on the amount of dilation which occurs during shear.

Moriyama et al. (1985), measured the wall pressure ratio after filling and during discharge, with the pressure measurements taken at the hopper gate zone near the transition in the bin for two different filling methods, central and peripheral feeding, and for six

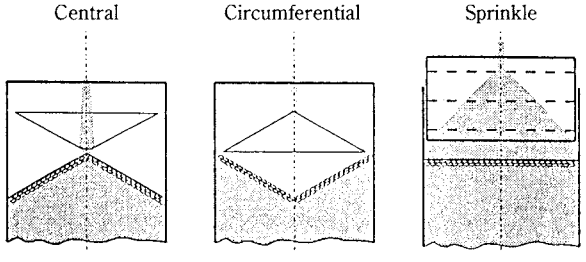

Fig. 1 Schematic of bin filling methods (Molenda et al., 1994)

different types of bulk solids. They found that the wall pressure ratio was different for the two different filling methods (pressure ratios were generally higher for central fill vs. peripheral fill) and was also affected by different hopper angles. That the method of bin filling influences the pressure distribution has also been reported by Aoki (1976), Nielson (1983), Munch-Anderson et al. (1990), and Kwade et al. (1994).

Large capacity reactors with packed bed of catalysts find important applications in the chemical industry. One of the problems associated with such reactors is the local preheating of the catalyst, an exothermic reaction, preferentially occurring at the inhomogeneities of the packed bed structure. The packed bed structure is a function of the method of filling the reactor with the catalyst. Since local preheating has an adverse effect on reactor efficiency, researchers have investigated various methods of filling reactors with catalysts. Smid et al. (1993) have studied the effect of three different filling methods on the bulk density of the resultant packed bed structure. The three filling methods used were: the free pouring method, which is characterized by the angle of repose of the material and two so-called "rainy" filling methods with horizontal top surfaces which were implemented with a special distributing grid, located either close to bed surface or higher up. It was found that a more homogenous distribution of the catalyst was obtained in the case of the "rainy" filling method as compared to the free pouring method. Several methods of producing catalyst layers with high bulk densities have been patented of which Johnson et al. (1976), Baillie (1977) and Cermak et al. (1989) are but three examples.

Bocchini (1987) has conducted experiments to try to establish the influence of small die openings on the powder fill bulk density. Using rectangular dies of various widths and copper and mixed elemental bronze powder, Bocchini showed that filling bulk density decreases with decreasing die opening. Bocchini proposes that the decrease of filling density caused by decrease in die thickness can be explained by introducing the concept of boundary layers existing at the die walls.

Faikin et al. (1976) have studied the influence of the rate of die filling on the bulk density of the powder fill. They varied the intensity of filling the same die with powder by employing hoppers with different discharge orifice diameters using different powders. They determined that with increase in pouring rate, the bulk density of the powder fill falls to a certain limit, beyond which further increase in filling inten-

sity produces no further decrease in density, and, conversely, decreasing the intensity of filling increases the bulk density of the powder in the die. The variation in pouring intensity was found to change powder fill density by 7-10%. They explain this phenomenon by observing that at a sufficiently low intensity of powder filling, particles dropping onto the free surface of the powder can move unhindered to sites corresponding to minimum potential energy, as a result of which their arrangement will approximate one of the regular systems of stacking and that by enabling particles to perform free, optimum movements in the course of filling, a decrease in powder pouring intensity reduces the probability of bridge formation or even completely prevents it and consequently increases the density of powder fill.

Similar results have been obtained by Readey et al. (1995) in their study on the pressure-compaction response of a spray-dried, 94% alumina powder containing a polymeric binder. They have reported that fill bulk density is a strong function of both die diameter and aspect ratio (compact thickness-to-die diameter).

All the studies reviewed above are those in which researchers have investigated the effects of different particulate filling methods in grain bins and hoppers, formation of catalyst beds, and the material *discharge* characteristics from model bins and hoppers. No study could be located in the literature that expressly addresses the issue of experimental analysis of the process of deposition of particulate materials *into* confined spaces achieved by different deposition methods vis-à-vis the fill density distribution.

2.2 Density distribution measurement:

Smid et al. (1993) subjected a filled packed catalyst bed to the passage of gamma radiation emanating from an external radioactive source located on one side of the reactor model. After passing through the bed, attenuation of radiation was detected by a scintillation probe situated outside the second wall. This so-called radiogaging technique is based on the assumption that the attenuation of a beam of gamma photons is proportional to the material's bulk density.

A similar, and more refined technique, is Computerized Axial Tomography (CAT) scanning using x-rays (wavelength 10^{-4} to 10 nm). In x-ray CAT scanning, a source delivers a series of short pulses of x-ray radiation as it and an electronic detector are rotated around the object being tested. The attenuated x-ray responses of the detector are fed to a computer that analyzes and integrates the x-ray data from the numerous scans to construct a detailed cross-sectional image of the object. The most well known and wide spread use of CAT scanning is for medical purposes for scanning of the human body. Apart from its application in the medical field, CAT scanning has been found in many other areas with most of the non-medical application of CAT scanning being in the areas of petroleum engineering where extensive analysis of porous media is required. For example, Coshell et al. (1994), have successfully imaged, by x-ray CAT scan, oil shales in Australia. Phogat et al. (1991), have applied CAT scanning to dual-source gamma-ray attenuation in soil columns to determine nondestructively the spatial distribution of volumetric water content and bulk density. Tollner et al. (1992), have used x-ray CAT scanning to image interior regions of 'Red Delicious' apples under varying moisture and, to a limited extent, density states. Kantzas (1994) has used x-ray CAT scanning to study fluidized and trickle beds in chemical reactors using glass beads and nitrogen.

Process Tomography is a technique very much similar to CAT scanning except for the spatial relationship between the object under investigation and the source and detector array. In CAT scanning, the test object is kept stationary and the source and detector array are in motion. In Process Tomography, the test object is in motion and the source and detector array are kept stationary. Similar to CAT scanning, in Process Tomography, the basic idea is to install a number of sensors around the pipe or vessel to be imaged. Although the applications of Process Tomography lie in analysis of flowing mass, it is conceivable that if the stationary particulate mass in a die or mold were analyzed by a source and detector array being moved along the outside of the die cavity, it might be possible to analyze the internal structure, i.e., mass distribution, of the particulate deposited in the die. Toward this end, literature review in the area of Process Tomography was also carried out.

Hosseini-Ashrafi and Tuzun (1993) have worked on the tomographic study of voidage profiles in axially symmetric granular flows. The state-of-the-art literature about process tomography has been compiled by Williams and Beck (1995).

Kondoh et al. (1996) carried out a study aimed at clarifying the powder deposition process in filling the die cavity. They observed the deposition process with the help of a videographic imaging apparatus. They have shown that particle size segregation in filling occurs independently of the shoe speed and die cavity shape. Further, coarse particles gather in places where powder flows along the angle of repose, while

fine particles gather in places where empty spaces within the die cavity are initially produced and which gradually get filled.

The ability to measure the in-situ density distribution within the particulate mass inside the die volume is of paramount importance to the objectives of the proposed research work. The literature review was carried out to locate instances where researchers might have carried out such an in-situ density distribution measurement of particulates in dies or molds. No such study could be found but the literature review provided a starting point with which to evaluate the different techniques for the purposes of this study.

3. Methodology

Based upon findings from the literature review, two potential techniques, x-ray CAT scanning and MRI were investigated. After considering the pros and cons of these and other lesser known techniques such as vacuum assisted epoxy impregnation, radiogaging and process tomography, a new tester — the real-time spatial particulate mass deposition tester — has been invented (for which a provisional patent has been obtained, Dhanoa and Puri, 1997), to determine the in-situ pre-compaction particulate density distribution. Details about the new real-time spatial particulate mass deposition tester that has been invented are given in the following sections.

3.1 Real-time Cumulative Mass Distribution Determination Load Cell Tester

Principle of Operation

The tester is based on the principle that an anisotropic fill density distribution would result in an uneven particulate vertical pressure distribution on the inside surface at the bottom of the die. Further, this uneven vertical pressure distribution can be detected by placing multiple, sensitive enough load cells on the inside surface at the bottom of the die and analyzing the output signals acquired from the load cells using any suitable data acquisition system.

Construction and Operation

The tester consists of a tiered arrangement of load cells such that the load cell load application points (tops of the custom fitted buttons) are just about flush with the uppermost plate top surface as shown in **Figure 2**. The dimensions of the die used in the tests are also shown in Figure 2. The die was cut from a clear acrylic pipe. The load range of the load cells is 0-4 grams. Combined with a state-of-the-art data acquisition system (model #AT-AI-16XE-10 by National Instruments Corp.), resolution of 0.002 gram can be obtained from the load cells. **Figure 3** shows the schematic of the operation of the tester for the two filling methods used in this study. The tester is placed on a level horizontal surface. A thin plastic film (such as those used in wrapping foods) is placed over the tester to isolate the fill particulate material from the load cells. The open-ended die is then placed over the tester. The output voltage signals from the five load cells during the die filling process are recorded using the data acquisition system. The resultant data captured by the data acquisition system can then be subjected to statistical analysis to determine the fill distribution. The vibratory feeder (model #F-T01-A by FMC Corp.) was used in this study to obtain precise control over the rate of particulate flow into the die as well as to achieve different rates of die fill to analyze the effect of flow rate on the fill density distribution as mentioned earlier in the introduction section.

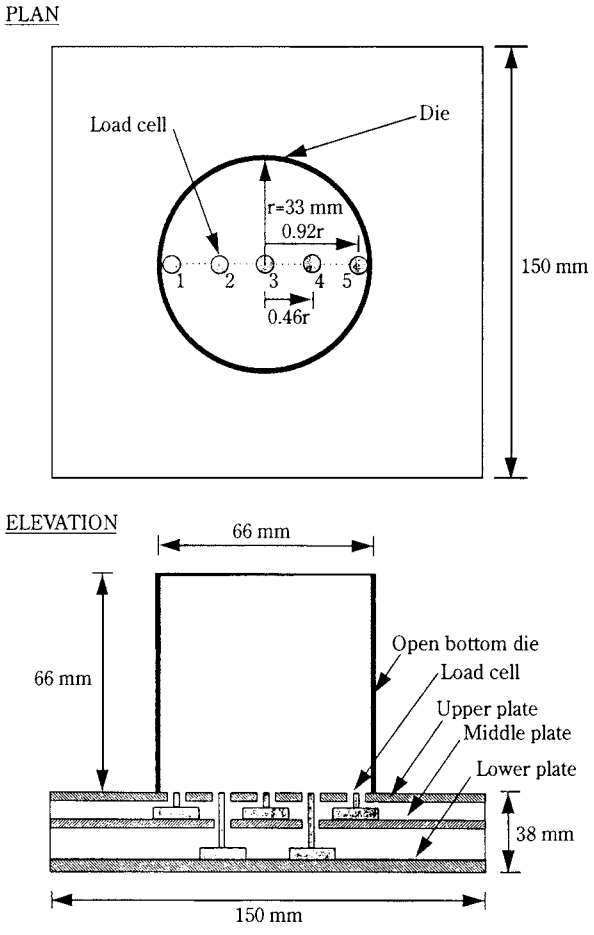

Fig. 2 Schematic of tester (not to scale)

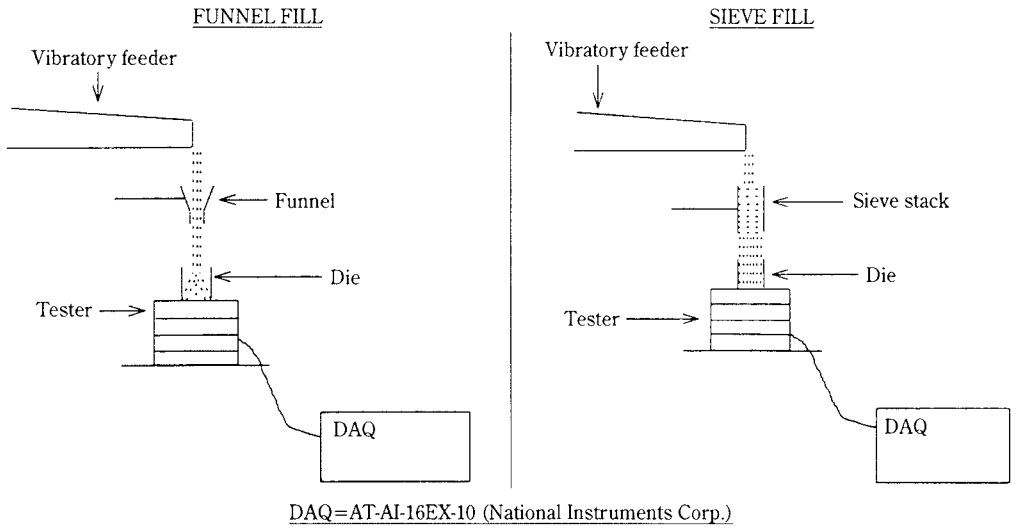

DAQ=AT-AI-16EX-10 (National Instruments Corp.)

Fig. 3 Schematic of test apparatus set-up (not to scale)

4. Results

The first phase of experimental analysis was to carry out proof-of-concept verification tests of the designed and fabricated real-time spatial cumulative mass distribution determination load cell tester (tester). The next step was to carry out the preliminary experimental analysis. Since this is still a work-in-progress, results and qualitative data interpretation for only one powder, spray-dried Alumina (d_{50}=100 microns, 4% PolyVinyl Alcohol binder), and one fill rate (18 g/s) are reported here. Each test was repeated five times. The powder was allowed to fall into the die from a fixed height of 300 mm.

4.1 Proof-of-concept verification of test method

Due to its inherent nature whereby a liquid exerts uniform pressure in all directions at any depth, water was considered to be an acceptable material with which to determine the functioning of the tester. The die was filled with water to various depths (quarter, half, three-fourths and full) and the output from a load cells was recorded. A waterproof seal between the die wall bottom and the plastic film was obtained by applying a layer of high vacuum silicone grease (made by Dow Corning) between the two. The test results are shown in **Figure 4**. The plots show the load cell readings at any depth are within a ±5% range of the average reading from the five load cells at that fill depth. Also, the average readings at different depths are linear (r^2=0.99) with negligible intercept (−0.0032 g) thus demonstrating the location independence of the load cells and linearity with fill height. Calculations showed that the ratio of measured to theoretical values for the load at different depths of fill ranged from 2.14 to 2.19. As expected, measured values were higher than theoretical values. This is most likely due to the fact that the load cell extensions (2 mm diameter) are seated in a hole which is covered with a thin plastic wrap which would contribute to increased effective area (compared to the load cell extension's cross-sectional area) and hence the measured load.

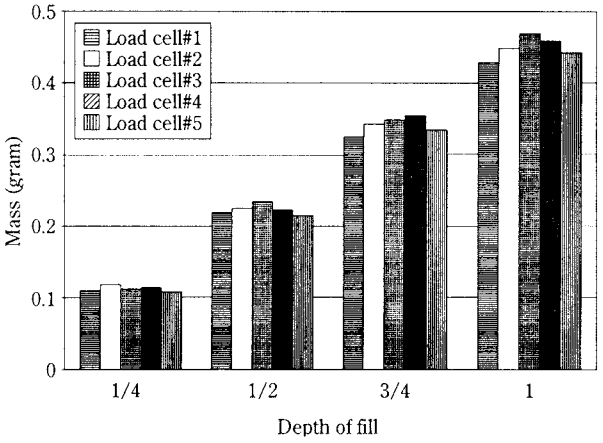

Fig. 4 Load measurements across load cells at different die fill depths with water

4.2 Experimental results

Figure 5 shows typical data for the case where the die was filled by the funnel fill method. The figure shows plots of the real-time cumulative mass vs. time data captured at the rate of 10 per second at each of five load cell locations as shown in Figure 2. From the plots it can be seen that maximum cumulative mass at the end of the filling process is recorded at the center of the die (load cell #3). The two load cells on either

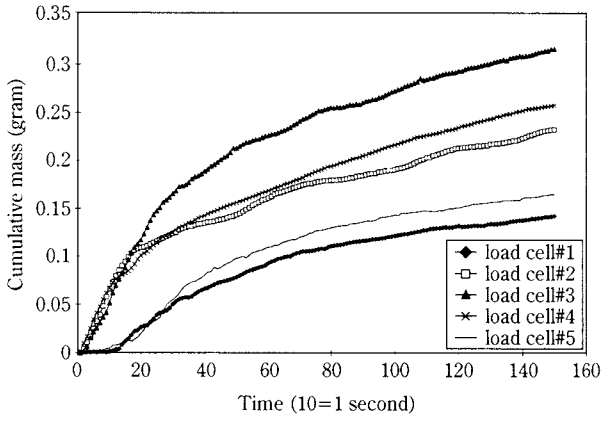

Fig. 5 Typical data for die filled with Alumina by the funnel fill method

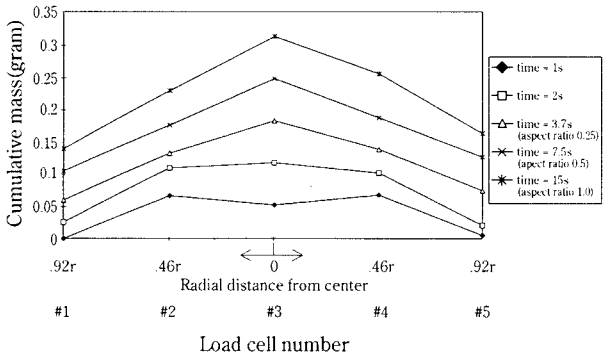

Fig. 6 Cumulative mass profile across the load cell locations at the end of successively increasing time periods from the start of the die fill process (funnel fill, die radius r=33 mm)

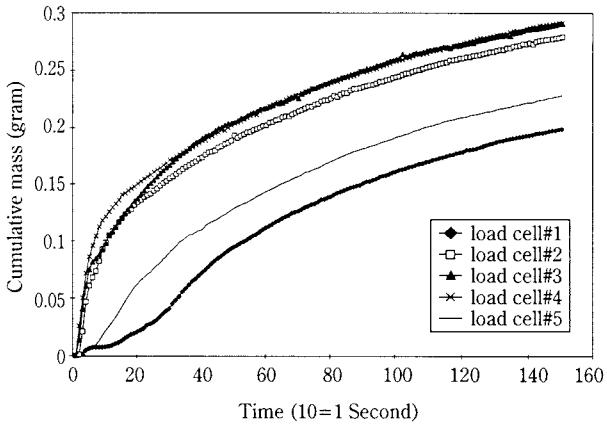

Fig. 7 Typical data for die filled with Alumina by the sieve fill method

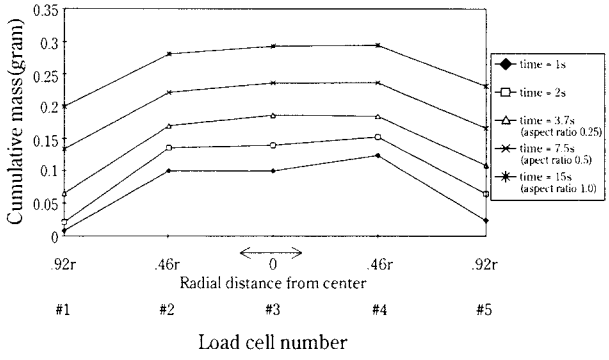

Fig. 8 Cumulative mass profile across the load cell locations at the end of successively increasing time periods from the start of the die fill process (sieve fill, die radius r=33 mm)

side (±0.46r, load cell #2 and #4) recorded the next two highest readings. The two load cells near the walls of the die (±0.92r, load cell #1 and #2) recorded the lowest readings. In the vicinity of the die wall, the powder wall interaction and wall friction is expected to reduce the loads at the bottom of the die. This finding is consistent with Bochinni's (1987) and others' observations. **Figure 6** shows plots of cumulative mass profile across the load cell locations at the end of successively increasing time periods from the start of the die fill process. The load cells indicate a powder fill, and hence density, distribution that decreases radially outwards from the center of the die towards the walls.

Figure 7 shows a typical dataset for the case of sieve filling method of Alumina. **Figure 8** shows plots of cumulative mass profile across the load cell locations at the end of successively increasing time periods from the start of the die fill process. Again, similar observation can be made regarding the particulate deposition as in the funnel fill case. The load cells near the walls record less load than the three in the middle. A comparison of data in Figures 6 and 8 shows that the load cells record a more flatter profile in the case of sieve fill than the funnel fill case. This suggests a more uniform powder fill for the sieve filling method compared to the funnel fill method.

Data in Figures 5 and 6 include the effect of heap formation as the surcharge on top of the deposited material. To discount the effect of heap formation, **Figure 9** shows the plot of load cells readings for the two fill methods at the end of the die fill process wherein the loadcell readings for the funnel fill case have been reduced in proportion of the surcharge height above the load cell location. The surcharge corresponds to the heap that had an angle of 27° (measured from digitized video still frames) for the funnel fill method. For the sieve fill method, the free surface was nearly horizontal. In Figure 9, the slopes of the profile plots on either side of the center of the die (on both sides of load cell #3) are shown. The slope values shown in Figure 9 were obtained by regressing the three data points in each case. It can be seen that the sieve fill plots are more flatter than

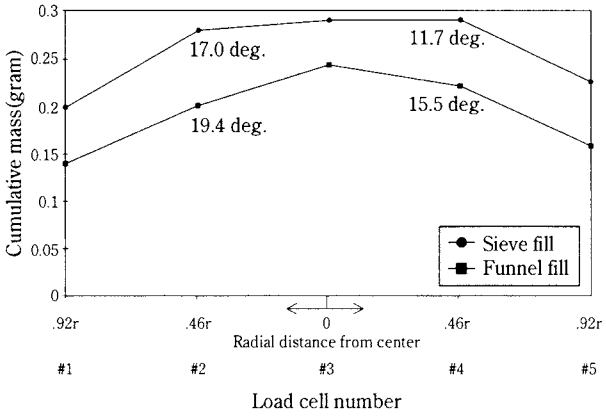

Fig. 9 Comparison of cumulative mass profile across the load cells at the end of die filling process by the funnel fill and sieve fill methods (die radius r=33 mm)

the funnel fill case thus reflecting the ability of the developed tester to distinguish between the two filling methods. For both methods, the powder fill is asymmetric as indicated by the slope values in Figure 9. This asymmetry is expected to influence the subsequent processing of the powder although to a lesser extent in the sieve filling case than the funnel fill case.

5. Future Activities

Based upon the results and experiences gained from this preliminary experimental analysis, a comprehensive design of experiments has been designed. In addition to spray-dried Alumina, four more powders will be tested. These are, 1) microcrystalline cellulose, 2) wheat flour, 3) silicon nitride powder, and 4) glass beads. In addition to the die filling factor, all powders will be tested in a randomized sequence for other factors mentioned earlier in the introduction section, namely, die cross-section, die aspect ratio, and rate of die filling. Statistical analysis will then be applied to the collected data to determine whether any of the factors under consideration significantly effect spatial die fill density distribution. Validation of the tester will be done by the CAT Scan experimental analysis technique.

6. Acknowledgement

The financial support provided by the Penn State Particulate Material Center and The Pennsylvania Agricultural Experimental Station is gratefully acknowledged.

References

1) Aoki R. 1976. Stresses of powders and granular materials in bins and hoppers. Theoretical and Applied Mechanics 26: 9-24.
2) Baillie L.A. 1977. US-Pat. 4 039 431, Atlantic Richfield Comp.
3) Bocchini G.F. 1987. Influence of small die width on filling and compacting densities. Powder Metallurgy 30(4): 261-266
4) Cermak J., J. Novosad, J Smid, O.P. Klenov and V.S. Lachmotsov, J.S. Matros. 1989. Czech Pat. 257 561.
5) Coshell L., R.G. McIver, R. Chang. 1994. X-ray computed tomography of Australian oil shales: nondestructive visualization and density determination. Fuel 73(8): 1317-1321.
6) Dhanoa P.S., V.M. Puri. 1997. Provisional Serial #60/054,981.
7) Faikin V.I., V.P. Levin, Y.N. Gribenyuk. 1976. Influence of the rate of die filling on the density of the powder. Soviet Powder Metallurgy and Metal Ceramics 15(8): 590-592.
8) Hosseini-Ashrafi M.E. and U. Tuzun. 1993. Tomographic study of voidage profiles in axially symmetric granular flows. Chemical Engineering Science 48(1): 53-57
9) Johnson J.A. and H.R. Wesler. 1976. US-Pat. 3 972 686, Universal Oil Products Comp.
10) Kantzas A. Computation of hold-ups in fluidized and trickle beds by computer assisted tomography. AIChE Journal 40(7): 1254-1261.
11) Kondoh M. And S. Takemoto. 1996. Visualization of powder behavoir for gravity filling. Toyota Central R&D Labs, Inc.
12) Kwade, A., D. Schulze and J. Schwedes. 1994. Determination of the stress ratio in uniaxial compression tests, Part 1. Powder Handling and Processing. 6(1): 61-65.
13) Molenda M., J. Horabik and I.J. Ross. 1994. Effect of filling method on load distribution in model grain bins. ASAE Paper no. 94-4517. St. Joseph, MI.
14) Moriyama R. and J Genji. 1985. Effect of filling methods on the wall pressure near the transition in a bin. Bulk Solids Handling 5(3): 603-609.
15) Moysey E.B. 1984. The effect of grain spreaders on grain friction and bin wall pressures. J. Agric. Engng. Res. 30: 149-156.
16) Munch-Anderson, J. and J. Nielsen. 1990. Pressures in slender grain silos. Measurements in three silos of different sizes. In Proc. 2nd European Symposium on the stress and strain Behavior of Particulate Solids — Silo Stresses, Praha, Czechoslovakia.
17) Nielsen, J. 1983. Load distribution in silos influenced by anisotropic grain behavior. International Conference on Bulk materials Storage, Handling and Transportation, Newcastle, NSW, Australia. August 1983.
18) Phogat V.K., L.A.G. Aylmore and R.D. Schuller. 1991. Simultaneous measurement of the spatial distribution of soil water content and bulk density. Soil science Society of America Journal 55(4) 908-915.

19) Readey M.J and F.M. Mahoney. 1995. Compaction of spray-dried ceramic powders: an experimental study of the factors that control green density. International SAMPE Technical Conference. 27: 622-634.
20) Smid J., P.V. Xuan and J. Thyn. 1993. Effect of filling method on the packing distribution of a catalyst bed. Chem. Eng. Technol. 16: 114-118
21) Tollner E.W., Y.C. Hung, B.L. Upchurch and S.E. Prussia. 1992. Relating x-ray absorption to density and water content in apples. Transactions of the ASAE 35(6): 1921-1928.
22) Williams R.A. and M.S. Beck. 1995. Process Tomography – Principles, Techniques and Applications. Butterworth Heinemann Ltd., Oxford.

Author's short biography

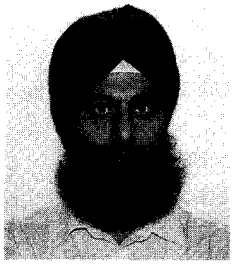

Premdeep S. Dhanoa

Premdeep S. Dhanoa is a Ph.D. candidate in the Department of Agricultural and Biological Engineering at The Pennsylvania State University from where he graduated in 1995 with a M.S. in Agricultural and Biological Engineering. He received a Master of Technology degree in Management and Systems from Indian Institute of Technology Delhi in 1989 and a Bachelor of Technology degree in Agricultural Engineering in 1987 from Punjab Agricultural University.

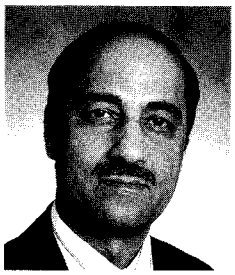

Professor Virendra M. Puri

Dr. Virendra M. Puri is Professor and Graduate Program Coordinator in the Department of Agricultural and Biological Engineering at the Pennsylvania State University. Professor Puri is also the research thrust leader of *Powder Storage, Flow and Handling* group of the Particulate Materials Center. Dr. Puri received his B.S. from Indian Institute of Technology and M.S. and Ph.D. from the University of Delaware in Mechanical Engineering. Professor Puri's research interests include: measurement of fundamental engineering properties of powders, development and validation of constitutive models, and use of numerical methods to model flow and compaction behavior of powders. He has served as the chairperson of the Bulk Solids Storage Systems Committee of the American Society of Agricultural Engineers. Professor Puri is an editorial board member of the *Particulate Science and Technology, An International Journal.* Dr. Puri regularly offers a postgraduate course in the area of powder mechanics and a hands-on industrial short course. Professor Puri has received several teaching and research awards.

Nucleation Control in Precipitation Processes by Ultrasound†

C. Gatumel, F. Espitalier, and J. Schwartzentruber
*Ecole des Mines d'Albi**
B. Biscans and A.M. Wilhelm
*ENSIGC-LGC Toulouse***

Abstract

The effect of an ultrasonic field on the precipitation process of barium sulphate has been investigated.

Experiments in a semi-batch precipitator showed that small crystal sizes with narrow distribution are obtained with ultrasound in a very reproducible way; however, this effect could not be assigned to an improvement in micromixing.

Experiments on continuous precipitation of barium sulphate in two reactors in series were carried out in order to characterise the effect of ultrasound on precipitation, by separating the nucleation and growth processes. It was concluded that the main effect of ultrasound is an enhancement of secondary contact nucleation by acoustic cavitation.

This change in the precipitation process allows small crystals with uniform size and shape to be obtained without effect of mechanical mixing. It is only necessary to sonicate the mixing volume of the reactants with a low level of ultrasonic power: this is very promising for industrial applications.

1. Introduction

The quality of particles produced by precipitation is largely determined by the very fast nucleation step, and is therefore difficult to control in industrial processes. Nucleation in precipitation depends strongly on the way the reactants are put into contact (1). In general, this results in a non-reproducible polymodal particle size distribution which makes it necessary to carry out sieving, grinding or agglomeration to obtain the required particle size.

It is well known that power ultrasound causes unstable cavitation in liquids, resulting in violent collapse of cavitation bubbles; therefore, ultrasound is expected to improve the micromixing of the liquid reactants (2), thus giving better control of supersaturation and nucleation. In addition, ultrasound can have effects on the solid particles by erosion and desaglomeration (3).

The main objective of this work was to investigate the role of ultrasound in the precipitation of a model product: barium sulphate. We divided this investigation into two parts. At first, we studied a semi-batch precipitation with micromixing characterisation. In a second phase, the direct effects of ultrasound on nucleation and growth were shown in a continuous precipitation. And finally, we tried to highlight the most important parameters in ultrasound-enhanced precipitation.

2. Materials and methods

2.1 Experimental apparatus

We studied the precipitation of barium sulphate at 20°C in accordance with the following equation:

$$Na_2SO_4 + BaCl_2 \rightarrow BaSO_4 \downarrow + 2NaCl$$

The solvent was demineralized water. The reactant concentration was chosen so as to avoid agglomeration: 1 mol/m^3 after mixing of reactants.

In both cases ultrasound is emitted directly in the solution. The frequency is 20 kHz, and the power involved is between 30 and 220 W. Under these conditions, ultrasound causes acoustic cavitation in liquids.

The ultrasound power levels reported in our experiments always signify the electrical power consumed by the generator, as measured with a wattmeter. The power dissipated in the liquid medium can be estimated by calorimetry. We found that the dissipated power is only 40% of the electrical power consumed by the generator.

* Route de Teillet, 81013 Albi, France
**Chemin de la Loge, 31078 Toulouse, France
† Received May 25, 1998

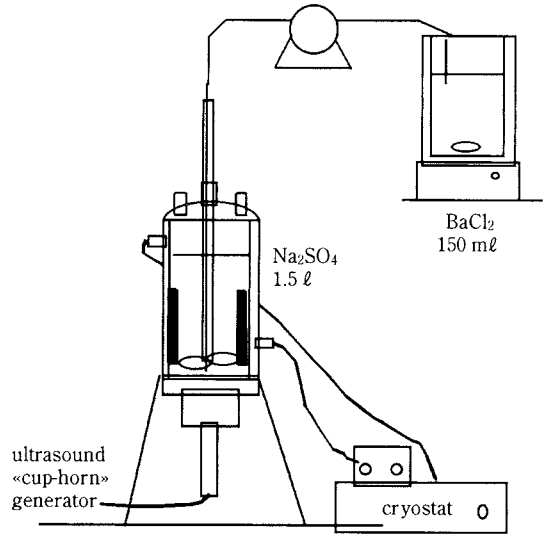

Fig. 1 Experimental equipment for semi-batch precipitation

2.1.1 Semi-batch precipitation

Figure 1 shows the apparatus used to study the semi-batch precipitation. The precipitator is baffled reactor, stirred with a marine propeller. Stirring speed is between 200 and 1000 rpm. Ultrasound is emitted directly into the liquid at the bottom of the reactor.

A solution of sodium sulphate (1.5 ℓ) is already in the reactor. Barium chloride (150 mℓ) is added by means of an inlet tube located in the stirrer spindle. Under these conditions, reactants are mixed just above (2 cm) the ultrasound emitter, so that the nucleation zone is well sonicated.

2.1.2 Continuous precipitation

The equipment consists of two reactors in series (see **Figure 2**). Each reactor can be sonicated separately. The first one is a small, stainless steel cell (0.05 ℓ) where nucleation is expected to be the dominant process. Ultrasound is emitted by means of a probe inside the cell. Reactants are introduced through a coaxial tube and mixed just under the ultrasonic probe. The second reactor is a one-litre, stirred reactor with baffles, and ultrasound emitted at the bottom (similar to the semi-batch reactor described in section 2.1.1); a longer residence time allows particles to grow. The stirrer speed in the growth reactor is 440 rpm and the total flow rate is 480 mℓ/min.

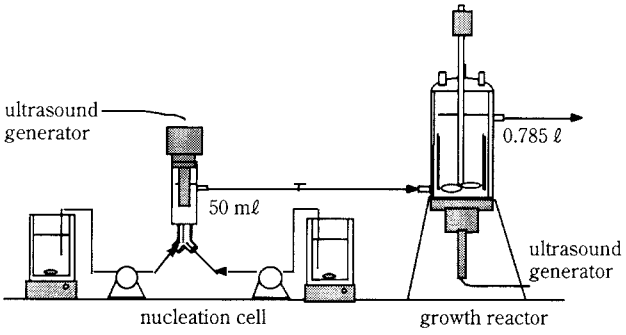

Fig. 2 Experimental equipment for continuous precipitation

2.2 Characterisation of the micromixing in the semi-batch reactor

The mixing of two miscible fluids can be analysed in terms of **macromixing** (dispersion of aggregates from one fluid into the other) and **micromixing** (molecular scale mixing of the reactants). The micromixing level was determined using the Bourne reaction (4) (a diazo coupling reaction involving consecutive competitive reactions):

$$A+B \rightarrow p\text{-}R \quad (1)$$
$$A+B \rightarrow o\text{-}R \quad (2)$$
$$p\text{-}R+B \rightarrow S \quad (3)$$
$$o\text{-}R+B \rightarrow S \quad (4)$$

where A is 1-naphthol, B is diazo sulphanilic acid, p-R and o-R are mononitric dyes, and S is a bi-nitric dye. Initial concentrations are chosen to give a slight excess of A with respect to B. The solution of A is already present in the reactor, and B is introduced slowly.

In the case of bad micromixing, aggregates of B remain in solution, so that the p-R or o-R formed by reactions (1) and (2) are still in contact with unreacted B: there is a high conversion of B into S. On the other hand, if the micromixing is good, very little S is produced.

The segregation index is defined as:

$$X_S = \frac{2C_S}{2C_S + C_{o-R} + C_{p-R}}$$

Reactions (1) and (2) are instantaneous, and (3) and (4) are very fast. X_S is close to unity for a very bad micromixing and will tend towards zero if micromixing is perfect.

2.2.1 Experimental procedures

The reaction is performed in the semi-batch apparatus described in section 2.1.1. The reactor contains initially 1.5 ℓ of solution 1-naphthol (0.527 mol/m^3) buffered a pH=10, and 150 mℓ of a solution of diazotised sulphanilic acid (5 mol/m^3) are added in 10 minutes.

The concentrations of the products are determined by spectrophotometry in the visible range. We used the molar absorption coefficients of the three dyes determined by Wenger et al (5).

2.2.2 Calculation of the mixing times

The Segregated Feed Model (SFM) developed by Villermaux (6) was adapted to a simple jet feed in

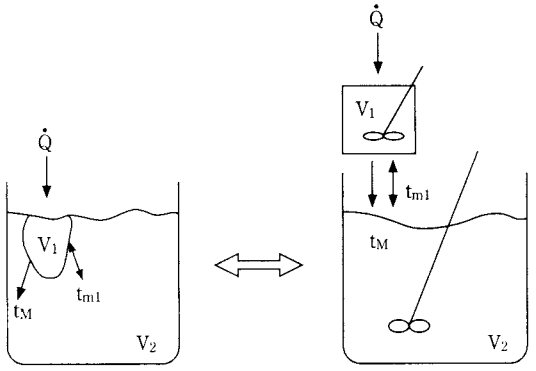

Fig. 3 Principle of SFM model for a simple jet reactor

order to deduce the mixing times from the measured segregation index.

This phenomenological model takes into consideration that the reactor is divided into two zones (see **Figure 3**). Each zone is a perfectly mixed reactor. We considered two different types of mass transfer between these two zones:

- an irreversible transfer from the feed to the reactor volume. This is the macromixing and its characteristic time is t_M.
- a reversible transfer between the two zones, which represents the micromixing and its characteristic time is t_m.

The corresponding set of ordinary differential equations is solved numerically (see appendix 1). This model allows calculation of the dye concentrations and the segregation index X_S from t_M and t_m. Reciprocally, it is possible to fit values of mixing times t_M and t_m to measured dye concentrations by means of a standard parameter estimation method.

2.3 Precipitation characterisation

Following a precipitation requires knowing both the solution composition and the solid product characteristics.

2.3.1 Solution

As the reaction is performed with salts, we can measure the concentration of unreacted species in the precipitation by conductimetric measurements. The mean relative supersaturation can be calculated with:

$$S=\frac{C_{BaSO_4}}{\sqrt{K_S}}\cdot\gamma\pm$$

K_S: solubility product; C_{BaSO4} is the concentration of $BaSO_4$; $\gamma\pm$ is the mean activity coefficient. It is calculated with the Bromley equations for an electrolyte (7).

2.3.2 Solid product

At the end of the experiments, crystal size distributions are measured with a Malvern Mastersizer laser diffraction instrument. The samples are taken and analysed immediately and without dilution. We can also filter a sample of solution and observe the crystals' shape with a Scanning Electron Microscope.

3. Results and discussion

3.1 Investigations of the role of mixing during the semi-batch sonicated precipitation

We first investigated the influence of mixing conditions on the precipitation of barium sulphate. Experiments were conducted in the semi-batch equipment. At first, we determined that, under the experimental conditions we used, macromixing was not a limiting step. We therefore present only the study of micromixing in the experimental apparatus.

3.1.1 Effect of ultrasound on micromixing

The micromixing level in the precipitator subjected to ultrasound was determined as a function of the stirrer speed in a liquid phase without precipitation. Very similar results were obtained in a synthetic liquid-solid suspension, showing that the presence of solid particles does not significantly affect the micromixing (8).

In **Figure 4**, we report the segregation index obtained by the Bourne characterisation method for several stirrer speeds and ultrasonic power levels. For the lowest agitation levels, micromixing is improved by an increase of the ultrasonic power, but this effect of ultrasound on micromixing disappears at high stirrer speeds. Similar results have been obtained by other authors (9), and could be explained by an interaction between turbulence and cavitation caused by high-speed stirring and the acoustic waves propagation.

It can be noticed that our segregation indexes

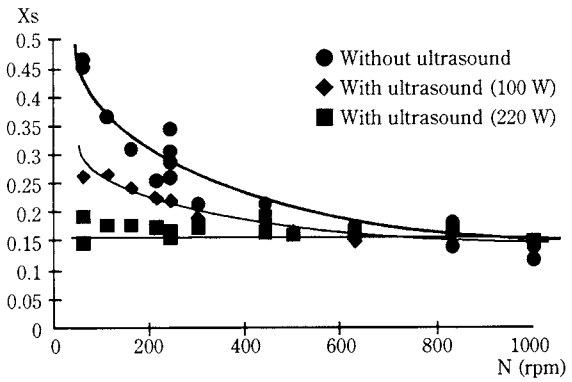

Fig. 4 Influence of stirrer speed and ultrasound on the segregation index

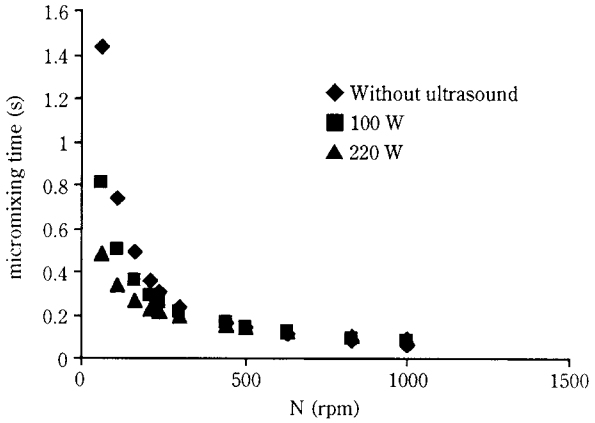

Fig. 5 Micromixing times calculated from the segregation indexes

remain rather high, and that the best micromixing is obtained at a high stirrer speed: 600 rpm for a 2-litre reactor. This is probably because the reactants are introduced at a very low point in the reactor (just above the ultrasound transducer).

We have noticed that the results are more reproducible with ultrasound. The mixing times calculated from the micromixing experiments are shown in **Figure 5**. In all our experiments, the micromixing times were larger than 0.05 s. On the one hand, these values are much larger than the characteristic time of the Bourne reaction (10^{-5} second), which means that this reaction is really controlled by micromixing in our experimental conditions, even for the highest agitation levels. And on the other hand, the mixing times are greater than the characteristic time of precipitation (induction time) which is of the order of magnitude of 10^{-3} second. This confirms that precipitation should be affected by micromixing conditions, since nucleation will occur before mixing is complete.

3.1.2 Effect of ultrasound on the precipitation product

The precipitates formed both with and without ultrasound were compared for shape and particle size distribution. **Figure 6** shows photographs of crystals.

Without ultrasound, there are some platelets topped with crystallites, and some "roses of the desert". These last ones do not seem to be agglomerates of platelets, but probably platelets which have grown on top of each other.

When precipitation is carried out under ultrasonic irradiation, crystals are smaller but they still have the same shape. It may be concluded that the presence or absence of ultrasound does not change the morphology of particles.

Figure 7 shows the particle size distributions obtained for several ultrasonic powers at 240 and 1000 rpm. For both agitation speeds, ultrasound leads to a reduced crystal size and a narrower particle size distribution. It was also observed that our results are much more reproducible in the presence of ultrasound.

The mean crystal size obtained for several ultrasonic powers are reported as a function of the stirrer speed in **Figure 8**.

Without ultrasound, when the stirrer speed is increased, the mean particle size seems to remain constant or to increase slightly between 200 and 600 rpm, and then decreases. This shows the importance and complexity of mixing phenomena during precipitation. These results suggest that the production of supersaturation is controlled by the contacting of reactants, and thus by the micromixing conditions. At low stirrer speeds, reactants are badly mixed, local supersaturation is quite low, few nuclei are formed and the mean supersaturation is high enough to

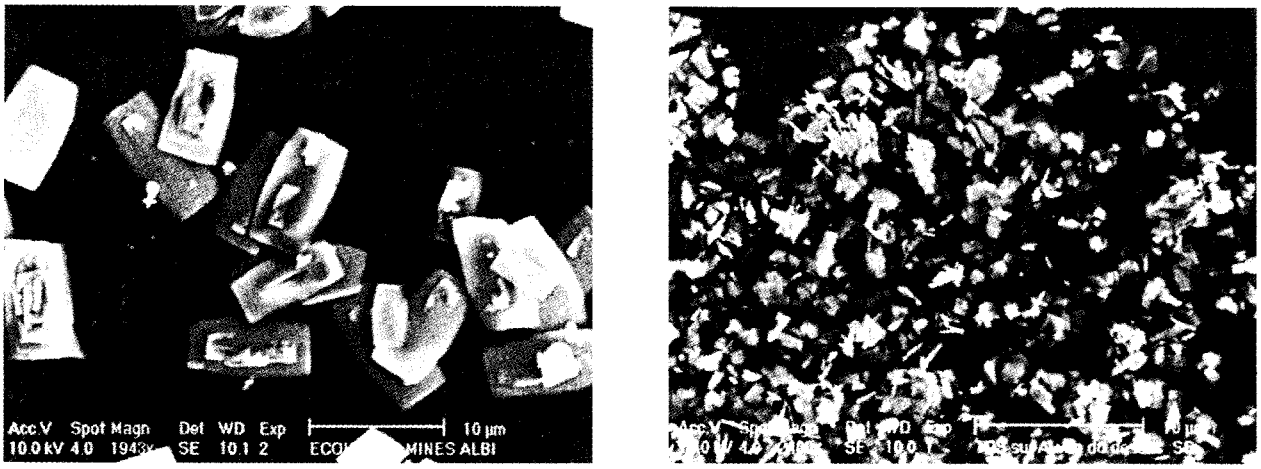

Without ultrasound 200 Watt

Fig. 6 Crystal shapes observed with a S.E.M. microscope for precipitation with or without ultrasound

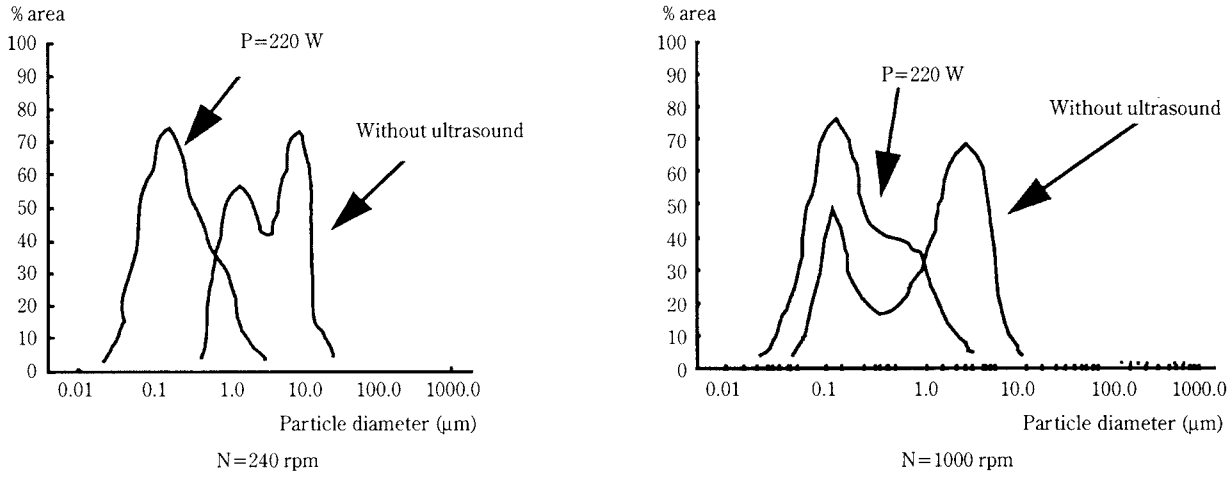

Fig. 7 Influence of ultrasound on particle size distribution (in surface) for two stirrer speeds

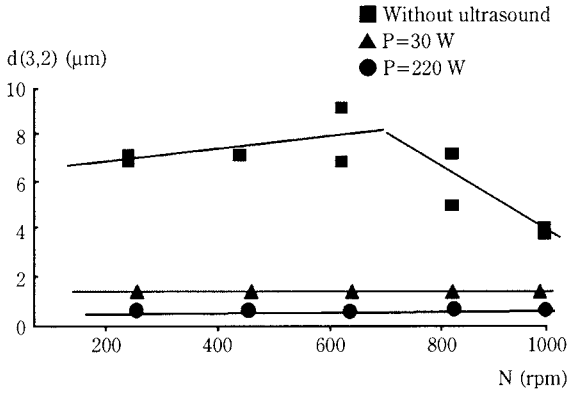

Fig. 8 Influence of stirrer speed and ultrasound on the mean particle size of crystals

permit crystal growth. Improving the mixing will enhance both crystal growth and nucleation, and there is no clear effect of mixing on particle size. But, when local mixing in the nucleation zone is sufficient, local supersaturation increases, resulting in abundant nucleation and a strong decrease in crystal size. We conclude from these results that without ultrasound, the precipitation process seems to be very sensitive to the mixing conditions in the reactor.

In the presence of ultrasound, **Figure 8** shows that for all stirrer speeds, the mean crystal size decreases with increasing ultrasonic power; considering the resolution of the particle size analysis, there is no significant effect of stirrer speed on the mean particle size.

As a first conclusion, we can see that the effects of the micromixing conditions disappear in the presence of ultrasound. Moreover, one can see (Figure 4) that when the stirrer speed is greater than 600 rpm, the micromixing index is the same with and without ultrasound; however, the mean crystal size is strongly affected by ultrasound.

This shows that the effect of ultrasound on precipitation is not due to an improvement in micromixing, but there must be a specific effect of ultrasound on the precipitation mechanisms, namely nucleation or growth, since there is no agglomeration in our experiments.

3.2 Ultrasound effect on nucleation

In order to determine the influence of ultrasound on nucleation and growth, we chose to work in continuous mode by physically separating these two processes. The experimental device is described in 2.1.2. Reported mean sizes are calculated from the size distribution on the surface. Numbers of particles are given for 100 mℓ of suspension. These last quantities could not be determined with great precision and should be considered only as orders of magnitude. The ultrasonic power used in these experiments was 200 W.

3.2.1 Ultrasound in the nucleation cell

Results in terms of supersaturation, size and number are presented in **Table 1**. The shapes of crystals obtained in the cell without ultrasound and for 200 W are presented in **Figures 9-a** and **9-b**, respectively.

Without ultrasound, crystals are in the form of "roses of the desert" and platelets, and they are topped with growing crystallites. With ultrasound there are only platelets, and no more crystallites.

Table 1 Ultrasound effect in the nucleation cell

	without ultrasound	200 Watt
Supersaturation	46.5	15.2
mean size (μm)	4.1	0.9
number for 100 mℓ	~1e10	~1e11

Ultrasound allows the creation of more and smaller crystals. But these crystals do not seem to be broken crystals, and the final supersaturation is divided by two when ultrasound is used. The effect of ultrasound in the cell is clearly an increase of nucleation rate (primary or secondary).

3.2.2 Ultrasound in the growth reactor

Table 2 presents supersaturation, size and number of crystals obtained in the growth reactor, either with or without ultrasound in the cell. **Figures 9-c** and **9-d** represent the shape of crystals formed with and without ultrasound in the growth reactor, when there is no ultrasound in the nucleation cell.

If ultrasound is applied to the cell, supersaturation at the exit of the cell is very low (lower than 15), and so there is not much solute remaining to nucleate or to feed the crystals by growth. The number of particles is the same in both reactors; supersaturation is slightly lower in the growth reactor and the mean size is slightly larger.

If neither the cell nor the growth reactor is sonicated, values in **Table 2** indicate that there is only growth and no nucleation in the growth reactor. As in the cell, Figure 9-c shows that crystals present platelets and "roses of the desert" shapes. The difference is that there are more crystallites on the crystals.

If the growth reactor only is sonicated (200 W), one sees that supersaturation and mean crystal size are smaller in the growth reactor than in the cell, and that there are more crystals in the growth reactor. Crystal shapes are mainly platelets, with some "roses of the desert" shape (see Figure 9-d). But as in the cell with

Table 2 Ultrasound effect in the growth reactor

Ultrasonic power in the nucleation cell	Ultrasonic power in the growth reactor	supersaturation n	mean size (Nm)	number for 100 mℓ
0 W	0 W	26.4	6.9	~1e10
0 W	200 W	16	0.80	~1e11
200 W	0 W	10.4	0.80	~1e11
200 W	200 W	10.2	0.85	~1e11

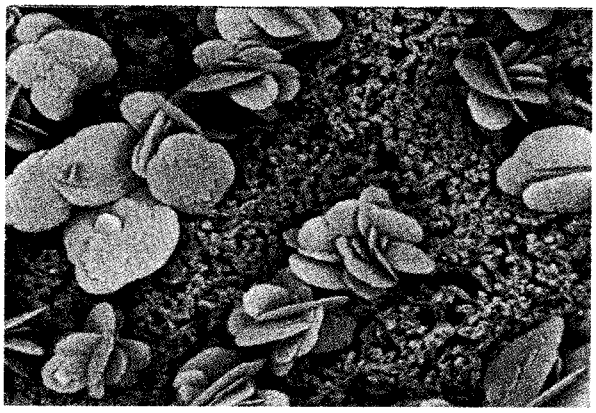

a 9 μm

Nucleation without ultrasound

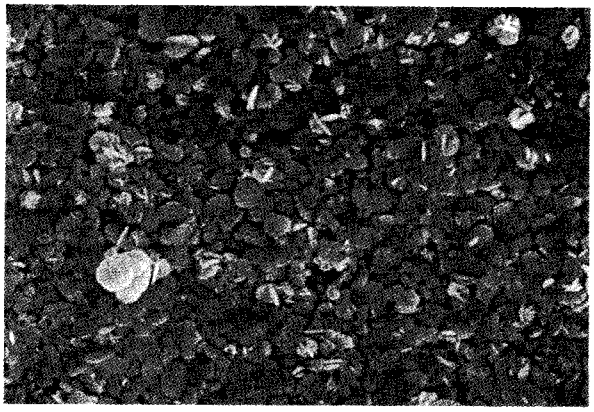

b 9 μm

Nucleation with ultrasound (200 W)

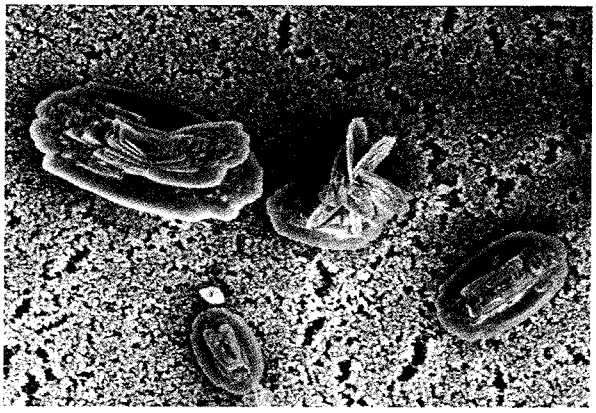

c 32 μm

Growth without ultrasound

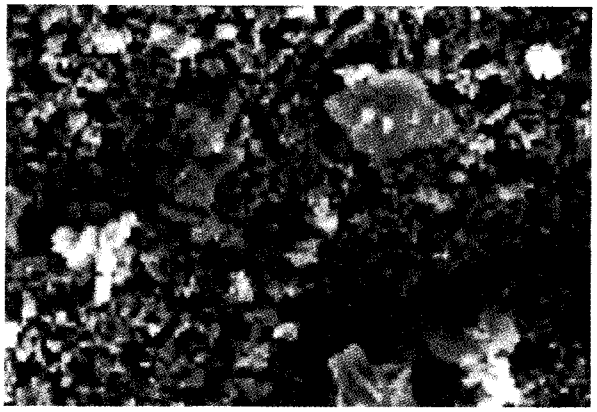

d 9 μm

Growth with ultrasound (200 W)

Fig. 9 Ultrasound effect on crystal shape in the continuous reactors

ultrasound, they are not topped with crystallites any more. In this case, it seems that creation of crystals in the growth reactor is not due to breakage but to nucleation.

3.2.3 Proposed mechanism

Results obtained with the continuous sonicated precipitators show that ultrasound has a strong effect on nucleation. As far as very small supersaturations are concerned (only 10 in the growth reactor with ultrasound when there is no ultrasound in the cell), it may be secondary nucleation. The probable mechanism could be contact nucleation (10): when a cavitation bubble implodes near a growing crystal, it can remove clusters forming on a crystal surface or petals of roses in formation and thus produce new nuclei in solution.

3.3 Validation by the population balance

The two reactors in series were modelled on the basis of a simple population balance. They are supposed to be MSMPR (Mixed Suspension Mixed Product Removal), and we have chosen to describe the growth rate as being dependent on the crystal size. The model equations are presented in appendix 2. The kinetic parameters have been fitted to experimental crystal size distributions. These calculations should not be considered as a precise quantitative study, but rather as a tool to determine tendencies in order to validate our assumptions.

3.3.1 Nucleation at the "zero size"

At first, we assumed that secondary nucleation was contact nucleation rather than breakage. In the population balance, this could be expressed by nucleation at the "zero size", which is equivalent to the first class of crystals. The computed nucleation rates are reported in **Tables 3** and **4** for the nucleation cell

Table 3 Nucleation rate values in the cell calculated by population balance

	B, crystals/m³/s
cell without ultrasound	1.22 e 15
cell with 200 Watt	3.53 e 15

Table 4 Nucleation rate values in the growth reactor calculated by population balance, crystals/m³/s

	Growth reactor without ultrasound	Growth reactor 200 Watt
cell without ultrasound	0	9 e 13
cell 200 Watt	0	0

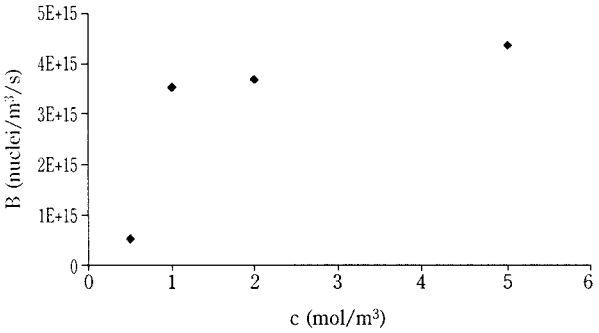

Fig. 10 Nucleation rate in the small cell as a function of the initial concentration

and the growth reactor. These values allow good representation of the experimental size distributions. This shows that nucleation occurs at the minimum crystal size and can therefore be primary or secondary contact nucleation. The method cannot discriminate between these assumptions; however, secondary nucleation is more likely to occur in an ultrasonic field.

3.3.2 Influence of initial concentration

We calculated nucleation rates in the small cell subjected to ultrasound (200 W) for different initial concentrations: 0.5 mol.m^{-3}, 1 mol.m^{-3}, 1.5 mol.m^{-3}, and 2 mol.m^{-3}. The results are plotted in **Figure 10**. The nucleation rates depend on initial concentrations. This reinforces the hypothesis of secondary contact nucleation (10), since the breakage nucleation rate should be independent of supersaturation.

4. Influence of the ultrasonic parameters on the crystal's characteristics during the continuous precipitation process

We found that the most important effect of ultrasound in the precipitation of barium sulphate is to cause secondary nucleation. Characterisation of the ultrasound effect on the process requires knowing the influence of the power involved and the ultrasound location. We ran experiments by separately sonicating the cell and the growth reactor with different powers. The values observed are the mean crystal size and the number of crystals in the cup-horn. The results are reported in **Figure 11**.

In terms of final product number and size, applying ultrasound to the small cell or to both reactors leads to the same results and the ultrasonic power does not seem to have a significant effect. There are indications that a 100 W power level could be somewhat more efficient than 200 W. This is perhaps because

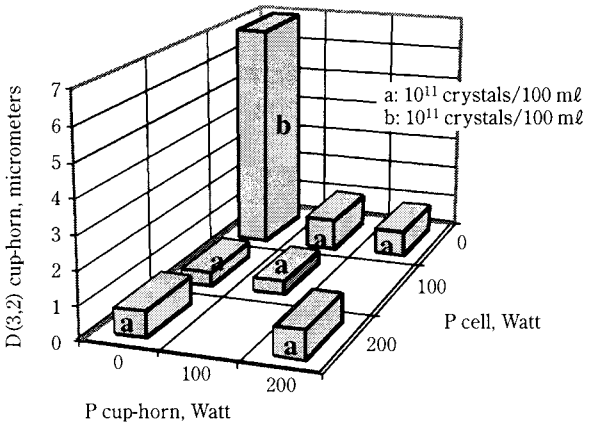

Fig. 11 Effects of ultrasound power and location on mean crystal size and number of crystals

when the ultrasonic power increases, the number of cavitation bubbles also increases, thus hindering the propagation of the acoustic wave. We also did some experiments at 50 W, which is the lowest power delivered by our ultrasound generator, and the results were essentially the same as for 100 W.

5. Conclusion

It has been shown that applying an ultrasonic field during barium sulphate precipitation leads to much more reproducible results. Without changing the morphology of the crystals, it brings about a large reduction in the mean particle size and a narrower size distribution.

These beneficial effects cannot be attributed to an improvement in reactant micromixing; it is demonstrated that ultrasound has a direct effect on the nucleation process (mainly on secondary contact nucleation), which is promoted by acoustic cavitation. These effects can be obtained with a low acoustic power, and it is only necessary to apply ultrasound in the small nucleation volume where the reactants are put into contact. Ultrasound therefore appears to be a very promising way of improving the control of industrial precipitation processes.

Nomenclature

a	: coefficient for growth rate	[m^{-1}]
B	: nucleation rate	[crystals/m^3/s]
C_i	: concentration of product i	[mol/m^3]
d(3,2)	: mean particle size (in surface)	[μm]
G	: growth rate	[m/s]
G_0	: growth rate at zero size	[m/s]
k	: kinetic constant	[m^3/mol.s]
L	: crystal size	[mm]
Q	: feed rate	[m^3/s]
n	: population density	[crystals/m^4]
r_{ij}	: production rate of component i in zone j	[mol/m^3.s]
t_M	: macromixing characteristic time	[s]
t_m	: micromixing characteristic time	[s]
t	: mean residence time	[s]
V_i	: volume of zone i	[m^3]
X_s	: segregation index	

References

1) GARSIDE. Tailoring crystal products in precipitation processes and the role of micromixing. AIChE Symposium series, 87(284), 16-25, 1991
2) OKADA, S. FUSEYA, Y. NISHIMURA, M. MATSUBARA. Effect of ultrasound on micromixing. Chem. Eng. Sci., 27(3), 529-535, 1972
3) LEBRAS. Action des ultrasons sur les processus physico-chimiques. Revue de chimie minérale, 4, 283-315, 1967
4) BOURNE, F. KOSICKI and P. RYS. Mixing and fast chemical reaction1: test reaction to determine segregation. Chem. Eng. Sci., 36 (10), 1643-1648, 1981
5) WENGER, E.H. DUNLOP and I.D. MACGILP. Investigation of the chemistry of a diazo micromixing test reaction. A.I.Ch.E. Journal, 38 (7), 1105-1114, 1992
6) VILLERMAUX. A simple model for partial segregation in a semi-batch reactor. A.I.Ch.E. Annual Meeting, paper 114-A (1st page), A1-B2, 1989
7) BROMLEY. Thermodynamic properties of strong electrolytes in aqueous solution. A.I.Ch.E. Journal, 19, 313-320, 1973
8) GATUMEL, F. ESPITALIER, O. LOUISNARD, J. SCHWARTZENTRUBER, B. BISCANS and A.M. WILHELM. Micromixing and ultrasonic precipitation of barium sulphate. Proceedings of the ECCE-1 congress, vol. 2, P.1511, 1997
9) MONNIER, A.M. WILHELM and H. DELMAS. Ultrasonic mixing: preliminary results. A.I.Ch.E. Symposium series, San Diego, California, 214-219, 1996
10) GARSIDE and R.J. DAVEY. Secondary contact nucleation: kinetics, growth and scale-up. Chem. Eng. Com., 4, 393-424, 1979

Appendix 1

Differential equations system for the SFM model in the case of a simple jet reactor

$$A + B \rightarrow p - R,\ k_{1\text{-}p} = 12238$$
$$A + B \rightarrow o - R,\ k_{1\text{-}o} = 921$$
$$p - R + B \rightarrow S,\ k_{2\text{-}p} = 1.835$$
$$o - R + B \rightarrow S,\ k_{2\text{-}o} = 22.25$$

For zone 1 reaction rates are:

$$r_{A1} = -(k_{1\text{-}p} + k_{1\text{-}o})C_{A1}C_{B1}$$
$$r_{B1} = -(k_{1\text{-}p} + k_{1\text{-}o})C_{A1}C_{B1} - k_{2\text{-}p}C_{pR1}C_{B1} - k_{2\text{-}o}C_{oR1}C_{B1}$$
$$r_{pR1} = -k_{1\text{-}p}C_{A1}C_{B1} - k_{2\text{-}p}C_{R1}C_{B1}$$
$$r_{opR1} = -k_{1\text{-}o}C_{A1}C_{B1} - k_{2\text{-}o}C_{R1}C_{B1}$$

Equations for zone 2 are strictly analogous.
Volume balances are:

$$\frac{dV_1}{dt} = -\frac{V_1}{t_M} + Q$$
$$\frac{dV_2}{dt} = -\frac{V_2}{t_M}$$

Partial mass balances are:

$$\frac{d(V_1C_{i1})}{dt} = -\frac{V_1C_{i1}}{t_M} + \frac{V_1V_2}{V_1+V_2}\frac{C_{i2}-C_{i1}}{t_m} - r_{i1}V_1$$
$$\frac{d(V_2C_{i2})}{dt} = -\frac{V_1C_{i1}}{t_M} + \frac{V_1V_2}{V_1+V_2}\frac{C_{i1}-C_{i2}}{t_m} - r_{i2}V_2$$

Initial conditions

t = 0, $V_1 = 0$, and $V_2 = V_o$

Appendix 2

MSMPR population balance

Population balance in the nucleation cell:

$$\frac{n_1}{\tau_1} + \frac{d(n_1G_1)}{dL} = 0$$

with

$$n_1(L_0) = \frac{B_1}{G_0^1}$$

In the growth reactor:

$$\frac{n_2 - n_1}{\tau_2} + \frac{d(n_2G_2)}{dL} = 0$$

with

$$n_2(L_0) = \frac{B_2}{G_0^2}$$

Crystal growth rate (Canning and Randolph model, order 1):

$$G_i(L) = G_0^i(1 + a_iL)$$

After integration, the population balance in the cell becomes:

$$n_1 = n_0^1(1 + a_1L)^{-\frac{1+a_1G_0^1\tau_1}{a_1G_0^1\tau_1}}$$

with

$$n_0^1 = \frac{B_1}{G_0^1}$$

The equation for the growth reactor must be integrated numerically:

$$G_2(L)\frac{dn_2(L)}{dL} + n_2(L)\left(\frac{dG_2(L)}{dL} + \frac{1}{\tau_2}\right) = \frac{n_1(L)}{\tau_1}$$

Author's short biography

Cendrine Gatumel

(main author) holds an engineering degree from the Ecole Nationale Supérieure d'Ingénieurs du Génie Chimique (Chemical Engineering Institute) in Toulouse, and a PhD degree from the Institut National Polytechique de Toulouse. She now has a postdoctoral position at LAGEP (Laboratoire d'Automatique et de Génie des Procédés – Process Engineering and Process Control Laboratory) in Lyon.

Fabienne Espitalier

(corresponding author) holds an engineering degree from the Ecole Nationale Supérieure d'Ingénieurs du Génie Chimique (Chemical Engineering Institute) in Toulouse. She is presently Assistant Professor in Chemical Engineering at the Ecole des Mines in Albi, where she works on precipitation and crystallisation processes.

Jacques Schwartzentruber

Holds a civil engineering degree from the Ecole des Mines in Paris, and a PhD degree from the Ecole Nationale Supérieure des Techniques Avancées in Paris. He is presently Professor of Chemical Engineering at the Ecole des Mines in Albi.

Béatrice Biscans

Dr Béatrice BISCANS was born in 1958. She graduated from the Ecole Nationale Supérieure de Génie Chimique of Toulouse (ENSIGC) in 1982. She prepared a PhD thesis on the separation of proteins by ion exchange chromatography in the Chemical Engineering Laboratory of Toulouse (UMR CNRS 5503) and obtained her doctor's degree in 1985. She then undertook post-doctoral research on the electrophoretic separation technique.

Since 1987, she has developed and supervised several studies in the field of crystallization as a researcher of CNRS (French National Scientific Centre of Research), working in the Chemical Engineering Laboratory of Toulouse (UMR CNRS 5503). In particular, her work involves the development of research studies on spherical crystallization.

Acoustic Monitoring of Pneumatic Transport Lines: From Noise to Information

"Mass flowrate measurements in dilute phase pneumatic transport lines using acoustic sensors"†

Maths Halstensen[1)], **Sunil de Silva**[2)] **and Kim Esbensen**[3)]
*Telemark College/Tel-Tek, Porsgrunn, Norway**

Abstract

Acoustic chemometrics is an interdisciplinary approach covering diverse fields including applied engineering, electronics, signal analysis and chemometrics. The applications of acoustic chemometrics are manifold, but quantitative analysis (chemical/physical) and process monitoring and physical characterisation of products are areas in which it can be beneficially used. Potential applications in many industry sectors abound. In one particular sense, acoustic chemometrics is simple: Acoustic signals from any process or equipment, followed by some form of pertinent signal analysis, are subjected to chemometric data analysis. In this context it is often the power of multivariate calibration that comes to the fore. Here, we give one major example of the use of applied acoustic chemometrics – non-invasive monitoring of a pneumatic transport line. Noise and acoustics have been defined as follows: ***noise*** *– Irregular fluctations accompanying, but not relevant to, a transmitted signal (Concise Oxford Dictionary),* ***acoustics*** *– science of sound (Scribner Bantam Dictionary). The irregular fluctations referred to above contain much valuable information, and it is the line acquisition, conditioning and analysis of such fluctations that we are concerned with in this paper.*

1. Introduction

Industrial and technological processes are always accompanied by stronger or weaker energy outputs (heat, sound, vibration, etc.). Emission of audible noise is an inherent characteristic of very many production, manufacturing, transportation and/or propulsion processes – indeed, on reflection it is well nigh impossible to conceive of any industrial/technological *processes* which are not accompanied by at least some form of apparently incoherent acoustic energy output – **noise**. Some of this noise invariably shows up in the form of vibrational energy which can be measured, and whatever can be measured can in turn be subjected to chemometric data analysis. In this context, by "acoustic output" we mean not only "true noise" in the audible range, i.e. 5-20 KHz, but we also include vibrational energy outputs in contiguous frequency ranges which for many practical purposes of technological applications of acoustic chemometrics cover the range 0-25KHz.

There are many communalities for acoustic chemometrics applications – the common ground can be outlined (the "data path" from noise to information). **Figure 1** is a schematic flow-sheet for a generic data path from the acoustic phenomenon to the final multivariate calibration model, including future *prediction* facilities.

During its first 2-3 years of operations, the Applied Chemometrics Research Group at Telemark College/Tel-Tek has designed, built and implemented most of the necessary electronic and computer equipment, covering both fixed as well as portable sets of data acquisition tools needed for any type of acoustic chemometrics (laboratory or field-based) in close collaboration with the Oslo-based entrepreneur company "SENSORTEKNIKK A/S", which specialises in dedicated sensor technology.

Acoustic sensor technologies include generic accelerometers (often standard industrial units are quite adequate, but sometimes also tailor-made special accelerometers). Both portable recorders and desk-top or laboratory bench PC-based data I/O links are in use.

* Applied Chemometrics Research Group (ACRG), Institute of Process Technology, Kjolnes Ring, 3914 Porsgrunn, Norway
1) Corresponding author, 2) Head, POSTEC group, Tel-Tek, 3) ACRG-Leader
† Received May 25, 1998

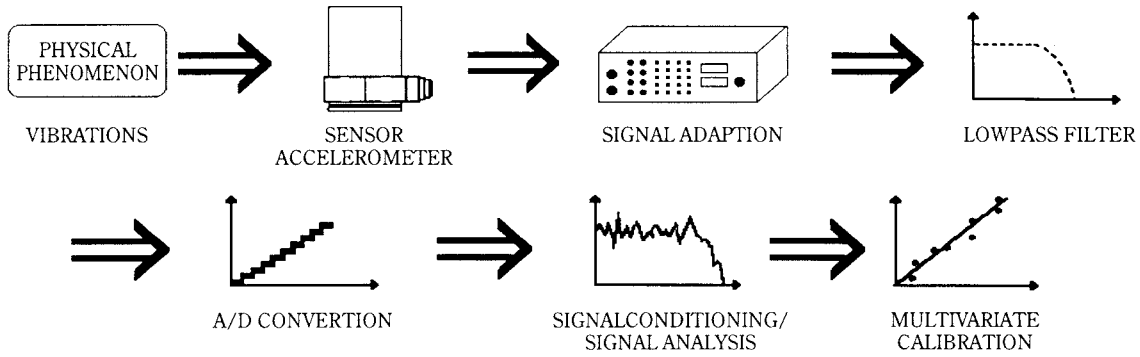

Fig. 1 Generic data path flow-sheet in acoustic chemometrics

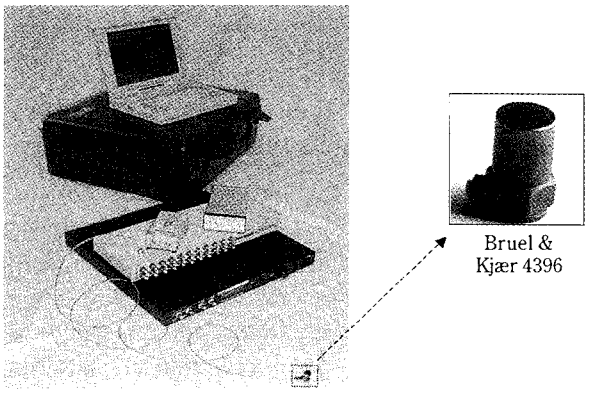

Fig. 2 ACRG portable acoustic chemometric "travelling suitcase" – (top to bottom): Portable PC (laptop); shock-proof case for total equipment complement; power supplies; universal connector array; amplifier/filtering unit; cabling; accelerometer(s), one or two in present configuration

All hardware solutions are backed by the powerful LabVIEW software system (National Instruments Inc.), allowing for dedicated virtual instruments through the use of the graphical programming facility, G.

2. Non-invasive monitoring of the pneumatic flow behaviour of particulate materials

2.1 Context of pneumatic acoustic chemometric studies

A new concept for characterising the flow of particulate materials in pneumatic conveying pipelines has been developed experimentally by ACRG and POSTEC (Powder Science and Technology Group, Tel-Tek) during the last two to three years. By means of chemometrics, several attempts have been made to establish *empirical regression models* describing the connection between the flow behaviour of representative types of materials and non-invasive acoustic measurements of pipeline surface vibrations. The aim is real-time characterisation of the material flow through *prediction* from these non-invasive acoustic measurements, an objective which in general is too complicated for a physical first-principles approach. Experimental data are needed to develop the necessary predictive model(s). Several pilot-scale & semi-plant-scale conveying tests have been carried out on a horizontal 21-m-long, 2″ pipeline with a 90° bend (see **Fig. 3**). "Clamp-on" surface-mounted accelerometers were used to measure the compound acoustic vibrations resulting from the internal material flow. The effect of the different radial and axial position of the sensors on the accuracy of the predicted values has been investigated for different representative types of materials, e.g. PVC granules, sand, rape seed, cement and dolomite. Here, we give some selected highlights of these studies.

At the outset, it would appear reasonable to assume that the "noise" caused by pneumatic conveying systems is a reflection both of the relevant transport system settings as well as of the material properties themselves, e.g. solids feed rate, air flow, particle size distribution, particle density, humidity – and potentially many others. Although inseparable by the human ear, each property must be assumed to contribute in principle in a tractable manner (qualitatively as well as quantitatively) to the composite acoustic impact. It is the objective of acoustic chemometrics to be able to *decompose* such (noisy) signals with the aim of *quantification* of the parameter(s) of interest. In pneumatic transport lines, the ability to measure the solids loading by a robust, non-invasive technique as well as to use this to stay clear of blockages is of critical economic importance.

2.2 Experimental

The pneumatic conveyor is designed for batch transport. The main components of the test rig are *the blow tank*, *the test-section pipeline* and *the receiving tank*. Recharging of the blow tank is taken care of by a movable silo carried by an overhead crane. The solids feed rate is either controlled by the bypass to

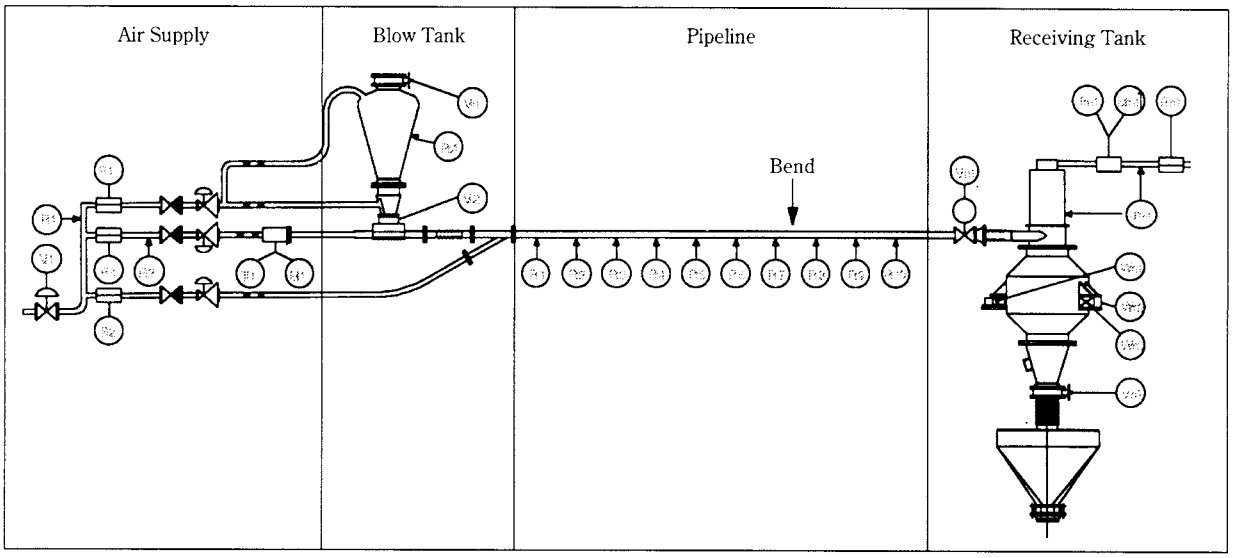

Fig. 3 Schematic sketch of the pneumatic test rig – location of accelerometers in present study corresponds to the first and last position (before bend) on the straight pipeline section (P1 and P7, respectively).

transport air ratio, or by a piston-operated knife valve at the bottom of the blow tank. The overall air flow rate is the summarised flow rate of transport air, fluidising air and bypass air. Each supply is controlled by a globe valve and monitored by a turbine flowmeter. The transport air is additionally equipped with a pneumatic actuator for accurate adjustment. Humidity, temperature and pressure are also monitored on the air supply side.

The conveying line used for the experiments was 21 m long and had an inside diameter of 53 mm. Apart from a 90° "long radius bend" placed 13 m away from the outlet of the blow tank, no hindrances disturb the material flow. Ten equally spaced pressure transmitters enable monitoring of the pressure progress along the pipeline and calculation of specific pressure drops. This is the "traditional" pressure drop monitoring approach. The receiving tank is placed upon three load cells enabling continuous measurements of the average mass flow – massflow solids, Mf_{solids} – to be made. This parameter will serve here to illustrate one important "parameter of interest" in the present context. Thus the acoustic chemometric modelling will specifically be oriented towards predicting Mf_{solids} directly from calibrated acoustic models. Our experiments have also included three other related parameters which are more or less correlated to Mf_{solids}, which accordingly is the only variable described here.

The acoustic investigations required only a few instrumentation extensions to be made to the traditional approach. One or two *uniaxial* accelerometers were used to pick up the characterising system vibrations. The accelerometers act as portable "clamp-on" sensors, easily mounted on the surface of the system to be monitored. They are clearly *non-invasive* measuring devices as there are no hindrances placed in the stream. In our application, the accelerometers are mounted directly on the outside of the enclosing pipeline with ceramic glue and/or via welded brackets, allowing the accelerometers to be screwed tight firmly. This leads to a beneficial elimination of wear and plugging compared with standard instrumentation. **Figure 4** shows details of the mounting alternatives of the acoustic sensors, as compared with the standard pressure transmitters.

A dedicated *Data Acquisition (DAQ) Board (National Instruments Inc.)* enabling an overall high-frequency

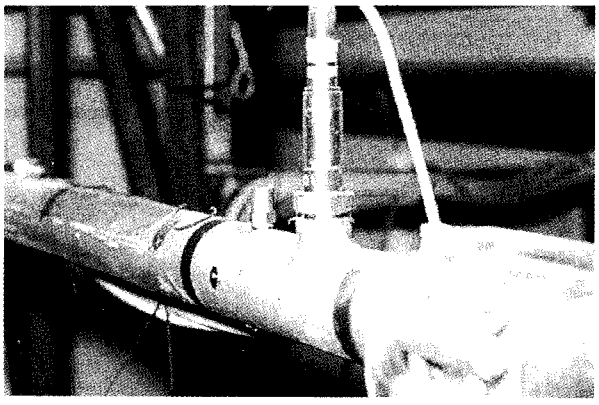

Fig. 4 Front: Pressure transducer with thick cabling (invasive) – Middle: Accelerometer with thin cabling (non-invasive). The difference between traditional pneumatic transportation equipment and the present acoustic chemometric alternative.

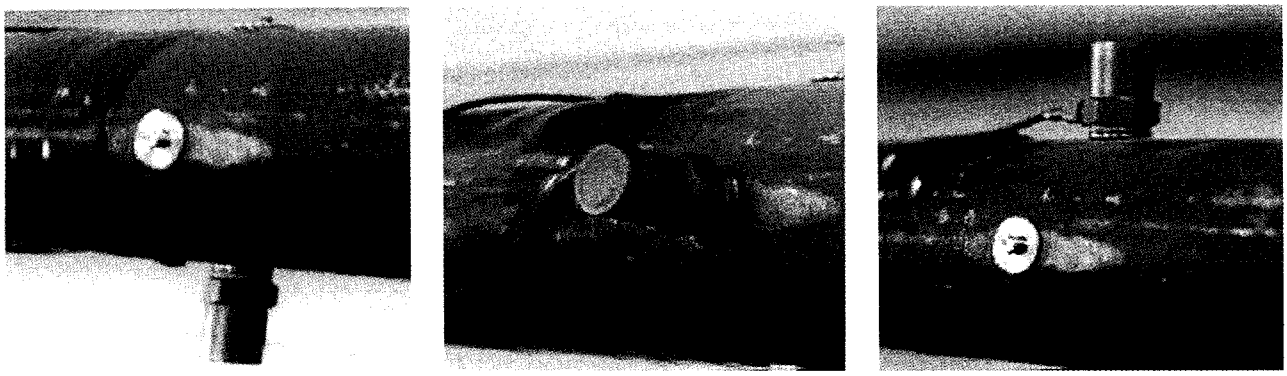

Fig. 5 Details of accelerometer mounting (from left to right): bottom mounting – side mounting – top mounting. Note that it is imperative to affix cabling firmly to pipeline surface to ensure that the cabling receives the same vibrations as the accelerometer bracket(s). Also note bracket preparations on pipeline surface.

sampling rate of 50 kHz was used to handle the acoustic signals. Signal conditioning is taken care of by a *Programmable Differential Amplifier and Low-Pass Filter Board* (*Alligator Technologies*), needed to enhance the *signal to noise ratio* and to reduce the *aliasing effects* always present to some extent in the analogue-to-digital conversion of real-world signals. The amplified and band-limited signals (still analogue) from this board enter the DAQ board for a digital representation, A/D conversion.

The time-domain acoustic signals from the surface-mounted accelerometers are characterised by a great deal of irregularity and may well, at a first casual inspection, appear to be no less than pure noise. Information concerning interesting phenomena is very much hidden from the human eye, and has to be uncovered by some data analytical means. The *Power Spectral Density* (PSD) is an advantageous signal representation in that it enables the comparison of the signal frequency contents from one acoustic record to the other, especially when using a full-spectrum approach in the subsequent multivariate calibration stage. There are many easily available facilities for virtually real-time calculation of PSDs – i.e. the effective FFT (Fast Fourier Transform) approach – e.g. Ifeachor & Jervis (1993).

LabVIEW™ 4.0 (*National Instruments Inc.*) was used throughout to control signal conditioning and the data acquisition board and to estimate the X-block FFTs. The virtual program stores both acquired (time domain) and processed (frequency domain) data; it is also equipped with useful sonogram (time-frequency) display features etc.

2.2.1 Types of powders used in the study

Five granular materials were included in the present study – see **Table 1**. They were chosen from a set of reference materials which are frequently used in the process industry, all of which are included in POSTEC's standard test program. Some physical characteristics of these selected materials, determined by standard laboratory testing equipment, are also listed in Table 1. As can be seen, the chosen materials cover a reasonably wide range of physical characteristics.

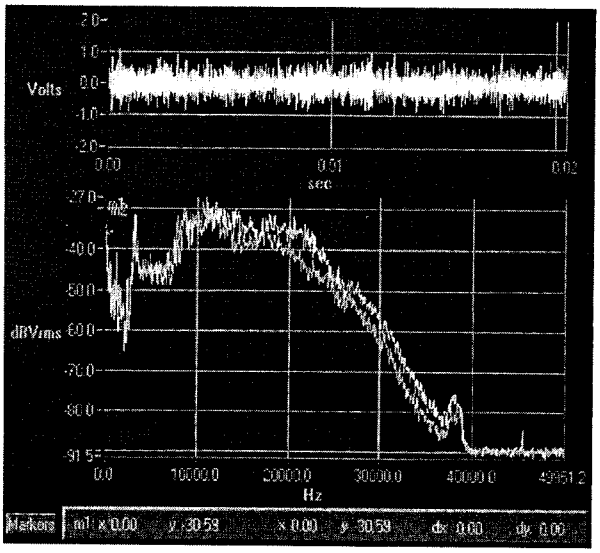

Fig. 6 Time-domain (top panel) to frequency-domain representation (FFT)

The present studies all relate to representative pneumatic transportation in the "dilute phase", which is the area of greatest industrial interest.

2.4 Implementation/data recording optimisation

Several initial series of investigations were carried out in order to facilitate an optimised basis for establishing accurate and representative prediction models for the materials; such experimentation was directed towards all the necessary basic implementa-

Table 1 Physical and pneumatic conveying characteristics of test materials

Material	Partiole density [kg/m^3]	Poured bulk density [kg/m^3]	Mean particle size [μm]	Minimum fluidisation velocity [m/s]	Wall friction angle against ST37 [°]	Static angle of repose [°]	Dynamic angle of repose [°]
PVC granules	1414	518	472	$8.1 \cdot 10^{-2}$	19.7°	37°	35°
Sand	2645	1590	687	$2.5 \cdot 10^{-1}$	16.3°	36°	33°
Rape seed	1164	687	1650	$4.3 \cdot 10^{-1}$	18.7°	30°	30°
Microdol 100	2865	1212	66	$3.2 \cdot 10^{-4}$	26.1°	63°	39°
Cement	3095	734	11	$1.0 \cdot 10^{-3}$	29.3°	65°	33°

tion optimisation of, e.g. *air flow rate* and *solids flow rate* regarding accelerometer/amplification/filtering responses, etc. It is of importance to acquire acoustic signals with the highest possible quality, and this is effected by signal conditioning optimisation, i.e. grounding, gain setting, cut-off frequency as well as different amplification gain settings. In order to optimise *PSD (Power Spectral Density)* estimation, the number of *periodograms* (temporary *PSD*) used to produce one final average *PSD* and the number of samples used to compute each periodogram are two essential parameters. The use of a frame size of 4096 together with 75 averages proved to be useful average data acquisition parameters over all the selected materials. Care also has to be taken when estimating the *PSD*s in order to preserve the information and minimise "spectral leakage", Ifeachor & Jervis (1993). We do not report the full range of these basic, but nevertheless crucial, results here; suffice it to refer to M.Sc. theses by Saudland (1996), Svalestuen (1997) and Halstensen (1997).

All initial implementation/recording optimisation (see below) was based on traditional so-called experimental screening designs, while the subsequent application runs were for the most part based on the random design approach, Esbensen et al. (1994).

2.5 Optimising acoustic sensor position(s) – main experiment series

First results were based on a bottom-mounted accelerometer located near the pipeline inlet, at the first straight pipeline position (Fig. 3). Because most practically obtainable flow patterns have a positive vertical concentration gradient (top to bottom), and since homogeneity certainly increases along the pipeline, it was quickly discovered that it was also of great interest to try out different *vertical* as well as *horizontal* downstream sensor positions. **Figure 7** shows the six principal sensor positions investigated in one of our main experimental series, in which four

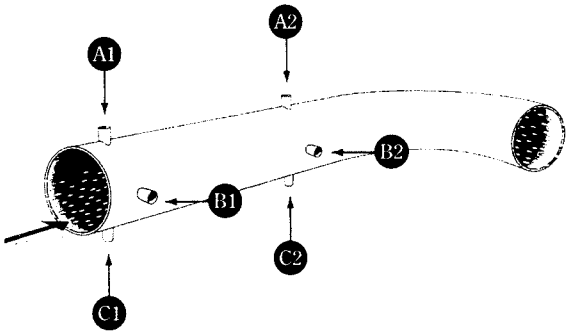

Fig. 7 Main vertical and horizontal positions of alternative accelerometer locations in the present study. The distance between locations A1/B1/C1 and A2/B2/C2 are not to scale.

vertical and two horizontal principal positionings were tested out. It was decided early on to focus on the straight part of the pipeline to avoid *roping* and other additional unpredictable effects caused by the bend – and later follow-up experiments have indeed verified impressively that it is not possible to characterise the in-line transportation regimen immediately after the bend with any similar degree of precision as for our other acoustic results to be presented, or at least that it requires considerably more sophistication to even try this. Besides this, the straight pipeline results are fully adequate for the present feasibility study, because such straight pipe sections are – needless to say – an integral part of *any* pneumatic transportation system.

2.5.1 Data analysis

The regression model to be developed through the use of multivariate Partial Least Squares(PLS) calibration describes the relationship between the acoustic signals and – in this context – the measured flow characteristics, and is thus typically to be used in future real-time predictions of flow behaviour, Mf_{solids}. Multivariate calibration in general deals with the two matrixes X and Y containing the independent input variables and the dependent response or output vari-

ables, respectively. The input variables may well be correlated (which is certainly the case here with the *PSD* spectra) and therefore not suited for standard Multiple Linear(ML) regression analysis. *Partial Least Squares Regression* (*PLS-R*), the most often-used chemometric tool, handles this situation with dispatch. It is of course of critical importance that the (X,Y) data contain *relevant information* for the relationships to be modelled, which has been verified abundantly by our preliminary studies: Saudland (1996), Svalestuen (1997), Martinussen (1996). Descriptions of the two most frequently used methods *Principal Component Analysis* (PCA) and *Partial Least Squares Regression* (PLS-R) will not be given here: Those interested are referred to Martens & Næs (1989), Wold et al. (1984), Geladi & Kowalski (1986) and Esbensen et al. (1994).

The two multivariate calibration matrixes in the present experimental context contain the FFT spectra in the X-block (PSD spectra), and Mf_{solids} as the Y-vector. We have investigated several other parameters of interest, but will not report these here, partly because there is often a moderate degree of correlation between most of these parameters, but mostly because we are only interested in showing the principal feasibility of the acoustic chemometric approach. The validity range of the Mf_{solids} model is determined by the range of the design variables in the X-block. It is, of course, imperative that the calibration data sets span the important process variations in a way representative for future industry use/operation, and this is ensured by POSTEC. Thus the present X-data contain the optimally recorded, relevantly signal-analysed (Fourier-transformed) acoustic spectra, characterising a broad set of operating conditions for industrial pneumatic powder transportation, while the Y-vector consists of the traditionally measured (integrated load weighting) solids flow rate, Mf_{solids}.

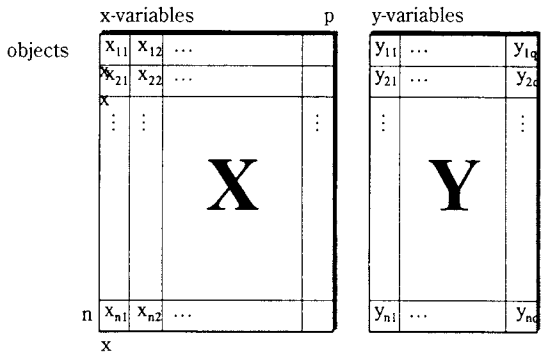

Fig. 8 Multivariate calibration set-up (training data set)

2.5.2 Results

The first result to be presented concerns deployment of one single accelerometer – in the very first straight pipeline position, only some 70 cm downstream of the powder inlet (this position corresponds to C1 in Fig. 7). We are currently collecting synoptic experience on all 7 principal powder types for the whole range of relevant operating conditions, in order – hopefully – to get some initial insights into the underlying systematics of acoustic X→Y relationships. For this inaugural acoustic chemometric application, a satisfactory first-order model can be achieved, explaining (82.75)% of the (Y, X) variance, and giving rise to the *predicted vs. measured* evaluation shown in **Figure 9**.

Clearly this model merits further sophistication; the slope of a *fitted* pred. vs. meas. regression line is only 0.79 and the correlation coefficient: r^2=0.82. This result required four PLS components, as validated by full cross-validation based on a total of 20 objects/runs. The choice of full cross-validation was guided by inspection of the pertinent t-u plots (Esbensen et al.1994). This result constitutes only the very first (ever) acoustic prediction of intrinsic pneumatic transportation monitoring parameters, derived directly from simple, inexpensive, robust passive on-line sensors. As such it must be characterised as promising, although clearly not yet optimised by any means.

Second-generation refinements were carried out as a direct continuation, but now focusing on which combination of two accelerometers in vertical positions 1 and 2, respectively (Fig. 7) – in any permutation – did the best job of laying the foundation for on-line prediction of the solids mass flow rate. These comparisons were based upon identical *predicted vs. measured* multivariate calibration cross-validations in order to ensure that all influencing factors were incorporated

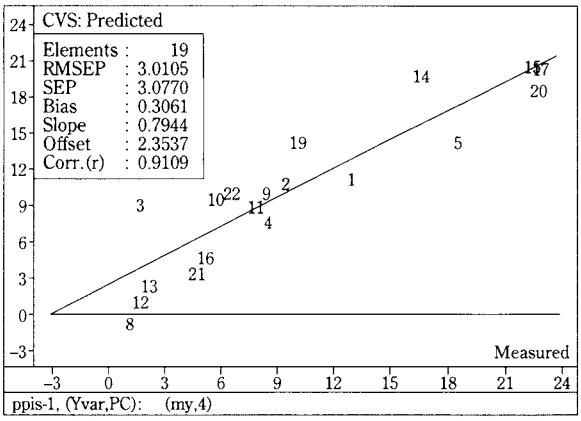

Fig. 9 Predicted vs. measured evaluation plot. Statistics refer to a **fitted** regression line of the CVS predictions vs. the reference measurements, which is used as a measure of **deviation** from an ideal relationship.

Table 2 Comparative statistics for **fitted** regression models pertaining to alternative two-accelerometer configurations, cf. text.

Sensor positions	Slope	Offset	Correlation (r^2)	RMSEP	PLS components
C1-C2	1.04	−0.68	0.88	362.22	2
B1-C2	1.04	5.75	0.88	376.70	2
C1-B2	1.02	20.87	0.86	392.48	2
B1-B2	1.02	29.32	0.85	406.75	1

similarly in the empirical models.

This table demonstrates that it is possible to obtain much-improved prediction validations based on these second-generation refinements. For the best four two-sensor combinations (**Table 2**), slopes are very close to 1.00, for a fraction Y-variance explained spanning 85-88%. The combination **B1-C2** was chosen, Svalestuen (1977). From Figure 7 it will apparent that this corresponds to a side-mounted position "close" to the powder inlet, in combination with a bottom-mounted position well "downstream". There are many powder-science reasons why this particular combination is readily acceptable as a likely "best". But most especially because a bottom-mounted sensor in the C1 position is not generally desirable, as it is sure to be affected by "bottom-drag", i.e. self-damping.

We end this section by showing final results for PVC spherules, sand, cement & microdol.

These are very satisfactory results for a first attempt at developing a novel technique for on-line acoustic chemometric monitoring:

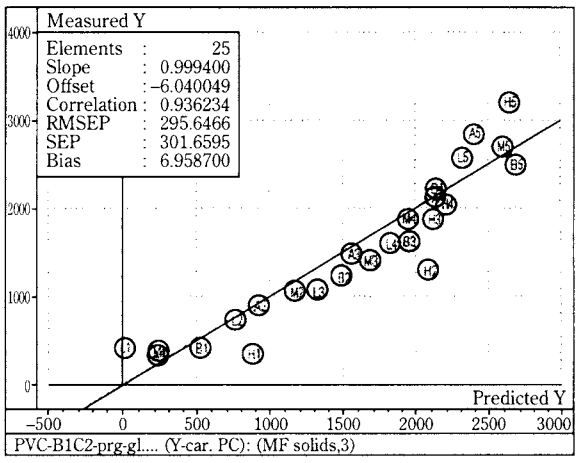

Fig. 10 Final predicted vs. measured evaluation plot for PVC- see text for details. Note how the **fitted** regression line is very close to origin.

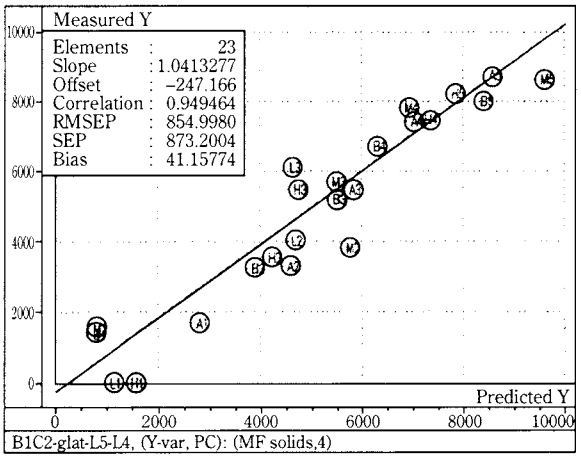

Fig. 11 Final predicted vs. measured evaluation plot for sand. Note how the **fitted** regression line is very close to origin.

	Slope (fitted)	Corr. coef. r^2	RMSEP %	# PLS components
PVC	1.00	0.88	9.8	4
Sand	1.04	0.90	8.5	4
Cement	0.92	0.85	11.2	2
Microdol 100	0.92	0.85	8.6	3

*) RMSEP% calculated w.r.t. half the spanning X-range

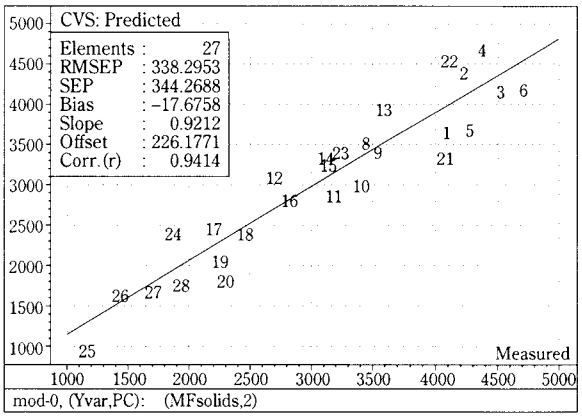

Fig. 12 Predicted vs. measured evaluation for cement

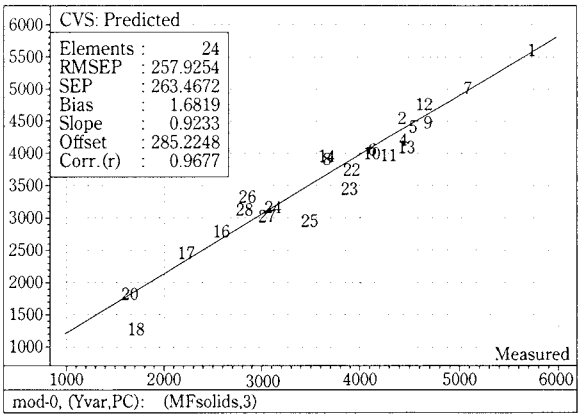

Fig. 13 Predicted vs. measured evaluation for microdol

The final model evaluations for PVC and for sand were based on 25 **new** runs/objects; full cross-validation was again used. Cement and dolomite evaluation is based on the direct calibration cross-validation results. These results were also corroborated by other internal re-runs carried out as independent, part test-set confirmations, alas with slightly too few objects for a complete test-set validation yet – the prime objective being to investigate the ***feasibility*** of the technique being developed. Work continues on characterising all seven powder types used by Martinussen [1997] in his Ph.D research, including pertinent test-set validations, etc., and will be reported in due time.

3. Discussion

By any standards we call the above very promising first results. We envisage a fertile and flowering immediate future for this type of *non-invasive* (non-interfering) acoustic process/product monitoring. The very last point to be made here in fact concerns the distinction between a non-interfering and an actively interfering mode of acoustic chemometrics. All of the above has been concerned with acoustic chemometric listening in completely "as is" – there is absolutely no interference or modification necessary, nor any other active interaction with the object/process being characterised – by passive acoustic chemometrics.

5. References

General technical references:

National Instruments Corp:
DAQ AT-MIO/AI E Series – User Manual, 1996
Alligator Technologies:
AAF-3 Filter/Amplifier – User's Guide, 1996
National Instruments Corp:
LabVIEW® 4.0 for Windows 95 – User Manuals, 1996

1) Box, G.E.P., W.G. Hunter, J.S. Hunter: *Statistics for experimenters*, Wiley, N.Y., 1978
2) Esbensen, K., Schonkopf, S. & Midtgård, T.: *Multivariate Analysis – A Training*
3) *Package*, Camo AS, Trondheim 1994, ISBN 82-993330-0-8
4) Esbensen, K.H. et al.: *Acoustic chemometrics II: One constriction will go a long way!*
5) ***in preparation*** (1998)
6) Halstensen, M.: *Akustisk kjemometrisk karakterisering av væsketransport: flowregime, konsentrasjonsmåling (olje i vann), lydgenerering, opptaksopptimalisering og datamodellering.* M.Sc. thesis (in Norwegian), Aug. 1997, 239 p.
7) Ifeachor, I.C. & Jervis, B.W.: *Digital Signal Processing, a Practical Approach*, Addison-Wesley Publishing Company, 1993
8) Geladi, P. & Kowalski, B.R.: *Partial least Squares Regression: A Tutorial.* Anal. Chim. Acta. vol. 185, p. 1-17. 1986
9) Geldart, D.: *Types of gas fluidization.* Powder Techn. Vol. 7, p. 285-297. 1973
10) Martens, H. og Næs, T.: *Multivariate Calibration*, John Wiley & Sons Ltd., UK 1989 (reprint 1994)
11) Martinussen, S.E.: *The Effect of Physical Characteristics of Particulate Materials on their Conveyability in Pneumatic Transport Systems* (Ph.D. Thesis), University of Greewich July, 1996 Telemark College.
12) Saudland, A.: *Vurdering av effekten av mateselsjonens utformning samt akustisk, kjemometrisk karakterisering av pulvertilstand utfra eksperimentelle forsøk med pneumatisk transportsystem.* M.Sc. thesis (in Norwegian), Aug. 1996, 137 p.
13) Svalestuen, J.: *Akustisk kjemometrisk karakterisering av pneumatisk pulvertransporttilstand – videreutvikling av opptaksoptimalisering og data modellering.* M.Sc. thesis (in Norwegian), Aug. 1997, 117 p.
14) Wold, S., Albano, C., Dunn III, W.J., Edlund, U., Esbensen, K.H., Geladi P., Helberg, S., Johansen, E., Lindberg, W. & Schostrom, M.: *Multivariate data analysis in chemistry.* ***in*** B.R. Kowalski (Ed) Chemometrics, Mathematics and Statistics in Chemistry. D. Reidel Publ., p. 17-95, ISBN 90-277-1846-6

Author's short biography

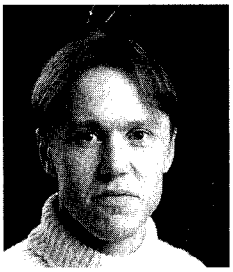

Maths Halstensen

Maths Halstensen recieved his BE of industrial-electronics (1994) from Gjøvik College. He obtained his M.Sc. (eng.) in process-automation (1997) from Telemark Institute of Technology, Porsgrunn. He is currently in a four-year Ph.D.program at the same institution; the subject of his thesis is: Multivariate sensor technology/chemometrics.

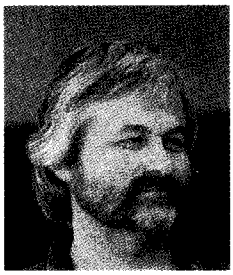

Kim H. Esbensen

Kim H. Esbensen received his M. Sc. degree in geology/geochemistry from the University of Århus, Denmark in 1979. Following a three-year research fellow-ship at the Chemometrics Research Group, Umeå, Sweden and two years as a consultant in the geochemical exploration industry, he was for 8 years at the Norwegian Computing Center, Oslo (research scientist), followed by four years as a senior research scientist at SINTEF, Oslo (The foundation for science and industrial research at the norwegian institute of technology). Since 1994 he has been professor in chemometrics at Telemark Institute of Technology, Porsgrunn. He is also department head (applied chemometrics) at Tel-Tek (Telemark Technological R & D Center), Porsgrunn, Norway.

Sunil de Silva

Sunil de Silva received his B.Tech (Honours) and Ph.D degree from Loughborough University in England. Having completed research for his Ph.D in 1970, he worked for Prof. Kurt Leschonski at the Universities of Karlsruhe and Clausthal in many areas of gas/solids flow until 1976. He then spent six years in industry as the Engineering Manager of the Majac Department of Donaldson Europe in Belgium, before returning to research in Powder Technology at Chr. Michelsen Insitute in Bergen, Norway in 1982. Since 1988 he has been adjunct, later full Professor of Powder Technology at Telemark College, and Manager of the Department of Powder Science and Thecnology (POSTEC) at Tel-Tek.

The Population Balance as a Tool for Understanding Particle Rate Processes†

M.J. Hounslow
*Particle Products Group, Department of Chemical and Process Engineering, The University of Sheffield, UK**

1. Abstract

This article discusses the use of population balance techniques in the understanding of particulate processes. Population Balance Equations (PBEs) describe how properties of a group of particles change with time and position. These "properties" are frequently some measure of particle size, so PBEs are most often used to describe how particle size distributions (PSDs) change during the processing of particulate materials. After a brief review of how PBEs are formulated and solved, three case studies, from the author's research, are considered.

Crystallisation: Aggregation During Precipitation From Solution.

This case study reports a decade of work on the aggregation of calcium oxalate monohydrate crystals in supersaturated solutions. Our knowledge of the dependence of growth and aggregation rates on solution composition is reported and physical models explaining the dependencies are discussed. The main conclusion for this study is, apart from a description of COM, that substantial microscopic lessons may be drawn from observations made at a mesoscopic (i.e. many particle) scale.

Fluidisation: Spray Coating Of Grass Seeds

The objective of this work was a description of how seed particles increase in size as new material is sprayed on. This study is unusual in that the PBE was solved analytically and gave rise to a model with no adjustable parameters. At first sight the model is capable of very high fidelity predictions; it is not until each particle is considered to have *two* properties, and not just one, in size, that failings in the model become apparent.

Granulation: Extracting Kinetics

This study reports a substantial experimental and numerical investigation of the rates at which size enlargement occurs in high-shear granulation equipment. It is shown that breakage is extremely important and that its rate can be quantified. It is also shown that it is not possible to uncouple the effects of particle size, age and other properties without careful experimental design.

The main conclusions of this work are:

- It is possible to pose and solve PBEs for a variety of problems
- It is possible to extract physical information about particle rate processes by means of PBEs
- There are indications that this type of work must move on from representing particles by a single property, i.e. their size, and recognise that most particles have a variety of properties that affect their behaviour.

2. Introduction

2.1 Descriptions of groups of particles

2.1.1 One particle

The starting perspective of this paper is that the first property of a particle is its size. We will view "size" perhaps as a linear dimension, l, or with less ambiguity, as a particle volume, v. There are cases where a single size co-ordinate can completely and un-ambiguously describe a particle. It is more common, however, for descriptions of particle shape, composition and even age to be required for a complete description. Each of these descriptions is, after the work of Hulburt and Katz[1], termed an *internal co-ordinate*. The properties of a particle may then be described as a list, or vector, of internal co-ordinate, $\mathbf{x}_i$.

The other properties of a particle that might determine the rates with which it changes are its co-ordinates in physical space (x,y,z) – its *external co-ordinates*, $\mathbf{x}_e$. The complete characteristics of a particle will be given by the combination of these two vectors to give, as Hulburt and Katz have it, the position in phase space, $\mathbf{x}$.

* Mappin Street, Sheffield, S1 3JD, UK
† Received June 9, 1998

2.1.2 Groups of particles

A description of the rates of particle processes is of necessity a description of many particles at once. In so doing we most naturally seek a statistical description of a very large number of particles; so large in fact that we may assume that the distribution of particle properties is continuous and so we may use continuous *probability density functions* to describe how these properties are distributed.

In this work we use *number* density functions, n, and *mass* density functions, w. These relate the differential number or mass of material in a differential region of phase space as

$$dN = n(\mathbf{x},t)d\mathbf{x} \text{ and } dW = w(\mathbf{x},t)d\mathbf{x} \tag{1}$$

For clarity, consider the simplest case where the only phase-space co-ordinate is size: the number of particles with sizes in the range $(l, l+dl)$ is $dN = n(l)dl$.

The usual expectation when using probability density functions is that they will be normalised in such a way that integrating them over the domain of their arguments leads to a value of one. It is quite common, however, when modelling particulate systems, to allow some other value that contains information on the amount of material present. For example, in the study of crystallisation, it is usual to use a basis of 1 m^3 of suspension, so that dN in equation (1) is the number of crystals *per unit volume of suspension* in the indicated size range.

2.2 The Population Balance Equation (PBE)

The PBE is described by many authors – most notably Hulburt and Katz[1], Randolph and Larson[2], and Ramkrishna[3] – as a statement of continuity, or of conservation, for particulate systems. Just as conservation statements lie at the heart of descriptions of chemical rate processes, so they do in the description of particle rate processes.

At every point in phase space, the local rate of destruction of particles $r(\mathbf{x},t)$ must exactly balance the local rate of accumulation and divergence in the flow field. The PBE is then

$$\frac{\partial n(\mathbf{x},t)}{\partial t} + \nabla\cdot\left(\mathbf{u}(\mathbf{x},t)n(\mathbf{x},t)\right) + r(\mathbf{x},t) = 0 \tag{2}$$

In this equation – termed the micro-continuity equation by Randolph and Larson – $\mathbf{u}$ is the vector of velocities in phase space. It is this equation that must be used in systems where there is dependence on spatial position, i.e. on the external co-ordinate position. If, however, the system under consideration is sufficiently well mixed for there to be no spatial dependence, equation (2) can be averaged over the extent of the external co-ordinates to yield the so called macro-continuity equation:

$$\frac{\partial V(t)n(\mathbf{x}_i,t)}{\partial t} + V(t)\nabla\cdot\left(\mathbf{u}(\mathbf{x}_i,t)n(\mathbf{x}_i,t)\right) + V(t)r(\mathbf{x}_i,t) = \sum_{k\in \text{in}} Q_k(t)n_k(\mathbf{x}_i,t) - \sum_{k\in \text{out}} Q_k(t)n_k(\mathbf{x}_i,t) \tag{3}$$

where the Q_k are flow rates of streams in to or out of the well-mixed region, which has a size V. If the basis used for n is 1 m^3 of suspension, the Q will be volumetric flow rates and V the volume.

2.3 The Rate Processes

Of the many processes that might change the behaviour or characteristics of a particle we concentrate here on those that will change the particle size distribution. In so doing, we are already making the implicit assumption that the particles are described by a single internal co-ordinate i.e. size.

Once this assumption is made, we need only consider four distinct mechanisms: nucleation, growth, aggregation and breakage.

2.3.1 Nucleation

Nucleation is the process by which new particles are formed from matter that is recognised as non-particulate. In fields such as crystallisation, precipitation or aerosol science, this usually entails the formation of a new particle from some clustering together of ions or molecules. In some other fields, such as granulation, it is allowed that the very fine primary powder is not, in fact particulate, and grains of this powder must clump together, i.e. nucleate, before they can be reckoned particulate.

Quantitative descriptions of the rate of nucleation date from the time of Gibbs[4]; in general these take account of the energy barriers that exist to generating new particles and then compare this barrier with the energy available.

The rate at which this process takes place is given by the nucleation rate B^0 ($m^{-3}s^{-1}$) i.e. the rate of appearance of particles per unit of, typically, bulk volume. This rate must then be combined with information on the size distribution of nuclei, f_N. It is quite common to assume that the nuclei will be mono-disperse in size so that $f_N = \delta(l-l_0)$ where δ is the Dirac distribution and l_0 is the size of the nuclei. In general however, the appropriate rate term for inclusion in the PBE is

$$-r_N = B^0(\mathbf{x},t)f_N(\mathbf{x}_i,t) \tag{4}$$

2.3.2 Growth

Growth is the process by which non-particulate matter becomes incorporated within a particle. Since the distinction between particulate and non-particulate matter is that the former is available in very small units only, growth must of necessity be a differential process. The growth rate of a particle can then be described by a rate of change of size; as such the growth rate is simply a velocity along the particle-size axis. So if linear dimension is used to measure size, the growth rate is

$$G_l(\mathbf{x}_e, l, t) = \frac{dl}{dt} \tag{5}$$

and if volume

$$G_v(\mathbf{x}_e, v, t) = \frac{dv}{dt} \tag{6}$$

Values for these growth rates are usually deduced from rates of mass transfer or rates of surface reactions and are well known for very many types of systems. In those systems where the rate of reaction (per unit surface area of particle) is independent of size, the linear rate of growth defined in equation (5) is independent of particle size – which makes for considerable analytical convenience when seeking solutions to the PBE.

2.3.3 Aggregation

Aggregation is the other size-enlargement mechanism; new large particles are formed by combinations of smaller particles. By contrast with nucleation and growth, aggregation is a poorly understood phenomenon. It is usual to assume that aggregation involves only two-body interactions and so may be described by a second order rate constant, or kernel, as it is often known. The rate of aggregation events, per unit volume, for particles of types 1 and 2 is given by

$$r_{1,2} = \beta(\mathbf{x}_e, \mathbf{x}_{i,1}, \mathbf{x}_{i,2}, t) N_1 N_2 \tag{7}$$

where N_1 and N_2 are the number concentrations of particles of each type. By restricting the internal co-ordinates to particle size, using volume as the measure of size, this definition may be integrated over appropriate size ranges to give the net rate of aggregation

$$-r_A(\mathbf{x}_e, v, t) = \frac{1}{2}\int_0^v \beta(\mathbf{x}_e, v-\varepsilon, \varepsilon, t) n(\mathbf{x}_e, v-\varepsilon, t) n(\mathbf{x}_e, \varepsilon, t) d\varepsilon - n(\mathbf{x}_e, v, t)\int_0^\infty \beta(\mathbf{x}_e, v, \varepsilon, t) n(\mathbf{x}_e, \varepsilon, t) d\varepsilon \tag{8}$$

Little is known about the prediction of aggregation rate constants. In some applications it is often assumed that the rate of aggregation is independent of particle size, while in others quite complicated empirical dependencies are fitted to experimental results. Two well-known functional forms are those of Von Smoluchowski[5] for ortho- and for peri-kinetic aggregation.

2.3.4 Breakage

Breakage is that set of processes that reduce the size of a particle while producing more, smaller particles. The description of the rate of breakage requires definition of two functions: the selection rate constant $S(\mathbf{x}, t)$ with units of s^{-1} and a breakage function, $b(\mathbf{x}_e, \mathbf{x}_{i,\,new}, \mathbf{x}_{i,\,old}, t)$. S is sometimes termed the specific rate of breakage and is, in fact, the first order rate constant for the selection of particles. The breakage function, b, gives the distribution of "daughter" particles formed when a "mother" particle is broken. The subscript "old" denotes the co-ordinates of the mother particle and "new" those of the daughter particles being born. It is worth noting the convention that the first set of internal co-ordinates is those of the daughter particles and the second that of the mother.

Once more, it is very unusual to use more than size as the measure of the internal co-ordinate, in which case the rate of breakage may be reckoned as

$$-r(\mathbf{x}_e, v, t) = \int_0^\infty S(\mathbf{x}_e, \varepsilon, t) b(\mathbf{x}_e, v, \varepsilon, t) n(\mathbf{x}_e, \varepsilon, t) d\varepsilon - S(\mathbf{x}_e, v, t) n(\mathbf{x}_e, v, t) \tag{9}$$

For conservation of mass (or more strictly, volume, as equation (9) uses volume as the internal co-ordinate) it is necessary that

$$\int_0^v \varepsilon b(\mathbf{x}_e, \varepsilon, v, t) d\varepsilon = v$$

It is possible to define forms of b corresponding to certain kinds of limiting behaviour. For example attrition, the process by which a single small daughter particle of volume v_0 is broken off a mother particle has

$$b(\mathbf{x}_e, v, \varepsilon, t) = \delta(v - v_0) + \delta(v - \varepsilon + v_0)$$

Uniform fragmentation where the mother particle is broken entirely into daughter particles of size v_0 has

$$b(\mathbf{x}_e, v, \varepsilon, t) = \frac{\varepsilon}{v}\delta(v - v_0)$$

There is little theoretical basis for the choice of either S or b.

2.4 Using the PBE

There are very, very few useful analytical solutions to the PBE. Indeed, the author knows of no solution when all four mechanisms are active, even when the most simplistic assumptions are made for the various

rate constants. It is frequently necessary, then, to use numerical methods; these fall into two broad groups: finite difference techniques[6,7,8] (so-called discretised population balances, DPBs) and finite element methods[9,10]. It is not the intention here to explore these numerical methods, but simply to report that they exist and that it is now possible to solve PBEs (with one internal co-ordinate and at most one external co-ordinate) relatively routinely.

By solve, here, it is meant simulate a size distribution; i.e. given initial and/or feed information and a complete set of kinetic parameters, PSDs can be calculated as functions of time or spatial position. The so-called inverse problem presents a far greater challenge. In their full form, inverse problems require that the kinetic parameters be determined as functions of size and time from experimental measurements. Muralidar and Ramkrishna[11] show that even with quite elaborate treatment, data of an exceptional, probably unattainable, quality are required.

It is, however, possible to address a much reduced form of the inverse problem. Bramley *et al*[12] have recently shown that if the dependence on size of the kinetic parameters is known, it is possible to extract the dependence on time, spatial position or some other driving force.

3. Case Study 1. *Crystallisation*: Aggregation During Precipitation From Solution

The author's group has for approximately 10 years studied the aggregation of calcium oxalate monohydrate crystals while they grow in supersaturated saline solutions. The processes active in this case are growth and aggregation; so, for the well mixed batch systems studied, the PBE is

$$\frac{\partial n(v,t)}{\partial t}+\frac{\partial}{\partial v}\left(G_v(v,t)n(v,t)\right)=\frac{1}{2}\int_0^{\infty}\beta(v-\varepsilon,\varepsilon,t)n\cdot$$

$$(v-\varepsilon,t)n(\varepsilon,t)d\varepsilon-n(v,t)\int_0^{\infty}\beta(v,\varepsilon,t)n(\varepsilon,t)d\varepsilon \qquad (10)$$

The purpose of this study is to develop knowledge of how G and β depend on particle size and on solution conditions, such as supersaturation (which accounts for the dependence on time).

3.1 Experimental Detail

The experimental techniques employed is an adaptation of that of Ryall[13]. A saline metastable (i.e. supersaturated, but non-nucleating) is prepared by mixing NaCl, $Na_2C_2O_4$ and $CaCl_2$ solutions with buffer at 37°C. At $t=0$, a thermostated agitated flask of the metastable solution is inoculated with a small volume of seed crystals. There after small volumes are extracted at regular intervals for particle size analysis by Coulter Counter.

3.2 Typical Results

Two key results are shown in **Figures 1** and **2**. In **Figure 1**, the size distribution of crystals at the start and at the end of a typical one hour experiment are shown. It is clear from the location of the curves that the crystals have increased in size; from the area under each curve it is also clear that the number of crystals has decreased substantially. This immediately suggests that crystal aggregation is occurring. In **Figure 2** – which shows results corresponding to an extended, 24 hour experiment – it is very clear that aggregates are present.

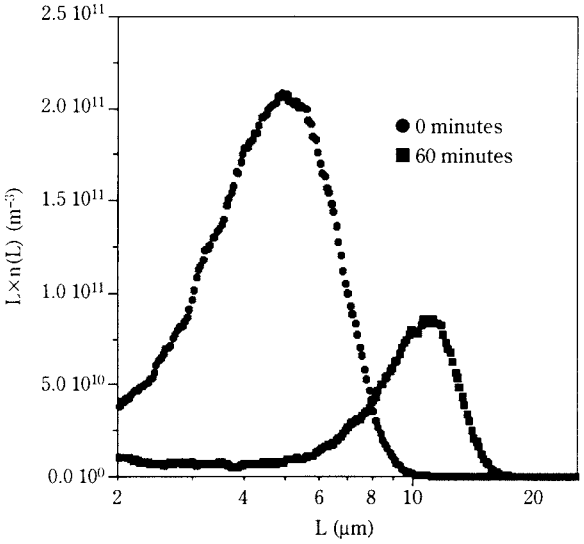

Fig. 1 Number density functions of the seed and of the product after one hour

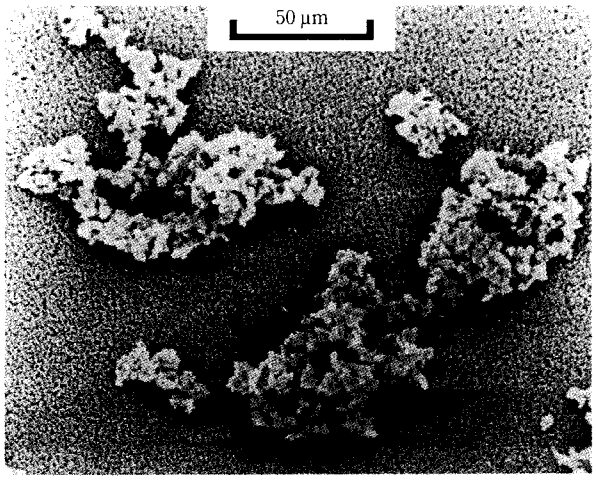

Fig. 2 Scanning Electron Micrograph of the product after 24 hours

3.3 Data Extraction, Modelling & Simulation

For a batch system in which growth and aggregation are active, the PBE is given by equation (10). We expect that growth will be size independent, but have little knowledge of how the aggregation rate will depend on size. The method we adopted[14] uses an iterative technique in which we first assumed a size dependence of the aggregation rate, then extracted the values of the growth rate G_l, and the size independent portion of the kernel, β_0, using the method of Bramley and Hounslow[12]. We then simulated the size distribution using the method of Hounslow *et al*[6]. We considered initially a great many kernels (some of which can be found in Hartel and Randolph[15]). Of these, some kernels could be eliminated immediately as they show gelling behaviour (as described by Smit et al[16]). Of those that remained, the most frequently used kernels are those shown in **Table 1**.

We then characterised the ability of each kernel to describe our results by considering the sum of square error in predicting the PSDs. Complete results are tabulated in Bramley et al[14], but as **Figure 3** illustrates, the shear kernel is incapable of describing the results while the Brownian and size-independent kernels do quite well. In what follows, and in our further work, we adopt the size-independent kernel as giving the best fit and, as indicated in **Table 1**, as best corresponding to our recent *a priori* predictions[17].

Table 1 The three kernels used in Figure 3

Kernel, $\beta(l_1, l_2)$	Physical rationale
Size Independent, β_0	None; but Mumtaz *et al*[17] show that when the effect of particle size on collision rate and on collision efficiency is considered, only weak size dependence should be expected.
Brownian motion, $\beta_0 \times (l_1+l_2)/\left(\frac{1}{l_1}+\frac{1}{l_2}\right)$	Corresponds to perikinetic motion as described by Von Smoluchowski
Shear, $\beta_0 \times (l_1+l_2)^3$	Corresponds to orthokinetic motion as described by Von Smoluchowski

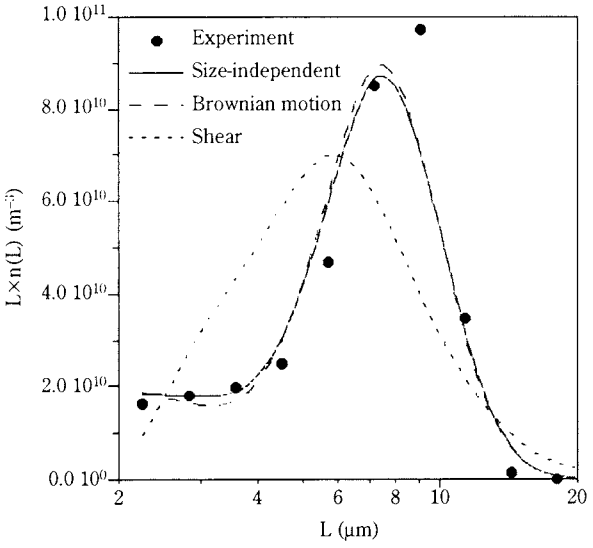

Fig. 3 Predicted and experimental PSDs for three assumed forms of the aggregation kernel

3.4 The effect of process conditions

Having established that we can describe our experiments in terms of a size-independent growth rate, G_l and a size independent aggregation rate constant, β_0, we then explored how these kinetic parameters depend on operating conditions. In Bramley and Hounslow[14], and Bramley *et al*[18] we report the effect of changing supersaturation S, and initial ion ratio, α_0.

3.4.1 Growth Rates

In **Figure 4** the square root of growth rate is plotted against supersaturation. There is an excellent correlation between the variables from which it is apparent that growth rate is directly proportional to the square of supersaturation and is independent of the ion ratio. This result is entirely expected: being equivalent to the results of Nancollas *et al* [19]. We conclude from this that the rate of growth is determined by the rate of reaction, or incorporation, of ions on the surface of the crystals.

3.4.2 Aggregation Rates

Figure 5, is the aggregation analogue of **Figure 4**. We see now that while the aggregation rate constant also increases with increasing supersaturation, there is very clear dependence of the rate on the ion ratio.

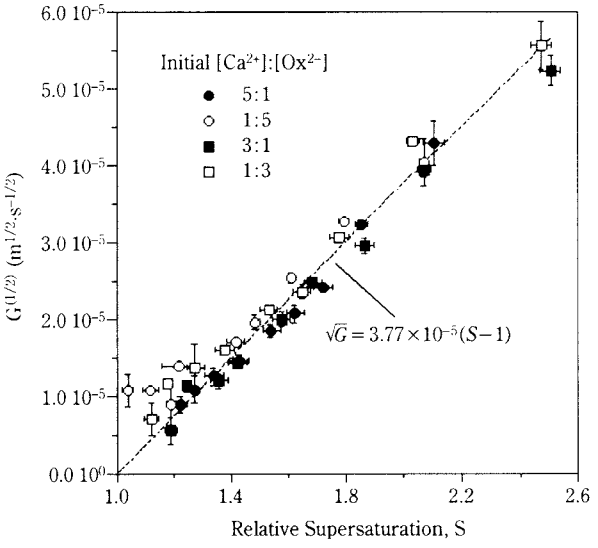

Fig. 4 The effect of relative supersaturation and initial ion ratio on the growth rate

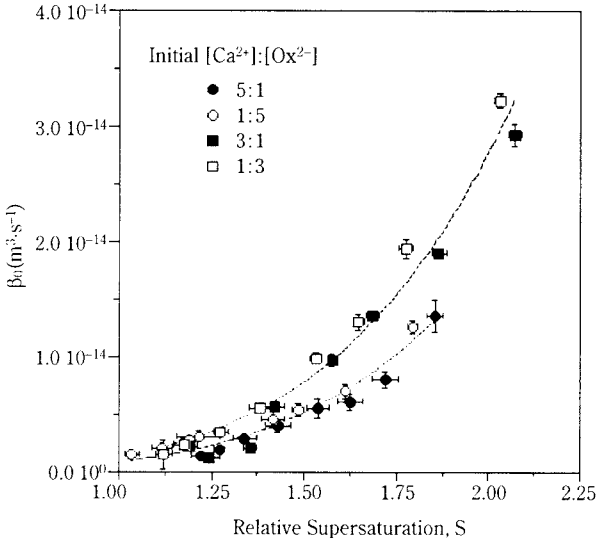

Fig. 5 The effect of relative supersaturation and initial ion ratio on the aggregation rate constant

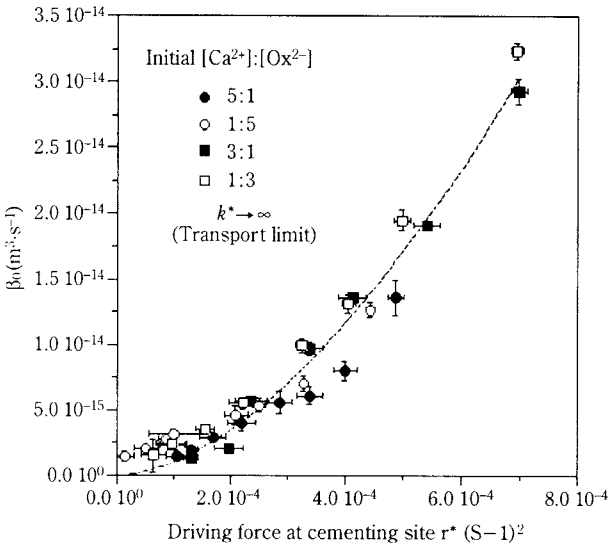

Fig. 6 The dependence of aggregation rate constant on the calculated driving force at the cementing site

On the basis of these data it can be seen that the further the ratio is from 1:1, the lower the rate of aggregation. Furthermore, it is apparent that this effect is symmetrical, so that a system with a ratio of 1:5 behaves the same as one with 5:1. These observations have been confirmed by Hounslow et al[18] who considered ratios from 1:10 through to 10:1.

These results are, to us, reminiscent of sequential chemical reactions of the first and second order. This observation led us to propose a pore diffusion reaction model[18]. In this model we propose that in order for two particles to aggregate they must first meet and then form a sufficiently strong bridge of new material, or cement as we have it, before they experience disruptive forces (induced by fluid motion). The process of laying down this cement involves diffusion (a first order process) to a cementing site (down some pore) and then reacting (a second order process) to form the new, solid, cement.

If we assert that the transport down the pore and the reaction at the cementing site are in pseudo steady state, we may write

$$r_c = \frac{D}{X}\left(T^{S}_{Ca^{2+}} - T^{C}_{Ca^{2+}}\right) = \frac{D}{X}\left(T^{S}_{Ox^{2-}} - T^{C}_{Ox^{2-}}\right) = k(S^C - 1)^2$$

where r_c is the rate of reaction in mol m^{-2} s^{-1}, the symbols T refer to total concentration of dissolved ions, D is the diffusivity, X is the pore length, k is the reaction rate constant and S^C the relative supersaturation at the cementing site. From this equation we can deduce that the rate of deposition at the cementing site and the rate at the crystal surface are related by

$$r^* = r_c / r_s = \Phi(k^*, S, \alpha)$$

where k^* is a Thiele modulus.

Figure 6 shows the results of **Figure 5** plotted now against the calculated value for the driving force at the cementing site. The results have now collapsed onto a single curve showing no dependence on the ion ratio.

3.4.3 The effect of agitation

The results shown above were obtained in simple shaken flasks; those reported in Hounslow et al[18], were collected using a one litre baffled stirred tank vessel. For that system we find that the results are described by a Thiele modulus of $k^* = 0.3$, rather than the diffusion limited value of $k^* = \infty$. Our most recent work, Barrick[20], shows that for the stirred vessel, the value of k^* is very strongly dependent on the stirrer speed.

3.5 Observations on crystallisation

This case study represents, by far, our most mature work. We now very routinely use the PBE – equation (10), in this case – to extract the growth rate G_l and the aggregation rate constant β_0 as functions of time. Since we are also capable of determining the solution composition and therefore supersaturation, as functions of time, we can very easily explore the kinetics of both processes. The whole thrust of our work is the investigation of how these kinetics change under various conditions. This approach of using the PBE to reduce extensive experimental data to just a few fundamental kinetic parameters is the perfect illustration of what is meant by the title of this paper: *The Population Balance as a Tool for Understanding Particle Rate Processes.*

4. Case Study 2. *Fluidisation*: Spray Coating of Grass Seeds

Of the three case studies presented in this paper, the first represents approximately a decade's work and the last approximately three year's. By contrast the analysis presented here stems from about two week's work.

The problem to be considered is one of coating grass seeds with a layer of fertiliser in a bottom-sprayed spouted fluidised bed – as shown in **Figure 7**. Details of the experimental arrangements can be found in Litster *et al*[21]. The aim of the work is to predict first how the distribution of particle sizes varies with time and then to consider the variability of the coating thickness.

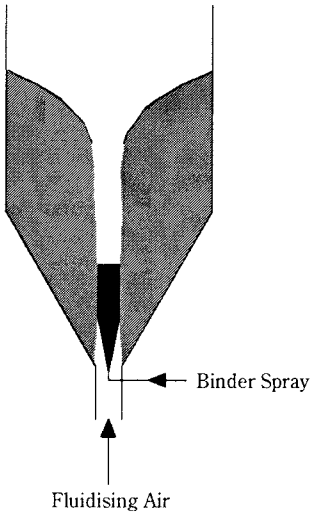

Fig. 7 Schematic of the seed coating device

We adopt a simple model: we take the bed to consist of a plug flow "coating zone" representing the spout where we expect to find droplets of binder, and a well mixed "bed"; as shown in **Figure 8**.

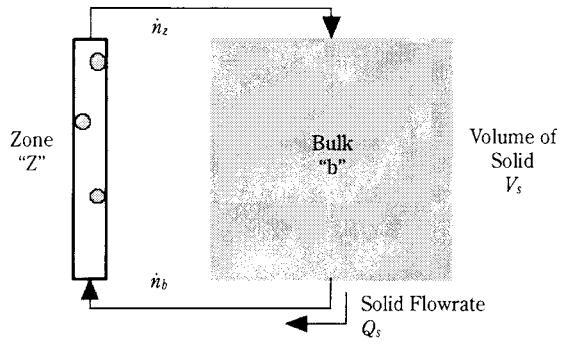

Fig. 8 Schematic of the two zone model for a spouted fluidised bed

4.1.1 Plug flow model for the coating zone

The coating-zone model will, in due course, be required to relate the size distribution of particles coming into the zone (from the bed) to the distribution leaving the zone and passing back to the bed. In order to do so an expression for the population density is required as a function of height, x, in the zone, and of particle size, in this case the particle volume, v. In principle this would require a description of the aggregation of binder droplets and particles. Rather than proceed along these lines, we treat the binder as non-particulate developing an effective rate of growth of the larger particles. To do so we now develop a binary population balance; we consider two populations, population 1 being the spray droplets, and 2 the seeds. We then allow that the numbers of particles per unit volume are N_1 and N_2.

We first calculate the rate of collisions per seed:

$$\begin{aligned} f &= N_1 \times \text{rate seeds sweep out volume} \\ &= N_1 a_2 (U-V) \\ &= N_1 a_2 U \end{aligned}$$

where the velocities U and V are as shown in **Figure 9**, U has been taken to be much greater than V, and a_2 is the projected area of a seed. The population balance for droplets may then be reckoned as

$$U\frac{dN_1}{dx} = -fN_2 = -N_1 N_2 U a_2$$

$$\therefore N_1 = N_1(0)\exp(-A_2 x)$$

where

$$A_2 = N_2 a_2 = \frac{3}{2}\frac{1-\varepsilon}{d_2}$$

where ε is the void fraction in the coating zone. In this last result we see that the concentration of spray droplets decays exponentially with a decay length proportional to the diameter of the seeds and inversely proportional to the volume fraction of seeds. We deduce from this that collisions between seeds and droplets occur only over a few, perhaps 10, particle

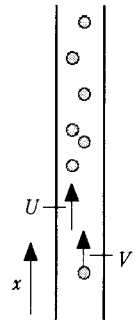

Fig. 9 The coating zone

diameters of length. This observation requires that attention be paid to the region at the very bottom of the bed where we expect the particles to have relatively low velocity.

The population balance for the coating region may now be deduced by application of equation (2), with two co-ordinates (x, v) and $r = 0$.

$$\frac{\partial}{\partial x}\left(\frac{dx}{dt}n(x,v)\right) + \frac{\partial}{\partial v}\left(\frac{dv}{dt}n(x,v)\right) = 0 \tag{11}$$

In what follows, it is more convenient to work with a basis for the population density of 1 second rather than 1 m^3, as naturally arises in equation (11). Defining $\dot{n}(x,v)$ as the number density passing a point at a height, x, per second, equation (11) becomes

$$\frac{\partial \dot{n}(x,v)}{\partial x} + \frac{\partial}{\partial v}\left(\frac{dv}{dt}\dot{n}(x,v)\Big/V\right) = 0 \tag{12}$$

To calculate the dependence of particle velocity, V, on position, the equation of motion, allowing for size and slip dependence of drag, was solved numerically to give

$$\frac{dx}{dt} = V \propto \sqrt{x/v^{0.4}} \tag{13}$$

The velocity along the size axis may be calculated as

$$\begin{aligned}\frac{dv}{dt} = G_v &= \text{rate of droplet collisions per seed} \times \\ &\quad \text{droplet volume} \\ &\propto f \\ &\propto a_2 N_1 \\ &\propto v^{2/3}\exp(-A_2 x)\end{aligned} \tag{14}$$

Equation (12) becomes

$$\frac{\partial \dot{n}(x,v)}{\partial x} + \frac{kv^{0.87}e^{-A_2 x}}{\sqrt{x}}\frac{\partial \dot{n}(x,v)}{\partial v} = -n(x,v)\frac{kv^{0.87}e^{-A_2 x}}{\sqrt{x}}$$

where k is a combined constant of proportionality from equations (13) and (14).

This equation can be solved with considerably greater ease if the exponent of v, 0.87 is replace with a value of 1, in which case the PBE is

$$\frac{\partial \dot{n}}{\partial x} + \frac{kve^{-A_2 x}}{\sqrt{x}}\frac{\partial \dot{n}}{\partial v} = -n\frac{kve^{-A_2 x}}{\sqrt{x}}$$

which has the solution

$$\dot{n}(x,v) = \dot{n}\left(0, ve^{-k\,\mathrm{erf}(\sqrt{A_2 x})}\right)e^{-k\,\mathrm{erf}(\sqrt{A_2 x})} \tag{15}$$

If we allow that the length of the coating zone is much greater than the decay length of the droplet concentration, the error function in this last equation tends to 1, so

$$\dot{n}_z(x) = \frac{\dot{n}_b(v/K)}{K} \tag{16}$$

where $K = e^{-k}$.

Consequently, for each pass through the zone a particle's volume increases by a *size-independent* factor: the coating parameter, K. We can now relate the number densities entering and leaving the coating zone by

$$\dot{n}(x,v) = \frac{\dot{n}(0, v/K)}{K} \tag{17}$$

4.1.2 Two-compartment population balance model

We now write a PBE for the well mixed fluidised bed, and then combine it with that for the plug-flow coating zone. We take equation (3), allow that there is no change in particle size in the bed, and use a basis of unit time to obtain

$$\frac{\partial \dot{n}_b}{\partial t} + \frac{\dot{n}_b}{V_s}\frac{dV_s}{dt} = \frac{\dot{n}_z - \dot{n}_b}{V_s/Q_s} \tag{18}$$

where V_s is the volume of solid in the bed and Q_s is the volumetric flow rate of solid from the bed into the coating zone. Combining this last result with equation (17) yields

$$\frac{\partial \dot{n}_b(v)}{\partial t} + \frac{\dot{n}_b(v)}{V_s}\frac{dV_s}{dt} = \left(\frac{\dot{n}_b(v/K)}{K} - \dot{n}_b(v)\right)\frac{Q_s}{V_s} \tag{19}$$

Defining the moments of the size distribution as

$$\dot{m}_{b,j} = \int_0^\infty v^j \dot{n}_b(v)\,dv$$

allows (19) to be transformed to

$$\frac{\partial \dot{m}_{bj}}{\partial t} + \frac{\dot{m}_{bj}}{V_s}\frac{dV_s}{dt} = \dot{m}_{bj}(K^j - 1)\frac{Q}{V_s} \tag{20}$$

Before proceeding, some assumption concerning the flow of material from the bulk to the coating zone is required. The obvious choices are constant number flow of particles or constant mass flow. Since it is likely that the rate of entrainment is dependent on momentum transport from the gas to the particles, it seems most appropriate to assume constant mass flow. In which case, the first moment leaving the bulk will be constant. From (20), with $d\dot{m}_{b1}/dt = 0$, it follows that

$$Q_s = \frac{dV_s}{dt}\frac{1}{K-1}$$

We may now solve (20) eliminating time as the independent variable and replacing it with the volume of solid in the bed V_s.

$$\frac{\dot{m}_{bj}(t)}{\dot{m}_{bj}(0)} = \left(\frac{V_s(t)}{V_s(0)}\right)^{\frac{K^j - K}{K-1}} \tag{21}$$

We may use this last result to calculate the mean size and variance:

$$\bar{v}(t) = \bar{v}(0)\frac{V_s}{V_s(0)} \tag{22}$$

$$\sigma^2(t) = \left(\frac{V_s}{V_s(0)}\right)^{K+1}\sigma^2(0) + \bar{v}^2(0)\left(\left(\frac{V_s}{V_s(0)}\right)^{K+1} - \left(\frac{V_s}{V_s(0)}\right)^2\right) \tag{23}$$

Preliminary calculations, and common sense, suggest that $K << 1$. In which case (23) becomes

$$\sigma(t) = \left(\frac{V_s}{V_s(0)}\right)\sigma(0) \tag{24}$$

Quit unusually, it is also possible to solve the PBE itself, (19). If the initial condition is $\dot{n}_b(v, V_s(0)) =$

$\dot{n}_f(v)$, some time later the size distribution in the bulk is

$$\dot{n}_b(v, V_s) = \left(\frac{V_s}{V_s(0)}\right)^{\frac{-K}{K-1}} \cdot \sum_{j=0}^{p_{max}} \left(\frac{1}{K(K-1)}\right)^j \frac{1}{j!} \ln^j \left(\frac{V_s}{V_s(0)}\right) n_f(v/K^j) \quad (25)$$

where $p_{max} = \text{int}\left(\frac{\ln(v/v_{min})}{\ln(K)}\right)$ and v_{min} is the smallest particle size present.

Although deduced directly from the population balance, the form of this solution and some of the terms it contains may be given physical significance. Each time a particle passes through the coating zone its size increases by a factor, K. It follows, that in determining the number of particles currently of size v, one may add up the numbers of particles that have been through the coating zone no times, once twice *etc.* (as counted by j) which initially had sizes v, v/K, v/K^2 etc. The maximum number of passes through the coating zone (p_{max}) is the largest integer satisfying $v_{min} \leq v/K^{p_{max}}$. The remaining terms account for the probability of a particle having passed through the zone j times and normalisation of the density function to maintain a constant third moment.

4.2 Comparison with Experiment

The striking thing about the predictions of the previous section is that according to equations (22) and (24) the mean size and standard deviation are directly proportional to the volume of solids added and further, the model has *no adjustable parameters*.

Figure 10 shows results from 14 different experiments[22], from which we may conclude that the model gives a good description of the mean and standard deviation.

Further evidence of the quality of the model may be obtained by comparing an observed and predicted size distribution; as shown in **Figure 11**. Here equation (25) has been used with $K \approx 1$, so that once again, the prediction is *free of adjustable parameters*. Both the position of the curve shown in **Figure 11** and its shape depend only on the amount of solid added.

For most problems in Particle Technology, predictions of the quality shown in **Figure 10** and **Figure 11** would be considered very strong verification of the model proposed. However, in this case it is also possible to test the model further by considering the thickness of coating applied to each seed. It is not shown here, but by means of a two-dimensional population balance, it is possible to show that taking a value of $K \approx 1$ requires the coating thickness (expressed as a volume of coating material) to depend only on the initial seed size for each particle. A plot of coating volume versus seed size (such as **Figure 12**) should show no dispersion. Quite clearly, the model prediction is not verified in this case.

What is seen is that the amount of coating a seed of a given size receives depends quite strongly on the seed's initial size (as predicted) but also on some random variable. This is likely to be the number of passes through the coating zone and indicates, perhaps, a more detailed description of how particles flow from the bulk of the bed into the coating zone is

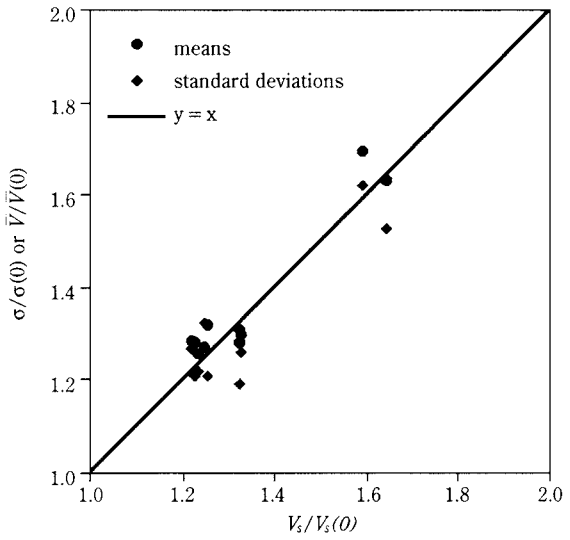

Fig. 10 Comparisons of theory and experiment. Equations (22) and (24) predict that both mean size and standard deviation should be directly proportional to the volume of solid sprayed on *i.e.* the data should lie along the $y = x$ line.

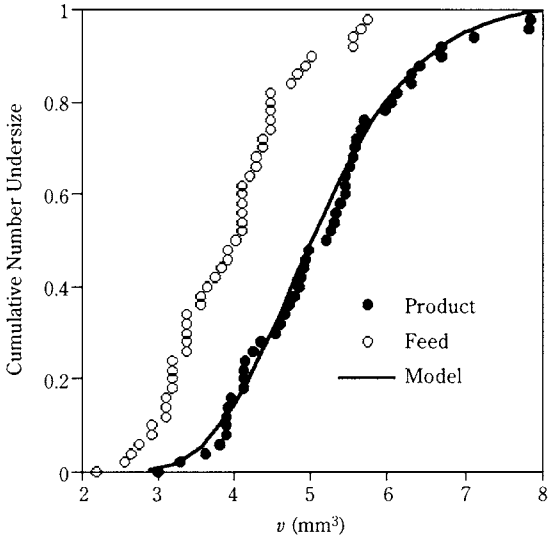

Fig. 11 Predicted and observed particle size distribution for spray coating. The prediction is made using equation (25), and is free of adjustable parameters.

required. Prediction of coating thickness is of some importance in this type of equipment as it is often desirable that uniform coatings be achieved. Two points of importance emerge here: a complete model requires better knowledge of the flow pattern and the particle's state needs to be described by two internal co-ordinates (seed size and coating size).

4.3 Observations on spray coating

The development of the PBE in this case study took place while Dr J.D. Litster was on sabbatical leave from the University of Queensland, Australia, at the University of Cambridge. We sought first to explain how size increase proceeds – we conclude that it is by means of a constant coating factor, K – and then to predict the overall size distribution. Both of these objectives were quickly met, but we came to the conclusion that explanation of the discrepancies shown in **Figure 12** would require considerable additional experimental work.

5. Case Study 3. *Granulation*: Extraction of Rate Constants

This last example concerns the application of population balance techniques to the process of granulation. PBEs have been used to describe this unit operation for many years, most notably by Sastry[23] and recently by Litster and his co-workers[24]. The work reported here differs from those authors in that it refers to high-shear rather than pan or drum granulation, and, as will be seen, requires the consideration of more than one mechanism.

5.1 Experimental

We have studied the granulation of finely divided calcium carbonate powders (mean size 15 μm) with the addition of liquid polyethylene glycol binder (PEG 1600) at 50°C in a Fukae 30 litre high-shear mixer. For further details see Knight *et al*[25] and Pearson *et al*[26]. Samples of granules are removed from the mixer at regular intervals, cooled to solidify the binder and then sieved on a fourth-root-of-two series of sieves.

We also conduct tracer studies, in which additional granules – marked with blue dye – are added to the mixer, typically eight minutes after commencement of operation. The distribution of dye with time and size can then be followed by means of sieving and spectrophotometry to determine dye concentrations.

5.2 Key Results

The two most important results are that the PSDs observed are clearly bi-modal and that dye added in large tracer particles rapidly becomes distributed to much smaller sizes. This last point is most readily illustrated by considering the fraction of dye that remains in particles larger than the smallest tracer particle added. An example of these data is shown in **Figure 13**. It may be seen that the fraction decays exponentially with a time constant of approximately 1000 s.

5.3 Modelling

The standard approach to PBE modelling of granulating systems is to assume a functional form of the aggregation kernel – i.e. how it depends on granule size, and perhaps time – and then to choose parame-

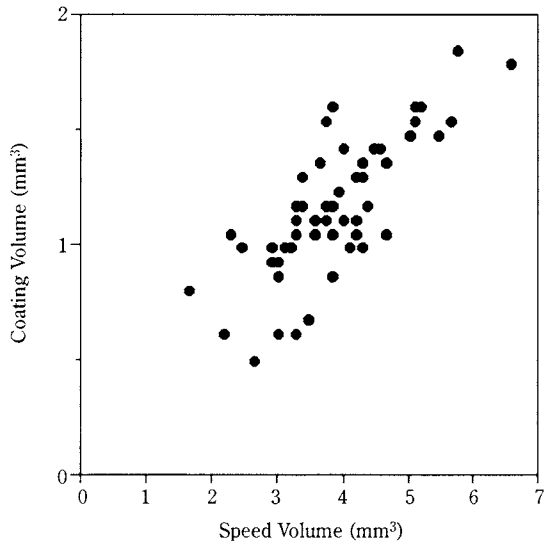

Fig. 12 The coating size as a function of initial seed size. The model incorrectly predicts *no* dispersion of coating size for any given seed size.

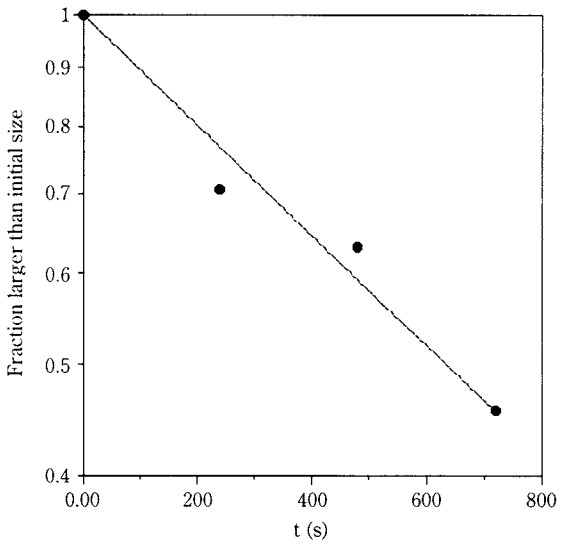

Fig. 13 The fraction of dye found in granules of size greater than or equal to the size of tracer granules added

ters for the kernel (perhaps exponents of the size dependence) so that the model fits the data well in some least-squares sense. In so doing the differential equations of the PBE are solved – integrated, as is often said – using varying values of the parameters until the fit is optimal.

The approach adopted here is a different one. We take the differential approach that we developed for our crystallisation work (Bramley *et al*[12]) which requires *a priori* knowledge of the size dependence of the rate constants and extracts the time dependence. At this early stage of our work we simply propose, from first principles, the forms of the size dependencies and asses their performance. The two mechanisms to be considered are size enlargement by aggregation and size reduction by breakage.

5.3.1 Aggregation

Visual observation of the bed of granules in a high-shear mixer reveals that while the granules adopt significant rotational velocities they also display noticeable deviations from the local average velocity. This may be likened to turbulent flow of a fluid or to molecular motion in a gas.

Consider the rate of collisions between particles of size l_1 and l_2, each with time varying velocities V_1 and V_2. We take Smoluchowski's approach and write

Rate of collisions = Collsion cross-section × average relative speed

$$\propto (l_1+l_2)^2\,|\overline{V_1-V_2}|$$

We borrow from the study of turbulence and write that $V(t)=\overline{V}+V'(t)$, where we assume that the average velocity of a granule does not depend on its size (being the average tangential velocity of the bed of solid) but that the random component does. Making this assumption allows

$$|\overline{V_1-V_2}| = |\overline{V'_1-V'_2}| \approx \sqrt{\overline{(V'_1-V'_2)^2}} = \sqrt{\overline{V'^2_1}+\overline{V'^2_2}}$$

In the kinetic theory of gases it is assumed that kinetic energy is equally distributed between differing molecular species, so that the square of random velocity is inversely proportional to the molecular mass of the species. That assumption couples naturally with the assumption that all collisions are elastic and that all energy is manifested as translational kinetic energy. In the current situation such an assumption seems rather implausible. Instead we assume that each granule is subject to the same random fluctuating impulses (in the mechanical sense) so that the random component of translational momentum will be constant, and that the random component of velocity will be inversely proportional to a granules mass, or the cube of its size

$$V' \propto 1/l^3$$

Combining these last results, and allowing that the aggregation rate constant and the rate of collisions differ by an efficiency that will at least be a function of operating conditions, and thus time, we write

$$\beta(l_1,l_2,t) = \beta_0(t)\,(l_1+l_2)^2\sqrt{\frac{1}{l_1^6}+\frac{1}{l_2^6}} \qquad (26)$$

5.3.2 Breakage

To define the breakage rate we need to specify a breakage selection function $S(l,t)$ and a breakage distribution $b(l_1,l_2)$. Our tracer data indicates that the breakage rate is not strongly size or time dependent and from the slope of the line in **Figure 13**, $S=0.001$ s^{-1}. We attribute the presence of the small-size mode to the breakage process and make the assumption that breakage proceeds by fragmentation. We then take b to be a log-normal distribution with a mass-weighted geometric mean size of 125 μm (the location of the samll-size mode) and geometric standard deviation of 1.15 (the width of that mode).

5.3.3 Simulations

Figure 14 below shows how well the PBE is able to predict the observed size distributions.

The input to the simulation is the dependence of the aggregation rate constant, β_0, on time. The values for β_0, extracted from the measured PSDs, and the curve used in the simulations are shown in **Figure 15**.

These data, then, suggest that the aggregation rate constant increases with time; which must almost

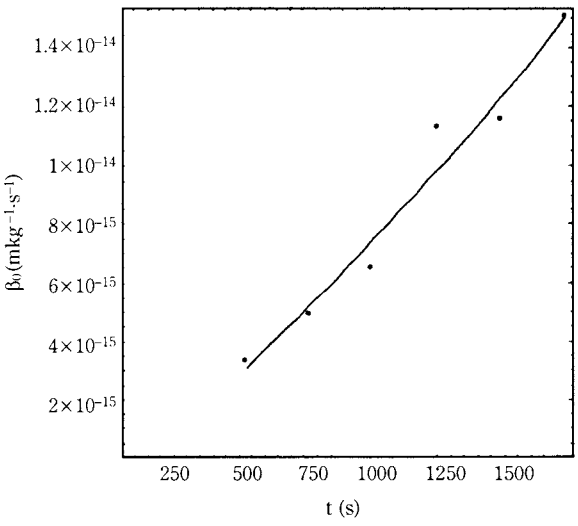

Fig. 15 The dependence of the aggregation rate constant on time

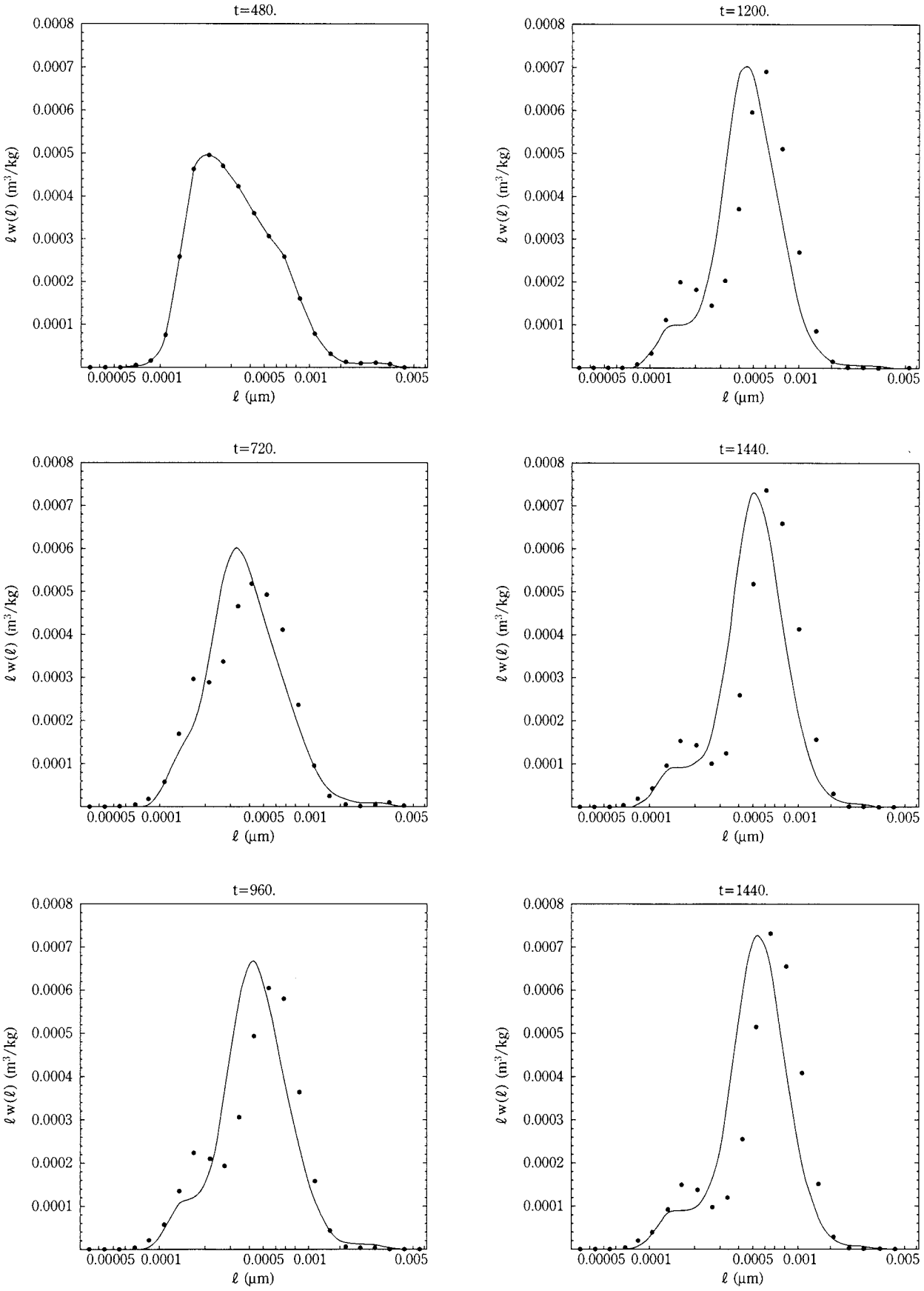

Fig. 14 Measured and predicted mass density functions

certainly mean that some property of the granules is changing with time. The current focus of our research is the identification of what that property might be. We conclude, once again, that the behaviour of each particle is governed by more than just its size – that a physically sound model must incorporate additional internal co-ordinates.

5.4 Observations on granulation

Our experiments and population balance analysis leave us confident that breakage is important in this system. We have proposed that the rate of breakage is independent of time and size and that the fragments formed are nearly mono-disperse. We have developed a collision model to predict the effect of particle size on aggregation rate.

6. Conclusions

It is possible now to solve population balance equations routinely when particles can be described by one internal co-ordinate (i.e. size) and at most one external co-ordinate. In the three case studies reported, size was variously characterised as equivalent volume diameter, particle volume and sieve size. In the second case study it was allowed that the size distribution varied with position in the coating zone of a spray coating apparatus.

It is also possible to extract rate constants, by means of PBEs, provided the size dependence of the rates is known. This approach was used in the first and third case studies. It is perhaps this activity that can reveal most about the processes under study. For in this way all of the behaviour of a system – or at least, such of it as is captured by the model – is reduced to a simple list of rate constants. In the first case study it was shown that simultaneous growth and aggregation can be described by standard supersaturation dependence of the growth rate, but that a rather more elaborate description was needed for aggregation. Without taking this rate-based approach, it would have been quite impossible to interpret our experimental data. The second case study, however, revealed that the PSDs produced are entirely independent of any rate constant; the spray coating system behaves as the analogue of the equilibrium chemical reactor, the product being determined in this case solely by the amount of material sprayed on. In the final case study a second internal co-ordinate (dye concentration) was added to the experimental data (but not, at this stage, the model) in order to identify the active mechanisms and determine their rates.

It is surely noteworthy that all of the modelling reported here has one common flaw. In every case it has been shown that description of particles by one internal co-ordinate – size – is, eventually, inadequate. In the first case study, it eventually becomes apparent that some internal structure of the aggregates (presented here as a Thiele modulus) determines the rate of aggregation. In this case it seems possible to assume that all particles have the same value of the modulus, so no difficulty is encountered. In the second case study, inspection of a second internal co-ordinate (coating size) revealed that the model was not capable of predicting the observed dispersion in coating thickness – despite the excellent predictions of the overall size distribution. In the last case study it was shown that the aggregation rate constant is strongly dependent on time – which must arise out of some changing property of the granules other than their size.

The need to represent a particle by more than just its size is a reflection that particles are heterogeneous and that the heterogeneity is in general not uniform over different particle sizes. A different kind of heterogeneity, this time external to the particles, – imperfect mixing – was also suspected of being important in the eventual shortcomings of the model in the second case study. It is these areas – heterogeneity within and without particles – that are the focus of our current research in population balance techniques.

7. Acknowledgements

I am grateful to many people for their contributions over the last decade and more to this work. First and foremost these are the people who have done most of the work, my students and collaborators: on population balance methods Denis Smit, Ed Wynn, Mark Nicmanis; on aggregation during precipitation Allan Bramley, Dean Ilievski, Bill Paterson, John Gooch, Alan Collier, Hassan Mumtaz, Jason Barrick; on spray coating Lian Liu, Jim Litster and on granulation Terry Instone, Peter Knight, Judith Pearson, Alison Scott and Yong Qi Chen. We all in one way or another owe thanks to NH&MRC of Australia, SERC, EPSRC, Du Pont, ICI, Bayer, Romaco and Unilever for funding.

Most of the results presented here have been published previously (as is indicated in the footnotes), some of the text used in the second case study forms part of the proceedings of the 5th International Symposium on Agglomeration, Nagoya, Japan, 1993.

8. Nomenclature

8.1 Roman symbols

a cross sectional area of a particle (m^2)
b breakage function (m^{-1} or m^{-3})
B^0 nucleation rate ($m^{-3}s^{-1}$)
D diffusivity (m^2/s)
f size dependent portion of a rate constant
K coating parameter (–)
k reaction rate constant (kmol $m^{-2}s^{-1}$)
l particle size (m)
m moment
n number density function per unit volume of suspension (m^{-4})
N number of particles per unit volume (m^{-3})
Q volumetric flowrate (m^3/s)
r rate of destruction
S selection rate constant (s^{-1}) or supersaturation (–)
t time (s)
T Total species concnetration ($kmol/m^3$)
v particle volume (m^3)
V volume (m^3) or velocity (m/s)
w mass density function per unit volume of suspension (kg m^{-4})
W mass of particles per unit volume (kg m^{-3})
x axial position (m)
X pore length (m)

8.2 Vectors

$\mathbf{x}$ Position in phase space
$\mathbf{u}$ velocity in phase space

8.3 Greek Symbols

α ion ratio
β Aggregation rate constant (m^3/s)
δ Dirac distribution
ε integration variable
σ standard deviation

9. References

1) Hulburt, H.M. and Katz, S., "Some problems in particle technology. A statistical mechanical formulation", *Chem. Eng. Sci.*, **19**, 555, (1964)
2) Randolph, A.D. and Larson, M.A., *Theory of Particulate Processes 2nd ed,* Academic Press, New York, 1988
3) Ramkrishna, D., "The status of population balances", *Reviews in Chemical Engineering*, **1**, 49, (1985)
4) Gibbs J.W., *Collected Works*, Vol. 1, *Thermodynamics*, Yale University Press, New Haven, 1948
5) Smoluchowski, M.V., "Mathematical theory of the kinetics of the coagulation of colloidal solutions", *Z. Phys. Chem.*, **92**, 129, (1917)
6) Hounslow, M.J., Ryall, R.L. and Marshall, V.R., A Discretized Population Balance for Nucleation, Growth and Aggregation, *AIChEJ*, **34**, no. 11, 1821, 1988
7) Hounslow M.J., "A Discretized Population Balance for Continuous Systems at Steady State", *AIChE J*, **36**, 1, 106, 1990
8) Hill, P.J and Ng, K.M., "New discretization procedure for the breakage equation", *AIChEJ*, **41**(5), 1204-1216, (1995)
9) Nicmanis M. and Hounslow M.J., A finite element method for the steady state population balance equation, in press *AIChEJ*, 1998
10) Gelbard, F. and Seinfeld, J.H., "Numerical solution of the Dynamic Equation for Particulate Systems", *J. Comp. Physics.*, **28**, 357, (1978)
11) Muralidar, R. and Ramkrishna, D., "An inverse problem in agglomeration kinetics", *J. Colloid Interface Sci.*, **112**, 348, 1986
12) Bramley A.S. and Hounslow M.J. "Aggregation during Precipitation from Solution: A Method for Extracting Rates from Experimental Data", *J. Coll. Interf. Sci.*, 183, no 1, 155, 1996
13) Ryall, R.L., Harnett, R.M. and Marshall, V.R., "The effect of urine, pyrophosphate, citrate, magnesium and glycosaminoglycans on the growth and aggregation of calcium oxalate crystals in vitro", *Clin. Chim. Acta.*, **112**, 349, (1981)
14) Bramley A.S., Hounslow M.J. and Ryall R.L., Aggregation during precipitation from solution: Kinetics for Calcium Oxalate Monohydrate., *Chem Engg Sci*, **52**, no 5, 747-757, 1997
15) Hartel, R.W. and Randolph, A.D., "Mechanisms and Kinetic Modeling of calcium oxalate crystal aggregation in a urinelike liquor", *A.I.Ch.E. J.*, **32**, No. 7, 1186, (1986)
16) Smit D.J., Hounslow M.J. and Paterson W.R., "Aggregation and gelation: I. analytical solutions for CST and batch operation", *Chem Engg Sci*, **49**, 7, 1025, 1994
17) Mumtaz H.S., Hounslow M.J., Seaton N.A. and Paterson W.R., Orthokinetic aggregation during precipitation: a computational model. *Chem Eng Res Des.*, **75**, Part A, 152-159, 1997
18) Hounslow M.J., Bramley A.S. and Paterson W.R., Aggregation during precipitation from solution. A pore diffusion-reaction model for calcium oxalate monohydrate, in press *J. Coll. Interf. Sci*, 1997
19) Nancollas, G.H. and Gardner, G.L., "Kinetics of crystal growth of calcium oxalate monohydrate", *J. Crystal Growth*, **21**, 267, (1974)
20) Barrick J.P., CPGS report, Department of Chemical Engineering, The University of Cambridge, 1997
21) Litster J.D., Hounslow M.J. and Liu L.X., "Bottom sprayed granulation and coating in a spouted bed", *Proceedings of the VIth International Symposium on Agglomeration*, 123-128, Nagoya, Japan, 1993
22) Liu, L.X., "Coating of seeds with fertilizer in a spouted bed", PhD thesis, University of Queensland, Australia, 1991.

23) Sastry, K.V.S., "Similarity size distribution of agglomerates during their growth by coalescence in granulation or green pelletization", *Int J Min Proc*, **2**, 187, (1975)
24) Adetayo, A.A., Litster, J.D., Pratsinis, S.E. and Ennis, B.J., "Population balance modelling of drum granulation of materials with wide size distributons", *Powder Technol.*, **82**, 37-49, (1995)
25) Knight, P.C., Instone, T., Pearson, J.M.K. and Hounslow, M.J., "An investigation into the kinetics of liquid distribution and growth in high-shear mixer agglomeration", *Powder technol.*, **97/3**, 246-257, (1998)
26) Pearson, J.M.K., Hounslow, M.J., Instone T. and Knight P.C., "Granulation kinetics: the confounding of particle age and size"

Author's short biography

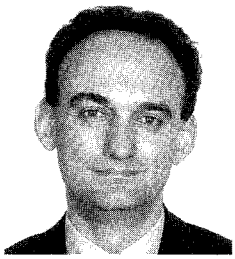

Professor M.J. Hounslow BE (Hons), PhD, MIChemE, CEng

Michael Hounslow graduated with an honours degree in Chemical Engineering from the University of Adelaide, Australia, in 1980. He then spent four years with ICI Australia (Operations) Ltd in a variety of production and design roles. In 1984 he joined the University of Adelaide as a Lecturer where, among other things, he undertook a PhD on the subject of aggregation during crystallisation. That work was concerned mainly with population balance modelling for the purposes of understanding human kidney stone production. In 1990 he moved to the University of Cambridge in the UK as a Lecturer where he continued his work on crystallisation, population balance modelling and, more recently, granulation. In August 1998 he left Cambridge to take up a Chair in Chemical Engineering in the Department of Chemical and Process Engineering at the University of Sheffield, in the UK, where he leads the Particle Products Group.

Modelling and Numerical Calculation of Turbulent Gas-Solids Flows with the Euler/Lagrange Approach†

M. Sommerfeld
*Martin-Luther-Universität**

Abstract

The paper summarises recent developments of the Euler/Lagrange approach for the prediction of particulate two-phase flows. Based on detailed experiments, the modelling of particle-wall collisions, including the effect of wall roughness, could be considerably improved. Moreover, a stochastic approach was developed for modelling inter-particle collisions which were found to be quite important even for low particle mass loading. Model calculations with inter-particle collisions were validated based on large eddy simulations for a homogeneous isotropic turbulence field. The effect of inter-particle collisions on the development of a particle-laden horizontal channel flow was analysed in detail by varying particle size and mass loading. Numerical predictions were performed for pneumatic conveying in a horizontal pipe and compared with measurements by phase-Doppler anemometry in order to further validate the developed models.

1. Introduction

Gas-particle flows in wall-bounded systems are frequently found in technical and industrial processes. Examples are pneumatic conveying, fluidised beds, vertical risers, particle separation in cyclones, classification of particles, mixing devices and others. In most of these processes, the particulate phase is more or less homogeneously dispersed and the fluid dynamic transport of the particles plays a significant role. Two-phase flows in such processes are characterised by a number of complex fluid dynamic features, as for example:

- strong velocity gradients near walls and in shear layers,
- particle interactions with solid boundaries,
- spatial non-uniformities in the particle distribution with regions of dilute and dense flow regimes,
- modification of mean flow and turbulence by the presence of particles.

Hence, the particle behaviour in these kinds of flows is influenced by a number of physical effects such as gravity, inertial effects, transverse aerodynamic lift forces, turbulence, particle-wall collisions, and at higher particle loading, also by inter-particle collisions. In addition, mean flow and turbulence properties are modulated by the presence of the particles, especially at higher mass loading.

For supporting the lay-out and optimisation of the above mentioned processes, numerical computations are increasingly applied also by industry. A reliable numerical calculation of confined gas-solid flows requires that all important physical transport phenomena have to be appropriately modelled. In most of the above-mentioned applications, the dispersed phase is characterised by a relatively wide size spectrum and the concentration is not too high. Therefore, numerical predictions of such flows may be satisfactorily performed by using the Euler/Lagrange approach which allows consideration of an arbitrary particle size spectrum. Moreover, this approach has the advantage that micro-physical phenomena affecting the particle motion, such as wall collisions and collisions between particles, can be easily described by models based on physical principles. The application of the Euler/Lagrange approach for the prediction of pneumatic conveying was recently summarised by Huber and Sommerfeld [1]. The present paper summarises recent developments in modelling and calculating gas-particle flows based on the Euler/Lagrange approach.

2. Numerical approach

In the developed Euler/Lagrange method, the fluid flow is calculated by solving the time-averaged Navier-

* Fachbereich Ingenieurwissenschaften, 06099 Halle (Saale), Germany
† Received July 28, 1998

Stokes equations in connection with the well-known k-ε turbulence model and accounting for source terms describing the effect of the dispersed phase on the mean flow and turbulence properties [1]. The resulting set of conservation equations is solved using a finite volume discretisation scheme with collocated grid arrangement.

The dispersed phase is simulated by tracking a large number of parcels through the flow field and determining the averaged phase properties by ensemble averaging. Each parcel represents a number of real particles with the same properties in order to allow representation of the dispersed phase concentration by a reasonable number of computational particles. The parcels are tracked through the flow field by solving the equations of motion, a set of ordinary differential equations for the calculation of the new parcel position, the parcel linear velocity components and the components of the angular velocity. The forces considered to act on each particle are the drag force, gravity, the slip-shear lift force, and the lift force resulting from particle rotation. Furthermore, the torque acting on the particles as a result of rotation is accounted for. Details of the individual forces are given by Sommerfeld [2].

The instantaneous fluid velocity components at the particle location which have to be known to solve the equations of motion, were determined from the local mean fluid velocity interpolated from the neighbouring grid points and a fluctuating component generated by the Langevin model described by Sommerfeld et al. [3]. In this model, the fluctuating velocity components are composed of a correlated part from the previous time step and a random component sampled from a Gaussian distribution function. The correlation function is composed of a Lagrangian and an Eulerian part to account for the crossing trajectories effect, and is calculated using appropriate time and length scales obtained from the k and ε values [3].

The influence of the particle phase on the fluid flow, i.e. the mean flow and turbulence properties, is accounted for by calculating the source terms in the Navier-Stokes equations by a modified PSI-CELL method [4]. In order to obtain a converged solution for the coupled phases, an iteration procedure with under-relaxation was developed [5].

3. Modelling of wall collisions

In wall-bounded particulate flows, the collision of particles with the walls may considerably alter the development of the flow and also result in an increase of pressure loss. The importance of wall collisions on the particle behaviour may be assessed by comparing a characteristic length scale of particle motion with the dimensions of the confinement, e.g. the pipe diameter. If the particle motion after being rebound from the wall is insignificantly affected by the flow before it reaches the opposite wall, the regime may be regarded as wall-collision-dominated. This is the case when the particle response distance is larger than the dimension of the confinement, i.e. $\lambda_p > D$. The particle response distance is the product of the particle response time τ_p and a characteristic velocity W_p, which in pneumatic conveying is the average conveying velocity.

The wall bouncing process is influenced by a number of parameters, particularly the impact angle, the particle velocity, the angular velocity, the particle and wall material, the particle shape, and the wall roughness. The change of particle velocities by a wall collision may be calculated by solving the momentum equations in conjunction with Coulomb's law of friction. This derivation results in two sets of equations for a sliding and non-sliding collision [6], [7]. Several experimental studies revealed that wall roughness considerably alters the wall collision process. In order to account for the effect of wall roughness, a stochastic model was developed [8], where the instantaneous impact angle is composed of the particle trajectory angle with respect to the plane wall and a component randomly sampled from a normal distribution function:

$$\alpha_1' = \alpha_1 + \Delta\gamma\,\xi \tag{1}$$

Here, $\Delta\gamma$ is the standard deviation of the roughness angle distribution and ξ is a Gaussian random number with zero mean and a standard deviation of one. The assumption of a normally distributed roughness angle was confirmed by optically scanning a stainless steel plate [9]. The standard deviation $\Delta\gamma$ is of course a function of particle size and exponentially decreases with increasing particle size, which implies that the roughness effect is more pronounced for smaller particles. All the required model parameters, such as restitution ratio and friction coefficients as a function of impact angle, were obtained from experiments in a horizontal particle-laden channel flow [9]. The channel used for these experiments had a height of 30 mm, a width of 300 mm, and a length on 3 m. The wall plates were interchangeable in order to study the effect of different wall material on the wall collision process. The conveying velocity was about 15 m/s. These data were used to improve and validate the developed stochastic wall collision model [10].

A comparison of the model calculations with the experimental data is shown in **Figure 1** for 100-μm glass beads colliding with a polished plate and an untreated stainless steel plate. The plot of the rebound angle versus impact angle clearly reveals the effect of wall roughness. For small impact angles, the rebound angle is considerably larger than the impact angle, which is associated with an increase of the velocity component normal to the wall after rebound. This is the result of the so-called shadow effect [7], which implies that particles hitting the wall at a shallow angle will impact with a higher probability on a positive inclined roughness structure. This is generally associated with an increase of the rebound angle. The resultant so-called mean roughness angle decreases with increasing particle impact angle and approaches zero for a normal impact. The model calculations are in very good agreement with the data, for both the untreated stainless steel and the polished wall (Fig. 1), which shows that the wall roughness effect is modelled appropriately.

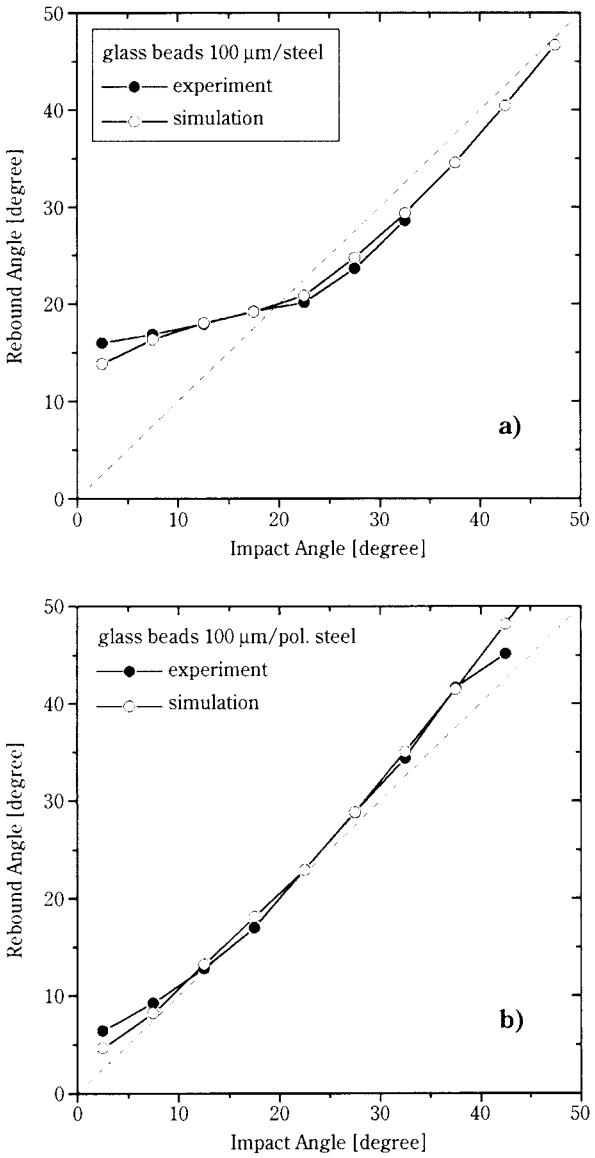

Fig. 1 Comparison of measurement and model calculations for the rebound angle versus impact angle (glass beads with a diameter of 100 μm, impact velocity of particles 12 m/s), a) stainless steel wall ($\Delta\gamma$=7°), b) polished steel wall ($\Delta\gamma$=2.3°)

The effect of the wall roughness on the rebound characteristics of a particle is illustrated in **Figure 2**, where simulated probability distributions of the rebound angle are shown for two impact angles, i.e. 5° and 45° and two different degrees of wall rough-

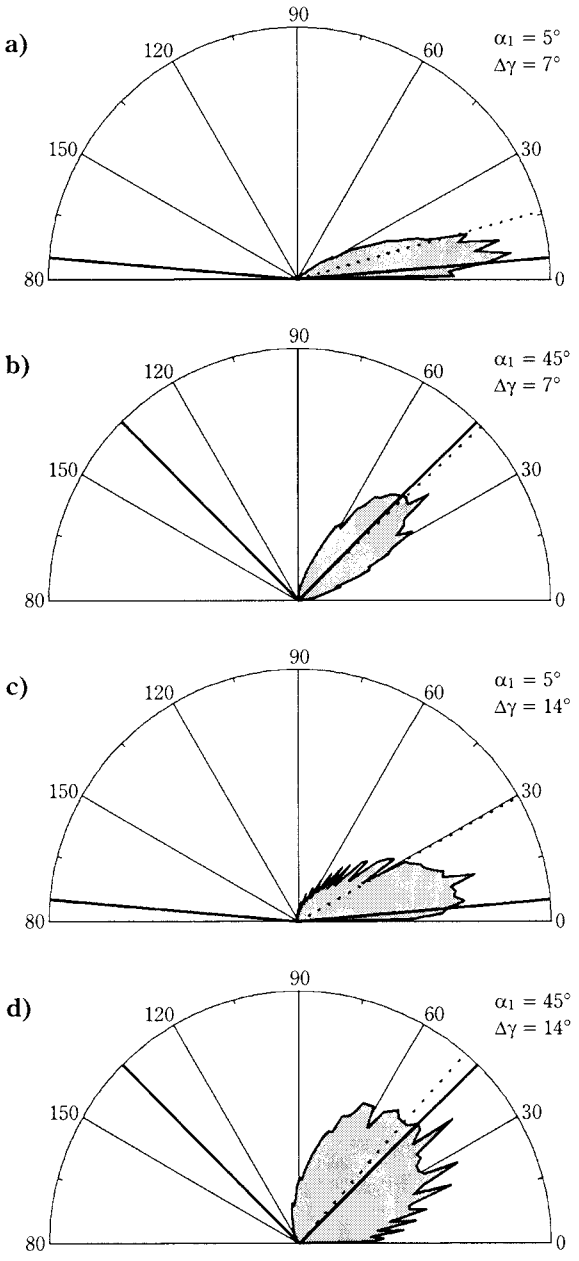

Fig. 2 Distributions of the rebound angle for different degrees of roughness and different impact angles, a) α_1=5°, $\Delta\gamma$=7°, α_2=15.07°, b) α_1=45°, $\Delta\gamma$=7°, α_2=43.55°, c) α_1=5°, $\Delta\gamma$=14°, α_2=29.65°, d) α_1=45°, $\Delta\gamma$=14°, α_2=48.69° (solid line: impact angle, dashed line: mean rebound angle)

ness. As a result of wall roughness, the rebound angle scatters over a wide range. With increasing degree of roughness (i.e. increase of $\Delta\gamma$ from 7° to 14°) the rebound angle distribution becomes more broadened. For the shallow impact angle, the mean rebound angle becomes considerably larger than the impact angle as a result of the shadow effect. Increasing the degree of roughness also causes a further increase of the average rebound angle. In horizontal pneumatic conveying, the shadow effect causes a re-suspension of the particles as demonstrated by Huber and Sommerfeld [1]. Even for a polished wall, remaining surface structures cause a slight increase of the mean rebound angle at low impact angles.

The results presented above also demonstrate the importance of taking into account wall roughness effects in numerical calculations of wall-bounded particulate flows. In gas-solid flows, wall collisions of particles largely contribute to the additional pressure loss of the dispersed phase. This pressure loss is directly correlated with the momentum loss during a wall collision and the way the particles are rebound, since the re-acceleration of the particles extracts momentum from the gas phase.

4. Inter-particle collision model

Even in dilute two-phase flows, inter-particle collisions may considerably affect the flow development as demonstrated by Sommerfeld [2] for a horizontal channel flow. The importance of inter-particle collisions may be estimated by comparing the particle response time with the mean inter-particle collision time [11]. If the particle response time is much smaller than the collision time, the particle motion is controlled by fluid dynamic transport and turbulence. This regime is referred to as dilute two-phase flow. In dense two-phase flows, the particle collision time becomes much smaller than the particle response time, which implies that the particles will not be able to respond fully to the fluid flow between successive collisions. Hence the particle motion is dominated by inter-particle collisions.

With the Lagrangian approach, it is in principle possible to apply a direct simulation approach to detect and calculate collisions between particles if all particles are tracked simultaneously through the flow field, as for example using the method adopted by Tanaka and Tsuji [12]. This method is, however, relatively time consuming, since it requires a search for a collision partner in the vicinity of the considered particle at each time step of the trajectory calculation.

To avoid such a procedure, a stochastic inter-particle collision model was developed [2]. This model is also applicable if a sequential tracking of the particles is adopted, as is usually done for stationary flows. During each time step of the trajectory calculation of the considered particle, a second fictitious particle is generated. The size and velocity of this fictitious particle are randomly sampled from local distribution functions. This approach implies, however, that for each control volume the particle size and the velocity distribution functions have to be determined and stored. The local distribution functions of the particle phase properties are updated after each Lagrangian calculation through an iterative procedure until these properties approach steady-state values. Since no particle phase properties are available in the first iteration, the particle collision calculation begins with the second Lagrangian calculation. When the effect of the particles on the fluid flow is accounted for, this procedure is combined with the two-way coupling iteration procedure [5].

In turbulent flows, the velocities of colliding particles may be correlated since they are transported in the same eddy. The degree to which the particle velocities are correlated depends on their response to the turbulent fluctuations. The velocities of small particles will be strongly correlated while those of very large particles are completely de-correlated. The response of particles to turbulent fluctuations may be characterised in terms of the Stokes number, i.e. the ratio of the particle response time to the Lagrangian integral time scale:

$$St_t = \frac{\tau_p}{T_L} \tag{2}$$

The particle response time is determined from the calculations accounting for non-linear drag, and the Lagrangian integral time scale is obtained from the turbulent dispersion model [3]. In the developed collision model, the correlation of the velocity components of the fictitious particle $u_{fict,i}$ with those of the real particle $u_{real,i}$ is accounted for in the following way by using the turbulent Stokes number:

$$u_{fict,i} = R(St_t)u_{real,i} + \sigma_{p,i}\sqrt{1-R(St_t)^2}\xi \tag{3}$$

Here, $\sigma_{p,i}$ is the local rms value of the particle velocity component i, and ξ is a Gaussian random number with zero mean and a rms value of one. Hence, the sampled velocity components are composed of a correlated and a random part. With increasing Stokes number, the correlated term (first term in Eq. (3)) decreases and the random term increases accordingly. Comparing model calculations with large eddy

simulations, the following dependence of the correlation function $R(St_t)$ on the Stokes number was found.

$$R(St_t) = \exp(-0.55 St_t^{0.4}) \quad (4)$$

The next step in the collision model is to determine the probability of the occurrence of a collision between the considered and the fictitious particle within a time step. This probability is obtained by the product of the time step size Δt and the collision frequency given by the kinetic theory of gases:

$$P = f_c \Delta t = \frac{\pi}{4} (D_{p1} + D_{p2})^2 (\vec{U}_{p1} - \vec{U}_{p2}) N_{p2} \Delta t \quad (5)$$

where, D_{p1} and D_{p2} are the particle diameters, $(\vec{U}_{p1} - \vec{U}_{p2})$ is the instantaneous relative velocity between the considered and the fictitious particle, and N_{p2} is the number of particles per unit volume in the respective control volume. In order to decide whether a collision takes place or not a random number from a uniform distribution in the interval [0.1] is generated. A collision is simulated when the random number becomes smaller than the collision probability.

Once a collision occurs between the considered and the fictitious particle, the collision process is calculated in a coordinate system where the fictitious particle is stationary and the velocities are transformed accordingly. In this situation, the point of impact on the surface of the fictitious particle can only be located on the hemisphere facing the considered particle, and is obtained by a random sampling process [2]. For calculating the post-collision velocities of the considered particle (i.e. linear and angular velocities), the momentum equations for an oblique collision are solved by taking into account both sliding and non-sliding collisions [2]. Finally, the velocities of the considered particle are re-transformed into the original coordinate system. The velocities of the fictitious particle are of no further interest. This procedure is repeated for each time step of the trajectory calculation of the considered particle.

5. Validation of collision model

In order to validate the developed Lagrangian stochastic inter-particle collision model, data obtained by large eddy simulations (LES) were used [13], [14]. These simulations were performed for a homogeneous isotropic turbulence field (i.e. a cube with periodic boundary conditions) with the properties summarised in **Table 1** and different particle response times and concentrations. The adopted collision detection algorithm requires to consider rather large particles (i.e. D_p=656 μm). In order to have particle response times in a range to allow for a response of the particles to the turbulent fluctuations, the density of the particles was selected accordingly (**Table 1**). The resulting turbulent Stokes number (i.e. according to Eq. 2) is between about 0.8 and 6.0.

Table 1 Turbulence characteristics and particle phase properties for the large eddy simulations

Gas rms velocity, u'	0.3 m/s
Kinematic viscosity, ν	$1.45 \cdot 10^{-5}$ m²/s
Lagrangian integral time scale, T_L	23 ms
Eulerian integral time scale, T_E	26 ms
Longitudinal Eulerian length scale, L_f	7.25 mm
Lateral Eulerian length scale, L_g	3.71 mm
Particle diameter, D_p	0.656 mm
Particle density, ρ_p	25, 50, 100, and 200 kg/m³
Turbulent Stokes number	0.79, 1.5, 2.9, and 5.7
Volume fraction α	0.005–0.05
Restitution coefficient, e	1.0
Friction coefficient, μ	0.0

The calculations with the stochastic Lagrangian approach were performed by only considering the drag force acting on the particles. Gravity is neglected in these studies and the collision is assumed to be fully elastic. To generate the instantaneous fluid velocity along the particle trajectory, the Langevin equation model was applied [3]. Periodic boundary conditions were applied for the trajectory calculation. The gas flow and hence turbulent kinetic energy and the time and length scales of turbulence were prescribed according to the large eddy simulations. Two-way coupling is not considered in the present study, in order to isolate the effects due to inter-particle collisions.

As expected, the energy of the particles' fluctuating motion decreases with increasing Stokes number, since the particles become less responsive to the turbulent fluctuations. Both the model calculations and the simulations follow the same trend, indicating that the particle-turbulence interaction is modelled properly (**Fig. 3**). The collisions between the particles have no considerable influence on the particles' fluctuating motion, i.e. the results for the different volume fractions are only slightly different.

An important feature of the stochastic collision model is the consideration of the correlated motion of colliding particles. This effect is pronounced when the particle response time is in the order of the integral time scale of turbulence or even lower. The

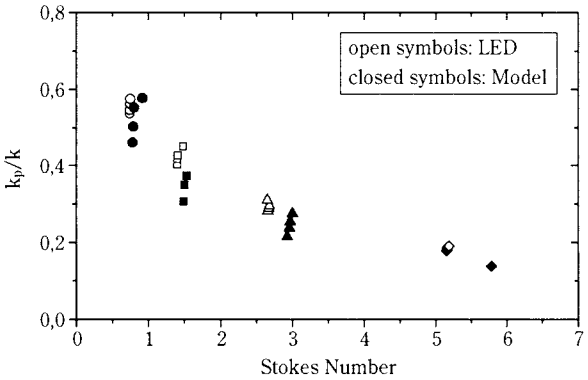

Fig. 3 Kinetic energy of the particles' fluctuating motion as a function of Stokes number (open symbols: LES, closed symbols: stochastic collision model with velocity correlation, symbols of one kind indicate the results for the different volume fractions (see Table 1))

relative velocity distribution function (PDF) for particles with a Stokes number of 0.794, shown in **Fig. 4a**), reveals the importance of accounting for this correlation. If the velocity of the fictitious particle is not correlated with that of the considered particle, a rather wide velocity distribution with a mean value of 0.45 m/s is obtained. In contrast, the correlated model gives a more narrow relative velocity distribution with a mean value reduced to 0.32 m/s. The comparison of the model calculations with the large eddy simulations shows a rather good agreement if the degree of correlation is modelled properly by appropriate specification of the model constants in the correlation function (Eq. 4).

Also, the distribution function of the angle between the trajectories of colliding particles is shifted considerably towards smaller angles when accounting for the correlation of velocities in the model (**Fig. 4b**). The calculated angle PDF (probability density function) agrees well with the LES result and a mean value of 1.07 rad is calculated. Without the velocity correlation, a larger mean value of 1.76 rad is obtained.

As a result of the reduction of the mean relative velocity due to the correlation effect, the average collision frequency will also be reduced. This effect may be illustrated by comparing the simulated average collision frequency with that resulting from the kinetic theory limit, which corresponds to the average collision frequency obtained without correlation. In **Figure 5**, the ratio of the calculated collision frequency to that predicted by kinetic theory is plotted versus the Stokes number. For very large Stokes numbers, the frequency ratio approaches the value of one. With decreasing Stokes number, the frequency ratio is continuously reduced due to the increasing degree of correlated motion of colliding particles.

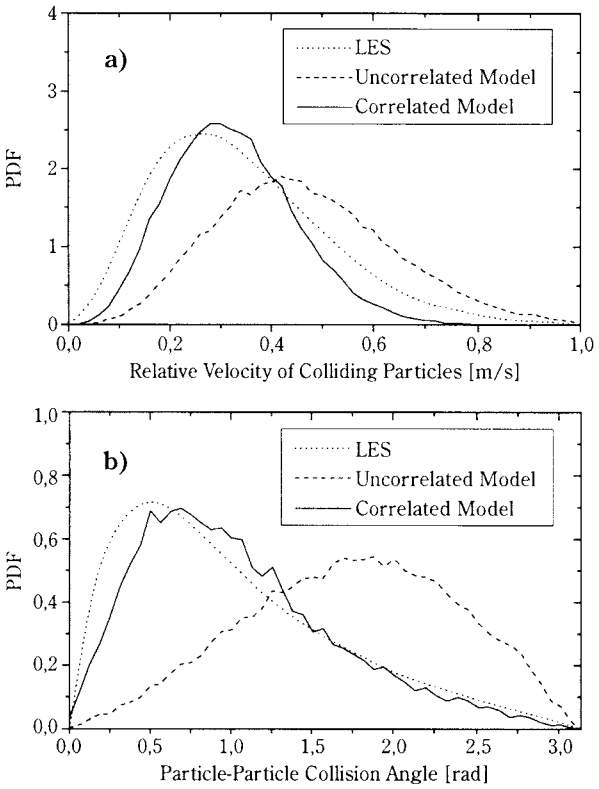

Fig. 4 Distribution of the relative velocity between colliding particles (a) and the particle-particle collision angle (b), comparison of the stochastic model with large eddy simulations (ρ_p=25 kg/m^3, St_t=0.794, α=0.0352)

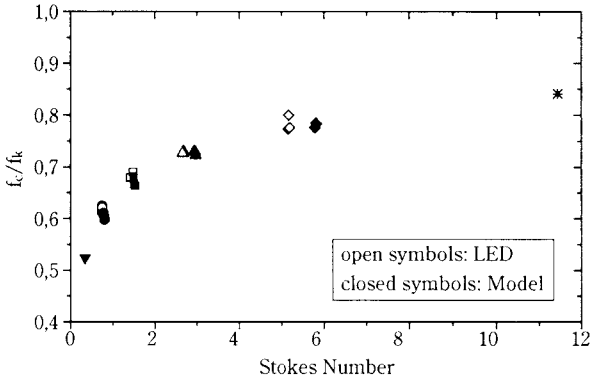

Fig. 5 Dependence of the ratio of simulated collision frequency to the collision frequency obtained from the kinetic theory limit on the particle Stokes number (open symbols: LES, closed symbols: stochastic collision model with velocity correlation, symbols of one kind indicate the results for the different volume fractions)

The predicted increase of the frequency ratio with Stokes number is in very good agreement with the LES data.

6. Channel Flow

In order to analyse the influence of inter-particle collisions on the development of particle-laden gas

flows, a closed two-dimensional horizontal channel with a height of H=50 mm and a length of L=5 m was considered. In order to isolate the effects of particle collisions from other effects, two-way coupling was not considered. Therefore, the gas flow field was prescribed according to the measurements of Laufer [15] for a fully developed channel flow with a centre line velocity of 20 m/s. The data for the gas flow include the profiles of the mean velocity in the direction of flow, U, the fluctuating components, $\overline{u'^2}$, $\overline{v'^2}$ and $\overline{w'^2}$, and the Reynolds stress $\overline{u'v'}$. The gas density was given a value of 1.18 kg/m^3 and the dynamic viscosity was selected to be $18.8 \cdot 10^{-6}$ N s/m^2. The particle motion was calculated by solving the equation of motion including drag force, gravity, transverse lift forces due to shear and particle rotation, and turbulence effects. The wall collision of particles was treated as inelastic and the change of the velocities was calculated by solving the momentum equations in connection with Coulombs law of friction. Wall roughness was not considered for the channel flow calculations. The particles considered in the calculations were glass beads with different diameters in the range between 25 and 500 μm and a solids density of ρ_p=2.5 g/cm^3.

The particle motion in channel flows in the dilute regime (i.e. with minor importance of inter-particle collisions) is controlled by turbulence and wall collisions. The importance of either of these effects depends on the particle response time and the turbulence intensity (i.e. the resulting particle Stokes number). The motion of small particles is mainly affected by turbulence, while large particles will continue to bounce from wall to wall without being strongly affected by flow and turbulence. The transition from turbulence-dominated transport to the wall collision regime is illustrated in **Figure 6** where vertical profiles of the normalised particle mass flux are shown

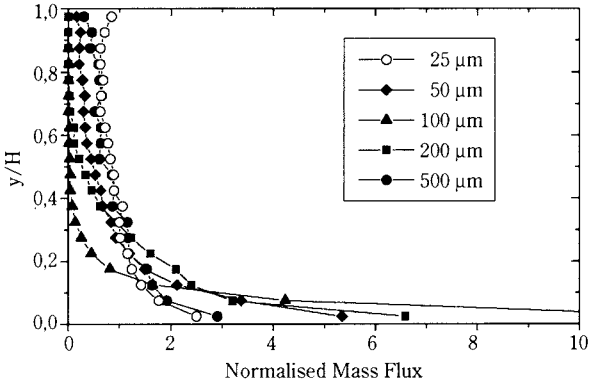

Fig. 6 Effect of particle size (diameter specified in the legend) on the developed profiles of the normalised particle mass flux in a horizontal channel flow (numerical calculation without inter-particle collisions)

for different particle sizes. Note that these calculations were performed without inter-particle collisions. It is obvious that small particles (i.e. diameter 25 μm) are almost homogeneously dispersed over the channel since gravitational settling is to a large extent balanced by turbulent dispersion, only a slight accumulation of the particles is found near the bottom of the channel. With increasing particle size, gravitational settling becomes more important and the particle mass flux near the bottom of the channel increases. The maximum is reached for the 100-μm particles. By further increasing the particle size, wall collision effects become more important and the particle mass flux distribution again becomes more uniform in the channel. For the 500 μm-particles, the profile of the particle mass flux is almost identical to that of the 25-μm particles.

The effect of inter-particle collisions is first analysed by comparing the particle mass flux distributions for different particle sizes as a function of mass loading. For the smallest particles considered (i.e. 25 μm), the influence of inter-particle collisions on the mass flux profile is very small and the profiles only change slightly with increasing mass loading (**Fig. 7a**), indicating again the dominance of turbulent transport. With increasing importance of gravitational settling (i.e. increase of particle size) and the associated increase of the particle mass flux near the bottom of the channel, inter-particle collisions become more important and the particles are re-dispersed by the collisions (**Fig. 7b** and **c**). It is observed that with increasing mass loading and hence increasing collision frequency, the mass flux near the bottom of the channel is reduced. Up to a mass loading of about one in most cases, however, an exponential increase of the mass flux with loading is still predicted towards the channel bottom. At the highest mass loading (i.e. η=2.0), the maximum in the mass flux is found at some distance above the channel bottom. The effect of inter-particle collisions is most pronounced for the 100-μm particles and at a mass loading of η=2.0, the particles are almost homogeneously dispersed over the channel.

The influence of inter-particle collisions on the profiles of the linear and angular velocities is illustrated in **Figure 8** for the 100 μm particles. Even for a rather low mass loading of η=0.1, the horizontal component of the particle mean velocity is considerably affected by inter-particle collisions. Near the bottom of the channel, the particle velocity becomes larger and in the core region smaller compared to the result without taking account of collisions. This is associ-

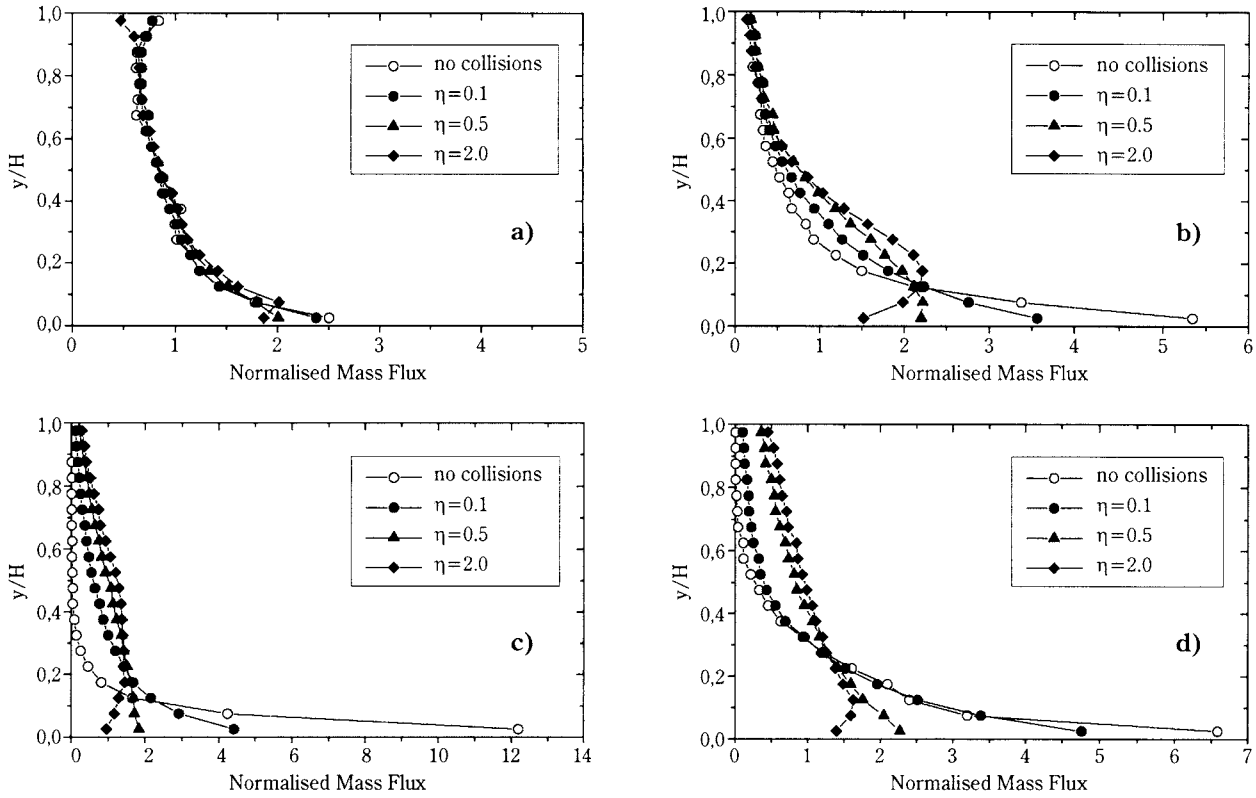

Fig. 7 Influence of inter-particle collisions on the developed profiles of the normalised particle mass flux for different mass loading and particle sizes, a) D_p=25 μm, b) D_p=50 μm, c) D_p=100 μm, d) D_p=200 μm

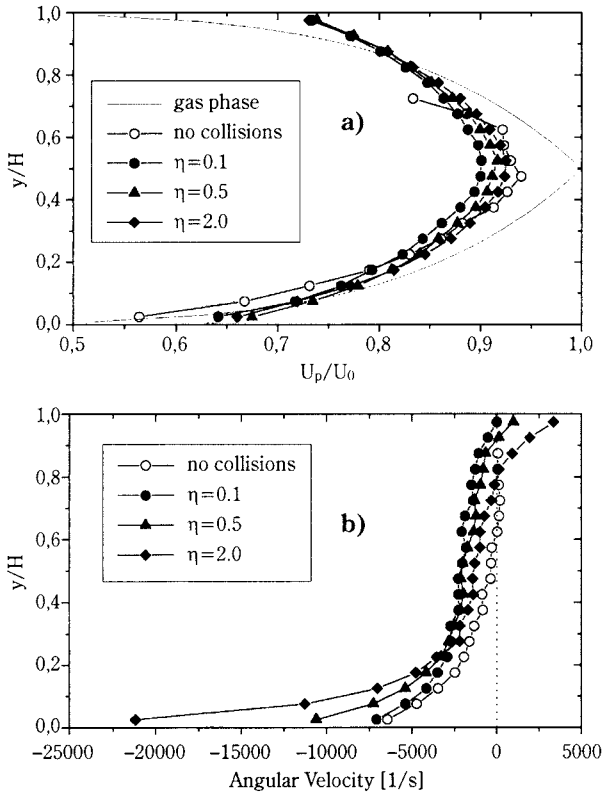

Fig. 8 Influence of inter-particle collisions on the profiles of the particle velocities, a) stream-wise component of the particle velocity, b) angular velocity, (particle diameter: 100 μm)

ated with two effects:

- Collisions between particles cause a re-dispersion of the particles whereby low speed particles from the region of high concentration near the bottom of the channel are transported to the core region.
- The average collision frequency of particles with the lower wall is reduced by inter-particle collisions [2] associated with a lower momentum loss and hence higher mean particle velocities near the bottom of the channel.

When the particle mass loading is increased further, i.e. from η=0.1 to 2.0, the collision frequency between particles is also increased further and the particle concentration near the bottom of the channel is reduced considerably. This is also associated with a further reduction of the wall collision frequency. The particles lose less momentum thereby and hence the particle mean velocity in the core region of the channel again slightly increases with mass loading. The angular velocity of the particles, especially in the vicinity of the channel bottom, is also considerably enhanced by the collisions between the particles (**Fig. 8**). For a mass loading of 2.0, the angular velocity reaches values of more than 20,000 1/s near the bottom of the channel.

Considering the fluctuating velocity components,

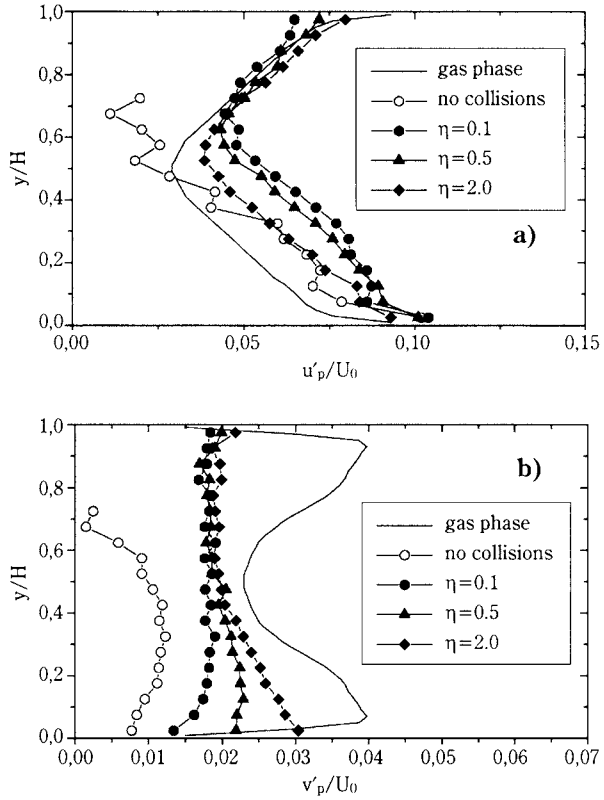

Fig. 9 Influence of inter-particle collisions on the profiles of the fluctuating velocities of the particles, a) stream-wise component, b) lateral component (particle diameter: 100 μm)

significant effects of inter-particle collisions are also obvious from **Figure 9**. The stream-wise component is first of all significantly higher than that of the gas phase and moreover higher in the lower part of the channel than in the upper part (**Fig. 9a**). This is again provoked by wall collision effects and the higher wall collision frequency with the lower wall. Obviously, the collisions between particles enhance the stream-wise fluctuation of the particles initially, when comparing the results without and with accounting for collisions at a loading ratio of 0.1. A further increase of the mass loading, associated with an increasing inter-particle collision frequency, causes a decrease of the particle fluctuating velocity. On the other hand, the lateral component of the particle fluctuating velocity continuously increases with increasing particle collision frequencies (**Fig. 9b**). Hence, the particles' fluctuating motion becomes more isotropic as a result of inter-particle collisions. The importance of modelling collisions between particles even for relatively low mass loading becomes obvious from these results.

7. Pneumatic Conveying

As a means of further validating the developed models also in a more complex flow situation, numerical calculations were performed for the pneumatic conveying of fine particles in different pipe elements such as horizontal pipes, pipe bends and vertical pipes. Detailed experimental data were obtained by phase-Doppler anemometry in pipes of different diameter, i.e. 80 mm [1] and 150 mm [16]. The particles used in the experiments were spherical glass beads with a density of ρ_p=2.5 g/cm^3 and a number mean diameter of 40 μm. In the present study, the calculations for pneumatic conveying systems were performed for the 80 mm pipe, by accounting for the influence of the particles on mean flow and turbulence properties (i.e. two-way coupling) by introducing the appropriate source terms in the Navier-Stokes equations [1]. The particle motion was calculated by solving the equation of motion including drag force, gravity, transverse lift forces due to shear and particle rotation, and considering turbulence effects based on the Langevin equation model [3] and inter-particle collisions. Wall collisions and wall roughness was modelled as described above.

As demonstrated previously [2] and [7], wall roughness also has considerable consequences for the development of the distribution of the particles in the cross-section of a horizontal pipe. The average increase of the rebound angle compared to the impact angle due to roughness causes a re-suspension of particles, whereby the effect of gravitational settling is reduced [7]. A comparison of calculated particle mass flux profiles at the end of a 4-m-long horizontal smooth glass pipe and a stainless steel pipe reveals this effect clearly (**Fig. 10**). In the smooth pipe, turbulence is not sufficiently strong to disperse the particles and they tend to accumulate in the lower half of the pipe cross-section (**Fig. 10a**). In the case of the stainless steel pipe, particles colliding with the lower wall are in average rebound at a larger angle and hence are re-entrained in the flow. Therefore, the maximum in the particle mass flux is close to the centreline of the pipe (**Fig. 10b**).

The comparison of the predictions with the measurements for both cases reveals that the wall roughness effect is modelled properly (**Fig. 10**). Some larger differences between calculation and experimental data are observed for the glass pipe (i.e. smooth wall), especially in the upper cross-section of the pipe.

The additional pressure loss in pneumatic convey-

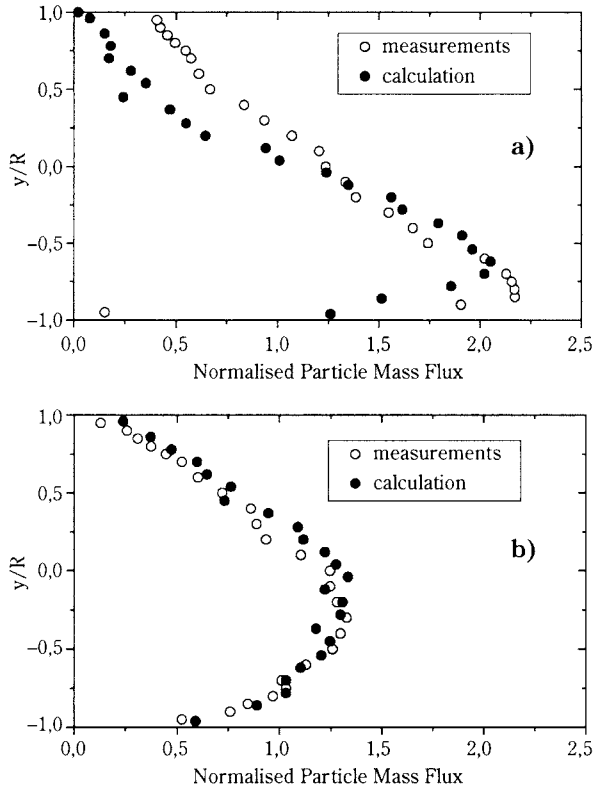

Fig. 10 Profiles of normalised particle mass flux in a horizontal pipe (diameter 80 mm) after a conveying distance of 4 m, a) smooth glass pipe, b) stainless steel pipe (average conveying velocity: 24 m/s, mass loading: 0.3 kg particles/kg air)

ing due to the particles is mainly associated with the re-acceleration of the particles by the gas phase after a wall impact and depends on the way the particles are rebound from the wall. Hence, wall roughness should also considerably alter the pressure loss. This is associated with an average reduction of the particle velocity component in the main stream direction, since the average rebound angle is larger than the impact angle. This effect requires more momentum to re-accelerate the particles in the stream-wise direction compared to the situation for a smooth wall and hence, the additional pressure loss increases considerably for the rough wall in the considered case compared with the smooth wall. It should be noted that this may not be observed under different conditions (i.e. ratio of pipe diameter to particle response distance), since the pressure loss depends strongly on the modification of the wall collision frequency by the wall roughness.

Numerical calculations with and without wall roughness predict for the present case an increase in pressure drop (**Fig. 11**). The measured pressure loss for the stainless steel pipe shows the same trend as the predictions, except for the development region where different flow conditions may exist in experiment and

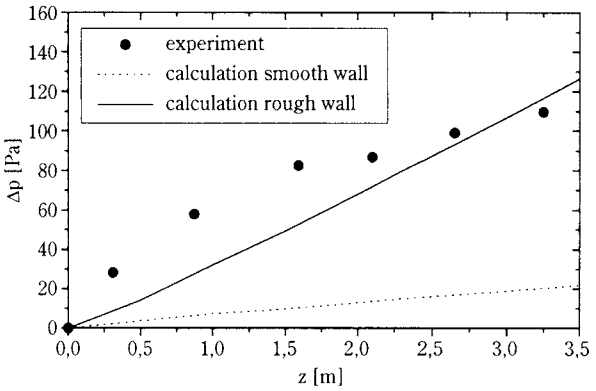

Fig. 11 Pressure drop along a horizontal pipe, comparison of calculations for a smooth and rough pipe (pipe diameter: 80 mm, average conveying velocity: 24 m/s, mass loading: 0.3 kg particles/kg air)

calculation, i.e. the particles were assumed to be homogeneously distributed at the inlet which was not the case in the experiment. Unfortunately, the pressure loss was not measured in the glass pipe to prove the effect described above. These results demonstrate that wall roughness plays an important role for the development of particle-laden confined flows.

8. Conclusions

Recent developments of the Euler/Lagrange approach for the prediction of gas-particle flows were summarised with emphasis on modelling particle-wall collisions and inter-particle collisions. The wall collision process was calculated by solving the momentum equations in conjunction with Couloumb's law of friction. Wall roughness was simulated for spherical particles by adding a stochastic component to the particle impact angle using a correlation of the particle diameter with the characteristic dimensions of the wall roughness determined from experiments. Moreover, the required parameters for the wall collision model were derived from detailed experiments in a horizontal particle-laden channel flow. The comparison of model calculations with the experimental results showed a very good agreement.

The concept of a stochastic inter-particle collision model which accounts for the correlated motion of colliding particles in turbulent flows was introduced. To permit refining and validating the developed stochastic inter-particle collision model, large eddy simulations for a homogeneous isotropic turbulence field were used.

Calculations for a particle-laden horizontal channel flow revealed the importance of inter-particle collisions even for a moderate mass loading. For larger particles, inter-particle collisions tend to re-disperse

particles accumulating near the bottom of the channel due to gravitational settling. Moreover, collisions cause the fluctuations of the particle phase to become more isotropic.

Calculations of pneumatic conveying in a horizontal pipe demonstrated the effect of wall roughness on the development of the particle concentration distribution and pressure drop. Wall roughness also tends to reduce the effect of gravitational settling, but yields a considerable increase in pressure drop for the considered flow conditions.

The good agreement of the calculations with measurements for all the considered cases gives confidence in the use of numerical predictions based on the Euler/Lagrange approach for the optimisation of process equipment whenever dispersed two-phase flows are present.

9. Acknowledgements

The present studies were partly supported by the European Commission under contract nos. 7220-ED/105 and 7220-ED/036, and the Deutsche Forschungsgemeinschaft under contract So 204/12-1. The author thanks Professor O. Simonin and Dr. E. Lavieville for providing the LES data and for helpful discussions.

10. Nomenclature

D_p	particle diameter
e	restitution coefficient
f_c	inter-particle collision frequency
f_k	inter-particle collision frequency according to kinetic theory
H	channel height
k	turbulent kinetic energy
k_p	kinetic energy of particle fluctuation
L_f	longitudinal Eulerian length scale
L_g	lateral Eulerian length scale
$\dot{m}_g$	mass flow rate of gas phase
$\dot{m}_p$	mass flow rate of particles
N_p	number density of particles [particles/m^3]
P	probability
Δp	pressure loss
$R(St_t)$	correlation function
R	pipe radius
St_t	turbulent Stokes number
T_E	Eulerian integral time scale
T_L	Lagrangian integral time scale
Δt	time step
$\vec{U}$	instantaneous velocity vector
U_0	centre line velocity
U, V, W	components of mean velocities
u′, v′, w′	components of fluctuating velocities
x, y, z	co-ordinates

Greek symbols

α	particle phase volume fraction
α_1	particle impact angle
α_2	particle rebound angle
ε	dissipation rate
γ	roughness angle
$\Delta\gamma$	standard deviation of roughness angle distribution
$\eta=\frac{\dot{m}_p}{\dot{m}_g}$	mass loading ratio
λ_p	particle response distance
μ	wall friction coefficient
ν	molecular viscosity
ρ_p	particle material density
$\sigma_{p,i}$	rms value of particle velocity distribution for component i
τ_p	particle response time
ξ	Gaussian random number

Acronyms

PDF	probability density function
LES	large eddy simulations

11. References

1) N. Huber, and M. Sommerfeld, *Modelling and numerical calculation of dilute-phase pneumatic conveying in pipe systems*, Powder Technology, 99, 90-101, 1998.

2) M. Sommerfeld, *The importance of inter-particle collisions in horizontal gas-solid channel flows*, Gas-Particle Flows (Eds.D.E. Stock, M.W. Reeks, Y. Tsuji, E.E. Michaelides and M. Gautam), ASME Fluids Engineering Conference, Hiltons Head, USA, ASME, FED-Vol. 228, 335-345, 1995.

3) M. Sommerfeld, G. Kohnen, and M. Rüger, *Some open questions and inconsistencies of Lagrangian particle dispersion models*, Proceedings Ninth Symposium on Turbulent Shear Flows, Kyoto Japan, Paper No. 15-1, 1993.

4) C.T. Crowe, M.P. Sharma, and D.E. Stock, *The Particle-source-in-cell (PSI-cell) model for gas-droplet flows*, J. of Fluids Eng. Vol. 99, 325-332, 1977.

5) G. Kohnen, M. Rüger, and M. Sommerfeld, *Convergence behaviour for numerical calculations by the Euler/Lagrange method for strongly coupled phases*, Numerical Methods in Multiphase Flows 1994, (Eds. C.T. Crowe, R. Johnson, A. Prosperetti, M. Sommerfeld, and Y. Tsuji), ASME Fluids Engineering Division Summer Meeting, Lake Tahoe, U.S.A., FED-Vol. 185, 191-202, 1994.

6) Y. Tsuji, N.Y. Shen, and Y. Morikawa, *Numerical simulation of gas-solid two-phase flow in a two-dimensional horizontal channel*, Int. J. Multiphase Flow, Vol. 13, 671-684, 1987.
7) M: Sommerfeld and G. Zivkovic, *Recent advances in the numerical simulation of pneumatic conveying through pipe systems*, Computational Methods in Applied Science (Eds. Ch. Hirsch, J. Periaux and E. Onate) Invited Lectures and Special Technological Sessions of the First European Computational Fluid Dynamics Conference and the First European Conference on Numerical Methods in Engineering, Brussels, 201-212, 1992.
8) M. Sommerfeld, *Modelling of particle-wall collisions in confined gas-particle flows*, Int. J. Multiphase Flows, Vol. 18, 905-926, 1992.
9) M. Sommerfeld and N. Huber, *A laser strobe technique combined with digital image analysis to study particle-wall collisions*, Modern Measuring Techniques for Multiphase Flows (Eds. Xu, Y. and Wang, S.), Proceedings of the International Symposium on Measurement Techniques for Multiphase Flows, Nanjing, China, April 1995, pp. 428-440.
10) M. Sommerfeld and N. Huber, Experimental analysis and modelling of particle-wall collisions. Submitted to Int. J. Multiphase Flows, 1998.
11) C.T. Crowe, *On the relative importance of particle-particle collisions in gas-particle flows*, Proc. of the Conf. on Gas-Borne Particles, Paper C78/81, pp. 135-137, 1981
12) T. Tanaka and Y. Tsuji, *Numerical simulation of gas-solid two-phase flow in a vertical pipe: On the effect of inter-particle collision*, Gas-Solid Flows (Eds. Stock, D.E., Tsuji, Y., Jurewicz, J.T., Reeks, M.W. and Gautam, M.), ASME, FED-Vol. 121, 123-128, 1991.
13) J. Lavieville, E. Deutsch, and O. Simonin, *Large eddy simulation of interactions between colliding particles and a homogeneous isotropic turbulence field*, Gas-Particle Flows, (Eds.D.E. Stock, M.W. Reeks, Y. Tsuji, E.E. Michaelides and M. Gautam), ASME Fluids Engineering Conference, Hiltons Head, USA, FED-Vol. 228, 359-369, 1995.
14) A. Berlemont, O. Simonin, and M. Sommerfeld, *Validation of inter-particle collision models based on large-eddy simulations*, Gas-Particle Flows (Eds.D.E. Stock, M.W. Reeks, Y. Tsuji, E.E. Michaelides and M. Gautam), ASME Fluids Engineering Conference, Hiltons Head, USA, FED-Vol. 228, 359-369, 1995.
15) J. Laufer, *Investigation of turbulent flow in a two-dimensional channel*, National Advisory Committee for Aeronautics, Report 1174, pp. 417-434, 1952.
16) N. Huber and M. Sommerfeld, *Characterization of the cross-sectional particle concentration distribution in pneumatic conveying systems*, Powder Technology, Vol. 79, 191-210, 1994.

Author's short biography

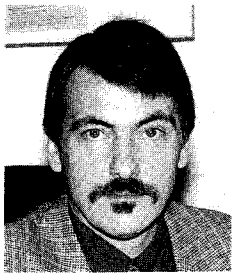

M. Sommerfeld

Martin Sommerfeld studied aeronautical engineering at the Technical University of Aachen and received his Dipl.-Ing. degree in 1981. Thereafter, he worked as a research assistant at the Shock Wave Laboratory of the Technical University of Aachen on shock wave propagation through gas-particle mixtures. In 1984 he received his doctoral degree (Dr.-Ing.) with a thesis related to this topic. From 1984 to 1985 he spent a year at the Kyoto University in Japan on a research fellowship from the Japan Society for Promotion of Science and the Alexander von Humboldt Foundation. After returning from Japan he worked another year as a research assistant at the Shock Wave Laboratory in Aachen and then moved to the University of Erlangen. At the Institute of Fluid Mechanics of the University of Erlangen Martin Sommerfeld was heading a research group on Two-Phase Flow from 1986 to 1994. During this period he completed a Habilitation on Modelling and Calculation of Turbulent Two-Phase Flows using the Euler/Lagrange Approach. In October 1994 he was appointed as a full Professor of Mechanical Process Engineering at the Martin-Luther-University of Halle-Wittenberg. Since 1997 he is Head of the Department of Process Engineering at the University of Halle-Wittenberg.

Martin Sommerfeld organised a continuing series of workshops on two-phase flow predictions, ASME symposia, and several other international conferences. He is currently Associate Editor of the Journal of Fluid Engineering and in the editorial board of a number of international journals. In 1997 he received the DECHEMA Award 1996 for his contributions to multiphase flow measurements, modelling, and numerical prediction. His present research activities are mainly concentrated on the following topics:

- fundamentals of multi-phase flows with the aim of developing physical models for describing relevant transport phenomena,
- detailed experimental analysis of multi-phase flows using modern optical instrumentation,
- development of numerical methods for the prediction of multi-phase flows,
- application of numerical methods for design and optimisation of industrial processes involving multi-phase flows.

In-Situ Characterization of Nanoparticles by Polarized Light Scattering and Laser-Induced Incandescence†

Reiner Weichert
Institute for Particle Technology and Environmental Engineering
*Technical University of Clausthal**

Abstract

Two different optical methods for the determination of particle size distributions in the nanometer range are described. One method uses the scattering of polarized light at different angles and applies a regularized inversion algorithm and is applicable for arbitrary materials. In the other method, light-absorbing particles are heated by a short laser pulse up to evaporation temperature, and the temperature of the particles is determined by the measurement of the thermal radiation. This method has been applied since many years; the detailed analysis, however, shows that one has to be careful with interpretation of the measured data.

1. Introduction

Nanoparticles are becoming of increasing interest in various fields. They have been used as catalysts since a long time because of their high specific surface, but improvements will be achieved by still finer nanoparticles or by nanoparticles coated with active layers only a few nanometers thick. Since nanoparticles are able to penetrate barriers, new forms of pharmaceutical applications are expected. Quantum effects in nanoparticles might be used for future sensors.

Well-known examples for the formation of nanoparticles are colloids in liquids and soot particles in gases. In general, nanoparticle generation occurs from supersaturated solutions. This is achieved either by rapid mixing of chemically reacting liquids or by reactions in the gas phase, sometimes supported by microwaves or laser radiation. Other developments are rapid expansion of supersaturated liquids or evaporating the material in an inert gas atmosphere by plasma heating or high-energy laser radiation. In all cases, molecules are formed and aggregate spontaneously if they collide, driven by Brownian motion.

The mechanisms of nanoparticle formation are understood in principle, but not in detail. Supersaturation in the fluid, diffusion of molecules and clusters of molecules, condensation and coagulation determine the size of resulting primary nanoparticles and of agglomerates. Temperature, concentration and mixing state are essential parameters, but even now it is difficult to control particle size. Intense research in nanoparticle formation is ongoing. Methods for monitoring the formation of particles are required, and since the processes are fast, the measurement has to be fast, too. During combustion in engines, for example, the formation and subsequent oxidation of soot nanoparticles occurs in milliseconds. At the present time, two different methods for the fast in-situ measurement of nanoparticles are being developed: scattering of polarized light and laser-induced incandescence.

2. Scattering of polarized light

2.1 Principle

Particles illuminated by a light beam form a scattered light pattern. If the particles are larger than the wavelength of light, diffraction effects dominate, and the scattering occurs mainly in the forward direction. Every particle size has its individual scattered light pattern which makes particle sizes distinguishable. If many particles are in the light beam at the same time, then their scattered light patterns superpose. The resulting angular intensity distribution is measured in laser diffraction instruments by a multiple element detector. With inversion algorithms, the particle size distribution can be computed from measurements [1].

The method applied in laser diffraction instruments fails if the particles are substantially smaller than the wavelength of light. Then, the scattered light patterns

* Leibnizstr. 19, 38678 Clausthal-Zellerfeld, Germany
† Received August 24, 1998

of different particles differ only in intensity, not in angular distribution. One larger particle generates the same scattered light pattern as many small ones. There is one exception to this rule: if the detection of scattered light is measured in the plane of polarization and at scattering angles around 90 degrees, then the scattered light patterns of particles smaller than the wavelength of light depends on particle size. To explain the principle, eqn. (1) describes the scattered light intensity I as a function of the intensity I_0 of the illuminating light beam of the wavelength λ [2],

$$I = I_0 \, (\lambda/(2\pi r))^2 \, (i_1 \sin^2\phi + i_2 \cos^2\phi) \qquad (1)$$

where r is the distance from the particle, i_1 and i_2 are the scattering functions dependent on the complex refractive index m of the particle material, the scattering angle θ, and the Mie-parameter $\alpha = \pi x/\lambda$ with x as particle size. The polarization is characterized by the angle ϕ.

In the plane of polarization, i.e. $\phi = 0$, the first term in eqn. (1) vanishes and I is proportional to i_2. The scattering function i_2, computed according to [3], is plotted in **Figure 1** for soot and shows minima in the vicinity of the scattering angle $\theta = 90$ degrees dependent on the Mie-parameter α, i.e. on the particle size.

This permits the analysis of the size distributions of nanoparticles from scattered light data. The scattered light intensity $I(\theta)$ of an assembly of particles described by the volume distribution of particle size $q_3(x)$ is given by eqn. (2).

$$I(\theta) = \text{const.} \int_0^\infty \frac{q_3(x)}{x^3} \, i_2 \, dx \qquad (2)$$

For the solution of this equation, inversion algorithms can be used as are known from laser diffraction methods.

An instrument for the particle size analysis by polarized light scattering has been developed as shown in **Figure 2** [4], [5]. A laser beam (250 mW, 488 nm, 1.5 mm diameter) passes polarization optics (Glen Thompson polarizer, extinction ratio $1:10^{-8}$) and illuminates the soot particles to be analyzed in the flame. The scattered light intensity as a function of the scattering angle is measured by photomultiplier PM1 via a lens, a oscillating mirror and a pinhole. Photomultiplier PM2 measures the intensity at another wavelength, giving information on the thermal light emission of the particles for corrections. In addition to the scattered light intensity $I_S(\theta)$, the light intensity I_0 before, and I_E after passing the flame are measured for the determination of the particle concentration according to the Lambert-Beer law [6].

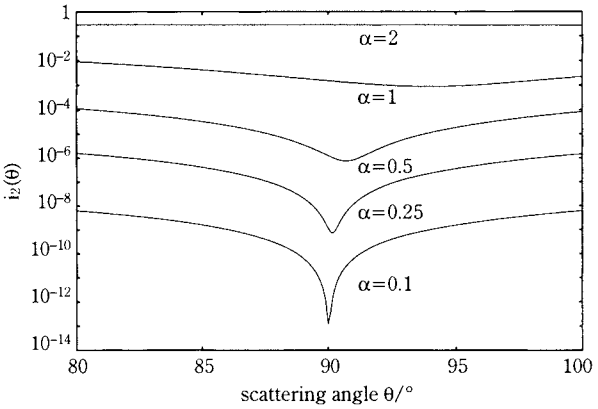

Fig. 1 Scattering function i_2 for soot particles (m=1.57−0.53i)

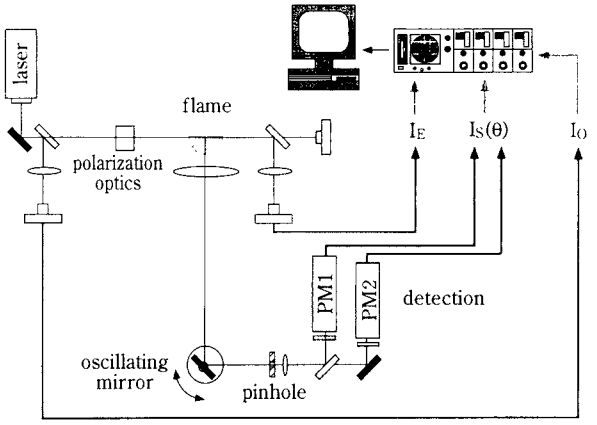

Fig. 2 Experimental setup for the determination of size distributions of soot particles in a premixed flame

2.2 Experimental results

The experimental set-up has been tested on a premixed acetylene-oxygen-argon flame. **Figure 3** shows the scattered light signals as measured at two different heights above a burner, and **Figure 4** the particle size distributions computed from these signals, using a computer code for non-negative regularization [7].

The soot particles seem to be rather big for a premixed flame. For verification, particles were sampled at the same (hab) for electron microscopy. The sampling device has two concentric hypodermic needles as shown in **Figure 5**. The sampling is done by the inner needle. Argon flows into the gap between the two needles, diluting and cooling the aerosol at the inlet and preventing chemical reactions and agglomeration of the soot particles. Particles sampled at (hab)=7.5 mm and collected on a nuclepore filter are shown in **Figure 6**. Their size distribution corresponds to that computed from scattered light data.

The described instrument is rather slow and appropriate only for the measurement of particle size distri-

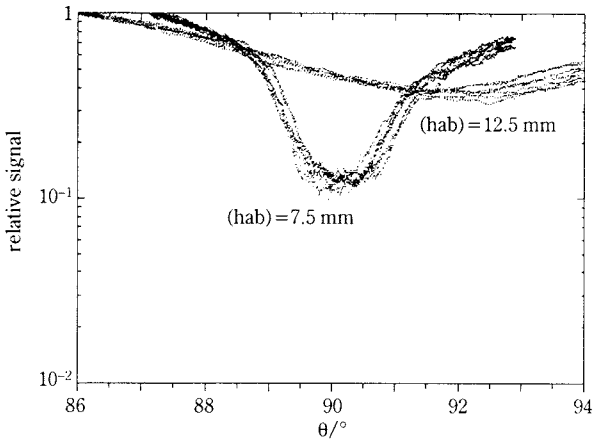

Fig. 3 Scattered light signal from soot particles in a flame at two different heights above burner (hab) = 7.5 mm and (hab) = 12.5 mm; 10 runs for both heights.

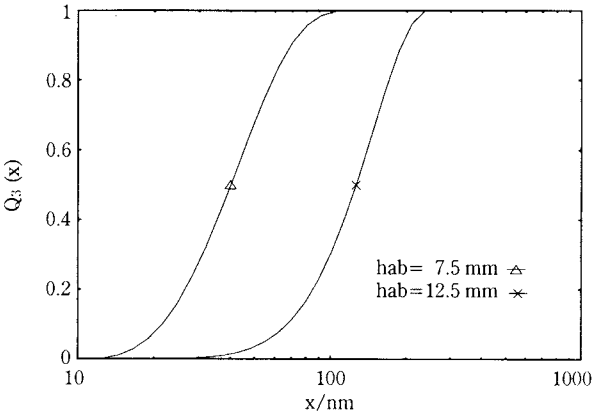

Fig. 4 Size distributions of soot particles at two different heights above burner (hab) = 7.5 mm and (hab) = 12.5 mm, averaged over 10 runs

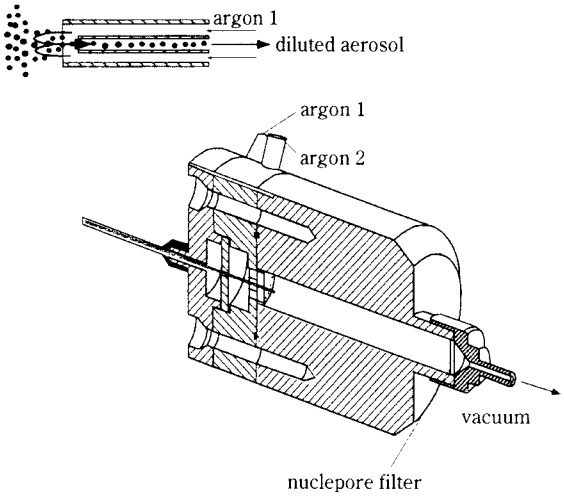

Fig. 5 Sampling device for nanoparticles

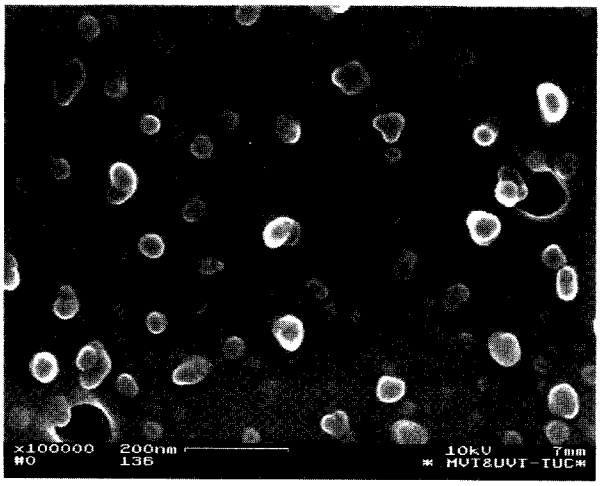

Fig. 6 Scanning electron micrograph of soot particles, sampled at (hab) = 7.5 mm

butions in stationary processes. An improved version of the instrument is under development, using a pulsed Nd-YAG laser and a gated CCD camera. The new instrument is planned for highly instationary processes with measuring times of only a few nanoseconds. The range of particle sizes will be – as with the present instrument – from about 15 nm to 250 nm.

It should be emphasized that the particles have to be spherical but that the method works for any material – absorbing or non-absorbing – as long as the refractive index is known.

3. Laser-induced incandescence

3.1 Principle

The idea of heating particles by means of a short, intense laser pulse and to monitor the cooling of the particles by measurement of the emitted thermal light radiation goes back to Weeks and Duley [8]. They showed theoretically that the cooling time of particles can be used for the determination of their size, and verified this idea with alumina particles and a CO_2 laser pulse. Some years later, Eckbreth [9] extended the theory to partial evaporation of the particles and showed by experiments with soot that the fluence of the laser has a strong effect on the emitted light signal. The theory has been refined by Dasch [10], Melton [11], Hofeld [12], Roth and Filippov [13], Mewes [14] and Will et al [15]. Many other authors applied the method to a variety of different combustion processes ranging from diffusion flames to Diesel engines. The advantage of the method is that with the laser pulse as a light sheet, it can be used for the two-dimensional analysis of soot particle size and concentration. The following detailed analysis,

however, shows that one has to be careful with interpretation of the measurements.

3.2 Modeling

The model described here uses – in principle – the theory developed by the authors cited above. It differs, however, in some details and considers the change of particle size during evaporation. It gives the detailed derivation of the equations used for computations and shows computed results accurate within the simplifying approximations.

Laser-induced incandescence, LII, is modeled by an energy rate equation. Absorbing light of intensity I from the laser pulse, the particle gains energy dW_{abs} in unit time dt. Increasing the particle temperature needs heat dW_{heat}. If the temperature of the particle is high enough, it loses energy dW_{vap} by evaporation. The particle loses dW_{con} by thermal conduction to the surrounding gas and dW_{rad} by radiation. So we obtain eqn. (3) for the description of laser-induced incandescence.

$$dW_{abs}+dW_{heat}+dW_{vap}+dW_{con}+dW_{rad}=0 \tag{3}$$

The assumption that there are no temperature gradients inside the particle is reasonable for particle sizes below 100 nm and pulse durations above 1 ns [11].

The absorption is described by

$$dW_{abs}=C_{abs}\, I\, dt \tag{4}$$

where C_{abs} is the absorption cross-section of the particle and can be computed from Mie theory or from the Rayleigh approximation [2].

$$C_{abs}=\pi^2 x^3 \delta/\lambda_\lambda \tag{5}$$

$$\delta=\mathrm{Im}(-(m^2-1)/(m^2+2)) \tag{6}$$

where x is the particle diameter, m the complex refractive index, Im stands for imaginary part and λ_λ is the wavelength of the laser. The change of latent heat with changing temperature is described by

$$dW_{heat}=\frac{\pi}{6} c \rho x^3 dT \tag{7}$$

where dT is the change of temperature, c the specific heat and ρ the density of the particle material. The rate j_v of molecules leaving an evaporating surface is given by [16]

$$j_v=u_v p_v/(4kT) \tag{8}$$

where u_v is the average velocity of the evaporating molecules

$$u_v=\sqrt{8kT/(\pi m_v)} \tag{9}$$

k the Boltzman constant and p_v the vapor pressure expressed according to the Clausius-Clapeyron equation

$$p_v=a \exp(-b/T) \tag{10}$$

With the mass m_v of one evaporating molecule and the mass-specific heat of evaporation H, the energy loss by evaporation is given by

$$dW_{vap}=\pi x^2 m_v H j_v dt \tag{11}$$

The molecular description of evaporation neglecting molecules returning to the particle by diffusion is usual in all LII-papers and will be used here, too. The practicability of this assumption should be checked in the future.

Modeling the thermal conduction is still a problem. Melton [11] and Hofeld [12] use the results of McCoy and Cha [17] and make corrections of the continuum thermal conductivity of the gas, taking the mean free path of molecules into account. Roth and Filippov [14] model the diffuse reflection at the particle surface following [18] – but they all assume that the gas molecules hit the particle with the thermal energy of the gas far away from the particle and that the molecules leave the particle surface with the thermal energy corresponding to the temperature of the particle.

The latter assumption is not supported by experiments. Following the considerations of Goodman and Wachman [19], we write for the thermal conduction

$$dW_{con}=\pi x^2 j_g (E_{sca}-E_g) dt \tag{12}$$

where

$$j_g=p_g u_g/(4kT_g) \tag{13}$$

is the rate and E_g the energy of molecules arriving on the surface of the particles, with the pressure p_g and the temperature T_g of the gas and the average velocity u_g of the arriving gas molecules having the mass m_g,

$$u_g=\sqrt{8kT_g/(\pi m_g)} \tag{14}$$

The energy of the gas molecules leaving the particle is E_{sca}. Using the definition of the energy accommodation coefficient α_{eac},

$$\alpha_{eac}=(E_{sca}-E_g)/(E-E_g) \tag{15}$$

where E is the average energy of a molecule in thermal equilibrium with the surface having the temperature T and using the streaming correction [19]

$$E-E_g=2k(T-T_g) \tag{16}$$

we finally get

$$dW_{con}=2\pi x^2 p_g u_g j_g k T_g (T/T_g-1) \alpha_{eac} dt \tag{17}$$

which differs by the term α_{ea} from the equation for the thermal conduction according to [13].

The energy accommodation coefficient α_{eac} depends on the gas, the surface and the temperature. Experimental data of the interaction of various gases with graphite surfaces [20], [21] in combination with the simplified hard sphere model of energy accommodation [18] suggest for a first approximation $\alpha_{eac}=0.5$. In any case, the assumption made in cited LII-papers, i.e. that the molecules leave the particle with the thermal energy corresponding to the particle temperature ($\alpha_{eac}=1$), overestimates the cooling rate of the particles.

The heated particles emit radiation which can be used to monitor the temperature of the particle and which gives a contribution to the loss of heat. The flux of emitted light in the Rayleigh approximation is according to Planck's law

$$J\, d\lambda = C_{abs}\,(\lambda)\; hc_l^2/\lambda^5 .\; 1/(\exp(hc_l/(\lambda kT) - 1)\, d\lambda \quad (18)$$

where h is the Planck constant, c_l the velocity of light and C_{abs} given in eqn. (5)

Integrating the flux over all wavelengths gives the energy loss by thermal radiation

$$dW_{rad} = \int_0^\infty J d\lambda \quad (19)$$

which is – under atmospheric conditions – small compared with the loss of heat by thermal conduction, W_{con}, and is therefore neglected here.

During evaporation, the particle loses mass dM

$$dM = m\, j_v\, \pi\, x^2\, dt, \quad (20)$$

this loss changes the volume of the particle

$$-dM/\rho = \pi\, x^2\, dx/2 \quad (21)$$

and we get for the change of particle size

$$-dx = (2\, m\, j_v/\rho)\, dt \quad (22)$$

The set of two differential equations (3) and (22), in combination with the other equations in this paragraph, describe the process of laser-induced incandescence. It should be emphasized that diffusion is neglected in the description of evaporation and thermal conduction.

Putting everything together, we get

$$dT = f\,(I, T, T_g, x)\, dt \quad (23)$$
$$dx = -h\,(T)\, dt \quad (24)$$

where the functions f and h are known from the model outlined above.

In order to compute the change of temperature, vapor pressure and particle size as a function of time, the intensity of the laser beam has been modeled as

$$I = W/(\tau\sqrt{\pi})\, \exp((-t/\tau - 2)^2) \text{ for } 0 < t/\tau < 4 \quad (25)$$
$$I = 0 \text{ else}$$

where W is the laser fluence in J/m^2 and τ the characteristic time of the laser pulse.

There is a complication in the evaporation of soot particles since in addition to C-atoms, molecules C_2 and C_3 evaporate with different partial pressures, different evaporation enthalpies, and different velocities. This has been taken into account in the development of the computer code for the description of laser-induced incandescence.

3.3 Results

For the computations, the following data were used: Refractive index m=1.56-0.46i [22], density $\rho=2100$ kg m^{-3}, specific heat $c=2200$ J kg^{-1} K^{-1} [10], the constants for the Clausius Clapeyron equation for the vapor pressures of C, C_2, C_3 were computed from data from [23], evaporation enthalpies of C, C_2, C_3 were taken from [24]. The molar mass of the gas was set to 28 gram per mol, the gas temperature to $T_g=2000$ K and the pressure to $p_g=1\ 10^5$ N m^{-2}. The energy accommodation coefficient was set to $\alpha_{eac}=0.5$.

In **Figure 7**, the laser intensity I, the vapor pressure p_v, the particle size x and the particle temperature T are plotted in a normalized form as a function of time. The temperature rises just after the begin of the laser radiation starting from gas temperature 2000 K and reaches about 3734 K after 8 ns, when evaporation becomes substantial. 11 ns after onset of the radiation, the temperature with 4708 K and vapor pressure with 12.8 10^5 N/m^2 (sum of the partial pressures of C, C_2 and C_3) reach their maxima. At that

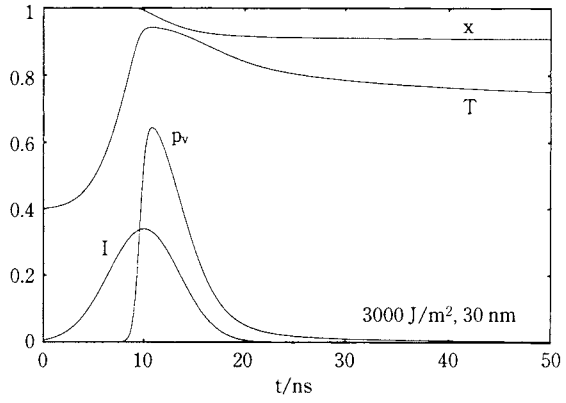

Fig. 7 Laser intensity I, vapor pressure p_v, particle size x and particle temperature T in normalized form as a function of time t. Initial particle size x(t=0)=30 nm, laser fluence W=3000 J m^{-2}. Laser intensity is normalized to 1 10^{12} Wm^{-2}, vapor pressure to $2{\cdot}10^6$ Nm^{-2}, temperature to 5000 K

time, the particle diameter has shrunk from 30 to 29.3 nm. After 20 ns, when the laser radiation stops, the temperature has dropped to 4204 K, vapor pressure to 1 10^5 N/m^2. At 50 ns, the temperature has dropped to 3754 K and vapor pressure to 6.3 10^3 N/m^2, but the heat losses by evaporation are still larger than by heat conduction. The particle size is now 27.2 nm. Detailed analysis shows that only at temperatures below 3600 K does heat conduction become dominant under atmospheric conditions. The following tables show how laser fluence affects maximum temperature T_{max}, maximum pressure P_{max}, temperatures at times t=50 and 100 ns and particle size x, for initial particle size x(t=0)=20 nm in **Table 1** and for x(t=0)=50 nm in **Table 2**. The gas temperature was T_g=2000 K in all cases. This information in the tables is supplemented by the following figures. The temporal change of particle temperature is plotted for various laser fluence for particle size x=20 nm in **Figure 8** and for x=50 nm in **Figure 9**. The temporal change of particle temperature for various particle sizes for laser fluence W=1000 J m^{-2} is shown in **Figure 10** and for W=5000 J m^{-2} in **Figure 11**.

Table 1 x(t=0)=20 nm

fluence	T_{max}	P_{max}	T(50ns)	T(100ns)	x/x(t=0)
Jm^{-2}	K	10^5 Nm^{-2}	K	K	—
500	2822	.00	2799	2760	1.000
1000	3633	.03	3544	3434	0.998
2000	4430	3.42	3719	3535	0.960
5000	4436	14.48	3702	3509	0.840
10000	4880	26.95	3664	3458	0.670

Table 2 x(t=0)=50 nm

fluence	T_{max}	P_{max}	T(50ns)	T(100ns)	x/x(t=0)
Jm^{-2}	K	10^5 Nm^{-2}	K	K	—
500	2827	.00	2818	2802	1.000
1000	3649	.03	3608	3549	0.999
2000	4588	7.39	3892	3721	0.961
5000	4960	37.46	3875	3698	0.839
10000	5118	69.89	3837	3655	0.667

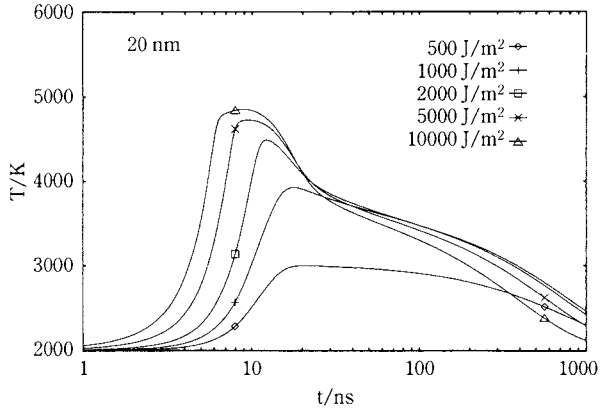

Fig. 8 Particle temperature as a function of time, particle size x=20 nm, parameter fluence W

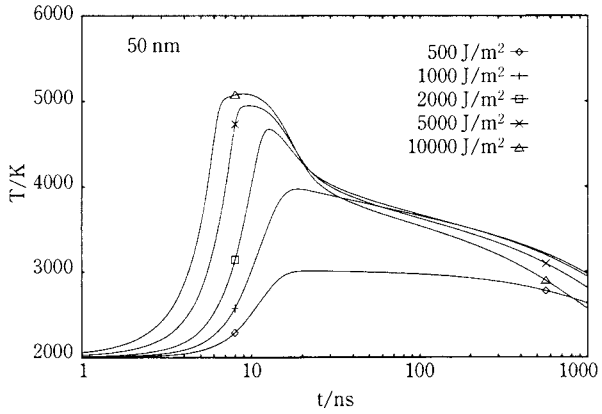

Fig. 9 Particle temperature as a function of time, particle size x=50 nm, parameter fluence W

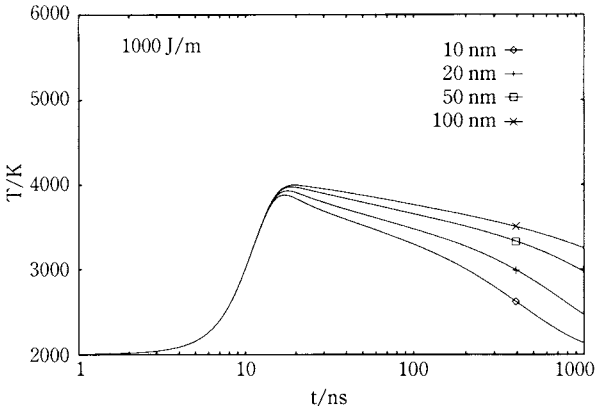

Fig. 10 Particle temperature as a function of time, fluence W=1000 J m^{-2}, parameter particle size x

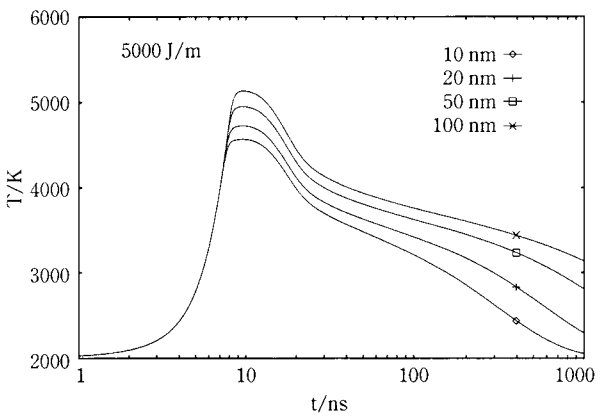

Fig. 11 Particle temperature as a function of time, fluence W=5000 J m^{-2}, parameter particle size x

3.4 Discussion

a) Accuracy

The 4-digit values in the tables suggest an accuracy which is not attainable. For short periods, when light absorption, latent heat and evaporation are dominant, the poor knowledge of the refractive index [25] is one weak point in the calculation. Further, the Rayleigh approximation leads to errors at larger particle sizes. Compared with exact Mie-calculations using [3], the absorption of a 100-nm soot particle at 530 nm wavelength is underestimated by about 30% in the Rayleigh approximation. In the evaporation term, only carbon atoms/molecules leaving the particle were considered. Since evaporation can be important even for times beyond 100 ns, back diffusion will no longer be negligible – the computed pressures of tens of atmospheres suggest that the particles are surrounded by a dense cloud of carbon molecules. The inaccuracy caused by poor knowledge of the energy accommodation coefficient has been mentioned before. A hot cloud of carbon molecules around the particle will cause an additional uncertainty in the convective transport. In spite of the complications, the physics of LII is understandable and in future investigations, it should be possible to improve the accuracy substantially. In the following, we assume that the current accuracy is high enough for the determination of soot parameters in a flame.

b) Role of laser fluence

The LII method is used by several authors – measuring the intensity of thermal radiation – for the determination of soot concentration and particle size. As Figures 10 and 11 suggest, particle size can be computed from temperature at a known time after the laser pulse, provided that the fluence is known. Figures 9 and 10 indicate how accurately the fluence has to be known. Only in the range from 30 to 100 ns and at fluences between 1000 and 5000 Jm^{-2} does an evaluation of the particle size from radiation signals seem feasible. At lower fluences, the evaporation temperature is not reached, making the temperature of the particle strongly dependent on the fluence. At fluences above 5000 Jm^{-2}, the loss of particle mass becomes substantial. It is not reasonable to use focused laser beams for LII where a whole range of fluences heats the particles to different temperatures, depending on their position in the beam.

Acknowledgements

The author thanks Dipl.-Ing. R. Sanders and Dipl.-Ing O. Rulik for preparing the figures. Financial support for the experimental investigation by the Deutsche Forschungsgemeinschaft is gratefully acknowledged.

Nomenclature

a	constant in Clausius-Clapeyron equation/N m^{-2}
b	constant in Clausius-Clapeyron equation/K
c	specific heat/J kg^{-1} K^{-1}
c_l	velocity of light/ms^{-1}
C_{abs}	absorption cross-section/m^2
E_g	energy of molecules arriving on the particle/J
E_{sca}	energy of the gas molecules leaving the particle/J
h	Planck's constant/J s
(hab)	height above burner/m
H	mass-specific heat of evaporation/J kg^{-1}
i_1, i_2	scattering functions
I_s	scattered light intensity/Wm^{-2}
I_0	light intensity of an incident beam/Wm^{-2}
I_E	transmitted light intensity/Wm^{-2}
J	light flux/W sr^{-1} m^{-1}
j_g	rate of gas molecules on surface/$s^{-1}m^{-2}$
j_v	rate of evaporating molecules/$s^{-1}m^{-2}$
k	Boltzmann's constant/JK^{-1}
m	complex refractive index
m_g	mass of gas molecule/kg
m_v	mass of evaporating molecule/kg
dM	loss of mass by evaporation/kg
p_g	vapor pressure of gas molecules/Nm^{-2}
p_v	vapor pressure of evaporating molecules/Nm^{-2}
$q_3(x)$	differential size distribution/m^{-1}
r	distance between particle and detector/m
t	time/s
T	temperature of the particle/K
T_g	temperature of the gas/K
u_g	average velocity of gas molecules/ms^{-1}
u_v	average velocity of evaporating molecules/ms^{-1}
W	laser fluence/Jm^{-2}
dW_{abs}	absorbed energy/J
dW_{heat}	latent energy/J
dW_{vap}	energy loss by evaporation/J
dW_{con}	energy loss by thermal conduction/J
dW_{rad}	energy loss by radiation/J
x	particle diameter/m
α	Mie-parameter
α_{eac}	energy accommodation coefficient
δ	see eqn. (6)

θ scattering angle
λ wavelength of light/m
λ_λ laser wavelength/m
ρ density/kgm^{-3}
τ characteristic time of the laser pulse/s
ϕ polarization angle

References

1) Heuer, R.; Leschonski, K.: Erfahrungen mit einem neuen Gerät zur Messung von Partikelgrößenverteilungen an Beugungsspektren. 3rd European Symposium Particle Characterization, PARTEC, Nürnberg 1984, 515-538.
2) Kerker, M.: The Scattering of Light and other Electromagnetic Radiation. Academic Press New York, 1969.
3) Wiscombe, W.J.: Mie Scattering Calculations: Advances in Technique and Fast Vector Speed Computer Codes. NCR Boulder (1979), Report No. NCAR/TN-140+STR.
4) Niemann, J.; Weichert, R.: Measurement of Concentration and Particle Size Distribution of Soot Particles in Flames. 4th International Congress Optical Particle Sizing, PARTEC 95, Nürnberg, March 1995, 375-384.
5) Niemann, J.: Entwicklung eines photometrischen Meßverfahrens zur Rußanalyse in Flammen. PhD Diss, Techn. Univ. Clausthal, 1996.
6) Sanders, R.; Niemann, J.; Weichert, R.: In-situ Determination of Size Distribution and Concentration of Nanoparticles in Gases. 7th European Symposium Particle Characterization, PARTEC 98, Nürnberg, March 1998, 89-98.
7) Mühlenweg, H.; Weichert, R.: Optical Particle Sizer: A New Development with Mathematical Correction of Spread Measurement Data. Part Part Syst Char 14 (1997), 205-210.
8) Weeks, R.; Duley, W.: Aerosol-particle Sizes from Light Emission during Excitation by TEA CO_2 laser pulses. J Appl Phys 45 (1974) 10, 4661-4662.
9) Eckbreth, A.: Effects of Laser-modulated Particulate Incandescence on Raman Scattering Diagnostics. J Appl Phys 48 (1977) 11, 4473-4479.
10) Dasch, C.: Continuous-wave Probe Laser Investigation of Laser Vaporization of Small Particles in a Flame. Appl Opt 23 (1984) 13, 2209-2215.
11) Melton, L.: Soot Diagnostics Based on Laser Heating. Appl Opt 23 (1984) 13, 2201-2208.
12) Hofeldt, D.: Real-Time Soot Concentration Measurement Technique for Engine Exhaust Streams. SAE Technical Paper Series (1993), SAE Paper 930079, 33-45.
13) Roth, P.; Filippov, A.: In-Situ Ultrafine Particle Sizing by a Combination of Pulsed Laser Heatup and Particle Thermal Emission. J Aerosol Sci 27 (1996) 1, 95-104.
14) Mewes, B.; Seitzman, J.: Soot Volume Fraction and Particle Size Measurements with Laser-induced Incandescence. Appl Opt 36 (1997) 3, 709-717.
15) Will, S.; Schraml, S.; Bader, K.; Leipertz, A.: Performance characteristics of soot primary particle size measurements by time-resolved laser-induced incandescence. Appl Optics 37 (1998) 24 (in press).
16) Hirschfelder, J.; Curtiss, C.; Bird, R.: Molecular Theory of Gases and Liquids. Wiley 1964.
17) McCoy, B.; Cha, C.: Transport Phenomena in the Rarefied Gas Transition Regime. Chem Eng Sci 29 (1974), 381-388.
18) Williams, M.; Loyalka, S.: Aerosol Science – Theory and Practice. Pergamon Press 1991.
19) Goodman, F.; Wachman, H.: Dynamics of Gas-Surface Scattering. Academic Press 1976.
20) Meyer, L.; Gomer, R.: Energy Exchange between Cold Gas Molecules and a Hot Graphite Surface. J Chem Phys 28 (1958) 4, 617-622.
21) Siekhaus, W.J.; Schwarz, J.A.; Olander, D.R.: A Modulated Molecular Beam Study of the Energy of Simple Gases Scattered from Pyrolytic Graphite. Surface Sci 33 (1972), 445-460.
22) Dalzell, W.; Sarofim, A.: Optical Constants of Soot and Their Application to Heat Flux Calculations. Heat Transfer 91 (1969) 100-103.
23) Landoldt-Börnstein: Zahlenwerte und Funktionen, II. Band, Eigenschaften der Materie in ihren Aggregatzuständen. 2. Teil Bandteil a, Gleichgewichte Dampf-Kondensat und osmotische Phänomene, Springer 1960, p. 6.
24) Touloukian, Y.S.: Thermophysical Properties of High Temperature Solid Materials, Vol I: Elements. The Macmillan Company, New York 1967, p. 105.
25) Faeth, G.M.; Köylü, J.Ö.: Soot morphology and optical properties in non premixed flames. Combustion science and technology 108 (1995) 207-229

Author's short biography

Reiner Weichert

Reiner Weichert received his diploma in physics in Karlsruhe in 1969. He joined the Institute of Mechanical Engineering of the University of Karlsruhe, working with Hans Rumpf and Klaus Schönert. In 1976 he obtained his Dr.-Ing. with a thesis on physical processes at breakage of brittle materials. He was a visiting professor at the Comminution Centre of the University of Utah between 1983 and 1984, subsequently returning to Karlsruhe where he habilitated in powder technology in 1984.

He has been professor of environmental process technology at the Technical University of Clausthal since 1989. His current research activities are in the field of turbulent particle deposition for gas cleaning and in the field of nanoparticles: generation of nanoparticles by laser ablation and high-energy milling, mixing of nanoparticles, characterization of nanoparticles by optical methods.

He was dean of the faculty of mechanical engineering and process engineering between 1993 and 1995. He is chairman of the board of PARTEC and of the Particle Characterization working party of the German Institute of Chemical Engineers.

Electrification of Fine Particles in Gas-Solids Pipe Flow†

Hiroaki Masuda, Shuji Matsusaka, Satoshi Akiba and Hiroaki Shimomura
*Dept. of Chem. Eng., Kyoto Univ.**

Abstract

The electrification of fine particles in a gas-solids pipe flow is investigated theoretically and experimentally. Flowing particles are charged through their collisions with a pipe wall. When a part of the pipe is electrically isolated and grounded, the charge transferred from the particles to the wall is detected as an electric current from the wall. The current generated and the electric charge of fine particles (fly-ash: D_{p50}=3.4 and 12 μm) and relatively large particles (quartz sand: D_{p50}=320 μm) are measured. The relationship between the current per unit powder flow rate I/W_p and charge-to-mass ratio $(q/m_p)_0$ is represented by a linear equation irrespective of particle diameter as long as the mass flow ratio is below 0.0058. However, the absolute value of I/W_p of fine particles decreases with increasing mass flow ratio m when m exceeds 0.011. It is found that the current I/W_p is represented by a quadratic equation of $(q/m_p)_0$. The fact is readily explained by introducing the concept of electrification efficiency.

1. Introduction

In a gas-solids pipe flow, particles move with the gas flow while repeatedly colliding with the pipe wall, and they are electrified by charge transfer upon collision. Generally particle electrification in a pipe flow is considered as an undesirable phenomenon because it increases the amount of particles deposited on the wall, hampers subsequent powder operations, and causes other problems, while static electrification is sometimes used positively, e.g., electrostatic powder coating using a tribo gun [1] and powder flow rate measurements based on particle electrification [2, 3]. However, the electrostatic phenomenon in a gas-solids pipe flow is complex because it varies in response to particle diameter, particle density, and other conditions of two-phase flows, making good predictions difficult at present. There is especially little knowledge about the electrification of fine particles smaller than several tens of microns in diameter. This paper analyzes the electrostatic characteristics of the continuous process from powder supply to a fully developed gas-solids pipe flow.

* Yoshida-honmachi, Sakyo-ku, Kyoto 606-8501, Japan

† This report was originally printed in J. Soc. Powder Technology, Japan. **34**, 91 (1997) in Japanese, before being translated into English by KONA Editorial Committee with the permission of the editorial committee of the Soc. Powder Technology, Japan.

2. Theory

When a section of a pipe carrying a gas-solids flow (length: Δx) is electrically isolated and grounded, the charge transferred per unit time from particles to pipe wall in that section is measured as an electric current. If one considers as the mechanism of particle-wall charge transfer the contact potential difference V_c, which is based on the work functions of the particles and wall surface, the image charge effect of particle electrification, and the space charge effect of charged particles, then the generated current I under powder flow rate W_p can be approximated as follows [2, 4].

$$I \approx W_p \left\{ \left(\frac{q}{m_p} \right)_0 - \left(\frac{q}{m_p} \right)_\infty \right\} \frac{n(\Delta x)}{n_0} \tag{1}$$

Where:

$(q/m_p)_0$ and $(q/m_p)_\infty$ are the particle charge per unit mass at $x=0$ and $x=\infty$, respectively, $n(\Delta x)$ is the number of collisions per particle in pipe section Δx, and n_0 is the characteristic number called the relaxation number of collisions.

$(q/m_p)_\infty$ and n_0 are given by Equations (2) and (3), respectively.

$$\left(\frac{q}{m_p} \right)_\infty = \frac{3 \varepsilon_0 V_c}{(1+\alpha) \rho_p D_p z_0} \tag{2}$$

$$n_0 \approx \frac{\pi D_p^2}{2(1+\alpha) S \dfrac{\Delta t}{\tau}} \tag{3}$$

The parameter α in Equations (2) and (3) is the ratio of the space charge effect to the image charge effect, which is given by the following equation.

$$\alpha = \frac{3\,q\,z_0\,W_p\,\rho\,D\,\bar{u}}{2\,\pi\,\varepsilon_0\,Q\,\rho_p\,D_p{}^3\,\bar{v}} \Big/ \frac{2\,q\,z_0}{\pi\,\varepsilon_0\,D_p{}^2}$$
$$= \frac{3\,W_p\,\rho\,D\bar{u}}{4\,Q\,\rho_p\,D_p\,\bar{v}} = \frac{3\,m\,\rho\,D\bar{u}}{4\,\rho_p\,D_p\,\bar{v}} > 0 \qquad (4)$$

Equations (1) through (3) provide the following equation.

$$\frac{I}{W_p} = a(1+\alpha)\left(\frac{q}{m_p}\right)_0 + b \qquad (5)$$

Where:

$$a = \frac{2\,n(\Delta x)\,S\,\Delta t}{\pi D_p{}^2\,\tau} \geq 0 \qquad (6)$$

$$b = -\frac{6\,\varepsilon_0\,V_c\,n(\Delta x)\,S\,\Delta t}{\pi D_p{}^3\,\rho_p\,z_0\,\tau} \qquad (7)$$

a always has a positive value when particles collide with the pipe wall ($n(\Delta x)\neq 0$), but b can be either negative or positive depending on contact potential difference V_c. Here the sign of contact potential difference V_c was determined so as to agree with particle charging direction. If average flow velocity and other items are made constant and conditions for particle-wall collisions made uniform, then a and b are constants, and I/W_p becomes a linear equation with a positive gradient on $(q/m_p)_0$. Further, since α is directly proportional to powder flow rate W_p, I becomes a quadratic equation of W_p when $(q/m_p)_0$ is constant. If here we reduce the powder-to-air mass flow ratio m (powder flow rate W_p / air flow rate Q), i.e., $\alpha << 1$, Equation (5) is simplified to:

$$\frac{I}{W_p} = a\left(\frac{q}{m_p}\right)_0 + b \qquad (8)$$

We shall call the straight line (with a positive gradient) produced by Equation (8) the "characteristic line of electrification" [3]. If $(q/m_p)_0$ is constant, generated current I is directly proportional to powder flow rate W_p.

3. Experimental Apparatus and Procedure

In our experimental apparatus (**Fig. 1**) powder supplied by a table feeder (Sankyo Piotech MFOV-1) is dispersed in air through an ejector (Japan Pisco VHL15-1002J or VRL50-080108). In experiments requiring that a fine powder be supplied at a small flow rate (W_p<10 mg·s^{-1}), we used a method that involved partially remodeling the table feeder so as to suck powder directly from a powder bed on a rotating table into a capillary tube to improve continuous stability [2, 3]. The current detecting pipe, which is the test section for particle electrification, was the same as that in our previous paper [3], a nickel pipe 70 mm long having a 6 mm inside diameter, which was attached behind the fore-flow region extending 400 mm from the ejector outlet. Other than the detecting pipe section, the rest is JIS SUS 304 stainless steel. To electrically isolate the detecting pipe, it is connected with acrylic joints having insulators 1 mm long. An electric shield around the detecting pipe shuts out external noise. Current flowing from the detecting pipe to the ground was measured with an electrometer (Advantest TR8651, minimum measurement range of 10^{-14} A), and readings were fed to a personal computer at 0.1 sec intervals. Even when increasing data by taking readings at 1/10th that interval, there was no difference in measurement accuracy. Powder flow rate was determined from the amount ejected by the table feeder or from that collected with a filter attached to the detecting pipe outlet, and the particle charge amount per unit mass $(q/m_p)_0$ at the detecting pipe inlet was measured with a Faraday cage. Experimental powders (**Table 1**) were quartz sand with a comparatively large median diameter, and two kinds of fine fly ash of differing particle diameters (JIS Z8901 test powders No. 5 and No. 10). We set average air velocity to 30 m·s^{-1} in accordance with the condition that a layer of deposited particles not form on the inside pipe wall [3, 5]. The experiment was conducted at an ambient temperature of 289-296 K, and relative humidity of 40-60%.

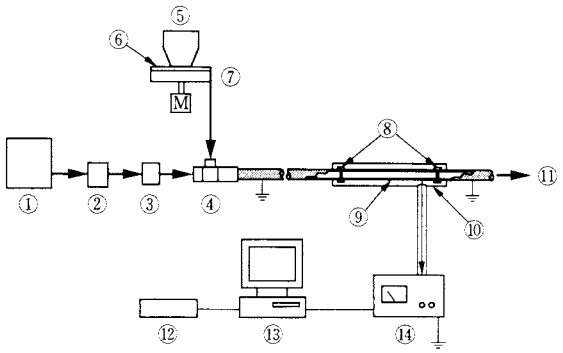

① Compressor
② Condenser
③ Mist separator
④ Ejector
⑤ Hopper
⑥ Powder layer
⑦ Table feeder
⑧ Insulator
⑨ Detecting pipe
⑩ Electric shield
⑪ Bag filter
⑫ Printer
⑬ Computer
⑭ Electrometer

Fig. 1 Experimental Apparatus

Table 1 Test Powders

Material	D_{p50}(μm)	σ_g(−)	ρ_p(kg·m^{-3})
Quartz sand	320	1.11	2700
Fly ash (JIS Z8901 No. 5)	12	2.30	2300
Fly ash (JIS Z8901 No. 10)	3.4	2.14	2300

4. Experimental Results and Discussion

4.1 Current Generated and Particle Charge

When using quartz sand with a mass median diameter of 320 μm (**Fig. 2**) we varied powder flow rate W_p across about two orders of magnitude, and the current I generated from the detecting pipe was almost proportional to the powder flow rate. This relationship corresponds to Equation (8) whose right side is a constant.

When using fly ash No. 10, which has a mass median diameter of 3.4 μm (**Fig. 3**), generated current I increases with powder flow rate W_p, though the rate of increase gradually declines. **Fig. 4** shows the relationship between charge-to-mass ratio at the detecting pipe inlet, i.e., $(q/m_p)_0$ and powder flow rate W_p. In the graph, the broken line indicates particle charge in the hopper as measured with a Faraday cage, and shows that the particles have almost no charge. The difference between the plot and the broken line corresponds to the charge accumulated by particles caused by passing through the table feeder, ejector, and fore-flow region. The particle charge decreases as powder flow rate increases.

The results shown in **Figs. 3** and **4** give the relationship between I/W_p and $(q/m_p)_0$ (circles in **Fig. 5**). In the theoretical Equation (8) or the more general Equation (5) with the space charge effect, I/W_p must increase steadily with $(q/m_p)_0$, though in the experiment it actually tended to decrease. Triangles (△) in the same graph show the experimental results from our previous report [3] using the same powder and detecting pipe, although experimental conditions differed: powder-to-air mass flow ratio m in the experiment is between 0.0011 and 0.0058. Even at the largest ratio, α is sufficiently small (α=0.0040), and the space charge effect can be ignored. Therefore, this straight line is the characteristic line of electrification that satisfies the conditions of Equation (8). In the experiment we artificially vary $(q/m_p)_0$ by electrifying particles in advance. If in Equation (5) one substitutes a and b obtained from the characteristic line

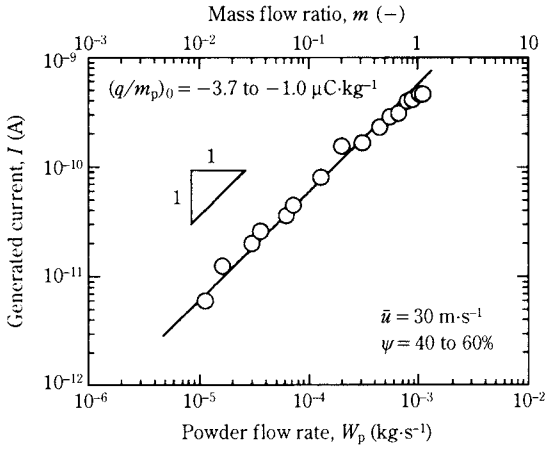

Fig. 2 Generated Current from the Detecting Pipe as a Function of Powder Flow Rate (Quartz sand: D_{p50} = 320 μm)

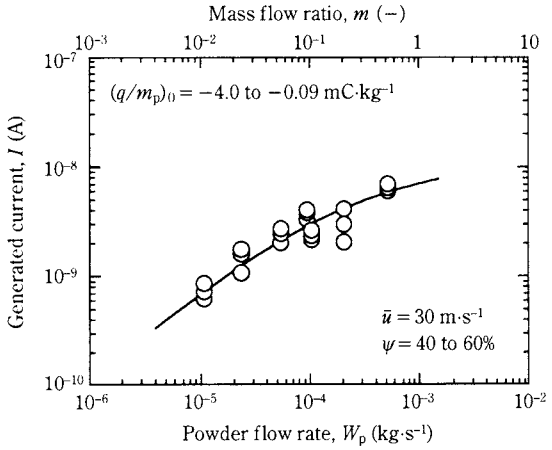

Fig. 3 Generated Current from the Detecting Pipe as a Function of Powder Flow Rate (Fly ash No. 10: D_{p50} = 3.4 μm)

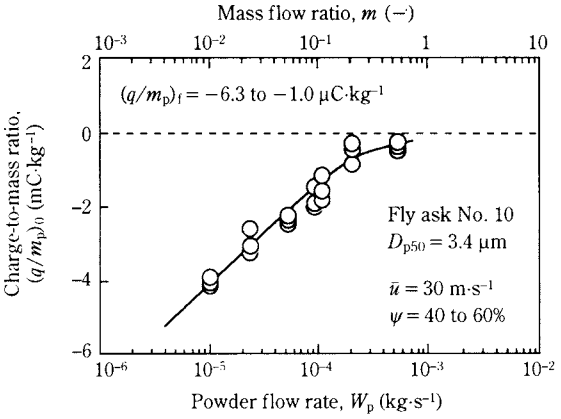

Fig. 4 Charge-to-Mass Ratio of Particles at the Inlet of the Detecting Pipe

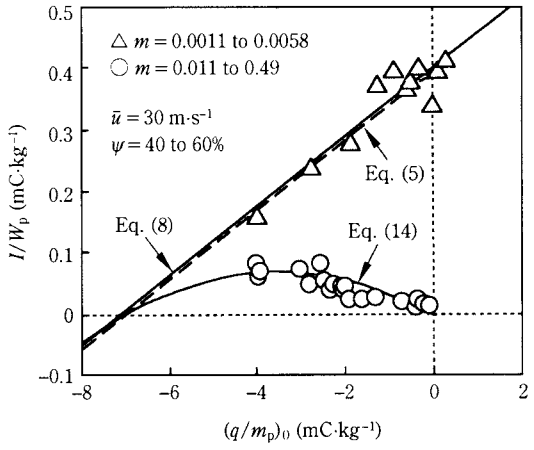

Fig. 5 Characteristic Line of Particle Electrification (Fly ash No. 10: D_{p50} = 3.4 μm)

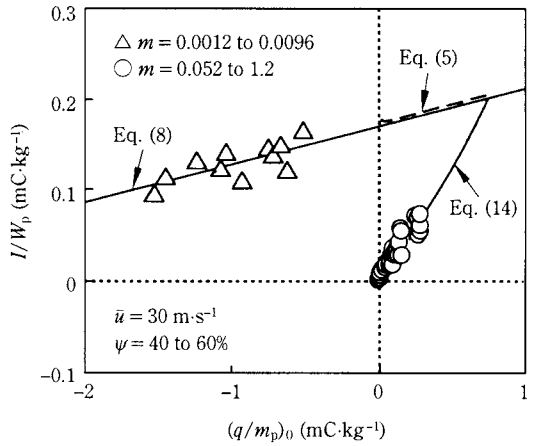

Fig. 6 Characteristic Line of Particle Electrification (Fly ash No. 5: D_{p50} = 12 μm)

of electrification, and the relationship between $(q/m_p)_0$ and W_p shown in **Fig. 4**, one obtains the relationship between I/W_p and $(q/m_p)_0$ including the space charge effect (the broken line in **Fig. 5**). The experimental results were lower than I/W_p as calculated with Equation (5), showing that charge transfer was not adequate in the detecting pipe, which means there was a decrease in particle electrification efficiency.

Fig. 6 shows the relationship between I/W_p and $(q/m_p)_0$ for fly ash No. 5, which has a slightly larger particle diameter of D_{p50}=12 μm. The results for m=0.052 to 1.2 (○) were lower than the value calculated from Equation (5) based on the results for m=0.0012 to 0.0096 (△).

4.2 Analysis of I/W_p and $(q/m_p)_0$ Using Particle Electrification Efficiency

The results in **Figs. 5** and **6** can be explained using particle electrification efficiency $\eta\,(0\leq\eta\leq1)$, which will be analyzed in detail in Section 4.3 below. To begin with, we shall consider this process by dividing it into two parts: The anterior section consisting of powder supply, powder dispersion, and the fore-flow region, and the posterior section consisting of the fully developed gas-solids pipe flow (detecting pipe). Although the anterior section comprises several operations, the following simple equation is obtained from Equation (5) by introducing overall particle electrification efficiency η_f in this section.

$$\frac{I_f}{W_p}=\eta_f\left\{a_f(1+\alpha)\left(\frac{q}{m_p}\right)_f+b_f\right\} \tag{9}$$

Where:

$(q/m_p)_f$ is the particle electrification per unit mass in the hopper. Similarly, if particle electrification efficiency in the detecting pipe is η, the following equation is obtained for the posterior section.

$$\frac{I}{W_p}=\eta\left\{a(1+\alpha)\left(\frac{q}{m_p}\right)_0+b\right\} \tag{10}$$

The charge balance yields the following equation.

$$\left(\frac{q}{m_p}\right)_f+\left(\frac{q}{m_p}\right)_0=\frac{I_f}{W_p} \tag{11}$$

Since particle electrification arises primarily through collisions with the pipe wall as long as gas-solids pipe flow conditions are unchanged, particle electrification efficiency will be constant. Although particle velocity accelerates when passing through the ejector, subsequent velocity is nearly constant, and the mass flow ratio remains unchanged throughout the entire process. Thus, if we approximate that particle electrification efficiency is constant ($\eta_f\approx\eta$) and delete η_f and η from Equations (9) through (11), I/W_p is represented by a quadratic equation of $(q/m_p)_0$ as follows:

$$\frac{I}{W_p}=\frac{-a(1+\alpha)}{a_f(1+\alpha)\left(\frac{q}{m_p}\right)_f+b_f}\left\{\left(\frac{q}{m_p}\right)_0-\left(\frac{q}{m_p}\right)_f\right\}\times\left\{\left(\frac{q}{m_p}\right)_0+\frac{b}{a(1+\alpha)}\right\} \tag{12}$$

$(q/m_p)_0$ in Equation (12) is determined here by particle electrification in the anterior process. It is limited by the following equation, which is derived from Equations (9) and (11).

$$\left(\frac{q}{m_p}\right)_0=\left\{1-\eta_f a_f(1+\alpha)\right\}\left(\frac{q}{m_p}\right)_f-\eta_f b_f \tag{13}$$

When the space charge effect is small and powder in the hopper is considered $(q/m_p)_0\approx0$, which is applicable to this experiment, Equations (12) and (13) are simplified as follows:

$$\frac{I}{W_p}\approx-\frac{a}{b_f}\left(\frac{q}{m_p}\right)_0\left\{\left(\frac{q}{m_p}\right)_0+\frac{b}{a}\right\} \tag{14}$$

$$\left(\frac{q}{m_p}\right)_0=-\eta_f b_f \tag{15}$$

The absolute value of b_f becomes larger with the increase in particle transport distance in the anterior process, while b_f can be zero when that distance is very short. And if the condition $0\leq\eta_f\leq1$ is added to Equation (15), $(q/m_p)_0$ is limited to within the following range.

$$-b_f\leq\left(\frac{q}{m_p}\right)_0\leq0,\quad\text{for } b_f>0, \tag{16}$$

$$0\leq\left(\frac{q}{m_p}\right)_0\leq-b_f,\quad\text{for } b_f<0, \tag{17}$$

Therefore, I/W_p is represented by a quadratic equation of $(q/m_p)_0$ passing through the origin, though the parabola's orientation changes according to the sign

Table 2 Experimental Values

Material	a(−)	b(mC·kg^{-1})	b_f(mC·kg^{-1})
Fly ash (JIS Z8901 No. 10)	0.056	0.40	10
Fly ash (JIS Z8901 No. 5)	0.042	0.17	−0.73

of b_f or $(q/m_p)_0$ (see Equation (15)).

To compare this analysis with the experimental results, we added the results of calculations with Equation (14) to **Figs. 5** and **6**. The constants used in calculations are presented in **Table 2**. There is good correspondence between the theoretical results and the experimental results. Thus it is possible to explain the fine powder electrification phenomenon in gas-solids pipe flows using the corrected equation (quadratic equation) for the relationship between I/W_p and $(q/m_p)_0$. Further, substituting $\eta_f=1$ in Equation (15) yields $(q/m_p)_0=-b_f$, and substituting this in Equation (14) gives the same form as Equation (8).

4.3 Analysis of Particle Electrification Efficiency

In order to quantitatively assess the extent to which I/W_p departs from electrification theory in **Figs. 5** and **6**, we analyzed the ratio of experimental values to theoretical values (corresponding to particle electrification efficiency η). **Fig. 7** shows the relationship between particle electrification efficiency η and powder-to-air mass flow ratio m of the two types of fly ash with different median diameters and the quartz sand. We observed hardly any decline in particle electrification efficiency in quartz sand, which has a large median diameter, though the electrification efficiency for fly ash decreases when the mass flow ratio is large. Electrification efficiency of fly ash No. 10, which has a small median diameter (D_{p50}=3.4 μm), begins to fall at mass flow ratios smaller than that for fly ash No. 5 (D_{p50}=12 μm). A possible cause is a decrease in the effective number of particle collisions with the pipe wall ($n(\Delta x)$) due to an increase in the

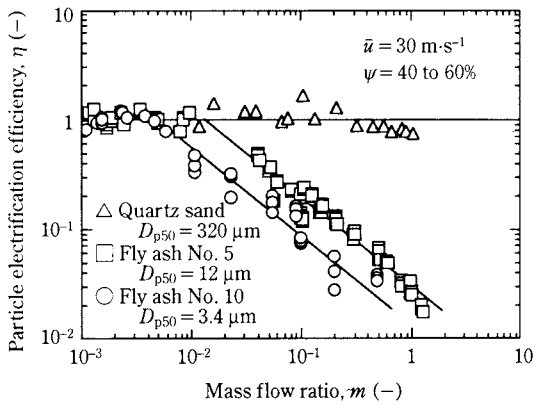

Fig. 7 Effect of Mass Flow Ratio on Particle Electrification

mass flow ratio. According to Equations (6) and (7), when $n(\Delta x)=0$, a and b are both zero, and no current is generated. There is still incomplete understanding of the relationship between the number of collisions with the pipe wall and the mass flow ratio of fine powders, so here we shall focus our investigation on mutual interference between particles. Specifically, when particle concentration near a pipe wall increases, particles moving toward the wall are hindered, making it possible that collisions with the wall will decrease. Further, since the air velocity of 30 m·s^{-1} in this experiment is well over the reentrainment velocity of these fine powder types [5], a powder layer was not formed on the pipe wall, which means we should be able to disregard a decrease in particle electrification efficiency due to particle deposit on the wall.

The complexity of particle behavior in turbulent flows makes it impossible to precisely determine the number of particle-particle collision. However, there is the following equation to show the number of collisions N per unit time and per unit volume [6].

$$N = Kc^2 \tag{18}$$

Where:

K is a constant that is directly proportional to the third power of the particle diameter, and c is the concentration in number of particles, which is inversely proportional to the third power of the particle diameter when the mass flow ratio is constant. This means that, according to Equation (18), the number of particle-particle collisions N is inversely proportional to the third power of particle diameter. The count median diameter for fly ash No. 10 (CMD=0.6 μm), for example, is about 1/500th that of quartz sand (CMD=310 μm), so with the same mass flow ratio the number of collisions is about 10^8 times larger. Further, since the fly ash has a broader particle size distribution than quartz sand (see Table 1), the difference in collision frequency is larger still owing to the added effect of mobility based on particle inertia. This suggests that particle-particle collisions affect the electrification efficiency of fine particles.

Additionally, since particle adhesion in fine powders promotes agglomeration when particles collide with each other, it is no longer possible for the interior particles of agglomerates to collide directly with the pipe wall. Even particles on the surfaces of agglomerates can collide with the wall only with certain small parts of themselves, so their electrification efficiency decreases. We used a cascade impactor (Kanomax 5600) to measure the size of particles pass-

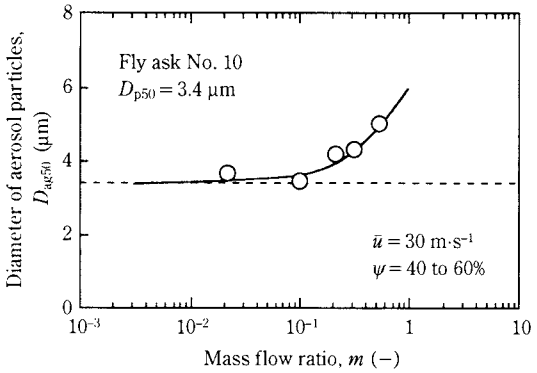

Fig. 8 Effect of Mass Flow Ratio on Diameter of Agglomerated Aerosol Particles

ing through the detecting pipe. The mass median diameter D_{ag50} of the particles increases when the mass flow ratio is over 0.1, which shows that the particles are agglomerating (**Fig. 8**). The broken line in this graph is the mass median diameter measured with the sedimentation method (Sedigraph 5000) after fully dispersing in an aqueous solution.

5. Conclusion

We conducted an electrification experiment that envisioned the continuous process from powder supply to a fully developed gas-solids pipe flow, and examined, both theoretically and experimentally, the electric current generated in the test section (detecting pipe) and particle charge. Following are our conclusions.

1) When using comparatively coarse particles with a mass median diameter of 320 μm, the current generated in the detecting pipe was almost proportional to the powder-to-air mass flow ratio, but when using fine particles (mass median diameter of 3.4 μm) the rate of increase in the generated current gradually declines as the mass flow ratio increases.

2) Even with fine particles, when the mass flow ratio is small, the current generated per unit powder flow rate I/W_p and the charge-to-mass ratio $(q/m_p)_0$ are represented by a characteristic line of electrification (linear equation) having a positive coefficient. However, when the mass flow ratio is large and the efficiency of particle-wall collisions decreases, the line departs from electrification theory. Further, electrification characteristics (the relationship between I/W_p and $(q/m_p)_0$) change greatly in accordance with the sign of initial particle charge.

3) Regardless of the initial charge sign, it is possible to explain the electrostatic phenomenon of fine powders in gas-solids pipe flows using the corrected equation (quadratic equation) for I/W_p and $(q/m_p)_0$ derived by introducing particle electrification efficiency.

4) The reason why particle electrification efficiency decreases with increasing mass flow ratio is thought to be that mutual interference between particles diminishes particle-wall collisions.

Acknowledgment

This research was conducted under a Grant-in-Aid for Scientific Research No. 08455355 from the Ministry of Education, Science and Culture, Japan.

Nomenclature

a	: constant defined by Eq. (5)	(−)
b	: constant defined by Eq. (6)	(C·kg^{-1})
c	: particles per unit volume	(m^{-3})
D	: inner diameter of a pipe	(m)
D_{ag50}	: mass median diameter of aerosol particles	(m)
D_p	: particle diameter	(m)
D_{p50}	: mass median diameter	(m)
I	: electric current	(A)
K	: constant in Eq. (18)	(m^3·s^{-1})
m	: powder-to-air mass flow ratio ($=W_p/Q$)	(−)
m_p	: particle mass	(kg)
N	: rate of collisions between particles	(m^{-3}·s^{-1})
$n(\Delta x)$	: number of collisions of a particle between x and $x+\Delta x$	(−)
n_0	: relaxation number of collisions defined by Eq. (3)	(−)
Q	: air flow rate	(kg·s^{-1})
q	: particle charge	(C)
$(q/m_p)_0$	: charge-to-mass ratio at $x=0$ (at the inlet of a detecting pipe)	(C·kg^{-1})
$(q/m_p)_f$	: charge-to-mass ratio of powder in a hopper	(C·kg^{-1})
$(q/m_p)_\infty$	: charge-to-mass ratio at $x=\infty$	(C·kg^{-1})
S	: contact area between particle and wall	(m^2)
Δt	: duration of contact	(s)
$\bar{u}$	: average air velocity	(m·s^{-1})
V_c	: contact potential difference based on work function	(V)
$\bar{v}$	: average particle velocity	(m·s^{-1})
x	: length from a point	(m)
Δx	: length of a pipe	(m)
W_p	: powder flow rate	(kg·s^{-1})
z_0	: gap between contact bodies	(m)
α	: ratio of space charge effect to image charge effect	(−)

ε_0	: permittivity of air	$(F \cdot m^{-1})$
η	: particle electrification efficiency	$(-)$
ρ	: air density	$(kg \cdot m^{-3})$
ρ_p	: particle density	$(kg \cdot m^{-3})$
σ_g	: geometric standard deviation	$(-)$
τ	: time constant of electrification	(s)
ψ	: relative humidity	$(-)$

References

1) Hughes, J. F.: "Electrostatic Powder Coating", Research Studies Press (1984)
2) Masuda, H., S. Matsusaka and S. Nagatani: "Measurements of Powder Flow Rate in Gas-Solids Pipe Flow Based on the Static Electrification of Particles", *Advanced Powder Technol.*, **5**, 241-254 (1994)
3) Masuda, H., S. Matsusaka and H. Fujimoto: " On-Line Simultaneous Measurement of Powder Flow Rate and Electric Charge of Particles in Gas-Solids Pipe Flow −effect of air velocity on accuracy of measurement−", *Kagaku Kogaku Ronbunshu*, **21**, 573-580 (1995)
4) Masuda, H., T. Komatsu and K. Iinoya: "The Static Electrification of Particles in Gas-Solids Pipe Flow", *AIChE J.*, **22**, 558-564 (1976)
5) Matsusaka, S., M. Shimizu and H. Masuda: "Formation of Wall Particle Layers by Simultaneous Deposition and Reentrainment of Fine Particles in Turbulent Aerosol Flows", *Kagaku Kogaku Ronbunshu*, **19**, 251-257 (1993)
6) Saffman, P. G. and J. S. Turner: "On the Collision of Drops in Turbulent Clouds", *J. Fluid Mechanics*, **1**, 16-30 (1956)

Author's short biography

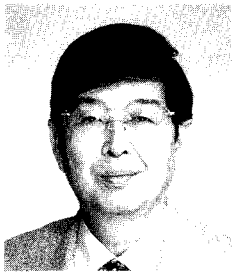

Hiroaki Masuda

- Professor, Department of Chemical Engineering, Kyoto University.
- 1966 B.S. (Hiroshima Univ.), 1968 M.S. (Hiroshima Univ.), 1973 Ph.D. (Kyoto Univ.).
- 1973 Research Associate (Kyoto Univ.), 1979 Associate Professor (Hiroshima Univ.), 1986 Professor (Hiroshima Univ.), 1989 Professor (Kyoto Univ.).
- Excellent Paper Award by The Society of Chemical Engineers, Japan (1980), Excellent Paper Award by The Society of Powder Technology, Japan (1985), Excellent Paper Award by Japan Association of Aerosol Science and Technology (1991), Iinoya Award by Japan Association of Aerosol Science and Technology (1995), Distinguished Achievements Award by The Institute of Electrostatics Japan (1996), Naito Award by The Society of Chemical Engineers, Japan (1998).
- Research Interests: Electrostatic characterization of powder, Deposition and reentrainment of fine particles, Dry-dispersion of powder, Surface cleaning by air-jet.

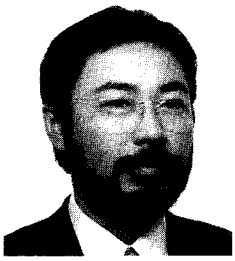

Shuji Matsusaka

- Associate Professor, Department of Chemical Engineering, Kyoto University.
- 1981 B.S. (Hiroshima Univ.), 1983 M.S. (Hiroshima Univ.), 1993 Ph.D. (Kyoto Univ.).
- 1983 Toray Engineering Co., 1989 Research Associate (Kyoto Univ.), 1996 Lecturer (Kyoto Univ.), 1997 Associate Professor (Kyoto Univ.).
- Iinoya Award by Japan Association of Aerosol Science and Technology (1995).
- Research Interests: Deposition and reentrainment of fine particles, Particle electrification and its application, Particle interactions and assembly mechanics.

The Electrostatic Force Between a Charged Dielectric Particle and a Conducting Plane†

Tatsushi Matsuyama, Hideo Yamamoto
*Dept. of Bio-eng., Soka Univ.**

Abstract

The electrostatic force between a uniformly charged dielectric particle and a conducting plane was carefully calculated including the effect of higher-order polarizations. The potential distribution problem was solved using spherical coordinates by considering the symmetry of the image and using a re-expansion technique of the Legendre functions. On the basis of the results, the electrostatic force was calculated using the orthogonality of the Legendre terms. In this method, numerical calculations are required for each condition, such as the contact gaps and the dielectric constants of the particle. This would be avoidable if an approximate formula was available. Thus, for convenience, an approximate formula was searched for by trial and error, and $F_e=F_e(d=0)/\{1+(d/a)^{\alpha}\}^{\beta}$ *was found to be a good approximation. This was the simple expansion of the contact gap dependence of the particle with a relative dielectric constant* $\varepsilon=1$*, i. e., with no effect of polarization.*

1. Introduction

Suppose that a uniformly charged spherical dielectric particle is located in the vicinity of a conducting plane. The electrostatic field generated around this particle is, in many cases, approximated by the superposition of the fields generated by the center-point charge and its image. This is the 0-th order approximation which neglects the effect of higher polarization. In the stricter sense it is necessary to consider the following effects: the image of the center-point charge, which is equivalent to a uniform charge on the surface of the sphere, induces a polarization of the particle: the image of this polarization induces a higher order polarization, and so on; therefore the electrostatic field around the particle is given by the superposition of all the fields which are due to all the higher polarizations and their images. The problem to find this field can be reduced into the problem of solving Laplace's equation around two equivalent spheres, considering the symmetry and including the sign of the image. This problem was solved by Xiaopin [1] and Stoy [2] using bi-spherical coordinates. However, this method requires very complex analytical calculations. The authors solved this problem using simple spherical coordinates [4,5], using the re-expansion technique [3] of Legendre harmonics around two spheres. By directly using this result, we can treat strictly the electrostatic force between a charged dielectric particle and a conducting plane. This method is equivalent to the "multipole method" of Fowlkes et al. [8], but has the advantage of simpler mathematical expressions. It can be more easily extended other boundary conditions such as the condition for partially charging [5], and has better perspective for analytical calculations. This paper will describe this solution.

2. Out-line of the Analytical Procedure

The method to solve the potential distribution for given boundary condition was described in detail in a previous paper [4, 5]. Here it will be shown in outline and then, the derivation of the electrical force, which is the subject of this paper, will be described in detail.

Figure 1 shows the coordinate system used including the location of the two spheres. The sphere S1 is

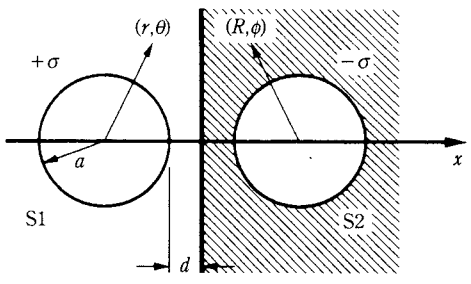

Fig. 1 The coordinate system for two spheres

* 1-236 Tangi-cho, Hachioji-shi, Tokyo 192

† This report was originally printed in J. Soc. Powder Technology, Japan. **34**, 154 (1997) in Japanese, before being translated into English by KONA Editorial Committee with the permission of the editorial committee of the Soc. Powder Technology, Japan.

the object of the discussion. This is charged uniformly on its surface with charge density σ, and a and ε represent its radius and relative dielectric constant, respectively. The mirror sphere S2 with a charge of opposite polarity is displaced by a contact gap $2d$; this means that d represents the contact gap between the S1 and conducting plane which is assumed to lie symmetrically between these two spheres. The x-axis passes through the centers of the two spheres, and the distance between these two centers is written as $x=2(a+d)$. However, we mainly use spherical coordinates (r, θ) whose origin is set at center of S1.

Generally, with no space charge, the potential distribution, ϕ, satisfies Laplace's equation:

$$\nabla^2\phi = 0 \tag{1}$$

The general solution, in the case of axi-symmetric distribution on the spherical coordinates, is given as:

$$\phi = \frac{a\sigma}{\varepsilon_0}\sum_{k=0}^{\infty} A_k \left(\frac{r}{a}\right)^{-k-1} P_k(\cos\theta) + \frac{a\sigma}{\varepsilon_0}\sum_{k=0}^{\infty} B_k \left(\frac{r}{a}\right)^{k} P_k(\cos\theta) \tag{2}$$

Here, $P_k(x)$ represents a Legendre function of the first kind, and $a\sigma/\varepsilon_0$ is a normalizing factor. Note here that the first term of this equation represents the potential around S1 due to the charge and the polarization of S1 and the second term represents the potential around S1 due to S2 with its net charge and induced charge due to polarization, according to the singularity at $r\to\infty$ and at $r\to 0$. For the present problem, the symmetry, including the sign of the image, requires symmetry between the potential distribution around S1 due to S1 and that around S2 due to S2, including its sign. This symmetry condition can be expressed by the re-expansion theory for Legendre harmonics (refer eqs. (3), (11) and Appendix A and B of ref. [4], or eqs. (3), (17) and Appendix A and B of ref. [5]). Using this symmetry condition and the following boundary conditions on the surface of S1 (for all θ at $r=a$):

continuation of potential: $\phi_{ext} = \phi_{int}$
continuation of flax: $\varepsilon\partial\phi_{int}/\partial r - \partial\phi_{ext}/\partial r = \sigma/\varepsilon_0$

we can obtain the coefficients A_k and B_k of eq.(2) (see eq.(16) of ref. [4] or eq.(23) of ref [5]).

Now that the potential distribution is obtained the result directly can be used to calculate the electrostatic force acting on the particle. Let us write σ_t as the whole charge distribution existing on the S1 surface. Note here that this charge includes both of the net surface charge held by S1 originally and the induced charge due to the polarization of S1. Let us also write $\boldsymbol{E}$ as the external electrostatic field applied to S1. Here, according to the method of Coulomb's Law Committee [7], the force $\boldsymbol{F}$ acting on S1 is given by:

$$\boldsymbol{F} = \int \sigma_t \boldsymbol{E}\, \mathrm{d}s \tag{3}$$

For this problem, only a scalar force, F, aligned with the x-axis results because of the symmetry; therefore, this equation can be rewritten as,

$$F_x = \int \sigma_t E_x\, \mathrm{d}s \tag{4}$$

Here E_x represents the component of the field in the x-direction. The terms σ_t, $\boldsymbol{E}$, and E_x can be obtained from their definitions as:

from $\dfrac{\sigma_t}{\varepsilon_0} = -\dfrac{\partial\phi_{ext}}{\partial r} + \dfrac{\partial\phi_{int}}{\partial r}\Big|_{r=a}$

$$\sigma_t = \sigma\sum_{k=0}^{\infty}\{(2k+1)A_k\}P_k(\cos\theta), \tag{5}$$

and from $\boldsymbol{E} = -\mathrm{grad}\,\phi$, $E_x = \boldsymbol{E}\cdot\hat{\boldsymbol{x}}$

$$E_x\Big|_{r=a} = -\frac{\sigma}{\varepsilon_0}\sum_{k=1}^{\infty} kB_k P_{k-1}(\cos\theta). \tag{6}$$

Substituting eqs. (5) and (6) into eq. (4), the force F_x can be obtained as,

$$F_x = -\frac{q^2}{4\pi\varepsilon_0(2a)^2}\times 2\int_{-1}^{1}\sum_{k=0}^{\infty}(2k+1)A_k P_k(x) \times \sum_{k=0}^{\infty} kB_k P_{k-1}(x)\,\mathrm{d}x \tag{7}$$

The net total charge held by the particle is given by: $q(=4\pi a^2\sigma)$. It is shown here that the force is normalized by the force acting between two point charges q and $-q$ displaced by a distance $2a$. This is equivalent to the force acting on the contact of two no-polarized particles, i.e., with relative dielectric constant $\varepsilon=1$ and radius a. The integration can be performed analytically because of the orithogonality of the Legendre functions. The attractive electrostatic force acting on the two spheres is finally obtained as:

$$F_x = -\frac{q^2}{4\pi\varepsilon_0(2a)^2}\times 4\sum_{k=0}^{\infty}(k+1)A_k B_{k+1} \tag{8}$$

3. Examples of Calculations

In this section some examples of calculations of the attractive force between a uniformly charged particle and a conducting plane will be shown. In all these results, the contact gap, d, between the particle and the wall is normalized by the radius of the particle, a. The electrostatic force, F_e, is also normalized by a force given by: $F^0=q^2/4\pi\varepsilon_0(2a)^2$. This is the force which would exist without polarization, i.e., the force when a particle with a relative dielectric constant $\varepsilon=1$ is in contact with a conducting plane.

Figure 2 shows the result of calculations of force

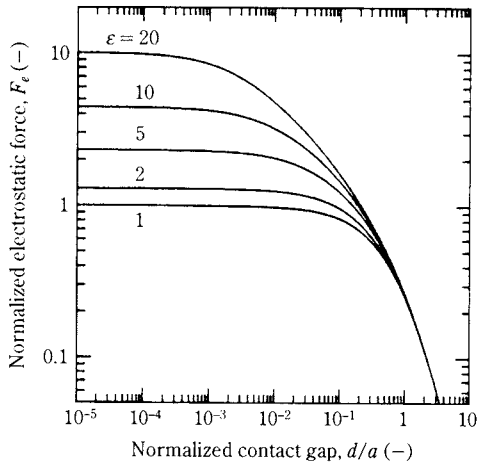

Fig. 2 The electrostatic force as a function of the normalized contact gap

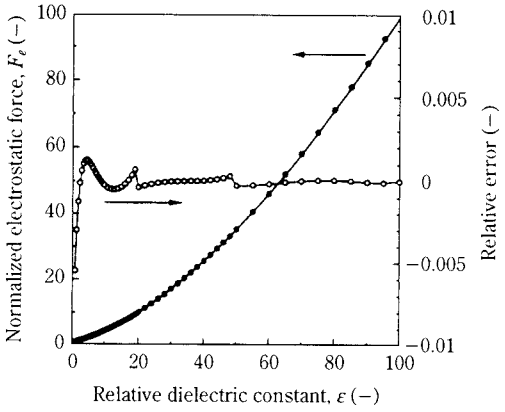

Fig. 3 The relation between the electrostatic adhesive force and the relative dielectric constant of the particle

as a function of the contact gap between the particle and the conducting plane for $1<\varepsilon<20$. The higher order polarization show their effect when the contact gap becomes less than the particle radius. This result shows that the attractive force can be bigger, in the case of particles in contact, than that of the normally used point charge approximation depending on the dielectric constant. The effect of the polarization is negligible in the case of particles farther from the wall than the particle radius. These results agree with the results given by Fowlkes et al. using the "multipole method", and by Davise using bi-spherical coordinates. In that paper, the calculated result was shown for only one particle with a diameter and one charge. In this paper the results were normalized by the particle diameter and charge (eq.(8)), which is more convenient.

Figure 3 shows the electrostatic attractive force on a particle in contact with the wall ($d=0$) as a function of the dielectric constant of the particle for $1<\varepsilon<100$. In this figure, the black dots indicate each calculated result, whilst the solid line shows a empirical approximation; The following 6-th order polynominal gives a good approximation,

$$F_e = 0.721_3 + 0.261_0\varepsilon + 1.220_7\times10^{-2}\varepsilon^2 - 1.206_8\times10^{-4}\varepsilon^3 + 1.402_6\times10^{-6}\varepsilon^4 - 9.44_8\times10^{-9}\varepsilon^5 + 2.62_7\times10^{-11}\varepsilon^6 \quad (9)$$

4. Approximation

In order to determine the coefficients A_k and B_k of the Legendre harmonics, a numerical calculation is required for each given condition, that is relative dielectric constant of the particle, ε, and normalized contact gap d/a. Thus, some effort will be required to calculate the electrostatic force. Thus, we give here empirical approximations based on each calculation, which may be convenient for some users.

We calculated the electrostatic force, F_e, as a function of the normalized contact gap, d/a, between the particle and the wall in the range of the dielectric constant $1<\varepsilon<20$, and found an approximation by trial-and-error. We thus obtained the following equation which gives a good approximation for wide range of the contact gap:

$$F_e = \frac{F_e\big|_{d=0}}{\{1+(d/a)^{\alpha}\}^{\beta}} \quad (10)$$

Here the value of F_e as $d\to0$ is found in eq.(9). This formula is rather weak since it is not amenable to analytical integration. Nevertheless, it is interesting because it is a very simple expansion of the analytical solution for the case of a particle with relative dielectric constant 1:

$$F_e^{\varepsilon=1} = \frac{1}{\{1+(d/a)\}^2} \quad (11)$$

Figure 4 shows a comparison between the approxi-

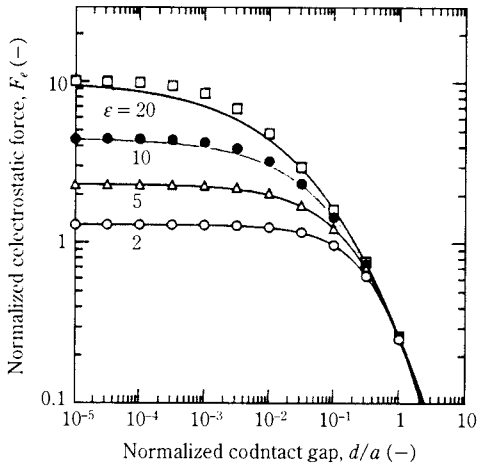

Fig. 4 The comparison between the strictly calculated values and the approximations

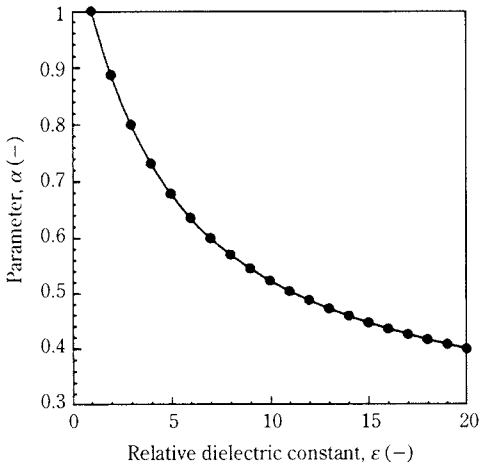

Fig. 5 The parameter α as a function of the dielectric constant of the particle

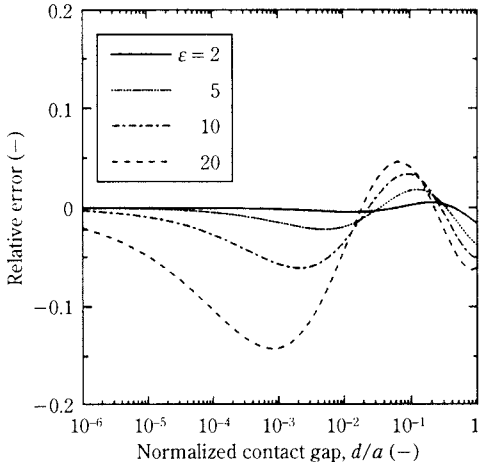

Fig. 6 The relative error due to the approximation as a function of the contact gap

mation and the numerical solution. This indicates good agreements over a wide range of the contact gap.

Nevertheless, a detailed check on the relative error of the approximation showed that the relative errors increase rapidly in the range of $d/a>1$. This is caused not only by the fact that the absolute value of the force becomes very small but also mainly by the fact that we used only simply approximation eq.(10) over the whole range despite the reduced effect of the polarization in this range. Thus we consider that it is rather useful if the constants in eq.(10) are determined to combine with eq.(11) which is applicable with no polarization effect in the bigger range of d. This connecting condition between eq.(10) and eq.(11) at $d/a=1$ is given as:

$$\beta = 2+\log_2 F_e\Big|_{d=0} \tag{12}$$

For each value of β given in this way, the term α was determined for a range of relative dielectric constant $1<\varepsilon<20$ using a least square method. We tried to reproduce the increasing behavior especially in the range of the contact gap of $0.01<d/a<1$. **Figure 5** shows this result. The determined parameter α was expressed well by the following empirical equation:

$$\begin{aligned}\alpha = {} & 1.145_6-0.1650_0\varepsilon+2.11_6\times10^{-2}\varepsilon^2 \\ & -1.749_2\times10^{-3}\varepsilon^3+8.71_1\times10^{-5}\varepsilon^4 \\ & -2.36_5\times10^{-6}\varepsilon^5+2.68_0\times10^{-8}\varepsilon^6\end{aligned} \tag{13}$$

Figure 6 shows the relative error, as a function of normalized contact gap, between the numerical data and the approximation with the parameters α and β as given above. It shows that the relative error increases with an increase of the relative dielectric constant of the particle. However, they all lie within ±10% for the range of $0.01<d/a<1$. This approximation can be accepted as being useful over this range by noting the fact that the value of F_e at $d=0$ is fixed by the original result in eq.(10) and that **Fig.6** is drawn on a log-scale on the horizontal axis.

5. Comparison Between the Electrostatic Force and van der Waals Force

In this last section we will show briefly a comparison between the van der Waals force and the electrostatic attractive force. **Figure 7** shows the attracting forces as a function of the contact gap between the

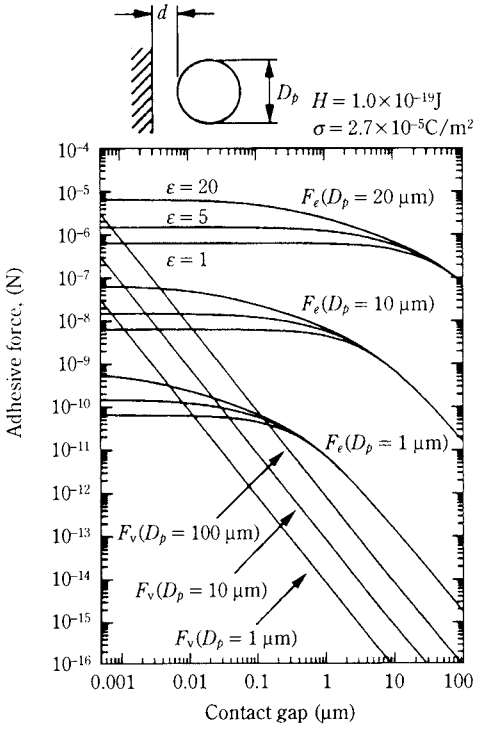

Fig. 7 Examples of comparisons between the van der Waals forces and the strict electrostatic forces

particle and the conducting plane for particles of 100, 10 and 1 μm in diameter. Here, for the evaluation of the van der Waals force, we used the most simple equation:

$$F_v = \frac{H}{12d^2} D_p \tag{14}$$

We assumed a value of $H=1.0\times10^{-19}$ J for the Hamaker constant which is the most commonly assumed value. It is open to question what value should be used as the surface charge density of the particle in these comparisons (see ref. [9] by Masuda et al.): Here we used $\sigma=2.7\times10^{-5}$ C/m^2 as a reasonable value.

It is well known that the van der Waals force decreases very rapidly with an increase of the contact gap between the particle and the wall. On the other hand, the electrostatic force is a macroscopic interaction which depends on the particle size. Indeed, **Fig.7** shows that the electrostatic force is constant to a displacement equal to the particle radius. In this paper, the strict treatment of the electrostatic force including the effect of the higher polarization has been described in detail: This effect is not so big for polymer materials, the figure shows that the effect does not work to change the force in the order of magnitude. Also, it is shown, and is well known, that the van der Waals force is the dominant adhesive force when the particles in contact is smaller particle than 10 μm.

6. Conclusions

The electrostatic force acting between a uniformly charged particle and a conducting plane was treated strictly to include the effect of the higher order polarization. Also an approximation was found to avoid the necessity to perform a numerical calculation for each condition. The formula found is $F_e=F_e(d=0)/\{1+(d/a)^{\alpha}\}^{\beta}$. This is a very simple expansion of the case with no polarization, and gives a good approximation in the range of the normalized contact gap $d/a<1$; the parameters α and β were obtained empirically. As the next step, it is important to expand these results to the case of non-uniformly charged particles.

Nomenclature

a	: radius of a particle	(m)
A_k	: coefficients for the Legendre terms	(−)
B_k	: coefficients for the Legendre terms	(−)
D_p	: diameter of a particle	(m)
$\boldsymbol{E}$	: electrostatic field applied on a particle	(V/m)
E_x	: x-direction component of the electrostatic field	(V/m)
$\boldsymbol{F}$	: electrostatic force acting on a particle	(N)
F_e	: electrostatic force acting on a particle	(N)
F_x	: x-direction component of the electrostatic force	(N)
F_v	: van der Waals force	(N)
H	: Hamaker constant	(J)
$P_k(x)$	: Legendre function of the first kind	
q	: charge	(C)
$\hat{\boldsymbol{x}}$	: a unit vector of x-direction	
α	: coefficient of Eq. (10)	(−)
β	: coefficient of Eq. (11)	(−)
ε	: relative dielectric constant	(−)
ε_0	: dielectric constant of free space	(F/m)
ϕ	: potential	(V)
σ	: surface charge density	(C/m^2)

References

1) Xiaopin, C. : "The electrostatic problem of a dielectric sphere near a plane", *J. Electros.*, **19**, 201 (1987)
2) Stoy, R. D.: "Solution procedure of the Laplace equation in bispherical coordinates for two spheres in a uniform external field", *J. Appl. Phys.*, **65**, 2611 (1989)
3) Washizu, M.: "Precise calculation of dielectrophoretic force in a arbitrary field", *J. Electros.*, **29**, 177 (1992)
4) Matsuyama, T. and H. Yamamoto: "The electrostatic field around a dielectric particle located near a conducting plane", *AIChE/Part. Tech. Forum* Vol. 2, p. 30 (Denver; 1994)
5) Matsuyama, T., H. Yamamoto and M. Washizu: "Potential distribution around a partially charged dielctric particle located near a conducting plane", *J. Electros.*, **36**, 195 (1995)
6) Fowlkes, Wm. Y. and K. S. Robinson: "The electrostatic force on a sphere resting on a conducting substrate", in "Particle on Surfaces vol. 1", p. 143, Plenum, New York (1988)
7) Coulomb's law committee: "The teaching of electricity and magnetism at the college level", *Amer. J. Phys.*, **18**, 1 (1950)
8) Davis, M. H.: "Electrostatic field and force on a dielectric sphere near a conducting plane – a note on the application of electrostatic theory to water droplets", *Am. J. Phys.*, **37**, 26 (1969)
9) Masuda, H. and S. Matsusaka: "Maximum electrostatic force acting on a particle", *J. Soc. Powder Technol. Japan*, **30**, 27 (1993)

Author's short biography

Tatsushi Matsuyama

Tatsushi Matsuyama was born in 1964 in Kanagawa, Japan, and grew in Nagano in his early days. He graduated from the Department of Chemical Engineering, the University of Tokyo, in 1987. He received the Ph.D. degree from the University of Tokyo, in 1995.

He joined the Department of Bioengineering, Soka University, as an Associate Researcher in 1992, and in 1998 to become an Associate Professor. His field at present is particle technology and applied electrostatics. His current researches involves contact charging of polymer particle and metal plate, and to calculate the potential distribution around the dielectric particle located near a conducting plane.

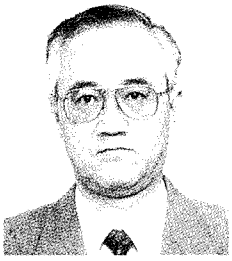

Hideo Yamamoto

Hideo Yamamoto was born in 1943 in Tokyo and graduated from the Department of Chemical Engineering, the University of Tokyo, in 1967. He received the Dr. Eng. degree from the University of Tokyo, in 1979.

He joined the Department of Chemical Engineering, University of Tokyo in 1976, and in 1989 to become an Associate Professor at the Institute of Industrial Science, University of Tokyo. He was a Visiting Researcher at the Delft University of Technology, in The Netherlands, from 1984 to 1986. He joined the Department of Bioengineering at Soka University, as a Professor in 1991.

His field is particle technology and applied electrostatics. His current researches are particles separation from gases, fine powder dispersion in gas, particle size analysis, production and application of ultra fine particles, triboelectric charging of polymer particles, high temperature electrostatic precipitation, electrostatic formation of ceramic membrane, chemical reaction in surface corona plasma, and electrostatically handling of biomaterials.

New Methods for Detecting Physical Phenomena in a Silo†

Yotaro Hatamura, Takatsugu Takeuchi and Masayuki Nakao
*Dept. of Eng. Synthesis, Fac. of Eng. Tokyo Univ.**

Abstract

To ascertain the stress inside silos we developed several kinds of sensors with specific applications: (1) pressure cells, (2) two-directional stress cells, (3) slipping velocity detectors, (4) surface temperature detectors, and (5) internal temperature and slipping velocity detectors.

The detecting sections of pressure cells and two-directional stress cells comprise a parallel plate structure and strain gauges that can detect pressure, and pressure and frictional stress, respectively.

Measurements of physical phenomena in silos lead to the following conclusions: Pressure cells and two-directional stress cells (1) work as designed, and (2) they are capable of elucidating the fundamental physical phenomena in silos.

1. Introduction

Designing a silo with adequate functions and controlling its processes requires that we conceive the overall phenomena occurring in a silo as physical phenomena.

Those physical phenomena are the deformation, force, heat, sound, and others that arise in silo contents and silo walls, and those translate into content flows and internal stress, the stress acting on walls, the load acting on the silo as a whole, the heat quantity generated by grain slippage, the amount of that heat transmitted to silo walls, the sound generated among granules or between granules and walls, and others. However, research heretofore has not investigated these physical phenomena comprehensively [1-12].

The purpose of this research was to develop an "intelligent silo" that can predict future events and control phenomena themselves by using sensors to ascertain these phenomena and comparing the information obtained with a previously prepared knowledge base [13]. This paper explains the sensors developed in order to perform the essential job of acquiring this information and providing the control for turning it into knowledge, and gives examples of measurements obtained in actual use. This silo research comprises five parts: Sensor development, dynamic silo data, elucidation of physical phenomena in silos, silo analogy, and making silos intelligent.

* 7-3-1 Hongo, Bunkyo-ku, Tokyo 113 Japan

† This report was originally printed in J. Soc. Powder Technology, Japan. **34**, 312 (1997) in Japanese, before being translated into English by KONA Editorial Committee with the permission of the editorial committee of the Soc. Powder Technology, Japan.

Ascertaining the phenomena that arise in silo contents generally requires the use of sensors for granular material, which differ from those for liquids. This necessity is particularly evident when measuring stress. To begin with, internal stress in granular material has two components: the force transmitted by contact between granules, and the force transmitted through the liquid or gas filling the interstices among granules (**Fig. 1(a)**). Wall stress acting on inside walls of silos consists of both forces, as shown in **Fig. 1(b)**. For this reason sensors for granular material must accurately measure the sum total of forces from many granules in discontinuous contact with each other.

What is more, as shown in **Fig. 1(c)**, wall stress is actually measured as the vector sum of the component running parallel to the wall (tangential) and the component running perpendicular to it (normal). Because there is great granule-wall friction in silos holding granular material, the tangential force is much larger than the wall stress generated in containers holding only liquids. Granule sensors therefore

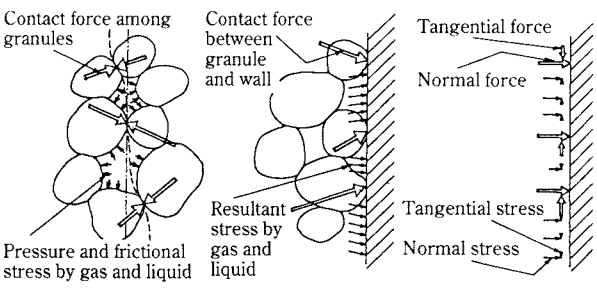

Fig. 1 Granular Stresses

must be able to measure a total of forces in three directions including the normal and tangential forces. Also, localized contact stress is large owing to the small area of contact between granules and the wall, and because granules roll around, wall stress is measured as a discontinuous value. To measure this large discontinuous value accurately, sensors must have resistance to abrasion and a high natural frequency [14].

Following is a discussion of granule sensors that satisfy these requirements.

2. The Newly Developed Sensors

2.1 Stress Sensor

2.1.1 Parallel Plate Structure in Detector

In order to measure granular stress the authors have developed stress sensors whose detectors have a parallel plate structure (**Fig. 2(a)**) [13-15]. The structure consists of a square beam with a square hole in the side, i.e., a movable part and fixed part linked by two parallel plates, upper and lower. When subjected to force in a vertical direction, the movable part is displaced selectively in the downward direction alone, and tensile or compressive strain is generated at both ends of the plate. As this strain is proportional to force, the force can be determined by detecting the strain with four strain gauges incorporated into a wheatstone bridge circuit. This structure has the following features: (1) It can detect force in one direction only, making for little component interference from forces in other directions and from moment; (2) assembling this structure makes it possible to configure various kinds of multiple-force component measuring instruments; and (3) this structure provides greater rigidity than the simple beam, diaphragm, and other structures normally used. **Fig. 2(b)** and (c) show examples of detection blocks using this parallel plate structure. We used (b) in the pressure cell and slipping velocity meter, and (c) in the two-directional stress cell, all of which are described below.

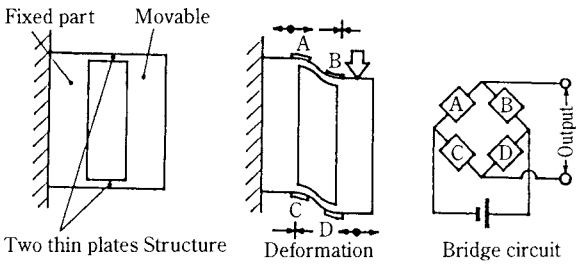

(a) Parallel plate structure [P. P. S.]

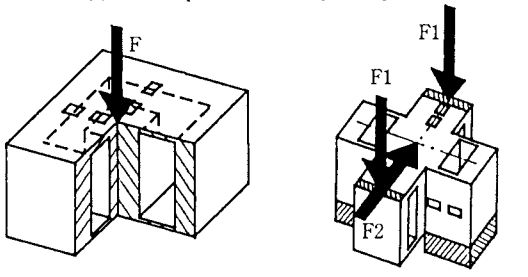

(b) One-directional force detection be P. P. S. arranged in box shape

(c) Two-directional force detection be P. P. S. arranged in cross shape

Fig. 2 Parallel Plate Structure and Its Application

2.1.2 Pressure Cell

Pressure cells are used to detect stress (pressure) acting on the wall vertically. Generally their structure involves the use of flexible, soft diaphragms as detecting sections, so they are susceptible to abrasion and their output characteristics vary. In our research we gave the detecting section and detecting block different functions, and had a hard steel plate as the detecting block (i.e., the part that deforms when exposed to a force). Using this structure allowed us to make sensors capable of obtaining more stable output characteristics.

The pressure cell we developed in this research (**Fig. 3**) is structured so that pressure is transmitted from the detecting surface to the interior quadrangular pyramid, which is supported, through an upper and a lower plate, by the suspending block surrounding it. Pressure is ultimately detected as changes in electrical resistance by the strain gauges attached to the bottom plate. This pressure cell's pressure detection performance has good linearity, nonhysteresis, and sensitivity (**Fig. 4(a)**). It is thought that grains come in contact with the pressure cell's detecting surface at random locations, where a concentrated

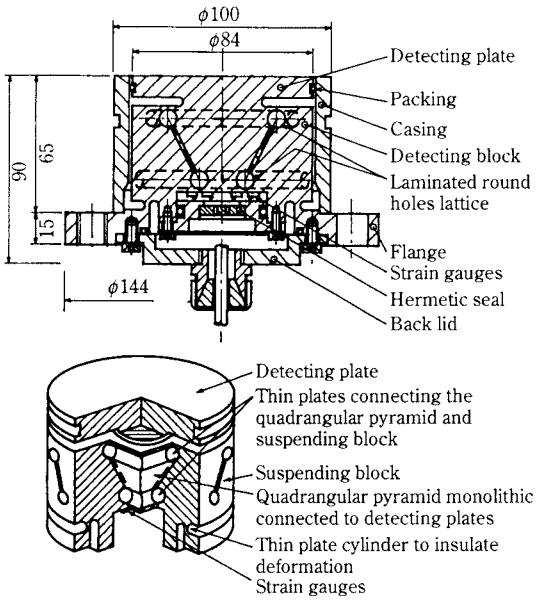

Fig. 3 Pressure Cell Structure

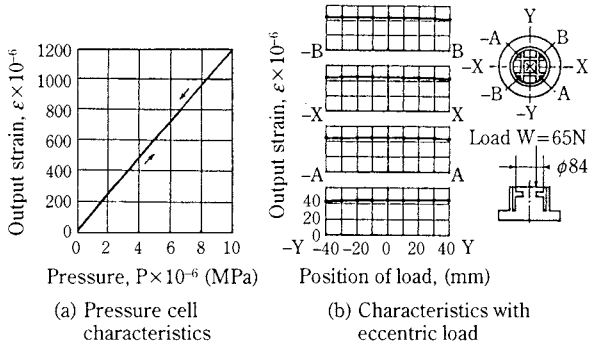

Fig. 4 Pressure Cell Performance

load acts. The graphs show the cell's corresponding performance (i.e., eccentric load characteristics; **Fig. 4(b)**). It is evident that no matter where grains contact the detecting surface, strain gauges get about the same output.

2.1.3 Two-Directional Stress Cell

Because the measurement of frictional stress was important to achieving the objective of this research, we developed a sensor for that purpose as there were none up to that time, the mid-size model silo treated herein releases granules from its bottom. Because grains flow downward, the wall is subjected to mainly vertical and perpendicular (tangential and normal) force components. But as a later report notes, because in large silos large rotational movements are generated around vertical axes, one should take note of the horizontal frictional stress. For the sake of simplification, this paper ignores horizontal frictional stress and focuses exclusively on that in the vertical direction. The stress cell we developed uses two parallel plate assemblies in the detecting block: one for detecting frictional stress and one for detecting pressure. These allow the cell to detect the principal two of the three stress components acting on the wall.

It is the two-directional stress cell that simultaneously detects both stress acting vertically on the wall (i.e., pressure) and stress acting horizontally on the wall (which we shall call either frictional stress or shearing stress) with a single instrument. It detects the two force components: the single-component frictional stress and the pressure created by the granular material inside a silo (**Fig. 5**) [16]. Pressure and frictional stress are transmitted through the detecting section to the cruciform detecting block, which is in contact with the underside of the detecting section's outer edge, pass through the cruciform block from one side and are transmitted to another side intersecting at a 90° angle. At this point pressure and frictional stress are detected separately by two parallel plate

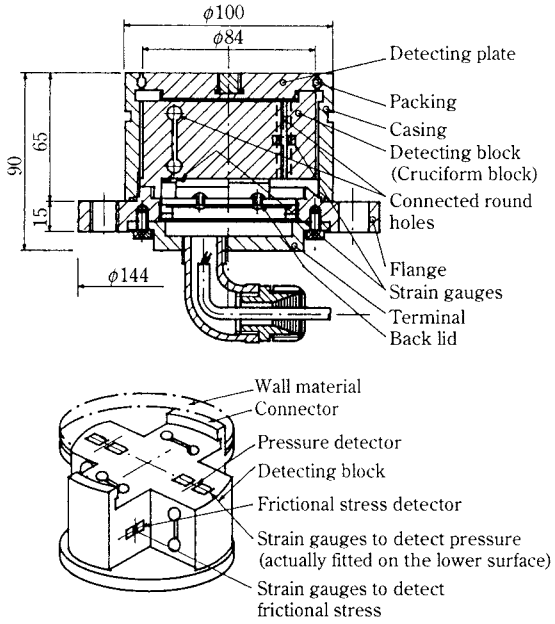

Fig. 5 Structure of Two-Directional Stress Cell

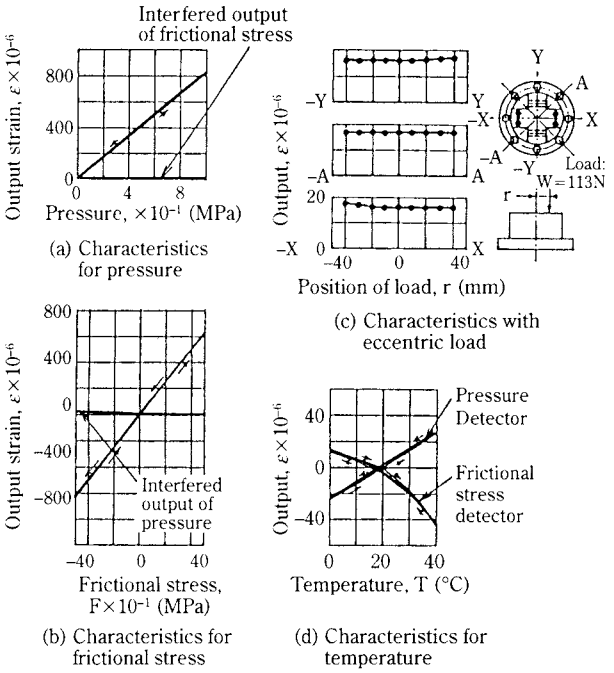

Fig. 6 Performance of Two-Directional Stress Cell

structures inside the cruciform detecting block. Just as in the pressure cell, pressure and frictional stress are detected as changes in electrical resistance from the strain gauges attached to the plates.

Performance graphs for this two-directional stress cell (**Fig. 6**) show pressure detection performance (**a**) and frictional stress detection performance (**b**). All show good linearity, nonhysteresis, and sensitivity. They also indicate that pressure interference in frictional stress output and frictional stress interference

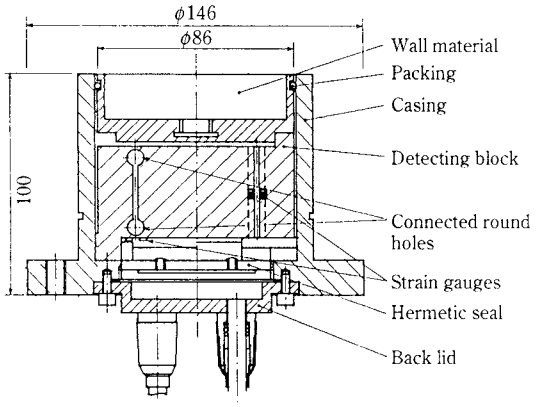

Fig. 7 Two-Directional Stress Cell Exchangeable Wall

in pressure output are very small. The graph for eccentric load (**c**) shows that there is only a small 8% effect on the output at the point on the 84 mm diameter detecting surface upon which the load concentrates. This figure can be ignored in actual use because the largest granule size of our experimental sample was small at under 3 mm, making it impossible for a concentrated granule load to be imposed on that part. The graph for the effect of temperature on output (**d**) was plotted with data that had not been corrected for resistance variation among the four strain gauges, so with correction it would be possible to further reduce the effect of temperature to under 3 μst/°C.

In measuring stress on walls, the material and surface state of the sensor's pressure detecting section must be the same as those of the wall that is being observed, or it is impossible to correctly measure stress because of changes in the frictional state of the granules. This makes it necessary to have a structure capable of changing the material and surface state of the detecting surface at will. An example of this structure (**Fig. 7**) shows how the desired detecting section can be affixed by means of screws.

2.2 Deformation Sensor [17]

2.2.1 Determining Structural Deformation from Overall Information

Generally the supporting structure for a working part deforms in response to the working part's force. Measuring the deformation of the supporting structure therefore makes it possible to estimate the magnitude of the working part's force. This holds for a silo as well, for measuring the deformation of supports makes it possible to find the weight and eccentric load of grains in a silo.

2.2.2 Deformation Sensor

Let us examine the principle by which displacement-caused structural deformation is measured (**Fig. 8**). Affixed to two points on the structure and parallel to it is an assembly connected with a deformation detector having a high-rigidity rod and a parallel plate structure. The parallel plate structure and notch in the rod's center allow this detector to measure deformation of the structure in the x direction alone. Using a deformation sensor to directly detect the amount of change over the distance between two points far apart provides a significantly larger S/N ratio and guarantees sensor protection from changes in the immediate environment, making this method superior to installing direct strain gauges that detect localized strain. The advantage of this method is that it allows stable, accurate detection of force phenomena in a silo.

The deformation sensor we made (**Fig. 9**) is 900 mm long, has a parallel plate detecting section measuring 45×80×20 mm, and a connecting rod 10 mm

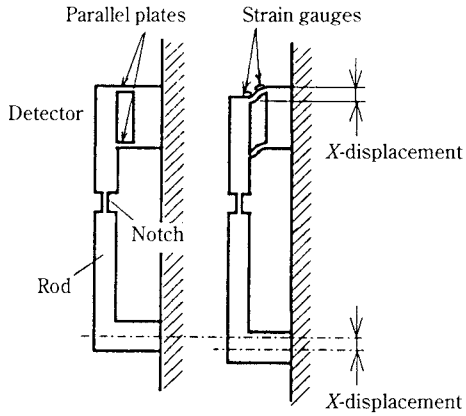

Fig. 8 Detecting Principle of Deformation Sensor

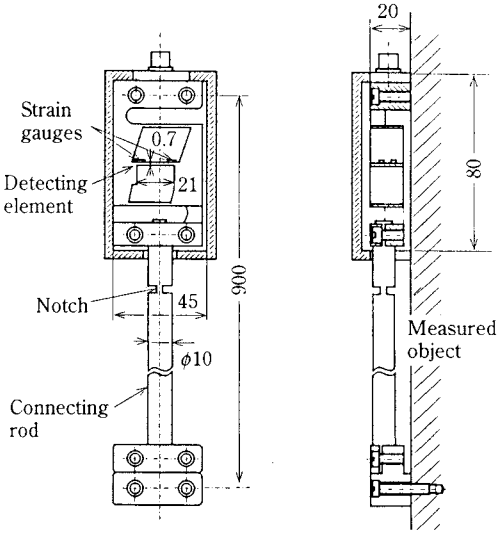

Fig. 9 Deformation Sensor Structure

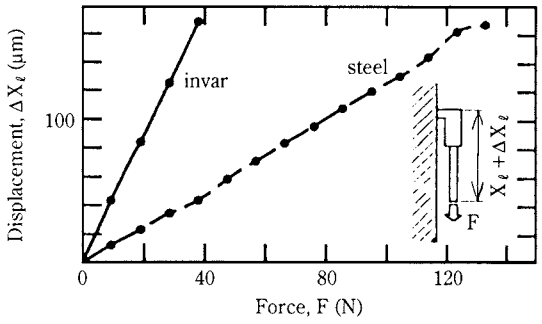

(a) Relation between displacement and force

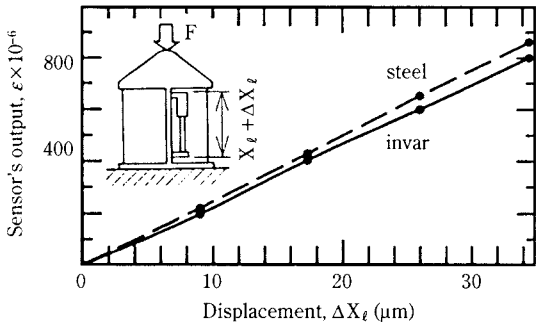

(b) Relation between sensor output and displacement

Fig. 10 Deformation Sensor Performance

in diameter and 820 mm long for joining two points. Deformation of a structure is determined from the strain gauges attached to the parallel plates on the deformation detecting section. Sensor material is steel or invar. The latter has small thermal expansion of 1×10^{-6}/°C, and can be suitably applied to the thermal deformation of steel structures.

We have graphically represented deformation sensor performance (**Fig. 10**). In order to investigate sensor rigidity, one end of a sensor was left free and a weight placed on the bottom. **Fig. 10(a)** shows the relationship between load and load direction displacement. Using this to determine rigidity shows that when the detecting section is made of steel it is 0.83 N/μm, and when invar it is 0.24 N/μm, far smaller than the rigidity of the structure. This sensor's natural frequency is 400 Hz even when using invar. **Fig. 10(b)** shows the relationship between output and deformation when both ends of the sensor are affixed to the structure. Results show that sensitivity to deformation is 24 μst/μm, and that the smallest resolution is 0.05 μm. Also evident is that linearity and nonhysteresis (under 1%) are excellent.

Investigating interference on deformation in other directions showed that while output in the main direction (X) was 24 μst/μm, that in the y and z directions was 0.001 μst/μm, with 2 μst/deg for θ_x, small values showing there is very little interference.

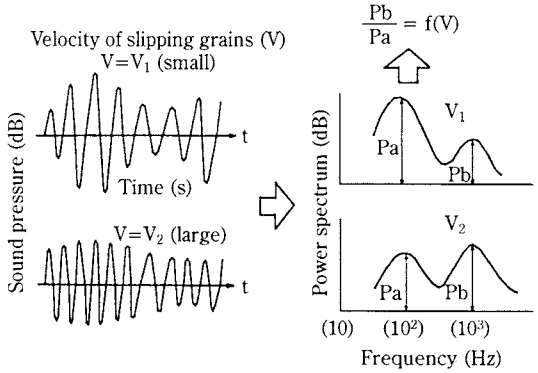

(a) Sound pressure measured by microphone or pressure cell

(b) Power spectrum of sound pressure

Fig. 11 Principle of Detecting Slipping Velocity by Sound Pressure Power Spectrum

2.3 Slipping Velocity Meter

2.3.1 Principle of Detecting Slipping Velocity with the Spectrum Method

Grains produce sound when they slip against a silo wall. As shown in the diagram (**Fig. 11(a)**), the waveform of that sound changes in accordance with slipping velocity magnitude. Frequency analysis of that waveform shows that the height of two representative peaks change relative to one another (**Fig. 11(b)**). For example, when slipping velocity is small (V_1), the higher frequency with the 1,000 Hz peak value (Pb) is lower, while the frequency with the lower 100 Hz peak (Pa) is higher. But when the slipping velocity is large (V_2), it is the opposite: the peak with the higher frequency is high, while that with the lower frequency is low. In view of these findings, our research proposes a method, called the spectrum method, of finding slipping velocity from the ratio between the two peak values by using the correlation between that ratio and slipping velocity. A possible reason for that correlation is inter-granular collisions. Specifically, the larger the slipping velocity, the greater the frequency of inter-granular collisions, and the greater generation of pressure with a high-frequency component.

The development of such a sensor would produce a detector that would detect a totally new physical quantity.

2.3.2 Slipping Velocity Meter Types

The authors used the principle described in 2.3.1 to devise several ways of measuring slipping velocity in granular material. First we tried a way of directly measuring sound pressure. One structural type is the slipping velocity meter using a microphone (**Fig. 12**) [18], which has a condenser microphone connected

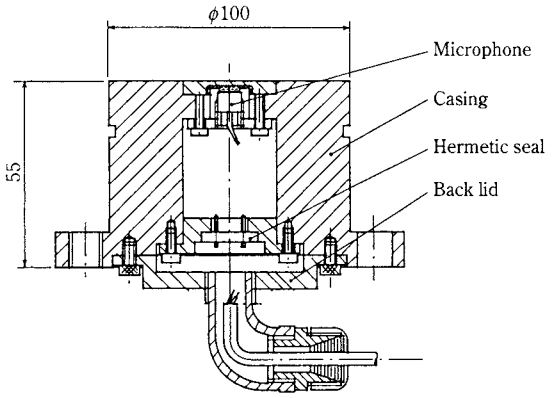

Fig. 12 Slipping Velocity Meter Using Microphone

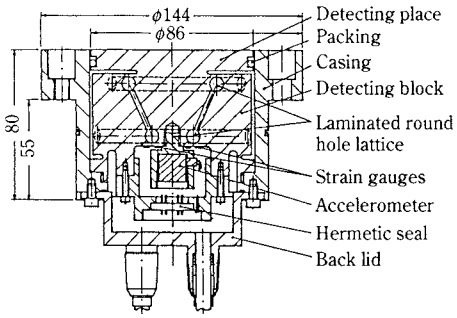

Fig. 13 Slipping Velocity Meter Using Accelerometer

through an ultra-thin pressure plate. Sound pressure is detected as a voltage that is proportional to change in static electricity capacity. But despite the excellent sensitivity of this microphone type, its drawback is that the thinness of the plate over the pressure detecting section makes for poor abrasion resistance and results in varying detection performance owing to abrasion by granules.

To eliminate this shortcoming we devised a method that detects wall acceleration. The slipping velocity meter using an accelerometer (**Fig. 13**) [18] consists of an accelerometer installed in the bottom of the detecting block of the pressure cell described in section 2, and works by using the accelerometer to detect vibration impinging vertically on the detecting surface due to pressure. The spectral distribution obtained in actual use was the same as that obtained with the microphone meter in **Fig. 12**.

Because the structure of the pressure detecting section in **Fig. 13** is the same as that of pressure cells, we next conceived a method of using direct spectral analysis on the output of strain gauges attached to a pressure cell. Using this method yielded the same spectral distribution as the two methods described above. It is therefore possible to determine slipping velocity by analyzing pressure cell output, thereby

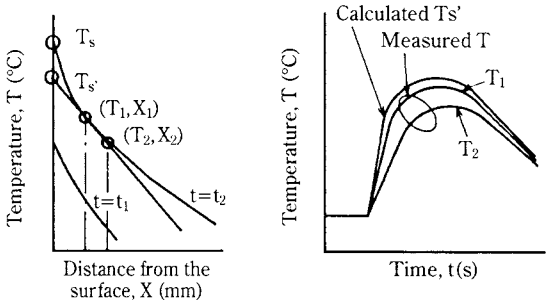

(a) Temperature distribution

(b) Measured temperature and calculated surface temperature

Fig. 14 Surface Temperature Detecting Principle

eliminating the need for making and using separate slipping velocity meters. In future related research we shall adopt this method of determining slipping velocity by spectral analysis of pressure cell output.

2.4 Surface Temperature Sensors

2.4.1 Surface Temperature Detection Principle

Using the principle of finding surface temperature and thermal flux from the temperature difference between two points at different depths (**Fig. 14(a)**), it is possible to find surface temperature T_s from temperatures T_1 and T_2 at two points X_1 and X_2 located at different depths using an inverse Laplace transformation when temperature distribution at a certain time ($t=t_2$) is given [19].

This transformation's linear approximation entails finding surface temperature by a linear extrapolation from temperature change in a micro-area. Surface temperature is found as T_s' in this case. Temperature changes for T_1, T_2, and T_s' as found in this manner are represented in a graph (**Fig. 14(b)**). As temperature change in a silo is not rapid, there is no problem with using the linear approximation value of T_s' for surface temperature even if a precise inverse Laplace transformation is not used. It is possible to calculate thermal flux using the same principle. If such a sensor were developed it would detect totally new physical quantities.

2.4.2 Surface Temperature Sensors

The surface temperature meter used to measure internal silo wall temperature (**Fig. 15**) [20] has two sheathed thermocouples set at different depths from the detecting surface. As the casing material's heat transfer characteristics and thermocouples' positions are known, one can calculate silo wall surface temperature from the temperatures at the thermocouple positions.

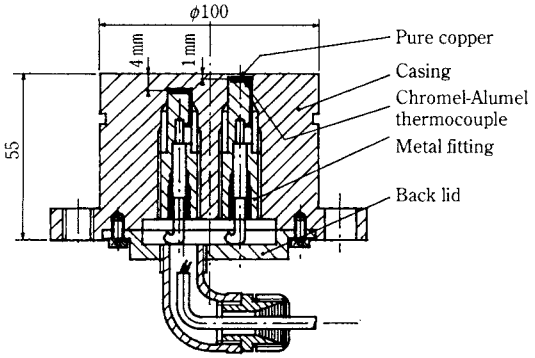

Fig. 15 Surface Temperature Meter

This detector can also detect the thermal flux passing vertically through its own surface (i.e., the heat quantity passing through per unit time per unit area), but owing to the differences between the materials and shapes of the silo and the detector's detecting section, problems remain with regard to the differences between detector readings and actual temperatures in other locations. For this reason we decided not to deal with thermal flux in our research.

2.5 Internal Temperature/Velocity Meter

The authors made a new internal temperature/velocity meter to measure the internal temperature and the velocity of granular material in silos (**Fig. 16**) [21]. This sword-shaped sensor is inserted into the side of a silo at the height where measurements are desired. There it measures the temperature of granular material with thermocouples, and its slipping velocity relative to a beam with a microphone.

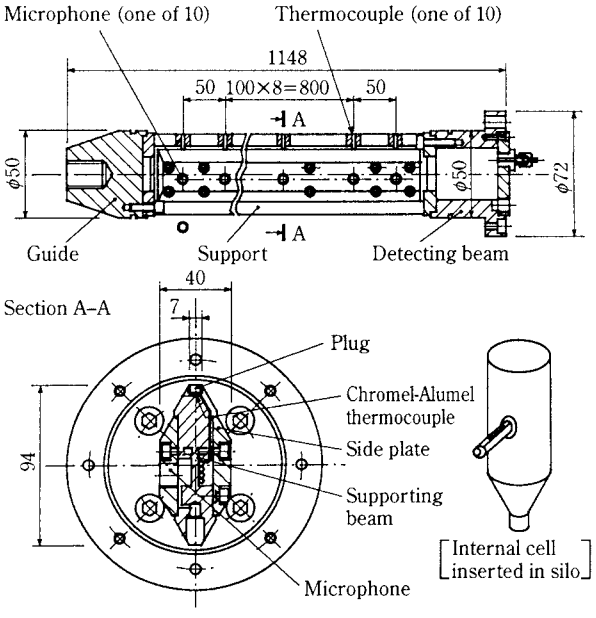

Fig. 16 Internal Temperature/Velocity Meter for Granular Material

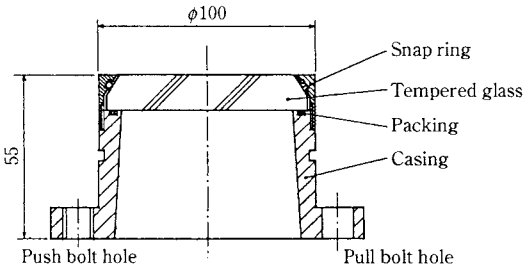

Fig. 17 Observation Window

2.6 Window for Observing Internal Flow

We made an observation window for directly observing the flow of granular material near a silo wall (**Fig. 17**) [21]. It has the same shape as sensors so as to be interchangeable with them. The window has these features: (1) The combination of the push and pull bolts in the outer frame allow one to adjust the glass flush with the silo wall to eliminate indentations or protrusions that would interfere with granule flow, and (2) the use of reinforced glass provides excellent resistance to abrasion.

3. Measurement Examples

To check the performance of the detectors we developed, we gave each a performance test and also verified their practicality by installing them in model silos or real silos.

3.1 Measurement of Stress on Wall

We measured silo wall stress by installing the two-directional stress cells described previously in a mid-sized silo having a cylindrical section 1 m in diameter and 3 m high, and a conical section 0.9 m high with an angle of 60°. These two sections are supported by separate piers and load cells. We installed a total of seven two-directional stress cells, five on the cylindrical section and two on the conical section (**Fig. 18**).

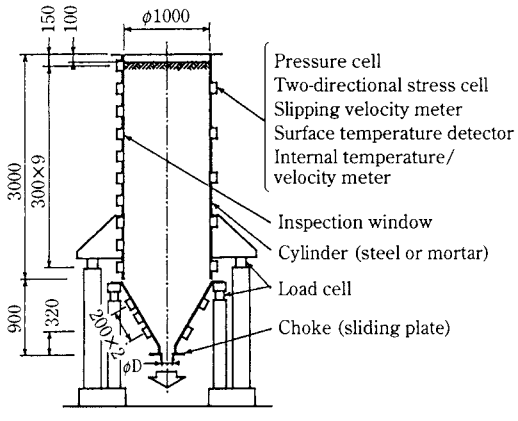

Fig. 18 Medium-size Model Silo and Detectors

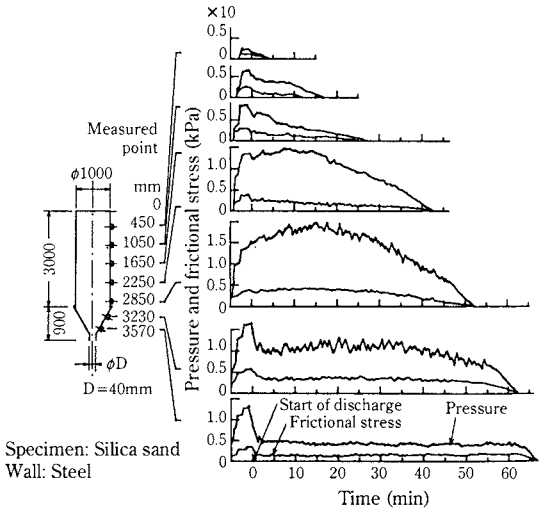

Fig. 19 Example of Measured Pressure and Frictional Stress in Silo Using Two-Directional Stress Cell

Readings for changes in pressure and frictional stress in the mid-size model silo have been graphically represented (**Fig. 19**). The experimental granular material was silica sand with an average granule size of 0.38 mm. The graphs show that when the sand is put in the silo beginning at −5 min, stress rises beginning with the lowest cell and proceeding in order to the highest. As the valve opens and begins releasing the sand at 0 min, the two cells in the conical section register decreases in pressure and frictional stress, while the fourth and fifth cells near the cylinder's bottom show that pressure starts to gradually build, then subsequently decreases. These measurements reveal a phenomenon in which, as granular material begins to exit the silo bottom, the conical section is no longer able to support the silo contents, and the cylindrical section takes over the job of supporting the weight of the material above.

3.2 Measurements of Slipping Velocity at the Wall

We have plotted, as a sound pressure spectrum for each slipping velocity, the output from pressure cells arising when granules slip in a mid-size silo 1 m in diameter and 4 m high (**Fig. 20(a)**). The silo was filled with coal, and the graphs show the spectral analysis results when slipping velocity relative to the wall (i.e., flow velocity) is 6, 12, and 24 cm/s. In all cases peak readings appeared at around 100 Hz and 1,000 Hz (correctly, 150 Hz and 1150 Hz).

Fig. 20(b) shows the relationship between the ratio (*Pa/Pb*) of the peak values (*Pa*, *Pb*) and flow velocity. There were three measured points, and the results show it is possible to measure slipping velocity at the wall from the slipping sound at the wall.

3.3 Measurements of Wall Temperature

We have plotted the temperature changes measured at two points inside a temperature sensor and 1 mm and 4 mm from the silo wall surface, and the changes in inside wall temperature as determined by

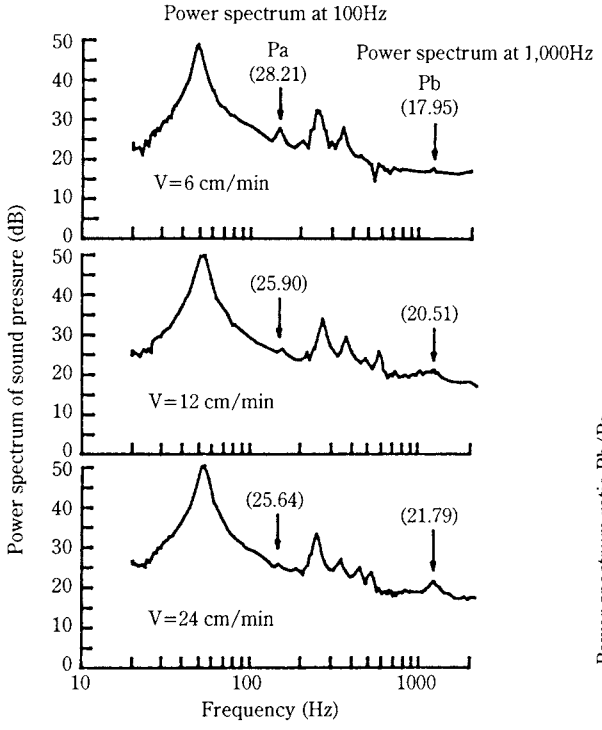

(a) Power spectrum of pressure cell output

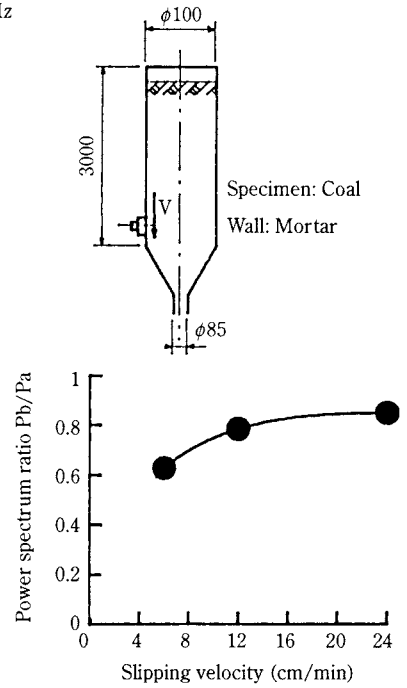

(b) Relation between slipping velocity and power spectrum ratio

Fig. 20 Example of Measured Power Spectrum of Pressure Cell Output in Silo

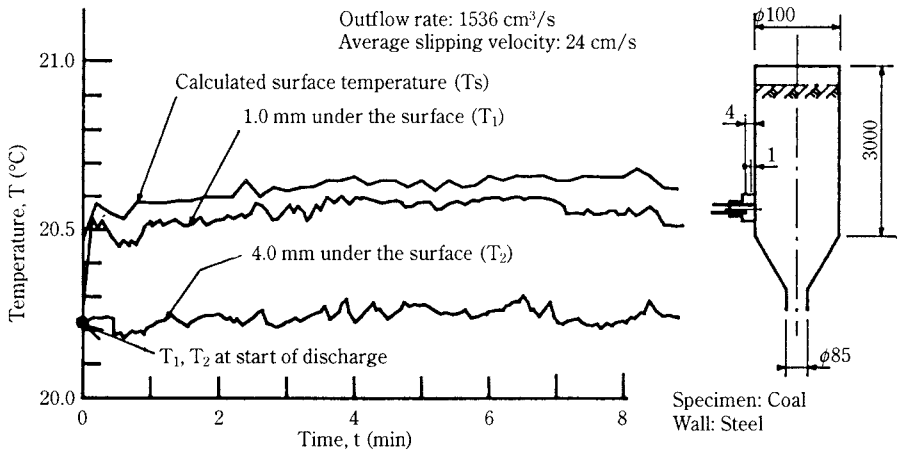

Fig. 21 Example of Surface Temperature in Silo Measured by Temperature Meter

linear approximation calculations from the readings at those two points (**Fig. 21**). After beginning to release silo contents at 0 min, surface temperature immediately rises, and then gradually climbs about 0.4°C while fluctuating.

3.4 Measurements of Internal Flow Velocity and Internal Temperature

The internal temperature/velocity meter shown in **Fig. 16** was used to measure the temperature and flow velocity inside a silo (**Fig. 22**). Temperature increase was very small at a maximum of 1°C, and the peak appears closer to the wall than to the center. This shows that more heat is generated by wall-granule friction than by inter-granule friction.

Flow velocity is higher in the silo center than at the wall. Additionally, velocity immediately after discharge begins is generally greater than that during a steady flow, something that is especially evident in the silo center. These results indicate that immediately after discharge begins, granules at the center start flowing before those near the silo wall.

3.5 Measurements of Silo Structural Deformation

To measure structural deformation we used a silo 1.5 m in diameter and 4 m high (cylindrical section 1.6 m), with a wall thickness of 1.6 mm and central outlet (**Fig. 23**). Deformation sensors were installed at four equidistant points – N, S, E, and W – around

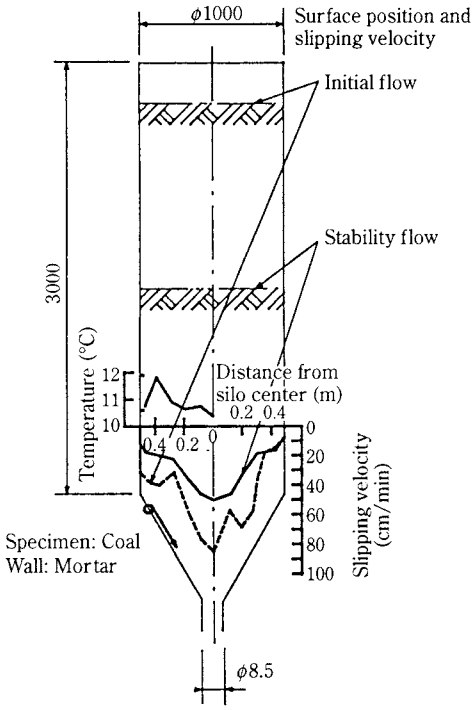

Fig. 22 Example of Slipping Velocity and Heat Generation in Silo Measured by Internal Temperature/Velocity Meter

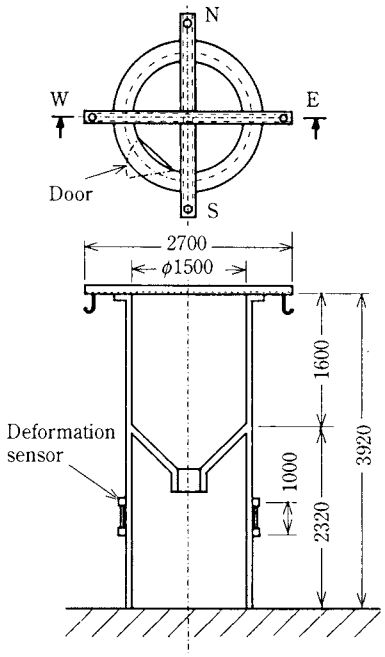

Fig. 23 Method of Measuring Stored Volume in Silo by Deformation Sensors

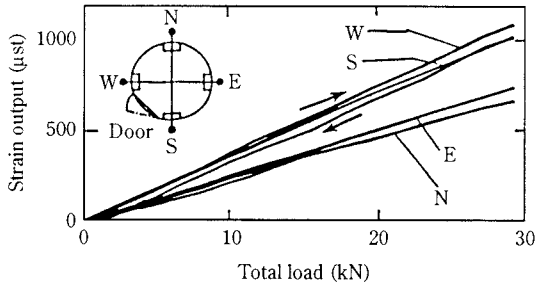

(a) Relation between equalized load and outputs of deformation sensors

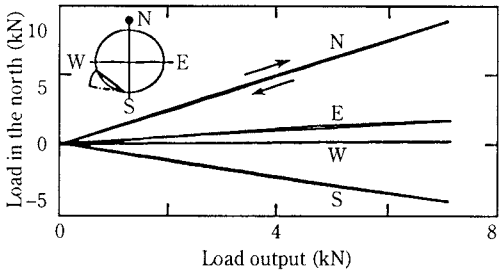

(b) Relation between load in the north and outputs of deformation sensors

Fig. 24 Outputs of Deformation Sensors for Loading on Silo

the silo skirt. Before making measurements we placed two horizontal bars in a plus shape on the silo's top in the N-S and E-W directions so that an eccentric load would be imposed. First we measured the output of all deformation sensors with equal loads in all four directions (**Fig. 24(a)**), and found that W and S deformation was greater than E and N deformation. This was because of the door on the silo skirt in the SW position, which lowered the rigidity of that area. We then read sensor output with an eccentric load at N alone (**Fig. 24(b)**), and found that as a result the north side of the skirt shrank, while the south side was extended. Totaling these load outputs showed that they are equal to the eccentric load at N within 5%.

These data indicate that if silo deformation is measured with a suitable method it may very well be possible to directly measure, with considerable accuracy, the weight of silo contents without the use of a load cell.

4. Discussion

We used the sensors developed in this research to perform measurements for three to four months. While the detecting sections were slightly rusted and abraded, there was hardly any change in their detection performance, results which show they have adequate long-term stability, durability, abrasion resistance, and other qualities.

In stress detection we compared the integral of frictional stress in the entire silo cylinder with the total of the load outputs measured at the three piers supporting the cylinder, and found they were nearly equal. From this we know that the detector correctly detected frictional stress. And because the flow velocity measured with the slipping velocity meter was nearly equal to the velocity as measured visually while granules flowed by observation windows, we know that the slipping velocity meters using pressure cells are correctly measuring the slipping velocity.

As little heat is generated by slipping between granules and the silo wall or among granules, temperature changes found by measurements were very small. Thus, we found that to correctly measure transitional temperature changes it is necessary to place the temperature sensor's internal temperature measurement points closer to the surface than we did in our research (for example, 0.5 mm and 1 mm). Also, when using the internal temperature/velocity meter it is possible that the beam inserted into the silo will disrupt the measuring system itself, but we found that nevertheless it is useful in finding the approximate values for a silo's internal temperature and flow velocity. We also discovered that finding the deformation in a silo's structure makes it possible to measure things such as the total quantity it holds and the eccentric volume, which indicates the need to further develop the methods used here and devise a method using deformation sensors that are easier to install.

5. Conclusion

This paper describes the use of several sensors we developed for granular materials in order to detect physical phenomena in silos. In particular, the use of a parallel plate structure in stress sensors made it possible to develop stress sensors for granular materials that can simultaneously detect the pressure and frictional stress acting on a single pressure-sensitive part, and that have excellent non-interference, eccentric load qualities, and abrasion resistance.

We also developed slipping velocity and temperature sensors that can measure flow velocity and temperature, which could not be checked until now, as well as a deformation sensor that measures the structural deformation of silos. We used these sensors three to four months in experiments on actual silos and found that they have good qualities including long-term stability, durability, and abrasion resistance. Experiments showed that the surface tempera-

ture sensor alone still has room for improvement.

The development of these sensors was necessary to create intelligent silos, and the development of the sensors described here has made it possible to directly obtain data on the physical phenomena occurring inside silos. Building on this will allow development of technologies for intelligent silos. Further papers will report on the analysis of the data obtained, their application to intelligent silos, and other matters.

Acknowledgment

We would like to express our appreciation to Ikeda Manufacturing Co., Ltd. for its cooperation in the development of the sensors described in part 2, and to the Technical Research Center of Takenaka Komuten Co., Ltd. for its cooperation in the measurement experiment (mid-size silo) described in part 3.

Nomenclature

X_ℓ	: distance between measuring points	(m)
ΔX_ℓ	: displacement of X_ℓ	(μm)
F	: force	(N)
V	: velocity of slipping grains	(m/s)
Pa	: power spectrum at 100 Hz	(dB)
Pb	: power spectrum at 1,000 Hz	(dB)
t	: time	(s)
T	: temperature	(°C)
X	: distance from surface of silo	(m)
X_1	: 1.0 mm under the surface	(m)
X_2	: 4.0 mm under the surface	(m)
T_1	: temperature at X_1	(°C)
T_2	: temperature at X_2	(°C)
Ts'	: calculated surface temperature	(°C)
Ts	: calculated surface temperature using an inverse Laplace transformation	(°C)
D	: outlet diameter	(m)

References

1) Richards P.C.: "Bunker design (1)", *Trans ASME Ser. B*, **99-4,** 809 (1977)
2) Rotter J.M.: "Structural design of light-gauge silo hoppers", *J. Am. Conr. Inst.*, **88**, 443 (1990)
3) Sugita M.: "Flow and pressure of non cohesive granular materials in deep bin", *J. Soc. Powder Technol.* Japan, **7**, 513 (1970)
4) Dumbaugh G.D.: "Flow from bulk-solids storage bins", *Chem. Eng.*, **86,** 189 (1979)
5) Jenke A.W. and J.R. Johanson: "Bin loads -Part 2,3,4", *J. Eng. Ind.*, **Feb.**, 1 (1973)
6) Nguyen T.Y., C. Brennen and R.H. Sabersy: "Gravity flow of granular materials in conical hoppers", *Trans ASME, J. Appl. Mech.*, **46**, 529 (1979)
7) Okamoto H.: "Experimental investigation by acoustic method on flow noise of granular mass", *J. Fac. Eng., Univ. Tokyo,* **XXXVI**, 37 (81981)
8) Hidaka J., A. Shimosaka and S. Miwa: "The effect of the particle properties on the parameter of impact sound between two particles", *J. Soc. Powder Technol.* Japan, **24**, 151 (1985).
9) Sindel J.A.: "Temperature differentials in the wall of a clinker-filled silo"., *J. Am. Conc. Inst.*, **82**, 73 (1985)
10) Askegard V. and J. Munch-Andersen: "Results from tests with normal and shear stress cells in a medium-scale model silo", *Powder Technol.*, **44**, 151 (1985)
11) Schulze D. and C. Lyle: "Die Entwickung einer Fuenfkomponenten-Spannungsmesszelle fuer Spannungsmessungen und Silos", *Messtech Briefe,* **24**, 33(1988)
12) Schulze D. and C. Lyle: "A new load cell for measuring normal and shear stresses", *Chem. Eng. Technol.*, **12**, 318 (1989)
13) Hatamura Y. & T. Takeuchi: "A proposal for intelligent silo based on measured phenomena", *Proc. of Sec. World cong. Tech., Tokyo, Japan,* **Sep.** 19-22 (1990)
14) Hatamura Y. & T. Takeuchi: "A new detecting method of granular stresses acting on the silo wall", *Proc. of the First Intl. Conf. on MCGM, Syenyang of China*, **Sep.** 288 (1982)
15) Hatamura Y.: "Development of pressure cell for granular materials", *Prepr. J. Soc. Mech. Eng.* Japan, **825-5**, 7 (1982)
16) Takeuchi T. & Y. Hatamura: "Development of 2-directional stress cell for granular materials", *Prepr. J. Soc. Mech. Eng. Japan*, **827-2**, 171 (1982)
17) Nakao M., T. Okumura, Y. Hatamura, Nagao T. and Ikeda G.: "Development of deformation sensor for extract change of structure", *Prepr. J. Soc. Prec. Eng.* Japan, **k24**, 411 (1993)
18) Okamoto H. & Y. Hatamura: "Development of slipping velocity meter using power spectrum of sound pressure", *Prepr. J. Soc. Mech. Eng. Japan*, **827-2**, 171 (1982)
19) Syoji M.: "Study on an inverse problem of transient heat conduction", *Trans. JSME*, **44-381**, 1633 (1978)
20) Hatamura Y., T. Takeuchi & H. Okamoto: "A trial of surface temperature detector for granular materials", *Prepr. J. Soc. Mech. Eng.* Japan, **827-2**, 233 (1982)
21) Hatamura Y., T. Takeuchi & H. Okamoto: "A trial of inner temperature/velocity meter for granular material", *Prepr. J. Soc. Mech. Eng.* Japan, **807**, 182 (1982)
22) Okamoto H.: "Analysis of power spectrum of sound-pressure on flow noise of grain using simple equipment", *Prepr. J. Soc. Mech. Eng. Japan*, **820-14**, 168 (1982)

Author's short biography

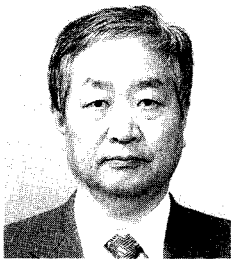

Yotaro Hatamura

After graduating from the Graduate School of the University of Tokyo as a master in mechanical engineering, Yotaro Hatamura joined Hitachi Co. Ltd. in 1966. He became an assistant at the Department of Mechanical Engineering for Production, Faculty of Engineering at the University of Tokyo in 1968. Obtaining his doctorate in 1973, he has been a professor at the Department of Engineering Synthesis since 1983, researching in various fields including nano-micro machining, intelligent manufacturing system, medical engineering, transmission of technology and Creative Design Principle.

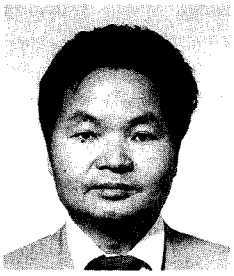

Takatsugu Takeuchi

Takatsugu Takeuchi is Research Associate of Department of Engineering Synthesis of The University of Tokyo since 1967.
His major research interests are development of pressure cell for slurry, development of detector for measuring stress between construction machinery and soil, a study of the compression of granular materials in a square box, a study of silo.

Masayuki Nakao

Masayuki Nakao was born in Tokyo, Japan on September 24, 1958. He received the B.E., M,E. and Dr. Eng. degrees from the University of Tokyo, Tokyo, in 1980, 1982, and 1991, respectively.
Since 1982, he had been engaged in the development of thin film disk in Hitachi Metals, Ltd., Saitama, Japan, and HMT Technology Corporation, Fremont, CA, Since 1992, he has been involved with the research of micro manufacturing as an associate professor in the Department of Engineering Synthesis, the University of Tokyo.

The Characterization of Microgranules Produced by Tumbling Fluidized Bed Granulator with Opposed Pulsed Jet Assembly†

Hiroyuki Tsujimoto, Toyokazu Yokoyama
*Hosokawa Micron Corporation**
Isao Sekiguchi
*Dept. of Applied Chemistry, Chuo Univ.***

Abstract

A new granulation method by a tumbling fluidized bed granulator equipped with opposed pulsed air-jet assembly applied to produce the microgranules having the size distribution in less than 100μm region was investigated. Powdered remedy material, consisting of diclofenac sodium as the main component was microgranulated by the granulator to investigate the effects of the pulsed air-jet on the microgranule properties, and also discuss its growth model. It was confirmed that the microgranules produced by the new method have not only the smaller granule size but the remarkably larger surface area, better solubility and higher compressibility compared with those of the granules made by conventional tumbling fluidized bed granulation. The microgranule growth mechanism was characterized by the following three steps. The first step was the formation process of smaller granules by the agglomeration of feed particles. The smaller granule size depended on the spray mist size. The next step was the successive coating process of the smaller granules. The final step was the coalescence of the smaller granules into final microgranules.

1. Introduction

A tumbling fluidized bed granulation[1] is a modern technology which combines in both tumbling and agitating as granulation principles with batch fluidized bed granulation. Such granulation using the powdered materials less than 100μm in a mean particle size, generally produces the spherical granules with high bulk density having several 100μm average granule size.

Recently, the miniaturization of various kinds of granules has been strongly desired for the development in advanced composite materials. For examples, in the case of ceramics materials applied for several electronic components, the fine spherical microgranules less than 100μm in average with heavy high bulk density, which can not be attained by spray dry granulation, have been frequently required to realize the high density filling of the materials into tiny cells. The miniaturization of the core-particle[2] applied for remedy granules also has been examined.

Although the application of the tumbling fluidized bed granulation to above-mentioned demands has been expected, the miniaturization of granules by using the tumbling fluidized bed granulator has not been yet reported.

In this paper, we examined experimentally the miniaturization limit of granules produced by using a new tumbling fluidized bed granulator equipped with an opposed pulsed jet assembly abbreviated as PJ system hereafter[3),4)]. This PJ system is an advanced dispersion technology using particle to particle collision accomplished by focusing three or more compressed air jet nozzles at the center of a fluidized bed. The compressed air was spouted intermittently from the jet nozzles installed at the sidewall of a granulation chamber for restraining the turbulence of fluidization by the inflow of compressed air into the fluidized bed. The bed particles were partially and intermittently forced into intense movement by the strong shearing and mixing effects of the air jet. Thus, the tumbling fluidized bed granulator with PJ system was expected to apply for manufacturing the microgranules by restraining unwanted large granules generation[3),4)].

Therefore, we attempted to produce the microgranules with granule size below 100μm to find out the advantages of the PJ system by comparing the new

* 1-9 Shoudai-Tajika, Hirakata Osaka 573-1132, Japan
** 1-13-27 Kasuga, Bunkyo-ku Tokyo 112-8551, Japan
† This report was originally printed in J. Soc. Powder Technology, Japan. **35**, 256 (1998) in Japanese, before being translated into English by KONA Editorial Committee with the permission of the editorial committee of the Soc. Powder Technology, Japan.

granulation using the PJ system with the conventional tumbling fluidized bed granulation. Physical properties of the microgranules obtained were also investigated to evaluate the new granulation method.

2. Experimental Apparatus and Procedure

2.1 Feed material and liquid binder

Table 1 shows the physical properties of feed particle. The particles shown in **Fig. 1** were diclofenac sodium (hygroscopic and crystalline powder) widely used as paregoric-antiphlogistic remedy. **Fig. 2** shows its size distribution measured by the Coulter Counter and its volume mean diameter was 4.5μm. The feed particle having both a light bulk density (ρ_b=240 kg/m^3) and a high angle of repose (α=44.0 deg.) showed a bad fluidity of 37 points expressed in term of the flowability index evaluated by Powder Tester (model PT-N, made by Hosokawa Micron Corp.). In addition, an aqueous solution of 5wt% hydroxypropylcellulose (HPC-SSL) was used as a liquid binder and was sprayed from a binary nozzle.

Table 1 Physical properties of feed particles

Feed particles		Diclofenac Sodium
Volume mean diameter of feed particles measured by Coulter Multisizer	[μm]	4.49
Surface area measured by BET method	[m^2/kg]	6200
True density	[kg/m^3]	1490
Bulk density	[kg/m^3]	240
Angle of repose	[deg.]	44.0
Ununiformity expressed by d_{90}/d_{10}	[−]	3.08

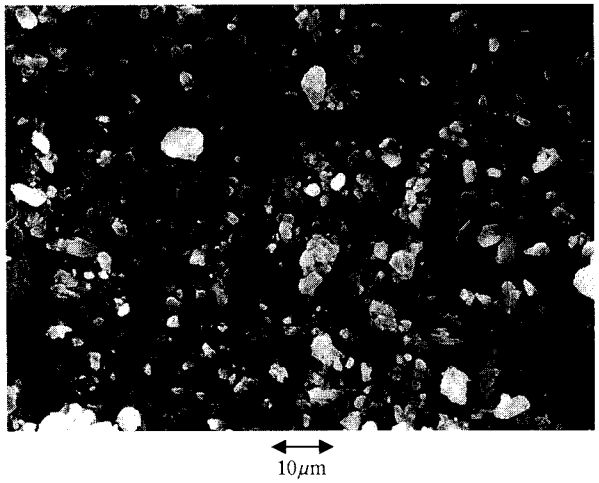

Fig. 1 SEM photograph of feed particles (⟷; scale) (Diclofenac sodium)

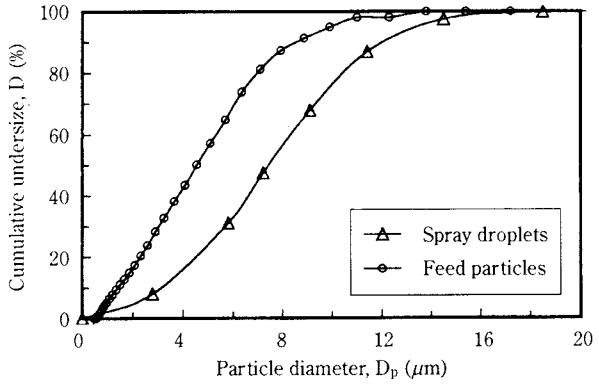

Fig. 2 Size distributions of feed particles and spray droplets

2.2 Experimental apparatus

2.2.1 Tumbling fluidized bed granulator

Fig. 3 shows a schematic diagram of the experimental apparatus employed. The main body of the tumbling fluidized bed granulator (AGM-2A-PJ, Hosokawa Micron) consisted of two parts made of acrylic fiber; a lower cylindrical granulation chamber with a capacity of 2×10^{-3} m^3 and an upper conical-cylindrical chamber in the free board area. A distributor made of a sintered porous stainless steel plate was provided at the bottom of the granulation chamber. A rotor ① with the air slits in the radius directions and the agitator on the distributor was turning on a central axis for creating tumbling and agitating actions of the bed particles. The heated fluidizing air generated by an electrical heater ⑪ and a suction blower ② was blown from both the air slits and the gap between the periphery of rotor and the inner face of granulation chamber to create the tumbling fluidization. Fine particles accompanied by fluidizing air were entrapped at four bag-filters ⑫ and blown down by a pulsed air jet ⑮.

The flow rate of fluidizing air and its temperature were measured using an orifice meter ③ and two

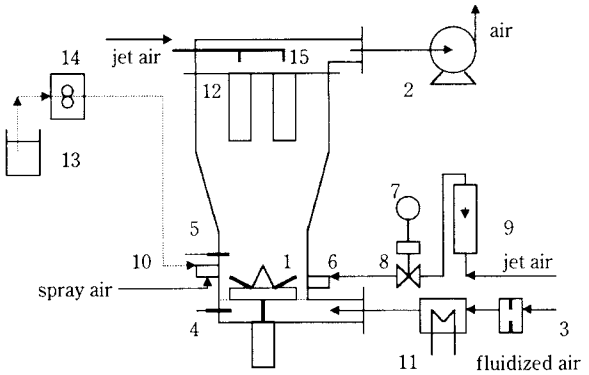

Fig. 3 Schematic diagram of experimental apparatus
1. Rotor equipped with agitator, 2. Fan, 3. Orifice flow meter, 4. Thermometer, 5. Thermometer, 6. Jet nozzle, 7. Timer, 8. Electromagnetism valve, 9. Flow meter, 10. Spray nozzle, 11. Heater, 12. Filter bag, 13. Liquid binder, 14. Pump, 15. Jet nozzle

thermoresistances respectively. The thermoresistances were located at both a lower chamber under the distributor for measuring an inlet air temperature ④ and an upper part of fluidized bed for the bed particle temperature ⑤. The binary nozzle ⑩ located at 4×10^{-2}m high from the distributor was used for atomizing a liquid binder toward the center of fluidized bed.

2.2.2 PJ system.

As the PJ system, three air jet nozzles ⑥ focusing at the center of fluidized bed were installed in the granulation chamber in 120deg. arrangement as shown in **Fig. 4**. An electromagnetic valve ⑧ with the timer ⑦ (**Fig. 3**) controlled both the supplied time t_1 of pulsed air jet from these nozzles and its interval time t_2. The total flow rate of these air jet was measured by a flow meter ⑨, and it was regulated at a constant flow rate of $6.67 \times 10^{-3}\,m^3 \cdot s^{-1}$ with $5kgf \cdot m^{-2}$ in this experiment. When the air jet was injected intermittently, the bed particles were distributed partially as shown in **Fig. 5**.

2.3 Experimental procedure.

Table 2 shows the granulation conditions. The amount of feed particles was 0.5kg in every batch. Anhydrous-silica of 0.675 wt% against the feed particles was added beforehand to improve the fluidity of raw material. The preliminary mixing of feed particles for 700s was performed before the beginning of granulation for not only mixing the feed particles but also increasing the bed temperature. The drying operation after the granulation was pursued for 1200s. These operations involving the granulation were continuously accomplished in the same fluidized bed

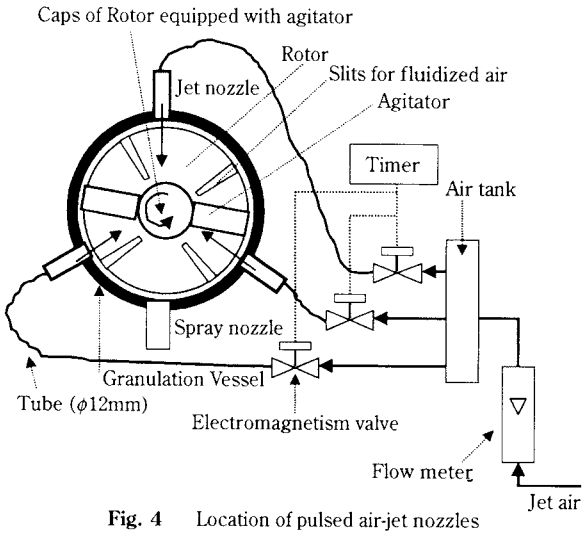

Fig. 4 Location of pulsed air-jet nozzles

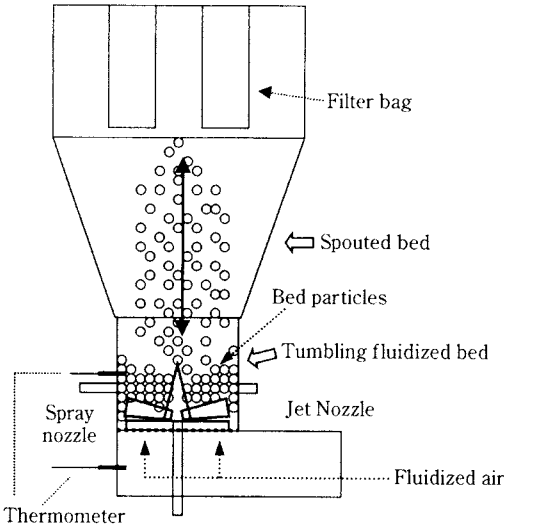

Fig. 5 Flow pattern of the bed particles when pulsed jet in use

Table 2 Granulation conditions

Granulation conditions		R-1	R-2	R-3	R-4	R-5	R-6
Pulsed air-jet		not used	used	used	not used	used	used
Supplied time of pulsed air-jet	[s]	–	0.5	0.5	–	0.5	0.5
Interval time of pulsed air-jet	[s]	–	15	7.5	–	6	3
Supplied number of pulsed air-jet	[–]	–	928	1848	–	1095	2180
Feed weight	[kg]	0.500	0.500	0.500	0.500	0.500	0.500
Granulation time	[s]	13980	13920	13860	6600	6570	6540
Concentration of HPC in liquid binder	[%]	5.00	5.00	5.00	5.00	5.00	5.00
Concentration of HPC in product	[%]	10.39	10.39	10.39	4.76	4.76	4.76
Liquid binder weight	[kg]	1.16	1.16	1.16	0.50	0.50	0.50
Averaged feed rate of liquid binder	[kg/s]	8.30×10^{-5}	8.33×10^{-5}	8.37×10^{-5}	7.58×10^{-5}	7.61×10^{-5}	7.65×10^{-5}
Spray air flow rate	[m^3/s]	9.5×10^{-4}	9.5×10^{-4}	9.5×10^{-4}	9.5×10^{-4}	9.5×10^{-4}	9.5×10^{-4}
Revolution of rotor	[r.p.s.]	9.2	9.2	9.2	9.2	9.2	9.2
Inlet air temperature	[K]	333	333	333	333	333	333
Outlet air temperature	[K]	303~304	302~304	302~304	301~305	302~305	302~305
Fluidized air flow rate	[m^3/s]	5.8×10^{-3}	5.8×10^{-3}	5.8×10^{-3}	5.8×10^{-3}	5.8×10^{-3}	5.8×10^{-3}

granulator for each batch.

The peripheral velocity of the rotor, the inlet fluidized air temperature and its flow rate in above series operations were set at 9.2 rps, 333 K and 5.83×10^{-3} $m^3 \cdot s^{-1}$ respectively as fixed conditions. The PJ system was only used in the granulation operation for the batch tests, which examined the influence of the PJ system upon the granulation performance. In addition, the above-mentioned operational factors reached each set value within about 90s after setting in every batch. The bed temperature reached 304-305K at the end of preliminary mixing and it was raised to 314-316K at the end of the drying operation. The ratio of the additional liquid binder ⑬ to the feed particles Cb was set at 10.4wt% in the case for producing the microgranules having a heavy bulk density and granule strength. Moreover, Cb was set at 4.8wt% considering the balance of granules collapsibility and its fluidity for examining the miniaturization limit of granules. In each case, the liquid binder was continuously supplied at a constant rate by the binary nozzle with the roller pump ⑭ (**Fig. 3**). Besides, the feed rate of liquid binder in each batch was set at a suitable value that the bed temperature was maintained within 302 ± 1K. The amount of compression air for the binary nozzle was set at the maximum value (9.5×10^{-4} $m^3 \cdot s^{-1}$) for the generation of fine spray mists. Consequently, the median mean size of spray mists measured by a particle size analyzer using laser diffraction (2600 Particle Sizer, Malvern) was 7.5μm as shown in **Fig. 2**.

According to the above-mentioned granulation operation, the moisture content of granule product and the recovery ratio of granules in each batch were below 3.5 wt% (wet basis) and over 90 wt% (weight basis) respectively.

The other experimental procedures are described individually in the following part of experimental results.

3. Results and Discussion

3.1 Properties of fine granules at Cb=10.39%

3.1.1 Granule size distributions

The granules size distribution was measured using the sieves (JIS standard sieves) and expressed as a cumulative pass percentage, D (%). **Fig. 6** shows the granule size distributions obtained at Cb=10.39%. The mean size of granules on mass basis prepared by the conventional granulation without using the PJ system of Run 1 was 54μm. Moreover, the granule size at

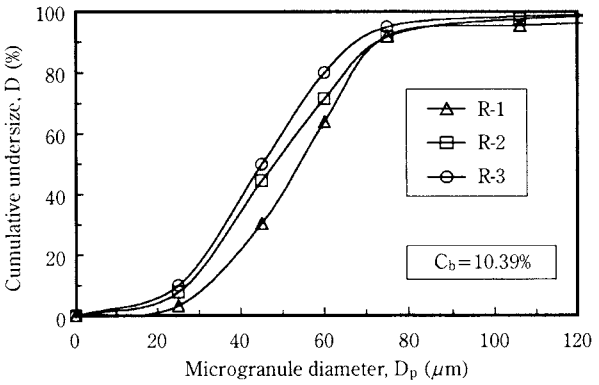

Fig. 6 Size distributions of microgranules

D=95% became 80μm and all granules were below 100μm. An uniformity of granule size distribution D_{90}/D_{10} expressed as the granule size ratio of D=90% to D=10% in cumulative pass percentage was 2.26. According to a previous report [2], the uniformity of the core granules having a mean granule size of 116-181μm prepared using ethenzamide particles in a similar tumbling fluidized bed granulator was from 2.1 to 3.0. As seen from these results, the granulation in this experiment was understood to have obtained the microgranules having the narrow size distribution in less than 100μm region which had been difficult previously.

On the other hand, the granules size distributions were shifted wholly to the fine size area corresponding to the increase of supplied number of air jet in the cases of Run 2 (t_1=0.5s, t_2=15s, n=928) and Run 3 (t_1=0.5s, t_2=7.5s, n=1848), using the PJ system based on the operating conditions of Run 1. As the result, these mean granule sizes decreased to 48μm and 45μm respectively. These uniformity of R-2 and R-3 became 2.73 and 2.68 respectively. The increases of uniformity by using the PJ system were caused by finer granules generation directly leading to the decrease of the value of D_{10}. In this way, at the granulation using the PJ system, the survival of feed particle and the generation of smaller particles by crushing and/or wearing of the granules by the dispersion effect of the air jet were suspected. Then, to examine the presence of these particles, **Fig. 7** (a-1) and (b-1) show the electron microscope photographs of products passed through a 25μm sieve in Run 1 and Run 3. Especially, neither feed particles nor fine particles by crushing and wearing of the granules were observed in the product in Run 3 produced with higher ability of the PJ system as well as the product obtained in R-1 without the PJ system.

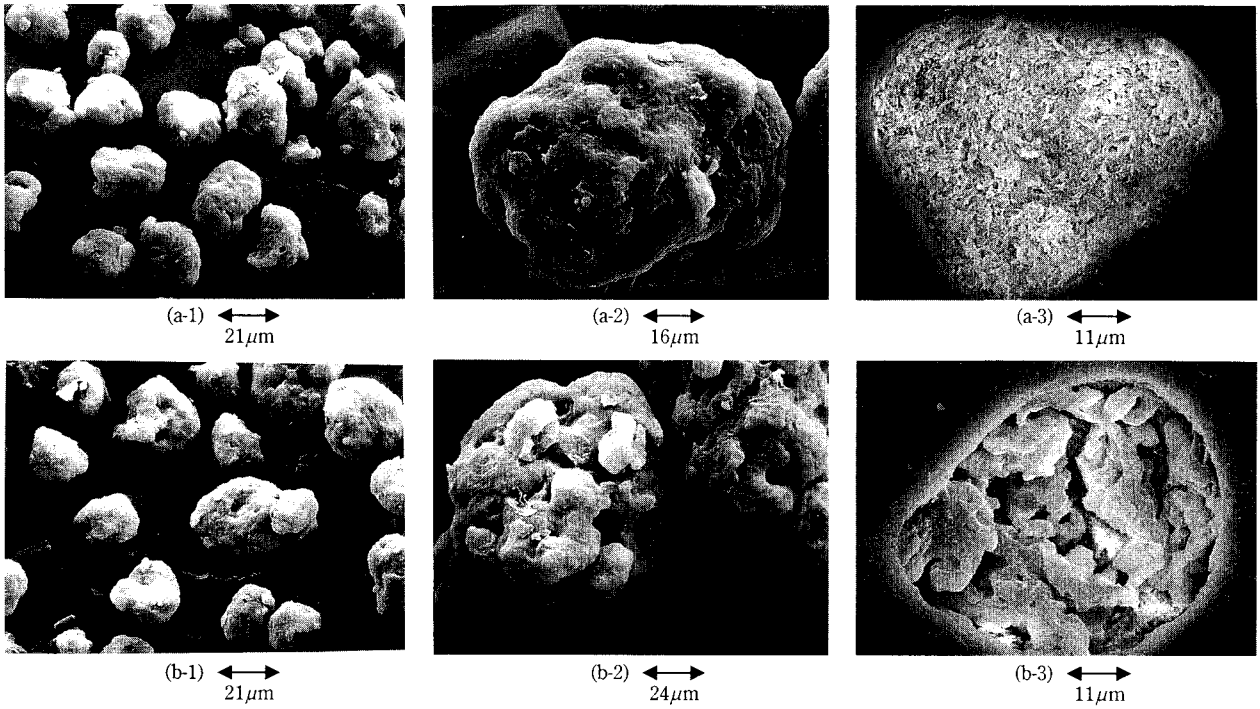

Fig. 7 SEM photographs of microgranules obtained in R-1 and R-3 (⟷; scale)
(a-1): R-1, Products under 25μm (b-1): R-3, Products under 25μm
(a-2): R-1, Products from 45 to 75μm (b-2): R-3, Products from 45 to 75μm
(a-3): R-1, Cross section photograph (b-3): R-3, Cross section photograph

3.1.2 Properties of granules

The photos (a-2) and (b-2) in **Fig. 7** show the surface photographs of granules from 45 to 75μm in R-1 and R-3 respectively. Besides the photos (a-3) and (b-3) similarly show the sectional photographs of granules obtained in R-1 and R-3 respectively, for examining the effect of difference in the granulation method on the granule properties. The granules (R-1) produced by the conventional granulation without the PJ system were recognized to have thicker binder component spread onto the surface of granules as compared with those (R-3) using the PJ system. Moreover, the sectional photograph of granules in R-1 indicated the dense agglomeration resulting in the formation of granules having high bulk density. On the other hand, in the case of R-3, the spreading of binder component onto the surface of granules was less as compared with R-1. The sectional structure of the granules, showing the loose agglomeration formed by primary granules below about 10μm, obviously differed from the case of R-1. The granules in R-2 also indicated similar tendencies as in the case of R-3.

3.2 Lower limit of granule size at Cb=4.76%

3.2.1 Granule size distribution

Fig. 8 shows the granule size distributions obtained at Cb=4.76% for examining the miniaturization limit of granules. Here, the mean granule size and the uniformity of product (R-4) obtained with the conventional granulation became 45μm and 2.56 respectively. The cumulative undersize at D=95% was 75μm. Both R-5 (t_1=0.5s, t_2=6s, n=1095) and R-6 (t_1=0.5s, t_2=3s, n=2180) used additionally the PJ system based on the operating conditions of R-4. Especially, the interval time of pulsed air jet t_2 in R-6 was set at 3s as a maximum condition. Because the formulation of stable tumbling fluidization for pursuing the granulation, became difficult when t_2 was set at shorter than 3s. Namely, the operating condition of R-6 was a limit condition to use stably the PJ system. The mean granule size in both R-5 and R-6 decreased to 36.0μm and

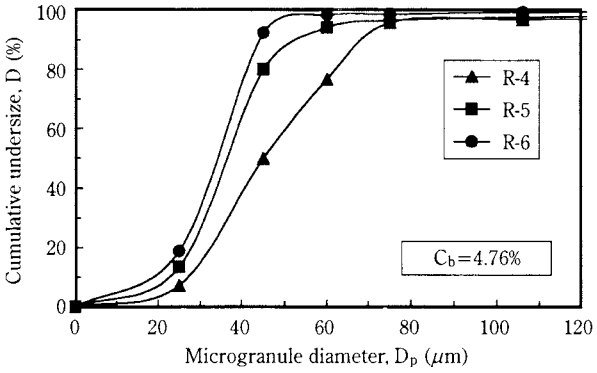

Fig. 8 Size distributions of microgranules

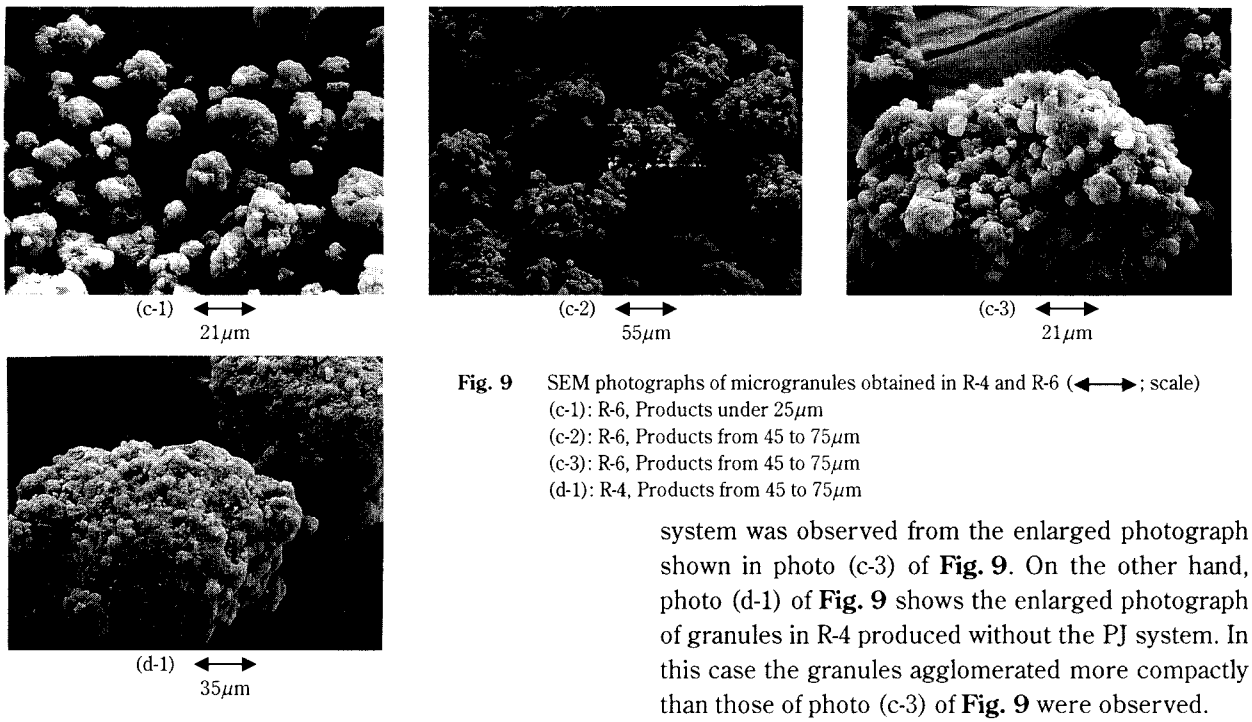

Fig. 9 SEM photographs of microgranules obtained in R-4 and R-6 (◀—▶; scale)
(c-1): R-6, Products under 25μm
(c-2): R-6, Products from 45 to 75μm
(c-3): R-6, Products from 45 to 75μm
(d-1): R-4, Products from 45 to 75μm

33.5μm respectively as compared with R-4, and the cumulative undersize at D=95% attained to the fine region less than 50μm. Moreover, the uniformity also decreased to 2.33 and 2.32 respectively as compared with R-4. Using the PJ system contrary to the results of granulation at Cb=10.39% described in 3.1 led to the decreases of uniformity. The reasons were presumed that the D_{90} value depending on the generation of coarse granules was extremely suppressed by reducing the amount of liquid binder (HPC) by half, and increasing the supplied number of the air jet as well. In addition, the photo (c-1) in **Fig. 9** shows the electron microscope photograph of granules under 25μm of R-6 produced using the maximum ability of the PJ system. The existence of the ungranulated particles also was not observed here. In this way, it was confirmed that the tumbling fluidized bed granulation in the region of microgranules under 50 μm without ungranulated particles was realized by using the PJ system as shown in **Fig. 8** for R-6.

3.2.2 Properties of microgranules

The photo (c-2) in **Fig. 9** shows the granules from 45 to 75μm at Cb=4.76% to examine the influence of the PJ system on the surface properties of granules. This photograph indicated the decrease of the binder component spread onto the surface of granules reducing the Cb by half. Moreover, the formation of porous granules (secondary agglomerated particles) made by soft agglomeration of the fine granules (primary agglomerated particles) from 3 to 10μm using the PJ system was observed from the enlarged photograph shown in photo (c-3) of **Fig. 9**. On the other hand, photo (d-1) of **Fig. 9** shows the enlarged photograph of granules in R-4 produced without the PJ system. In this case the granules agglomerated more compactly than those of photo (c-3) of **Fig. 9** were observed.

3.3 Growth model of microgranules

Fig. 10 shows the growth model of microgranules in accordance with the foregoing observation results. The first step was the formation process of smaller granules (primary agglomerated particles) from 3 to 10μm formed by the agglomeration of feed particles. The size of primary agglomerated granules produced in this process nearly corresponds to the spray mist size. It was presumed that the primary agglomerated granule size was prescribed by the spray mist size. The next step was the successive coating process onto the surface of primary agglomerated particles. The final step was the formation process of final microgranules formed by the coalescence of primary

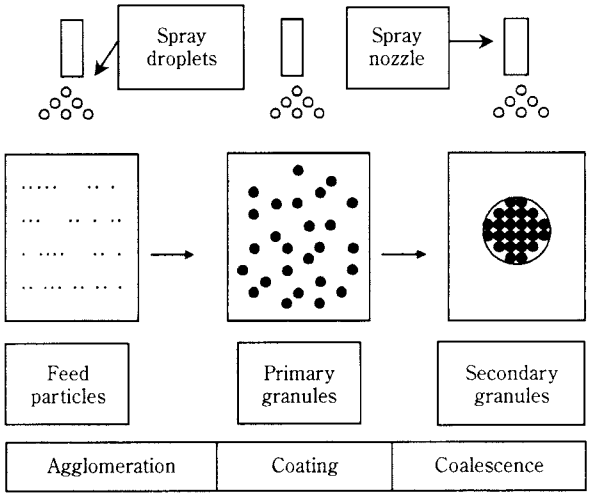

Fig. 10 Schematic diagram of microgranule growth mechanism

agglomerates. Namely, the granulation process of microgranules was categorized as the following three steps, agglomeration/coating/coalescence.

3.4 Other granules properties

The others granules properties such as bulk density, angle of repose, specific surface area, dissolution-disintegration and compression-tension characteristics of microgranule bed were evaluated for examining the effectiveness of the PJ system.

The test samples used for the measurement of both the bulk density and the angle of repose were the final granule product without the sieving. On the other hand, the granules from 25 to 45μm were used for the other tests for eliminating the influence of granule size distributions on the measurement results.

3.4.1 Bulk density and angle of repose

Fig. 11 shows the measurement results by using the powder characteristic tester (PT-N). The bulk density and the angle of repose showed the tendency of decrease and increase respectively corresponding to the increase of the supplies number of the air jet. Moreover, the granules produced at Cb=4.76% showed low bulk density and high angle of repose comparing with that of Cb=10.39%. That is, the bulk density became high in consequence of porous agglomeration in the case of both increasing the supplied number of the air jet and decreasing the added liquid binder as comprehended from the above-mentioned Photographic observation. Furthermore, it was presumed that the increase of the angle of repose was resulted from the increase in the sliding friction between granules due to the increase of the holes of granule surface in the operation using the PJ system.

3.4.2 Specific surface area

Fig. 12 showed the specific surface area obtained by a BET method using liquid nitrogen as an adsorbate at 343K as the deaeration temperature. A rapid surface area analyzer 2200 (Shimadzu Seisakusho) was used as an analyzer. The values of specific surface area were increased corresponding to the increase of the supplied number of the air jet. Especially, the specific surface area obtained at Cb=4.76% were from 100 to 500 times larger as compared with the result at Cb=10.39%. It was thought that the measurement results at Cb=10.39% mainly corresponded to the surface area of secondary agglomerated particles and the measurement results at Cb=4.76% relied on the surface area of primary agglomerated particles.

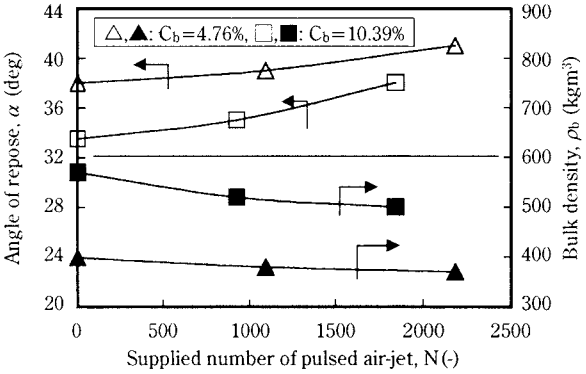

Fig. 11 Bulk density and angle of repose of microgranules

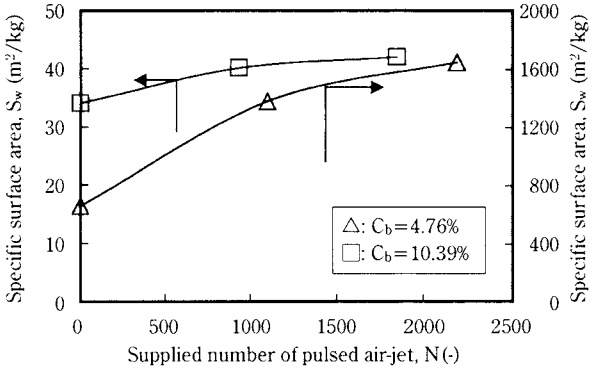

Fig. 12 Specific surface area of microgranules from 25 to 45μm
• Feed particles; Sw=6200m²/kg

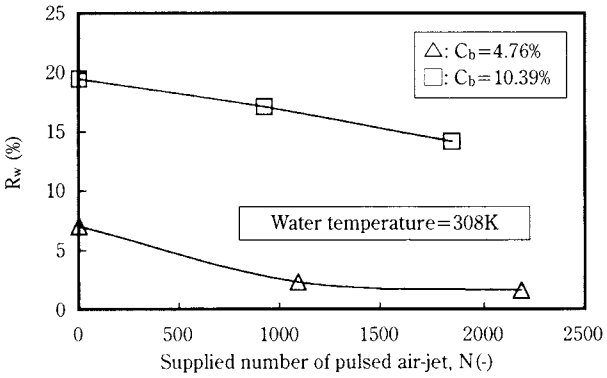

Fig. 13 Mass percentage of residue of microgranules from 25 to 45μm in dispersibility test, Rw
• Feed particles; Rw=22.1%

3.4.3 Dissolution and disintegration

When the produced granules were put into agitated water, a great deal of granules were dissolved easily, but a part of granules formed a comparatively coarse aggregates over 500μm. **Fig. 13** shows the dissolution and disintegration ability of granules in water by evaluating the above aggregates. The granules of 1.5g were put into 100ml water agitated by a stirrer in a beaker of 200ml. The water temperature was fixed at 308K. The dispersed water containing the sample was

passed through the sieve having 500μm opening size after 10s from putting the granules into the water. The weight of the aggregates remaining on the sieve was measured after drying and it was expressed as mass percentage of residue of microgranules in **Fig. 13**. The results were improved in proportion to the specific surface area as shown in **Fig. 12**.

3.4.4 Properties of compaction and tension of microgranule bed

The properties of microgranule bed was measured by a full automatic testing system for tensile strength of compressive powder beds (Hosokawa micron, AGR)[5]. The microgranules were filled in a stainless steel split cell having 15mm inner diameter and 40mm length to be split to upper and lower parts. The compression test was performed by compacting the bed with the compression piston at a fixed speed (0.1 $mm \cdot s^{-1}$) till attaining the set compression stress (1.1×10^{11} $N \cdot m^{-2}$) for measuring both the displacement of the bed caused by the compaction and its compaction stress. After maintaining the compression state at a set stress for 5 minutes, the tensile breakage force, σ_T was measured by raising the upper cell vertically at a fixed speed (0.64 $mm \cdot s^{-1}$).

The symbol L_s shown in **Fig. 14** represents the logarithmic strain expressed using both the initial bed height L_0 and the bed height at maximum compression state L_1.

$$L_s = -\log (L_1 / L_0)$$

The microgranule bed at Cb=4.76% exceeded 0.7 in this L_s value indicating the high compressibility of the bed. On the other hand, the logarithmic strain L_s in the case of Cb=10.39% showed a low value of about 0.3. It was attributable to the production of the microgranules having heavy bulk density with high granule

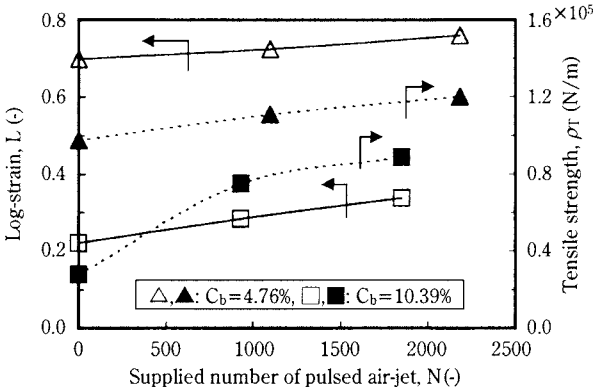

Fig. 14 Log-strain and tensile strength of microgranules bed in the compressive-tensile test at $\sigma_p = 1.1 \times 10^{11} N/m^2$
• Feed particles; $L_s = 0.852$, $\sigma_T = 4.38 \times 10^4 N/m^2$ at $\sigma_p = 2.04 \times 10^6 N/m^2$

strength corresponding to the added liquid binder. In each liquid binder condition, the microgranules formed more porous structure due to the increase of the supplied number of the air jet. Consequently, the compressibility of microgranules and the logarithmic strain L_s were increased. Next, the tensile breakage stress of microgranule bed, σ_T at Cb=4.76% in spite of small amount of added liquid binder indicated a higher value than at Cb=10.39%. The σ_T closely depended on the compaction state of microgranules at the breakage of bed. Namely, the formability by compression of microgranule bed at Cb=4.76% was improved.

4. Conclusions

The production of microgranules using the new tumbling fluidized bed granulator equipped with the PJ system was examined. Properties of the microgranules obtained were evaluated. The conclusions are as follows;

1) The extremely fine granules, having 45-48μm and 33.5-36μm in a mean granule size at the condition of Cb=10.39% and Cb=4.76% respectively, were produced using the PJ system. By means of the PJ system, the granule size distributions shifted wholly to finer size area compared with the conventional granulation without the PJ system. It was clearly found that the new granulation proposed here was a effective method for the miniaturization of granules.
2) The agglomeration of primary agglomerated particles, which leads to the formation of secondary agglomerated particles as a product, was restrained by injecting the air jet. Consequently, the new granulator using the PJ system produced the advanced microgranules having various features such as large specific surface area, good dispersibility and high compressibility.
3) By the observation of the electron microscope photographs, the granulation process of microgranules in this study using fine feed particles was characterized by the following three steps; Agglomeration/Coating/Coalescence.

Nomenclature

C_b	: concentration of solid binder (HPC) in feed particles	[%w.b.]
D	: cumulative mass percentage of under size	[%]
D_p	: particle or microgranule size	[μm]
D_{10}	: 10% particle diameter on a mass basis	[μm]

D_{90}	: 90% particle diameter on a mass basis	[μm]
L_s	: log-strain of compressive microgranule bed	[−]
N	: supplied number of pulsed air-jet in granulation	[−]
R_w	: mass percentage of residue of microgranules in dispersibility test	[%w.b.]
S_w	: specific surface area	[m^2/kg]
t_1	: supplied time of pulsed air-jet	[s]
t_2	: interval time of pulsed air-jet	[s]
α	: angle of repose	[deg]
ρ_b	: bulk density	[kg/m^3]
σ_T	: tensile strength of pre-compressed microgranules bed	[N/m^2]
σ_P	: pre-compressive stress in tensile strength test	[N/m^2]

References

1) Sekiguchi, I.: "Recent Trend in Powder Technology 1991, Granulation", Funtaito kougyou 23, 27-33 (1991)
2) Chu, I., H. Sunada and Y. Yano: "Shuyaku wo beesutosita kakuryuusi no setkkei", Preprints of 13th Symposium on Particulate Preparations and Designs, Soc. of Powder Technology., Japan, pp.96-100, Toyohashi (1996)
3) Tsujimoto, H., and T. Yokoyama: "Fluidized Bed Granulator Equipped with Opposed Pulsed Jet Assembly", *J. Soc. Powder Technology., Japan*, 33, 476-480 (1996)
4) Tsujimoto, H., and T. Yokoyama: "Palusujetto bunsankikou wo tousaisita ryuudousou zouryu coutingu souti niokeru zouryuu coutingu gijyutu", *Funsai*, 40, 57-64 (1996)
5) Tsujimoto, H., Y. Inoue and T. Yokoyama: "Funtaisou asshuku hippari kyoudo jidoukeisoku sisutemu AGGROBOT", *Funsai*, 38, 57-64 (1994)

Author's short biography

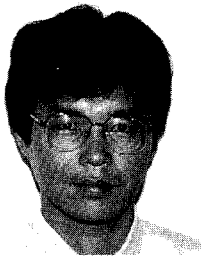

Hiroyuki Tsujimoto

Hiroyuki Tsujimoto received the master degree in chemical engineering from the Chuo University in 1988. His M.S. thesis focused on the research of agglomeration of polymeric powder in a hot fluidized bed granulator. Since his graduation he has been working mainly at R&D section of Hosokawa Micron Corporation, where he developed "Tumbling Fluidized Bed Granulator with Opposed Pulsed Jet Assembly" in 1994. His primary research interest is in new granulation technology of "Direct Granulation Method of Liquid Material in a Fluidized Bed Granulator".

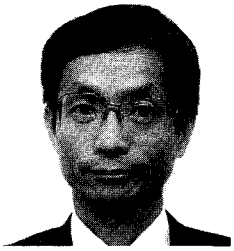

Toyokazu Yokoyama

Toyokazu Yokoyama graduated in Chemical Engineering from Kyoto University and received M.S. in 1975. Then he spent six years in Europe to study powder technology at Karlsruhe University and to work as an engineer for Hosokawa Europe Ltd. in Cologne and near London. After another six year work in the engineering division and laboratory of Hosokawa Micron Corp. in Osaka, he was engaged in research at Nagoya University, where he received Ph.D. on the subject of fine wet grinding by ball media mills. Since 1992, he is a manager of Hosokawa Micromeritics Laboratory. His major interests are particle design and processing for advanced functioning by mechanical composing and granulation methods as well as fine grinding and particle characterization.

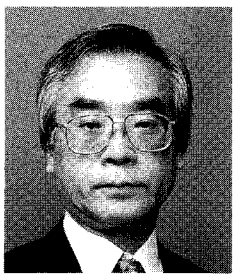

Isao Sekiguchi

Dr. Isao Sekiguchi graduated from the Department of Industrial Chemistry, Chuo University in 1958, and obtained the Doctor degree of Engineering from Tohoku University in 1975. Since 1977, he is a professor in the Department of Applied Chemistry, Chuo University. His main research in the field of granulation techniques is concerned with fundamentals and extended application which cover three areas: fluidized bed granulation, tumbling granulation and spray drying or prilling. Additional research topic being pursued at present is a new development in the use of microcapsuled asphalt powder as an auxiliary in soil stabilization.

The 32nd Symposium on Powder Technology

The 32nd lecture and debate symposium on powder technology was held on August 27, 1998, at the Hotel Laforet, Tokyo under the sponsorship of the Hosokawa Powder Technology Foundation and with the support of Hosokawa Micron Corporation. With more than 210 people in attendance and with inspired lectures and heated debates, the symposium was a great success.

The present symposium focused on powder agglomeration and particulate design. In particular, lectures were given on basic and applied technology for medical products and the foodstuff industry.

The 32nd Symposium on Powder Technology

Theme : Recent Agglomeration and Particulate Design
— focusing on medical products and foodstuff manufacturing processes —

Session 1 KONA award commemorative lecture (Agglomeration and Particulate Design)
Chairmanship: Prof. Yoshinobu Fukumori (Kobe Gakuin University)

- Various Basic Phenomena in the AFBG Process and a Few Other Topics — Prof. Isao Sekiguchi (Chuo University)
- Design of Polymer Nano-particle Systems and DDS Development — Prof. Yoshiaki Kawashima (Gifu College of Pharmacy)

Session 2 (Particulate Design and Simulation)
Chairmanship: Prof. Kei Miyanami (University of Osaka Prefecture)

- Discrete Particulate Simulation (Practicability and Issues) — Prof. Yutaka Tsuji (Osaka University)
- Particulate Micro-Design in the Manufacture of Foodstuff — Teruo Yoshida (Foodstuff Central Research Center, Ajinomoto Co., Inc.)

Session 3 (Application to the Pharmaceutical and Foodstuff Industries)
Chairmanship: Yoshitaka Kuwahara (National Industrial Research Institute of Nagoya)

- Design of Dry Powder for Steroid Type Bronchial Asthma Medicine KSR-592 — Kazuhiko Ikegami (Formulation Research Center, Kissei Pharmaceutical Co., Ltd.)
- New Agglomeration and Coating Technique Using a Fluid Bed Applied Apparatus — Hiroyuki Tsujimoto (Hosokawa Micron Corporation)

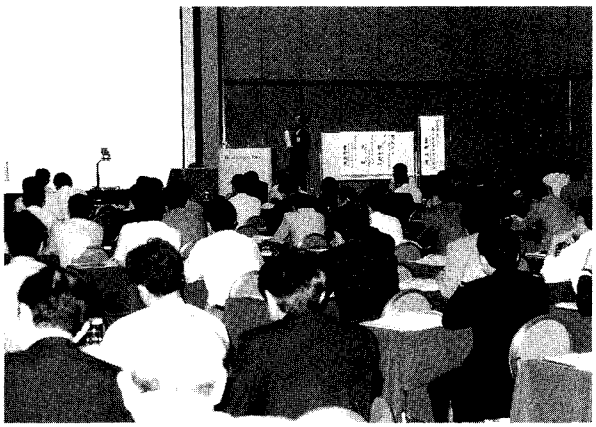

The 7th KONA Award

The 7th KONA Award sponsored by Hosokawa Powder Technology Foundation and given to the scientists or groups who have achieved excellence in the researches related to the basic powder technology, was presented to Professor Yoshiaki Kawashima of Gifu College of Pharmacy and to Prof. Isao Sekiguchi of Chuo University by Masuo Hosokawa, President of the Foundation on January 19, 1998 at the R&D Center of Hosokawa Micron Corporation in Hirakata.

Prof. Kawashima's achievement consisted mainly of developing an original design method for the production of agglomerates with various medical functions (quick solubility, slow release characteristics, fluidity, tableting characteristics, consistency of content), by agglomeration processing in a liquid.

Firstly, various characteristics can be given to the primary and secondary properties of various medicines obtained by spray-drying under controlled drying temperature and spraying conditions. This showed that micro-capsules can be made in various shapes as well as methods for regulating the slow release characteristics, etc., of medicines.

Secondly, Prof. Kawashima made kinetic studies on the wet spherical agglomeration method by model experiments using calcium carbonate powder and computer simulations to clarify the agglomeration mechanism. On the basis of this basic study, the functional characteristics of produced agglomerates were researched in regards to various liquid systems and systems in which the various medicines would be used, and ways were developed for their application as coatings for medicines and for the DDS method.

Thirdly, spherical crystallization was developed as a further extension of the wet agglomeration method mentioned in the 2nd paragraph above, and a composite processing method of simultaneous crystallization and agglomeration was developed for the first time. This method was further expanded to reaction systems, and it was shown that reaction and agglomeration could be achieved simultaneously.

The above three methods enabled simultaneous control over the primary characteristics of particulates and secondary characteristics of particulates after agglomeration, and have been widely accepted as a process proposal by which various high function medicines can be easily made. In this way, Prof. Kawashima's achievements have resulted in the development of many new conceptions and application aspects, and consequently have established a new method for designing particulates of superior functioning for medicines.

In contrast to the agglomeration in liquids by Prof. Kawashima , Prof. Sekiguchi's research mainly concerned agglomeration in a gaseous phase. This operation has been widely performed since ancient times, but it is an unstationary phenomenon in which an extremely great number of factors are involved and for which theoretical analysis is extremely difficult to make. In view of the technical importance of this operation, Prof. Sekiguchi proceeded with research in this field.

Basic research was conducted on a number of typical agglomeration methods and outstanding results were obtained, including a particle size distribution rule. Also, the various and diverse agglomeration methods and agglomeration apparatuses used in the respective industries were classified by their principle of operation, characteristics of materials and demands placed on products. This helped systematize the overall agglomeration technology. Furthermore, he introduced a large number of technical books and handbooks covering many technical fields, giving substantial guidance to technicians and researchers in related industries.

Academic publication concerning powder technology in Japan (1997)

Journal of the Society of Powder Technology, Japan Vol.34 (1997)

Title	Author(s)	Page
〈**Research Papers**〉		
• The Fractal Dimension of a Particle's Projected Shape by the Area-perimeter Method	M. Suzuki, S. Yamada, H. Kada, M. Hirota and T. Oshima	4–9
• The Mechanochemical Polymerization of Methyl Methacrylate Initiated by the Grinding of Quartz and Quartz Glass	M. Hasegawa, M. Sato, S. Sakuyama and M. Kimata	10–16
		17–26
• The Dividing and Packaging Characteristics ruring Dispensing and the Content Uniformity of Fine Granules	M. Ohkuma, Y. Kato, T. Ishikawa, Y. Ohtani, K. Kawano, S. Takamatsu K. Kawada and S. Nakajima	
• A Study of Variable-Pressure Consolidation	W. Xiaomin	84–90
• Electrification of Fine Particles in Gas-Solids Pipe Flow	H. Masuda, S. Matsusaka, S. Akiba	91–96
• Mixing and Surface Modification of Raw Materials for Poly-vinyl-alcohol (Vinylon) Fibers-reinforced Cement-based Building Materials Using a High-velocity Pneumatic Double-stage Impactor	S. Taniguti and M. Nakamura	97–106
• The Electrostatic Force between a Charged Dielectric Particle and a Conducting Plane	T. Matsuyama and H. Yamamoto	154–159
• Production of Monodispersed TiO_2 Particles by the Three-Phase Alkoxide Method	T. Mineo, A. Tsutsumi and K. Yoshida	160–164
• The Formation of Dispersed Calcium Hydroxide Fine Particles by Alkoxide Method	T. Tsuruoka, M. Yokota, M. Sakurai A. Tsutsumi and K. Yoshida	165–169
• Preparation of Fine Mullite Powders with High Surface Area by Agglomeration Control of Alkoxide-derived Precursor Sol	H. Suzuki, M. Shimizu, H. Kamiya M. Takahashi and T. Ota	170–175
• Coating on Barium Sulfate and Magnetite by Hydrolysis of Metal Alkoxides	M. Kimata, M. Koizumi and M. Hasegawa	206–211
• The Stress-strain Rate Relationship for Flowing Coarse Particle Powder Beds Obtained by the 3-Dimensional Distinct Element Method and Experiments	S. Yuu, A. Hayashi, M. Waki and T. Umekage	212–220
• The Improvement of a New Estimation Method of Particle Size Distribution by Anisokinetic Sampling –The Estimation of both Median Diameter and the Deviation of Distribution by Changing the Particle Inertial Parameter–	H. Tsuji, H. Makino, M. Kimoto H. Yoshida and K. Iinoya	221–227
• The Fluidization of Fine Particles under Vibrated or Reduced Pressure Conditions	K. Noda, Y. Sakae, H. Iijima S. Uchida and T. Suzuki	228–232
• The Mechanism of the Break-down and Coalescence by Impacting Particles	S. Taniguchi, M. Nakamura and T. Higuchi	233–240
• New Methods for Detecting Phenomena in a Silo	Y. Hatamura, T. Takeuchi and M. Nakao	312–323
• The Correlation between Size Reduction and the Mechanical Activation of Talc by a Multi-ring Media Mill	K. Hamada, S. Yamamoto and M. Senna	324–329
• Evaluation of the Mixing Process Based on a Disintegrating-rate-model of the Powder Agglomerates	M. Satoh, T. Yoshida, T. Yanagida T. Iwasaki and H. Kimura	330–336
• The Rapid Dissolution of Trace Amounts of the Iron Formed by Abrasion in Wed Grinding	T. Katsuyama, K. Takekoshi and Y. Kanda	337–341
• The Effect of the Mechanical Properties of Powder on the Characteristics of Dense Phase Horizontal Conveyance of Powder	M. Hirota, T. Matsumoto, M. Adomi Y. Kita and M. Suzuki	394–399
• A Study of a Particle Suction Nozzle with an Injection Port	T. Nozaki, Y. Horinouchi, M. Fukuhara	400–404
• Critical Plug Length at Natural Plug Formation	M. Takei, M. Ochi and Y. Takabe	405–410

Title	Author(s)	Page
• The Investigation of a Screening Model by the Information Theory −Verification and Development of Miwa's Probability Model−	T. Ozaki, S. Miwa and K. Hara	750−758
• The Evaluation and Expression of Fine Grindabillty Using a Ball Mill Grinding	N. Kotake, S. Abiko, S. Yamaguti and Y. Kanda	759−766
• The Miing and Deagglomeration Characteristics of an Agitationg-type Mixer	Y. Sugai, M. Satoh and M. Kobayashi	767−772
• Homogeneous Precipitation of Alumina Precursors with the Enzymatic Decomposition of Urea	H. Unuma, S. Kato, T. Ota and M. Takahashi	773−777
• The On-line Monitoring of the Electrostatic Field Strength in Fluidized Bed Granulation and Drying Using a Newly Developed Electrostatic Field Detecting System	S. Watano, Y. Ito, T. Suzuki and K. Miyanami	778−784
• The Dispersion Behavior of Coarse Particles by Lateral Vibration under Microgravity	Y. Ohyama, H. Takeuchi and A. T. Pyatenko S. Chiba and K. Shinohara	834−839
• The Effect of Particle Properties on the Morph-ological Change Induced by Impaction against a Solid Surface for Tristearin Powder Mixed with Hard Particles	K. Fukui, H. Masuda, K. Nakao M. Suzuki, K. Baba and K. Hashimoto	840−848
• The Preparation of Coated Particles Using a Precipitant Precursor Injection Method	H. Nakamura, N. Yamada, E. Abe and H. Takeyama	849−854
• An Advanced Method for the Measurement of the Particle Size Distribution by Anisokinetic Sampling −Investigation of a Method Using Three Probes with Diffetent Diameters−	H. Tsuji, H. Makino, H. Yoshida and K. Iinoya	904−912
• The Effect of Particle Size on the Movement of a Striped Pattern Deposition Layer in an Aerosol Flow	I. Adhiwidjaja, S. Matsusaka, T. Hamamura and H. Masuda	913−918
• Measurement of the Mass Flow Rate of a Polymer Powder Based on the Static Electrification of Particles	H. Masuda, S. Matsusaka and H. Shimomura	919−923

Kagaku Kougaku Ronbunnshu Vol.23 (1997)

Title	Author(s)	Page
• Synthesis of Processes for Recovering Metals from Incineration Fly Ash of Municipal Solid Wastes	J. H. Kim, J. G. Yang and E. Kunugita	47−52
• Controlled-Release Behavior of Nicotine from Chitosan Microparticles Coated with Artificial Lipids	K. Yoshizuka, H. Ohta, K. Ohto and K. Inoue	53−58
• Hydrodynamic Behavior in Spout-Fluid Beds of Binary Mixtures of Particles	T. Ishikura, H. Nagashima and M. Ide	59−66
• Analysis of Mixing Mechanism of Wet Particle System in Kneading Process with Dispersion Model	Y. Kawaguchi, M. Kaminoyama, K. Nishi and M. Kamiwano	103−109
• Preparation of Polymeric Hollow Microspheres	K. Ijichi, H. Yoshizawa, T. Ashikari Y. Uemura and Y. Hatate	125−128
• Preparation of Fine Ammonium Perchlorate by Freeze-Drying	M. Kohga nd Y. Hagihara	163−169
• Iron Powder Production through Spontaneous Agglomeration and Sedimentation in a Fluidized Bed	T. Mikami, H. Kamiya and M. Horio	208−215
• Flux and Particle Concentration of Induction-Charged Powder Coating in a Field with Horizontally Set Parallel Plate Electrodes	Y. Ohkubo and Y. Takahashi	216−223
• Preparation of Ultraviolet Shielding Composite Fine Particles by the Spray Dry Method and Their Optical Properties	K. Ohshima, K. Tsuto, K. Okuyama and N. Tohge	237−242
• Application of Fuzzy Control to Stable Operation of a Fluidized Bed Granulator	H. Tsujimoto, T. Yokoyama and I. Sekiguchi	353−362
• Elaborate Classification of Flyash Particles by Bench Scale Air Cyclone	H. Yoshida, T. Yamamoto, K. Okanishi H. Morisaki, T. Nakamura and K. Iinoya	363−370

New Product News

Mikro Classifier CC

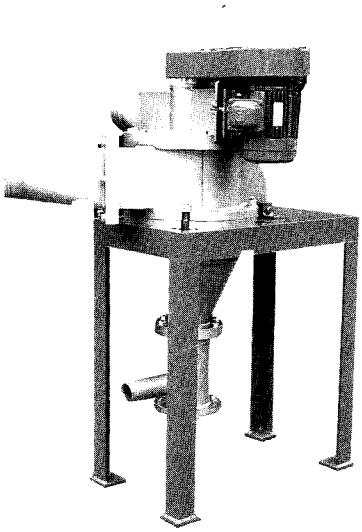

With this new classifier from Hosokawa MikroPul, powder coating production can be much more efficient. By using air classification with a high sharpness of cut, yield can considerably be increased, while losses decrease in similar scales.

An improved rotor design, secondary air flow and integrated central fittings create an optimum of material and air flow. As a result, agglomerates are significantly well dispersed.

The new MikroClassifier operates in a wide range of cut sizes between 5 μm and 100 μm. Off-line and Inline classification is possible.

Tests showed that this system is in an ideal way suitable for powder coating products (epoxy or acrylate based) with enormous positive appeal to production. Other products which can be processed are minerals, food (sugar) and other fine or finest materials.

MikroTemp™

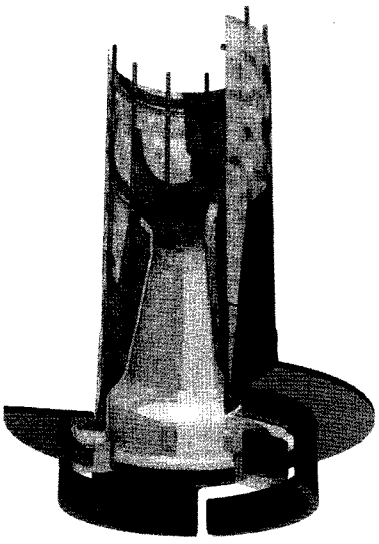

Stabilised glass fiber is a less expensive alternative to other high temperature filter media.

Ceramic coating of the glass fibers, together with a special design of the bag retainers (patent pending), allows a significant increase of the operational temperature level up to 450°C (842°F), which cannot be achieved by usual glass fiber bags. At the same time, the mechanical stress of common pulse-jet cleaning can be reduced.

High filtration efficiencies of more than 99,9% with clean gas concentrations significantly below 5 mg/m^3 can be achieved, adapting filtration conditions to the dust features. Existing dust collector installations can easily be retrofitted by a wide range of available filter element lengths and the employment of standard tube sheet fastenings.

For more information contact; **HOSOKAWA MIKROPUL GmbH**
Welserstraße 9-11
D-51149 Köln, Germany
Tel.: +49-2203-308-0
Fax: +49-2203-308-293
E-mail: info@hmgmbh. hosokawa. com

HOSOKAWA MICRON AGGLOMASTER AGM-SD

Hosokawa Micron has developed a spray-drying type fluid bed agglomeration apparatus, the Agglomaster AGM-SD (patent filed for in 1998) which produces spherical particulates directly and continuously from various types of liquid materials using a single apparatus.

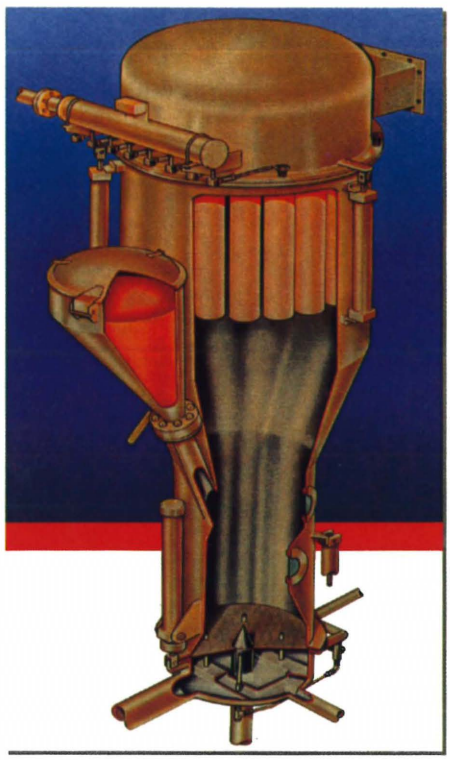

Features

With its unique agglomerating principle, this apparatus possesses the following features which differ compared with conventional spray-drying systems.

- Batch operation enables multiple model production which is difficult with a spray-drying system.
- Large processing capacity up to 1500 kg/hr by continuous operation (based on solid concentration of 50%w.b. with air temperature of 130°C at inlet and of 50°C at outlet).
- A built-in bag filter is provided in the product collection unit and, moreover, since an agglomeration apparatus or final drying apparatus is not required, the conventional production process can be greatly shortened and installation space can be reduced. Accordingly, equipment and running costs may be substantially reduced.
- This system enables production of large spherical particulates (controllable to an average particle size range of 30−3000μm) which cannot be produced by spray-drying systems.
- Product water content (exhaust temperature) can be maintained at a high level since a fluid bed apparatus is used and, therefore, highly heat efficient operation is possible. Also, the liquid additions and after-drying processes for the purpose of agglomeration found in conventional production processes are not required since layered agglomeration is performed together with spray-drying. This results in increased efficiency.
- By making the liquid material into extremely fine particulates (average liquid droplet size about 8−15μm), solid and gaseous contact inside the apparatus is substantially improved and high heat efficiency is obtained, leading to substantial downsizing of the apparatus compared with conventional spray-drying apparatuses.

Application

With the AGM-SD, spherical particulate products may be produced from various liquid materials (water slurry, aqueous solutions, etc.) within a single unit.

- Foodstuff additives (aqueous solutions)
- Others, water soluble foodstuff materials
- Medical product additives (aqueous solutions)
- Sodium acetate (water soluble), water type slurries, others.

For more information contact: **HOSOKAWA MICRON CORPORATION**
5-14, 2-chome, Kawaramachi, Chuo-ku,
Osaka 541-0048, JAPAN
Telephone: 81-6-6233-3968
Facsimile : 81-6-6229-9267

HOSOKAWA MICRON

Hosokawa Micron Ltd. is a member of the Hosokawa Micron Group, responding to global needs through an emphasis on materials science and engineering. The Group is an international provider of equipment and Technology for powder and particle processing, product recovery, plastics processing and confectionery products. The Group maintains facilities for research, engineering, manufacturing, and service in each of the world's major industrial markets.

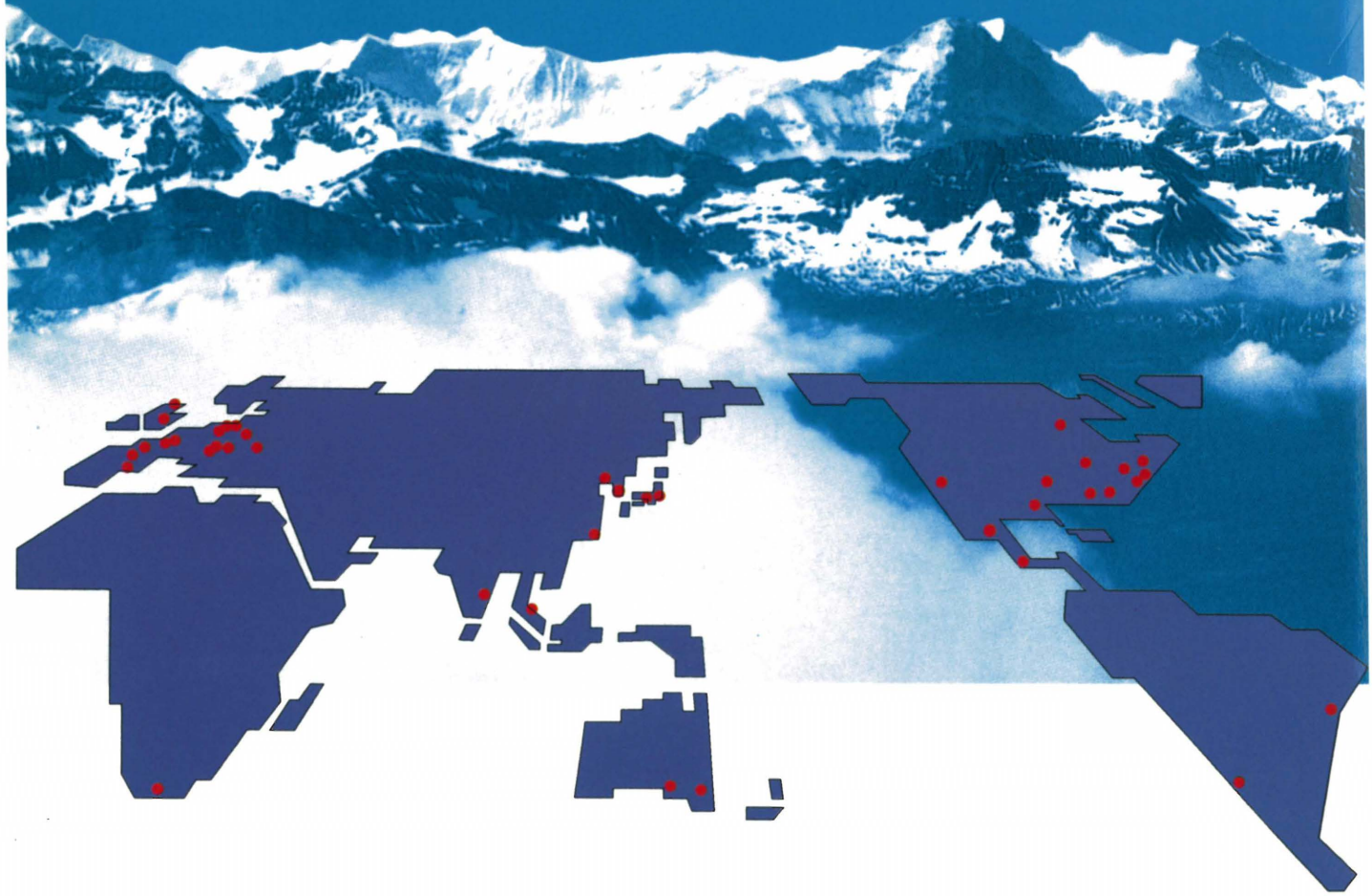

Process Technologies for Tomorrow

HOSOKAWA MICRON

Headquarter Locations;

HOSOKAWA MICRON CORPORATION

5-14, 2-chome, Kawaramachi, Chuo-ku,
Osaka 541-0048, Japan
Tel: 81-6-6233-3968
Fax: 81-6-6229-9267
http://www.hosokawamicron.com/japan

HOSOKAWA MICRON INTERNATIONAL INC.

780 Third Avenue, New York,
NY 10017, U.S.A
Tel: 1-212-826-3830
Fax: 1-212-826-6612
http://www.hosokawamicron.com